ABSTRACT

GLOTFELTY, TIMOTHY WILLIAM. Assessing the Impact of Global Air Quality and Climate Interactions in a Changing World using Two Advanced Global Models: Improvement of Organic Aerosol Formation and Application to Decadal Simulations. (Under the direction of Dr. Yang Zhang).

In this study, two advanced global models are used to simulate future climate policy and air quality scenarios. The Global-through-Urban Weather Research and Forecasting Model with Chemistry (GU-WRF/Chem) is used to simulate the changes in future air quality, climate, deposition, intercontinental transport, and aerosol-cloud interactions following the IPCC AR4 SRES A1B scenario. The Community Earth System Model modified at North Carolina State University (CESM-NCSU) is further developed in this work to include new treatments for the formation of organic aerosol (OA) and its impact on aerosol-climate interactions. Then this modified version of CESM-NCSU is employed to simulate future changes in air quality, climate, deposition, and aerosol-cloud interactions following the IPCC AR5 RCP4.5 and RCP8.5 climate policy scenarios. The objectives of this work are to improve the representation of OA in CESM-NCSU, evaluate and quantify changes in future air quality and climate using both advanced models, quantify the impact of chemistry on climate following future emission projections using both advanced models, and determine if the use of these advanced models provides additional insights into future climate change and air quality compared to models with less advanced chemistry.

Air quality is degraded in the future following the IPCC AR4 SRES A1B scenario using GU-WRF/Chem with global average increases in maximum 8-hr ozone ($O_3$8hr) of 2.5 ppb and $PM_{2.5}$ of 0.3 μg m^{-3}. Increases in future emissions and enhanced transport from

climate change increase the global impact of pollution from East Asia, especially in North America and the Arctic. The enhanced aerosol and cloud formation lead to decreases in short-wave radiation reaching the earth's surface by 1.2 W m^{-2}. However, the use of prescribed sea surface temperatures in GU-WRF/Chem limits the impact of this change in radiative forcing on climate. GU-WRF/Chem shows differences in simulated future climate compared to NCAR's CCSM3 model with less advanced chemistry, indicating that chemical treatments can have a strong impact on climate change predictions.

The new OA treatments in CESM-NCSU increase simulated levels of oxygenated organic aerosol (OOA) and total organic matter (TOM), but decrease simulated levels of primary organic matter (POM). The reduced POM level decreases the aerosol direct effect of OA, while the increase in OOA increases the aerosol indirect effect of OA within CESM-NCSU. The new OA treatments improve model performance compared to most OA observations, except hydrocarbon-like aerosol (HOA) that becomes largely underpredicted. The new OA treatments also improve the simulated seasonal patterns of OA and bring the relative contributions of POM and OOA to TOM into better agreement with observations. Overall, CESM-NCSU with the new OA treatments provides an improved representation of the current atmosphere and is thus suitable for future climate simulations.

There are reductions in the future levels of many pollutants following the RCP4.5 and RCP8.5 scenarios simulated by CESM-NCSU, due to reductions in future emissions. However, there are differences in future O_3 projections in both scenarios with a 1.4 ppb global average decrease following RCP4.5 and a 2.3 ppb global average increase following the RCP8.5. The reduced anthropogenic aerosol levels decrease the aerosol direct and

indirect effects in many regions following both scenarios, but increases in marine cloud formation dominate radiation changes. The reduced emissions under the RCP4.5 scenario lead to a global average warming of 0.2ºC in response to reductions in the aerosol direct and indirect effects. This leads to a weakening of the Walker circulation that impacts global precipitation and cloud cover distributions. Overall, the advanced global models used in this work provide additional insights into climate change compared to models with less advanced chemistry.

© Copyright 2016 Timothy William Glotfelty

All Rights Reserved

Assessing the Impact of Global Air Quality and Climate Interactions in a Changing World using Two Advanced Global Models: Improvement of Organic Aerosol Formation and Application to Decadal Simulation

by
Timothy William Glotfelty

A dissertation submitted to the Graduate Faculty of
North Carolina State University
in partial fulfillment of the
requirements for the degree of
Doctor Philosophy

Marine, Earth, and Atmospheric Sciences

Raleigh, North Carolina

2016

APPROVED BY:

_____
Dr. Yang Zhang
Committee Chair

_____
Dr. Nicholas Meskhidze

_____
Dr. Markus Petters

_____
Dr. Anantha Aiyyer

_____
Dr. Andrew Grieshop

BIOGRAPHY

Timothy William Glotfelty was born in Cumberland, Maryland in 1988, and has been a resident of Grantsville, Maryland for the majority of his life. He attended St. Michael's Catholic Elementary school for kindergarten through sixth grade, after which he transferred to Northern Garrett County Middle school and later attended Northern Garrett County High School to complete his secondary education. During this time period, Timothy had developed an interest in the Earth sciences; especially the weather. While embarking on this educational journey, he enjoyed all manners of science and mathematics classes that provided him with an opportunity to develop a greater understanding and appreciation of the processes that control the Earth and its ecosystems. Upon graduating from Northern Garrett County High School in 2006, he became interested in pursuing a degree in Meteorology.

To accomplish this goal, he enrolled at Frostburg State University in Frostburg, Maryland in fall of 2006 to complete his general education requirements. Later in 2008, he transferred to the Pennsylvania State University (Penn State) in University Park, Pennsylvania where he completed the majority of his meteorological coursework. During his final summer at Penn State, Timothy undertook an internship at the Pennsylvania Department of Environmental Protection where he developed an interest in air quality modeling and forecasting. After this experience, he began to consider graduate school as a vehicle that would enable him to study air quality and climate change in greater detail. He obtained his B. S. in Meteorology and graduated with high distinction from Penn State in May of 2010.

Later, in May of 2010 he accepted an early summer internship at the Air Quality Forecasting Lab in the Department of Marine, Earth, and Atmospheric Sciences at the North

Carolina State University (NCSU), so that he could get a head start on his thesis research. During the course of his studies at NCSU, he was able to participate in two research internships, including two summers working as part of the Advanced Studies Program at the National Center for Atmospheric Research (NCAR) and another summer position as part of the Oak Ridge Institute for Science and Education at the United State Environmental Protection Agency (U. S. EPA). These internships provided essential and beneficial real world experience in the fields of urban scale meteorological modeling and data assimilation. Both experiences better prepared him for a career in atmospheric research. Additionally, the real world experience from the first internship at NCAR is what inspired him to switch from an M.S. degree program to a Ph. D degree program.

ACKNOWLEDGMENTS

Now that I have reached the capstone of my education, there are several individuals and agencies I would like to like to acknowledge for their guidance and support. I would first like to thank my entire committee including, Drs. Yang Zhang, Nicholas Meskhidze, Markus Petters, Andrew Grieshop, and Anantha Aiyyer for their guidance and scientific input. I would like to especially thank Dr. Yang Zhang for all the opportunities that she has offered and the patience and dedication she has shown in guiding me to be a research scientist in a challenging field. Special thanks are also due to Drs. Jason Ching formerly of the U.S. EPA, Fei Chen of NCAR, and Kiran Alapaty of the U.S. EPA for providing me moral support, real world training, and other necessary skills for my career and the completion of my degree. The inspiration and memories that came from my experiences with them have provided me the motivation to finish my degree and some of the best memories of my Ph. D studies. Thanks are also due to the following individuals who provided support of data necessary for this research including, Drs. Gary Howell and Eric Sills from the High Performance and Grid Computing Center at NCSU. Dr. Prakash Karamchandani of ENVIRON International Corporation, Dr. David Streets of Argonne National Lab Energy Systems Division, and Drs. Louisa Emmons, Mark Richardson, William C. Skamarock, and Francis Vitt of NCAR.

I would like to thank the agencies that funded this work including, the United States Environmental Protection Agency Science to Achieve Results Program Grant no. R83337601 and the National Sciences Foundation (NSF)/United State Department of Agriculture Earth System Modeling Program Grant No. AGS-1049200 at NCSU and 2012-67003-30192 at the University of Chicago/ANL. I would like to acknowledge high-performance computing

support from Yellowstone (ark:/85065/d7wd3xhc) provided by NCAR's Computational and Information Systems Laboratory, sponsored by the National Science Foundation. MODIS data and CERES data are provided by NASA via http://ladsweb.nasa.gov/data/search.html and http://ceres.larc.nasa.gov/order_data.php, respectively. Other surface network data were downloaded from their respective web sites. AQMEII emissions for CONUS were prepared by U.S. EPA, Environment Canada, Mexican Secretariat of the Environment and Natural Alessandra Balzarini, Research on Energy System (RES), Italy. MEIC emissions for China were provided by Qiang Zhang and Kebin He, Tsinghua University, China.

I am especially grateful for the support of my past and current colleagues at the NCSU Air Quality Forecast Laboratory, including Kai Wang, Jian He, Khairunissa Yahya, Patrick Campbell, Brett Gantt, LeeAnna Young Chapman, Catalina Segura, Ashley Penrod, Ying Chen, Xin Zhang, Changjie Cai, Shuai Zhu, Maslin Gudoshava, Yao-Sheng Chen, Nan Zhang, and many others.

Lastly, I would like to thank my parents Kimberly B. Glotfelty and Timothy K. Glotfelty, my brother Brandon K. Glotfelty, and my close friends Amanda Baker and Peter Seanez. I would never have made it this far without their support.

TABLE OF CONTENTS

LIST OF TABLES

LIST OF FIGURES

LIST OF ACRONYMS

Acronym	Definition
1-D	One dimensional
1.5-D	One and a half dimensional
3-D	Three dimensional
ΔHvap	Enthalpy of vaporization
ACCMIP	Atmospheric Chemistry and Climate Model Intercomparison Project
AF	Africa
AIM	Asian-Pacific Integrated Model
ALKH	Long chain alkanes
AMS	Aerosol mass spectrometer
ANL	Argonne National Laboratory
AOC	Average of current years
AOD	Aerosol optical depth
AOF	Average of future years
APIN	α-pinene
AQS	Air Quality System
AR4	Fourth assessment report
AR5	Fifth assessment report
ASOA	Anthropogenic secondary organic aerosol
ASOC	Anthropogenic secondary organic carbon
AUS	Australia
AVOC	Anthropogenic volatile organic compounds

BB	Biomass burning
BC	Black carbon
BCTD	Black carbon total deposition
BDQA	Base de Donnẻes sur la Qualite de I'Air
BE07	Bennartz (2007)
BFM	Brute force method
BHM	Birmingham, AL
BIR	Birkenes, Norway
BPIN	β-pinene
Br	Bromine
BSOA	Biogenic secondary organic aerosol
BSOC	Biogenic secondary organic carbon
BSRN	Baseline surface radiation network
BVOC	Biogenic volatile organic compounds
C*	Effective saturation concentration
CAM5	Community Atmosphere Model version 5
CAM-Chem	Community Atmosphere Model with Chemistry
CB05	2005 Carbon Bond Mechanism
CB05GE	2005 Carbon Bond Mechanism with global extension
CB6	Version 6 of Carbon Bond Mechanism
CCM	Chemistry-Climate model
CCN5	Cloud condensation nuclei at a supersaturation of 0.5%
CCS	Carbon capture and storage technologies

CCSM	Community Climate System Model version 3
CDC	Climate Diagnostic Center
CDNC	Cloud droplet number concentration
CERES	Clouds and the Earth's Radiant Energy System
CESM	Community Earth System Model
CESM1	Community Earth System Model version 1
CESM1.2.2	Community Earth System Model version 1.2.2
CESM-NCSU	Community Earth System Model modified by the North Carolina State University
CF	Cloud fraction
CFCs	Chlorofluorocarbons
CH_4	Methane
Cl	Chlorine
Cl^-	Particulate chloride
CMIP5	Coupled Model Intercomparison Project Phase 5
CMU	Carnegie Mellon University
CO_2	Carbon dioxide
COT	Cloud optical thickness
CRI	Critical refractive index of water
CTM	Chemical transport model
CWP	Condensed water path
Dcs	Critical diameter for ice crystal autoconversion
E10	Epstein et al. (2010)

EA	East Asia
EAAE	East Asian Anthropogenic Emissions
EaSM	Earth System Model
EBAF	Energy balanced and filled
EMEP	European Monitoring and Evaluation Programme
EFA	Anthropogenic emission factors
EFBB	Biomass burning emission factors
ELVOCs	Extremely low volatility organic compounds
EU	Europe
FF	Functionalization and fragmentation
FLDS	Downwelling long-wave radiation at the Earth's surface
FLNS	Net long-wave radiation at the Earth's surface
FSDS	Downwelling short-wave radiation at the Earth's surface
FSDSC	Clear-sky downwelling short-wave radiation at the Earth's surface
FSNS	Net short-wave radiation at the Earth's surface
FT	Free troposphere
F-TUV	Fast Tropospheric Ultraviolet-Visible Model.
GCM	General Circulation Model
GEOS/Chem	Goddard Earth Observing System model with Chemistry
GHG	Greenhouse gases
GHGF	Greenhouse gas forcing
GLSOA	Organic aerosol from glyoxal
GLSOC	Organic carbon from glyoxal

GLW	Downwelling long-wave radiation flux at the Earth's surface
GOME	Global Ozone Monitoring Experiment
GPCP	Global Precipitation Climatology Project
GRSM	Great Smokey Mountains National Park, TN
GSW	Net downwelling short-wave radiation flux at the Earth's surface
GU-WRF/Chem	Global-through-Urban Weather Research and Forecasting Model with Chemistry
GWRF	Global Weather Research and Forecasting Model
HE15	He et al. (2015a)
Hg	Mercury
HgTD	Mercury total deposition
HNO_3	Nitric acid
HO_2	Hydroperoxyl radical
H_2O_2	Hydrogen peroxide
HOA	Hydrocarbon-like organic aerosol
HTAP	Hemispheric Transport of Air Pollution
HUM	Humulene
IAT	Inorganic aerosol thermodynamics
ICs	Initial conditions
IMAGE	Integrated Model to Assess the Global Environment
IMN	Ion mediated nucleation
IMPROVE	Interagency Monitoring of Protected Visual Environments
INON	Inorganic oxidized nitrogen

IOLE	Internal olefins
IPCC	Intergovernmental Panel on Climate Change
ISOP	Isoprene
ISP	Ispra, Italy
ITAP	Intercontinental transport of anthropogenic pollution
ITCZ	Intertropical convergence zone
IVOCs	Intermediate volatility organic compounds
J	Nucleation rate
J09	Jimenez et al. (2009)
JFD	January, February, and December
JJA	June, July, and August
JNO_2	Photolysis rate of NO_2
KMOE	Korean Ministry of the Environment
L13	Lewondowski et al. (2013)
LHX	Latent heat flux
LIM	Limonene
LOWR	Lostwood Wildlife Refuge, ND
LTRH	Lower troposphere relative humidity
LTT	Lower troposphere temperature
LWCF	Long-wave cloud forcing
LWP	Liquid water path
MADE	Modal Aerosol Dynamics Model for Europe
MADRID	Model of Aerosol, Dynamics, Reaction, Ionization, and Dissolution

MAM	March, April, and May
MAM3	3 mode Modal Aerosol Model
MAM7	7 mode Modal Aerosol Model
MB	Mean bias
MBO	2-Methyl-3-buten-2-ol
MEGAN	Model of Emissions of Gases and Aerosols from Nature
MEPC	Ministry of Environmental Protection in China
MLS	Microwave Limb Sounder
MODIS	Moderate Resolution Imaging Spectroradiometer
MOPITT	Measurements Of Pollution In The Troposphere
MOZART-4	Model for Ozone and related chemical Tracers version 4
Na^+	Particulate sodium
NAM	North America
NAP	Naphthalene
NCAR	National Center for Atmospheric Research
NCDC	National Climatic Data Center
NCEP-FNL	National Centers for Environmental Prediction Final Operational Reanalysis
NCP	Net chemical production
ND	Nitrogen deposition
NH	Northern hemisphere
NHIR	Northern hemisphere industrial regions
NH_3	Ammonia
NH_4^+	Particle ammonium

NMB	Normalized mean bias
NME	Normalized mean error
NO	Nitrogen oxide
NO_2	Nitrogen dioxide
NO_3^-	Particulate nitrate
NO_3	Nitrate radical
NO_x	Nitrogen oxides
NO_y	Reactive nitrogen
N_2O	Nitrous oxide
N_2O_5	Dinitrogen pentoxide
NOAA	National Oceanic and Atmospheric Administration
NOAH	The National Center for Environmental Prediction (NNR), Oregon State University, Air Force, and Hydrologic Research Lab
NUM	Column particle number concentration
O^1D	Singlet oxygen
O_2	Molecular oxygen
O_3	Ozone
$O_3$8hr	Maximum eight hour ozone
OA	Organic aerosol
OC	Organic carbon
OCI	Ocimine
OD08	O'dell et al. (2008)
OH	Hydroxyl radical

OIN	Other unspeciated inorganic aerosol
OLE	Terminal olefins
OLR	Outgoing long-wave radiation
OM	Organic matter
OMI	Ozone Monitoring Instrument
ON	Oxidized nitrogen
OOA	Oxygenated organic aerosol
OPOM	Oxidized primary organic matter
OSR	Outgoing short-wave radiation
PAH	Polycyclic aromatic hydrocarbons
PAMS	Photochemical Assessment Monitoring Stations
PAN	Peroxyacetyl nitrate
PBL	Planetary boundary layer
PBLH	Planetary boundary layer height
PHO	Phoenix, AZ
$PM_{2.5}$	Particulate Matter with diameter less than or equal to 2.5 μm
PM_{10}	Particulate Matter with diameter less than or equal to 10.0 μm
POC	Primary organic carbon
POM	Primary organic matter
PSFC	Atmospheric surface pressure
PR	Precipitation rate
PRC	Convective precipitation rate
PRL	Large scale precipitation rate

PWV	Precipitable water vapor
Q2	2m Water vapor mixing ratio
R	Pearson's correlation coefficient
RACM	Regional Atmospheric Chemistry Mechanism
RCP	Representative Concentration Pathways
RCP2.6	RCP pathway with radiative forcing of 2.6 W m^{-2} by 2100
RCP4.5	RCP pathway with radiative forcing stabilizing at 4.5 W m^{-2} by 2100
RCP6	RCP pathway with radiative forcing stabilizing at 6.0 W m^{-2} by 2100
RCP8,5	RCP pathway with radiative forcing of 8.5 W m^{-2} by 2100
Reff	Column average cloud drop effective radius
RESTOA	Net radiation at the top of the atmosphere
RHMINL	Threshold relative humidity for low level cloud formation
RMSE	Root mean square error
RN	Reduced nitrogen
RRTM	Rapid radiative transfer model
RTP	Research Triangle Park, NC
S08	Shrivastava et al. (2008)
SA	South Asia
SAF	Southern Africa
SAM	South America
SCIAMACHY	SCanning Imaging Absorption SpectroMeter for Atmospheric CHartographY
SEA	Southeast Asia
SEARCH	Southeastern Aerosol Research and Characterization Network

SH	Southern hemisphere
SHX	Sensible heat flux
SLP	Sea level pressure
SO_2	Sulfur dioxide
SO_4^{2-}	Particulate sulfate
SO_x	Oxidized sulfur
SOA	Secondary organic aerosol
SOAG	Gases that form SOA
SON	September, October, and November
SRES	Special Report on Emissions Scenarios
SSPs	Shared socioeconomic pathways
SSTs	Sea-surface temperatures
STE	Stratosphere-Troposphere exchange
STN	Speciation Trend Network
SVOA	Semi-volatile organic aerosol
SVOCs	Semi-volatile organic compounds
SWCF	Short-wave cloud forcing
SWDOWN	Downwelling short-wave radiation flux at the Earth's surface
T2	2-m Temperature
TAQMN	Taiwan Air Quality Monitoring Network
TC	Total carbon
TCO	Tropospheric carbon monoxide
TER	Terpinene

THCHO	Tropospheric formaldehyde
TND	Total nitrogen deposition
TNO_2	Tropospheric nitrogen dioxide
TNTD	Total nitrogen total deposition
TNVOC	Total non-methane volatile organic compounds
TOL	Toluene
TOM	Total organic matter
TOMS	Total Ozone Mapping Spectrometer
TOR	Tropospheric ozone residual
UD	Urban downwind
VBS	Volatility basis set
VMRS	Volume mixing ratios
VOC	Volatile organic compounds
VSOA	SOA from volatile organic compounds
WACCM	Whole Atmosphere Community Climate Model
WSP10	10-m Wind speed
WSP5500	5500-m Wind speed
XYL	Xylene
YSU	Yonsei University
Z07	Zhang et al. (2007)

CHAPTER 1. INTRODUCTION

1.1 Background

Two of the most important issues facing the scientific community during the current era are the prospect of global climate change and air pollution. As the global population increases, there is an increasing demand for energy and food resources. The by-products of producing these resources are the release of trace gases and aerosol particles into the atmosphere. Some of these gases known as the greenhouse gases (GHGs) (e.g., CO_2, CH_4, and N_2O) perturb the earth's radiation balance. With the exception of CH_4, other gases and particles are typically referred to in the literature as short-lived climate pollutants (e.g., ozone (O_3) and particles with aerodynamic diameter less than or equal to 2.5 μm ($PM_{2.5}$)), both perturb the earth's radiation balance and are hazardous to human and ecosystem health (Pierrehumbert, 2014). Hence, understanding the impact of future air quality/ climate interactions is necessary for policy makers to develop the most optimum climate mitigation and air pollution control strategies.

One of the biggest steps in understanding the impact of future air quality/ climate interactions is the development of future climate and emissions scenarios. This work has been undertaken by the Intergovernmental Panel on Climate Change (IPCC) since its formation in 1988. Two very different types of future climate and emissions scenarios are available from their most recent Fourth and Fifth Assessment Reports (AR4 and AR5, respectively). In the IPCC AR4, future climate scenarios were compiled into the Special Report on Emissions Scenarios (SRES). These scenarios are socio-economic based scenarios in which future emissions are based on future changes in population, globalization, economic

growth, technology change, and energy generation (IPCC, 2001). However, one key limitation of the IPCC AR4 SRES scenarios is that they do not reflect changes from future emission control policies (IPCC, 2007). Thus, as part of the IPCC AR5 the Representative Concentration Pathway (RCP), scenarios were developed. These scenarios are also based on socio-economic factors such as population and economic growth, but they assume major changes in energy generation technologies as a result of climate policy implementation, with a special emphasis on Carbon Capture and Storage (CCS) technologies that help to mitigate the emission of greenhouse gases (van Vuuren et al., 2011b). In addition to major changes in energy generation technologies, these scenarios include the implementation of current and proposed air pollution control measures and the implementation of such control measures in developing countries when the income gap between these countries and developing world decreases (van Vuuren et al., 2011b).

Another key element of future air quality/ climate interaction studies is the modeling tool. Traditionally, future air quality studies used models with offline-coupled architecture (Jacob and Winner, 2009). In this architecture, the climate scenario information (e.g., GHG levels and prescribed aerosol levels) are used to drive an atmospheric General Circulation Model (GCM). GCMs are global weather models that simulate the atmosphere's dynamical and physical processes and that have usually been calibrated for long-term climate simulations. These GCMs are typically limited as they either prescribe or used highly simplified representations of atmospheric chemistry and they tend to rely on prescribed land use, sea ice, and sea surface temperatures (SSTs). The GCM meteorology information is then used as an input to drive a global Chemical Transport Model (CTM) that simulates trace gas

levels and aerosols based on future climate GCM meteorology and projected future emissions. Future climate and air quality studies using this offline architecture are simple ways to estimate future air quality given a specific scenario. However, they are limited as they cannot simulate air quality/climate interactions, such as direct radiative forcing from prognostic changes in O_3 and aerosols, and the aerosol indirect effects on clouds.

To overcome these limitations, online-coupled GCM-CTM models, also known as Chemistry-Climate Models (CCMs), have been developed (Eyring et al., 2005; 2006). These models simulate chemical species and metrological processes within the same model framework, allowing for the prediction of not only future air pollutant levels but also the impact of changing pollutant concentrations on future climate through the aerosol direct and indirect effects. In addition to GCMs, CTMs, and CCMs, future air quality/climate studies can be carried out using Earth System Models (EaSMs) (Claussen et al., 2002). EaSMs differ from both GCMs and CCMs as they simulate a wide range of Earth processes, including component models that simulate the atmosphere, the land surface, the oceans, sea ice, and land ice. Within the EaSM architecture, various component models pass information to each other via a coupler program. This architecture is more computationally-expensive than GCMs or CCMs, but allows for more complex studies such as the study of aerosol direct and indirect effects on large-scale global circulations (Cai et al., 2006), the impact of short-lived climate pollutants on sea ice retreat (Gagne et al., 2015), and biogeochemical studies that focus on global carbon storage (Arora et al., 2013). EaSMs can be configured like CCMs, but many of the recently-developed EaSMs still use prescribed chemistry in a manner similar to GCMs (He and Zhang, 2014). All these architectures for chemistry-climate studies are still in

use and models with each of these configurations have taken part in the Atmospheric Chemistry and Climate Model Intercomparison Project (ACCMIP). ACCMIP compared an ensemble of simulated fields from various global air quality models predicting historical and future air quality following the IPCC AR5 RCP scenarios (Lamarque et al., 2013).

Despite the availability of many modeling tools for future air quality/climate studies, these studies can be limited by the use of simplistic parameterizations for meteorological and chemical processes. For example, the recently-developed Community Earth System Model (CESM) (Hurrell et al., 2013) and the CCM version known as the Community Atmosphere Model with Chemistry (CAM-Chem) (Lamarque et al., 2012) do not consider the role of inorganic aerosol thermodynamics (IAT). IAT is a fairly imperative process to be considered as part of air quality studies because an IAT module is necessary to accurately simulate the formation of aerosol ammonium (NH_4^+) and nitrate (NO_3^-) and the sea-salt acidification process. These processes are neglected in even the most advanced aerosol module in the officially-released version of CESM from NCAR (Liu et al., 2012). This omission may be somewhat justified based on the application of the CESM model as the abundance of sulfate (SO_4^{2-}) is generally larger than other inorganic aerosol components over the Northern Hemisphere based on aerosol mass spectrometer (AMS) measurements (Zhang et al., 2007; Jimenez et al., 2009). However, this lack of IAT means that certain important scientific questions cannot be addressed, such as, how much NO_3^- will compensate SO_4^{2-} from future sulfur dioxide (SO_2) emission reductions? (Fiore et al., 2012). Nonetheless, this limitation has recently been addressed in the version of CESM modified at the North Carolina State University (CESM-NCSU) (He and Zhang, 2014).

There are similar or perhaps larger issues regarding the formation of organic aerosols (OA) within CCMs. OA is a major component of total aerosol comprising roughly (18-70%) (Zhang et al., 2007; Jimenez et al., 2009). Typically OA is treated in global models as two separate classes of aerosol. The first is primary organic matter (POM) that is emitted directly into the atmosphere via combustion and behaves similar to a tracer compound. The second is secondary organic aerosol (SOA) that is formed in the atmosphere through the condensation and partitioning of certain low volatility organic vapors. This two species treatment is typical in global models such as the 3 mode or 7 mode Modal Aerosol Model (MAM3 or MAM7) within CESM (Liu et al., 2012). However, there are many CCMs that partially or entirely neglect the formation of SOA (Jacob and Winner, 2009; Fiore et al., 2012). These representations of OA in CCMs are problematic in light of the scientific progress regarding OA formation within the last decade. OA research has shown that POM is volatile and thus a significant portion of it evaporates into organic vapors (Lipsky and Robinson, 2006; Shrivastava et al., 2006). Another key finding is that organic vapors in the atmosphere, including those from evaporated POM, undergo many generations of oxidation that decrease their volatility and lead to much greater SOA formation (Robinson et al., 2007). This has led to the development of a new framework for simulating OA within air quality models known as the volatility basis set (VBS) (Donahue et al., 2006). Some progress has been made regarding the incorporation of a VBS framework into global CTMs and CCMs (Farina et al., 2010; Jathar et al., 2011; Jo et al., 2013; Shrivastava et al., 2015), Such a step is critical for future air quality/climate interaction studies as it is likely that OA will become the dominant form of aerosol in the future due to more rapid declines in the precursor emissions of other

aerosol components and the increase of biogenic volatile organic compound (BVOC) emissions (Tagaris et al., 2007; Heald et al., 2008).

1.2 Objectives, Hypothesis, and Proposed Research

The overall objectives of my Ph. D research are to quantify changes in future air quality and air quality/climate interactions by the year 2050 using two advanced global air quality models. These models include the Global through Urban Weather Research and Forecasting Model with Chemistry (GU-WRF/Chem) (Zhang et al., 2012b) and the Community Earth System Model developed at the North Carolina State University (CESM-NCSU) (He et al., 2015a, b). The GU-WRF/Chem model is roughly equivalent to a GCM-CTM architecture CCM, although it has not undergone the extensive calibrations needed for long-term climate simulations. CESM-NCSU is an EaSM that is configured in a CCM mode. The specific objectives of this research are:

(1) To implement, evaluate, and perform sensitivity analysis on new OA treatments in the CESM-NCSU model;

(2) To evaluate the ability of the GU-WRF/Chem and CESM-NCSU models to represent the current atmosphere;

(3) To quantify changes in future air quality between the current time period and the mid-21st Century, following the IPCC AR4 SRES A1B and IPCC AR5 RCP4.5/RCP8.5 scenarios using the GU-WRF/Chem and CESM-NCSU models, respectively;

(4) To determine the impact of future emission changes on climate and the impact of climate change on air quality by 2050 following the IPCC AR4 SRES A1B and

IPCC AR5 RCP4.5 scenarios using the GU-WRF/Chem and CESM-NCSU models, respectively;

The ultimate goal of this research is to demonstrate the importance of using advanced modeling tools for doing future air quality and air quality/climate interaction studies and provide quantifications of these future climate scenarios to the scientific community so that the results are available to be compared with other studies or used as part of future emission control and climate mitigation strategies. The main hypothesis of this work is that chemical processes especially those related to aerosol are important for climate change predictions and conversely the changes in climate are important for predicting future air quality. Several science and policy-related questions will be addressed. For example, how will changing global climate and emissions impact global air quality? What are their relative contributions? How will intercontinental transport of pollution change in the future and what factors dominate those changes? Will updated treatments for OA improve a climate model's ability to predict OA and subsequently improve the accuracy of predicted aerosol, cloud properties, and radiative forcing through the aerosol direct and indirect effects? How will these processes be affected by future changes in biogenic emissions and changes in oxidant levels? How much biogenic SOA is controllable by controlling anthropogenic emissions?

Table 1.1 compares the level of complexity of the different treatments from GU-WRF/Chem, CESM-NCSU, and the standard version of CESM (CESM-CAM5), and a modified version of CESM-CAM5 by NCSU in this work and previous work by He and Zhang al. (2014), Gantt et al. (2014), and He et al. (2015a,b). From this comparison it is clear that CESM-NCSU and CESM-CAM5 are the better choice of model for climate simulations,

due to more advanced model representations of land use, sea-surface temperatures, and sea ice. However, CESM-CAM5 uses relatively simplistic treatments for many chemical processes except for the gas-phase chemical mechanism that can be configured to be either simple or complex based on the user's needs. However, all climate applications of CESM-CAM5 thus far used the simple chemical mechanism. This facilitated a need to develop CESM-NCSU that combines advanced chemical treatments similar to those found in GU-WRF/Chem for the superior climate modeling of CESM-CAM5. This development also included improving processes that are treated in a simplistic way in GU-WRF/Chem, such as new particle formation (He and Zhang, 2014), aerosol activation (Gantt et al., 2014), and organic aerosol formation (this work, and also in Glotfelty et al., 2016a).

The first portion of this research includes evaluating the model performance of GU-WRF/Chem and using it to quantify the impact of future climate and emission on global air quality, estimating the impact of climate change alone on global air quality, and estimating the impact of future changes in global air quality on future climate due to the aerosol direct and indirect effects. Current climate evaluations are performed by comparing simulated fields against available satellite estimates, reanalysis data, and surface network observations to determine statistical biases and model errors. Future climate trends are determined by averaging the simulated fields of the current period (2001 and 2010) and the future period (2020, 2030, 2040, and 2050) and taking the difference of the two periods. GU-WRF/Chem is also used for a future climate sensitivity study of 2050 using 2001 period emissions. The difference of this simulation with the GU-WRF/Chem 2001 simulation reveals the changes in future air quality caused by climate change. The difference between this simulation and the

GU-WRF/Chem 2050 simulation indicates the changes in future climate caused by future emissions changes. GU-WRF/Chem is an older model with an online-coupled GCM-CTM style CCM structure similar to many of the classic chemistry-climate studies. Since GU-WRF/Chem is comparable to models that took part in phase three of the IPCC Coupled Model Intercomparison Project (CMIP3), this study follows the older IPCC AR4 SRES A1B scenario. Trends in GU-WRF/Chem simulated fields are compared against those predicted by the Community Climate System Model version 3 (CCSM3) that also follows this scenario. Since CCSM3 does not simulate prognostic chemistry, this comparison illustrates the importance of using online-coupled CCM structure.

GU-WRF/Chem is also used to investigate the current and future role of ITAP from East Asia. This is achieved by conducting additional 2001and 2050 simulations with East Asian Anthropogenic Emissions (EAAE) removed. This will quantify how ITAP will change under this scenario, determine what factors dominate these changes, and also allow for the impact of EAAEs on biogenic SOA (BSOA) levels to be investigated.

Although GU-WRF/Chem has advanced parameterizations to simulate atmospheric chemistry, the model is limited by a number of factors discussed in Chapter 2. GU-WRF/Chem is designed primarily for short term air quality simulations. As a result, GU-WRF/Chem has static land use changes between current and future periods and sea ice/se surface temperatures are prescribed. Additionally, GU-WRF/Chem's transport scheme is not positive definite allowing to errors in the transport of chemical tracers. Due to these limitations GU-WRF/Chem was replaced by the CESM model in the remainder of this work. Until recently the officially-released version of CESM had very simplified representations of

gas-phase chemistry and still contains simplified representations of inorganic and organic aerosol formation. These limitations have been overcome due to modifications made by NCSU, leading to a new CESM-NCSU model (He and Zhang, 2014; Gantt et al., 2014) that is further developed and used for decadal climate simulations in the second portion of this work.

The second portion of this research focuses on further development, evaluation, and application of the CESM-NCSU model. In order to further develop CESM-NCSU, new treatments for OA are implemented into the model. These include (1) a VBS framework treatment for the simulation of POM volatility and SOA formation, including OA aerosol formed from semi-volatile organic compounds (SVOCs) generated from POM evaporation, (2) the addition of an OA generation pathway from glyoxal, and (3) the addition of a treatment for the conucleation of organic vapors and sulfuric acid. These new treatments allow for a more detailed and potentially more realistic simulation of OA in the model. Simulations of the current atmosphere with these updated treatments are evaluated under current climate conditions and compared against current climate simulations of the baseline model to determine differences and improvements in model performance. Sensitivity analysis is also carried out by adjusting various aspects of the new OA treatments to estimate the uncertainties associated with the new OA treatments.

A preliminary version of the new OA treatments has been implemented into a newer version of CESM-NCSU. This preliminary version of CESM-NCSU has been used to conduct future climate simulations following the newer IPCC AR5 RCP4.5 and RCP8.5 scenarios. A more detailed description of the differences between this version of CESM-NCSU and the

finalized OA treatment is discussed in Chapter 4. The procedure for this study is similar to the GU-WRF/Chem study but with a future time period focused closer to 2050 on a decadal scale (2046-2055). The current climate period (2046-2055) is evaluated using emissions of both scenarios and this evaluation is compared against a CESM-NCSU simulation using more detailed emissions to determine potential limitations of the RCP emissions inventory. Furthermore, this study also focuses on the impact of climate change on future air quality and the impact of future emission changes on climate following the RCP4.5 scenario. This is performed by comparing the future and current period RCP4.5 simulations against a sensitivity simulation of the 2046-2050 period using the current era RCP emissions. Future trends under both RCP scenarios are compared between CESM-NCSU and a version of CESM that uses highly-simplified chemistry to again illustrate the impact of the more advanced chemical treatments on future climate projections.

This work differs from previous studies by examining not only the impact of changing emissions and climate on air quality, but how these future projections are impacted by the used of detailed chemical treatments. The new OA treatments implemented into CESM-NCSU are focused not only on improving model performance of OA, like other studies in the literature, but on how the changes in OA and new particle formation from advanced OA treatments impact aerosol/climate interactions. This work also provides a comprehensive model evaluation of the current climate, as predicted by the RCP scenarios. This provides the scientific community with a bench mark that the performance of other advanced global models and other future climate scenarios can be compared against.

The research compiled here is a collection of scientific manuscripts that are either current published or will be part of future publications, The majority of the GU-WRF/Chem climate application in Chapter 2 is part of a published manuscript (Glotfelty et al., 2016b), except for Section 2.9 that has been published as a standalone article (Glotfelty et al., 2014). Chapter 3, which focuses on the development of OA in CESM-NCSU, is currently being prepared for publication (Glotfelty et al., 2016a). Lastly, Chapter 4 is currently being revised into a two part publication (Glotfelty et al., 2016c, d), with part 1 focusing on the comprehensive evaluation of CESM-NCSU and part 2 focusing on the future trends in climate/air quality following the RCP4.5 and RCP8.5 scenarios.

Table 1.1 Comparison of Treatments in GU-WRF/Chem, CESM-CAM5, and CESM-NCSU

Model	GU-WRF/Chem	CESM-CAM5	CESM-NCSU
Architecture	CCM	EaSM	EaSM
Land Use	Static	Dynamic Vegetation	Dynamic Vegetation
Sea-Surface Temperatures	Prescribed	Prognostic	Prognostic
Sea Ice	Prescribed	Prognostic	Prognostic
Gas-phase Chemistry	Advanced	Simple/Advanced[a]	Advanced
Aqueous Chemistry	Advanced	Simple	Simple
New Particle Formation	Simple	Simple	Advanced
Inorganic Aerosol	Advanced	Simple	Advanced
Organic Aerosol	Simple	Simple	Advanced
Aerosol Activation	Simple	Simple	Advanced
References	Z12b[b]	H13[c]	HZ14[d], G14[e], G16a[f]

[a]CESM-CAM5 can be configured with either simple or advanced gas-phase chemistry but all long-term climate simulations use the simple gas-phase chemistry, [b]Zhang et al. (2012b), [c]Hurrell et al. (2013), [d]He and Zhang 2014, [e]Gantt et al. (2014), [f]Glotfelty et al. (2016a)

CHAPTER 2. CHANGES IN FUTURE AIR QUALITY, DEPOSITION, AND AEROSOL-CLOUD INTERACTIONS UNDER THE IPCC AR4 SRES A1B SCENARIO USING GU-WRF/CHEM

2.1 Review of Climate Change Impacts on Air Quality

As the global population increases and industrialization grows in a changing climate, it is critical that governmental agencies account for changes in global air quality when forming successful climate change and air pollution mitigation strategies. A warmer and more humid climate with an increased abundance of atmospheric CO_2 is generally expected in the future and this has important ramifications for global air quality (Vautard and Hauglaustaine, 2007; Jacob and Winner, 2009; Weaver et al., 2009; Jacobson and Streets, 2009; Fiore et al., 2012). In addition, several studies have indicated that there is a higher probability of heat waves and air pollution episodes in the future due to increased stagnation. This results from a poleward shift in stormtracks and a general decrease in the frequency of mid-latitude cyclones (Mickley et al., 2004; Yin, 2005; Vautard and Hauglaustaine, 2007; Wu et al., 2008; Jacob and Winner, 2009; Monks et al., 2009; Young, 2009; Tai et al., 2012), which is consistent with the decreases in the frequency of mid-latitude cyclones observed during the 1980-2006 period (Leibensperger et al., 2008). The simulated impact of climate change on vertical transport is uncertain due to differences in model parameterizations (Murazaki and Hess, 2006; Jacob and Winner, 2009), but the impact could be larger than horizontal ventilation reductions as a 13% decrease in boundary layer export has been reported compared to a 2% reduction in interhemispheric transport

(Fang et al., 2011). However, there may be a potential increase in boundary layer export due to increases in convection (Zeng et al., 2008).

The warmer and wetter climate is expected to reduce the background ozone (O_3) level in regions with low NO_x levels, while increasing O_3 level in more polluted regions (Hauglaustaine et al., 2005; Liao et al., 2006; Murazaki and Hess, 2006; Stevenson et al., 2006; Hedegaard et al., 2008; Wu et al., 2008; Zeng et al., 2008; Jacob and Winner, 2009; Fiore et al., 2012; Doherty et al., 2013). The decreased background concentrations are the result of increased water vapor which reduces the lifetime of O_3 by removing O^1D to form the hydroxyl radical (OH), which in turn can destroy O_3 through HO_x reactions (Doherty et al., 2013). However, this general reduction in O_3 is compensated by increases in troposphere/stratosphere exchange due to strengthening of the Brewer-Dobson circulation expected in a warmer, CO_2 rich climate (Hauglaustaine et al., 2005; Buchart et al., 2010; Fiore et al., 2012). The O_3 level is increased in polluted regions due to higher temperatures leading to higher O_3 formation rates, increases in emissions of biogenic VOCs, and increased decomposition of peroxyacetyl nitrate (PAN), as well as reduced ventilation from source regions (Hedegaard et al., 2008; Liao et al., 2006; Wu et al., 2008; Zeng et al., 2008). In addition to changes in mean O_3, there is a tendency for increases in the 95^{th} percentile O_3 (Weaver et al., 2009; Langner et al., 2012), even in cases where the mean O_3 level decreases (Langner et al., 2012). Similarly, the impact of climate change alone results in over half the eastern U.S. exceeding a maximum 8-hr O_3 level of 75 ppb assuming emissions remain the same (Rieder et al., 2015). This indicates increases in the severity and duration of air

pollution episodes which have been estimated to increase in duration from 2 to 3-4 days with increased pollution levels of 5-10% in the U.S. (Mickley et al., 2004).

The impact of a changing climate on aerosols is less certain than that of O_3 because it is comprised of many different species that respond differently to perturbations in climate and emissions. The impact of future wet deposition is uncertain as it has been shown to both increase in the future resulting in decreases in $PM_{2.5}$ (Liao et al., 2006) and also potentially decrease globally due to reductions in annual large scale precipitation over land and seasonal changes in precipitation (Fang et al., 2011). Generally, precipitation changes are variable between models and the impacts are more regional, as wet deposition of soluble aerosols is not strongly dependent on global changes in precipitation (Fiore et al., 2012). $PM_{2.5}$ is also highly correlated with meteorological phenomena, such as the passage of cold fronts, but the projected increased stagnation in the future is not expected to induce a climate change penalty of more than 0.5 $\mu g\ m^{-3}$ (Tai et al., 2012).

Changes in climate and emissions are also expected to affect $PM_{2.5}$ speciation. The warmer and wetter climate is generally more oxidant rich which results in greater conversion of SO_2 to sulfate (Unger et al., 2006; Hedegaard et al., 2008; Jacob and Winner, 2009). This increased oxidation capacity along with potential increases in biogenic volatile organic compounds (VOCs) will lead to greater formation of both biogenic and anthropogenic secondary organic aerosol (SOA) (Tagaris et al., 2007; Heald et al., 2008). However, the increases in temperature may lead to reduced nitrate in the particulate phase (Jacob and Winner, 2009). These climate-induced changes in future aerosol levels can be either enhanced or offset by changes in future emissions depending on the emission

projection. Under the Intergovernmental Panel on Climate Change (IPCC) Fourth Assessment Report (AR4) Special Report on Emissions Scenarios (SRES) A1B scenario, the decreases by 2100 in emissions of sulfate, nitrate, and ammonium precursors are larger than those of primary organic matter (POM). This coupled with an increase in SOA may lead to organic matter (OM) as a dominant $PM_{2.5}$ species (Tagaris et al., 2007). It is also possible in certain regions that declining SO_2 emissions and increasing NH_3 emissions may lead to nitrate formation that is equivalent to current $PM_{2.5}$ levels (Fiore et al., 2012). This changing speciation over time may lead to variation in climate forcing. The work of Levy et al. (2008) showed that in 2030 following the SRES A1B scenario the climate is only weakly dependent on short lived climate forcers (sulfate, OM, black carbon (BC), O_3) due to compensating effects, but by 2100 enhanced BC emissions of 100% and a roughly 60% decrease in SO_2 emissions will contribute 1.5-2.0°C to global warming. This is a result of an enhanced warming effect from BC and a reduced cooling effect from sulfate (Levy et al., 2008). There may also be potentially large feedbacks to natural emissions of $PM_{2.5}$ including sea-salt, mineral dust, and wildfires (Jacob and Winner, 2009; Fiore et al., 2012).

Changes in future air quality will also have consequences on ecosystem health. O_3 deposition inhibits photosynthesis, damages plant cells, and has been shown to reduce both net primary productivity and carbon sequestration (Felzer et al., 2004). O_3 deposition is expected to increase due to an increase in the leaf area of broadleaf forests (Wu et al., 2012). However, these changes are uncertain as O_3 deposition can offset the CO_2 fertilization effect (Felzer et al., 2004). Plant damage from O_3 deposition may also have an indirect effect on climate as it will cause more CO_2 to remain in the atmosphere (Sitch et al., 2007). The

impact of O_3 on vegetation is also dependent upon emission scenario. Large increases in O_3 are to be expected under most of the IPCC AR4 SRES scenarios, making it difficult to achieve standards for crop damage and leading to speculation of possible agricultural concerns in the future (Prather et al., 2003). In contrast, the Representative Concentration Pathway (RCP) scenarios, from the IPCC Fifth Assessment Report (AR5), produce surface level O_3 improvements in all but the RCP8.5 scenario compared to present day (Lamarque et al., 2011, Young et al., 2013; Kim et al., 2015). However, under both types of scenarios nitrogen deposition is expected to increase (Dentener et al., 2006; Lamarque et al., 2011) due to increases in reactive nitrogen (NO_y) and NH_3 under the SRES scenarios and from increases in NH_3 that compensate losses of NO_y under the RCP scenarios. This may result in ecosystem changes, as 10.1% of natural terrestrial ecosystems are already exposed to nitrogen deposition higher than the critical load estimated to impact sensitive ecosystems (Dentener et al., 2006).

In this work, the Global-through-Urban Weather Research and Forecasting Model with Chemistry (GU-WRF/Chem) is employed to study the impact of climate change and emissions on global air quality under the IPCC AR4 SRES A1B emission scenario. The total impacts, as well as the separate contributions from changing emissions and climate, are investigated. The changes in ambient concentrations, deposition, and the impacts of chemistry on cloud and radiative parameters are discussed. The benefit of using this model for climate change studies is that it can represent the complex feedbacks between chemistry and meteorology and it employs the same level of complexity as regional air quality models, compared to the simplified treatments used by most contemporary global climate and

chemical transport models. However, this complexity comes at the cost of higher computational resource requirements.

2.2 Model Configuration, Evaluation Protocol, and Observational Datasets

2.2.1 Model Configuration and Inputs

GU-WRF/Chem (Zhang et al., 2012b) is an online-coupled model capable of simulating the interactions and feedbacks between the chemical and physical processes in the atmosphere. It is a hybrid model generated by replacing the WRF model in the National Oceanic and Atmospheric Association (NOAA)'s mesoscale WRF/Chem with the National Center for Atmospheric Research (NCAR)'s global WRF (GWRF) and then improving several model treatments for their applications on hemispheric to global scales. These improvements include online dust and BVOC emissions, gas-phase chemistry, a photolytic rate scheme, aerosol chemistry and microphysics, and aerosol-cloud interactions. Like GWRF and mesoscale WRF/Chem, GU-WRF/Chem has many different parameterizations for various atmospheric processes occurring on spatial and temporal scales smaller than those that can be resolved explicitly by the model. Table 2.1 contains a list of the chemistry and physics options used and the configuration of the simulations.

Gas-Phase chemistry in GU-WRF/Chem is simulated with the carbon bond mechanism with global extension (CB05GE) (Karamchandani et al., 2012), that simulates tropospheric chemistry as well as chemistry of the upper troposphere and stratosphere, chemistry of the marine boundary layer, mercury (Hg) chemistry (i.e., elemental (gas) and divalent (gas+aerosol) Hg), and Arctic chemistry. This is done through stratospheric reactions for CH_4, CO_2, O_2, N_2O, and excited atomic oxygen (O^1D), halogen reactions of 14

Cl and 11 Br species, heterogeneous reactions on cloud and aerosol particles, and reactions on polar stratospheric clouds all listed in Karamchandani et al. (2012) Tables 1-5. Aerosol chemistry is simulated using the WRF/Chem coupled Model of Aerosol, Dynamics, Reaction, Ionization, and Dissolution MADRID (Zhang. et al., 2004, 2010, 2012c). that simulates all major aerosol processes including inorganic aerosol thermodynamic equilibrium simulated based on version 1.7 of ISORROPIA (Nenes et al., 1998), nucleation, gas-to-particle mass transfer, condensation, coagulation, and the formation of 25 SOA species from anthropogenic (e.g., toluene and xylene) and biogenic (e.g., isoprene, monoterpene, and sesquiterpene) precursors.

Aerosol direct and indirect effects are simulated in GU-WRF/Chem. Aerosol radiative forcing is calculated based on Mie theory using the Goddard shortwave radiation scheme (Chou et al., 1998). Aerosol indirect effects in GU-WRF/Chem are only treated for large scale resolved clouds. Cloud condensation nuclei are determined based on Kohler theory calculated as a function of aerosol number concentrations and updraft velocity following the aerosol activation parameterization of Abdul-Razzak and Ghan (2002). Cloud droplet number concentrations (CDNC) are predicted based on major cloud processes including aerosol activation, collision/coalescence, collection by rain drops, snow, and ice crystals, formation of ice crystals thru freezing, and advection as part of the Ghan et al. (1997) parameterization that was incorporated into the existing Purdue Lin cloud microphysics scheme (Lin et al., 1983; Chen and Sun, 2002). The radiative forcing of clouds is then simulated by linking the CDNC simulated by the double moment Purdue Lin scheme

to the Goddard shortwave radiation scheme. More details on the chemical and aerosol-cloud interactions are discussed in Zhang et al. (2012b) and references therein.

GU-WRF/Chem simulations are conducted for a period of six years, with two current years (2001 and 2010) and four future years (2020, 2030, 2040, and 2050). This limited subset of years is used because each year represents a different stage of climate forcing and emissions changes, thus some of the decade to decade variability can be captured within the computational constraints. The initial meteorology and chemical conditions for O_3, N_2O, and CH_4 come from the Community Climate System Model version 3 (CCSM3) SRESA1B data set. Other chemical initial conditions for gas species with moderate lifetimes not found in the CCSM dataset (e.g., SO_2, PAN, and H_2O_2) are generated from the Goddard Earth Observing System Model with Chemistry v7-04-12-Run0 (http://wiki.seas.harvard.edu/geos-chem/index.php/GEOS-Chem_v7-04-12). Short-lived radical gas species (e.g., OH and NO_3) are initialized with clean conditions and aerosol initial conditions are set with the default values from mesoscale WRF/Chem. A one-month spin up period is then used to generate realistic ambient values for the short-lived species and aerosols. An additional two year simulation is conducted for the years 2001 and 2010 using meteorological initial conditions from the National Centers for Environmental Prediction Final Operational Reanalysis (NCEP-FNL), without data assimilation, so that the model can be evaluated to ensure that GU-WRF/Chem can reproduce the current atmosphere. A sensitivity simulation of the year 2050 is carried out using the same configuration as the base 2050 simulation but with unprojected 2001 emissions (2050_NPE). This sensitivity experiment is compared against both the 2001 simulation to investigate the impact that climate change alone will have on

future air quality and the 2050 simulation with projected emissions to examine the impact of changing emissions on the future climate.

The boreal spring months (March, April, and May (MAM)) of 2001 and 2050 during which ITAP is the strongest for the Trans-Pacific region are selected to study the role of intercontinental transport of east Asian air pollutants and their impacts on the U.S. and global air quality and climate. Simulations under different emission and climate scenarios for MAM 2001 and 2050 are conducted and compared to those of the MAM 2001 and 2050 simulations as part of the aforementioned multi-year simulations. The suite of model simulations conducted includes three baseline simulations with EAAEs from the multi-year simulations during MAM: 2001 with current climate conditions and emissions, 2050 with projected climate change and emissions, and 2050 with projected climate change only (referred to as 2001, 2050, and 2050_CCO, respectively), and three sensitivity simulations in which EAAEs are removed in the East Asia region including China, North and South Korea, Japan, and portions of India, Mongolia, Southeast Asia, and Russia. The years 2001 and 2050 were selected as they show the full changes in emissions and climate forcing between the current and near future periods, and additional sensitivity simulations without EAAEs for multiple years would require substantial computational resources that were not available for this study. However, as discussed in Section 2.9.2, the difference in the model simulations between the individual years (2001 and 2050) and the average of the current and future periods is smaller than the differences between the current and future time periods for several meteorological variables, indicating that the differences between the individual years largely represent changes in climate rather than just differences in model weather between both

years, although some degrees of internal model variability will affect the results. Unlike the 20% reductions of anthropogenic emissions used in other studies (discussed in Section 2.9.1), all Asian anthropogenic emissions are zeroed out in the sensitivity simulations in this work to estimate the maximum possible impacts of EAAEs on global air quality and climate. This will lead to significant nonlinear impacts on O_3 and fine particle formation but accounting for these processes is necessary to quantify the impact that East Asia has on the global chemical/climate system and to understand how this impact will change in response to changing climate and emissions.

The meteorological initial conditions as well as the sea surface temperatures (SSTs) for the non-evaluation simulations are 10 year averages of the CCSM3 data that are centered about each GU-WRF/Chem simulation year (e.g., the year 2030 is initialized with the average of 2025-2034 from the CCSM3 data), with the exception of 2001 which is initialized with the 5 year period 2000-2004 since the CCSM3 simulation started at the year 2000. The meteorology and the SSTs are reinitialized every month. This is especially important as the model uses static SSTs, which need to be reinitialized in order for the annual variation in SSTs to be represented. The chemical species in the model are reinitialized every 3 months. This allows for a mostly continuous chemistry simulation but prevents excess buildup of pollutants near the top of the model and near the polar singularities that can occur due to the lack of a positive-definite advection scheme in the model. This type of reinitialization technique is standard practice in online coupled regional air quality models such as those that took part in phase 2 of the Air Quality Model Evaluation International Initiative sponsored by the U.S. Environmental Protection Agency; including an updated version of mesoscale

WRF/Chem on which GU-WRF/Chem is based that employed reinitialization in 2 day intervals (Yahya et al., 2014; 2015).

The base anthropogenic emission inventory for the year 2001 has been provided in Table 2 of Zhang et al. (2012b). The natural emissions of biogenic volatile organic compounds (BVOCs), sea-salt, and dust are calculated online. The BVOCs are generated from the Model of Emissions of Gases and Aerosols from Nature (MEGAN) version 2 (Guenther et al., 2006), sea-salt is calculated using the formulation of Gong et al. (1997) with a correction for the smaller sea-salt particles from O'Dowd et al. (1997), and dust is generated from the scheme of Shaw (2008) with the modifications of Zhang et al. (2012b). Future emissions projections are based on the IPCC AR4 A1B scenario, which is a scenario of increasing economic and population growth that peaks in the mid-21st century and declines thereafter, with a focus on balanced energy sources (IPCC, 2001). The anthropogenic emissions projections for 2030 and 2050 are generated from region wide growth factors for 17 world regions developed by Argonne National Laboratory (ANL) using the Integrated Model to Assess the Global Environment (IMAGE) following the approach of Nakicenovic et al. (2000) and RIVM (2001), with the exception of the growth factors for primary organic carbon (OC) and black carbon (BC), which were derived following the approach of Streets et al. (2004). Tables 2.2 and 2.3 contain the SRES A1B emission growth factors for chemical species in GU-WRF/Chem. The emissions for 2010 and 2020 are a linear interpolation between the base emissions inventory and the projected 2030 emissions and 2040 emissions are a linear interpolation between the 2030 and 2050 emissions. The total global emissions of all major anthropogenic species for each simulated decade are listed in Table 2.4.

2.2.2 Evaluation Protocol

The model's performance with regards to meteorology and chemistry is evaluated for current years using a combination of satellite, global surface networks, and reanalysis data. The evaluation protocols are similar to those of Zhang et al. (2010, 2012a, 2012b) and include statistical evaluations and trend comparisons with observations for current years and a comparison of the climate trends in the CCSM3 data used to initialize the simulations for future years. The performance statistics include the correlation coefficient (R), the mean bias (MB), the normalized mean bias (NMB) and the normalized mean error (NME). The satellite data used for evaluation include the column abundance of CO from the Measurements Of Pollution In The Troposphere (MOPITT) , the column abundance of NO_2 from the Global Ozone Monitoring Experiment (GOME), the column abundance of NO_2 and SO_2 from the SCanning Imaging Absorption SpectroMeter for Atmospheric CHartographY (SCIAMACHY), the column tropospheric ozone residual (TOR) from the Total Ozone Mapping Spectrometer/ the Solar Backscatter UltraViolet (TOMS/SBUV) and the Ozone Monitoring Instrument/ Microwave Limb Sounder (OMI/MLS), downwelling long-wave radiation flux at the Earth's surface (GLW), downwelling short-wave radiation flux at the Earth's surface (SWDOWN), net downwelling short-wave radiation flux at the Earth's surface (GSW), and outgoing long-wave radiation at the top of the atmosphere (OLR) from the Clouds and the Earth's Radiant Energy System/ Energy Balanced and Filled (CERES/EBAF), and the cloud condensation nuclei at a supersaturation of 0.5% (CCN), the aerosol optical depth (AOD), the cloud optical thickness (COT), the cloud fraction (CF), the cloud liquid water path (LWP), and the precipitable water vapor (PWV) from the Moderate

Resolution Imaging Spectroradiometer (MODIS). Additional satellite datasets for the evaluation include remote sensing estimates of the cloud droplet number concentration (CDNC) in warm clouds from Bennartz (2007) (BE07) and LWP from O'Dell et al. (2008) (OD08). The data from global surface networks include GLW and SWDOWN from the Baseline Surface Radiation Network (BSRN) and the 2-m temperature (T2), the 2-m water vapor mixing ratio (Q2), the 10-m wind speed (WS10), surface pressure (PSFC), and precipitation rate (PR) from the National Climatic Data Center (NCDC). Reanalysis data used include PR from the Global Precipitation Climatology Project (GPCP) and OLR from the National Atmospheric and Oceanic Administration/ Climate Diagnostic Center (NOAA/CDC).

2.3 Model Evaluation

2.3.1 Operational Evaluation

Table 2.5 summarizes the model performance statistics for the various global networks listed above. Figure 2.1 shows a comparison of the zonal mean profiles of GU-WRF/Chem and the satellite/reanalysis datasets for the annual averaged current year period of 2001 and 2010 (AOC), while Figure 2.2 shows spatial distributions of simulated meteorological variables overlaid with observations from the surface networks. OLR and GLW are both well simulated in GU-WRF/Chem with correlations varying between 0.94-0.99 to the observations and NMBs within ±3%. There is a slight inconsistency between OLR datasets most likely because CERES/EBAF data are satellite retrievals and the NOAA/CDC data are from a model reanalysis. Despite the differences in magnitude, the zonal mean profile of both CERES/EBAF and NOAA/CDC datasets and the

GU_WRF/Chem simulation are quite similar with model predictions usually between both datasets, resulting in a slight overprediction compared to the NOAA/CDC data and a slight underprediction compared to the CERES/EBAF data.

Similar to most global climate/air quality models (Kay et al., 2012; Lauer and Hamilton, 2013), cloud parameters are not as well simulated in GU-WRF/Chem. The cloud fraction in GU-WRF/Chem is overpredicted by ~20% domain wide but the overprediction largely occurs over the oceans and at the higher latitudes while the interior of the continents are either close to the observations or slightly underpredicted. Despite the overprediction in CF; COT and LWP are largely underpredicted (an NMB of -82.6% for COT, and NMBs for LWP are -81.0% against MODIS, and -58.9% against OD08). LWP in GU-WRF/Chem only represents resolved clouds and as a result subgrid scale cloud water is missing compared to the observations, which most likely accounts for the large underprediction. Additionally, the Purdue Lin cloud microphysics scheme is fairly outdated and simplified compared to many of the newer microphysics schemes such as the Morrison double moment scheme (Morrison et al., 2005) in the WRF model and future work for coupling these microphysics schemes with chemistry and representing subgrid scale cloud water may lead to better agreement with the observations. The LWP from the OD08 dataset is a better match to the GU-WRF/Chem predictions. However, this OD08 LWP data is limited in spatial coverage to marine environments and not available at higher latitudes. This indicates that the larger underpredictions against the MODIS LWP data occur because of the inability of GU-WRF/Chem to simulate cloud water at higher latitudes and over the continental interiors with the underprediction over the continents being the result of underpredictions in cloud

formation. However, there is also large uncertainty in satellite retrievals at higher latitudes due to low solar zenith angle (Seethala and Horváth, 2010) and interference from radiatively active snow covers (Kay et al., 2012). COT is underpredicted in part because of the underprediction in LWP but also because only cloud water and ice are part of the calculation and additional optical thickness from rain, snow and graupel is not represented in the model. However, despite these model weaknesses, the performance of GU-WRF/Chem is comparable to that of mesoscale WRF and MM5/CMAQ (Zhang et al., 2012b).

Both SWDOWN and GSW are reasonably well simulated by GU-WRF/Chem with NMBs of ~20-26% and correlations of 0.89 and 0.92, respectively. The bulk of the overprediction in SWDOWN and GSW occurs in the higher and mid-latitudes. The overpredictions in both SWDOWN and GSW are the result of underpredictions in cloud parameters such as COT, especially over the continents and at higher latitudes. Additionally, based on the zonal mean plots in Figure 2.1, GSW has a larger overprediction in the Arctic compared to SWDOWN, indicating that the albedo in GU-WRF/Chem may be underpredicted, especially in polar regions.

The GU-WRF/Chem meteorological predictions are also in good or reasonably good agreement with observations. The PSFC is only slightly underpredicted (-0.4%) with a fairly high correlation of 0.65. Both PWV and Q2 are very well simulated with NMBs less than or equal to 2% and correlations of greater than or equal to 0.89. GU-WRF/Chem predicts a wetter atmosphere in the higher latitudes and drier tropics than that is observed. In both cases this may be the result of the warm bias from the model as higher temperatures in the high latitudes would lead to greater evaporation, while the warmer temperatures in the tropics

could result in a depletion of soil moisture and thus a drier atmosphere. The model does overpredict the surface temperature by 1.4°C with the overprediction focused on mostly at higher latitudes and the interiors of continents. These overpredictions are caused by the overpredictions in SWDOWN and GSW that result from the underpredicted LWP and COT. Despite the fairly high bias, the temperature is well correlated with the observations (0.94), indicating that the model can reproduce the spatial pattern in temperature rather well. The WS10 in GU-WRF/Chem tends to be underpredicted over the continents and overpredicted over the oceans with a domain average underprediction of -24.9%. The PRs from NCDC and GPCP are underpredicted by -6.1% and -3.4% respectively. The comparison of zonal mean PR of GU-WRF/Chem against GPCP observations (Figure 2.1) shows that GU-WRF/Chem generally captures the latitudinal variation in precipitation but overpredicts tropical convective precipitation and underestimates mid-latitude precipitation. The underpredictions in mid-latitude PR are due to underpredictions over the continents, as shown in Figure 2.2. The underprediction in the mid-latitudes is consistent with the underprediction of clouds over the continents in these regions. This is also consistent with the prediction of PWV as the enhanced PR in tropics have depleted the tropical PWV compared to observations and the underpredicted mid-latitude PR leaves more PWV in the atmosphere compared to observations.

The model AOD and CCN are both overpredicted (NMBs of 96.3% and 18.9%). The overprediction in AOD is the largest in biomass burning regions including South America, Africa, and Indonesia, as shown in Figure 2.3, indicating that either BC or OM emissions may be overestimated or that the strong convection in this region is leading to excess lofting

of fine particles. Underpredictions in precipitation may also be responsible for the overpredicted AOD and CCN as wet removal of particles will be underpredicted. The MODIS CCN data is only available in marine regions so the overprediction is largely caused by excess continental outflows resulting from the underpredictions in precipitation and also potential overpredictions in sea salt from overpredicted marine wind speeds. The model underpredicts warm cloud CDNC by 63.5% most likely due to the underpredicted aerosol activation from lack of cloud formation as evidenced by underpredicted LWP. The aerosol activation may be underpredicted in GU-WRF/Chem because the Abdul Razzak-Ghan activation scheme does not account for the adsorptive activation of hydrophobic aerosol which has been shown to increase aerosol activation and CDNC (Gantt et al., 2014). There are also uncertainties in the satellite derived CDNC. For example, the satellite-derived CDNC may be an underestimation of the actual CDNC since the CDNC is derived from the MODIS retrieval of effective radius (Bennartz, 2007). This parameter typically has very large values, especially in remote oceans regions due to the presence of broken cumulus clouds. This bias has been attributed to drizzle/rain contamination (Nakajima et al., 2010) and artifacts from cloud heterogeneity (Zhang and Platnick, 2011). Thus the overestimation of cloud effective radius would result in an underestimate of satellite CDNC.

The column abundances of CO and NO_2 are both overpredicted (NMBs of 54.7% and 74.8%). The overpredictions in both species are tied to overestimations of NO_x and CO emissions. As discussed in Zhang et al. (2012b), the emissions of CO and NO_x in the GU-WRF/Chem inventory are larger than most other available emission inventories and in this study their emissions are not scaled down to match the other inventories. The overestimated

CO appears again to come largely from the biomass burning regions in the tropics, indicating that biomass burning emissions may be generally overestimated. The zonal mean profile of column NO_2 in Figure 2.1 reveals that while the column NO_2 is overestimated it follows the same latitudinal variability as the observations. The TOR also appears to follow the same pattern as the observations but is overestimated by 24.3% most likely due to the overestimated NO_2 column. The model also captures the spatial variability of column SO_2 but it is largely underestimated (with an NMB of 81.2%). This is most likely the result of a number of factors including the lack of emissions and pathways for the formation of SO_2 from volcanoes and dimethyl sulfide emitted from the oceans.

2.3.2 Climate Trend Comparison

GU-WRF/Chem predictions are compared against available data from climate projections of both CCSM3 that utilizes a similar SRES A1B scenario projection and also against predictions from the Community Earth System Model version 1.0 /Community Atmosphere Model version 5.1 (CESM1-CAM5) from the Coupled Model Intercomparison Project Phase 5 (CMIP5) that follows the RCP8.5 scenario. The RCP8.5 scenario was chosen as it is the RCP scenario that is the most comparable to the SRES A1B scenario. Figure 2.4 shows the trend in T2, Q2, GSW, OLR, PR, and sulfate between the average of the current year period (AOC) and the average of the future year period (AOF) for both CCSM3 and GU-WRF/Chem. Figure 2.5 also shows trend comparison s of T2, Q2, OLR, and PR but shows additional trends in WSP10, PWV, LWP, CF, SWDOWN, and AOD between the AOF and AOC periods for GU-WRF/Chem and CESM1-CAM5. The domain mean increase in temperature between the two SRES A1B models is similar with an increase of ~1.0°C for

CCSM3 and 0.7°C for GU-WRF/Chem, but the RCP8.5 projection shows greater warming of ~1.4ºC. The SRES A1B models show similar patterns in warming and cooling with the exception of the Arctic where CCSM3 produces the strongest warming and GU-WRF/Chem either produces less warming or even cooling. The disagreement in this region likely contributes the most to the more modest warming trend in GU-WRF/Chem and is caused by increases in Arctic cloudiness that result in a decrease in GSW. The greater warming under the RCP8.5 scenario is the result of large increases in CH_4 emissions under this scenario and reductions in aerosol levels that have been show to increase future temperatures (Chalmers et al., 2012; Westervelt et al., 2015). Changes in Q2 between AOF and AOC predicted by both SRES A1B models are similar with global average increases of 0.4 g kg^{-1} for CCSM3 and 0.3 g kg^{-1} for GU-WRF/Chem. The smaller increase of GU-WRF/Chem is likely driven by the more moderate warming compared to CCSM3. The larger increase of 0.5 g kg^{-1} in the CESM1-CAM5 prediction is also likely linked to greater warming under the RCP8.5 scenario. This is also true for PWV between GU-WRF/Chem (e.g., global average increase of ~1.1 mm) and CESM1-CAM5 (e.g., global average increase of ~1.4 mm) although both models show increases across the almost the entire domain. Changes in PR are also similar in all projections with increasing PR in the tropics, mid-latitudes and polar regions and drying in the subtropics. The global average changes are an increase of 0.05 mm day^{-1} for CCSM3, 0.06 mm day^{-1} for CESM1-CAM5, and 0.02 mm day^{-1} for GU-WRF/Chem. The PR increase is likely less in GU-WRF/Chem since the atmosphere is slightly drier compared to CCSM3 and CESM1-CAM5.

In general, GU-WRF/Chem predicts a sometimes cloudier and more aerosol-rich future atmosphere, which will be discussed in more detail in subsequent sections. Processed cloud variables from CCSM3 are not available from the Earth System Grid repository for comparison against GU-WRF/Chem so cloud variable comparisons are limited to CESM1-CAM5. The global average change in CF is similar between both models with decreases of ~0.17% for CESM1-CAM5 and ~0.15% for GU-WRF/Chem. Declines in CF are also consistent with other studies due to the reduction of low and mid-level clouds from increasing temperatures (Zelinka et al., 2013). However, there is not much agreement in terms of spatial variability of the changes accept for increasing cloudiness in the Arctic. This lack of consistency in spatial variability could be related to differences in model parameterizations that effect clouds, but it is more likely that the discrepancies seen over land are related to large differences in radiative forcing due to opposing trends in aerosols and the discrepancies over the oceans are caused the use of static SSTs in GU-WRF/Chem compared to an online coupled ocean model in CESM1-CAM5. There are large differences in the change of LWP path projected by GU-WRF/Chem which increases by 1.41 g m^{-2} on global average and condensed water path (LWP+ice) predicted by CESM1-CAM5 that increases by 0.04 g m^{-2}. The increase from GU-WRF/Chem is a largely global increase and reflects both enhanced moisture availability from the warmer climate but also enhancements from the increasing aerosol levels that increase LWP by increasing cloud lifetimes. The condensed water path (CWP) from CESM1-CAM5 also experiences increased LWP from enhanced moisture availability but over the continents, especially in industrial regions, the CWP is

decreased due to the decreasing aerosol levels under the RCP8.5 scenario that reverse the cloud lifetime effect (Westervelt et al., 2015).

The increases in aerosols in GU-WRF/Chem increase AOD globally and by 0.03 on global average. Total AOD was not available from the processed CCSM3 output but a comparison against CESM1-CAM5 shows a contrasting decreasing trend in aerosols under the RCP8.5 scenario which cause AOD to decline on global average by 4.6×10^{-4}. GU-WRF/Chem predicts global mean decreases in GSW of 1.05 W m^{-2} and OLR of 0.72 W m^{-2}. This is because the greater aerosol and cloud water amounts reduce the amount of shortwave radiation reaching the surface, thus reducing GSW. The reduced GSW reduces the surface heating and leads to a smaller emission of longwave radiation and this combined with more longwave absorption by the clouds and greenhouse gases leads to a reduction in OLR. These changes are in contrast to the CCSM3 predicted global mean increases of 0.08 W m^{-2} in GSW and 0.32 W m^{-2} in OLR. SWDOWN is projected to decrease by 1.6 W m^{-2} on global average based on GU-WRF/Chem compared to a 0.6 W m^{-2} decrease from CESM1-CAM5. These changes largely mirror changes in LWP and CWP indicating that global mean reductions in both models result from increased cloud albedos. The reduction is smaller in CESM1-CAM5 due to declines in aerosol levels under the RCP8.5, which increases SWDOWN over land through the aerosol direct and indirect effects. OLR increases to a stronger degree in the CESM1-CAM5 projection (e.g., 1.4 W m^{-3} on global average) due to the reduced cloudiness and warmer temperatures following the RCP8.5 scenario. However, despite the differences in the global average trends, there are some similarities in the spatial distributions (e.g., the decreasing OLR in the tropics and increasing OLR in the subtropics).

The discrepancy in the trends between both SRES A1B projections could be the result of a number of factors. Examples of such factors include: (1) the simulation of additional aerosol species such as ammonium nitrate and additional aerosol chemistry treated in GU-WRF/Chem that are not treated by this version of CCSM; (2) changes in carbonaceous aerosols in CCSM3 are based on changes in SO_2 emissions rather than having independent emission changes like those treated in GU-WRF/Chem; (3) sea-salt and dust are static between the current and future CCSM3 simulations but are dynamically evolving with climate in GU-WRF/Chem; (4) differences in cloud microphysics, radiation, and cumulus parameterizations; and (5) the use of a static prescribed O_3 field with a varying radiative forcing for future predictions in CCSM3 whereas GU-WRF/Chem allows O_3 and its subsequent feedback to radiative forcing to evolve with changes in meteorology and precursor emissions. Changes in aerosols including sea-salt and dust, as well as changes in O_3 from GU-WRF/Chem are discussed in detail in Section 2.5.

These differences in chemistry and also potential differences in emissions and the method for applying emissions changes may possibly explain the discrepancies in sulfate between the two SRES A1B models. Both models predict an increase in the global mean sulfate concentration, with CCSM3 predicting an increase of 0.04 μg m^{-3} compared to a larger increase of 0.19 μg m^{-3} by GU-WRF/Chem. However, there are several regional discrepancies including Africa, where GU-WRF/Chem predicts an increase of 0.5 to 2.0 μg m^{-3} in contrast to the 0.25 to 2.0 μg m^{-3} decreases predicted by CCSM3, and Europe, where GU-WRF/Chem predicts a decrease of 0.25 to 1.0 μg m-^{3} in contrast to the 0.25 to 1.0 μg m^{-3} increase predicted by CCSM3. These discrepancies are caused by differences in emissions

since the SRES A1B emissions growth factors for GU-WRF/Chem emissions are derived from the IMAGE integrated assessment model rather than the Asian-Pacific Integrated Model (AIM) used for the CCSM3 projections. This type of divergence despite using the same story line occurs between integrated assessment models (Nakicenovic et al., 2000).

2.4 Projected Emissions

The emissions projection used in this work is the IPCC AR4 SRES A1B scenario. This scenario is one of the more moderate climate change scenarios from the IPCC AR4 that focuses on the diversification of energy sources. Figure 2.6 shows the spatial distribution of the changes in the anthropogenic emission fluxes of key species (NO_x, total non-methane VOCs (TNVOC), CH_4, CO, SO_2, NH_3, BC, POM, and other unspeciated $PM_{2.5}$) following this scenario between the AOF and AOC periods . A more detailed discussion of the trend in the emissions from year to year and how they compare against the IPCC AR5 RCP scenarios can be found in Section 2.9.3.

Globally, the emission fluxes of NO_x and TNVOC increase on average by 4.4×10^{-1} and 6.6×10^{-1} mol km^{-2} hr^{-1}, respectively. The largest increases in emissions fluxes of NO_x of up to 12.6 mol km^{-2} hr^{-1} and TNVOC of up to 45.4 mol km^{-2} hr^{-1} occur in South Asia and East Asia, indicating that increases in O_3 formation are likely to be the greatest in these regions. Enhanced emissions of NO_x (e.g., ~1.0-2.5 mol km^{-2} hr^{-1}) and TNVOC (e.g., ~1.0-3.0 mol km^{-2} hr^{-1}) are also seen in eastern Europe and the Middle East. Reductions in both NO_x and TNVOC occur in the U.S., Canada, western Europe, and south central Africa. The largest reductions in NO_x of 0.5 to 1.3 mol km^{-2} hr^{-1} occur in the eastern U.S. and south central Africa, while the largest decreases in TNVOC emissions of up to 8.0 mol km^{-2} hr^{-1}

occur in the U.S. The global change in biogenic emission flux of TNVOC (shown in Figure 2.7) is an increase of 0.9 mol km^{-2} hr^{-1}, of which 0.6 mol km^{-2} hr^{-1} is the result of increases in isoprene emissions and 0.06 mol km^{-2} hr^{-1} is a result of increases in the emissions of terpenes, with the remaining increase attributed to formaldehyde, acetaldehyde, ethene, olefins, organic nitrates, organic acids, and organic peroxides. Additionally, there is an increase in biogenic NO emissions of 0.02 mol km^{-2} hr^{-1}. This increase is small compared to the anthropogenic changes in NO_x emissions, however it will enhance the background level O_3 as rural regions with biogenic emissions are typically NO_x limited. These global increases in biogenic emissions are the result of warmer temperatures in the future climate over most continents.

The global average change in the anthropogenic CO emissions flux is an increase of 0.3 mol km^{-2} hr^{-1} due mostly to increases in northern portions of Africa, South Asia, Southeast Asia, and South America, while CO is reduced in the U.S., western Europe, and southern and central Africa. A similar pattern of changes occurs in CH_4 emissions with the largest increases occurring in western Asia and the Middle East, resulting in a global average increase of 1.6 mol km^{-2} hr^{-1}. These increases in anthropogenic emissions are also accompanied by global average increases in biogenic CO emissions of 0.2 mol km^{-2} hr^{-1} and biogenic CH_4 emissions of 8.2×10^{-3} mol km^{-2} hr^{-1}. These emissions changes will increase the global burden of CO and CH_4, which indicate enhanced CO pollution in the developing world and more radiative forcing from CH_4 leading to further warming.

SO_2 emissions fluxes increase on global average by ~0.3 mol km^{-2} hr^{-1} as a result of increasing emissions in the developing world including: Africa, South America, Central

America, South Asia, and Southeast Asia, where increases can be as large as 46.5 mol km^{-2} hr^{-1}. Changes in SO_2 emission fluxes are negligible in both the U.S. and Canada and also in most of East Asia. The largest declines in SO_2 emissions occur in Europe with decreases as large as ~20.8 mol km^{-2} hr^{-1}. The global average NH_3 emission flux decreases by 4.6×10^{-2} mol km^{-2} hr^{-1} in this scenario. NH_3 emissions increase in portions of the developing world including Central America, South America, Southeast Asia, and the majority of Africa (e.g., 0.2 to 1.5 mol km^{-2} hr^{-1}). The global decline in NH_3 emissions is the result of significant decreases (e.g., 0.2 to 8.3 mol km^{-2} hr^{-1}) in the emission fluxes in Europe, South Asia, and East Asia. Similar to the changes in SO_2 emissions, NH_3 emission changes are negligible in the U.S. and Canada. These emissions projections indicate that increases in secondary inorganic $PM_{2.5}$ formation will be favored in most of the developing world including Africa, Central America, South America, South Asia, and Southeast Asia. The impact on secondary inorganic $PM_{2.5}$ formation is uncertain in the U.S., Canada, and East Asia as SO_2 changes are negligible in all these regions and NH_3 is reduced in East Asia and has a negligible change in the other regions. Secondary inorganic $PM_{2.5}$ formation is also likely to decrease in Europe due to the declining SO_2 and NH_3 emissions in that region.

The emission fluxes of BC, POM, and other unspeciated $PM_{2.5}$ all decrease on global average by 1.4×10^{-5}, 5.9×10^{-4}, and 1.6×10^{-4} μg m^{-2} s^{-1}, respectively. BC emission fluxes decrease the most in the eastern U.S., East Asia, Africa, and western Europe (e.g., by ~5.0×10^{-4} to 4.5×10^{-3} μg m^{-2} s^{-1}), but increase in Central America, South America, and South Asia (e.g., by ~5.0×10^{-4} to 3.2×10^{-3} μg m^{-2} s^{-1}). A similar pattern is observed in the POM emission fluxes except that POM emission declines (e.g., ~1.0×10^{-3} to 1.8×10^{-2} μg m^{-2} s^{-1})

are larger than BC declines and POM emission fluxes are reduced in South Asia and Central America. The increases in POM emission fluxes in South America, Eastern Europe, and Indonesia are also greater than those of BC (e.g., ~1.0×10^{-3} -2.1×10^{-2} μg m^{-2} s^{-1}). Changes in unspeciated $PM_{2.5}$ are negligible over a majority of the Northern Hemisphere with a few exceptions; these include central portions of Europe, Central America, South Asia, and Southeast Asia. Unspeciated $PM_{2.5}$ decreases are the largest in Sub-Saharan Africa (e.g., by ~1.0×10^{-3} to 3.6×10^{-2} μg m^{-2} s^{-1}), while the largest increases occur in South America, Indonesia, and Australia (e.g., ~1.0×10^{-3} to 1.3×10^{-2} μg m^{-2} s^{-1}). The overall impacts from these changes are declining primary aerosol in the U.S., western Europe, East Asia, and Africa and increasing primary aerosol in South America, Indonesia, and Australia. The impacts on South Asia, Southeast Asia, and Central America are uncertain due to compensating changes from the different primary aerosol species.

2.5 Impact on Air Quality

2.5.1 Trace Gases

Figure 2.8 shows the response of trace gases including CO, NH_3, SO_2, NO_2, the maximum 8-hr O_3($O_3$8hr), peroxyacetyl nitrate (PAN), OH, HO_2, H_2O_2, nitrate radical (NO_3g), N_2O_5, and HNO_3, to changing climate and emissions. The changes in CO, NH_3, SO_2, and NO_2 mirror the changes in their emissions. Increased CO emissions lead to a global average increase in the CO level of 6.3 ppm (5.2%). The largest increases (20-78 ppm) occur in biomass burning regions of South Asia and Southeast Asia. Reductions in CO are smaller in magnitude (e.g., 5.0 to 33.0 ppm) and occur in the eastern U.S. and south central Africa. NH_3 declines on global average by 6.4×10^{-3} ppb (3.6%) due to the large declines in South

Asia, East Asia, and south central Africa of 0.1 to 1.5 ppb and smaller declines of 0.1 to 0.3 ppb in Europe. These offset increases of 0.1 to 0.8 ppb in central Africa and South America. SO_2 increases on global average by 0.08 ppb (42.5%) due to increases of 0.2 to 15.0 ppb in most of the developing world. The increased SO_2 level in these regions offset moderate decreases of 0.1 to 3.8 ppb in Europe and western Asia and smaller decreases of 0.2 ppb or less in the U.S. and Canada. The global NO_2 level increases by 0.1 ppb (40.7%) on average with increases as large as 1.0 to 6.3 ppb in South Asia and East Asia. Reductions in NO_2 of 0.8 ppb or less occur in western Europe, the U.S. and south central Africa. These changes are generally consistent with the work of Jacobson and Streets (2009) that utilize the same emissions scaling technique used here for the SRES A1B scenario, which reported changes of +12%, +51%, +40%, and -15% in near surface CO, NO_2, SO_2, and NH_3 by 2030.

The $O_3$8hr level increases by 2.5 ppb on global average with increases as large as 20.4 ppb in South Asia and East Asia. Similarly, annual average near surface O_3 increases by 2.2 ppb (11.7%) on global average and as 15.0 ppb in South Asia and East Asia (not shown). An exact comparison of these changes against previous studies is not possible due to differences in scenario, methodology, and simulated period. However, increase in O_3 during the AOF period are consistent with the 14% increase in near surface O_3 by 2030 following the SRES A1B scenario reported by Jacobson and Streets (2009). The O_3 enhancements seen here are less than the 13.7-18.0 ppb average increase reported by Liao et al. (2006) following the SRES A2 scenario by 2100, which is to be expected as A2 generally has higher pollutant emissions than A1B and warming is more intense by 2100 compare to 2020-2050. The global average change in O_3 from GU-WRF/Chem is also similar to the 2.1 ppb increase in

surface O_3 following the RCP8.5 scenario in 2050 reported by Kim et al. (2015), although the reasons for O_3 increases under this scenario are more related to increased temperatures and increased CH_4 levels since NO_x emissions decrease under this scenario. The changes in O_3 in this work are significantly different from all other RCP scenarios, where O_3 decreases as a result of stronger controls of pollutants and greenhouse gases (Lamarque et al., 2011; Young et al., 2013; Kim et al., 2015).

In order to better explain the increases in $O_3$8hr, the changes in $O_3$8hr are correlated with changes in both meteorological and chemical variables, and the correlation coefficients (R) are shown in Table 2.6. The primary cause of the increased $O_3$8hr level is increases in NO_x emissions and consequently, the increases in the surface NO_2 level, which correlates with $O_3$8hr by 0.57 and 0.65, respectively. The enhancements of the $O_3$8hr level by TNVOC are less pronounced with a correlation of 0.26 against TNVOC emissions and 0.44 against the surface anthropogenic VOC level (AVOC). These correlation values do not necessarily indicate a strong influence from TNVOC as the emissions of TNVOC and NO_x are highly correlated with each other (R of 0.60). There is a mild contribution to the $O_3$8hr level from increasing T2 (R of 0.20), which increases the reaction rates for O_3 formation. Other meteorological factors including Q2, planetary boundary layer height (PBLH), and the photolysis rate of NO_2 do not appear to contribute substantially to the increase in $O_3$8hr with R values that are near zero or negative. The near zero correlation likely indicates that the impact of water vapor destruction on O_3 reported in many studies (Fiore et al., 2012 and references therein) is compensated by the increasing NO_x emissions in this scenarios. However, this effect is seen in the 2050_NPE simulation discussed in Section 2.8.1. The

change in the isoprene level also does not appear to be leading to enhanced O_3 formation as it has a negative correlation of -0.32 against the increases in $O_3$8hr. However, this strong anti-correlation indicates that O_3 enhancements result in much greater isoprene oxidation and removal despite slight increases in biogenic emissions (e.g., 9.6% increase in isoprene and 9.5% increase in total biogenic VOC). The enhancement of isoprene in GU-WRF/Chem is greater that the approximate 1% increase in biogenic emissions reported by Jacobson and Streets (2009) for 2030 and less than the 22% increase reported by 2100 in Heald et al. (2008) following the SRES A1B scenario, indicating the changes are within the range of future possibilities following SRES A1B. The global PAN level increases by ~0.03 ppb on average. This occurs, despite the enhanced PAN decomposition from warmer climate, due mainly to the increases in NO_x emissions but also potentially from the increases in emissions of TNVOC precursors (i.e., acetaldehyde, isoprene, and aromatics such as toluene, xylene, and cresol). This is especially true in South Asia and East Asia where emissions of both NO_x and TNVOC increase, resulting in increasing PAN levels by 0.1 to 0.5 ppb.

The enhanced O_3 level in the future environment leads to greater formation of O^1D, 1.8×10^{-11} ppt (8.6%) on global average, from O_3 photolysis. This increase in O^1D and its subsequent reaction with the greater water vapor level lead to greater formation of near surface OH, which increases on global average by 1.6×10^{-3} ppt (7.3%) with the greatest enhancements in the tropic and subtropic continents of 5.0×10^{-2} to 0.4 ppt. The increases in O^1D and OH are small even though the enhanced O_3 level favors formation, because there is a decline in O_3photolysis due to greater aerosol scattering and cloudiness in the future atmosphere that will be discussed in more detail in subsequent sections. This increase in OH

differs from the decreases of 3.8% reported by Jacobson and Streets (2009), and also ensemble results using the RCP scenarios (Voulgarakis et al., 2013; Kim et al., 2015). The decreases following the RCP scenarios are potentially linked to large increases in CH_4 in the RCP8.5 scenario and decreased O_3 production in the remaining scenarios, as well as O_3 recovery in the stratosphere predicted under these scenarios (Voulgarakis et al., 2013; Kim et al., 2015). The discrepancy between GU-WRF/Chem and the work of Jacobson and Streets (2009) could potentially be due to differences in the chemical mechanisms and underlying parametrizations in both models.

The increase in O_3 and OH also lead to enhancements of the HO_2 level of ~0.3 ppt (4.8%) on global average but up to as much as 1.0 to 3.3 ppt in tropical regions. The enhancements of OH and HO_2 lead to a higher H_2O_2 level of 0.08 ppb (13.8%) with enhancements of 0.2 to 1.2 ppb over most continents. The increases in O_3 combined with the increased NO_2 levels lead to greater formation of NO_3g, which increases on global average by 0.6 ppt (33.3%). This shows that the impact of the increased NO_x emissions under the SRES A1B scenario is not only to increase the global O_3 level but to increase the global availability of the major atmospheric oxidants, thus increasing the atmosphere's near surface oxidation state. The increased NO_x emissions also increase the level of other nitrogen containing species such as N_2O_5 which increases by 0.9 ppt (48.7%) on global average. This, combined with the increased levels of NO_2, NO_3g, and other oxidants, leads to greater formation of HNO_3 (0.3 ppb or 99.8% on global average), creating a bigger reservoir for nitrate aerosol formation. This increased HNO_3 level is comparable to the 76% increase reported by Jacobson and Streets (2009).

2.5.2 $PM_{2.5}$

Figure 2.9 shows the impact of the changing climate and emissions on $PM_{2.5}$ and its components. The global $PM_{2.5}$ level increases on average by 0.3 μg m^{-3} (3.6%), slightly larger but comparable to the 1.6% increase predicted by Jacobson and Streets (2009). However, the changes are much more regional in nature compared to the $O_3$8hr level. Table 2.7 shows the correlations of the changes in $PM_{2.5}$ compared to changes in meteorological variables, chemical precursors, and emissions. The impact of changing climate on the overall $PM_{2.5}$ level appears to be minimal except in the cases of the WSP10 (R value of 0.12), which impacts the emissions of sea-salt, and Q2 (R of 0.28) which can lead to greater absorption of water into the aerosol. The impacts from changes in PBLH and precipitation are minimal with R values close to zero. However, this assessment only pertains to simulations in which both climate and emissions are changing as the impact of climate change alone has been shown to impact $PM_{2.5}$ in past studies (Jacob and Winner, 2009; Fiore et al., 2012) and will be demonstrated in the 2050_NPE simulation discussed in Section 2.8.1.

The global $PM_{2.5}$ level is influenced the most by changes in primary particle emissions of BC, POM, and other unspeciated inorganic $PM_{2.5}$ (OIN) (R values of 0.42, 0.40, and 0.56, respectively). The decreases in these primary particle emissions are the primary cause of the decline of 0.6 to 12.5 μg m^{-3} in central and southern Africa and the decline of 0.6 to 1.2 μg m^{-3} in East Asia, and partially contribute to the declines in the eastern U.S. and western Europe. Increases in these emissions also contribute to the 0.3 to 2.1 μg m^{-3} increase in Australia and partially contribute to the 0.9 to 8.8 μg m^{-3} increases in South Asia,

Southeast Asia, South America and Indonesia (mostly from increases in BC and OIN since primary organic carbon (POC) declines in all these regions except South America).

The changes in $PM_{2.5}$ over the oceanic regions can be either decreases or increases and are partially controlled by the WSP10 driven changes in sea-salt emissions of sodium and chloride over the oceans (R of 0.36 and 0.26, respectively). However, there is a difference in not only the R of both sea-salt components but in the global change of sodium, which increases by 0.02 μg m^{-3} on global average, and chloride which decreases by 0.14 μg m^{-3}. This decline in chloride largely occurs off the coast of most continents and is caused by enhancements in the levels of both SO_2 and HNO_3 in these coastal zones, resulting in much greater chloride displacement by sulfate and nitrate. The enhanced chloride displacement, from the increased HNO_3 level, increases the global average nitrate level by 0.2 μg m^{-3} with increases as large as 2.9 μg m^{-3} in these coastal zones. The replacement of chloride by sulfate and nitrate is one of the major contributors to the increasing global $PM_{2.5}$ level since both nitrate and sulfate have a higher molecular weight than chloride.

The impact from the secondary inorganic aerosol precursors is not as strong as the primary particle emissions. Changes in SO_2 emissions and the surface SO_2 level show the greatest impact (R of 0.20 and 0.31), followed by NO_x emissions and the surface HNO_3 level (R of 0.19 and 0.26), while changes in NH_3 emissions and the surface NH_3 level have the smallest impact (R of 0.14 and 0.12). The global sulfate level is enhanced under this scenario by 0.19 μg m^{-3} on average. These sulfate enhancements are the greatest in South Asia, Southeast Asia, Indonesia, and South America, where the enhancements range from 0.4 to 5.5 μg m^{-3} and are the second major contributor to total $PM_{2.5}$ enhancements in these regions.

These areas of enhanced sulfate are the result of both increasing SO_2 and primary sulfate emissions. Regions with negligible changes in SO_2 emissions, such as the U.S., also experience slight increases in sulfate (less than 0.5 μg m^{-3}), mostly likely in response to the atmosphere's higher oxidant level. The only region that shows a strong decline in sulfate is Europe, where sulfate decreases by 0.3 to 1.0 μg m^{-3} in response to declining SO_2 emissions. This is the primary cause of the decrease of 0.3 to 1.8 μg m^{-3} in the total $PM_{2.5}$ level over most of Europe. Despite a decrease in the global NH_3 level, there is an increase of 0.01 μg m^{-3} in the global ammonium level. This discrepancy is largely the result of increases of 0.1 to 0.6 μg m^{-3} in ammonium over South Asia and East Asia, which occurs despite declining NH_3 emissions. This increased conversion to ammonium is likely the result of increased bonding with the increased sulfate. Similar or smaller increases occur in Africa, the Middle East, Central America, and South America where NH_3 emissions increase. In Europe where emissions of both SO_2 and NH_3 decrease, the ammonium level is reduced by 0.1 to 0.3 μg m^{-3}. The global changes in nitrate are primarily the result of the chloride replacement mentioned previously.

The changes in SOA are negligible in most regions except South America and Indonesia, where SOA increases by as much as 1.2 μg m^{-3}. This is a result of greater oxidant levels leading to greater oxidation of isoprene and terpene species that form SOA in these regions. The changes are largely negligible even though the oxidant levels are enhanced, because there are only minor increases in the emissions of biogenic VOC precursors in regions outside the tropics and the declining POC levels leaves less organic material for the

SOA forming gases to partition onto to form aerosol. This result may also be a limitation of the SOA representation in the model, since the CB05GE-MADRID SOA formation mechanism only treats toluene and xylene as anthropogenic precursors, thus neglecting other precursors such as creosols, olefin, and long chain alkane species, and because the treatment is based on the classic multi-product method for SOA formation (Odum et al., 1996). This type of mechanism is more simplistic and underestimates SOA formation compared to the recently developed volatility basis set (Donahue et al., 2006) and molecular approaches (Couvidat et al., 2012). There are also some minor changes in the polar regions and these are artifacts that result from changes in SOA lofted in the tropics and subtropics that subside at the poles.

2.6 Aerosol-Climate Interactions

Figure 2.10 shows the changes in the column aerosol number concentration (NUM), CCN, CDNC, LWP, COT, AOD, SWDOWN, and the photolysis rate of NO_2. The global average NUM level increases by 1.2×10^8 cm^{-2}. The increases are the largest (3.0×10^8 to 1.1×10^9 cm^{-2}) in South America, South Asia, and South Africa, where SO_2 emissions increase the most, while the NUM level decreases mostly over Europe and northern/western Asia by 2.0×10^8 to 9.8×10^8 cm^{-2} in response to the largest decreases in SO_2 emissions. The comparable spatial trends between the NUM level and the SO_2 emissions indicate that the changes in NUM are dominated more by changes in the nucleation of new particles from sulfuric acid than by changes in primary aerosol emissions. However, the large decreases in primary particle emissions in central Africa do offset the impact of enhanced new particle formation sufficiently to result in a slight decrease in the NUM level (less than 1.0×10^8 cm^{-2}).

The changes in the CCN level mirror the changes in the NUM level with a global average increase in CCN of 6.0×10^5 cm^{-2}, and decreases in central Africa, Europe, and northern/western Asia due to declines in the NUM level.

LWP increases by 1.4 g m^{-2} on global average due to a combination of both increases in the CCN level and a global average increase in PWV of 1.1 mm (not shown). The impacts of increases in both cloudiness and CCN lead to a global average increase in CDNC of 2.2×10^3 cm^{-2}. The increased CCN tends to increases the CDNC and LWP the most in marine clouds. Over land, changes in CDNC are nosier with the exception of Europe and northern/western Asia, where the CDNC level declines by 5.0×10^4 cm^{-2} to 3.5×10^5 cm^{-2} in response to the declines in CCN, despite increases in LWP. The changes in COT mirror the changes in CDNC with a global average increase of 0.05 largely as a result of the increased CDNC in marine clouds.

Although surface concentrations of $PM_{2.5}$ can increase or decrease in some regions depending on the changes in surface emissions, the $PM_{2.5}$ concentration in the middle and upper troposphere (600-200 mb) generally increases by 0.1 to 1.2 μg m^{-3} (shown in Figure 2.11). This is a result of enhanced secondary formation of $PM_{2.5}$ from the enhanced oxidant levels and the poleward advection of global precursors and particles from tropical and subtropical regions. This increased $PM_{2.5}$ level in the upper portions of the troposphere leads to a global increase in AOD with an average increase of 0.03, despite regional decreases in the $PM_{2.5}$ level near the surface. AOD enhancements are the largest in the tropical and subtropical regions (0.1 to 0.2) due to both the increased formation of particles and the lofting of these particles due to strong vertical motion in this region. There are also strong

enhancements of AOD along the coasts of the continents due to the replacement of chloride by sulfate and nitrate that have higher refractive indices.

The combined enhancement of COT and AOD leads to dimming at the Earth's surface with SWDOWN declining by 1.6 W m^{-2} on global average. This declining in SWDOWN leads to a reduction in photolysis. For example, the NO_2 photolysis rate decreases on global average by 1.2×10^{3} min^{-1}. This decline in photolysis could decrease the production of O_3 as mentioned in section 2.5.1. However, the increases in NO_x emissions are able to overcome this feedback of the increasing aerosol level on photochemical activity. The dimming induced by aerosol enhancements to the global AOD and COT are also likely the cause for the milder warming of T2 compared to the CCSM3 model as mentioned in Section 2.3.2.

2.7 Deposition

Figure 2.12 shows the changes in the total deposition of O_3, nitrogen, NH_3, HNO_3, BC, and mercury between the AOF and AOC periods. The global increase in O_3 level leads to global increases in O_3 deposition (1.9×10^{-2} g m^{-2} $month^{-1}$ on average). The enhancements in O_3 deposition are the greatest in South Asia and East Asia, where enhancements range from 6.0×10^{-2} to 2.3×10^{-1} g m^{-2} $month^{-1}$. Similar enhancements in O_3 deposition occur in Africa, Central and South America, and Indonesia. The enhanced O_3 deposition will result in greater damage to crops in these developing regions with large populations.

The total nitrogen deposition (TND) is the sum of nitrogen deposited from NO, NO_2, NO_3g, HONO, HNO_3, PAN, N_2O_5, N_2O, NH_3, nitrate aerosol and ammonium aerosol. TND increases on global average by 1.4×10^{-3} g m^{-2} $month^{-1}$ due in large part to the increases in the

atmospheric oxidized nitrogen species from increasing NO_x emissions. An example is HNO_3 deposition that increases on global average by 3.8×10^{-3} g m^{-2} $month^{-1}$ with large increases in the tropics and subtropics, especially South Asia and East Asia, where HNO_3 deposition increases by 3.0×10^{-2} to 1.8×10^{-3} g m^{-2} $month^{-1}$. The increases in TND are more moderate than the changes in deposition of HNO_3 because the increases in the deposition of oxidized nitrogen species are offset by reductions in the deposition of reduced nitrogen species, due to declining NH_3 emissions. This is especially true in East Asia and Europe, where TND is reduced by 5.0×10^{-3} to 1.5×10^{-1} g m^{-2} $month^{-1}$ in response to decreases of 5.0×10^{-3} to 2.3×10^{-1} g m^{-2} $month^{-1}$ in NH_3 deposition. Overall, TND increases in the developing world including Central and South America, South and Southeast Asia, Indonesia, the Middle East, Indonesia, and the majority of Africa. This will add further stress to ecosystems that will also be exposed to vegetation damage from enhanced O_3 deposition.

BC deposition decreases on global average by 1.2×10^{-5} g m^{-2} $month^{-1}$, with the largest decreases (4.0×10^{-4} to 5.1×10^{-3} g m^{-2} $month^{-1}$) occurring in North America, East Asia, Europe, and Africa in response to decreasing BC emissions. BC deposition increases in the range of 8.0×10^{-4} to 6.7×10^{-3} occur in the Ural Mountains, the Andes Mountains, and the Tibetan Plateau, as a result of increasing BC emissions in South America, eastern Europe/western Asia, and South Asia and increasing precipitation. The enhanced deposition in these alpine regions has the potential to enhance snow melting by reducing the snowpack albedo (Warren and Wiscombe, 1980; Clark and Noone, 1985), which may impact water reservoirs that depend on alpine melt water (Qian et al., 2011).

Mercury total deposition increases on global average by 1.7×10^{-3} μg m^{-2} $month^{-1}$. Mercury, unlike the other pollutants in GU-WRF/Chem, does not have future emissions projections. Thus, the increasing deposition is the result of climate change. Mercury dry deposition (not shown) is mainly responsible for the increases (1.0×10^{-2} to 8.0×10^{-2} μg m^{-2} $month^{-1}$) over many continental areas including South Asia, East Asia, western Europe, central and southern Africa, and the Middle East. This is a result of both lower PBLH, which increases the surface concentration of mercury, and reductions in aerodynamic resistance due to declining wind speeds. Enhanced mercury wet deposition of 1.0×10^{-2} to 9.3×10^{-2} μg m^{-2} $month^{-1}$ from increased precipitation in the Tibetan Plateau and northeastern China also greatly contributes to the enhanced mercury deposition in these regions. The enhanced mercury deposition may lead to enhanced bioavailable methylmercury, which could increase the level of mercury in crops and aquatic life in these populated regions leading to greater human exposure (Zhang, H. et al., 2010; Meng et al., 2011].

2.8 Sensitivity Analysis

2.8.1 Impact of Climate Change on Air Quality

Figure 2.13 shows the changes in $O_3$8hr, $PM_{2.5}$, T2, Q2, WSP10, PBLH, PR, and the NO_2 photolysis rate between 2001 and the 2050_NPE simulation. The correlations between the changes in $O_3$8hr and $PM_{2.5}$ with these meteorological variables are listed in Tables 2.8 and 2.9, respectively. Under the 2050_NPE case, the $O_3$8hr level increases on global average by 0.6 ppb with increases of 1.0 to 3.8 ppb in many mid-latitude continental regions. This is largely in response to increases in temperature (R of 0.33), which increases by 1.2°C on global average but up to 4.2°C in these continental regions. The increasing temperature

increases the $O_3$8hr level by increasing reaction rates, increasing biogenic VOC emissions (1.8 mol km^{-2} hr^{-1} on global average), and increasing decomposition of PAN (e.g., PAN decreases by 10.0% on global average). However, in tropical and oceanic regions, the $O_3$8hr level is reduced by 0.3 to 1.8 ppb in response to increases in water vapor (0.8 to 2.6 g kg^{-1}) that cause greater O_3 destruction in these low NO_x environments. This explains the fairly substantial anti-correlation with Q2 (R of -0.29). Similar to the base 2050 case, the 2050_NPE case predicts a cloudier and more aerosol-rich future atmosphere. The increase in aerosols is the result of the increase in SOA from greater biogenic emissions and greater sulfate from increases in the level of H_2O_2 (0.1 ppb on global average) and available cloud water (2.7 g m^{-2} on global average). This leads to a global average decrease in SWDOWN of 2.5 W m^{-2} (not shown). The results are global average declines in PBLH of 27.9 m and the NO_2 photolysis rate of 1.6×10^{-3} min^{-1}. The decreased PBLH should lead to greater O_3 levels near the surface, increasing the $O_3$8hr level and thus changes in $O_3$8hr level and PBLH should be anti-correlated. However, there is a minor positive correlation (R of 0.16) with PBLH, indicating that the declining PBLH does not significantly impact the $O_3$8hr level. The correlations with WSP10 and the NO_2 photolysis rate are negligible, indicating that the $O_3$8hr level is not very sensitive to changes in photolysis and horizontal advection, These findings contrast somewhat with the multi-model ensemble predictions of O_3 increases over land and decreases in marine environments caused by climate change reported in Dentener et al. (2006) and Doherty et al. (2013). Since O_3 reductions from climate change are driven by increased water vapor in low NO_x environments, the dominant tendency for increased O_3 from climate change in GU-WRF/Chem is likely driven by smaller increases in water vapor

as seen compared to CCSM3 discussed in Section 2.3.2 and also the overprediction of column NO_2. The impact of increased temperatures on O_3 may also be exaggerated by the overprediction in T2.

The $PM_{2.5}$ level in the future is enhanced by 0.25 μg m^{-3} on global average in the 2050_NPE case. The changes in $PM_{2.5}$ are largely driven by changes in WSP10 (R of 0.38) especially over the oceans (R of 0.50), where the changes in WSP10 control the changes in emissions of sea-salt. In continental regions there is a smaller magnitude anti-correlation with WSP10 (R of -0.14), which indicates that some of the increasing $PM_{2.5}$ over land is in response to weaker horizontal advection. This is likely the cause of elevated $PM_{2.5}$ levels in south/central South America, western North America, western Russia, East and Southeast Asia, and off the coast of Indonesia, as the enhancements of 0.5 to 6.2 μg m^{-3} in these regions are caused largely by enhancements in BC, POC, and OIN that are more tracer-like than other $PM_{2.5}$ species. The future $PM_{2.5}$ level is also increased in response to increases of SOA, which increases as much as 0.6 to 1.0 μg m^{-3} in central Africa, South America, and Indonesia in response to increases in biogenic VOC emissions.

It is possible that reductions in PBLH height could contribute to increases in $PM_{2.5}$ but that contribution is likely minor compared to horizontal advection changes since the correlation of $PM_{2.5}$ to PBLH is close to zero (R of -0.01 globally and -0.06 over land). There is a small positive relationship between Q2 and the $PM_{2.5}$ level (R of 0.15), which could indicate enhanced $PM_{2.5}$ due to water availability and enhanced levels of H_2O_2, however, it is also likely that this is an artifact of changes in horizontal advection since Q2 would respond to changes in WSP10 in a similar fashion to $PM_{2.5}$. Changes in precipitation show little

impact on $PM_{2.5}$ (R of 0.01), consistent with findings of other studies reviewed in (Fiore et al., 2012). The findings here show a fairly strong influence of climate on $PM_{2.5}$ and contrast with the influence of climate on $PM_{2.5}$ discussed in section 2.5.2. This likely indicates that changes in emission dominate over these changes from climate; however, internal model variability from comparing only a single year may also play a role in this discrepancy.

The impact of climate change on O_3 and $PM_{2.5}$ provided here is generally consistent with large body of work focusing on the impact of climate change on future air quality (Jacob and Winner, 2009 and references therein; Fiore et al., 2012 and references therein). GU-WRF/Chem replicates increased O_3 in high NO_x environments, changes in $PM_{2.5}$ from sea-salt aerosols, higher SOA, and possible increases in regional stagnation. However, GU-WRF/Chem does not reproduce the significant loss of background O_3 from water vapor potentially due to biases in temperature, water vapor, and NO_2. The results presented here have not been proven to be significant compared to internal model variability as the resources are currently unavailable for long term unforced simulations against which the results can be compared. However, in Section 2.9.2 the climate change signals of at least T2 and Q2 in the simulations discussed in this work are shown to be statistically significant compared to current and predicted interannual variability.

2.8.2 Impact of Changing Emissions on the Future Climate

To examine the impact that changing emissions have on future climate, Figure 2.14 shows the absolute differences in AOD, NUM, CCN, CDNC, column average cloud drop effective radius (Reff), COT, SWDOWN, NO_2 photolysis rate, CF, PWV, LWP, PR, GLW, PBLH, T2, and Q2 between the 2050 simulation with projected emissions and the 2050_NPE

case. The general increase in emissions of some primary aerosol and precursor emissions increase the global AOD by 0.03 on global average. Changes in NUM and CDNC between these simulations are similar to the differences between the AOF and AOC periods. The NUM level increases on global average by 2.3×10^{8} cm^{-2}, which results in a global average increase of 1.2×10 cm^{-2} in CCN. This is primarily in response to increasing SO_2 and primary aerosol emissions in South America and South Asia. The projected emissions increase the global average CDNC level by 1.3×10^{3} cm^{-2}. The increases in CDNC primarily occur in the oceanic regions including the Indian Ocean, the South Atlantic Ocean, and the central Pacific Ocean. These regions experience increases in CDNC (5.0×10^{4} to 5.3×10^{5} cm^{-2}) due to a relatively high level of cloud formation (e.g., LWP of 50 to 192 g m^{-2}) that favors effective aerosol activation. The enhanced CDNC level leads to a reduction in the Reff by 2.0 to 65.5 μm in these regions, enhancing the cloud albedo and enhancing the COT by 0.1 to 1.9. In Europe and northern Asia, the NUM level is reduced by 1.0×10^{8} to 1.2×10^{9} cm^{-2}, in response to declining SO_2 and primary aerosol emissions. The result is a decrease in the CDNC level of 5.0×10^{4} to 5.2×10^{5} cm^{-2}. This reduction in CDNC allows the cloud droplets to grow larger (with Reff increases of 2 to 12 μm) resulting in decreases in COT of 0.1 to 1.0. The findings shown here for the SRES A1B scenario contrast with those of RCP scenarios discussed in the work of Westervelt et al. (2015). Under the RCP scenarios declines in primary aerosol and precursor emissions by the year 2100 result in consistent trends for reductions in AOD and also LWP of 0.5-1.0 g m^{-2} due to a reversal of the cloud lifetime effect. This allows for larger growth of existing droplets increasing Reff by 0.54-0.60 μm. Similar reductions in AOD and reductions in CDNC were reported with a subset of the RCP scenarios in the work of

Chalmers et al. (2012). A fairer comparison with the work of Jacobson and Streets (2009) show contrasting declines in NUM and subsequently CDNC following the SRES A1B scenario by 2030, but show increases in AOD, COT, and LWP that are qualitatively similar to those mentioned above from GU-WRF/Chem.

Over the remaining continental regions, the cloud-aerosol interactions are more complex. In Africa, portions of North America, north central South America, portions of East Asia, and Southeast Asia, the CDNC level is reduced with projected emissions despite increases in NUM and CCN. These reductions in CDNC occur in regions where cloud cover is reduced by 2.0 to 8.0 %, indicating that in these regions the atmosphere's ability to produce clouds and activate the aerosols is reduced with projected emissions. The reduced cloud cover in these regions is caused by a slightly drier atmosphere as evidenced by reductions in PWV of 0.1 to 0.9 mm and reductions in Q2 of 0.05 to 0.5 g kg^{-1}. It is difficult to pinpoint the exact reason for the reduction in cloud cover from the changes in emissions as the perturbation in emissions will perturb the surface radiation budget through direct scattering of radiation and also perturb the CDNC. The perturbed CDNC will, in turn, change the cloud structure and the stability of the atmosphere, which will modify the radiation budget again. However, there is one possible mechanism that would explain these declines in CDNC over some continental regions. In these continental regions, with declining CDNC there is a reduction in convective precipitation of 0.05 to 0.5 mm day^{-1}. Precipitation can either be enhanced or suppressed by changes in aerosol levels with low level clouds experiencing suppression and deep convective clouds experiencing enhancement (Rosenfeld et al., 2008). However, because convective cloud microphysics is not treated in GU-

WRF/Chem it is likely that the reduced convective precipitation is caused by a reduction in convective instability likely caused by reductions in SWDOWN from the increasing AOD (e.g., with an increase of up to 0.3 in the regions listed above). This reduced instability reduces the convective precipitation amount in some regions and also likely shifts the location of the precipitation as evidenced by the dipolar changes in precipitation. Similar mixed signals in tropical convective precipitation are seen under the RCP scenarios (Westervelt et al., 2015), and are conceptually similar to large scale perturbations in convective precipitation caused by aerosols shown to occur in the work of Lee et al. (2010). These movements or reductions in precipitation will eventually impact the hydrologic cycle by reducing the underlying soil moisture. This means that less moisture is available for evapotranspiration, which explains the drier atmosphere and reduced cloud formation in these regions. Since the atmosphere's moisture level is reduced, fewer aerosols can activate, leading to the reduction in CDNC. Since a fewer amount of aerosols can activate, only the larger particles that can reach the critical radius activate, leading overall to larger cloud droplets. This is evidenced by the slightly larger Reff (increase of approximately less than 6 μm) in these regions. The combination of reduced cloud coverage, reduced cloud water, or increases in Reff results in decreases of COT in these regions of 0.1 to 1.0. This reduction in COT can offset the initial impacts of the increased AOD in some of these regions (e.g., East and Southeast Asia, central Africa, and portions of North America), leading to increases in SWDOWN of 1.0 to 6.0 W m^{-2} and slight increases in T2 (0.2 to 0.4°C). This mechanism also explains why Q2 in these regions decreases despite increases in T2 that would cause enhanced evaporation. On a global scale, the enhanced COT and AOD from the projected

emissions results in a global average decrease in SWDOWN of 1.2 W m^{-2} and up to 18.5 W m^{-2} in the oceanic regions where COT increases the most. This reduction in SWDOWN reduces the NO_2 photolysis rate by 1.4×10^{-3} min^{-1} on global average. The changes in emissions do not have a substantial impact on global precipitation with a global average increase of 5.7×10^{-4} mm day^{-1}. However, as mentioned above, there can be regional shifts in precipitation. Despite the global decreases in SWDOWN, T2 increases on global average by 0.03°C. This is a result of the increases in SWDOWN over land from either the aforementioned mechanism or the reduced CDNC in Europe and northern Asia. There is no response in T2 over the oceans since GU-WRF/Chem uses prescribed sea surface temperatures. This illustrates a key limitation of such aerosol-climate interaction studies in atmospheric general circulation models and indicates that such a study is better suited for an Earth system model that has an active ocean model component. Westervelt et al. (2015) also reported increases in global average temperature and precipitation of 0.72-1.04ºC and 0.08-0.09 mm day-1, respectively following the RCP scenarios. However, these changes were linked to decreasing aerosol levels rather than the complex interactions discussed above. This increased temperature in all the regions except those mentioned above helps to enhance evapotranspiration on a global scale leading to global average enhancements of Q2 (3.0×10^{-3} g kg^{-1}), PWV (0.03 mm), and LWP (0.4 g m^{-2}). These global enhancements in atmospheric moisture variables lead to a slight enhancement in the downwelling of longwave radiation at the surface (0.1 W m^{-2} on global average).

2.9 The Impact of Climate and Emissions on East Asian Intercontinental Transport

2.9.1 Review of Intercontinental Transport Studies

Intercontinental transport of atmospheric pollution (ITAP) is of major concern as it can offset the impact of local emission control efforts in certain regions (Jacob et al., 1999; Lin et. al., 2008; Wang et al., 2009, 2012). ITAP of fine aerosols has also been shown to be a health hazard resulting in an estimated 90,000 premature deaths globally in 2000 (Liu et al., 2009). ITAP plays a large role in the Northern Hemisphere (NH), as this is the most populated part of the globe, with three major industrial centers including East Asia, North America, and Europe. East Asia is the most important source region as its lower latitudes and thus higher surface radiation and vertical transport make it more suitable for local ozone (O_3) photochemical production and transport (Bey et al., 2001; Wild and Akimoto, 2001; Stohl et al., 2002). As a result, the Asian free troposphere has been shown to have a large global impact on the seasonal variations and vertical structure of O_3 throughout the troposphere (Sudo and Akimoto, 2007). North America is also an important source to global pollution but it is the most affected receptor to Asian emissions and to a lesser extent to European emissions (Wild and Akimoto, 2001; Fiore et al., 2009). Europe is typically the weakest source region, as weaker convection and the dominance of high pressure systems in summer make horizontal boundary layer advection the primary transport mechanism and this type of transport is typically blocked by the Eurasian terrain and the pollutants are subject to greater local deposition, but transport to the Arctic makes Europe the most important contributor to Arctic haze especially in winter (Wild and Akimoto, 2001; Stohl et al., 2002).

Additionally, Europe is a receptor since East Asia has a large global impact (Wild and Akimoto, 2001).

Transport from East Asia to North America occurs primarily through uplifting associated with the warm conveyor belt of mid-latitude cyclones, which lofts the pollutants into the lower free troposphere (FT) where they are transported by westerly winds (Bey et al., 2001; Husar et al., 2001; Hess et al., 2003; Jaffe et al., 2003; Liu et al., 2003; Cooper et al., 2004; Wang et al., 2009, 2012). Additional transport pathways include planetary boundary layer (PBL) outflow behind cold fronts (Liu et al., 2003; Wang et al., 2009, 2012), orographic uplifting in China (Liu et al., 2003), and strong convection (Liu et al., 2003; Takigawa et al., 2005). This uplift is usually associated with fast transport that can occur in as quickly as six days (Jaffe et al., 1999, 2003). Intercontinental transport from North America to Europe has not only been linked to uplift from warm conveyor belts, but also to pyro-convection from wild fires (Ravetta et al., 2008). Wang et al. (2009) showed that certain pollutants such as CO, O_3, $PM_{2.5}$, and SO_4^{2-} favor transport in both the PBL and lower FT, while other pollutants such as PAN, SO_2, and NO_3^- primarily transport in the lower FT. Wang et al. (2012) showed that dust particles transport at altitudes above 5 km.

Although it may be counter-intuitive, ITAP plays a much larger role in the boreal spring and autumn months as compared to the summer when production of pollutants such as O_3 is higher (Wild and Akimoto, 2001; Shindell et al., 2008; Fiore et al., 2009; Jonson et al., 2010). This is because although convective uplift is greater in the summer, there is more stagnation and thus less significant horizontal transport. Additionally, the lifetime of O_3 is relatively shorter in the summer months due to the additional water vapor resulting from

greater evaporation. This occurs because (1) there is a greater chance for $O(^1D)$ to react with H_2O to form OH rather than O which reduces O_3 production, and (2) the increased OH or HO_2 from this process can react with O_3 directly. The decreased production and increased destruction occur in the remote marine environments and FT, where the mixing ratios of O_3 precursors are low and most O_3 transport occurs. However, it is important to note that the increased OH in the terrestrial PBL leads to greater production of O_3 from reactions with volatile organic compounds (VOCs) that dominates over its destruction. Thus, transport is most effective in spring as the frequency of uplift from mid-latitude cyclones is high and the westerly transport is more direct (Wild and Akimoto, 2001). However, it can still play a minor role in the summer, e.g., it accounts for 3% of the North American O_3 budget (Pfister et al., 2008).

The Task Force on Hemispheric Transport of Air Pollution (HTAP) was formed in 2004 to improve the understanding of ITAP in the NH. The HTAP program included a multi-model ensemble of experiments that compared the impact of 20% reductions in anthropogenic emissions from their baseline levels in the four largest industrial centers including Europe, North America, East Asia, and South Asia. The aim of these multi-model ensemble experiments was to estimate the sensitivity of each region's ambient pollution to these emission reductions. These studies, along with others, were compiled into the 2010 Task Force on Hemispheric Transport of Air Pollution report (TF-HTAP) (http://www.htap.org/). These experiments found that, during spring months, the 20% emissions reductions largely from Asia can reduce the ozone level by over 1 ppb or greater at Trinidad Head, CA at the surface and throughout the troposphere (Jonson et al., 2010). These

reductions in East Asia emissions typically result in a decrease in the maximum 8-hr O_3 mixing ratio $O_3$8hr by ~0.9 ppb regardless of its level in the western U.S., but its magnitude of decrease varies with the $O_3$8hr level in the eastern U.S. (e.g., decreasing by 0.65 and 0.3 ppb at lower and higher $O_3$8hr, respectively) (Reidmiller et al., 2009). The emission reductions of O_3 precursors from East Asia were estimated to decrease the annual mortality rate in North America by 200 deaths but could decrease the number of premature deaths by as much as 5,900 over the entire NH (Anenberg et al., 2009). The experiments also revealed that long-term responses of surface ozone concentrations to emissions reductions of CH_4 are as large as the impact from reducing emissions of nitrogen oxides (NO_x), total non-methane VOCs, and CO combined (Fiore et al., 2009). A subset of the HTAP models reveals that projected climate change increases the impact of reducing anthropogenic emissions in source regions but reduces the impact on receptor regions (Doherty et al., 2013). In addition to the impacts on O_3, these emissions reductions have been shown to decrease the reactive nitrogen deposition in North America by 1.3% (Sanderson et al., 2008). The HTAP modeling also showed that East Asia contributes 19%, 31%, 29%, and 28% to the Arctic sulfate, black carbon (BC), CO, and O_3, respectively during the spring months. During the summer months when the BC snow albedo feedback is the strongest, BC deposition from East Asia is important and comparable to that from North America (Shindell et al., 2008).

Other studies have also investigated the impact of long range transport of East Asian aerosols (Park et al., 2004; Hadley et al., 2007; Koch et al., 2007; Liu et al., 2008; Yu et al., 2008; Leibensperger et al., 2011). It is estimated that 4.4 Tg a^{-1} of fine aerosol pollution is imported to North America from Asia, which is equivalent to approximately 15% of local

emissions (Yu et al., 2008). This transport contributes 10-30% and 30-50% to the background sulfate over the eastern and western U.S., respectively, and 75% to the BC over North America (Park et al., 2004; Hadley et al., 2007; Liu et al., 2008). Emissions of other compounds such as NO_x and CO in East Asia have also been shown to increase the concentrations of fine particles ($PM_{2.5}$) by 1.0 μg m^{-3} in the eastern U.S. (Leibensperger et al., 2011). Additionally, aerosols emitted from East Asia can have several climatic impacts (Lau et al., 2006a, b; Menon et al., 2002; Roberts et al., 2006; Qian et al., 2003, 2006, 2007; Zhang, R. et al., 2007). Compared to ultrafine marine aerosols, long range transport of anthropogenic particles in stratified layers from 1000-7000 m above the surface of the Eastern Pacific have been shown to play a more important role in the aerosol direct and indirect effects as their larger size increases their likelihood of activation and thus effectiveness of scatter radiation (Roberts et al., 2006). Light absorbing aerosols have been linked to the enhancement of winter time convection over the North Pacific (Zhang, R. et al., 2007) and to dynamic and thermodynamic feedbacks that can alter the Asian monsoon (Lau et al., 2006 a, b). The light absorbing BC aerosols emitted in East Asia have also been shown to result in dimming of 1.45-1.47 W m^{-2} in the western U.S. (Hadley et al., 2007). In China, increasing aerosol emissions provides a plausible explanation for the decreasing solar radiation reaching the surface despite decreasing cloud cover (Qian et al., 2003, 2006, 2007). It has also been shown that areas with high anthropogenic emissions, such as East Asia, can contribute substantially to the formation of local biogenic secondary organic aerosol (BSOA) (Carlton et al., 2010 and references therein).

There are several methods that can be employed to calculate the sensitivity of a chemical species in the atmosphere to transport from a particular source. The simplest method is the so-called "Brute Force" method in which the sensitivity of atmospheric pollutant can be calculated by comparing two simulations, one with and one without emissions in the area of interest. The advantages of this method are that it is straightforward and it accounts for the full non-linear effects of chemistry. However, it has been shown that the results from this method are susceptible to model noises, since the contributions from the source regions can be of the same order of magnitude or smaller than differences between the two simulations resulting from model noises in some cases (Brandt et al., 2012). A more complex method is the so-called "tagged tracer" method, where the concentration of a particular species (i.e., a tracer species) in a particular region is modeled and calculated in parallel with the background species concentration. This method is typically applied for a limited number of species and thus does not represent the full non-linear effects of chemistry with the background concentration; but it works well for species that are tracer-like such as CO (Fischer et al., 2010; Brandt et al., 2012). This method has been recently updated to represent non-linear effects and is less susceptible to the influence from model noises (Brandt et al., 2012). The most complex method is an adjoint approach. The model is viewed as an operator that acts on various vectors representing the initial concentrations of a particular set of species and a vector representing a set of parameters that correspond to the evolved concentration at a later time. The adjoint model calculates the sensitivity of a scalar model response function based on the given parameters which can correspond to chemical species at

a given time or source location (Henze et al., 2009). This approach, however, does not account for the non-linear effects of chemistry.

This sensitivity experiment aims to determine the role of the ITAP from East Asian anthropogenic emissions (EAAEs) in global air quality and climate under current and future emissions and climate scenarios using the "Brute Force" method (BFM). The BFM is used because its implementation is straightforward and it also accounts for the non-linear effects of chemistry. Specifically, several science and policy-related questions will be addressed. For example, how will the role of ITAP change under future scenarios? What processes and factors will dominate such changes? How much BSOA can be reduced through reducing EAAEs? Such information would be very useful to guide the development of future emission control and climate mitigation strategies in a changing climate.

2.9.2 Representativeness of 2001 and 2050

The simulation results in 2001 and 2050 are first compared with the averages of AOC and AOF, respectively, to determine their representativeness as a typical year for current-year and future-year climatology. This is to illustrate that the changes in meteorology between 2001 and 2050 are representative of the climate change signal with longer runs and therefore the differences presented in this study are representative of climate change rather than differences in simulated meteorology or internal model variability. The predictions of GU-WRF/Chem are also compared with those from an established climate model, i.e., the NCAR's CCSM3 to demonstrate its skills in simulating current and future climate. Figure 2.15 compares the average MAM 2-m temperature (T2), 2-m water vapor mixing ratio (Q2), precipitation rate (PR), and planetary boundary layer height (PBLH) for the GU-WRF/Chem

2001 and AOC NCEP-FNL simulations and CCSM3 initial conditions (2000-2014). Similar plots for 2050 are shown in Figure 2.16 in contrast to the AOF from GU-WRF/Chem and CCSM3 initial conditions (2015-2055).

In general, the 2001 and 2050 simulations have the same general spatial pattern as the AOC and AOF from GU-WRF/Chem, respectively. The global average T2 in 2001 and 2050 is -~0.6°C cooler and 0.5°C warmer than the AOC and AOF values, respectively, while the 2001 mean is 0.75°C warmer than the CCSM3 current period and the 2050 mean is ~4.0°C warmer than the CCSM3 future period. The discrepancy between GU-WRF/Chem and CCSM3 most likely results from a warm bias of ~1.2°C against the National Climatic Data Center (NCDC) global observations for the 2001 MAM period, this level of bias is consistent with other global models (Bader et al., 2004; John and Soden 2007; Tian et al., 2013). The discrepancy between GU-WRF/Chem and CCSM3 predictions in the future period likely results from the GU-WRF/Chem simulation being initialized with CCSM3 data, which appears to generate a warmer atmosphere than the simulation with a shorter reinitialization interval. This is also evident in the current year period initialized with CCSM3 data shown in Figure 2.17. The differences between the individual years of 2001 and 2050 and longer term average AOF and AOC are smaller than the differences between the average current and future periods from both simulations initialized with CCSM3 data (1.37°C warming between 2050 and 2001, 0.79°C warming between AOF and AOC, and 1.46°C warming between CCSM3 AOF and CCSM3 AOC), indicating that the differences in T2 between the subset period, i.e., 2050 and 2001 are representative of the average climate change between future and current years. The global average Q2 is 0.08 g kg^{-1} less in 2001 than AOC and 0.02 g kg^{-}

^{1} more in 2050 than AOF. The differences against CCSM3 are higher (0.25 g kg^{-1} between 2001 and CCSM AOC and 0.84 g kg^{-1} between 2050 and CCSM AOF), which may be due to an over-prediction of ~0.4 g kg^{-1} in the GU-WRF/Chem baseline simulation. Similarly to T2, the climate change signal between the current and future simulations initialized with CCSM3 data (i.e., 0.67 g kg^{-1} increase between 2050 and 2001, 0.37 g kg^{-1} increase between AOF and AOC, and a 0.55 g kg^{-1} increase between CCSM3 AOF and CCSM3 AOC) is larger than the discrepancies between the single years and the longer term average AOF and AOC of GU-WRF/Chem simulations.

GU-WRF/Chem does not produce a strong climate signal for PR with only small increases of 0.02 mm day^{-1} between 2001 and 2050 and 0.01 mm day^{-1} between AOF and AOC. For comparison, the increase in PR between CCSM3 AOF and CCSM3 AOC is 0.08 mm day^{-1}. The differences in climate change signal in PR between the two models are mainly due to differences in the cumulus and resolved cloud schemes. These differences are similar in magnitude to the discrepancies between 2001 and AOC (0.01 mm day^{-1}) and 2050 and AOF (0.02 mm day^{-1}), indicating that differences in this parameter cannot clearly be differentiated from internal model variability. Changes in the PBLH between the CCSM3 output and GU-WRF/Chem are quite large. There is a trend of decreasing PBLH in GU-WRF/Chem with global average decreases of 29 m between 2001 and 2050 and 15 m between AOF and AOC, whereas the changes in PBLH are insignificant between CCSM3 AOF and AOC (with an increase of 1 m). This discrepancy in climate change signal in PBLH between models is due to differences in the PBL parameterizations used different models

(Murazaki and Hess, 2006). However, the climate change signal is much larger than the variability between years (11 m between 2001 and AOC and 8 m between 2050 and AOF).

In order to further illustrate that the differences between the years 2001 and 2050 are indicative of climate change, a number of meteorological variables including T2, Q2, PR, sea level pressure (SLP), the wind speed at 10-m (WSP10), the wind speed at 5500-m (WSP5500), net incoming shortwave radiation at the Earth's surface (GSW), downwelling longwave radiation at the Earth's surface (GLW), and outgoing longwave radiation at the top of the atmosphere (OLR) are evaluated against statistical criteria to determine if the differences between these individual years are statistically significant and if the differences are outside the range of current and future climate variability. Statistical significance is determined using a two tailed student t-test. The distributions of 2001 and 2050 are based on the hourly output from the MAM time period resulting in distributions of 2208 values with the exception of precipitation, which is evaluated daily with 92 values for each distribution. The differences in the mean MAM values are considered to be statistically significant if the probability that the values in each grid cell are from the same distribution is less than 5% (i.e., 95% confidence).We quantify interannual variability for a given variable using the standard deviation of the mean MAM values from a 13-yr current year period (2000-2013) and a 10-year future year period (2045-2054). In this study we determine that the difference is outside the range in current and future climate variability if the difference between the 2001 and 2050 MAM mean value is greater than one standard deviation of the mean MAM values from both the current and future periods. The current year standard deviation for each variable is computed from both the CCSM3 output and available satellite and reanalysis

datasets. These datasets include the National Centers for Environmental Prediction Final Operational Analysis (NCEP-FNL) used to compute the standard deviation in the current MAM means of T2, Q2, WSP10, WSP5500, and SLP, the Global Precipitation Climatology Project (GPCP) used for PR, and the Clouds and Earth's Radiant Energy System Data (CERES) used for GSW, GLW, and OLR. The standard deviation for the future period is also calculated from the CCSM3 output. GLW is not evaluated against CCSM3 data as it is not readily available.

Figure 2.18 shows the mean MAM difference between 2050 and 2001 that is statistically significant and greater than current and future climate variability for T2, Q2, WSP10, WSP5500, SLP, PR, GSW, GLW, and OLR. T2, Q2, and GLW pass the climate signal test mentioned above on a global scale with global increases of ~1.2°C, ~0.82 g kg^{-1}, and ~8.0 W m^{-2}, respectively. The differences in WSP5500, SLP, and OLR tend to be significant on a more regional basis. The regional changes in SLP near Alaska and changes in WSP5500 over East Asia and western North America have important consequences on intercontinental transport and are discussed in greater detail in section 5. Although the significant changes in OLR are regional in nature, there is a decrease on global average of ~1.2 W m^{-2}. This decline in OLR and increase in GLW is consistent with enhanced anthropogenic longwave radiative forcing from increases in greenhouse gases. Compared to the other variables, the significant differences in PR, WSP10, and GSW have much less spatial coverage, indicating that these variables have a much weaker climate change signal. This is also consistent with the above analysis of the differences in the PR means. However, some of the significant differences in WSP10 are important to changing transport patterns

discussed in Section 2.9.4. The significant differences in GSW show a global decrease of ~2.1 W m^{-2}, consistent with the cloudier and more aerosol rich atmosphere that is predicted in the future by GU-WRF/Chem. Similar analysis is performed on the difference between the MAM AOF and AOC time periods as shown in Figure 2.19. Figure 2.19 shows similar changes to Figure 2.18 in general with slightly less of a robust signal. This is a result of the fact that the AOF and AOC time periods are the averages of multiple years spaced 10 years apart and thus the trend between 2050 and 2001 is dampened during the averaging resulting in more of the values falling into the range of interannual variability or being less statistically significant.

Overall, although some differences between climate change signals obtained using single year differences (i.e., 2050-2001) versus multi-year average differences (i.e., averages of 2020, 2030, 2040, and 2050 minus averages of 2001 and 2010) are due to interannual variability, the above comparison suggests that the differences in meteorology and subsequently chemistry between the 2001 and 2050 simulations are generally representative of a climate change signal obtained using multi-year averages of GU-WRF/Chem simulations. The climate change signals from both the subset of years and the GU-WRF/Chem averages for temperature and humidity are comparable to those from CCSM3, demonstrating the skills of GU-WRF/Chem in simulating current and future climate. Some differences exist for PR and PBLH simulated by the two models, mainly because they are more sensitive to the individual models' physical parameterizations (i.e., cumulus/resolved cloud and PBL schemes) than temperature and water vapor. The changes in temperature, humidity, long wave radiation, wind speeds, and SLP between the individual years have also

largely been shown to be statistically significant and greater than one standard deviation of the mean MAM values from both a 13-year current and 10-year future climate period.

2.9.3 Changes in Future Emissions

As mentioned in Section 2.2, the future emissions projections for this work are generated using region-wide growth factors for seventeen world regions for the A1B emission scenario, thus the emissions projection in this case will be referred to as GU-WRF/Chem A1B since the future emissions are derived from the GU-WRF/Chem base emissions inventory. Figure 2.20 shows the logarithm of the effective growth factors for the 2050 emissions versus the 2001 baseline emissions. The anthropogenic emissions of O_3 precursors, NO_x and VOCs, increase over most of the globe, with the exception of the U.S., Canada, western Europe, Australia, and portions of northern Asia, leading to global average increases by 38% and 23%, respectively, according to the A1B scenario. The East Asian region NO_x increases by ~25-300% and VOC increases by ~25-150%, indicating a potential for increased O_3 and peroxyacetyl nitrate (PAN) production in East Asia. Anthropogenic CO emissions decrease by ~11% on global average. Developed regions in North America, Australia, Europe, and northern Asia show the largest declines (~20-97%), while developing regions in Africa, South America, and South Asia experience increasing emissions (25%-280%). The impact of these emissions on total East Asian CO emissions is uncertain, as the decrease over China and increases over South East Asia are similar (< 25%) and there are increases in biogenic emissions over Southeast Asia and northeastern China (Figure not shown) that may have some impacts (10-30%).

The trends vary in anthropogenic emissions of fine particulate matter ($PM_{2.5}$) precursors and primary anthropogenic emissions. SO_2 emission reductions over the northern hemisphere vary from smaller decreases (< 20%) in China, Japan, and the U.S. to larger decreases (60-92%) in Europe and northern Asia. These decreases are compensated by large increases (99%-1500%) in South Asia, South America, and Africa, leading to a global average increase by 20%. The trend is slightly different for NH_3 emissions (not shown) with decreases by less than 20% in the conterminous U.S., 20-37% in China, and 50%-83% in Europe and increases by 25-99% in Mexico, northern Asia, and South America and larger increases in Africa of up to 195%. Black carbon (BC) emissions are reduced largely in the U.S., Canada, Japan, western Africa, and western Europe (20-60%) with smaller decreases in China (< 20%) and increases over the remainder of the globe. Emissions of primary organic aerosol (POM) largely decrease by 20-75% over much of the globe, with the exception of northern Asia, North Africa, Australia, and portions of South America, leading to a global average decrease by ~19%. These emission changes give no clear insight into the possible changes in East Asian $PM_{2.5}$ as changes over Southeast Asia are typically opposite to those over China and Japan. Overall, North America, with the exception of Mexico, will experience a decline in local anthropogenic emissions by 2050 based on the A1B scenario. Thus, increases in ambient concentrations of pollutants in NA could be attributed to enhanced transport from other regions, enhanced natural emissions, or enhancements from climate change.

The SRES A1B emissions used in this study are not directly comparable to any of the current IPCC representative concentration pathway (RCP) emission scenarios because the

two sets of emission scenarios were derived using fundamentally different approaches. The A1B SRES scenario was developed for IPCC AR4 based on detailed socioeconomic storylines to generate emissions. RCP emissions were developed for AR5 by a parallel process for the identification of important characteristics for scenarios of radiative forcings for climate modeling (Moss et al., 2010). RCP emissions are thus climate policy scenarios that provide inputs for climate and atmospheric chemistry modeling; and they are not designed to span a range of socio-economic conditions. A set of emission scenarios that are based on updated socioeconomic pathways is being developed, i.e., the Shared Socioeconomic Pathways (SSPs) (Kriegler et al., 2012; van Vuuren et al., 2012), which is more comparable to the SRES emission scenarios.

Nevertheless, it is still useful to compare the two sets of emission scenarios because they provide an important outlook on future emissions and have been widely used. The moderate RCP pathway with a stabilization of anthropogenic radiative forcing at 6 W m^{-2} by 2100 (RCP6) is an updated version of the SRES B2 scenario which predicts less greenhouse gas emissions in the near future compared to A1B (IPCC, 2000; Masui et al., 2011). The RCP scenario with a stabilization of anthropogenic radiative forcing at 8.5 W m^{-2} by 2100 (RCP8.5) is an updated version of the SRES A2 scenario, which has similar or slightly larger increases in greenhouse gas emissions compared to A1B (IPCC, 2000; Riahi et al., 2011). A comparison of the temporal evolution of Global and East Asian emissions of NO, VOCs, BC, primary organic carbon (POC), CO, SO_2, and NH_3 for the GU-WRF/Chem A1B, RCP6, and RCP8.5 emissions scenarios is shown in Figures 2.21 and 2.22.

Globally all species, except CO and NO, have emissions that are larger than the RCP scenarios for the base year (2001 for GU-WRF/Chem A1B and 2000 for RCP). The largest differences between the emission inventories occur for VOCs, BC, and POC where the emissions used in GU-WRF/Chem A1B are roughly one to two orders of magnitude larger than those from the RCP scenarios. Assuming the same atmospheric conditions, this implies that the predictions of anthropogenic $PM_{2.5}$ and O_3 from GU-WRF/Chem will generally be larger than those predicted using the RCP scenarios. The global trend in VOC emissions between all scenarios is roughly the same, where emissions increase then decline to 2050. In the GU-WRF/Chem A1B scenario, the emissions of BC and POC decrease from 2001 to 2030 and then increase from 2030 to 2050. This is an opposing trend to the RCP scenarios, where BC and POC decline from 2000 to 2050. In the case of CO, the GU-WRF/Chem A1B scenario shows increasing emissions until 2030 followed by decreases in emissions to 2050 in contrast to the general decreasing trend in both RCP scenarios. NO and SO_2 emissions from the GU-WRF/Chem A1B scenario increase from the base year through 2050, while both RCP scenarios generally predict decreasing emissions. There is an opposing trend in NH_3 emissions as GU-WRF/Chem A1B predicts a slight increase by 2030 and then a much sharper decline to 2050 compared to the general increasing trend in NH_3 emissions from the RCP emission scenarios. Overall, these trends would suggest that the GU-WRF/Chem A1B scenario will predict a more polluted future compared to what would be predicted using the RCP scenarios.

The East Asia trends shown in Figure 2.22 differ from the general global trends discussed above in Figure 2.21. The trend in the emissions of NO, VOC, and SO_2 in East

Asia from GU-WRF/Chem A1B scenario are more comparable to the RCP6 scenario than RCP8.5, while the trends in BC, POC, and CO are more comparable to the RCP8.5 scenario. Also, the GU-WRF/Chem A1B trend in NH_3 emissions is strikingly different from the RCP scenarios. During the time period considered here, this implies that anthropogenic production of O_3 in East Asia would be the largest in 2050 following the GU-WRF/Chem A1B and RCP6 scenarios with greater production in the GU-WRF/Chem A1B scenario, while in the RCP8.5 scenario O_3 production would be at its greatest in the year 2020. This of course assumes that changes in emissions will dominate over changes in meteorology. The East Asian trend in primary aerosols from the GU-WRF/Chem A1B scenario is more comparable to the RCP8.5 scenario as both scenarios experience decreasing emissions by 2050, unlike the RCP6 scenario that predicts increasing primary aerosol emissions. However, because the primary emissions from GU-WRF/Chem are much larger than the RCP emissions, it will always predict greater concentrations than either RCP scenario. The differences in emissions also imply differing possible changes in secondary aerosol formation. In the GU-WRF/Chem A1B scenario and the RCP6 scenario, the sulfate formation in East Asia is expected to be enhanced around 2050 due to increasing SO_2 emissions with a greater enhancement in GU-WRF/Chem A1B, while the sulfate formation for RCP8.5 should be reduced in 2050 due to declining SO_2 emissions. The increasing NH_3 emissions in both RCP scenarios also allows for the possibility of increased secondary aerosol formation even with decreasing SO_2 emissions, since the increased availability of NH_3 may help enhance nitrate formation given suitable atmospheric conditions. Similarly, the decline in NH_3 emissions in GU-WRF/Chem

A1B may limit the impact of increased SO_2 emissions and could potentially reduce nitrate formation, given suitable conditions.

2.9.4 Impact of EAAE on Current and Future Air Quality

The predicted flow patterns at 10 m and 5500 m and the sea level pressure for 2001, 2050, AOC, and AOF are shown in Figure 2.23, which illustrates two major pathways of ITAP for East Asia. At the surface, there is both a southerly track that exports pollutants to the Arctic due to the cyclonic circulation around the Aleutian Low and a westerly track that transports pollution to western North America from anticyclonic circulation around the Pacific High. This is similar to the findings reported in Zhang et al. (2008), which indicated that these two transport pathways were considered to be representative of Trans-Pacific transport climatology. In general, the surface pressure patterns are similar among all scenarios with a few key exceptions. In 2050, 2050_CCO (Figure not shown), and AOF the Aleutian Low strengthens leading to greater circulation than in 2001 or AOC, which results in enhanced transport to the Arctic. Additionally, there is an increase in sea level pressure off the coast of Scandinavia (to a lesser extent in AOF than 2050) which increases the wind speeds over northern Europe and Scandinavia compared to 2001 and AOC. In the free troposphere, transport is primarily westerly. Simulated wind speeds aloft increase over polluted portions of East Asia and decrease over western North America in 2050, 2050_CCO, and AOF. This increases the westerly export of pollutants lofted into the free troposphere from East Asia, while simultaneously increasing the lifetime of these pollutants over North America, and thus increases the likelihood of subsidence to the surface in the receptor regions.

Figure 2.29 shows the differences in max 8-h O_3 mixing ratio and the differences in the 24°N to 60°N meridional averaged vertical profiles of O_3 between the simulations with and without EAAEs for 2001, 2050, and 2050_CCO. In 2001, O_3 generated by EAAEs contributes 1.2 ppb to the max 8-h O_3 on a global average, with higher values in several regions (e.g., 3-33.5 ppb in East Asia, 1-2 ppb in western North America, and 1-3 ppb in the Arctic). In 2050, this contribution increases to ~2 ppb of max 8-h O_3 on a global average, and in several regions (e.g., 4-44.6 ppb in East Asia and 2-5 ppb in western North America and the Arctic). This is primarily a result of projected increases in East Asian emissions of O_3 precursors in the future, with some regional enhancement from climate change. The 2050_CCO simulations have the same contribution of 1.2 ppb on global average as 2001, but a somewhat different pattern in regional contributions (e.g., 3-37.7 ppb in East Asia, 1-3 ppb in western North America and the Arctic). The differences in O_3 between the 2001 and 2050_CCO simulations are the result of the 1-3 ^{0}C increase in temperature over most of East Asia (except southeast China with cooling by ~1 ^{0}C) and changes in the atmospheric flow pattern. 2050 has enhanced Arctic transport from the enhanced circulation around the Aleutian Low, which leads to an increase of O_3 in the Arctic, especially Alaska and western Canada. The 2050_CCO simulations show eastward and northward transport of the plume that is stronger than 2001 due to higher temperatures but weaker than 2050 due to lower O_3 precursor emissions. There is also an enhancement in western Mexico, due to a combination of less water vapor, which increases the lifetime of O_3, and greater subsidence of O_3 from the reduction in wind speeds aloft.

The vertical cross sections of O_3 show large differences between 850 mb and 400 mb for all simulations and the gradients are tilted toward the east, indicating that the O_3 is uplifted and carried eastward. A strong gradient exists near the surface from 120°E to 120°W, indicating a significant transport of O_3 in the PBL between East Asia and western North America. In 2050, greater generation of O_3 from increased precursor emissions and temperatures leads to greater lofting of O_3 into the FT and subsequently greater subsidence of O_3 downwind compared to 2001. In 2050_CCO, there is less lofting and thus less of a downwind impact on O_3 as compared to 2001. This results from increases in atmospheric stability, particularly from the surface to ~850 mb, which inhibits vertical transport. This indicates that future emission changes may overwhelm natural transport restrictions from climate change.

EAAEs also enhance the levels of other trace gases such as carbon monoxide (CO), sulfur dioxide (SO_2), and peroxyacetyl nitrate (PAN). EAAEs contribute ~13 ppb and ~16 ppb to the global average CO level under the current and future scenarios, respectively; the increase in 2050 mainly results from emission increases in Southeast Asia as the 2050_CCO simulations with and without EAAEs show only a slightly increased contribution (~14 ppb on global average) as compared to 2001. The impact of EAAEs is fairly uniform across the entire NH where they typically account for 5-10 and 10-30 ppb of the CO level in 2001 and 2050, respectively, but the impact is greater in immediate downwind regions such as North America, where the impact is 10-25 ppb in 2001 and 15-35 ppb in 2050. EAAEs-induced SO_2 has a weak transport signal as it accounts only for ~1- 5 ppb in local areas of east China and northeast India under current and future scenarios, but has a negligible contribution

elsewhere. EAAEs contribute ~2 ppb SO_2 to the 24°N to 60°N meridional averaged surface concentrations with a decreased contribution of ~0.05 ppb up to ~450 mb between 75°E and 150°E and negligible contributions elsewhere. PAN exhibits a similar spatial distribution of contributions as O_3 since they share the same precursors. In 2001, EAAEs contribute ~0.04 ppb (0.2-1.0 ppb East Asia) to the global average PAN level and this nearly doubles to ~0.07 ppb (0.2-1.8 ppb in East Asia) in 2050 as a result of increased precursor emissions. The 2050 emission increase also generates contributions of 0.1-0.2 ppb to the PAN level over the majority of the NH compared to a more negligible contribution in 2001. The 24°N to 60°N meridional averaged vertical PAN contribution exhibits a similar trend. In 2001 EAAEs contribute ~0.3-0.5 ppb of PAN in East Asia between the surface and 700 mb. The contribution is ~0.1-0.2 ppb over much of the North Pacific and portions of western North America above 900 mb, indicating that there is transport aloft but the subsidence to the surface is negligible. In 2050, the contribution over East Asia increases to ~0.3-0.9 ppb from the surface to roughly 450 mb due to the increase in precursor emissions. The enhancement of PAN aloft leads to additional eastward transport with contributions of ~0.1-0.2 ppb at the surface in western North America, Europe, and North Africa due to subsidence.

Figure 2.25 shows the differences in the 24-hr averaged surface concentrations and the 24°N to 60°N meridional averaged vertical profiles of $PM_{2.5}$ with and without EAAEs for 2001, 2050, and 2050_CCO. The impact of EAAEs on $PM_{2.5}$ is not as homogeneous as the impact on some trace gases because its concentration and formation are more sensitive to changes in climate. On a global average, EAAEs account for 0.3-0.4 μg m^{-3} in all scenarios with a slight increase from 0.32 in 2001 to 0.39 μg m^{-3} in 2050 on a global average but larger

increases in some regions (e.g., up to 3 μg m^{-3} in the Pacific Ocean) (despite projected reductions in primary aerosol emissions in 2050), with most of the positive contributions over East Asia and the North Pacific. Over the interior of North America in all scenarios, EAAEs reduce the surface $PM_{2.5}$ level by 0.5 - 1.5 μg m^{-3}. This can be attributed to the increased PBLH generated by EAAEs in this region. The mechanism by which EAAEs can impact PBLH is discussed in greater detail in Section 2.9.5. A similar situation occurs over Scandinavia in the 2001 simulations, where EAAEs reduce the local $PM_{2.5}$ level (by ~0.5-3 μg m^{-3}). This impact is larger than that over North America due to low wind speed conditions over Scandinavia, during which vertical mixing becomes the strongest meteorological process impacting $PM_{2.5}$ (with wind speeds < 1 m s^{-1}), but does not occur in 2050 or 2050_CCO due to the low pressure center that moves into this area in the future scenarios. Feedbacks from EAAEs to the 10 m wind speed (see Figure 2.27) are distinctly different among all scenarios, which lead to differences in the concentrations of sea salt emitted in marine environments and concentrations of dust emitted over North Africa. This implies that such feedbacks are heavily dependent on both anthropogenic emissions and climate. The contribution to the vertical distribution of $PM_{2.5}$ shows distinct difference between the impact in the PBL and lower FT, where the impact can be either an increase or a decrease, and that in the middle and upper free troposphere, where the impact is entirely an increase. This occurs because only stratiform cloud feedbacks are treated in this version of the model and these clouds are typically not present above ~500 mb. At this altitude, EAAEs increase the $PM_{2.5}$ level by 0.1-1.0 μg m^{-3}. This is why the impact on aerosol optical depth (AOD) (see

Section 2.9.5) is almost entirely an increase over most of the NH despite the surface $PM_{2.5}$ impact being either positive or negative.

Figure 2.26 shows the contributions of EAAEs to surface BSOA and the total deposition fluxes of total nitrogen, black carbon, and mercury (TNTD, BCTD, and HgTD, respectively) (i.e., the differences in the surface BSOA, TNTD, BCTD, and HgTD between the simulations with and without EAAEs for 2001 and 2050). EAAEs demonstrate a strong impact on the BSOA in East Asia. EAAEs increase BSOA in East Asia by 0.1-1.2 μg m^{-3} (10-81%) with large areas experiencing an increase of 0.5-1.2 μg m^{-3} (50-81%) under all scenarios, indicating that a large fraction of BSOA in East Asia is controllable through controlling EAAEs that affect the oxidant levels for the oxidation of BSOA precursors. These results are consistent with the work of Carlton et al. (2010), who reported that over 50% of the BSOA is controllable over the southeastern U.S. by reducing the anthropogenic emissions that increase atmospheric oxidant levels. However, further downwind EAAEs can decrease the amount of BSOA as they reduce incoming shortwave radiation fluxes at the Earth's surface (SWDOWN), in turn decreasing the photolytic rate of NO_2 (JNO_2) and the amount of hydroxyl radical available to oxidize BSOA precursors.

EAAEs account for ~0.01-0.9 g m^{-2} $month^{-1}$ (40-98%) of TNTD in East Asia and the North Pacific in 2001 and ~0.01-0.6 g m^{-2} $month^{-1}$ (20-97%) in 2050. The decrease in 2050 is the result of a projected decrease in emissions of NH_3. This indicates that EAAEs are a contributor to the nitrogen fertilization of the Pacific Ocean and can enhance ocean productivity in areas that are nitrogen limited (Duce et al., 2008). Another key difference in 2050 is an increase of 0.001-0.002 g m^{-2} $month^{-1}$ (10-40%) in TNTD over Alaska and other

portions of the Arctic due to enhanced southerly transport as compared to 2001. This enhanced Arctic deposition may help fertilize Arctic vegetation increasing their growth (Schindler and Bayley, 1993), thus potentially amplifying the climate feedbacks from enhanced shrub growth in that region (Chapin et al., 2005). EAAEs increase the global average BCTD by ~3.0×10^{-3} g m^{-2} $month^{-1}$ under all scenarios. In all scenarios EAAEs increase Arctic BCTD by ~1×10^{-4}-8×10^{-4} g m^{-2} $month^{-1}$ (~10-80%). This implies that EAAEs may be a leading contributor to enhanced melting of Arctic snowpack as BC lowers the snowpack albedo (Warren and Wiscombe, 1980; Clarke and Noone, 1985). Additionally, EAAEs contribute to BCTD in both the Tibetan Plateau (1×10^{-3}-3×10^{-2} g m^{-2} $month^{-1}$ or 20-80%) and mountainous regions of western North America (1×10^{-3}-1×10^{-2} g m^{-2} $month^{-1}$ or 10-40%), which could impact the melting of snow that is an important reservoir of water for local populations (Hadley et al., 2010; Qian et al., 2011). EAAEs increase the global average HgTD by ~ 2.0×10^{-8} g m^{-2} $month^{-1}$ (~48%), with varying contributions in different regions (e.g., 40-98% in East Asia and the North Pacific and 20-70% in the Arctic). In particular, EAAEs increase HgTD in North America by 10-40%. These results are consistent with the work of Seigneur et al. (2004) and Strode et al. (2008), who reported that Asian anthropogenic emissions contribute 5-36% and 14% to the Hg deposition in North America, respectively. The large contributions over all these regions imply that EAAEs-induced HgTD could be a large source of methylmercury, which is bioavailable and can accumulate in rice crops and aquatic life leading to human exposure (Zhang, H. et al., 2010; Meng et al., 2011).

2.9.5 The Impact of EAAEs on the Climate System

EAAEs affect regional and global climate under all scenarios. Figure 2.27 shows the contributions of EAAEs to cloud condensation nuclei (CCN) at a supersaturation of 0.5%, cloud droplet number concentration (CDNC), cloud optical thickness (COT), AOD, SWDOWN, and JNO_2 between the simulations with and without EAAEs for 2001, 2050, and 2050_CCO. At a supersaturation of 0.5%, EAAEs increase the global average column CCN by ~3.2×10^7 cm^{-2} (9.5%), ~1.7×10^7 cm^{-2} (3.5%), and ~3.6×10^7 cm^{-2} (11.4%), respectively, where the reduced contribution in 2050 can be attributed to lower aerosol concentrations which result from reductions in primary aerosol emissions. The impacts across all scenarios are the largest in East Asia (5×10^7 - 1.3×10^9 cm^{-2}), the North Pacific (5×10^7 - 1.2×10^9 cm^{-2}), and portions of North America (5×10^7 - 1.5×10^8 cm^{-2}). The column CCN can also be reduced by EAAEs, as much as ~ -3.0×10^8 cm^{-2}, in regions including western Asia, Europe, and Africa, as a result of decreased aerosol number. Such decreases may result from decreasing nucleation of new particles or slight increases in precipitation over portions of those regions. The general increase in CCN translates to domain-wide increases of 8.3×10^4 cm^{-2} (11.5%), 5.3×10^4 cm^{-2} (8.5%), and 7.9×10^4 cm^{-2} (19.5%) in CDNC in 2001, 2050, and 2050_CCO, respectively. CDNC also increases the most in East Asia (2.0×10^5 - 2.7×10^6 cm^{-2}), the North Pacific (2.0×10^5 – 1.0×10^6 cm^{-2}) and portions of North America (1×10^5 - 4×10^5 cm^{-2}) but there are certain regions, such as Mexico in 2050, where EAAEs can result in a sizeable decrease (1.0×10^5 – 3.0×10^5 cm^{-2}). These decreases are associated with decreases (2-6 g m^{-2}) in the cloud liquid water path (LWP). The greatest impact of EAAEs on CDNC occurs in areas with the greatest LWP. In East Asia, these areas include Southeast Asia and Northeast

China. In 2050 and 2050_CCO, these areas of larger LWP migrate to the northeast and the impact on CDNC becomes stronger due to changes in SLP patterns. .

EAAEs increase the global average COT by ~0.2 with larger increases of 0.5-4.5 in East Asia and its downwind areas in both 2001 and 2050, as shown in Figure 2.13. In 2050, the impact on COT is spread more evenly over the North Pacific, while in 2001 the impact is concentrated in the vicinity of the Philippine Sea. This results from changes in the global distribution of cloud LWP between 2050 and 2001, where the LWP increases (by 2-18 g m^{-2}) in the northernmost portion of the Pacific and Alaska and also in the subtropical North Pacific, there is also a decrease (by 2 to 6 g m^{-2}) over the Philippine Sea which weakens the impact in that region. The 2050_CCO scenario experiences the largest impact on COT with a global average impact of 0.3 and a stronger impact (2.0-4.0) over the western North Pacific. This is due to the combination of a greater LWP in the 2050 climate and a greater number of particles to increase the CDNC using the 2001 emissions. Additionally, EAAEs-induced aerosols increase the global average AOD by ~0.02 but up to 0.5 in East Asia in all cases. In both 2050 and 2050_CCO, the impact on AOD is reduced in the Arctic as a result of the stronger zonal transport over East Asia, which reduces the meridional transport of particles.

The increase in COT and AOD reduce the SWDOWN by ~2.8 W m^{-2} in 2001, ~2.5 W m^{-2} in 2050, and ~3.0 W m^{-2} in 2050_CCO on global average. The reductions can be as large as 38.2 W m^{-2} (18.3%), 32.6 W m^{-2} (17.8%), and 41.8 W m^{-2} (21.7%), respectively, in East Asia and the North Pacific. Over East Asia, the changes in SWDOWN follow the pattern of CDNC, because increases in CDNC increase COT and result in decreasing SWDOWN. The reduced SWDOWN also leads to a reduction in JNO_2 by ~2.4×10^{-3}-2.8×10^{-3}

min^{-1} on global average across all scenarios. The reductions can be larger than 5×10^{-3} min^{-1} over East Asia, the North Pacific, and North America, indicating that EAAEs reduce photochemistry over the majority of the NH. This primarily reduces the production rate of atomic oxygen gas (O), which then leads to a reduction in the rate of formation of O_3 and OH. The amount of O_3 is not significantly impacted as changes in precursor amounts and transport are more dominant; however, the OH level is reduced slightly by ~1×10^{-3} ppt on global average. This slight reduction in oxidants can reduce the production of condensable organic gases and lead to slight reductions in aerosols, such as BSOA, as mentioned previously.

These changes in cloud properties and radiation from EAAEs propagate through the atmosphere and alter the meteorology of the globe. Figure 2.28 shows the differences in 2 m temperature, PBLH, and 10 m wind speed between the simulations with and without EAAEs for 2001, 2050, and 2050_CCO. The aforementioned EAAEs-induced changes result in global cooling of ~0.05°C in 2001, ~0.02°C in 2050, and ~0.04°C in 2050_CCO. In 2001, the temperatures decrease by 0.25-1°C in East Asia over regions where COT increases, indicating that changes in SWDOWN are the controlling force. In North America, the temperature decreases by -0.25-2°C over northwestern U.S. and western Canada, but increases by 0.25-0.75°C over eastern Canada. Both of these regions experience decreased SWDOWN from EAAEs, but the extra cloudiness over eastern Canada enhances the downwelling of longwave radiation, leading to an average temperature increase. In 2050, the cooling over East Asia from EAAEs is about 0.25-0.75°C and there is warming over northeastern China of 0.25-1.25°C again from greater downwelling of longwave radiation.

Over North America the cooling is also about 0.25-1°C, except over Alaska where stronger reductions in SWDOWN decrease the temperature by 0.5-1.5°C. It is important to note that changes in global 2-m temperature are not represented in marine environments as the configuration of GU-WRF/Chem simulations used in this work does not contain an ocean model component to simulate the response of sea surface temperatures to changes in radiation. In addition to the surface temperature over the ocean, humidity in the marine boundary layer and large scale pressure patterns which are controlled by sea surface temperatures will not be impacted by changes in chemistry since sea surface temperatures are static.

Despite their spatial and magnitude discrepancies, all the above impacts have similar trends under both the current and future scenarios with a few exceptions. PBLH is a good example of this exception, since there is no clear trend in the global average with and without EAAEs. In 2001 and 2050, the global average difference with and without EAAEs is a negligible increase of 0.03 m and decrease of 0.8 m, respectively, while the 2050_CCO simulation shows a more pronounced decrease of 2.5 m. The lack of a clear trend is most likely because PBLH is not only sensitive to changes in the atmosphere but also to the interactions with the underlying land and ocean surface. This sensitivity may also explain why there is no robust model trend in PBLH from climate change (Murazaki and Hess, 2006). However, despite the lack of a clear global trend, there are some stronger regional signals in East Asia, North America, and Scandinavia. The contributions of EAAEs to PBLH over East Asia and North America are complex but there is a general trend for decreases of 20-100 m that are spatially co-located with changes in CDNC and COT. The increases in

CDNC increase COT, reducing the amount of SWDOWN reaching the surface; this decreases the amount of energy that is exchanged between the atmosphere and the underlying surface and reduces either the sensible heat flux or the latent heat flux and thus reduces the average PBLH. The contribution of EAAEs to PBLH in Scandinavia is not consistent, with an increase of ~10-70 m in 2001 and a decrease of ~10-30 m in 2050. The pattern for 2050_CCO is even more complex with an increase over Norway and Sweden and decrease over Finland. In 2001, when Scandinavia experiences lower wind speeds, the increase in PBLH from EAAEs in this scenario has a strong impact and reduces the $PM_{2.5}$ level at the surface by ~1-3 $\mu g\ m^{-3}$ (see Figures 2.25 and 2.28). This implies that chemistry feedbacks to meteorology from emission reductions may have the opposite effect on air pollution (i.e., enhance pollution) in some locations under certain conditions. The impact of EAAEs on PR and 10-m wind speed varies with both emissions and climate scenario and since the differences between the current and future scenario are relatively small, no robust information can be gleaned.

2.10 Conclusions

The impacts of changing emissions and climate following the IPCC AR4 SRES A1B scenario are investigated using the online coupled GU-WRF/Chem model. The evaluation of the model performance from the current year simulations indicates that the model simulates radiation and meteorological variables reasonably well. Cloud parameters are not as well simulated in the model but are comparable to other WRF/Chem simulations. Evaluation of column chemistry variables indicates overpredictions in aerosols from underpredicted precipitation and possible overestimations of biomass burning emissions. Column

abundances of CO, NO_2, and TOR are overpredicted due to overestimates of CO and NO_x emissions, while the column SO_2 abundance is underpredicted due to missing sources of natural sulfur species. The comparison of GU-WRF/Chem and CCSM3 future climate predictions shows similar changes in T2, Q2, and PR compared to CCSM3. However, GSW and OLR decrease in GU-WRF/Chem in contrast to increases of GSW and OLR in CCSM3 due to the cloudier and more aerosol-rich atmosphere predicted by GU-WRF/Chem. Sulfate levels increase in both models on global average but the spatial patterns are different due to the differences in chemistry treatments and because the emissions projection are generated by different integrated assessment models. CESM1-CAM5 projections following the RCP8.5 scenario predict reduced CWP and AOD due to emissions reductions in primary aerosols and aerosol precursors, especially over the continents, reducing the aerosol direct and indirect effects. This leads to greater increases in T2, Q2, and PR compared to either GU-WRF/Chem or CCSM3 and opposing trends in radiation variables compared to GU-WRF/Chem.

Global air quality is projected to degrade by the mid-21st century following the IPCC AR4 SRES A1B scenario. Changes in the levels of CO, NH_3, SO_2, and NO_2 mirror the global average change and regional variation of their emissions. CO, SO_2, and NO_2 all increase on global average due to increases in emissions in the developing world. NH_3 decreases on global average largely due to decreasing emissions in East Asia. These changes are generally comparable to those reported using similar emission growth factors following the A1B scenario by 2030 in the work of Jacobson and Streets (2009).The $O_3$8hr level will increase by 2.5 ppb on global average with large increases of up to 20.4 ppb in heavily populated areas of South Asia and East Asia. This increase is primarily caused by increasing NO_x emissions in

this scenario but may also be due to increased emissions of TNVOC and increased reaction rates from a warmer climate. These findings of increasing O_3 are consistent with previous findings from the SRES A1B and A2 scenarios and in contrast to changes in O_3 projected by all the RCP scenarios except RCP8.5 (Liao et al., 2006; Jacobson and Streets, 2009; Young et al., 2013; Kim et al., 2015). Increasing O_3 by 2050 reported under the RCP8.5 scenario by 2050 is driven more by increases in CH_4 and TNVOC as emissions of NO_x are reduced (Young et al., 2013; Kim et al., 2015). The increases in NO_x and TNVOC emissions under the SRES A1B scenario also lead to global average increases in PAN and other nitrogen containing trace gases. The combined effect of enhanced O_3, NO_2, and Q2 enhances the near surface atmospheric oxidation state by increasing the abundance of OH, HO_2, H_2O_2, and NO_3g. The enhancement in OH is in contrast to decreases reported under the RCP scenarios due to recovery of stratospheric O_3, large increases in CH_4 under the RCP8.5 scenario, and decreased O_3 production in the remaining RCP scenarios (Voulgarakis et al., 2013; Kim et al., 2015).

$PM_{2.5}$ increases by 0.3 μg m^{-3} on global average but the changes are regional in nature. Changes in primary particle emissions of BC, OC, and OIN have the greatest impact on the $PM_{2.5}$ level, causing increases in South Asia, Southeast Asia, Indonesia, Australia, and South America, and reductions in Africa and East Asia. $PM_{2.5}$ changes in marine regions are driven by WSP10 changes except in coastal zones where increased levels of SO_2 and HNO_3 lead to greater replacement of chloride by sulfate and nitrate, increasing the mass concentration of $PM_{2.5}$. Reductions in SO_2 and NH_3 emissions also contribute to the reduced $PM_{2.5}$ level in Europe.

The increased SO_2 emissions and increased primary aerosol emissions in South America and South Asia in this scenario lead to enhancements in new particle formation and an increasing global CCN level. This enhanced CCN level, combined with a moister future atmosphere, leads to enhanced CDNC and LWP. The increased CDNC and LWP result in an increased COT of 0.05 on global average and the increased aerosol level increases the global AOD by 0.03. Thus, the cloudier and more aerosol-rich atmosphere predicted by GU-WRF/Chem leads to dimming at the Earth's surface of 1.6 W m^{-2} on global average, which reduces photolysis and results in more moderate warming compared to CCSM3. These changes in aerosol effects are in contrast to reduced AOD and aerosol indirect effects following the RCP scenarios due to reductions in aerosol and precursor emissions (Lamarque et al., 2011; Shindell et al., 2013).

Deposition of both total nitrogen and O_3 is enhanced under this scenario, especially in the developing world due to enhanced emissions of NO_x. This will enhance the possibility of crop damage and ecosystem system stress in these areas that are already heavily-populated. This trend is similar to those reported under other SRES scenarios (Prather et al., 2003). However, the trend in O_3 deposition is in contrast to most RCP scenarios and the trend in total nitrogen deposition tends to mirror that of the RCP scenarios but is caused primarily by increases in reactive nitrogen rather than increases in reduced nitrogen seen in the RCP scenarios (Lamarque et al., 2011). BC deposition is reduced on global average due to declining emissions but there are enhancements in the Ural Mountains, Andes Mountains, and Tibetan Plateau, which may impact the water supplies of populations that depend on meltwater from these regions. Mercury deposition is enhanced from reductions in

aerodynamic resistance and PBLH that can be regionally enhanced by increased precipitation. This may increase the amount of mercury that can become bioavailable and increase health impacts.

Sensitivity analysis of the year 2050 without projected emissions reveals that, with only the influence of climate change, both the $O_3$8hr and $PM_{2.5}$ levels are enhanced on global average by 0.6 ppb and 0.25 μg m^{-3}, respectively. The increased $O_3$8hr level is driven by increasing temperatures. However, there are some reductions in $O_3$8hr levels in the tropics from enhanced destruction of O_3 by enhanced water vapor. This contrasts slightly with other studies that show larger reductions from enhanced water vapor (Dentener et al., 2006; Doherty et al., 2013), likely due to model biases in temperature, water vapor, and NO_x. The enhanced $PM_{2.5}$ level is driven largely by reductions in horizontal advection from reduced WSP10 over land and enhanced sea-salt emissions from enhanced WSP10 in some marine regions. A comparison of the 2050_NPE simulation and 2050 simulation with projected emissions shows that the projected emissions under this scenario result in dimming of 1.25 W m^{-2} at the Earth's surface from an enhanced AOD and COT. The COT increase primarily occurs in marine regions as there is ample moisture for cloud formation and aerosol activation. In continental regions, the impact of projected emissions is more complex due to regional perturbations in the hydrologic cycle that impact atmospheric moisture and ultimately aerosol activation. However, despite this dimming induced by changing emissions, the response in T2 is limited to only continental locations due to the use of prescribed sea surface temperatures. This indicates that studies focusing on global scale aerosol-cloud interactions should use an Earth system model with an active ocean model component to

account for changes in marine radiation. These findings differ from findings utilizing the RCP scenarios that show increased warming from reductions in AOD, CDNC, and LWP due to reduced aerosol levels (Chalmers et al., 2012; Westervelt et al., 2015).

EAAEs have a strong impact on climate, air quality, and potentially the ecosystems of not only East Asia but other regions downwind under both current and future climate and emission scenarios. This is especially true for the Arctic which, in addition to the aforementioned impacts, is expected to undergo many changes (e.g., amplified warming, sea ice retreat, and strong ocean acidification) by the latter half of the 21st century (Steinacher et al., 2009; Vavrus et al., 2012). The dominant impacts of EAAEs are to increase chemical concentrations (e.g., O_3, CO, PAN, $PM_{2.5}$), total deposition fluxes of chemical species (e.g., total nitrogen, BC, Hg), most cloud/optical variables (e.g., CCN, CNDC, AOD, and COT) but decrease some radiation/photolysis variables (e.g., downward/net shortwave radiation and photolytic rate of NO_2). Controlling EAAEs can reduce not only the concentrations and depositions of anthropogenic-induced pollutants (by up to 100%) but also BSOA (by 10-81%). The extent to which these effects can be controlled is beyond the scope of this work as eliminating all emissions from this region is not a realistic possibility and the nonlinear responses in pollutant concentrations will vary based on the magnitude of the emission reduction.

The intercontinental transport of Asian pollution will likely play a more important role in the future due to enhanced eastward and northward transport, increased gaseous precursor emissions, and increased temperatures under the climate and emissions scenarios considered in this work. In particular, the O_3 and $PM_{2.5}$ concentrations caused by EAAEs in

2050 will increase by 0.8 ppb and 0.07 μg m^{-3}, respectively, on global average and by up to 3-12 ppb and 1-3 μg m^{-3} over some regions. This demonstrates a need for the governments of involved countries to consider the complex interplays between air pollutants and climate to develop integrated emission control strategies for optimal air quality management and climate mitigation.

Similar to other climate change and air quality studies, this study is based on a number of assumptions that may have introduced some uncertainties into the results and may be subjected to several limitations. Specifically, the lack of computational resources and limited time frame for simulations introduces some uncertainty. In the work of Doherty et al. (2013), climate simulations are performed for longer periods and compared against simulations without climate forcing to show that the magnitudes of the simulated changes from climate forcing are greater than those from internal model variability. This is an ideal case for discounting the impact of internal model variability but in this case computational resources were not available for such simulations. However, in Section 2.9.2 the response from climate and emissions in several variables from the simulations presented here are compared against the interannual variability of these parameters from the current period reanalysis and satellite estimates and the current and future interannual variability from the CCSM3 simulations. For many parameters (e.g., T2 and Q2) the change was shown to be robust but the changes in other parameters (e.g., PR and PBLH) are less likely to be robust. The use of the Brute Force method in the ITAP experiment may be another source of uncertainty as this method is more susceptible to model noises than adjoint or tagged tracer methods (Brandt et al., 2012). Therefore, possible future work may include adopting the

nonlinear tagged tracer method employed in Brandt et al. (2012), as it accounts for nonlinearities and is not as sensitive to model noise. Other uncertainties result from simplifying assumptions in GU-WRF/Chem, such as, neglecting the impact of changing vegetation on dry deposition and future land use changes. These two processes may have a strong impact on air quality in certain regions since losses in soil moisture have been shown to greatly reduce O_3 deposition from vegetation wilting in southern Europe (Andersson and Engardt, 2010) and changes in land use have been shown to impact O_3 by up to 20% under the SRES A2 scenario (Fiore et al. 2012). O_3 and $PM_{2.5}$ formation are also tied to changes in biogenic emissions, whose future changes may be highly uncertain. The use of a dynamic vegetation model has been shown to reduce isoprene emissions by 39 Tg yr^{-1}, which can reduce O_3 by 5-30 ppb in certain regions (Sanderson et al. 2003). The effect of CO_2 inhibition on isoprene emissions is also neglected but has been shown to be important, especially in non-polluted regions (Young et al., 2009). Future changes in O_3 are sensitive to the treatment of organic nitrates (Ito et al., 2009; Weaver et al., 2009), which are not treated explicitly in this version of GU-WRF/Chem. The effect of changing climate and emissions on $PM_{2.5}$ is more uncertain than that of O_3 since there are large uncertainties in the emissions of primary species and secondary formation. The largest emissions uncertainty is from wildfire emissions as they will be tied to changes in the frequency and duration of heat waves and drought conditions (Jacob and Winner, 2009; Fiore et al., 2012).

This work demonstrates that policy makers, especially those in developing countries, need to implement effective climate mitigation and emission control strategies, such as those that are part of the RCP climate scenarios, in order to avoid potential air quality degradation,

crop damage, and ecosystem system stress predicted following the SRES A1B scenario. This work also illustrates that policy decisions based on atmospheric general circulation models need to use information provided by models that simulate more complex chemistry and aerosol-cloud interactions as the inclusion of these process will impact not only the prediction of radiation variables but also T2, Q2, and PR, as evidenced by the differences between the GU-WRF/Chem and CCSM3 models. This has been done in many of the Earth System Models that have taken part in the CMIP5 comparison and also the Atmospheric Chemistry and Climate Model Intercomparison Project (ACCMIP) (Lamarque et al., 2013) and indicates that such models should be the basis of future policy decisions. This work further demonstrates the need to conduct aerosol-climate interaction studies using an Earth system model framework, like those in the CMIP5 and ACCMIP projects, in order to represent the impact of changing emissions on not only the atmosphere but also the land, oceans, and sea ice. The advantages of using detailed chemistry and aerosol treatments illustrated in this work will potentially enhance the skill of an Earth system model in simulating atmospheric processes and their interactions with other components in the Earth system.

Table 2.1. GU-WRF/Chem Model Configurations

Attribute	**Configuration**
Time period	2001, 2010, 2020, 2030, 2040, and 2050
Horizontal resolution	4° × 5°, 45 (latitude) × 72 (longitude)
Vertical resolution	27 layers from 1000–50 mb, with 17 layers in PBL (< 2.6 km)
Atmospheric Process	**Parameterization**
Longwave radiation	The rapid radiative transfer model (RRTM) (Mlawer et al., 1997)
Shortwave radiation	Goddard scheme (Chou et al., 1998)
Cloud microphysics	Purdue Lin (Lin et al., 1983; Chen and Sun, 2002)
Land surface	NOAH (Chen and Dudhia, 2001a,b; Ek et al., 2003)
Cumulus	Grell-Devenyi (Grell and Devenyi, 2002)
Planetary boundary layer	Yonsei University (YSU) scheme (Hong et al., 2006)
Surface-layer	Monin-Obukhov scheme (Monin and Obukhov, 1954; Janjic, 2002)
Gas phase chemistry	CB05GE (Karamchandani et al., 2012)
Aqueous chemistry	CMU mechanism (Fahey and Pandis, 2001)
Aerosol dynamics/thermodynamics	MADRID (Zhang. et al., 2004, 2010, 2012c)
Photolysis	F-TUV (Tie et al., 2003)
Aerosol Activation	Abdul Razzak-Ghan (Abdul-Razzak and Ghan, 2002)

NOAH - The National Center for Environmental Prediction (NNR), Oregon State University, Air Force, and Hydrologic Research Lab, CB05GE – carbon bond mechanism version 2005 with global extension, CMU – Carnegie Mellon University, MADRID – Model of Aerosol, Dynamics, Reaction, Ionization, and Dissolution, F-TUV – Fast Tropospheric Ultraviolet-Visible Model.

Table 2.2. Emissions Growth Factors for the Year 2030

Species	Source	Canada	USA	Central America	South America	North Africa	West Africa	East Africa	South Africa	OECP Europe	Eastern Europe	Former USSR	Middle East	South Asia	East Asia	Southeast Asia	Oceania	Japan
ALD2	BB	1.08	1.05	0.90	0.97	0.97	0.76	0.89	0.46	0.91	0.62	1.02	0.83	1.48	0.94	1.28	1.32	1.40
	BF	0.90	0.99	1.37	1.52	0.12	1.29	1.25	1.22	0.83	1.08	1.06	0.41	1.03	0.85	0.97	0.96	0.77
	AT	0.51	0.44	1.43	1.48	4.29	4.18	5.76	3.24	0.60	0.86	1.76	1.63	3.46	1.72	2.00	0.49	0.67
FORM	BB	1.07	1.04	0.90	0.90	0.98	0.82	0.98	0.56	0.90	0.65	1.02	0.84	1.55	0.93	1.33	1.00	1.42
	BF	0.90	0.99	1.37	1.52	0.12	1.29	1.25	1.22	0.83	1.08	1.06	0.41	1.03	0.85	0.97	0.96	0.77
	AT	1.06	1.29	2.65	2.51	4.61	4.68	6.71	3.48	1.22	2.72	2.48	2.09	5.93	4.21	3.42	0.95	1.22
ETOH and	BB	1.08	1.05	0.91	0.96	1.00	0.78	0.94	0.48	0.91	0.61	1.02	0.85	1.58	0.96	1.29	1.22	1.44
MEOH	BF	0.90	0.99	1.37	1.52	0.12	1.29	1.25	1.22	0.83	1.08	1.06	0.41	1.03	0.85	0.97	0.96	0.77
	AT	0.87	0.88	1.94	2.00	4.02	4.35	5.28	3.15	0.95	2.02	1.93	1.86	4.60	2.88	2.81	0.80	1.08
ETHA	BB	1.08	1.05	0.91	0.97	0.99	0.77	0.93	0.47	0.93	0.58	1.01	0.85	1.57	0.97	1.29	1.25	1.44
	BF	0.90	0.99	1.37	1.52	0.12	1.29	1.25	1.22	0.83	1.08	1.06	0.41	1.03	0.85	0.97	0.96	0.77
	AT	0.91	0.60	1.39	3.06	2.42	5.84	5.36	3.46	0.93	1.27	1.92	3.23	2.74	2.62	1.75	0.77	0.76
HC	Total	0.91	0.60	1.38	3.01	2.40	5.56	2.34	2.74	0.93	1.27	1.91	3.22	2.10	2.36	1.66	0.77	0.76
KET	BB	1.08	1.05	0.91	0.96	1.00	0.78	0.94	0.48	0.91	0.61	1.02	0.85	1.58	0.96	1.29	1.22	1.44
	AT	0.88	0.88	1.86	1.92	3.50	2.35	1.97	2.14	0.95	1.99	1.86	1.80	2.37	2.17	2.20	0.81	1.08
ETH	BB	1.08	1.06	0.90	0.93	0.94	0.78	0.90	0.50	0.93	0.57	1.01	0.82	1.44	0.94	1.30	1.23	1.38
	BF	0.90	0.99	1.37	1.52	0.12	1.29	1.25	1.22	0.83	1.08	1.06	0.41	1.03	0.85	0.97	0.96	0.77
	AT	0.92	0.80	2.10	2.09	4.30	4.20	5.02	3.19	0.96	2.35	2.72	1.76	6.32	4.47	3.43	0.86	1.09
OLE and	BB	1.08	1.05	0.91	0.97	1.00	0.78	0.96	0.49	0.93	0.58	1.01	0.86	1.62	0.98	1.30	1.19	1.45
IOLE	BF	0.90	0.99	1.37	1.52	0.12	1.29	1.25	1.22	0.83	1.08	1.06	0.41	1.03	0.85	0.97	0.96	0.77
	AT	0.55	0.51	1.45	1.56	4.24	4.18	5.69	3.24	0.62	0.80	1.17	1.63	3.46	1.55	2.03	0.51	0.70
AACD	Total	0.88	0.88	1.86	1.92	3.50	2.35	1.97	2.14	0.95	1.99	1.86	1.80	2.37	2.17	2.20	0.81	1.08
TOL	BB	1.07	1.02	0.88	0.95	0.73	0.76	0.81	0.46	0.86	0.83	1.03	0.74	1.09	0.76	1.28	1.43	1.18
	AT	0.92	0.92	1.94	1.99	3.70	3.03	2.79	2.48	1.00	2.20	1.92	1.82	3.37	2.72	2.65	0.86	1.12
XYL	BB	1.07	1.03	0.89	0.98	0.90	0.75	0.85	0.45	0.87	0.80	1.02	0.79	1.31	0.80	1.27	1.42	1.33
	AT	0.89	0.85	1.92	1.93	3.95	3.13	2.99	2.73	0.97	2.23	2.06	1.74	3.55	2.73	2.65	0.84	1.11
CO	BB	1.08	1.05	0.90	0.98	0.97	0.76	0.89	0.46	0.92	0.59	1.01	0.84	1.49	0.96	1.27	1.34	1.41
	AT	0.67	0.54	1.51	1.65	3.41	1.65	1.58	1.97	0.68	0.92	1.38	1.57	1.39	1.23	1.33	0.60	0.71
CH_4	BB	1.08	1.05	0.89	0.92	0.90	0.79	0.87	0.50	0.91	0.61	1.02	0.80	1.34	0.91	1.31	1.25	1.33
	AT	1.23	0.59	2.24	3.94	3.96	5.02	1.34	4.92	0.88	1.27	1.98	4.69	1.98	1.31	3.22	2.15	0.55
CRES	Total	0.88	0.88	1.86	1.92	3.50	2.35	1.97	2.14	0.95	1.99	1.86	1.80	2.37	2.17	2.20	0.81	1.08
NO_x, and	BB	1.08	1.05	0.91	1.10	1.02	0.71	0.86	0.39	0.91	0.60	1.01	0.87	1.56	0.99	1.11	1.54	1.47
NO_3	AT	0.77	0.71	2.35	2.94	4.18	2.67	2.75	2.56	0.79	1.96	1.54	2.29	3.90	2.22	2.42	0.79	0.76
N_2O	Total	1.07	1.07	1.07	1.07	1.07	1.07	1.07	1.07	1.07	1.07	1.07	1.07	1.07	1.07	1.07	1.07	1.07
NH_3	BB	1.08	1.05	0.90	1.01	0.98	0.75	0.89	0.44	0.92	0.59	1.01	0.85	1.52	0.97	1.25	1.39	1.42
	AG	1.02	1.35	1.83	1.35	1.78	2.26	1.80	2.18	1.14	1.11	1.41	2.28	1.19	0.95	2.00	0.95	1.51
	AT	1.20	1.15	1.14	1.21	1.29	1.05	0.99	1.12	1.05	1.24	1.15	1.56	0.84	0.79	0.81	1.06	1.06
SO_2 and	BB	1.07	1.03	0.89	0.98	0.95	0.76	0.87	0.45	0.89	0.68	1.02	0.82	1.42	0.90	1.27	1.37	1.38
SO_4^{2-}	AT	0.22	0.25	2.22	4.33	3.09	4.15	7.82	2.70	0.29	0.23	0.83	1.75	3.57	1.43	2.38	0.27	0.21
BC	BB	1.09	1.06	0.90	1.00	0.99	0.75	0.90	0.45	0.94	0.56	1.01	0.85	1.53	0.98	1.26	1.35	1.43
	AT	0.63	0.59	1.48	2.99	1.77	0.71	0.60	1.25	0.52	1.09	1.39	1.72	0.98	0.61	0.99	0.77	0.41
OC	BB	1.07	1.03	0.89	0.98	0.93	0.75	0.86	0.45	0.88	0.70	1.02	0.81	1.39	0.89	1.26	1.40	1.37
	AT	0.72	0.68	0.80	0.79	2.11	0.59	0.40	0.80	0.63	0.82	0.88	0.98	0.59	0.61	0.72	0.69	0.43
OIN	BB	1.07	1.03	0.88	0.89	0.76	0.80	0.82	0.53	0.87	0.74	1.02	0.75	1.15	0.79	1.32	1.22	1.21

Table 2.3. Emissions Growth Factors for the Year 2050

Species	Source	Canada	USA	Central America	South America	North Africa	West Africa	East Africa	South Africa	OECP Europe	Eastern Europe	Former USSR	Middle East	South Asia	East Asia	Southeast Asia	Oceania	Japan
ALD2	BB	1.19	1.05	0.81	1.37	1.72	0.78	1.30	0.40	0.86	0.74	1.04	0.73	1.72	1.00	0.96	1.45	2.13
	BF	0.66	0.94	1.32	1.16	0.30	1.45	1.64	1.06	0.63	0.74	0.93	0.26	0.93	0.68	0.90	0.68	0.56
	AT	0.31	0.26	0.56	0.55	4.03	3.58	7.97	2.34	0.36	0.43	0.90	0.85	3.04	0.77	1.10	0.29	0.49
FORM	BB	1.19	1.05	0.81	1.37	1.72	0.78	1.30	0.40	0.86	0.74	1.04	0.73	1.72	1.00	0.96	1.45	2.13
	BF	0.66	0.94	1.32	1.16	0.30	1.45	1.65	1.06	0.63	0.74	0.93	0.26	0.93	0.68	0.90	0.68	0.56
	AT	1.44	1.68	3.68	3.40	7.45	12.65	20.42	6.41	1.55	4.79	5.17	2.48	13.62	7.26	5.88	1.30	1.61
ETOH	BB	0.24	0.47	0.33	1.05	0.44	0.42	0.55	0.18	0.37	0.35	0.24	0.36	0.33	0.11	0.68	0.64	1.08
and	BF	0.66	0.94	1.32	1.16	0.30	1.45	1.65	1.06	0.63	0.74	0.93	0.26	0.93	0.68	0.90	0.68	0.56
MEOH	AT	0.96	0.97	2.38	2.20	4.68	7.97	10.71	3.64	1.01	3.54	3.76	1.54	8.88	4.74	4.21	0.88	1.24
ETHA	BB	0.01	0.27	0.19	0.74	0.31	0.26	0.32	0.10	0.21	0.26	0.03	0.26	0.18	0.02	0.49	0.39	0.87
	BF	0.39	0.55	0.78	0.69	0.18	0.86	0.97	0.63	0.37	0.44	0.55	0.15	0.55	0.40	0.53	0.40	0.33
	AT	0.48	0.47	1.07	3.22	1.38	3.21	9.34	5.88	0.74	0.89	1.37	2.31	2.86	2.86	1.40	0.39	0.67
HC	Total	0.47	0.47	1.07	3.13	1.37	3.07	3.20	4.20	0.74	0.88	1.36	2.31	1.99	2.49	1.29	0.39	0.67
KET	BB	0.24	0.47	0.33	1.05	0.44	0.42	0.55	0.18	0.37	0.35	0.24	0.36	0.33	0.11	0.68	0.64	1.08
	AT	0.52	0.67	0.44	0.35	1.58	0.26	0.90	0.40	0.86	0.79	2.28	0.40	0.45	0.52	0.35	0.95	0.33
ETH	BB	1.19	1.05	0.81	1.37	1.72	0.78	1.30	0.40	0.86	0.74	1.04	0.73	1.72	1.00	0.96	1.45	2.13
	BF	0.66	0.94	1.32	1.16	0.30	1.45	1.65	1.06	0.63	0.74	0.93	0.26	0.93	0.68	0.90	0.68	0.56
	AT	1.05	0.86	3.22	2.96	5.15	12.38	14.87	4.92	1.01	4.40	5.52	1.39	17.94	9.55	6.87	0.97	1.22
OLE	BB	0.02	0.31	0.26	1.00	0.38	0.36	0.44	0.14	0.24	0.31	0.04	0.33	0.22	0.02	0.64	0.52	1.02
and	BF	0.66	0.94	1.32	1.16	0.30	1.45	1.65	1.06	0.63	0.74	0.93	0.26	0.93	0.68	0.90	0.68	0.56
IOLE	AT	0.37	0.35	0.65	0.67	4.12	3.82	8.02	2.45	0.41	0.47	0.76	0.90	3.02	0.82	1.22	0.32	0.53
AACD	Total	0.94	0.97	2.23	2.02	4.10	3.71	3.27	2.29	1.00	3.46	3.53	1.49	3.91	3.32	3.11	0.87	1.23
TOL	BB	1.19	1.05	0.81	1.37	1.72	0.78	1.30	0.40	0.86	0.74	1.04	0.73	1.72	1.00	0.96	1.45	2.13
	AT	1.03	1.03	2.61	2.32	4.27	5.91	5.02	2.75	1.09	4.11	4.11	1.58	6.57	4.75	4.22	0.96	1.29
XYL	BB	1.19	1.05	0.81	1.37	1.72	0.78	1.30	0.40	0.86	0.74	1.04	0.73	1.72	1.00	0.96	1.45	2.13
	AT	0.97	0.92	2.56	2.25	4.49	5.84	5.27	2.91	1.03	4.10	4.13	1.38	6.72	4.73	4.16	0.93	1.25
CO	BB	0.03	0.72	0.50	1.83	0.71	0.62	0.79	0.22	0.58	0.57	0.07	0.59	0.48	0.03	1.26	0.96	2.56
	AT	0.54	0.44	0.94	1.05	3.82	1.82	2.19	1.72	0.53	0.57	1.10	1.04	1.38	0.81	1.11	0.46	0.69
CH_4	BB	0.03	0.78	0.30	2.13	0.75	0.72	0.80	0.22	0.67	0.66	0.07	0.54	0.39	0.04	1.27	1.10	3.58
	AT	0.78	0.39	1.82	3.87	1.97	4.86	1.91	9.15	0.84	0.42	2.18	6.99	1.75	1.73	1.86	1.74	0.44
CRES	Total	0.94	0.97	2.23	2.02	4.10	3.71	3.27	2.29	1.00	3.46	3.53	1.49	3.91	3.32	3.11	0.87	1.23
NO_x,	BB	0.04	0.98	1.30	1.50	1.23	0.47	0.67	0.18	0.75	0.82	0.10	1.02	0.89	0.04	1.69	0.76	2.88
and	AT	0.97	0.89	3.36	3.62	9.17	6.72	8.40	5.16	1.02	2.58	2.11	3.84	8.63	2.94	4.80	1.03	1.01
NO_3																		
N_2O	Total	1.07	2.07	3.07	4.07	5.07	6.07	7.07	8.07	9.07	10.07	11.07	12.07	13.07	14.07	15.07	16.07	17.07
NH_3	BB	1.16	1.01	0.91	1.35	0.76	0.82	1.28	0.36	0.79	0.58	1.00	0.48	1.78	0.96	1.01	1.54	1.85
	AG	1.05	1.42	1.91	1.40	2.27	2.99	2.21	2.80	1.20	1.23	1.60	3.21	1.30	0.76	2.14	0.86	1.96
	AT	0.62	0.89	1.34	1.23	0.16	1.67	1.85	1.20	0.61	0.60	0.37	0.30	1.04	0.64	0.96	0.74	0.90
SO_2 and	BB	0.03	0.80	0.93	3.40	1.17	1.15	1.50	0.42	0.64	0.85	0.08	1.15	0.99	0.06	2.36	1.84	6.81
SO_4^{2-}	AT	0.26	0.25	1.81	7.46	7.26	9.09	14.81	6.87	0.37	0.23	0.37	1.09	3.93	0.89	3.59	0.43	0.26
BC	BB	1.19	1.05	0.81	1.37	1.72	0.78	1.30	0.40	0.86	0.74	1.04	0.73	1.72	1.00	0.96	1.45	2.13
	AT	0.58	0.49	1.70	1.01	2.99	0.93	1.97	1.42	0.57	1.06	1.63	1.69	1.88	0.76	1.10	0.85	0.26
OC	BB	1.12	0.96	0.80	1.40	0.98	0.79	1.27	0.40	0.72	0.75	1.04	0.51	1.42	0.93	0.96	1.51	1.63
	AT	0.52	0.67	0.44	0.35	1.58	0.26	0.90	0.40	0.86	0.79	2.28	0.40	0.45	0.52	0.35	0.95	0.33
OIN	BB	1.19	1.05	0.81	1.37	1.72	0.78	1.30	0.40	0.86	0.74	1.04	0.73	1.72	1.00	0.96	1.45	2.13

Table 2.4. Emissions Totals of Anthropogenic Species for Each Simulated Decade

Year	2001	2010	2020	2030	2040	2050
NO (Tg yr^{-1})	70.9	79.5	88.0	96.6	115.3	134.1
NH_3 (Tg yr^{-1})	63.9	64.1	64.3	64.5	62.4	60.4
SO_2 (Tg yr^{-1})	143.0	161.0	179.0	196.0	220.8	224.7
CO (Tg yr^{-1})	851.8	880.2	908.7	937.1	893.3	849.6
AVOC (TgC yr^{-1})	292.4	334.8	377.3	419.8	419.4	419.2
POC (TgC yr^{-1})	880.1	827.1	774.2	721.2	724.8	728.5
BC (TgC yr^{-1})	194.5	191.3	188.0	184.8	192.6	200.5
OIN (Tg yr^{-1})	967.3	942.9	918.5	894.1	940.0	985.9

Table 2.5. Model Evaluation Statistics for the Average of the Current Years

Variable	Unit	Dataset	Mean Obs.	Mean Sim.	Corr.	MB	NMB	NME
OLR	W m^{-2}	NOAA/CDC	216.0	217.8	0.97	1.8	0.8	3.1
OLR	W m^{-2}	CERES/EBAF	224.1	217.8	0.97	-6.3	-2.8	3.7
GLW	W m^{-2}	BSRN	325.5	329.6	0.94	4.0	1.2	4.5
GLW	W m^{-2}	CERES/EBAF	307.5	313.6	0.99	6.2	2.0	3.8
SWDOWN	W m^{-2}	BSRN	185.5	211.9	0.89	26.5	14.3	17.2
SWDOWN	W m^{-2}	CERES/EBAF	163.7	184.3	0.89	20.6	12.6	17.2
GSW	W m^{-2}	CERES/EBAF	128.9	149.3	0.92	20.3	15.8	22.8
CF		MODIS	0.66	0.80	0.44	0.13	20.2	31.3
LWP	g m^{-2}	MODIS	144,5	27.4	0.46	-117.0	-81.0	81.1
LWP	g m^{-2}	OD08	84.5	34.7	0.01	-49.6	-58.9	60.9
PWV	cm	MODIS	1.93	1.92	0.99	-4.0×10^{-3}	0.2	13.6
COT		MODIS	16.9	2.9	-0.42	-14.0	-82.6	82.7
PSFC	HPa	NCDC	969.3	965.2	0.65	-4.1	-0.4	3.2
WS10	m s^{-1}	NCDC	3.8	2/9	0.24	-0.9	-24.9	42.7
T2	°C	NCDC	13.6	15.0	0.94	1.4	10.6	19.2
Q2	g kg^{-1}	NCDC	8.3	8.5	0.89	0.2	2.0	16.9
PR	mm day^{-1}	NCDC	1.9	1.8	0.38	-0.11	-6.1	82.4
PR	mm day^{-1}	GPCP	2.2	2.1	0.70	-0.08	-3.4	53.9
CCN	cm^{-2}	MODIS	2.5×10^{8}	3.0×10^{8}	0.38	4.8×10^{7}	18.9	57.6
CDNC	cm^{-3}	BE07	107.3	39.1	0.20	-68.2	-63.5	67.1
AOD		MODIS	0.15	0.29	0.40	0.14	96.3	107.1
TOR	DU	TOMS/SBUV (2001) OMI/MLS (2010)	29.6	34.7	0.75	5.1	17.3	21.7
NO_2	cm^{-2}	GOME (2001) SCIAMACHY (2010)	4.5×10^{14}	$7.8°10^{14}$	0.80	3.3×10^{14}	73.7	92.9
SO_2	DU	SCIAMACHY	0.20	0.04	0.40	-0.16	-79.7	81.3
CO	cm^{-2}	MOPITT	1.5×10^{18}	2.1×10^{18}	0.88	6.6×10^{17}	44.6	44.6

T2, 2-m temperature; Q2, 2-m water vapor mixing ratio; WS10, !0-m wind speed only evaluated for observed wind speeds greater than 1.54 m s^{-1}; PSFC, surface pressure; DP, total daily precipitation in mm day^{-1}; PR, average precipitation rate (mm day^{-1}); SWDOWN, incoming shortwave radiation flux at the Earth's surface; GLW, incoming longwave radiation flux at the Earth's surface; OLR, outgoing longwave radiation at the top of the atmosphere; PWV, precipitable water vapor; LWP, vertically integrated cloud water; CF, cloud fraction; $CCN_{S=0.5\%}$, vertically integrated cloud condensation nuclei at a supersaturation (S) of 0.5% ; COT, cloud optical thickness; AOD, aerosol optical depth; TOR, tropospheric ozone residual; NO_2, vertically integrated NO_2 column; CO, vertically integrated CO column; Corr., correlation coefficient; MB, mean bias; NMB, Normalized mean bias

Table 2.6. Correlation of $O_3$8hr Response to Climate and Emissions Variables

Variable	**R**
T2	0.20
Q2	3.4×10^{-4}
NO_2 Photolysis Rate	-0.28
PBLH	0.06
NO_x Emissions	0.57
TNVOC Emissions	0.26
NO_2 level	0.65
AVOC level	0.44
Isoprene level	-0.32

Table 2.7. Correlation of $PM_{2.5}$ Response to Climate and Emissions Variables

Variable	R
Precipitation	-0.01
Q2	0.28
WSP10	0.12
PBLH	-0.09
BC Emissions	0.42
POM Emissions	0.40
OIN Emissions	0.56
SO_2 Emissions	0.20
NH_3 Emissions	0.14
NO_X Emissions	0.19
SO_2 level	0.31
NH_3 level	0.12
HNO_3 level	0.26

Table 2.8. Correlation for Sensitivity of $O_3$8hr Response to Climate Variables

Variable	R
T2	0.33
Q2	-0.29
NO_2 Photolysis Rate	-7.0×10-3
PBLH	0.16
WSP10	0.01

Table 2.9. Correlation for Sensitivity of $PM_{2.5}$ Response to Climate Variables

Variable	R
Precipitation	0.01
Q2	0.15
WSP10	0.38
PBLH	-0.01

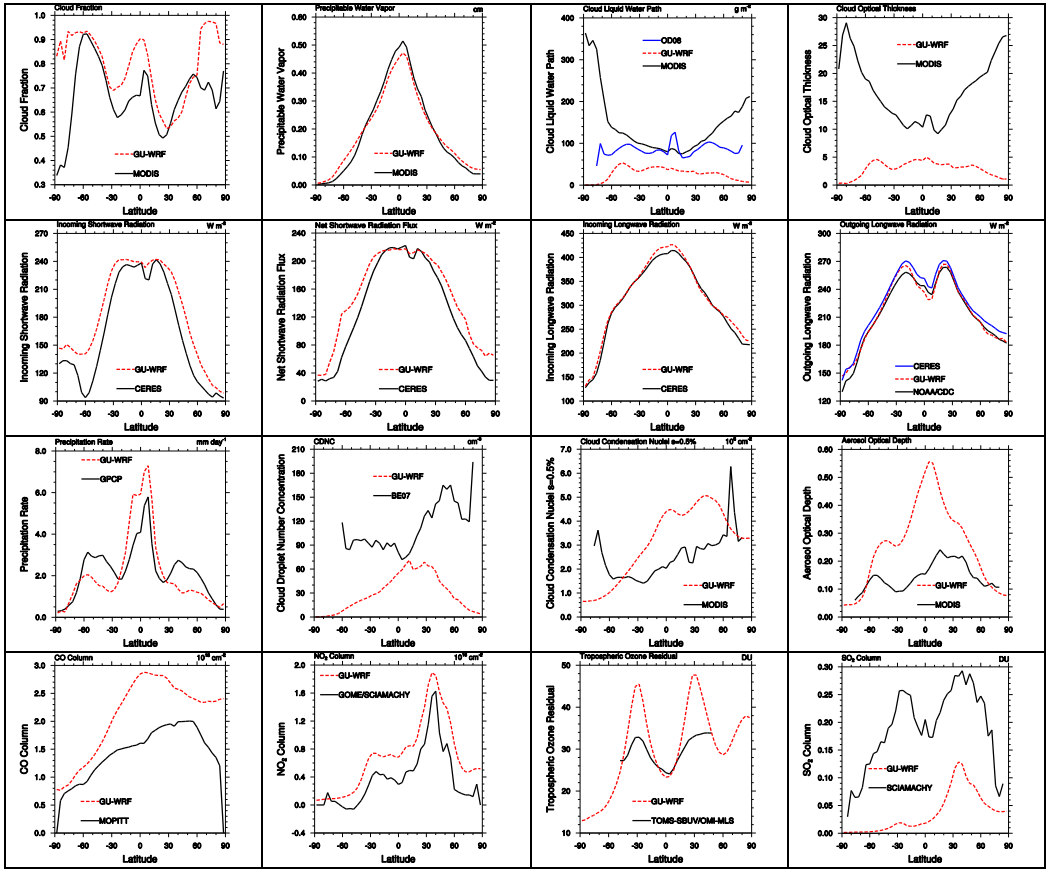

Figure 2.1. The zonal mean profiles of CF, LWP, COT, CCN, PWV, precipitation rate, OLR, AOD, column SO_2, column CO, column NO_2, and TOR from GU-WRF/Chem compared against the zonal mean profiles of observations from the MODIS, MOPITT, GOME, TOMS-SBUV, OMI-MLS, SCIAMACHY, NOAA/CDC, and GPCP satellite and reanalysis datasets for the average current year period (2001 and 2010).

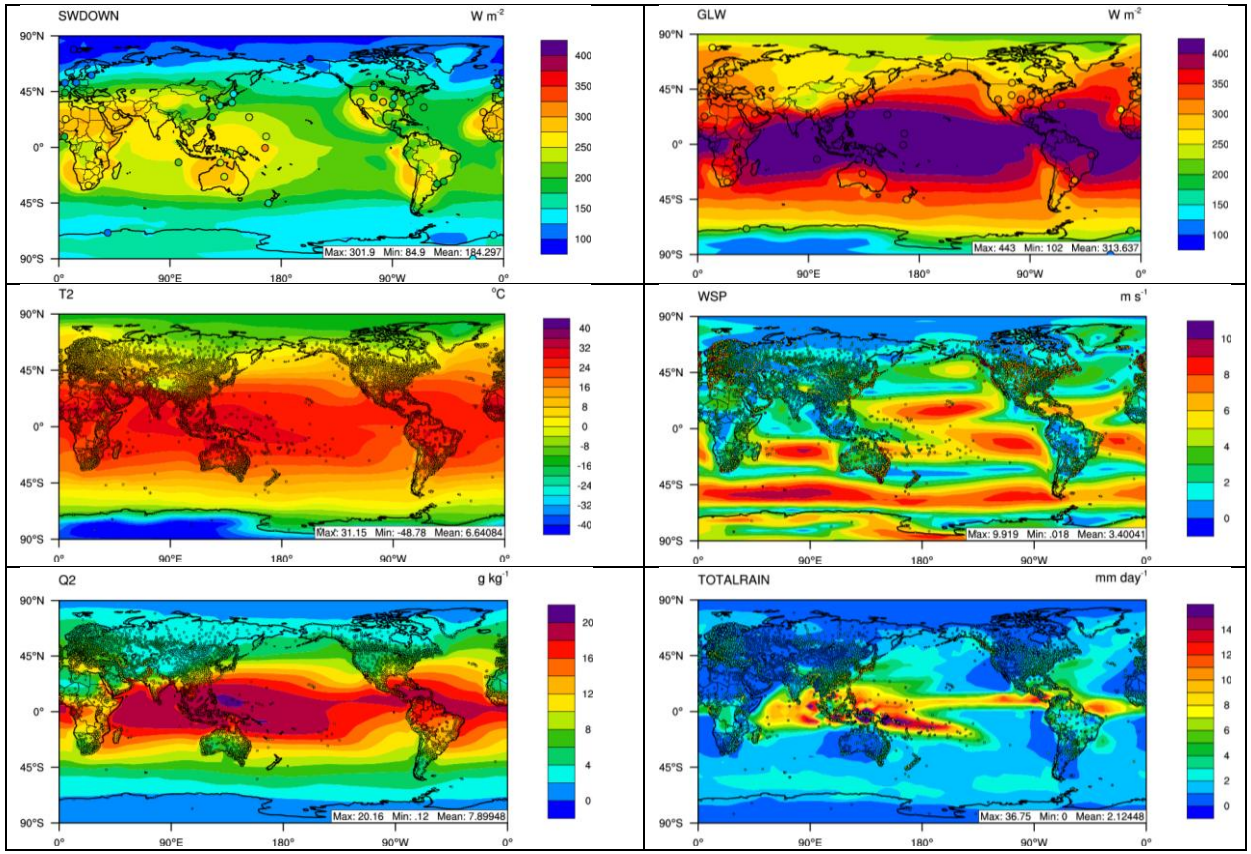

Figure 2.2. Spatial distributions of simulated SWDOWN and GLW overlaid with observations from the BSRN surface network and those of T2, Q2, wind speed at 10-m, and precipitation overlaid with observations from the NCDC surface network for the average current year period (2001 and 2010). The observations are symbolled as circles.

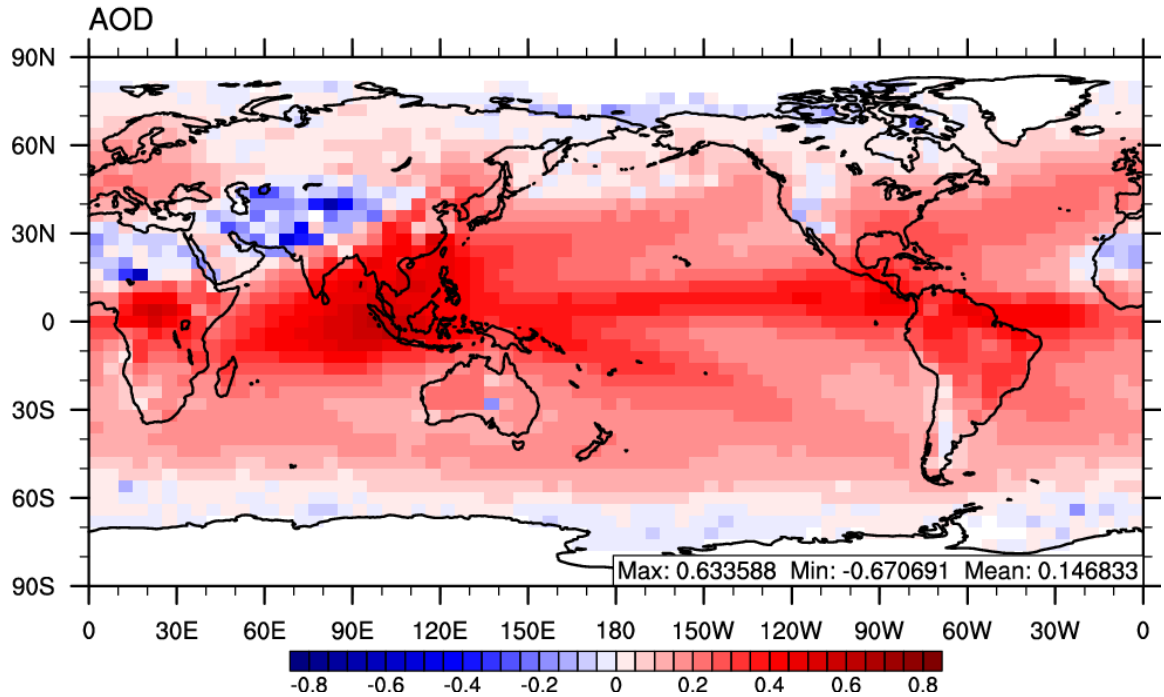

Figure 2.3. The absolute difference between simulated AOD and MODIS estimated AOD for the AOC period

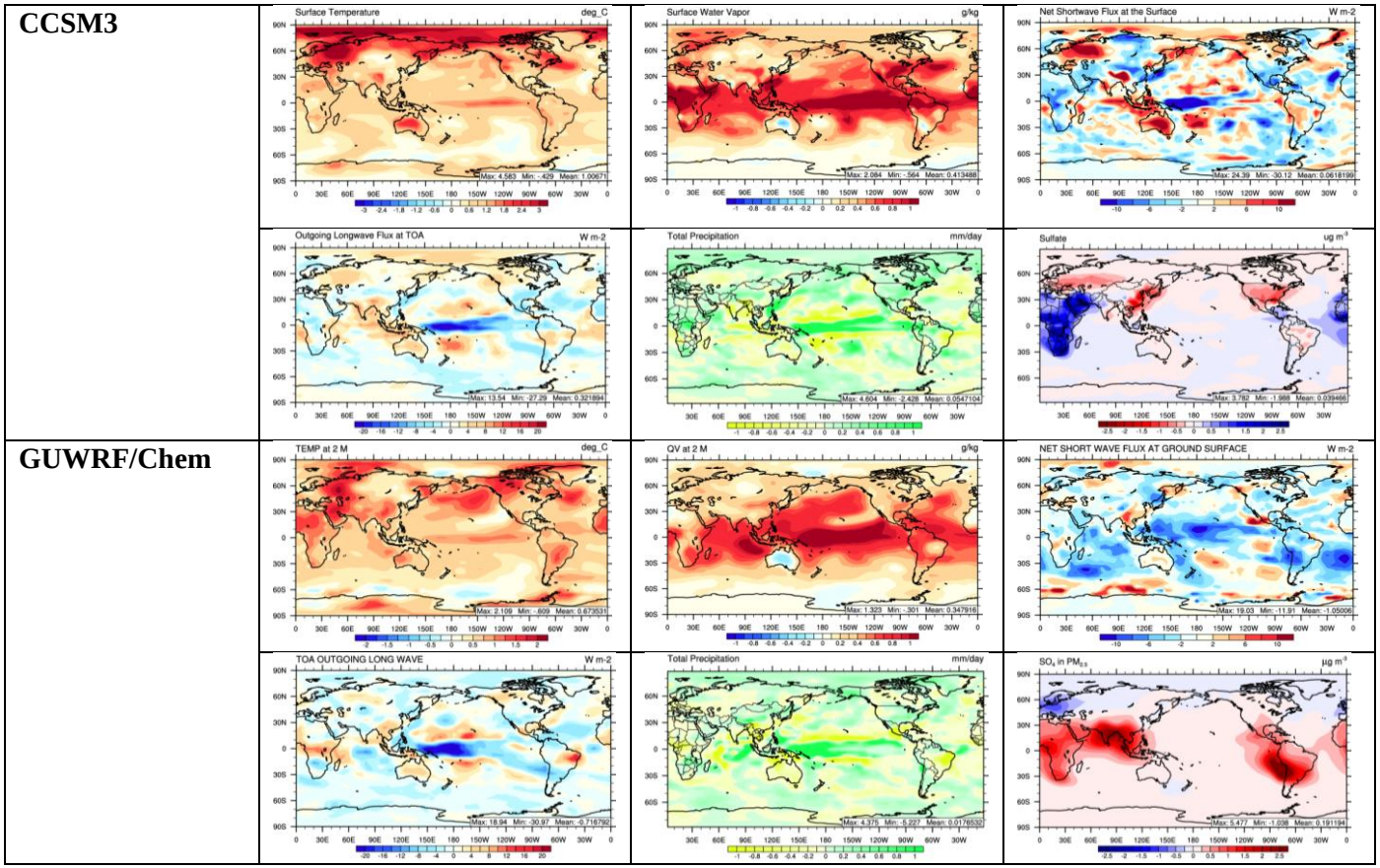

Figure 2.4. A comparison of the variation trends in surface temperature, surface water vapor, net shortwave radiation at the Earth's surface, outgoing longwave radiation at the top of the atmosphere, precipitation rate, and surface sulfate concentration between the average current year period (2001 and 2010) and the average future year period (2020, 2030, 2040, and 2050) for both the CCSM3 and GU-WRF/Chem simulation.

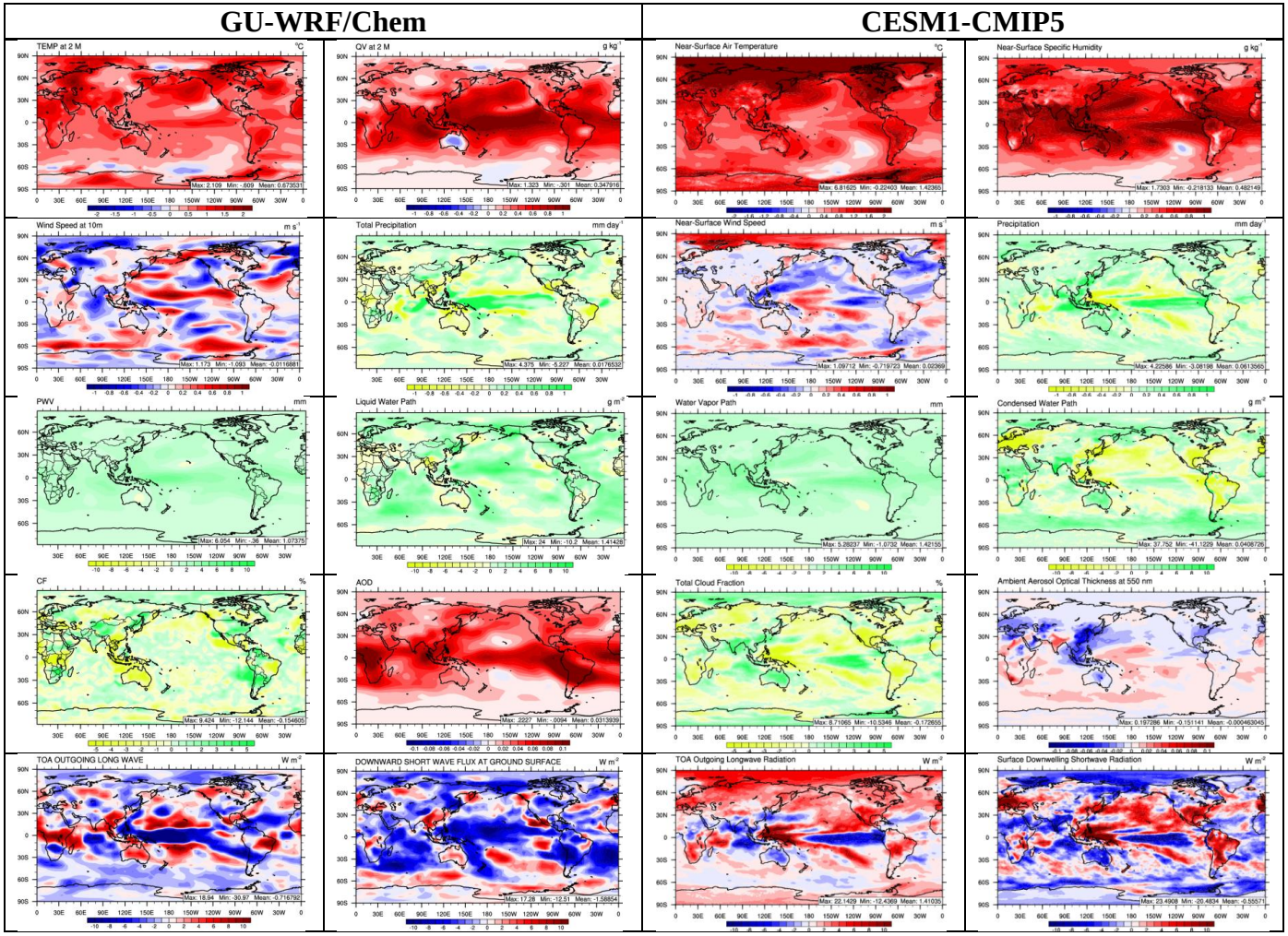

Figure 2.5. The absolute difference in meteorological, cloud, and radiation variables from GU-WRF/Chem and CESM1-CAM5 between the AOF and AOC periods.

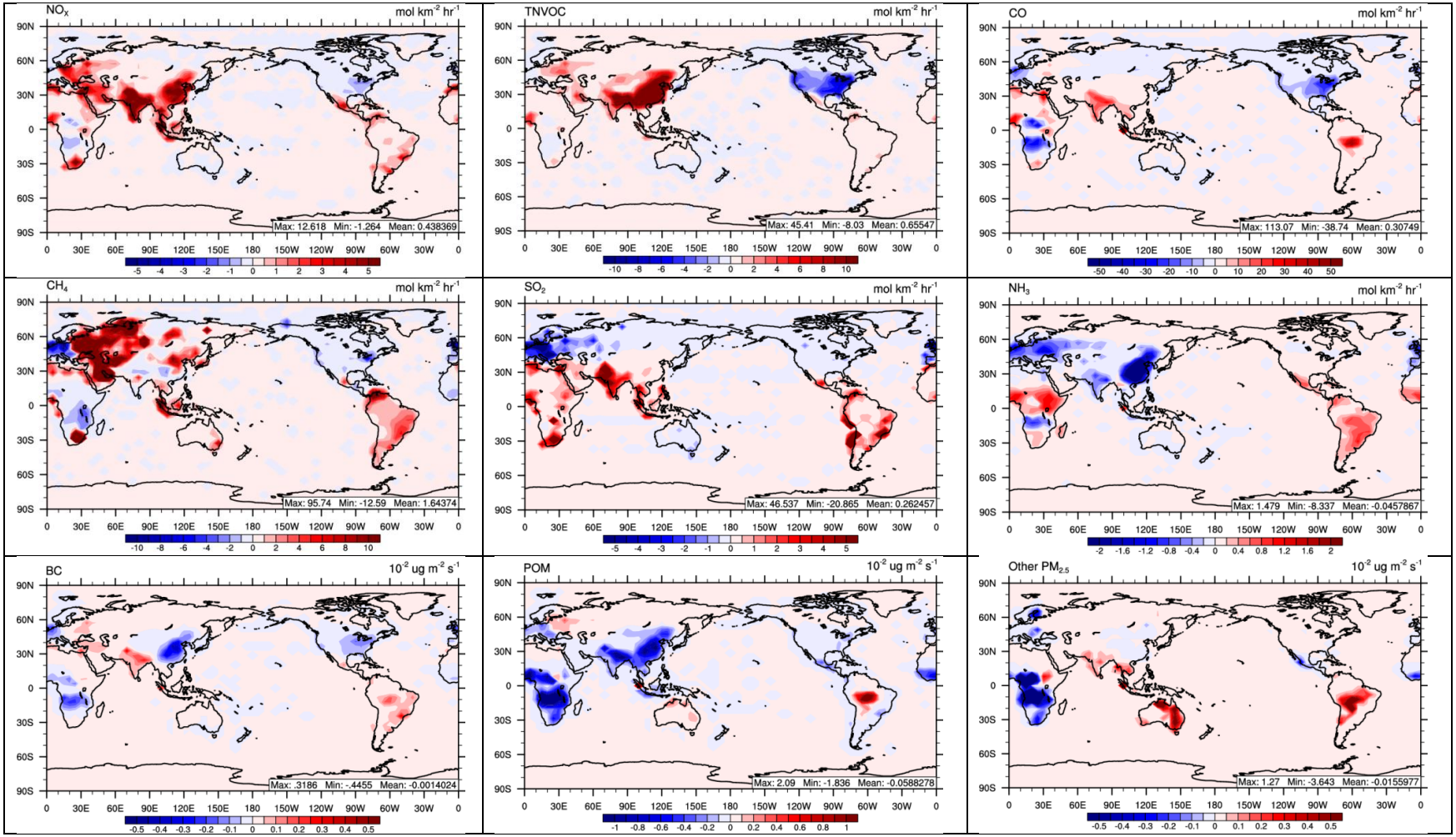

Figure 2.6. The absolute differences in anthropogenic emissions of TNVOC, NO_X, CO, CH_4, SO_2, NH_3, BC, POM, and other unspeciated $PM_{2.5}$ aerosol between the AOF and AOC time periods.

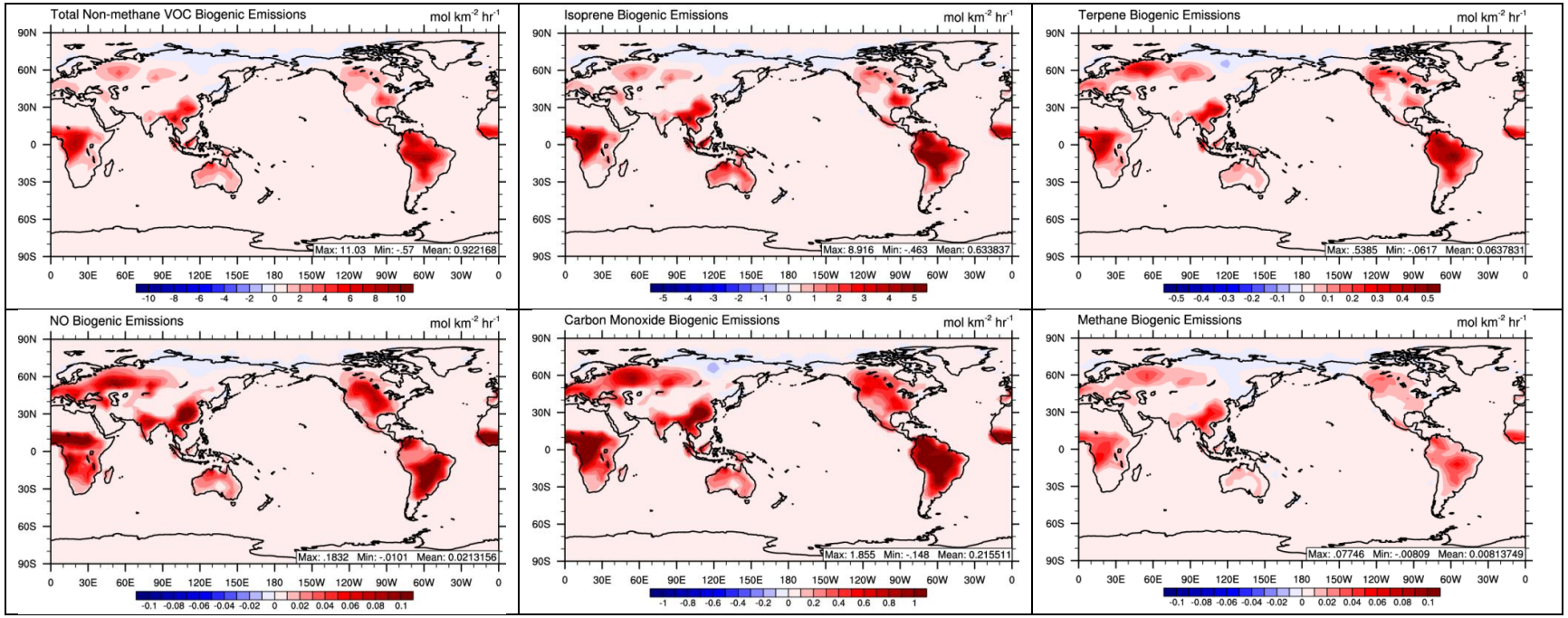

Figure 2.7. The absolute differences in the biogenic emissions of total non-methane VOCs, isoprene, terpenes, NO, CO, and CH_4 between the AOF and AOC periods.

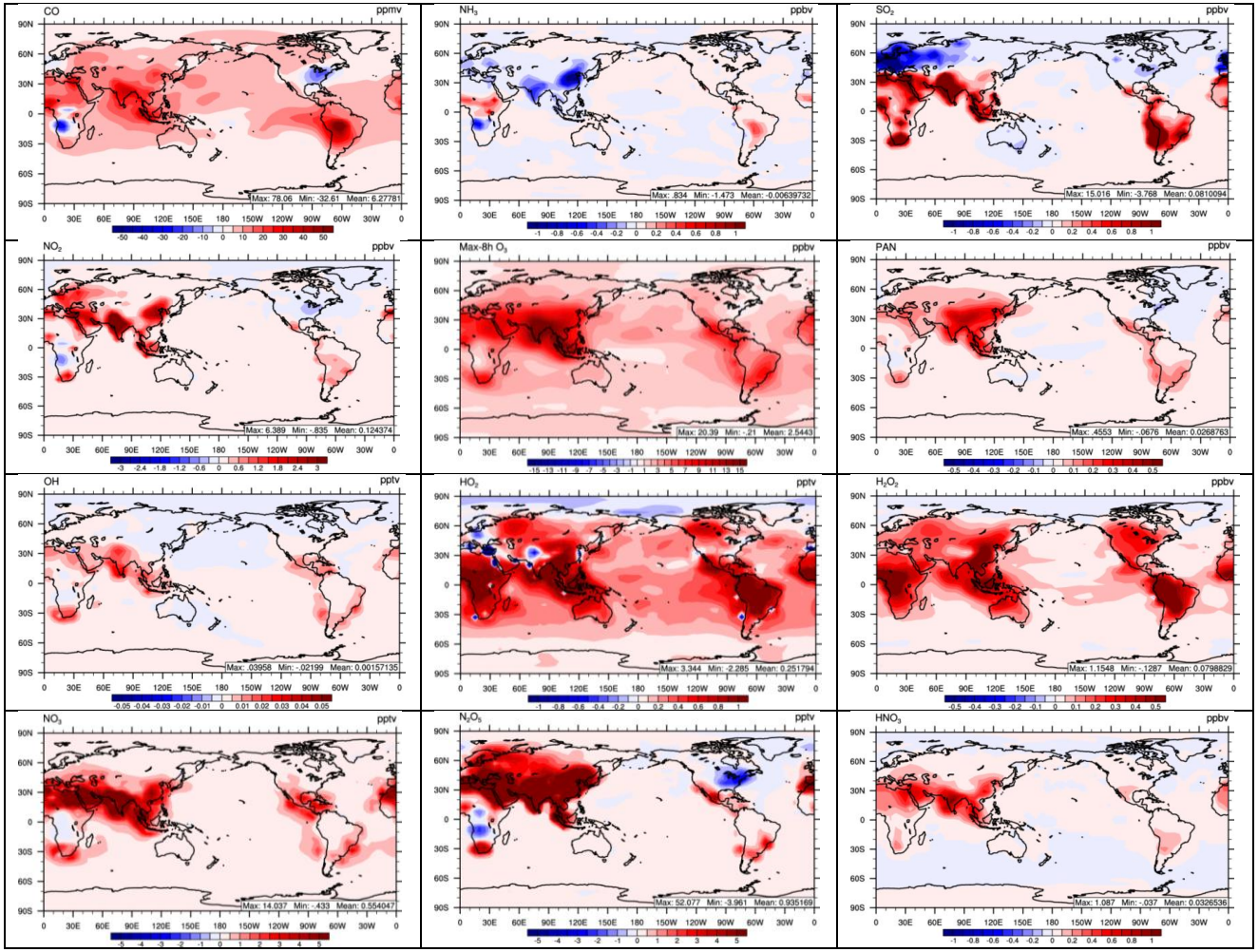

Figure 2.8. The absolute differences in the CO, NH_3, SO_2, NO_2, $O_3$8hr, PAN, OH, HO_2, H_2O_2, NO_3 radical, N_2O_5, and HNO_3 level between the AOF and AOC time periods.

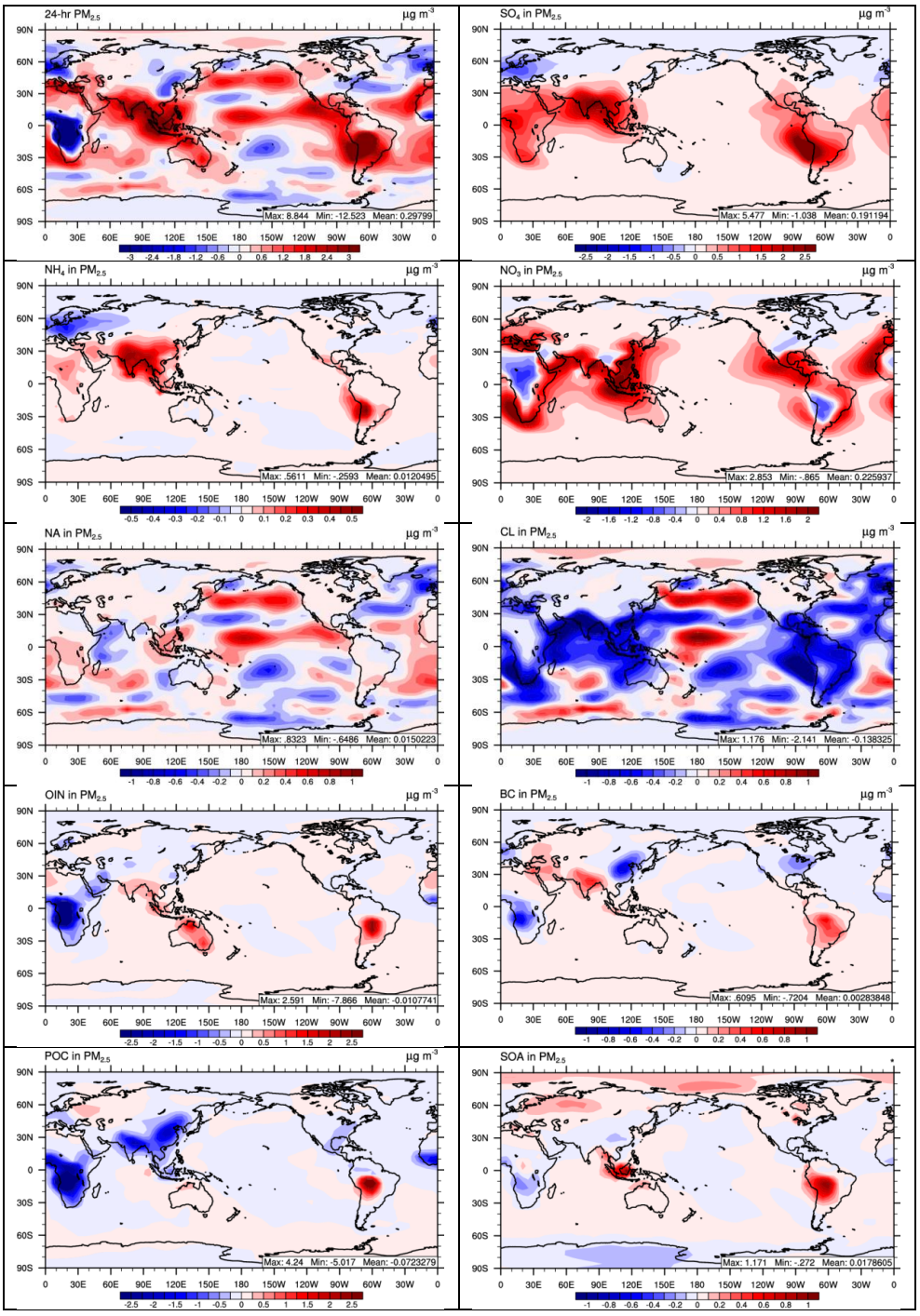

Figure 2.9. The absolute differences in average $PM_{2.5}$ level and its component species between the AOF and AOC time periods.

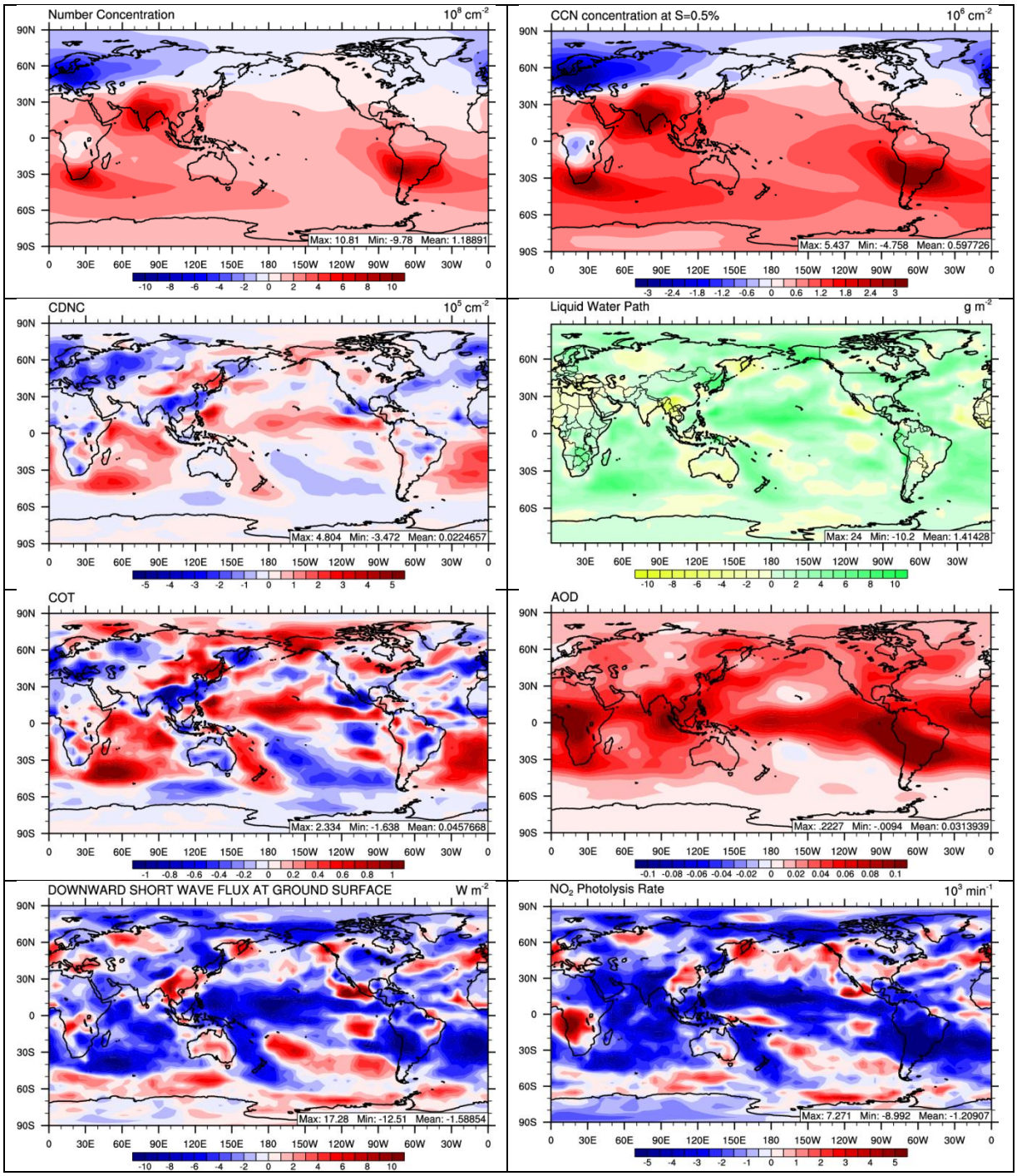

Figure 2.10. Absolute changes in aerosol number concentration, column cloud condensation nuclei concentration at a supersaturation of 0.5%, column cloud droplet number concentration, cloud liquid water path, cloud optical thickness, aerosol optical depth, incoming shortwave radiation, and NO_2 photolysis rate between the AOF and AOC periods.

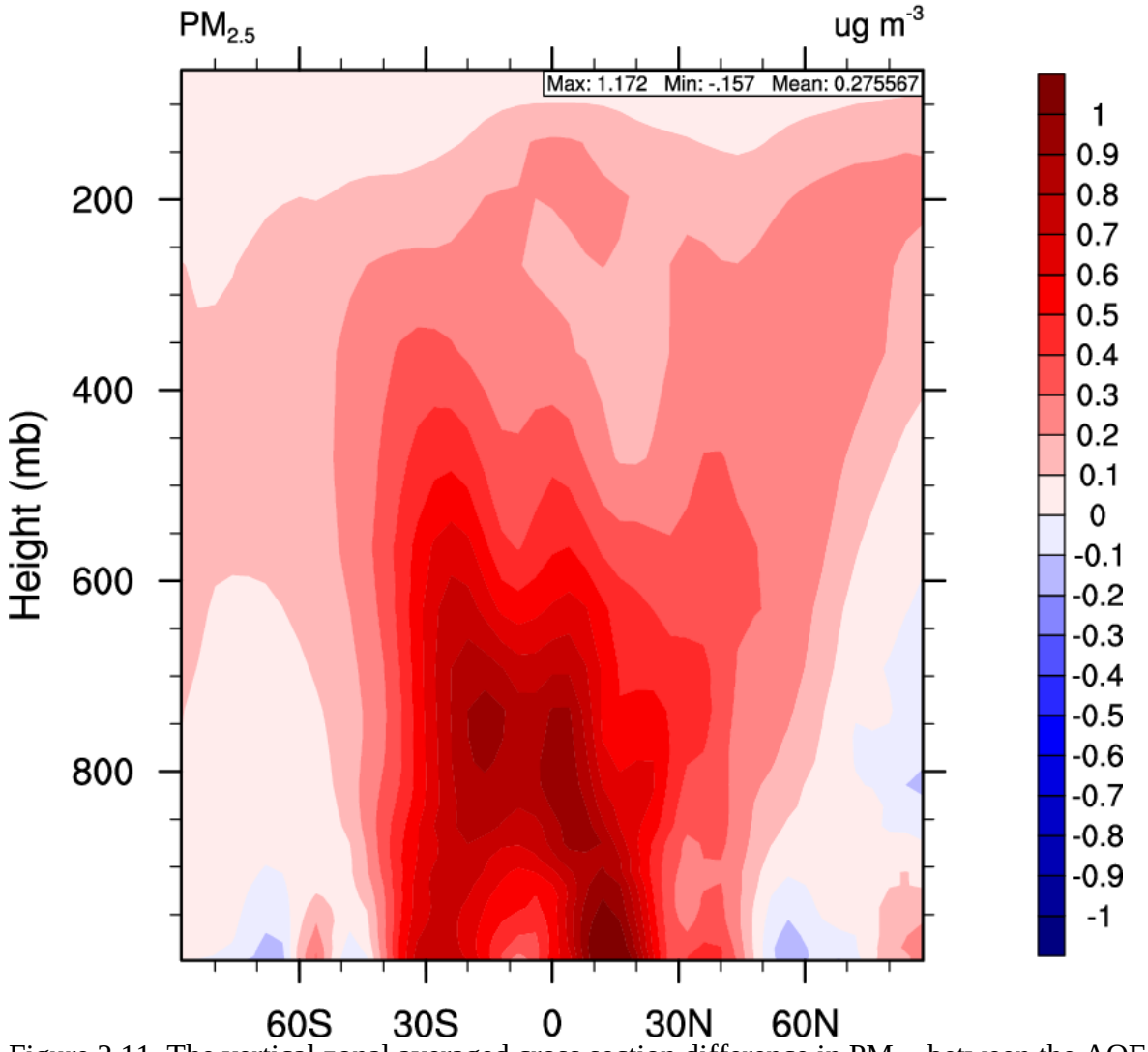

Figure 2.11. The vertical zonal averaged cross section difference in $PM_{2.5}$ between the AOF and AOC periods.

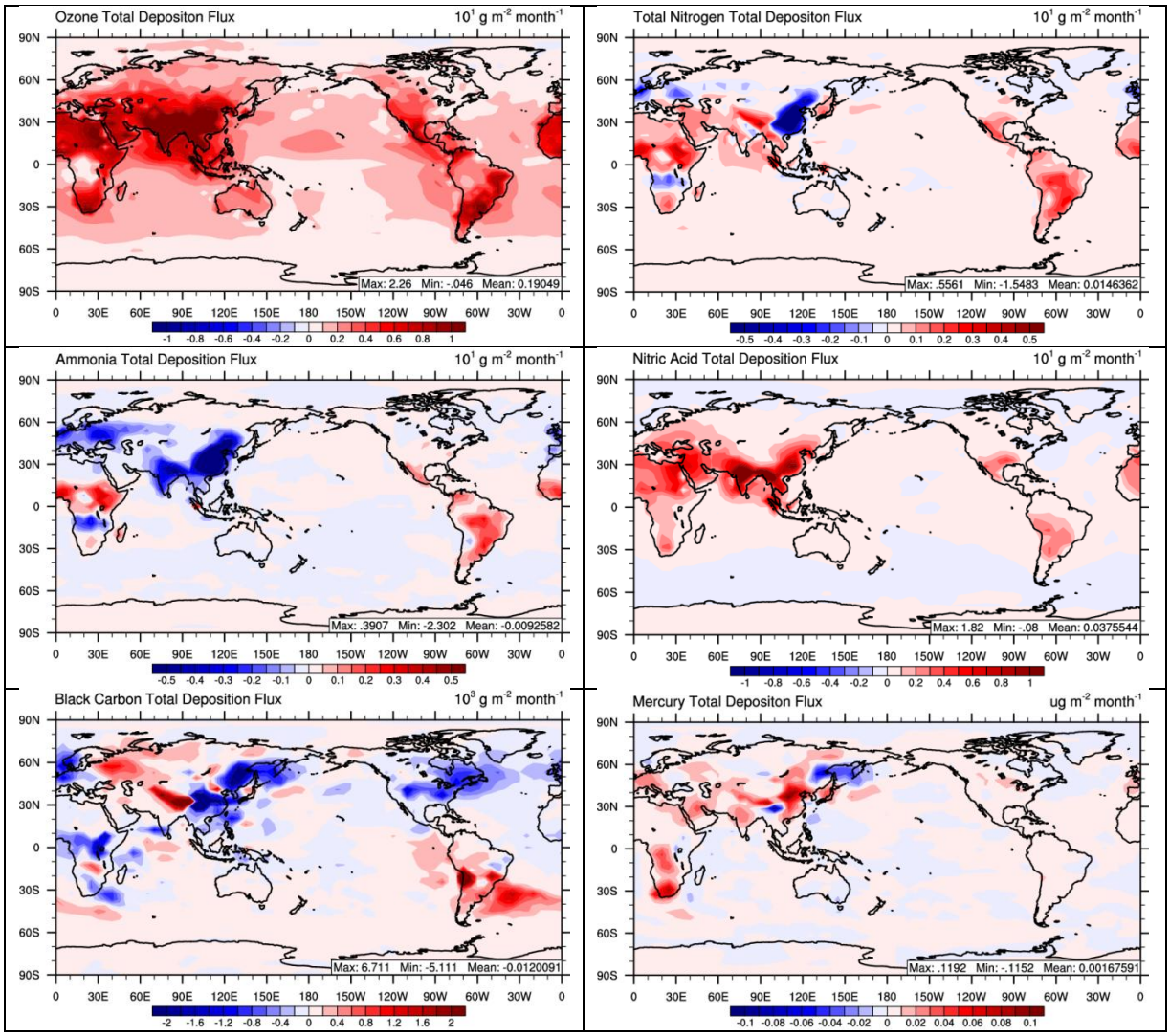

Figure 2.12. Absolute changes in the total deposition flux of O_3, total nitrogen, NH_3, HNO_3, BC, and Hg between the AOF and AOC periods.

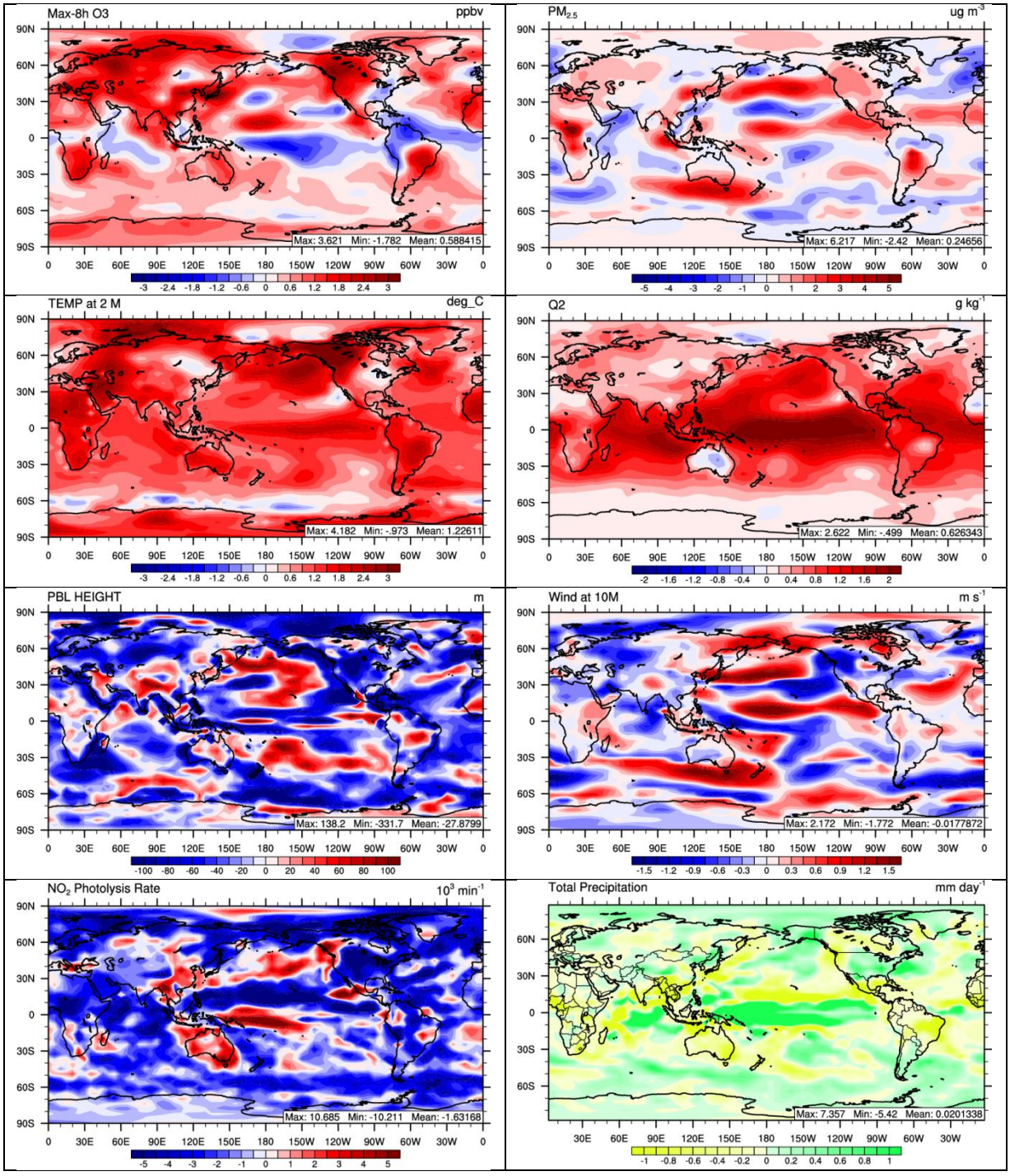

Figure 2.13. Absolute differences in $O_3$8hr, $PM_{2.5}$, T2, Q2, PBLH, WSP10, NO_2 photolysis rate, and precipitation between the 2050 climate change only simulation and 2001.

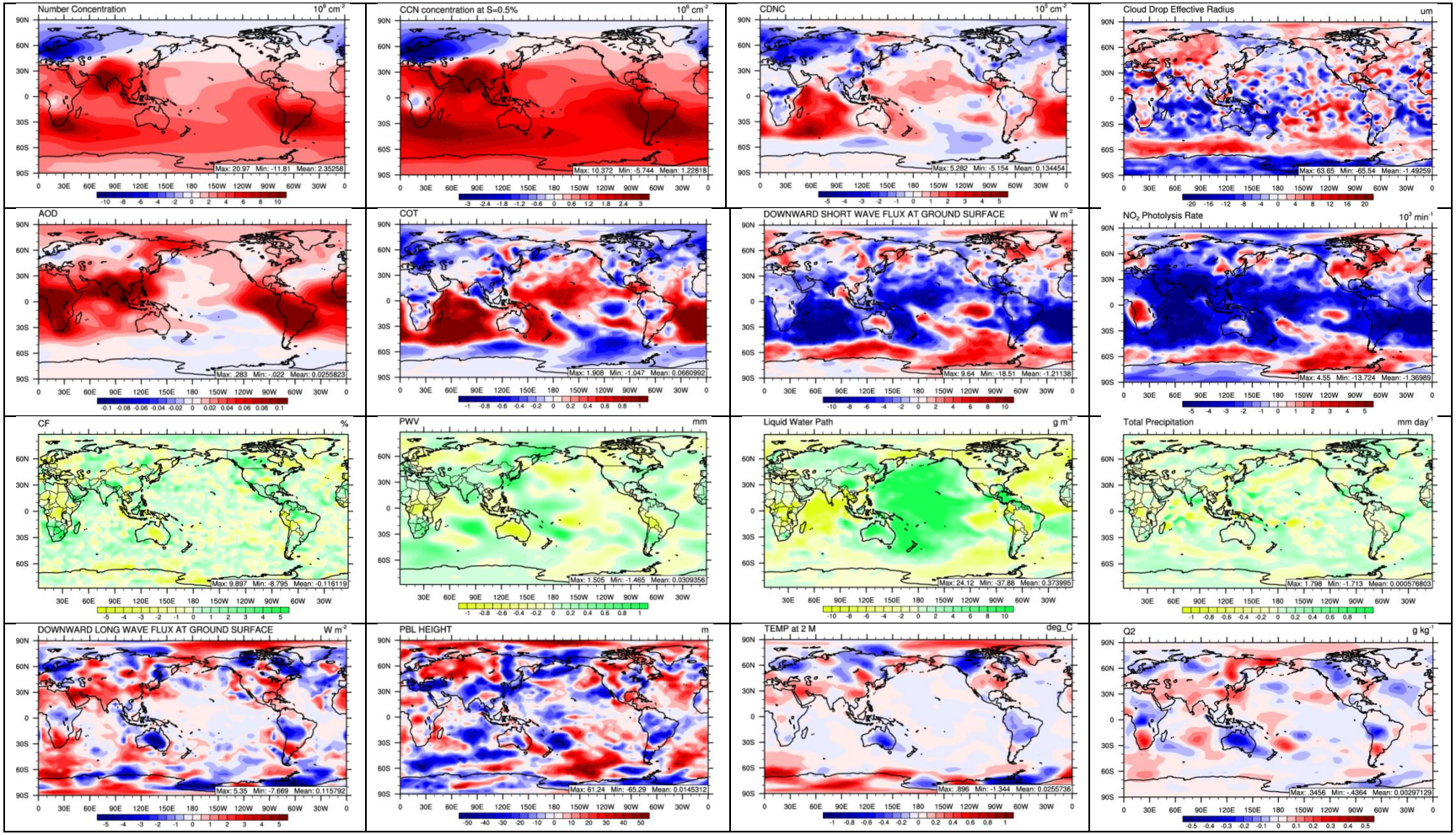

Figure 2.15. Absolute differences in NUM, CCN, CDNC, Reff, AOD, COT, SWDOWN, NO_2 photolysis rate, CF, PWV, LWP, PR, GLW, PBLH, T2, and Q2 between the 2050 simulation with projected emissions and the 2050 simulation without projected emissions.

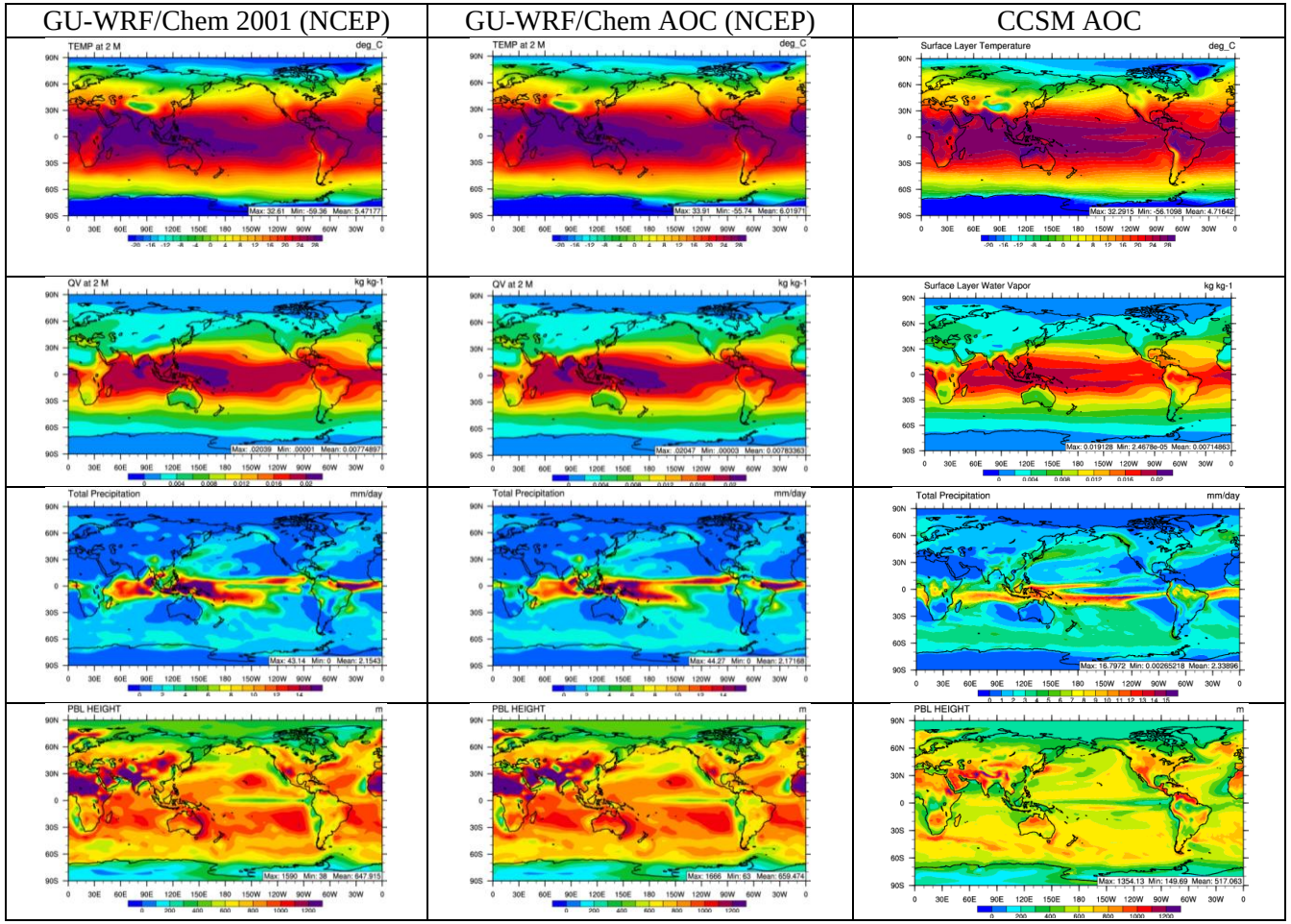

Figure 2.16. Average spring (MAM) 2-m temperature, 2-m water vapor, precipitation rate, and planetary boundary layer height fields from GU-WRF/Chem simulations of the year 2001 (left), averaged current period consisting of 2001 and 2010 (AOC) (center), and the average of the current period 2000-2014 from CCSM3 (right). GU-WRF simulations are initialized with the NCEP-FNL data.

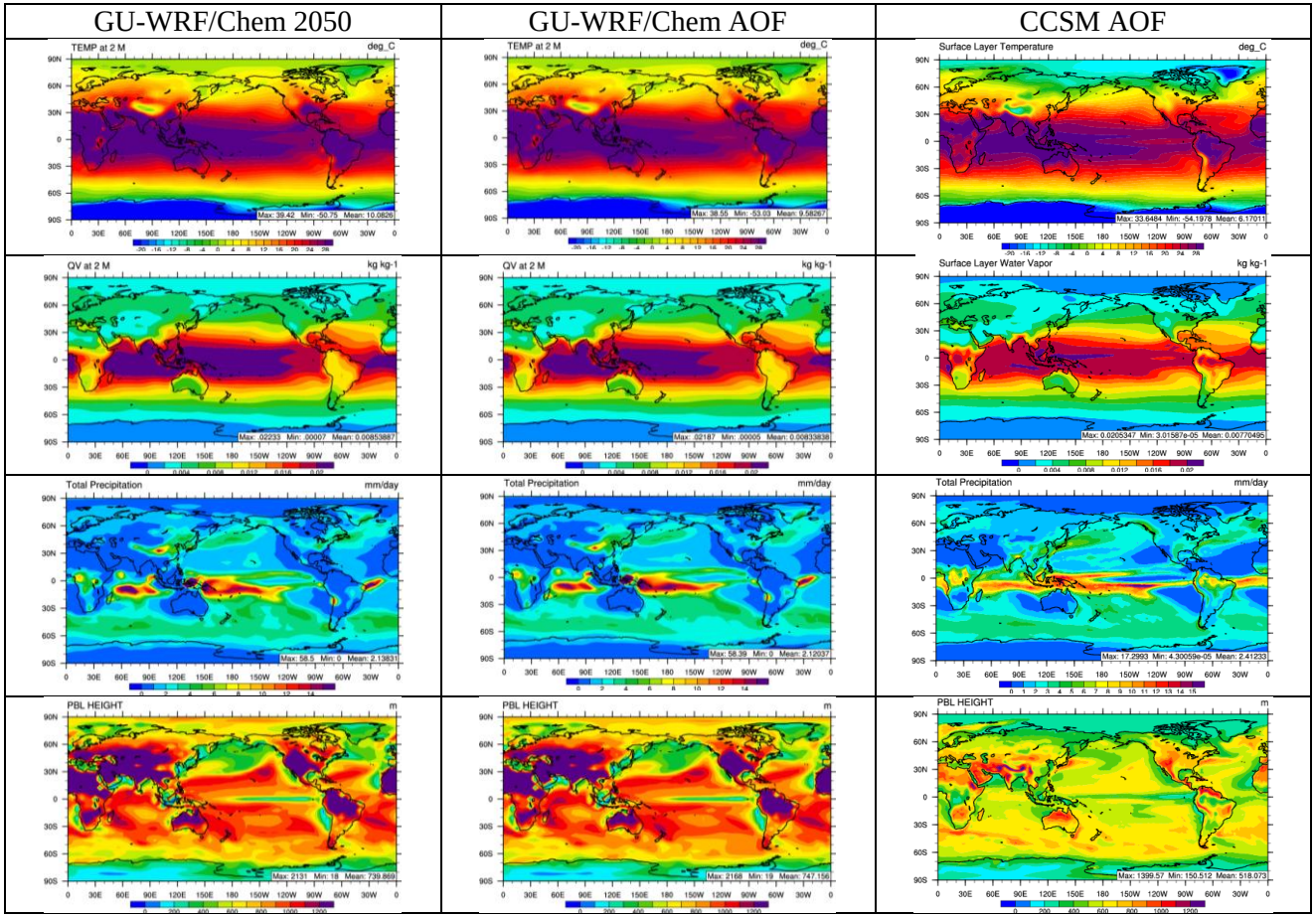

Figure 2.17. Average spring (MAM) 2-m temperature, 2-m water vapor, precipitation rate, and planetary boundary layer height fields from GU-WRF/Chem simulations of the year 2050 (left), averaged future period consisting of 2020, 2030, 2040, and 2050 (AOF) (center), and the average of the future period 2015-2054 from CCSM3 initial conditions (right).

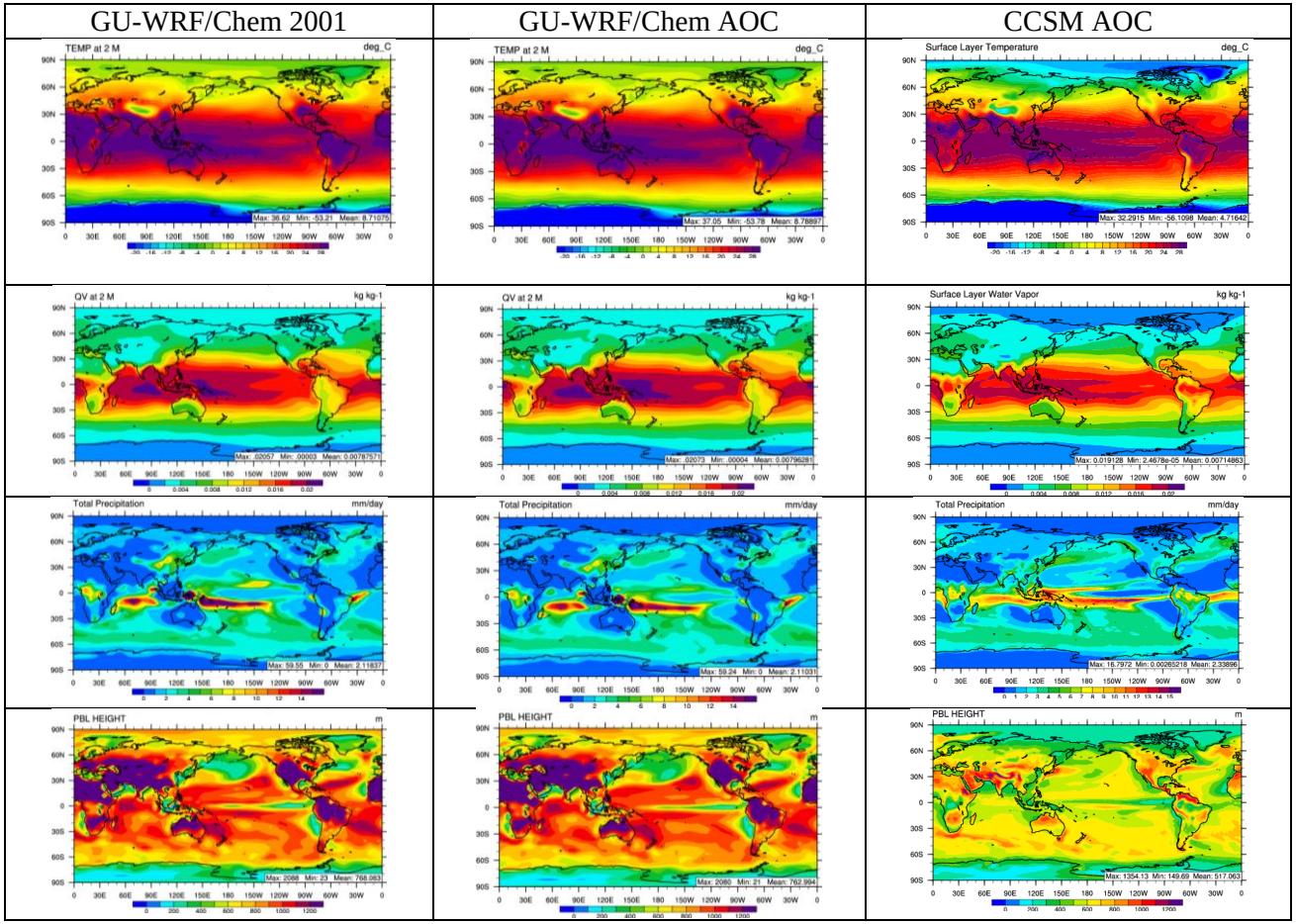

Figure 2.18. Average spring (MAM) 2-m temperature, 2-m water vapor, precipitation rate, and planetary boundary layer height fields from GU-WRF/Chem simulations of the year 2001 (left), averaged current period consisting of 2001 and 2010 (AOC) (center), and the average of the current period 2000-2014 from CCSM3 initial conditions (right)

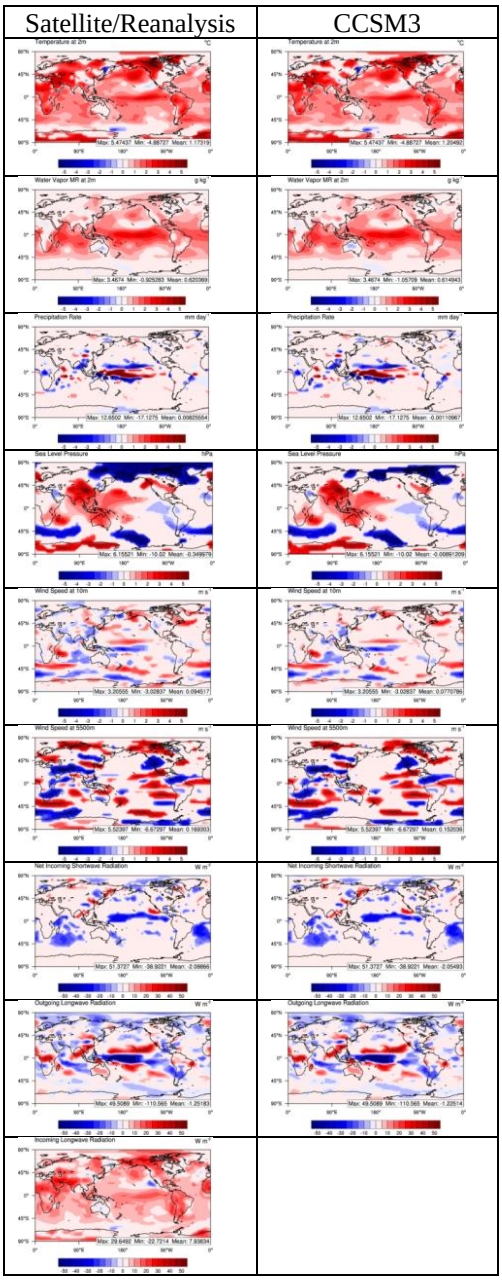

Figure 2.19. The statistically significant differences in T2, Q2, SLP, WSP10, WSP5500, PR, GSW, OLR, and GLW between MAM 2050 and 2001 that are greater than the variability in the current climate from reanalysis or satellite data (left) and greater than the variability in the current and future climate from CCSM3 (right). The GLW plot in the bottom row of the CCSM3 column was not generated since the CCSM3 GLW data was not readily available.

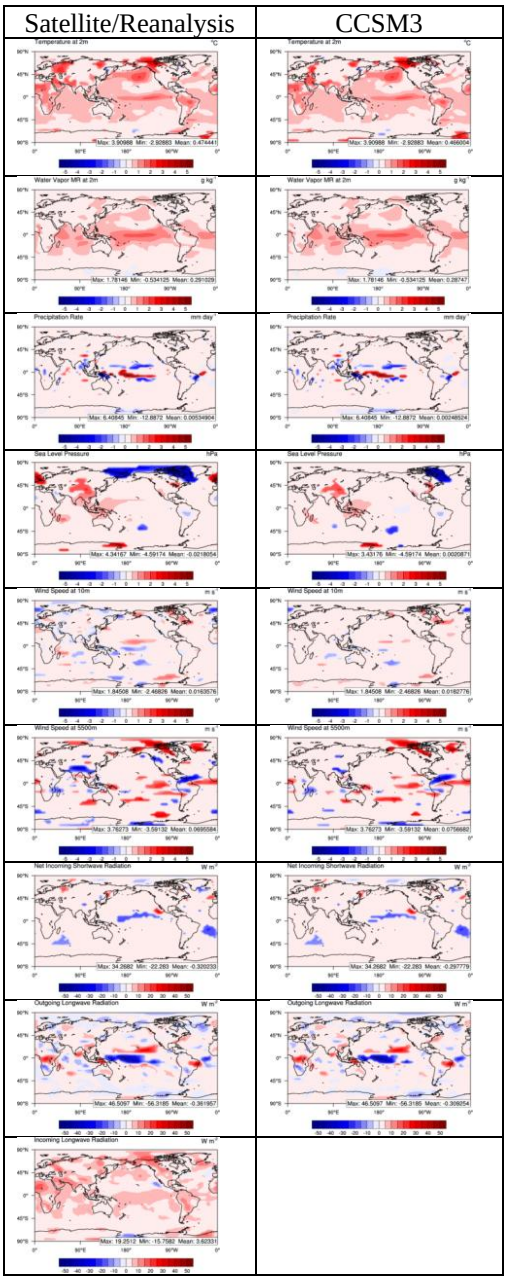

Figure 2.20. The statistically significant differences in T2, Q2, SLP, WSP10, WSP5500, PR, GSW, OLR, and GLW between MAM AOF and AOC that are greater than the variability in the current climate from reanalysis or satellite data (left) and greater than the variability in the current and future climate from CCSM3 (right). The GLW plot in the bottom row of the CCSM3 column was not generated since the CCSM3 GLW data was not readily available.

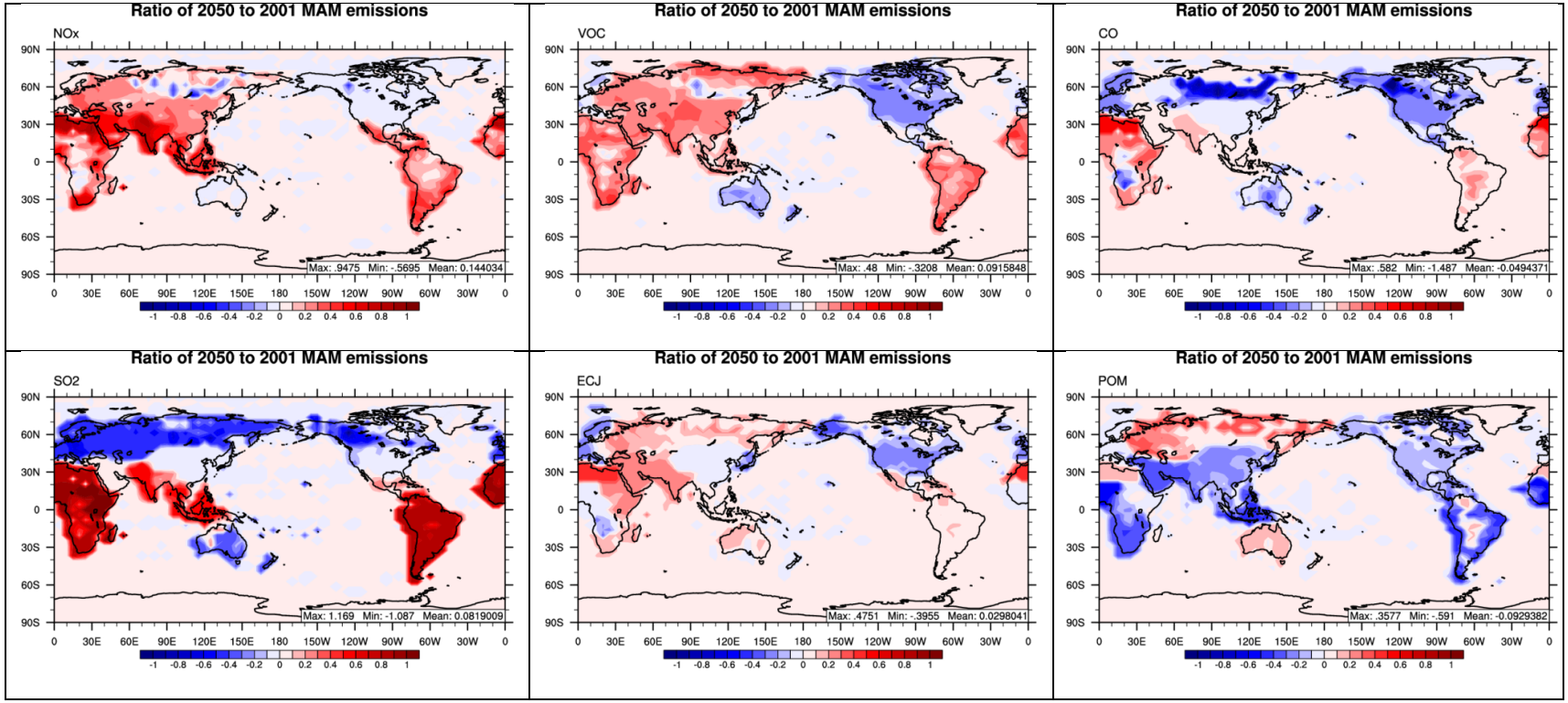

Figure 2.20. The logarithm of the ratio of 2050 spring (MAM) emissions to the 2001 MAM emissions of NOx, total non-methane VOC, CO, SO_2, black carbon, and primary organic carbon.

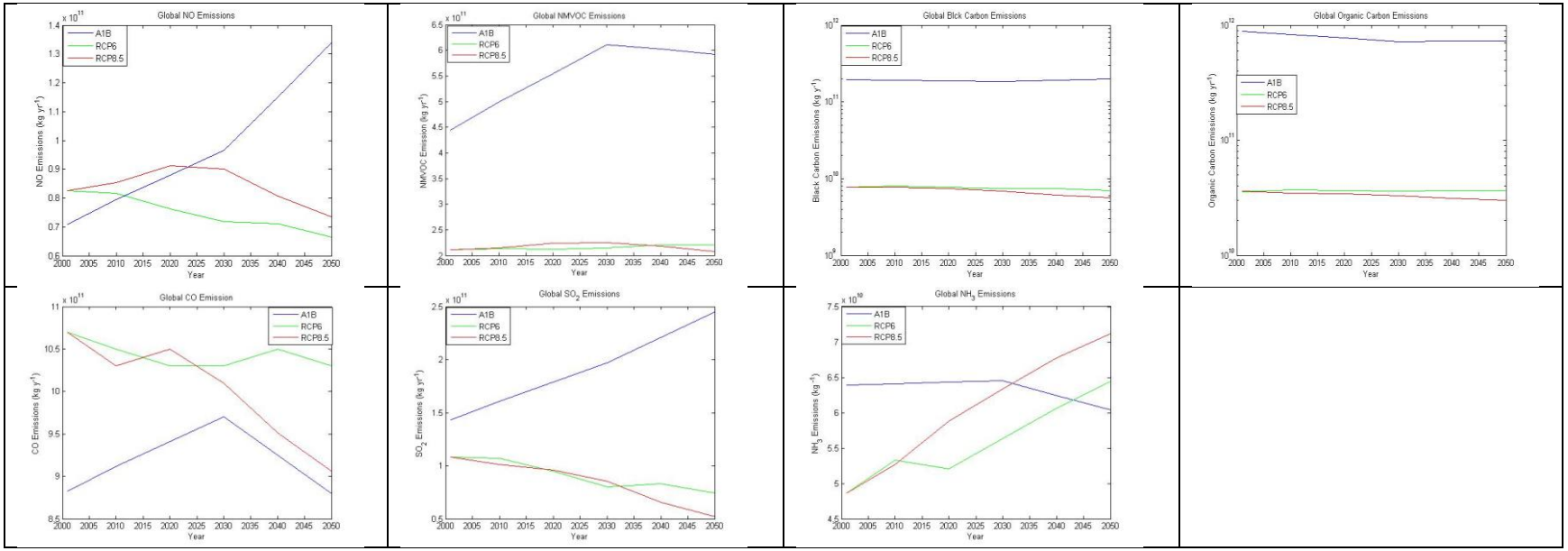

Figure 2.21. The time evolution of NO, volatile organic compound, black carbon, organic carbon, CO, SO_2, and NH_3 emissions in the GU-WRF/Chem A1B, RCP6, and RCP8.5 emission scenarios on a global scale.

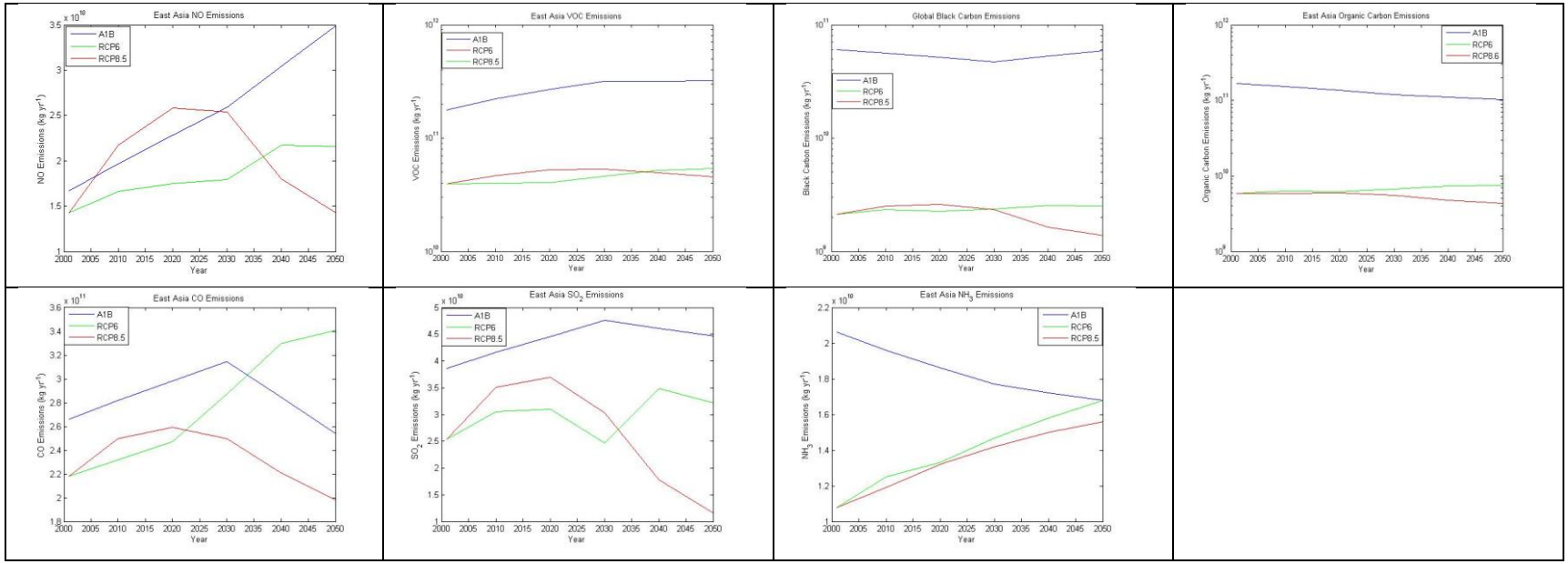

Figure 2.22. The time evolution of NO, volatile organic compound, black carbon, organic carbon, CO, SO_2, and NH_3 emissions in the GU-WRF/Chem A1B, RCP6, and RCP8.5 emission scenarios in East Asia.

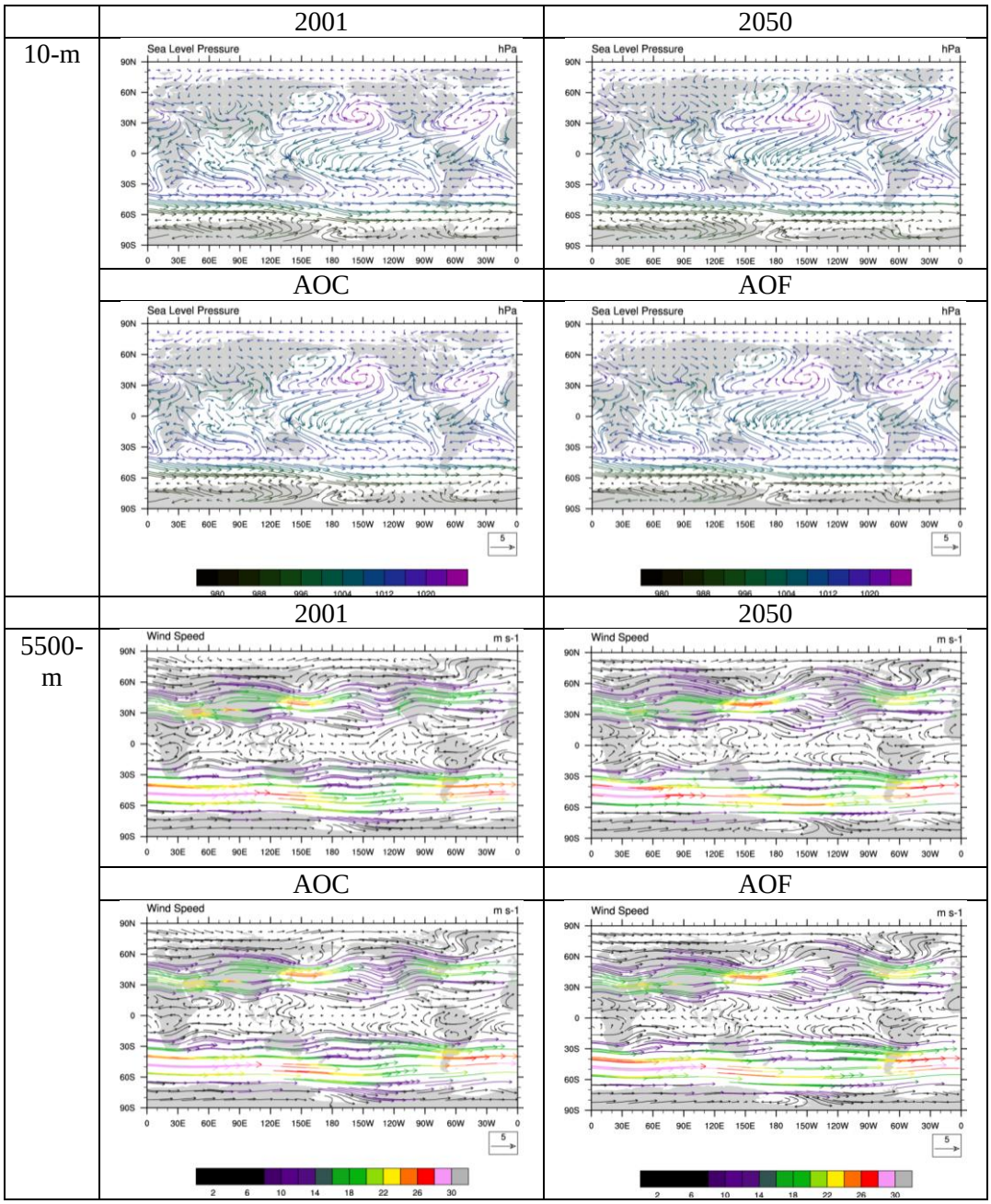

Figure 2.23. The average spring (MAM) weather patterns at the surface (top) and 5500 m (bottom) for 2001 and the average current period (left), 2050 and the average future period (right) from the baseline simulations. The surface plots depict the wind vectors from the 10 m wind components and the color scale is based on the sea level pressure. The 5500 m vectors are derived from the wind components interpolated to that height and the color scale is the magnitude of the wind speed.

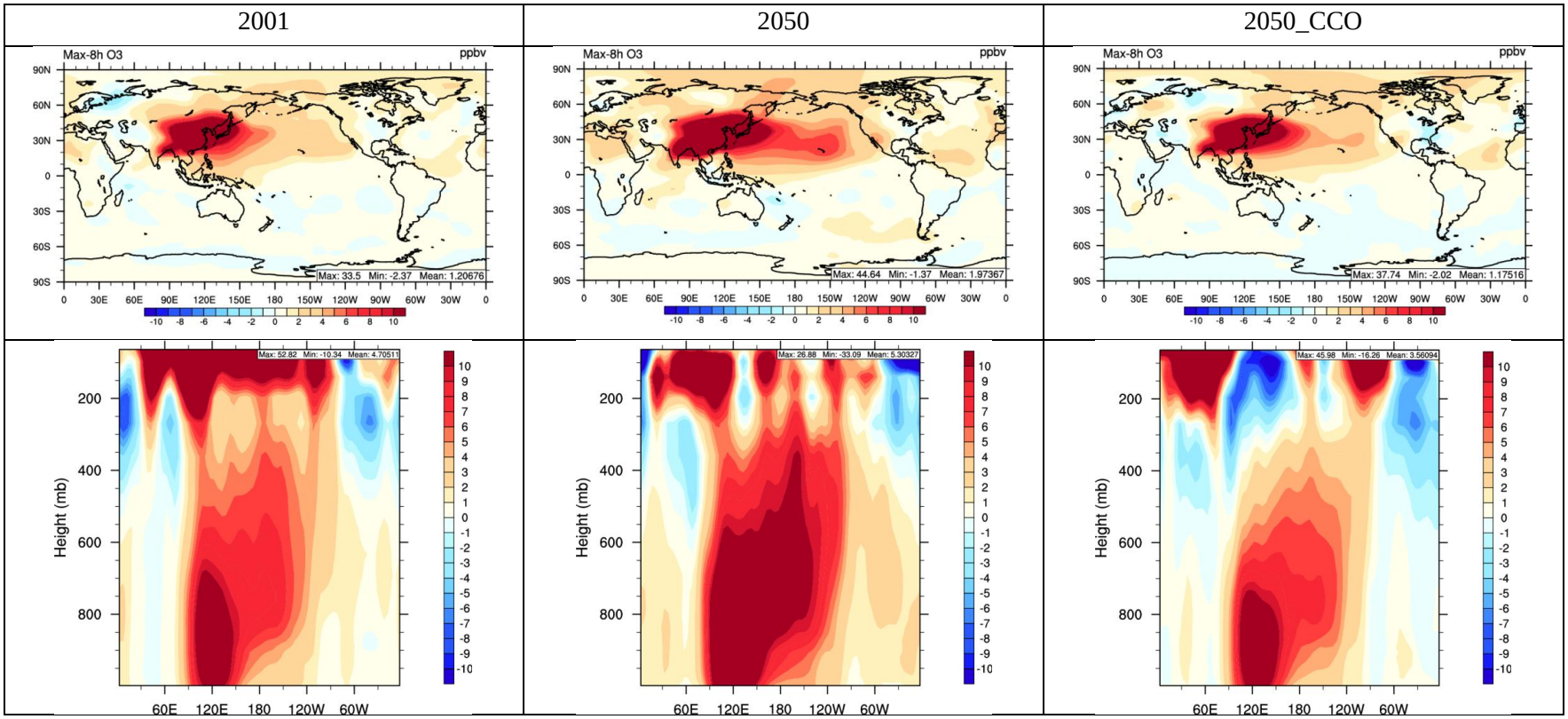

Figure 2.24. The difference in the spring (MAM) maximum 8-hr average surface ozone mixing ratio (top) and the mid-latitude (24°N to 60°N) meridional averaged vertical cross section of ozone (bottom) between the simulations with and without EAAEs for the current (2001) and future (2050 and 2050_CCO) scenarios.

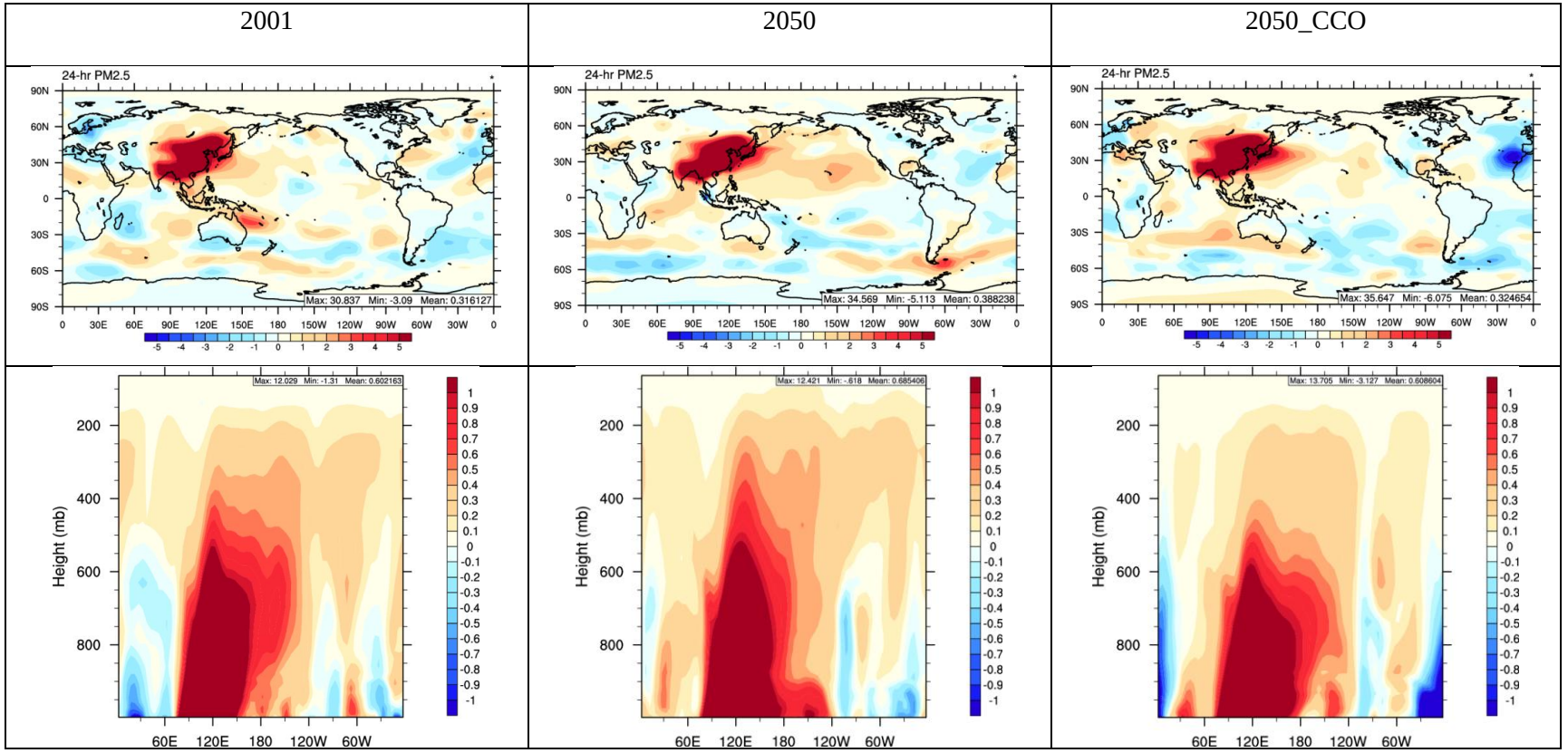

Figure 2.25. The difference in the spring (MAM) 24-hr average $PM_{2.5}$ concentration (top) and the mid-latitude (24°N to 60°N) meridional averaged vertical cross section of $PM_{2.5}$ (bottom) between the simulations with and without EAAEs for the current (2001) and future (2050 and 2050_CCO) scenarios.

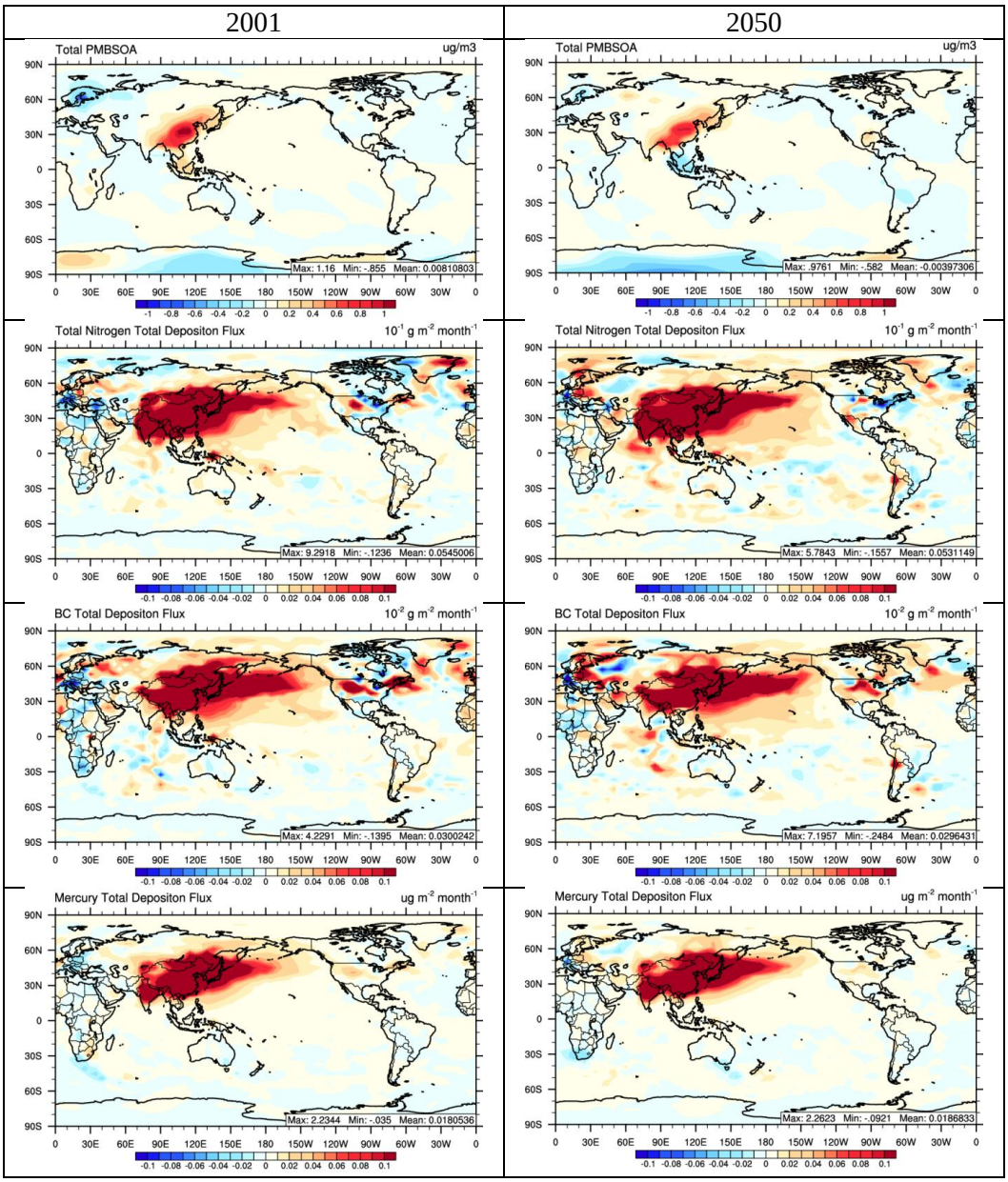

Figure 2.26. The difference in the spring (MAM) BSOA concentration (row 1), total deposition of total nitrogen (row 2), black carbon aerosol (row 3), and total gaseous and particulate mercury (row 4) between the simulations with and without EAAEs for the current (2001) and future (2050) scenarios.

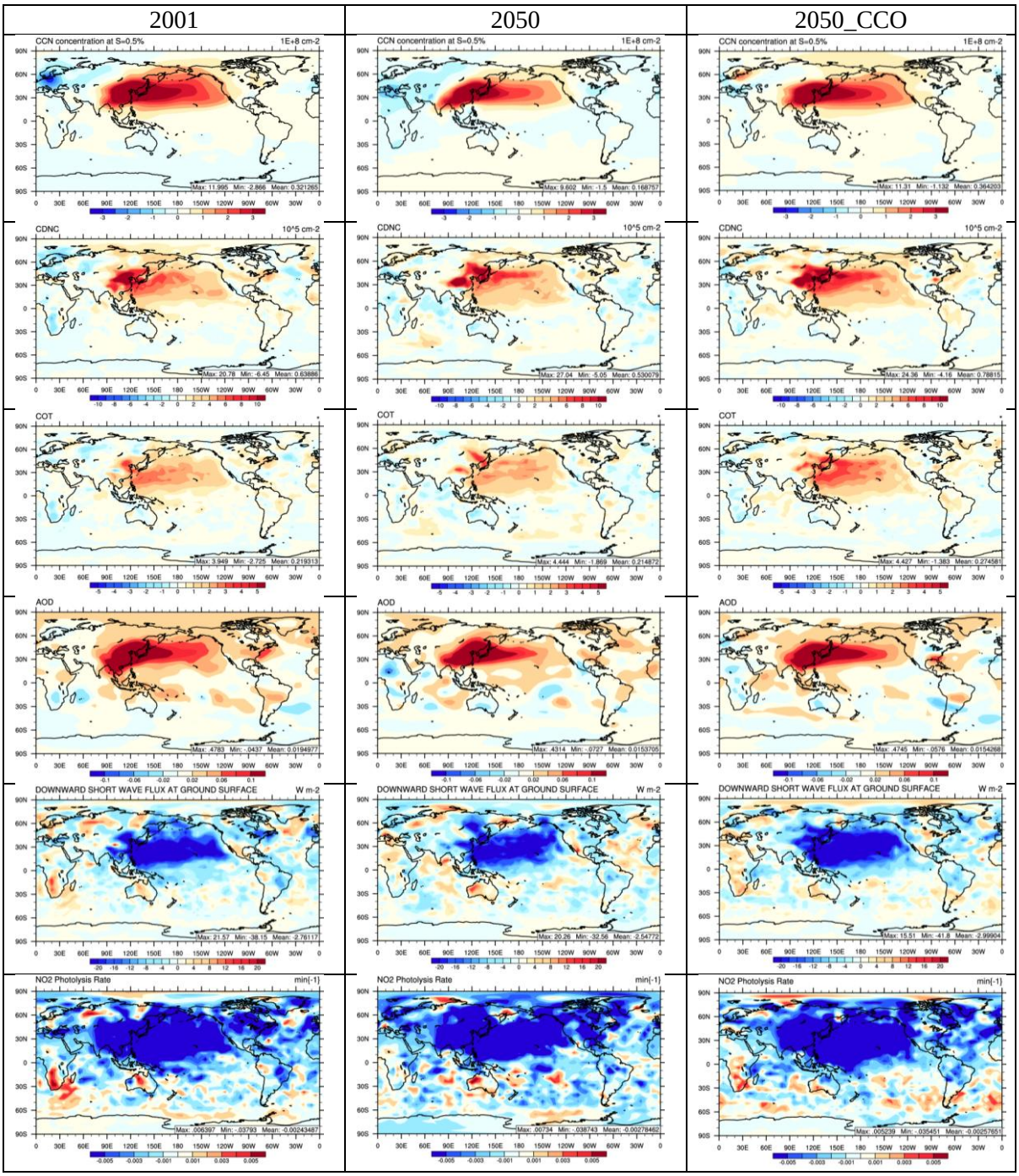

Figure 2.27. The difference in the spring (MAM) average cloud condensation nuclei (CCN), cloud droplet number concentration (CDNC), cloud optical thickness (COT), aerosol optical depth (AOD), downward solar radiation flux (SWDOWN), and the photolysis rate of NO_2 (JNO_2) between the simulations with and without EAAEs for the current (2001), future (2050), and climate change only (2050_CCO) scenario.

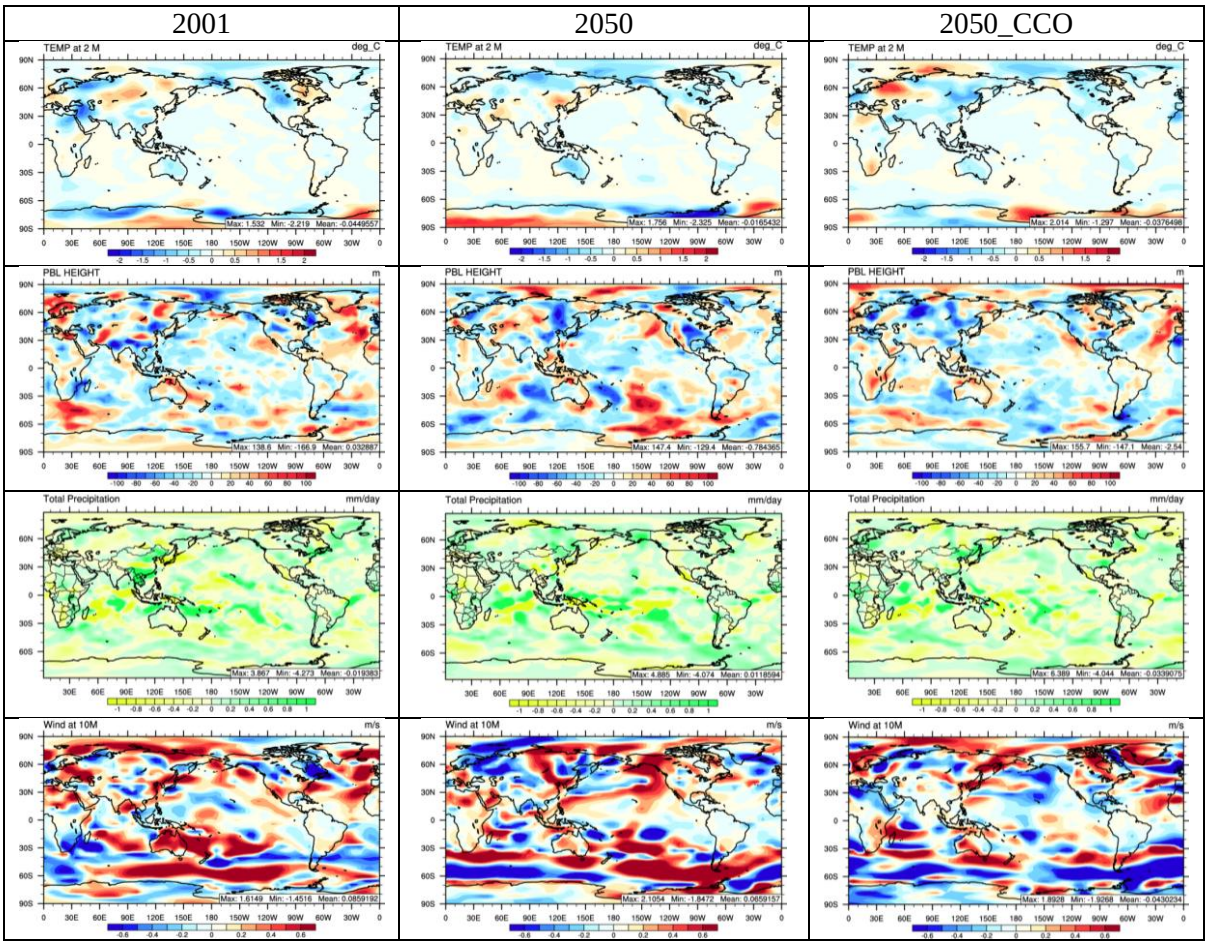

Figure 2.28. The difference in the spring (MAM) average 2 m temperature, planetary boundary layer height, total precipitation rate, and 10 m wind speed between the simulations with and without EAAEs for current (2001), future (2050), and climate change only (2050_CCO).

CHAPTER 3. INCORPORATION OF NEW ORGANIC AEROSOL TREATMENTS IN CESM-NCSU

3.1 Review of Organic Aerosol Modeling

Organic aerosol (OA) comprises a significant portion (18-70%) of submicron aerosol (Zhang, et al., 2007*; Jimenez et al.,* 2009). As a result, OA plays a role as a significant health hazard from an air quality standpoint (Nel, 2005), with the health impact of secondary organic aerosol (SOA) formed from aromatic hydrocarbons alone estimated to be responsible for 3,800 premature deaths in U.S. in 2006 (Von Stackelberg et al., 2013). OA, especially SOA, accumulates in the higher altitudes of the atmosphere where it has the ability to impact climate through direct radiative forcing (Henze and Seinfeld, 2006). OA is typically considered a light scattering aerosol, however, a portion of OA associated with certain biomass burning (BB) conditions referred to as "brown carbon" has varying light absorbing properties (Saleh et al., 2014). Previous model estimates of the top of the atmosphere direct radiative forcing of OA between the pre-industrial period and present day vary between -0.09 to -0.17 W m^{-2} assuming OA is an external mixture and -0.4 to -0.79 W m^{-2} treating OA as an internal mixture with black carbon (BC) and sulfate (Chuang and Seinfeld, 2002). However, more recent model estimates with updated pathways for OA formation show direct radiative forcing of SOA to vary between -0.12 to -0.31 W m^{-2} and the direct forcing of primary organic matter (POM) to vary between -0.06 and -0.11 W m^{-2} (Lin et al., 2014). In addition to direct radiative forcing, OA can also impact climate by acting as either cloud condensation nuclei (CCN) or ice nuclei, however, exactly how organic compounds impact these processes varies based on the organic compound and how these organic compounds interact with other

aerosol components (Sun and Ariya, 2006 and references therein; Hallquist et al., 2009 and references therein). Organic vapors have also been shown to help enhance new particle formation by forming highly stable organic acid – sulfuric acid complexes (Zhang, et al., 2004). The ability of OA to act as CCN in modeling studies varies with assumptions about the OA hygroscopicity parameter "κ", and uncertainties in κ have been shown to result in variations of 40-80% in CCN (Liu and Wang, 2010). These uncertainties in κ lead to a 0.4 W m^{-2} variation in total aerosol indirect radiative forcing between the preindustrial period and present day (Liu and Wang, 2010) and estimates of the aerosol indirect effect of SOA alone vary from -0.22 to -0.29 W m^{-2} (Lin et al., 2014).

Traditionally OA has been classified as either SOA, which forms in the atmosphere through the partitioning of low volatility organic vapors from the oxidation of anthropogenic and biogenic volatile organic compounds (AVOCs and BVOCs) into the aerosol phase, or POM that is non-volatile and directly emitted into the atmosphere from combustion. However, this conceptual framework does not account for many observed phenomena including: the high oxygen content of ambient OA (Zhang et al., 2005a; Aiken et al., 2008), small gradients in OA between urban areas and the surrounding environment (Zhang, et al., 2007; Donahue et al., 2009), and large increases in OA during periods of intense photochemical activity (Alfarra et al., 2004; Donahue et al., 2009). Dilution studies of fresh emissions from the combustion of diesel and wood show that significant amounts (50-80%) of the POM from these sources evaporate when diluted to clean or atmospheric conditions (Lipsky and Robinson, 2006; Shrivastava et al., 2006; Grieshop et al., 2009). It is also speculated that in past experiments semi-volatile organic compounds (SVOCs) are

misclassified as POM because the compounds are biased towards the aerosol phase, as a result of the dilution samplers used in these studies being operated with unrealistically high concentrations of organics (Donahue et al., 2009). Smog chamber experiments injected with diesel and wood combustion emissions reveal that the SVOCs generated from the evaporation of POM or emitted in the presence of POM can undergo oxidation in the presence of the OH radical and repartition into the aerosol phase as a more oxygenated OA (Robinson et al., 2007; Grieshop et al., 2009). This photochemical aging mechanism helps to explain many of the phenomena that cannot be explained by the traditional OA framework (Donahue et al., 2006, 2009; Robinson et al., 2007). These findings coupled with aerosol mass spectrometer (AMS) measurements indicate that OA may be better categorized using AMS terminology such as hydrocarbon-like organic aerosol (HOA) that corresponds to traditional POM or oxygenated organic aerosol (OOA) that includes traditional SOA, oxidized POM (OPOM), and also OA from the partitioning of SVOCs (SVOA) (i.e., OOA = SOA + SVOA) (Zhang et al., 2005b, 2007; Donahue et al., 2009; Jimenez et al., 2009). More recently the production of extremely low-volatility volatile organic compounds (ELVOCs) from the oxidation of BVOCs has been discovered (Ehn et al., 2014; Jokinen et al., 2015). The inclusion of these products that irreversible generate OA play a crucial role in atmospheric CCN production (Jokinen et al., 2015) and also may contribute to new particle formation in forested regions (Ehn et al., 2014).

In addition to partitioning of organic vapors onto existing aerosol, much attention has been put into understanding and simulating the formation of OA from aqueous reactions and oligometization in cloud and aerosol waters (Ervens et al., 2008; Fu et al., 2008; Hennigan et

al., 2008; Lim et al., 2010; Liu, et al., 2012; Liu, et al., 2012; Li et al., 2013). This pathway may be important as the partitioning of water soluble organic vapors has been shown to be enhanced with enhanced particle water in certain locations (Hennigan et al. 2008). Additionally, the degree of oxygenation of OA during foggy periods with low photochemical activity is as high as hazy days with greater photochemical activity (Li et al., 2013). One example of such partitioning is the formation of SOA from glyoxal. Glyoxal forms OA from either oligomerization after hydration in aerosol water or acid catalyzed heterogeneous reactions; these mechanisms have been proposed as an important glyoxal sink comparable to losses in the gas phase (Liggio et al., 2005a, b; Volkamer et al., 2007). OA formation from glyoxal also helps to partially explain the high oxygen content that is observed in ambient OA and the modeling framework for simulating glyoxal is adaptable to simulate OA formation from other carbonyl species such as methylglyoxal and glycolaldehyde (Ervens and Volkamer, 2010; Lim et al., 2010).

Simulating OA in chemical transport models (CTMs) requires a considerable simplification of the representation of organic species since OA is comprised of a complex mixture of millions of different organic species and the properties of only a small fraction of these species is known (Goldstein and Galbally, 2007*;* Andreae, 2009; Hallquist et al., 2009). There are currently three major methods for the simulation of OA in CTMs. These include the traditional approach, the volatility basis set approach (VBS), and the molecular approach. A comparison of these approaches is listed in Table 3.1. The traditional approach uses empirical data regarding the mass yields of SOA from the partitioning of AVOCs and BVOCs in smog chamber experiments and extrapolates those data to the atmosphere (Odum

et al., 1996). In this approach the data from the smog chamber experiments are fitted to represent the formation of OA from two or multiple OA forming products of VOC oxidation and the partitioning of these products is assumed to follow a quasi-ideal solution where the organic gases absorb onto preexisting organic material following the model of *Pankow* (1994) (Odum et al., 1996; Schell et al., 2001). The one dimensional version (1-D) of the VBS approach builds upon this traditional approach by lumping products from VOC oxidation indo different bins that represent the products volatility with an effective saturation concentration (C^*). This approach allows for the photochemical aging of these products which transfers their mass from higher volatility to lower volatility bins upon reaction with OH. This approach also allows for emissions of POM, SVOCs, and intermediate volatility compounds (IVOCs) to be mapped into similar bins and undergo similar photochemical aging (Donahue et al., 2006). The VBS approach can be expanded with additional dimensions beyond volatility with the most common second dimension being oxygen to carbon ratio (Donahue et al., 2011, 2012; Murphy et al., 2011). In the molecular approach, OA forming compounds are lumped together based on a number of identified molecular structures and the OA is formed according the different processes related to these surrogate compounds including not only the partitioning of hydrophobic species in the organic aerosol phase but also aqueous-phase reactions and oligomerization (Pun et al., 2002; Couvidat and Seigneur, 2011; Couvidat et al., 2012; Couvidat and Sartelet, 2014). In general both the VBS and molecular approaches provide a better representation of OA due to additional pathways for OA formation (Donahue et al., 2006; Couvidat et al., 2012). However, the VBS approach

may be a better choice in global CTMs because of its relative simplicity and adjustable complexity (Donahue et al., 2006).

The VBS approach has been adapted into many 3-D CTM studies at the local (Tsimpidi et al., 2010; Shrivastava et al., 2011; 2013), regional (Lane et al., 2008a; Shrivastava et al., 2008; Murphy and Pandis, 2009; Ahmadov et al., 2012; Bergstrom et al., 2012); and global (Farina et al., 2010; Jathar et al., 2011; Jo et al., 2013; Shrivastava et al., 2015) scales. A detailed comparison of the different VBS treatments in each modeling study is listed in Table 3.2. Comparisons of model performance over the U.S, Europe, and the NH from these modeling studies are compared against each other and the work modeling work presented in this study in Tables 3.3, 3.4, and 3.5, respectively. In general, models employing a VBS treatment perform well against observations but there are still discrepancies and large uncertainties in the treatments due to many unconstrained parameters. For example, many studies suggest that photochemical aging of biogenic SVOCs should not be treated because this leads to overpredictions of OA (Lane et al., 2008a; Murphy and Pandis, 2009; Farina et al., 2010; Jathar et al., 2010). However, it has been shown that satisfactory agreement with observations can be obtained while accounting for the aging of biogenic SVOCs with different assumptions regarding the deposition of SVOCs and fragmentation of SVOCs (Ahmadov et al., 2012; Shrivastava et al., 2013). There are also inconsistencies in model performance between the global and regional scales and different models. The most predominant difference between existing global and regional modeling studies is the lack of biogenic aging and the use of conservative photochemical aging assumptions that neglect functionalization (Farina et al., 2010; Jathar et al., 2011). Regional VBS studies over the U.S.

typically show overpredictions in OA against data from the Interagency Monitoring of Protected Visual Environments (IMPROVE) dataset, which represents rural locations, while underpredicting OA levels at locations in the Speciation Trend Network (STN), which is comprised of mainly urban and suburban sites (Lane et al., 2008a; Murphy and Pandis, 2009; Ahmadov et al., 2012). This differs from global modeling studies that show underprediction in OA against IMPROVE observations (Farina et al., 2010; Jathar et al., 2011; Jo et al., 2013). This could be related to both the more conservative aging assumptions in the global modeling studies and also the coarser model resolution that would lead to greater diffusion of surface concentrations. Additionally, the work of Shrivastava et al. (2015) showed that model performance against IMPROVE sites is dependent on fragmentation assumptions in the VBS treatment. Over Europe the regional scale study of Bergstrom et al. (2012) and global scale study of Jo et al. (2013) both showed underpredictions against limited observations from the European Monitoring and Evaluation Programme (EMEP) monitoring sites but the study of Farina et al. (2010) showed an overprediction.

In this study several new treatments from the simulation of OA are implemented into a modified version of the Community Atmosphere Model version 5.1 (CAM5.1) that is part of the Community Earth System Model version 1.0.5 (CESM1.0.5) released by the National Center for Atmospheric Research's (NCAR). These treatments include (1) A VBS approach for the simulation of SOA formed from VOCs (VSOA); (2) A VBS treatment for the volatility of POM and SVOA; (3) A simplified treatment for the simulation of OA formed from glyoxal; and (4) A treatment to represent the impact of conucleation of sulfuric acid and organics. As shown in Table 3.2, the VBS treatments in this work differ from many previous

studies by including both functionalization and fragmentation processes, as well as, biogenic aging. These processes are not accounted for in many of the previous global modeling studies, with the exception of Shrivastava et al. (2015). In general this study and the work of Shrivastava et al. (2015) implement similar VBS treatments into the same CESM-CAM5 model. However, there are some key differences including different configurations for the gas-phase mechanism, aerosol module, and aerosol activation parameterization. Additionally, the VBS treatment of Shrivastava et al. (2015) treats OA as non-volatile and neglects organic conucleation process whereas the VBS treatment implemented here treats OA as semi-volatile and includes a simplistic representation of the organic conucleation process. There are also differences in the approaches of both this work and Shrivastava et al. (2015). The model evaluation of Shrivastava et al. (2015) focused primarily on the performance against OC measurements from the IMPROVE network, measurements of OA taken over the Amazon rainforest, and AOD retrievals over regions with high OA levels. The model evaluation in this study has a greater focus surface performance across the NH from various measurement networks, to determine if the model can represent current atmospheric conditions, and focuses more on the impact of OA on cloud parameters. There are also differences in simulation style. The simulations of Shrivastava et al. (2015) are carried out in an air quality forecasting style using real meteorological fields for the year 2009 compared to this study where CESM simulation are run in a climate model style using meteorology and emissions representative of current climate, similar to the approaches of Farina et al. (2010) and Jathar et al. (2011).

The objectives of this work are to evaluate the updated model's performance for OA simulated under current atmospheric conditions to determine if the model should be applied for future climate simulations, and to investigate the impact of some of the many uncertainties associated with these treatments on OA and aerosol-cloud interactions. It is imperative that such a treatment for OA be included in global climate models such as CESM1.0.5/CAM5.1 since OA will likely become the most dominant aerosol species over time. This is due to enhanced biogenic VOC emissions and enhanced oxidation predicted in the future environment and because many emission projections indicate a more rapid decrease in emissions of other aerosol precursors such as SO_2 than POM and anthropogenic VOCs by the year 2100 (Tagaris et al., 2007; Heald et al., 2008).

3.2 Model Development and Improvements

The CESM1.0.5 model is a state of the art online-coupled earth system model that simulates the Earth's atmosphere, oceans, sea ice, and land surface and their interactions. This study focuses on the atmosphere component model, i.e., the CAM5. Details of the default physical and chemical parameterizations and options for the released standard version of this model can be found at http://www.cesm.ucar.edu/models/cesm1.0/cam/. The model used in this study is a version of CESM1.0.5/CAM5.1.that has been modified at the North Carolina State University (hereafter CESM-NCSU) (He and Zhang, 2014; Gantt et al., 2015). CESM-NCSU includes several new gas and aerosol treatments compared to the standard version of the model available for public release. As described in He and Zhang (2014) and Gantt et al. (2015), these updates include: (1) the addition of the Carbon Bond 05 mechanism with global extension (CB05GE) of (Karamchandani et al., 2012) for gas-phase

chemistry; (2) the addition of the computationally-efficient inorganic aerosol thermodynamic model ISORROPIA II of (Fountoukis and Nenes, 2007) that allows for the simulation of NO_3^- and NH_4^+ and the explicit treatment of Na^+, Cl^-, Mg^{2+}, K^+, Ca^{2+} ions from dust and sea-salt; (3) the inclusion of the ion mediated nucleation scheme (IMN) of Yu (2010) and that the use of the maximum nucleation rate (J) between the IMN and existing nucleation schemes as the simulated J; and (4) the inclusion of the Fountoukis and Nenes (2005) aerosol activation scheme, as well as a treatment for the activation of giant CCN (Barahona et al., 2010) and the adsorptive activation of insoluble aerosols (Kumar et al., 2009) to provide more aerosol cloud interaction pathways (hereafter the FN series). The complete list of chemical and physics options used in this work is listed in Table 3.6.

In this work, the original organic aerosol treatments are modified to include several new treatments to enhance the model's capability to simulate OA, in particular, SOA. The original and new OA treatments are described below and a flow chart indicating the differences between both treatments is shown in Figure 3.1.

3.2.1 Organic Aerosol Treatments in the Standard Version of CESM/CAM5.1

Organic and inorganic aerosols are both treated in the standard version of CESM/CAM5.1 using either the 3 mode or 7 mode Modal Aerosol Model (MAM3 or MAM7) (Liu, et al., 2012). In this study the organic aerosol updates have been implemented into the MAM7 aerosol module. MAM7 treats OA in a manner consistent with the traditional approach using two species representing POM and SOA. Fresh POM is emitted directly into the atmosphere in the primary carbon mode along with black carbon where they are treated as externally-mixed particles. These particles then age and grow into the internally-mixed

accumulation mode either through condensations of H_2SO_4, NH_3, HNO_3, HCl, and SVOCs or coagulation with sulfate, nitrate, ammonium, sea-salt, or SOA in the Aiken mode.

In the standard version of CESN1.0.5/CAM5.1, SOA is generated from a lumped SOA gas precursor (SOAG). This precursor is treated as an emitted species in the model framework and the emission is based on assumed mass yields of the alkanes, alkenes, toluene, isoprene, and monoterpene species from the Model for Ozone and related chemical Tracers version 4 (MOZART-4) (Emmons et al., 2010). However, with the addition of the CB05GE mechanism in the CESM-NCSU, the SOAG precursor has been modified to represent the lumped CB05GE SOA precursor products from the oxidation of the monoterpenes (i.e., α-pinene (APIN), β-pinene (BPIN), limonene (LIM), ocimine (OCI), and terpinene (TER)), sesquiterpene (i.e., humulene (HUM)), isoprene (ISOP), anthropogenic aromatics (i.e., toluene (TOL) and xylene (XYL)), polycyclic aromatic hydrocarbons (PAHs), and long chain alkanes (ALKH) (Karamchandani et al., 2012; He and Zhang, 2014). There is high uncertainty in this SOAG precursor in either the standard version of CESN1.0.5/CAM5.1 or the CESM-NCSU. For example, in the standard version, the mass yields used from the MOZART-4 species were artificially scaled up by a factor of 1.5 to achieve better agreement for anthropogenic aerosol indirect forcing (Liu, X. et al., 2012) and there are no SOA mass yields used to constrain the SOA forming potential of the SOA precursors from CB05GE.

The SOAG precursor undergoes condensation to and evaporation from the aerosol phase in either the accumulation or the Aiken mode of MAM7 following Raoult's Law. The equilibrium partial pressure of SOAG in each mode *m* (P_m^*) is expressed as:

$$P_m^* = \left(\frac{M_m^{SOA}}{M_m^{SOA} + 0.1\ M_m^{SOA}} \right) P^0 \quad (3.1)$$

where M_m^{SOA} is the molar fraction of SOA in mode *m*, M_m^{POA} is the molar fraction of POM in the mode *m* (10% is assumed to be oxygenated), and P^0 is the mean saturation vapor pressure of SOAG. The temperature dependence of P^0 is expressed using the Clausius-Clapeyron equation with a reference P^0 of 1×10^{-10} atm at 298 K and an enthalpy of vaporization (ΔHvap) of 156 kJ mol^{-1} (Liu et al., 2012).

3.2.2 The New OA Treatments Implemented into CESM-NCSU

3.2.2.1 The Volatility Basis Set Approach

The VBS approach implemented in CESM-NCSU consists of two major components. The first is a VBS approach for simulating VSOA from the oxidation of VOCs and the second is a VBS approach for simulating the volatility of POM and the formation of SVOA from the oxidation of the evaporated POM vapors. The VSOA treatment in CESM-NCSU is adapted from one of the methods used in the Weather Research and Forecasting Model with Chemistry (WRF/Chem) (Grell et al., 2005) that utilizes either the CB05 (Yarwood et al., 2005) or Regional Atmospheric Chemistry Mechanism (RACM) (Stockwell et al., 1997) gas-phase mechanisms and the Model Aerosol Dynamics Model for Europe (MADE) (Ackermann et al., 1998) aerosol mechanism (Ahmadov et al., 2012; *Wang et al.*, 2014). In this treatment, the products of VOC oxidation by OH, O_3, and the NO_3 radical (NO_3) are mapped onto a four-bin volatility basis set with C*'s ranging from 10^0 to 10^3 μg m^{-3} at 298°C. The mass yields for these products in each volatility bin are listed in Table 3.7. The yields for all VOC species except PAH are mapped to the species in CB05GE based on those

used for the SAPRC-99 mechanism (Carter, 2000) as described in Murphy and Pandis (2009). This mapping to SAPRC-99 species was also used for RACM in the work of Ahmadov et al. (2012). The mass yields for PAHs in each volatility bin are derived following the method of Stanier et al. (2008) using data from the smog chamber experiments of Chan et al. (2009), in which the SOA mass yields of naphthalene, 1-methylnaphthalene, and 2-methylnaphthalene are averaged as surrogates for PAHs. The PAH mass yields had to be generated separately as no mass yields for this species are available for this volatility basis set from previous studies.

In the CESM-NCSU approach, SOA partitions using the following equation:

$$c_n^{aer} = \frac{c_n^{tot}}{1 + \frac{c_n^*}{M}} \tag{3.2}$$

where c_n^{aer} is the SOA concentration in volatility bin *n*, c_n^{tot} is the sum of the SOA and anthropogenic and biogenic SVOCs capable of forming SOA in bin *n*, c_n^* is the saturation concentration calculated using the Clausius-Clapeyron equation with a ΔHvap value of 30 kJ mol^{-1} in bin *n*, and M is the total organic aerosol mass available for partitioning (Ahmadov et al., 2012). Equation (3.2) is solved using the Newtonian Iteration method. The amount of anthropogenic and biogenic SVOCs from the VOC precursor *i* available to form SOA in each volatility bin *n* ($SVOC_n^i$) is calculated as:

$$SVOC_n^i = a_n^i P_n^i \tag{3.3}$$

where a_n^i is the SOA mass yield of VOC species *i* in volatility bin *n* and P^i is the sum of the products of VOC species *i* oxidized by OH, O_3, and NO_3 (Ahmadov et al., 2012). The value

of a_n^i depends on the ambient NO_x level and varies between high and low NO_x conditions. a_n^i is calculated based on the following equation in the standard version of CESM:

$$a_n^i = B\ a_n^{i,high} + (1 - B)\ a_n^{i,low} \tag{3.4}$$

where B is the branching ratio, $a_n^{i,high}$ and $a_n^{i,low}$ are the SOA mass yields of VOC species *i* in volatility bin *n* under high and low NO_x conditions, respectively. The branching ratio in CESM-NCSU is generated using the formula (Lane et al., 2008b; Ahmadov et al., 2012):

$$B = \frac{k_{(XO_2+NO)}}{k_{(XO_2+NO)} + k_{(XO_2+XO_2)} + k_{(XO_2+HO_2)}} \tag{3.5}$$

where $k_{(XO_2+NO)}$ is the reaction rate of organic radicals against NO, $k_{(XO_2+XO_2)}$ is the reaction rate of the self-destruction of organic radicals, and $k_{(XO_2+HO_2)}$ is the reaction rate for loss of organic radicals from reaction with HO_2 (Lane et al., 2008b).

In the 1-D VBS framework, both anthropogenic and biogenic SVOCs are allowed to undergo photochemical aging against the OH radical to reduce the volatility of the SVOCs. In order to represent this process without the so called “zombie” effect mentioned in Bergstrom et al. (2012) where the SVOCs constantly reduce volatility, the functionalization (i.e., the addition of oxygen atoms from oxidation that increase the mass of the SVOCs) and fragmentation (i.e., the breaking of carbon bonds during oxidation that case an increase in the volatility of the SVOCs) (FF) of Shrivastava et al. (2013) are employed. In the method of Shrivastava et al. (2013), an additional dimension of oxidation generation (g) is added to the gas-phase SVOCs, thus effectively making the original 1-D VBS method a 1.5-D VBS framework. It is a 1.5-D VBS framework rather than a 2-D VBS framework because there

are two dimensions in the gas phase (e.g., volatility and oxidation generation) but only one dimension in the aerosol phase (e.g., volatility). This differs from 2-D VBS frameworks that have two dimensions in both the gas and aerosol phases (typically volatility and oxygen-to-carbon ratio) (Donahue et al., 2011, 2012; Murphy et al., 2011). In the 1.5-D VBS framework, the first two generations of oxidized SVOC undergo the following photochemical aging reaction:

$$SVOC_n^g + OH \rightarrow 1.15\ SVOC_{n-1}^{g+1} \quad (3.6)$$

where $SVOC_n^g$ is the SVOC of generation *g* in volatility bin *n* and $SVOC_{n-1}^{g+1}$ is the SVOC with a higher oxidation generation and a lower volatility bin. The factor 1.15 represents an increase in mass of 15% from the addition of oxygen atoms. This 15% corresponds to an assumption of 2 oxygen atoms added during oxidation for a precursor of $C_{15}H_{32}$ (Shrivastava et al., 2013). However, there are some uncertainties in this quantity as fragmentation reactions have been shown to add anywhere from 0-2 oxygen atoms (Jimenez et al., 2009; Shrivastava et al., 2013) and previous VBS modeling studies have assumed only the addition of a single oxygen atom (i.e., 7.5%) (Shrivastava et al., 2008). All oxidation generations from the third generation forward are lumped together into an n^{th} generation (g^n). In this n^{th} generation there is both an addition of mass from additional oxygen atoms but also an increase in volatility for some portion of the SVOCs in order to represent the process of breaking the carbon bonds (fragmentation). Thus in these generations, the aging is represented using the following reaction:

$$SVOC_n^g + OH \rightarrow 0.575\ SVOC_{n-1}^{g^n} + 0.4\ SVOC_{n_{max}}^{g^n} \quad (3.7)$$

where $SVOC_{n-1}^{g^n}$ is the SVOC in the smaller volatility of the lumped oxidation generations and $SVOC_{n_{max}}^{g^n}$ is the SVOC in the highest volatility bin, n_{max}, of the lumped nth oxidation generations. This is the moderate fragmentation case from Shrivastava et al. (2013) and it represents a case where 57.5% of the mass is transferred to the lower volatility bin, 40% is lost to the highest volatility level in the VBS frame work, and the remainder is assumed to be lost to species of volatilities higher than those described by the VBS framework. The exact value of functionalization and fragmentation fractions are not constrained by measurements as mentioned in Shrivastava et al. (2013) and are merely generated from box model sensitivity studies. However, the functionalization and fragmentation processes are documented to occur, with fragmentation shown to occur after 1-4 generations of oxidation in conjunction with the addition of functional groups (Kroll et al., 2011). In all photochemical aging cases the reactions proceed with a rate constant of 1.0×10^{-11} cm^3 moles^{-1} s^{-1}, which is a rate assumed to be characteristic of the OH degradation of products of aromatic VOC oxidation (Atkinson, 2000; Atkinson and Arey, 2003; Murphy and Pandis, 2009; Ahmadov et al., 2012).

The method for representing the volatility of POM and SVOA utilizes the same partitioning method as the VSOA treatment and simulates a similar aging process. The treatment for POM and SVOA is adapted from the treatment of Shrivastava et al. (2008) (S08) with a few minor updates. These updates include a new emission fraction spectrum for mapping the POM emissions into different volatility bins and the assumption that all the mass from volatility bins with C* of 10^5 and 10^6 μg m^{-3} remain in the gas-phase. These new

emission fractions as well as the emission fractions of S08 and enthalpy of vaporizations from both S08 and the parameterization of Epstein et al. (2010) (E10) are listed in Table 3.8. The E10 parameters are listed as an alternative to the S08 values and model performance using the E10 values will explored in a sensitivity experiment. The emissions fractions in this work differ between anthropogenic and biomass burning sources. The anthropogenic emission fractions (EFA) and the biomass burning emission fractions (EFBB) are based on the recommended emission fractions for gasoline vehicle exhaust from the work of May et al. (2013a) and for biomass burning from the work of May et al. (2013b), respectively. This updated emission spectrum is used because the S08 emissions spectrum is too volatile as will be demonstrated in Section 3.4.1. However, the updated emission spectrum does use the same factors as S08 to generate the additional unaccounted for IVOC emissions in the emission inventory representing 1.5 of the existing POM mass. It is important to note that these emissions are poorly constrained and could vary between 0.25 and 2.8 times the existing POM emissions (Shrivastava et al., 2008). The particulate phase of the two highest volatility bins has been shown to be negligible and is thus neglected to save computational cost (Shrivastava et al., 2008). Once the POM is emitted and undergoes gas/aerosol partitioning, the POM vapors can undergo the following oxidation reaction:

$$POAG_n + OH \rightarrow 1.15\ SVOC_{n-1} \tag{3.8}$$

where $POAG_n$ is the POM vapor in volatility bin *n* and $SVOC_{n-1}$ is the SVOC vapor in the lower volatility bin. After this initial oxidation step, the SVOC from the POM proceeds with the same functionalization and fragmentation method as the SVOC from VOC oxidation with a slightly higher rate constant of 4.0×10^{-11} cm^3 $moles^{-1}$ s^{-1}, that corresponds to OH

degradation of long chain hydrocarbons (Atkinson, 2000; Atkinson and Arey, 2003; Murphy and Pandis, 2009).

The SVOCs that have been added to the CESM-NCSU undergo both dry and wet deposition. The dry deposition velocity of SVOCs is assumed to be 0.25 times that of nitric acid in a manner consistent with WRF/Chem (Ahmadov et al., 2012). There is insufficient data readily available to describe the wet deposition of these species and as a result wet deposition is often neglected (Ahmadov et al., 2012). In order to represent this process in the CESM-NCSU, the Henry's law constants of 3.5×10^{5} M atm^{-1} for the SVOCs from AVOCs and oxidized POM and 1.9×10^{6} M atm^{-1} for SVOCs from BVOCs are used. These correspond to non-dissociative anthropogenic and biogenic organic vapors, respectively (Bessagnet et al., 2010). These non-dissociative acid species were chosen as surrogates for the SVOCs in CESM-NCSU because they are moderately hydrophilic. This seemed appropriate, since the lumped total SVOC in CESM-NCSU likely represents a range of oxidation products that are both hydrophobic and hydrophilic. Thus, the selection of the Henry's law constants of those moderately-hydrophilic species is likely a reasonable tradeoff between the portion of SVOC that is hydrophobic and the portion that is hydrophilic.

3.2.2.2 Glyoxal and Glyoxal SOA Formation

Glyoxal is not an explicitly-simulated species in CB05GE but it has been added as an explicitly-simulated species in the updated Version 6 of the Carbon Bond Mechanism (CB6) (Yarwood et al., 2010). In order to overcome the limitation of CB05GE, glyoxal and its reactions as well as several relevant reactions from CB6 are updated or included in the CESM-NCSU version of the CB05GE mechanism in this work. These modifications include

updating all reactions involving toluene, xylene, and isoprene and their products to the reactions from CB6 and also adding glyoxal as a product in the CB05GE reactions that contain glyoxal based on CB6. Additional species including benzene, ethyne, and glycolaldehyde and their reactions are also added into the CB05GE mechanism based on CB6 as they are glyoxal precursors.

Glyoxal is converted into SOA following the simple irreversible surface uptake approximation used in WRF/Chem expressed as:

$$\frac{\delta Gly_g}{\delta t} = 0.25 \cdot \gamma \cdot A \cdot \omega \cdot Gly_g \quad (3.9)$$

where γ =1.0×10^{-3} is the uptake coefficient (Liggio et al., 2005a; b), A is the aerosol surface area concentration (cm^2 cm^{-3}), and ω is the mean gas-phase velocity of glyoxal (cm s^{-1}) (Knote et al., 2014). This is similar to the approach that is commonly used in other glyoxal work on global scales (Fu et al., 2008; Stavrakou et al., 2009). However, because this approach does not account for any properties of the underlying particles, this approach represents an upper limit of SOA formation of glyoxal (Knote et al., 2014).

3.2.2.3 Organic Vapor – Sulfuric Acid Conucleation

In order to better represent the impacts of OA on aerosol-cloud interactions and because these interactions are driven partially by the aerosol number concentration, a simple treatment for the conucleation of organic vapors and sulfuric acid has been added to the CESM-NCSU model. This treatment is supported in part by laboratory work that shows new particle formation is enhanced in the presence of organic acids due to a reduction in the nucleation barrier from the formation of highly stable organic acid – sulfuric acid complexes

(Zhang et al., 2004). The simple parameterization of Fan et al. (2006) represents this process with the following the equation:

$$J = C \bullet P_{H_2SO_4} \bullet P_{org} \tag{3.10}$$

where J is the nucleation rate in m^{-3} s^{-1}, $P_{H_2SO_4}$ is the sulfuric acid concentration in molec. m^{-3}, P_{org} is the concentration of organic SVOCs in molec. m^{-3}, and C is a constant of 3.0×10^{25} m^3 s^{-1}. Although this parameterization is simplistic, the large uncertainties in understanding new particle formation make this a reasonable approach for representing this process in current modeling studies (Fan et al., 2006). Other methods for calculating the impact of organic compounds on new particle formation exist (Bonn et al., 2008); however these calculations are based on organic species not treated explicitly in CESM-NCSU such as ozonides from terpene oxidation and organic sulfates. The lack of many robust parameterizations for organic new particle formation stems from a lack of acceptance in the scientific community for this process as many ultra-fine organic substances are found to be from combustion sources (Zhang et al., 2005a). There is also a lack of confidence in process since the organic new particle formation in smog chamber experiments is considerable larger than those reported in the ambient atmosphere for all but heavily-polluted environments (Leskinen et al., 2008). The co-nucleation scheme described in Equation 3.10 has been added into the model as one of the options in the parameterization of He and Zhang (2014) that selects the highest nucleation rate, J, calculated from parallel calculations of all available new particle formation schemes.

3.3 Model Configurations and Evaluation Protocols

3.3.1 Model Setup and Simulation Design

A number of simulations are carried out to determine the impact of the new OA treatments on model performance and to estimate the uncertainty in these treatments. A simulation of CESM-NCSU with the treatments discussed in Section 3.2.2 is conducted for current climate conditions that approximately represent the year 2001 (hereafter New_OA). This simulation serves as a baseline simulation against which sensitivity simulations can be compared. Several sensitivity experiments are carried out to examine the uncertainties in different aspects of the new OA treatments. Table 3.9 summarizes the configuration of these experiments as well as their purposes. All sensitivity simulations are configured for the same 2001 time period as the New_OA simulation. The overall purpose of simulations 1-9 in Table 3.9 is to understand the uncertainty and impact of parameters that effect OA model performance and simulation 10 is to test the best combination for improving model performance. Four additional simulations that were targeting at understanding the uncertainty and impact of the OA treatments on aerosol-cloud interactions are separate from the first 10 sensitivity experiments and are listed as simulations 11-14. The OA_HGLY case explores how sensitive the model is to the glyoxal level by using scaled up emissions of glyoxal. The comparison of New_OA case against the OA_POM_SH08 experiment illustrates some of the uncertainty caused by allocating the total POM emissions to the different volatility bins by comparing the updated emissions fractions to those from S08. The uncertainties in the photochemical aging process are explored in the OA_NO_FF_BIOAGE, OA_HI_Fragmentation, OA_LOW_Fragmentation, and OA_NO_Fragmentation cases. A

comparison of the New_OA case against the OA_NO_FF_BIOAGE case provides some insight into how the OA treatments in CESM-NCSU deviate from other global modeling studies that do not treat FF or photochemical aging of biogenic SVOCs (Farina et al., 2010; Jathar et al., 2011). A comparison of the New_OA case against the OA_NO_Fragmentation case illustrates the impact of fragmentation, while the OA_LOW_Fragmentation and OA_HI_Fragmentation cases both estimate the uncertainty from different choices in amount of fragmentation. The OA_HVAP_SOA experiment illustrates the uncertainty of using a volatility bin dependent ΔHvap based on the parameterization of E10 compared against those from S08 and the constant ΔHvap value of 30 kJ mol^{-1} used for the VSOA. The E10 parameterization is used as it is the only alternative volatility bin dependent ΔHvap parameterization to the authors' knowledge and it has been used in other VBS modeling studies to explore ΔHvap sensitivity (Jathar et al., 2011). The OA_NO_WDEP and OA_LOW_WDEP experiments explore the impact of the wet deposition assumptions by examining the impact of neglecting and reducing SVOC wet deposition. The OA_Final_Mix case examines the impact from combining the OA_HVAP_SOA, OA_LOW_Fragmentation, and OA_LOW_WDEP configurations to improve OA performance within CESM-NCSU. This combination was selected since the OA_HVAP_SOA, OA_LOW_Fragmentation, and OA_LOW_WDEP configurations all lead to improvements in model performance independently as shown in Section 3.4.The uncertainty in aerosol-cloud interactions from OA is explored in the OA_HI_κ and OA_LOW_κ experiments, which represent the upper and lower possible hygroscopicities for different types of OA. Lastly, the OA_NO_CONUC and OA_SOA_CONUC simulations both illustrate the uncertainty in the conucleation treatment

in the CESM-NCSU. The first illustrates the full impact of the conucleation treatment, while the second illustrates some of the uncertainty in the treatment by allowing only the SVOCs formed from BVOCs and AVOCs to participate in the nucleation process.

To elucidate the impact of the OA updates on model performance, simulations that represent a longer current climate period from 2001-2010 are carried out with the New_OA configuration of the CESM-NCSU model (hereafter New_OAC). CESM-NCSU simulations are relatively computationally expensive utilizing ~4100 core hours per one simulated year for the BASE_OAC simulation, with an increase in computational costs to ~6400 core hours per one year of simulation with the new OA treatments. Because of limited computational resources, the longer time period consists of three discretely simulated years (i.e., 2001, 2006, and 2010). These years are selected for performance evaluation of the CESM-NCSU with new OA treatments under current climate conditions as they correspond to the three emission periods of He et al. (2015a) and thus represent the changing emissions of the current climate. Expanded current year simulations are also conducted using the OA_Final_Mix configuration of CESN-NCSU (hereafter Final_OAC). These simulations represent an alternative "best possible" performance case of the new OA treatments. Simulations of the current time period are also conducted with the version of CESM-NCSU described in Gantt et al. (2014) that does not include the OA updates from Section 3.2.2. These simulations are the baseline case (hereafter Base_OAC), against which the New_OAC and Final_OAC simulations will be compared.

All simulations are conducted at a horizontal resolution of $0.9^{o} \times 1.25^{o}$ and a vertical resolution consisting of 30 layers from the surface to roughly 3 hPa with approximately 7

layers in the planetary boundary layer (PBL). The simulations are configured with the F_AMIP_CAM5 component set of the CESM model. This component set has active atmosphere, land surface, and sea ice components but utilizes a climatological prescribed sea surface temperature that is provided by CESM's ocean model. The atmosphere model uses CAM5.1 physics and the land model has active biogeochemical cycling. This configuration minimizes the impact of ocean-atmosphere feedbacks and forcing on model results. The 2001 meteorological and chemical initial conditions for the Base_OAC, New_OAC, Final_OAC, and all other sensitivity simulations are derived from a 10-year (1990-2000) CAM5.1 standalone simulation with MOZART chemistry that is provided by NCAR. The data is used to drive a one-year spin-up simulation using the NCAR CESM B_1850-2000_CAM5_CN component set to provide initial meteorological and chemical conditions for all species that exist in both MOZART and CB05GE. Each simulation is then preceded by a 3-month spin up period to provide initial conditions for species that exist in CB05GE but not MOZART. The meteorological and initial conditions for the Base_OAC, New_OAC, and Final_OAC 2006 and 2010 simulations are derived from the simulation output of He et al. (2015a) for October of the previous year and are also preceded by a 3-month spin-up period.

The anthropogenic emission inventory used in these simulations is generated from several publically available global emissions inventories with several refinements from regional scale emissions inventories over East Asia, North America, and Europe regions descried in detail in He et al. (2015a). Assumptions on emissions of several species are made to generate emissions for several OA related species, including the emissions of ALKH, PAH, and glyoxal. The emissions of ALKH are generated from the Representative

Concentration Pathway with radiative forcing of 8.5 W m^{-2} (RCP8.5) (Riahi et al., 2011) emissions, publicly available from version 2 of the RCP database on the web at http://tntcat.iiasa.ac.at/RcpDb/dsd?Action=htmlpage&page=welcome. The ALKH emissions are assumed to correspond to hexanes and higher alkanes, since ALKH represents the long chain alkanes that would be contained in this emission category (Karamchandani et al., 2012). The emissions of PAH are also derived using naphthalene (NAP) emissions as a surrogate from the RCP8.5 inventory CO emissions using scaling factors of 0.0602 and 0.0701 mmol NAP mol CO^{-1} for biomass burning and anthropogenic emissions, respectively (Andreae and Merlet, 2001; Pye and Seinfeld, 2010). This is similar to the approach used in Pye and Seinfeld (2010) except that the emission factor for biofuel is assumed to be applicable for all anthropogenic emissions. In order to more accurately simulate OA the surface level POM and black carbon (BC) emissions from He et al. (2015a) are prescribed a vertical profile based on the CESM RCP POM and BC emissions provided by NCAR with the official-released model. More information on the vertical profiles of these emissions can be found in the supplementary material of Liu et al. (2012). Vertical and surface layer primary number emissions from POM, black carbon (BC), and primary sulfate are calculated from the mass emissions following the method describe in Table S1 of Liu et al. (2012). In all simulations without the OA_HGLY glyoxal emissions configuration mentioned in Table 3.9, glyoxal is generated from RCP8.5 CO biomass burning emissions using a scaling factor of 0.013 g GLY g CO^{-1} following the approach of Fu et al. (2008). Natural emissions of terpene species and isoprene are generated online from the Model of Emissions of Gases and Aerosols from Nature version 2.0 (Guenther et al., 2006), while natural emissions of dust and

sea-salt are generated from the emission schemes of Zender et al. (2003) and Martensson et al. (2003), respectively.

3.3.2 Available Measurements and Evaluation Protocol

A number of observational datasets from surface networks and field campaigns as well as satellite retrievals are available model performance evaluation. Table 3.10 provides a list of these datasets, the variables they are used to evaluate, the short name of that variable, the spatial coverage of that dataset, and the temporal coverage of that dataset. OA is evaluated using several different metrics, these include: (1) organic carbon measurements (OC) from the IMPROVE network that represents rural conditions in the CONUS region and the European Monitoring and Evaluation Programme (EMEP) that generally consists of rural background sites in Europe, (2) total carbon (TC) measurements from the STN that represents urban and suburban sites and IMPROVE datasets in the CONUS region, (3) HOA, OOA, and total organic matter (TOM) observations in a number of cities in the Northern Hemisphere representing urban, urban downwind, and rural conditions, compiled in the work of Zhang et al. (2007) (Z07) and Jimenez et al. (2009) (J09), and (4) SOA measurements representing a combination of background and urban environments for the CONUS region compiled in the work of Lewondowski et al. (2013) (L13). There is no temporally-consistent long-term monitoring of OC from the EMEP network available for model evaluation (Yttri et al., 2007). In order to overcome this limitation, all available OC measurements from EMEP for the periods of 2001-2013 are averaged into a current period climatology against simulated OC concentrations by CESM-NCSU. The observations in Z07, J09, and L13 datasets exist for limited time periods within the current climatological period (i.e., 2000-2006 for Z07 and

J09 and 2003-2010 for L13). Due to this limitation, these observations are assumed to represent climatological OA conditions of the season in which the measurements were taken for comparison with simulated fields. There are also potential inaccuracies in the comparison between HOA measurements and simulated POM. POM within the CESM-NCSU model is a lumped species containing POM from both anthropogenic and biomass burning sources. This imposes a limitation on the evaluation of POM since observed HOA only represents POM from anthropogenic sources and in reality POM should be evaluated against HOA plus OA from biomass burning (Zhang et al., 2011). This biomass burning OA component, however, is not available from Z07 and J09 datasets. The mixing ratios of VSOA precursors including ISOP, XYL, and TOL are compared against observations from the Photochemical Assessment Monitoring Stations (PAMS) in the CONUS region, and limited ISOP and TOL observations from the EMEP in Europe following a similar approach to that of OC.

Simulated concentrations of particulate matter with an aerodynamic diameter less than or equal to 2.5 μm ($PM_{2.5}$) is evaluated against the IMPROVE and STN networks over the CONUS region and the EMEP, Base de Donnėes sur la Qualite de I'Air (BDQA), and AirBase networks in Europe. Simulated concentrations of PM with an aerodynamic diameter of less than or equal to 10.0 μm (PM_{10}) are compared against observations from the U. S. Environmental Protection Agency's Air Quality System (AQS) in the CONUS regions, EMEP, BDQA, and Airbase in Europe, and data from the Ministry of Environmental Protection in China (MEPC), the Taiwan Air Quality Monitoring Network (TAQMN), and the Korean Ministry of the Environment (KMOE) in the East Asian region.

Simulated cloud and aerosol properties including, aerosol optical depth (AOD), cloud condensation nuclei at a supersaturation of 0.5% (CCN5), and cloud optical thickness (COT) are compared against satellite retrievals from the level 3 products of the Moderate Resolution Imaging Spectroradiometer (MODIS). Cloud droplet number concentration (CDNC) is compared against MODIS-derived estimates (Bennartz, 2007) (B07) and cloud liquid water path (LWP) is compared against a passive microwave-derived climatology (O'dell et al., 2008). Shortwave cloud forcing (SWCF) and downwelling shortwave radiation flux at the earth's surface (FSDS) are compared against satellite estimates from the Clouds and Earth's Radiant Energy System (CERES) dataset. It is important to note that there is a potential for inconsistencies when comparing this data against simulated fields because the monthly resolution of the CESM-NCSU simulations is not temporally consistent with the satellite overpass times.

The protocols for model performance evaluation primarily focus on statistical comparisons similar to the method of Zhang et al. (2012b) and He et al. (2015a). The statistical analysis will focus on mean bias (MB), normalized mean bias (NMB), normalized mean error (NME), and correlation coefficient (R). All performance statistics from the New_OA and sensitivity simulations are compared against observations from the year 2001 as the emissions used in these simulations represent this time period. The only exception is the aforementioned variables that have limited resolution and are assumed to be climatological. The BASE_OAC, New_OAC, and Final_OAC simulations, consisting of the average simulation results of 2001, 2006, and 2010, are compared against a ten-year averaged data spanning the period of 2001-2010 for satellite retrievals and the three-year

average (i.e., 2001, 2006, and 2010) of the surface network data to be consistent with the emission periods. In terms of spatial comparisons, all surface observations inside the same CESM-NCSU grid cell are average for comparison with the simulated value. Due to the complex nature of OA formation and the inability of any global model to represent the OA with complete accuracy, no true objective metric for acceptable model performance is used. Instead the model performance is considered acceptable if most of the bulk statistics are comparable to previous VBS modeling studies or if there is improvement in model performance compared to the unmodified CESM-NCSU model.

In addition to bulk annual statistic measures, model performance of seasonal trends in OA is evaluated based on the comparison of simulated and observed time series of OC and TC at selected sites in the IMPROVE, EMEP, and STN networks. Two IMPROVE sites: Great Smokey Mountains National Park, TN (GRSM) and Lostwood Wildlife Refuge, ND (LOWR) are selected from the IMPROVE network because both sites represent rural CONUS conditions, with the former in a high BVOC environment and the latter in a low BVOC environment. The STN sites of Phoenix, AZ (PHO) and Birmingham, AL (BHM) are selected as they are both urban locations with the former in a low BVOC environment and the latter in a high BVOC environment. Thus these selected sites should provide some insights into model performance in these four regimes in the CONUS region. The European sites Birkenes, Norway (BIR) and Ispra, Italy (ISP) are selected since they have fairly continuous temporal coverage during the 10-year period of interest compared to many of the other EMEP sites and they represent relatively low and high OC conditions, respectively.

Additionally, pie charts are used to evaluate the relative contributions of POM and OOA to the amount of TOM at selected sites in the Z07 and J09 dataset. The sites selected represent a range of seasons, a range of locations (e.g., sites located in East Asia, North America, and Europe), and a range of air quality and emission regime (e.g., urban, urban downwind, and rural/remote). Thus they provide a fairly diverse group of stations representing conditions throughout the Northern Hemisphere (NH). Similar pie chart analysis is performed comparing the fractions of ASOA and BSOA to total SOA from the L13 dataset at selected sites. The Research Triangle Park (RTP), NC and Pensacola, Florida sites are selected because they are in regions with relatively high BVOCs and the Detroit, MI and Bakersfield, CA sites are selected as they are in relatively low BVOC environments.

3.4 Uncertainty and Sensitivity Studies of Parameters within the New OA Treatments

3.4.1 Sensitivity of Organic Aerosol

In order to better understand the impact of some of the different parameters that control the formation of OA in the new OA treatment, the absolute differences in POM and OOA between sensitivity simulations 1-14 from Table 3.9 and the New_OA simulation are shown in Figures 3.2 and 3.3, respectively. Similar absolute difference plots for SOA, SVOA, and TOM are shown in Figures 3.4, 3.5, and 3.6, respectively. Normalized mean bias performance statistics for OA and cloud/radiative parameters for each sensitivity simulation are listed Table 3.11. Table 3.12 lists the probability values from a student's t-test analysis on OA and climate related fields from the sensitivity simulations compared to the New_OA simulations. In most of the sensitivity experiments, changes in OOA are statistically

significant at the 95% confidence level, but only POM changes from the OA_POM_SH08 and OA_Final_Mix simulations are statistically significant.

The enhanced glyoxal level in the OA_HGLY case does not have a global scale impact on either POM or SVOA, but there are enhancements in regions with large glyoxal and OA levels due to enhanced partitioning to the particulate phase from greater absorbing material. The enhanced glyoxal level increases the SOA level on global average by 0.03 μg m^{-3} with the largest increases ranging from (1.0-4.6 μg m^{-3}) in South Asia and East Asia (Figure 3.4.1), which are generally reflected in the changes of OOA (Figure 3.3.1). Some decreases occur in South America and Africa caused by perturbations in photochemistry, atmospheric stability, and precipitation. The large increases over South Asia and East Asia are related to the large biofuel emissions in these regions that were scaled up to represent the potential missing continental glyoxal source (Stavrakou et al., 2009) for the enhanced glyoxal emissions and the large amount of aerosol in these regions for glyoxal uptake.

The emission factors based on Shrivastava et al. (2008) used in the OA_POM_SH08 simulation to map POM emissions to the volatility basis set are far too volatile, resulting in much more evaporation of POM to the gas-phase. This reduces the POM level by 0.07 μg m^{-3} on global average and up to 30.3 μg m^{-3} in biomass burning regions compared to the factors used in the New_OA simulation (Figure 3.2.2). Using these factors would have further degraded model performance compared to the Z07 and J09 dataset for HOA to an underprediction of 70.8%, thus justifying the use of the New_OA simulation factors (Table 3.11). OOA increases on global average by 0.03 μg m^{-3} and up to 18.0 μg m^{-3} in regions with large anthropogenic and biomass burning POM emissions (Figure 3.3.2). The increases in

OOA are due to increases in SVOA. This is the result of enhanced SVOC levels from increases in gaseous POM. The result is an OOA prediction similar to the New_OA case with an underprediction of 45.5% (Table 3.11). The high POM volatility dominates the TOM changes with decreases of approximately 0.09 μg m^{-3} on global average. Based on this sensitivity, it is apparent that the emissions factors of S08 are likely not applicable to global scale OA simulations, since they further degrade HOA model performance.

The OA_NO_FF_BIOAGE simulation uses similar conservative photochemical aging assumptions as both Farina et al. (2010) and Jathar et al. (2011). There is little impact at the global level on POA between this simulation and the New_OA simulation. However, under these assumptions, OOA is reduced globally by 0.05 μg m^{-3}. The decreases are the largest in the Northern Hemisphere industrial regions (NHIR) (e.g., North America, Europe, South Asia, and East Asia), central Africa, and central South America (0.4 – 10.7 μg m^{-3}) (Figure 3.3.3). These decreases are the largest in regions with high BVOCs, thus reflecting both the lack of biogenic aging and functionalization. The decreased TOM in this simulation is generally the result of decreases in OOA. These assumptions degrade model performance of many OA parameters compared to the New_OA simulation. This illustrates the benefit of using biogenic aging in conjunction with the functionalization and fragmentation treatment over the conservative aging assumption, at least in a model that treats wet deposition of SVOCs. If wet deposition of SVOCs were to be applied to a model using this conservative aging assumption, it is likely to result in significantly greater OA underpredictions, since BSVOCs are more hydrophilic than ASVOCs (Hodzic et al., 2014).

Changes in the amount of fragmentation (i.e., simulations 4-6 in Table 3.9) do not substantially impact POM on a global level but do result in localized general trends of reductions or increases (Figures 3.2.4-3.2.6). These trends are generally due to changes in OOA absorbing material. In the OA_HI_Fragmentation case, OOA is reduced on global average by 0.03 μg m^{-3} with reductions of up to 5.3 μg m^{-3} in regions with high OA levels and photochemical activity (Figure 3.3.4), such as South Asia, East Asia, and the tropical Southern Hemisphere (SH). The OA_LOW_Fragmentation and OA_NO_Fragmentation simulations both lead to global average increases in OOA of 0.06 μg m^{-3} and 0.11 μg m^{-3}, with maximum increases of 9.9 μg m^{-3} and 9.1μg m^{-3} in the SH, respectively (Figures 3.3.5 and 3.3.6, respectively). Changes in OOA due to fragmentation are dominated by changes in SVOA. Global average changes in SVOA levels in both the OA_HI_Fragmentation (-0.02 μg m^{-3}) (Figure 3.5.4) and OA_LOW_Fragmentation (0.04 μg m^{-3}) (Figure 3.5.5) are roughly double the changes in SOA (i.e., ~-0.01 and 0.02 μg m^{-3}, respectively) (Figures 3.4.4 and 3.4.5, respectively). The relative change is even larger in the OA_NO_Fragmentation case, where the global average SVOA level increase (0.09 μg m^{-3}) (Figure 3.5.6) is over four times larger than the increase in SOA (0.02 μg m^{-3}) (Figure 3.3.6). This is likely because SVOA formation is primarily controlled by the photochemical aging process, unlike SOA formation which is controlled by both the photochemical aging process and the oxidation of VOCs. The overall impact of higher fragmentation on TOM is a global average reduction of 8.7×10^{-3} μg m^{-3} (Figure 3.6.4). This is smaller in magnitude than the global average increases of 0.02 μg m^{-3} (Figure 3.6.5) and 0.3 μg m^{-3} (Figure 3.6.6) that occur in the OA_LOW_Fragmentation and OA_HI_Fragmentation simulations, respectively.

In comparison to some of the other sensitivity experiments (e.g., Simulations 1-3 and 7-10), assumptions about the amount of fragmentation have a relatively small impact on the global TOM level. Nonetheless, there are some notable improvements in model performance with the OA_LOW_Fragmentation and OA_NO_Fragmentation simulations. These improvements include reductions in the NMBs of TC over the CONUS region from -37.4% to -34.3% and -33.8%, reductions in the NMBs of OOA over the NH from -45.9% to -37.8% and -38.2%, and reductions in the NMBs of TOM over the NH from -51.5% to -45.9% and -45.9%, respectively (Table 3.11). There is also a slight improvement in European OC with the OA_NO_Fragmentation configuration, reducing the NMB from -52.4% to -46.6%. However, model performance in both the OA_LOW_Fragmentation and OA_NO_Fragmentation simulations is degraded for both CONUS OC and SOA. The NMB in OC increases from -0.3% in the New_OA simulation to 7.0% and 9.0% in the OA_LOW_Fragmentation and OA_NO_Fragmentation simulations, respectively. Similarly, the NMB in SOA increases from -0.5% to 8.0% and 12.1%, respectively. Although the model performance is degraded compared to the New_OA simulation the NMB overall is still indicative of good model performance. Since the reduced fragmentation cases both result in improved model performance across most of the OA species, the configurations in both simulations are candidates for the final OA treatment in CESM-NCSU. The amount of fragmentation that occurs is not well understood and as a result the amount of fragmentation proposed in the work of Shrivastava et al., (2013) is based on sensitivity experiments and are therefore somewhat arbitrary. Thus the uses of the reduced fragmentation configurations are justified. However, the OA_LOW_Fragmentation configuration is likely the better choice as

it will avoid the VBS "zombie effect" discussed in the work of Bergstrom et al. (2012) that could potentially lead to overpredictions of OA in stagnant photochemically-active regions.

In the OA_HVAP simulation, the ΔHvap values of each volatility bin from the E10 parameterization are larger than those of S08 used in the New_OA simulation and much greater than the 30 kJ mol^{-1} used for the anthropogenic and biogenic SOA. As a result, the strength of the temperature dependence on gas to particle partitioning in each volatility bin in the model is increased. Since generally the annual average temperature in the model's surface layer is approximately 300K or less, this decreases the saturation concentrations of each volatility bin in nearly every grid cell of the model on annual average, thus shifting the mass from the gas to the particulate phase. The result is an increase in model POM on global average of 8.8×10^{-3} μg m^{-3} and up to 12.7 μg m^{-3} in regions with large ambient POM levels (Figure 3.2.7). This is most likely the effect of the ΔHvap values, but could also be due to general increases in OOA that functions as absorbing material. The OOA mass is increased by 0.06 on global average, with increases of up to 6.7 μg m^{-3} in the NHIR (Figure 3.3.7). The impact is the strongest across the entire NH, with general increases of 0.1 μg m^{-3} or greater, owing to the colder temperatures in this region that shift more mass to the particulate phase and the relatively high SVOC level. The increase in OOA is dominated by SOA, with SVOA decreasing slightly on global average by 1.3×10^{-3} μg m^{-3} (Figure 3.5.7). This decrease in SVOA can be attributed to either the reduction in available POA gases from the reduced volatility of POM or because SVOA levels are the highest in the tropical regions where temperatures are high enough to shift the saturation concentrations larger than the S08 case, and thus shift the mass from the particulate phase to the gas phase. The result of these

changes is a global average increase in TOM of 0.07 μg m^{-3} (Figure 3.6.7). The use of the E10 ΔHvap values tends to improve model performance of most OA related variables except OC and SOA over CONUS, which become strongly overpredicted (NMBs of 30.4% and 23.2%, respectively). The OA_HVAP simulation also shows the best improvement in HOA compared to the other sensitivity experiments, reducing the NMB -36.4% to -30.4%. However, the changes in POM from this simulation are not statistically significant, indicating that this improvement is also likely not statistically significant. These differences in model performance indicate that overall the E10 parameterization may be a better choice than the S08 values in the CESM-NCSU model. The developers of the VBS framework have indicated that using artificially-low ΔHvap values for SOA formation is necessary since insufficient information about the individual anthropogenic and biogenic SVOCs is available (Donahue et al., 2006). However, given that this is an assumption and other studies (Tsigaridis and Kanakidou, 2003) and the default treatment in CESM used much higher ΔHvap values, the use of volatility bin dependent ΔHvap for SOA is likely within the range of acceptable uncertainties.

In the OA_NO_WDEP and OA_LOW_WDEP simulations, POM is increased slightly on global average due to increases in OOA absorbing material. The lack of SVOC wet deposition in the OA_NO_WDEP simulation strongly increases the global OOA level by 0.18 μg m^{-3} on global average, and up to 21.8 μg m^{-3} in regions with high biogenic OA levels and precipitation rates (Figure 3.3.8). This enhanced OOA is dominated by enhanced SOA (~0.12 μg m^{-3} on global average) (Figure 3.4.8), which is roughly double the contribution from SVOA (~0.06 μg m^{-3} on global average) (Figure 3.5.8). The net impact is the largest

global average increase in TOM among all sensitivity experiments of 0.16 μg m^{-3} (Figure 3.6.8). The reduced SVOC wet deposition in the OA_LOW_WETD simulation leads to weaker enhancements in OOA compared to the OA_NO_WDEP case of 0.06 μg m^{-3} on global average, and up to 7.8 μg m^{-3} in regions with high OA and precipitation levels (Figure 3.3.9). Similar to the OA_NO_WDEP case, the contribution of SOA is roughly double that of SVOA (Figures 3.4.9 and 3.5.9). One of the key differences in the OA_NO_WDEP and OA_LOW_WDEP simulations, is the amount of OOA formed in the SH rainforests. For example, over the Amazon the OA_NO_WDEP configuration leads to increased OOA in excess of 1.0 μg m^{-3}, while the OA_LOW_WDEP configuration results in negligible or slight decreases in this region. This indicates that the use of the wet deposition scheme in CESM-NCSU for SVOCs may be problematic (i.e., there is overly efficient wet removal) in these areas, as even a 75% reduction in SVOC wet deposition cannot impact the OOA level. The OA_LOW_WDEP simulation has increased global average TOM of 0.04 μg m^{-3} (Figure 3.6.9), which is more comparable to increases in TOM from the reduced fragmentation simulations and the OA_HVAP simulation. The OA_NO_WDEP and OA_LOW_WDEP simulations have better performance against many of the OA metrics than the New_OA simulation, with the exception of CONUS OC and CONUS SOA which become largely overpredicted. These findings appear to indicate that wet deposition of SVOCs is overpredicted in the New_OA simulation. However, completely ignoring wet deposition is likely not a viable option since that would likely degrade model performance in certain locations. There are some indications that the wet deposition scheme of Horowitz et al. (2003) used in this version of the model is slightly inaccurate, as later versions of the CESM

model discussed in Chapter 4 have replaced it with the Neu and Prather (2012) scheme. The Neu and Prather (2012) scheme is a more advanced scheme that treats both in-cloud and below-cloud scavenging of trace gases. It contains a detailed treatment for scavenging by ice crystals, and a more realistic representation of precipitation and cloud spatial distributions within a model column compared to the Horowitz et al. (2003) scheme that uses the bulk diagnostic precipitation rates from the model and an effective Henry's Law constant (Lamarque et al., 2012). It is likely that the bulk approach used in the CESMv1.0.5 overpredicts wet deposition since in reality the clouds within each column would not cover the entire grid cell. Thus it is likely that the OA_LOW_WDEP simulation somewhat approximates the reductions that would occur with the Neu and Prather (2012) scheme.

The OA_Final_Mix simulation combines the configurations of the OA_LOW_Fragmentation, OA_LOW_WDEP, and OA_HVAP simulations. These three configurations were combined because in general each configuration lead to the improvement of simulated OA against most evaluation metrics, with the exception of CONUS OC and SOA, while still accounting for fragmentation and SVOC wet deposition. POM levels are enhanced by 1.6×10^{-2} μg m^{-3} on global average and by as much as 38.2 μg m^{-3} in the biomass burring regions of central Africa and South America (Figure 3.3.10). These enhancements are related to both the enhanced OOA absorbing material caused by all three of the configuration changes in this simulation and the enhanced partitioning from the change in ΔHvap values. Unlike the majority of the sensitivity experiments, the changes in POM from the OA_Final_Mix simulation are statistically significant. The increases in POM lead to improvements in HOA model performance, reducing the NMB from -36.4% in the

New_OA simulation to -31.5%. OOA is enhanced by 0.17 μg m^{-3} on global average (Figure 3.3.10) with the OA_Final_Mix configuration. OOA is enhanced in the range of 0.2-1.0 μg m^{-3} across most continental areas. The enhancements are even larger (e.g., in the range of 1.0-12.4 μg m^{-3}) over central Africa, central South America, Europe, East Asia, and the eastern U. S. The increase in OOA leads to significantly-improved OOA model performance, reducing the NMB from -45.9% in the New_OA simulation to -27.0%. SOA performance is degraded against the L13 dataset, increasing the NMB from -0.5% to 46.8%. However, the L13 SOA data is only derived from a small number of the SOA precursors that are treated in CESM-NCSU (this will be discussed in more detail in Section 3.5), meaning that the L13 dataset likely underestimates the actual ambient SOA level. The OA_Final_Mix simulation provides a significant enhancement in the TOM level of 0.13 μg m^{-3} on global average, which is comparable to TOM increases from the OA_NO_WDEP simulation. This leads to increased model performance in most total OA metrics compared to the New_OA simulation. These include, a reduction in the European OC NMB from -52.4% to -29.2%, a reduction in the CONUS TC NMB from -37.4% to 12.3%, and a reduction in the NH TOM NMB from -51.5% to -38.6% (Table 3.11). However, there is a degradation of CONUS OC performance from the IMPROVE network, with the NMB increasing from -0.3% to 45.7%. This overprediction against the IMPROVE network is common in many VBS studies as mentioned in Section 3.1. Nonetheless, the improvements across multiple OA metrics indicate that the configurations of the OA_Final_Mix simulation are an appropriate final configuration for the OA treatments in CESM-NCSU.

Changes in POM and OOA simulated by the OA_NO_CONUC, OA_SOA_CONUC, OA_HI_κ, and OA_LOW_κ are an order of magnitude smaller on global average than those simulated by the other sensitivity experiments (Figures 3.2.11-3.2.14 and Figures 3.3.11-3.3.14). This is in part because these simulations are targeted at changes in CCN rather than OA and because the impact on OA species in these simulations is minor, caused by numerical oscillations or feedbacks from chemistry into climate that cannot be easily separated from the changes in selected parameters within a fully-coupled climate-chemistry model like CESM. The student's t-test analysis from Table 3.12 indicates that OOA differences in the OA_HI_κ and OA_NO_CONUC simulations are not statistically significant and are thus likely model noise. The changes in OOA from the OA_LOW_κ experiment are statistically significant with a global average increase of 7.7×10^{-3} μg m^{-3}. The increased OOA in the OA_LOW_κ case is related to a number of factors. Firstly, the reduced κ values in this simulation reduced the ability of OA to activate, thus allowing for reduced wet removal of OA. This configuration also results in increasing FSDS over North America and Europe (Figure not shown). This leads to increases in OOA due to both increases in photochemistry, but also potential increases in BVOC emissions. However, the OOA perturbations in the SH are largely the result of perturbations in planetary boundary layer height (PBLH) from perturbations in cloud and radiation variables (Figure not shown). Similarly, the changes in OOA from the OA_SOA_CONUC simulation match closely with perturbations in FSDS and PBLH. These changes in OOA consist of many random dipoles, indicating that they are likely perturbations caused by differences in simulated feedbacks from chemistry into climate.

3.4.2 Sensitivity of Aerosol/Climate Interactions

The assumptions tested in the OA_HVAP, OA_NO_WDEP, and OA_Final_Mix simulations show a strong impact on cloud/radiative parameters. In order to examine this impact in greater detail, Figure 3.7 shows the zonally-averaged vertical cross section of the absolute differences in OOA, CCN, CDNC, and particle number concentration between these simulations and the New_OA simulation. In addition to surface increases in these three simulations, OOA is increased throughout the atmosphere. In the OA_HVAP simulation, the increased shift towards smaller saturation concentrations in the cooler atmosphere above the surface increase the partitioning of OOA by 0.05μg m^{-3} on vertical domain average, with the largest increases in the NH mid-latitudes (.e.g., 0.2-0.3 μg m^{-3} from the surface to roughly 750 mb). These increases occur in this region due to relatively high SVOCs and low temperatures. The OOA increase throughout the atmosphere is much greater in the OA_NO_WDEP simulation, with a vertical domain average increase of 0.14 μg m^{-3} and large increases (e.g., 0.2-0.6 μg m^{-3} from the surface to roughly 600 mb) throughout most of the NH and tropics (15ºS to 60ºN). OOA increases in the OA_Final_Mix simulation are comparable to the OA_NO_WDEP simulation, with a vertical domain average increase of 0.12 μg m^{-3} and increases of 0.2-0.5 μg m^{-3} from the surface to 600 mb in the 15ºS-60ºN zone. In addition to increases in OOA, all three simulations show increased CCN levels. CCN from the OA_HVAP simulation increases by roughly 5.8 cm^{-3} on vertical domain average, with the largest enhancements of 9.0-45.3 cm^{-3} in the lower latitudes and mid-latitudes of the NH from the surface to roughly 600 mb, although some perturbations near the surface exist. The increases are even larger in the OA_NO_WDEP simulation, with CCN

increases by 17.8 cm^{-3} on vertical domain average and by 12.0-81.1 cm^{-3} from the surface to 600 mb over the much of the NH and as well as the tropical and subtropical SH (20ºS to 60ºN). Increases in CCN in the OA_Final_Mix simulation are similar to the OA_NO_WDEP simulation, with a slight reduction in magnitude (i.e., 13.1 cm^{-3} on vertical domain average).

Despite increasing CCN in all three simulations, there are different trends in the CDNC. In the OA_NO_WDEP simulations, the lack of SVOC wet deposition has a twofold effect. The first effect is the obvious increase in OOA from greater available material for partitioning. Since OOA in the model is formed entirely through partitioning onto existing aerosol, the only way for increased OOA mass to increase CDNC is to increase the size and hygroscopicity of preexisting aerosols. Both these processes enhance the particles' ability to be activated. The second effect is an increase in aerosol number, because of enhanced conucleation from larger SVOC levels. This increases the atmospheres' particle number concentration by 2.9×10^{2} cm^{-3} on vertical domain average and up to 1.4×10^{3} cm^{-3} in the tropical atmosphere. The combined effects of greater aerosol number, larger aerosol, and more hygroscopic aerosols lead to an increase in CDNC of 0.4 cm^{-3} on vertical domain average with increases of 0.5 to 1.0 cm^{-3} in the tropical atmosphere and 1.5-7.5 cm^{-3} in the mid-latitude atmosphere from the surface to approximately 700 mb. The OA_HVAP simulation shows a very different impact on CDNC, with CDNC decreasing by 0.08 cm^{-3} on vertical domain average and up to 0.5-6.2 cm^{-3} from the surface to roughly 700 mb in the mid-latitude regions. These reductions in CDNC result from reductions of 1.6×10^{2} cm^{-3} on vertical domain average in particle number. The particle number in these regions is reduced due to reductions in SVOCs from greater partitioning to the particulate phase, which

decreases the rate of organic conucleation. The overall impact on CDNC indicates that although the aerosols in OA_HVAP simulation are likely larger in size and more hygroscopic, the reductions in particle number dominate the direction of CDNC changes. In the OA_Final_Mix simulation, the effect of the OA_HVAP greater partitioning dominates, leading to a vertical domain average reduction in particle number concentration of -1.5×10^{2} cm^{-3}. However, the greater increases in OOA in the OA_Final_Mix simulation compensate these reductions, leading to a complicated pattern in CDNC perturbations, with a vertical domain average increase of 0.03 cm^{-3}.

The combined impact of the CDNC, particle number concentration, and OOA enhancements in the OA_NO_WDEP simulation are global average increases in COT, SWCF, and AOD of 0.3, 1.4 W m^{-2}, and 8.8×10^{-3}, respectively, as shown in Figure 3.8. These changes improve model performance of AOD, COT, CCN, and LWP, which are underpredicted in the baseline simulation, but decrease model performance of CDNC and SWCF that are already overpredicted in the New_OA simulation. In the OA_HVAP simulation, the increase in OOA increases AOD on global average by 3.7×10^{-3}. Decreases in CDNC decrease COT on global average in the OA_HVAP simulation, but these reductions do not reflect the changes in SWCF. The global average increase in SWCF occurs because some maritime perturbations (i.e., increases) in COT have a stronger impact on SWCF than continental clouds, as they tend to contain more cloud water. Similar to the OA_NO_WETD simulation, the OA_Final_Mix simulation also increases COT, SWCF, and AOD on global average by 0.19, 0.69 W m^{-2}, and 7.7×10^{-3}, respectively. The enhancements from all three simulations to AOD are global wide with the exception of perturbations in

regions with large dust concentrations, indicating that both SVOC deposition and the choice of ΔHvap values generate a strong climate signal by controlling both the direct and indirect aerosol impact of OA.

The role of different OA treatment assumptions on aerosol/climate interactions are further explored in sensitivity experiments 11-14 as shown in Table 3.9. The simulations OA_HI_κ and OA_LOW_κ are performed to explore the impact of OA hygroscopicity on aerosol-cloud interactions. Figure 3.9 shows the zonally-averaged absolute differences in CCN, CDNC, and COT between the OA_HI_κ and OA_LOW_κ simulations and the New_OA simulation. The increased κ values of BSOA and SVOA in the OA_HI_κ simulation increase CCN on vertical domain average by 6.2 cm^{-3} with the largest increases (12.0-51.5 cm^{-3}), spanning the latitude range 15°S to 60°N from the surface to 700 mb. The reductions in κ values of all OA species in the OA_LOW_κ simulation induce a stronger impact than the OA_HI_κ simulation, with reductions in CCN of 9.2 cm^{-3} on vertical domain average and of 12.0-110.8 cm^{-3} in the same region from the surface to 700 mb. Smaller increases (less than 1.5 cm^{-3}) are found in tropics and subtropics. Changes in CDNC are more complex than changes in CCN; even though some of the patterns are discernible. In the OA_HI_κ simulation, the increased hygroscopicity increases CDNC by up to 3.9 cm^{-3} in clouds over the SH mid-latitudes, largely from 40°S-60°S, and the higher latitudes of the NH, from 60ºN-75ºN. Increases in CCN in the OA_HI_κ simulation do not necessarily mean the CCN will activate to form cloud droplets. In the OA_HI_κ simulation, thermodynamic perturbations in the model result in decreased cloud fractions over much of the NH mid-latitudes (Figure not shown). This reduces the CDNC in this region even though CCN are

increased. The reduced hygroscopicity in all of the OA species from the OA_LOW_κ simulation has a stronger impact on changes in CDNC compared to the OA_HI_κ simulation, with reductions of 0.19 cm^{-3} on average and the largest reductions (1.5-5.8 cm^{-3}) in clouds over the NH. The reductions in cloud fraction in the OA_HI_κ simulation dominate the changes in COT, leading to vertical domain average reductions. In the OA_LOW_κ simulation, COT is reduced by 9.1×10^{-3} on vertical domain average but up to 0.1-0.5 in mid-latitude cloud of the NH and the lower latitudes of the SH. Although some patterns exist from changes in these vertical cross sections, the spatial distributions of the changes in COT, LWP, and SWCF shown in Figure 3.10 are highly complex and have a "noisy" appearance. Additionally, the changes in SWCF in these simulations are not statistically significant based on the student's t-test analysis of Table 3.12. This indicates that the impacts from OA hygroscopicity on these parameters are not substantial compared to perturbations from different feedbacks of chemistry into climate between simulations, except over the NHIR and SH biomass burning regions in the OA_LOW_κ simulation. This finding is consistent with the work of Liu and Wang (2010) that showed a noisy response in SWCF to OA hygroscopicity between the current and pre-industrial periods. The NHIR and SH biomass burning regions have a substantial amount of POM, thus indicating that OA impacts on climate are more sensitive to the hygroscopicity of POM compared to OOA in this modeling system. These simulations also suggest that the impacts of OA hygroscopicity on climate are greater in the mid-latitudes compared to the tropics. This is likely because clouds in the mid-latitudes are more stratiform compared to the tropics, where cumulus clouds dominate and associated convection occurs. This is somewhat consistent with other findings in the

literature that report POM hygroscopicity and reductions in SOA hygroscopicity have the largest impacts on aerosol indirect forcing of OA and that the impacts on aerosol indirect forcing are the greatest in the NH (Liu and Wang, 2010).

The zonal-averaged vertical cross section of the absolute difference in particle number, CCN, and CDNC between the New_OA simulation and the OA_NO_CONUC and between the New_OA simulation and OA_SOA_NONUC are plotted in Figure 3.11 to illustrate the impact of the conucleation treatment. The inclusion of the conucleation treatment increases the number concentration by 5.6×10^{2} cm^{-3} on vertical domain average with the greatest increases concentrated in lower latitudes and the NH mid-latitudes of 1.0×10^{3} to 2.5×10^{3} cm^{-3} from the surface to 500 mb. The impact of including the SVOCs from oxidation of POM and IVOCs (POM-based S-IVOCs) is a vertical domain mean increase of 9.7×10^{1} cm^{-3}, with increases of 1.0×10^{1}-4.9×10^{1} cm^{-1} primarily in the lower latitudes from the surface to 500 mb. The impact of the full conucleation treatment used in the New_OA case on CCN is an increase of 4.3 cm^{-3} on vertical domain average (Figure 3.11). Generally CCN is enhanced by 3.0-66.3 cm^{-3} throughout the boundary layer (surface to 800 mb) of the lower and middle latitudes, with the largest increases (30-66.3 cm^{-3}) in the mid-latitudes of the NH. The impact of conucleation involving POM-based S-IVOCs is a minor decrease of 0.8 cm^{-3} on vertical domain average, despite the strong enhancements (12-29.6 cm^{-3}) in the lower and middle latitudes of the NH. This decrease is related to decreases in $PM_{2.5}$ (Figure not shown) in the subtropics of the NH due to different feedbacks of chemistry into climate impacting dust emissions. The increased CCN from the full conucleation treatment used in the New_OA case leads to an increased CDNC level of 0.6

cm^{-3} on vertical domain average, with the largest increases (2.0-7.1 cm^{-3}) in clouds of the NH and SH mid-latitudes (Figure 3.11). The impact from POM-based S-IVOCs is less with an average increase of 0.3 cm^{-3} and increases of up to 6.8 cm^{-3} in mid-latitude regions. The inclusion of the conucleation treatment enhances COT, LWP, and SWCF on global average by 0.5, 1.7 g m^{-2}, and 0.1 W m^{-2}, respectively (Figure 3.12). While the spatial changes in these parameters are also "noisy", as shown in Figure 3.12, there is a consistent impact with the greatest enhancements occurring in regions with high biogenic SVOCs. The impact from including POM-based SVOCs for co-nucleation is weaker (i.e., global average changes in COT, LWP, and SWCF of 0.2, 0.7 g m^{-2}, and 4.5×10^{-3} W m^{-2}, respectively). POM-based SVOCs were not included in the original Fan et al. (2006) conucleation treatment. Based on the above sensitivity analysis, anthropogenic and biogenic SVOCs play a dominant role in the conucleation treatment, thus minimal potential error is introduced by including POM-based SVOCs. Although these simulations demonstrate that organic conucleation has an impact on the aerosol indirect effects, one caveat is the simplistic and empirical nature of the conucleation parameterization used in this work. More complex and physically-based conucleation parameterizations should be considered in future work once they become available for 3-D model implementation.

3.5 Impacts of New OA Treatments and Current Period Evaluation

3.5.1 Evaluation and Comparison of OC, TC, and TOM

Figure 3.13 shows the absolute difference plots of POM, SOA, OOA, TOM, $PM_{2.5}$, AOD, Column Number Concentration (NUM), CCN, CDNC, COT, SWCF, and FSDS between the Base_OAC and Final_OAC simulations. Table 3.13 shows the p-values from a

students' t-test analysis on the differences between the Base_OAC simulation and the New_OAC and Final_OAC simulations in the Figure 3.13 variables. The t-test analysis indicates that the difference in OA and cloud/radiation parameters is statistically significant at the 95% confidence level for all parameters. Globally the final configuration of the OA updates reduces POM by 0.22 μg m^{-3} on global average, with the largest decreases (e.g., 3.0-67.3 μg m^{-3}) occurring in biomass burning regions of the SH, East Asia, and South Asia due to the POM volatility considered in the new treatments. SOA increases on global average by 0.21 μg m^{-3} with increase of 0.6-14.0 μg m^{-3} in portions of NHIR. These increases are caused by the increased SOA partitioning from the photochemical aging process, increased mass from the functionalization portion of the VBS treatment, due to a slight increase in the number of anthropogenic VOC precursors, and the addition of glyoxal SOA. In the SH, SOA is reduced by 0.3-2.2 μg m^{-3} primarily in the Amazon and Congo rainforests and Indonesia. This decrease could partially be the result of the SOA forming potential of ISOP being reduced in the New_OA updates. In the Base_OAC simulation, ISOP and terpene precursors have the same SOA forming potential because their oxidation products are lumped into a single gas for partitioning. In the Final_OAC case, the oxidation products of all VOC precursors are multiplied by the SOA mass yields in Table 3.7, which limits the SOA forming potential of ISOP oxidation products, compared to terpene oxidation products. Another more likely possibility for the reduction in SH SOA, is the potential inaccuracy of the biogenic SVOC wet deposition. Considering the large precipitation rate in the rainforest regions, it is possible that the biogenic SVOC wet deposition is overpredicted. This is illustrated by the OA_NO_WETD and OA_LOW_WETD sensitivity experiments in Section

3.4. The overprediction of SVOC wet deposition reduces the amount of organic material available to partition into aerosol. The total OOA (SOA + SVOA from oxidized POM and IVOCs) increases on global average by approximately 0.33 μg m^{-3}. The additional SVOA leads to further increases of OOA in the NHIR, especially in regions with high POM emissions such as South Asia, East Asia, and central Africa, resulting in OOA increases in the range of 3.0-35.6 μg m^{-3}. In the SH, the formation of SVOA somewhat compensates SOA reductions in biomass burning regions, leading to a less reduction or even a net increase in OOA. This is especially true in central Africa, where OOA generally increases by 0.9 μg m^{-3} or more despite negligible changes (e.g., decreases less than 0.6 μg m^{-3}) in SOA. However, there is not a substantial amount of compensation in the Amazon, where OOA can be reduced by up to 2.0 μg m^{-3}. The impact of the final configuration of the new OA treatments on TOM is a global average increase of 0.11 μg m^{-3}, with the increase in OOA dominating in the NHIR. Decreases occur in the SH and South Asia due to weaker increases in OOA, stronger decreases in POM, and loss of SOA in the Amazon.

The Base_OAC, New_OAC, and Final_OAC simulation performance statistics for all variables mentioned in Section 3.3 are listed in Table 3.14. Scatter plots corresponding to OC, TC, SOA, HOA, OOA, TOM, $PM_{2.5}$, and PM_{10} statistics between the Base_OAC and Final_OAC simulations are shown in Figure 3.14. In order to understand the OA evaluation, it is important to evaluate the performance of some of the SOA VOC precursors. Generally the performance of VOC precursors is similar between all simulations. Overall, ISOP, TOL, and XYL are simulated rather poorly with moderate to strong underpredictions ranging from -32.0 to -53.0%. One exception is European TOL, which has NMBs in the range of 0.6 to

5.8%. In addition to the fairly large bias, the NME for the VOCs in all simulations are greater than 60% and all the R values are near zero, with the exception of CONUS ISOP which has an R value of ~0.7 in all simulations. The poor VOC performance is likely either the result of inaccuracies in the global VOC emissions inventory or BVOC emissions module (Holm et al., 2014), uncertainties or inaccuracies in the VOC measurements (SCAQMD, 2004), inaccuracies in the mapping of the VOCs to the different chemical species in CB05GE, or inaccuracies in the oxidant levels (e.g., O_3) simulated by the CESM-NCSU model (He et al., 2015a). The inaccuracy of the emissions inventory is difficult to quantify, however, the CESM-NCSU model overpredicts O_3 by roughly 16.2% in the CONUS region and 47.8% in Europe (He et al., 2015a), indicating that there is an overabundance of oxidants that could be responsible for the underpredictions in VOC precursors. This overprediction has been attributed to both underpredictions of O_3 titration and underpredictions of O_3 deposition (Val Martin et al., 2014; He et al., 2015a).

OC statistics assuming OM:OC ratios of 1.8 are calculated for the CONUS region. The ratio of 1.4 is the typical assumption but 1.8 is a better assumption at the IMPROVE sites, since the OA in these environments is generally more aged than those in urban environments (Lane et al., 2008a). CONUS OC in the Base_OAC simulation is moderately underpredicted by -37.9%. This underprediction is improved to -25.3% in the New_OAC simulation and becomes a moderate overprediction of 31.4% in the Final_OAC simulation. This overprediction is consistent with many regional VBS studies including those on which the CESM OA treatments are based (Lane et al., 2008a; Murphy and Pandis, 2009; Ahmadov et al., 2012) as shown in Table 3.3. The NME is reduced by 8.0% and 5.5% in the

New_OAC and Final_OAC, respectively. Minimal changes occur in the R value in the New_OAC simulation, but the R value increases from 0.55 in the Base_OAC simulation to 0.66 in the Final_OAC simulation. This indicates an improvement in spatial pattern of CONIS OC, although the overall improvement in model bias is not large. The performance of CONUS OC is comparable to that of other studies listed in Table 3.3 in terms of bias, errors, and R values. However, the CONUS OC bias from the New_OAC and Final_OAC simulations are not as underpredicted and more overpredicted, respectively, compared to the simulations from the other global modeling studies of Farina et al. (2010), Jathar et al. (2011), and Jo et al. (2013). The differences compared to the other global modeling studies are due to the inclusion of greater functionalization and aging of biogenic SVOCs in the CESM-NCSU treatment.

There are improvements in simulated TC in the CONUS region with the new OA treatments. The NMB is decreased from -46.0% to -38.7% in the New_OAC simulation, but the model improvement is even more significant in the Final_OAC simulation (NMB to -0.7%) (Table 3.14). NME is also slightly improved in the New_OAC simulation from 51.1% in the BASE_OAC simulation to 47.6%, and improved more significantly to 37.5% in the Final_OAC simulation. There are only slight improvements in the R values from 0.53 in the BASE_OAC simulation to 0.57 and 0.59 in the New_OAC and Final_OAC simulations, respectively. This indicates that the new OA treatments improve TC more in terms of bias than spatial pattern. The scatter plots in Figure 3.14 show that CONUS OC and TC sites from the Final_OAC simulation are clustered much closer to the 1-to-1 line compared to those of the Base_OAC simulation, indicating an improvement in simulated OA over the

CONUS region from the final configuration of the new OA treatments. The model performance in terms of bias and error for CONUS TC is within the range of model performance of OC from STN reported from previous studies in Table 3.3. However, there are some caveats to this comparison since CONUS TC from CESM-NCSU contains both the IMPROVE and STN sites averaged together instead of a pure STN comparison reported in other studies. It is necessary to average STN and IMPROVE sites within the same grid cell together to compare with CESM-NCSU since the horizontal resolution of CESM-NCSU is coarse and thus the effect of urban/suburban sites in STN are diluted/diffused in such large grid cells. This issue is likely the reason why STN comparisons are not made in other global model studies and why sites close to urban areas are excluded (Shrivastava et al. 2015).

In Europe, there is poor OC performance in all three simulations with NMBs of -60.5%, -68.6%, and -49.3% in the Base_OAC, New_OAC, and Final_OAC simulations, respectively. The most likely cause of this poor performance is errors in European emissions. This evident in the smaller sensitivity of European OC model performance compared to the other OA metrics evaluated and also by the poor R values from nearly all chemical species simulated over Europe from CESM-NCSU (He et al., 2015a). However, it is possible that some of the difference between simulated and observed OC values is the result of inconsistent time periods between simulated and observed OC data mentioned in Section 3.3. Nonetheless, the Final_OAC simulation not only improves model performance in terms of bias but also improves the spatial evaluation of OC (e.g., increases in R from 0.17 to 0.38) (Table 3.14). The smaller R values and large underpredictions in European OC from CESM-NCSU are consistent with most other VBS studies that evaluated against OC measurements

from EMEP listed in Table 3.4. The only exception is Farina et al. (2010) which reports a large overprediction compared to EMEP measurements. This is likely because POM is treated as non-volatile in Farina et al. (2010), allowing for greater levels of OC mass in the aerosol phase.

Similarly, TOM is largely underpredicted in all simulations with NMBs of -68.3%, -61.9%, and -45.5% in the BASE_OAC, New_OAC, and Final_OAC simulations, respectively. The Final_OAC simulation also shows significant improvements in bias and NME (e.g., a decrease from 69.2% to 50.8%) (Table 3.14). The R values in all simulations are similar ranging from 0.82-0.89, with the new OA treatments reducing the R values slightly. Based on the scatter plot in Figure 3.14, a large number of the sites included in Z07 and J09 fall on or close to the 1-to-1 line in the Final_OAC simulation. Thus the large NMB is the result of underpredicted OA at a few sites and a small overall sample size of 37. The underprediction of TOM is consistent with the work of Jo et al. (2013) as shown in Table 3.5. However, the magnitude of the underprediction is larger in CESM-NCSU since HOA in CESM-NCSU is largely underpredicted as discussion in Section 3.5.2.

For a more in depth analysis, the monthly time series of TC and OC from the Base_OAC, New_OAC, and Final_OAC simulations are plotted at selected sites from the IMPROVE, STN, and EMEP networks in Figure 3.15. At the GRSM site, OC is underpredicted throughout the year in the Base_OAC simulation due to minimal SOA formation in the original OA treatments. The Final_OAC simulation overpredicts OC at the GRSM site throughout the year but is a better match to observed values during the boreal winter (JFD), spring (MAM) and autumn (SON) months than the Base_OAC simulation.

However, during the boreal summer (JJA) months and September OC is largely overpredicted, due to an overprediction of BSOA (i.e., BSOC: Biogenic Secondary Organic Carbon in the Figure) that is larger than observed total OC values. The New_OAC simulation has very good agreement with OC observations at this site, indicating that the impact of reduced wet deposition and fragmentation degrades JJA OC performance at some of IMPROVE sites in high BVOC environments. Contributions to TOA from OA species at the selected sites in Figure 3.15 are shown in Figure 3.16. At the GSRM site the contribution from the individual OA species are 14.3% from POM, 55.3% from BSOA, 21.8% from ASOA, 6.7% from SVOA, and the remaining 1.7% attributed to SOA from glyoxal (GLSOA) in the Final_OAC simulation. This is a significant shift towards OOA compared to the Base_OAC simulation that predicts a fairly even split between POM (51.5%) and SOA (48.5%). The LOWR site is one of the IMPROVE sites with underpredicted OC concentrations. The Base_OAC simulation predicts negligible OC at this site throughout the year, significantly underpredicting the magnitude and missing the seasonal pattern. The Final_OAC simulation provides a much better prediction of OC throughout the year and captures the bi-modal seasonal pattern of OC at this site. However, the simulated OC peak during MAM period occurs in April in the simulation rather than May in the observations. This is likely a result of an error in the temporal allocation of biomass burning emissions, since the simulated peak represents a spike in primary organic carbon (POC). The New_OAC simulation also captures the bi-modal pattern of OC at the LOWR site, but still strongly underpredicts the magnitude of OC. The final configuration changes appear to be critical for predicting sufficient BSOC to capture the peak in OC during the month of August. The

annual average composition of OA at this site consists of 12.9% from POM, 16.2% from SVOA, 38.6% from BSOA, 30.7% from ASOA, and 1.5% from GLSOA. This is an extreme change in OA speciation at this site, which is dominated but POM (74.4%) in the Base_OAC simulation.

The OC concentration is underpredicted at the BIR site in the Base_OAC simulation, as with many of the European OC sites. The simulated temporal pattern of OC at this site matches with the observed pattern in most seasons, except that it misses the peaks in February and August. In the Final_OAC simulation, the CESM-NCSU model captures most of the seasonal pattern of OC at this site but still misses the February peak. The missed peaks in February are likely from missing or miss allocated biomass burning emissions, since European increases in ambient levoglucosan levels near March and December indicate that biomass burning is a large contributor to OC during this time period (Puxbaum et al., 2007). The contributions of the different OA species to TOM at the BIR site are 20.8% from POM, 10.5% from SVOA, 35.3% from ASOA, 31.5% from BSOA, and 1.7% from GLSOA in the Final_OAC simulation. The ISP station is one of the few European sites with overpredicted OC concentrations in both the Base_OAC and Final_OAC simulations. It is fair to assume this overprediction in the Base_OAC simulation can be attributed to POM as the POM component of OC is greater than or roughly equal to the observed OC for most of the year as shown in Figure 3.15. The larger overprediction in the Final_OAC simulation can be attributed to overpredictions in SOA species as the ASOA component of OC is roughly equivalent to the total OC level throughout the year and the BSOA component of OC is roughly equivalent to the total OC level during the JJA season. The temporal pattern of OC is

roughly captured in both the Base_OAC and Final_OAC simulations, but similar to the temporal OC pattern at the BIR site, namely the peak in February is missed. As shown in Figure 3.16, the contribution of the different OA species to TOM is 18.9% from POM, 13.7% from 10.0% from SVOA, 43.0% from ASOA, 26.3% from BSOA, and 1.8% from GLSOA. Even though ISP is considered a rural background site (Yttri et al., 2007), the site is dominated by ASOA in the Final_OAC simulation and POM in the Base_OAC simulation (74.3%) (Figure 3.16). This is likely because of the course horizontal resolution of CESM-NCSU (i.e., 0.9º by 1.25º) allows more anthropogenic sources to be part of the ISP grid cell. Relative to the configuration of the New_OAC simulation, the Final_OAC configuration increases the relative contributions of BSOA and ASOA at all the selected IMPROVE and EMEP sites at the expense of decreases in the contributions of POM and SVOA. This has the greatest impact on the LOWR site where BSOA became the dominant OA species in the Final_OAC configuration, compared to SVOA dominating (27.3%) the TOM speciation in the New_OAC treatment. Comparing the EMEP and IMROVE OC sites, it is apparent that anthropogenic OA sources are more dominant in Europe compared to the CONUS region. The sample of stations tested here is too small for this difference in speciation between Europe and CONUS to be confirmed. Nonetheless, this speculation is consistent with the relative insensitivity of European OC to changes in model treatments, as these changes have the strongest impact on BSOA.

TC at the PHO site is likely driven by BC and POM considering the parabolic shape of the STN time series with maxima in the boreal winter season (JFD) when the atmosphere would be the most stable, the extent of photochemistry would be reduced comparing to other

warm seasons, and heating emissions would be large. This is reflected in the simulated annual average composition of OA at this site in the Final_OAC simulation, with POM and BC consisting of 25.4% and 24.5% of the carbonaceous aerosol, respectively. The remaining OOA breaks down into 27.0% ASOA, 13.4% SVOA, 8.3% BSOA, and 1.3% GLSOA. The dominance of POM and BC (67.4% and 27.4%) compared to SOA (5.2%) is even stronger in the Base_OAC simulation. In general the temporal profile of TC at this site is captured by both the Base_OAC and Final_OAC simulations. Both the Base_OAC and Final_OAC simulations have a peak in SON months due to increased SOA formation and significantly underpredict the JFD TC maxima, likely due to the coarse horizontal resolution of the CESM-NCSU model. This site also shows no significant improvement in TC model performance between the Base_OAC and Final_OAC simulations. At the BHM site, the CESM-NCSU model underpredicts TC throughout the year in the Base_OAC simulation. In the Final_OAC simulation, TC is simulated very well during the JJA period and is underpredicted throughout the rest of the year, but significantly less underpredicted compared to the Base_OAC simulation. The Base_OAC simulation somewhat captures the peaks in TC during the MAM and SON seasons, but fails to capture the JJA peak. The Final_OAC simulation captures the JJA peak, somewhat captures the MAM peak, and misses the SON peak. The JJA improvement is related to higher BSOA levels in the Final_OAC simulation, while the poorer performance of the MAM and SON peaks is likely related to underpredictions in POM, since these periods contain higher biomass burning emissions (Zhang et al., 2010). The total carbonaceous aerosol at the BHM site is comprised of 10.0% BC, 18.6% POM, 6.4% SVOA, 16.8% ASOA, 46.8% BSOA, and 1.4% GLSOA. There is

also a significant shift in carbonaceous aerosol speciation from the Base_OAC simulation, where total carbonaceous aerosol is comprised of 16.5% BC, 60.2% POM, and 23.3% SOA.

Overall, based on the analysis of OC and TC predictions at these selected sites, the Final_OAC configuration of the new OA treatments provides a much better representation of the magnitude and seasonal patterns of OA than the Base_OAC version of CESM-NCSU. However, deviations from observations still exist. The most striking of these is underpredictions of OC and TC during the JFD season, likely due to the underprediction of POM (discussed in detail below). Analysis of TC at the PHO site indicates that regions dominated by BC and POM will not experience significant improvements in model performance from the new OA treatments. The time series analysis also reveals that the modifications to fragmentation, SVOC wet deposition, and ΔHvap values in the Final_OAC simulation do not improve model performance at all locations, as evidenced by the OC performance at the GRSM site. Deviations from observations such as those reported here have occurred in other VBS studies (Lane et al., 2008a; Bergstrom et al., 2012), Indicating that while the VBS framework for OA leads to improved model performance compared to more traditional OA treatments, it may not be a "one size fits all" treatment and could benefit from the inclusion of other OA simulation techniques like those of the molecular approach.

3.5.2 Evaluation and Comparison of HOA, OOA, and SOA

OOA performance is significantly improved with the new OA treatments. OOA model performance is extremely poor in the Base_OAC simulation, with an NMB of -90.0%, an NME of 90.0%, and an R value of 0.48. This performance is improved in both the New_OAC and Final_OAC simulations (i.e., NMBs of -52.8% and -27.3%, NMEs of 53.2%

and 33.6%, and R values 0.92 and 0.89, respectively) (Table 3.14). Additionally, a large number of Z07 & J09 sites lie very close to the 1-to-1 line in the Figure 3.14 scatter plot. The OOA performance of CESM-NCSU is improved in terms of bias, error, and R vale compared to Jo et al. (2013) as shown in Table 3.5. The improved performance of CESM-NCSU is likely the result of the inclusion of the FF treatment and including aging of biogenic SVOCs. HOA performance is slightly degraded in terms of NMBs, changing from a slight 5.8% overprediction in the Base_OAC simulation to -62.1% and -59.2% underpredictions in the New_OAC and Final_OAC simulations, respectively. This indicates that POM in the VBS framework is too volatile. One potential reason for the underprediction of HOA is the rapid aging of POM from the primary carbon mode to the accumulation mode in the MAM7 aerosol module. This aging has been indicated to lead to extremely efficient wet removal of POM (Liu et al., 2012). In the VBS framework, the efficient wet removal of POM potentially leads to a feedback effect. The initial removal leads to a first-order underprediction of POM in the particulate phase. This in turn will lead to a shift in the OA equilibrium biasing the total POM mass towards the gas-phase in the Pankow (1994) partitioning parameterization, further enhancing underpredictions in POM. The HOA performance of CESM-NCSU contrasts with the findings of Jo et al. (2013) shown in Table 3.5, which show a large overprediction compared to HOA measurements. This could be related to differences in emissions between both studies, and also due to the potential POM wet removal errors in CESM-NCSU. Nonetheless, CESM-NCSU has better performance in terms of errors and R values compared to the work of Jo et al. (2013).

In Figure 3.17 the relative contributions of POM and OOA to TOM in the Base_OAC, New_OAC, and Final_OAC simulations are compared against the relative contributions of HOA and OOA to TOM in the Z07 and J09 dataset at selected sites. The POM contribution to TOM is largely overpredicted at urban locations in the Base_OAC simulation ranging from 86-89% of TOM across all locations and all seasons. In the Final_OAC simulation, the relative contributions of POM at the Mexico City and Mainz sites (37.8% and 34.3%, respectively) is in very good agreement with the Z07 & J09 contributions (38.2% and 42.1%, respectively). However, at the Manchester and Beijing sites, the contribution of POM is more underpredicted (49.5% and 21.7%, respectively) compared to the HOA observations (62.5% and 40.9%, respectively) than the Mexico City and Mainz sites. The underpredictions of POM at the Manchester and Beijing sites likely reflect the overall underprediction of POM in the new OA treatments, but the performance is still significantly better than the Base_OAC simulation.

There were no urban downwind (UD) stations available to evaluate during the SON and JFD seasons, thus two sites are selected from the MAM and JJA seasons. In the Base_OAC simulation the CESM-NCSU model also significantly overpredicts the contribution of POM to TOM, with POM contributions of ~73.0-79.0% over most of the sites and 44.5% at the NEAQS site. This is in comparison to HOA contributions of ~17.0-27.0% at most sites and 9.3% at the NEAQS site in the Z07 & J09 dataset. However, the Base_OAC simulation does at least capture the dominance of SOA (55.4%) at the NEAQS site. The NEAQS site is unique in the Z07 & J09 dataset, as it represents continental outflow from the CONUS region. The contribution of POM to TOM at the UD sites from the Final_OAC

simulation is in very good agreement with observations, being within ± 6.0% of the observed contribution.

In the rural/remote locations of the Z07 & J09 dataset, the Base_OAC is still consistently overpredicting the relative contribution of POM to TOM with contributions in the range of ~50.0-79.0%. This is in comparison to HOA contributions of ~0.0-12.0% in the Z07 & J09 dataset. At the Okinawa, Japan site, there is no reported HOA value, thus 1.0% is included for figure generation purposes. The relative contributions of POM to TOM at the Fukue Island and Chebogue Pt. (11.1% and 4.8%, respectively) sites in the Final_OAC simulation are in good agreement with observed HOA contributions (12.2% and 11.8%, respectively). However, the POM contribution is overpredicted at the Okinawa and Duke Forest sites (26.7% and 19.3%, respectively) compared to Z07 & J09 HOA contributions (0.0% and 8.3%, respectively). It is likely that the overprediction at the Okinawa and Duke Forest sites can be attributed to the use of a coarse horizontal resolution for the model simulation, as these sites are in proximity to anthropogenic OA sources. Thus the anthropogenic sources may be diffused into the grid cells representing these rural locations.

Overall all three CESM-NCSU simulations capture the decrease in relative contribution of POM from the urban to the rural sites. The new OA treatments in the Final_OAC simulation significantly improve the simulation of POM/OOA speciation in the CESM-NCSU model. Differences in the POM/OOA split between the New_OAC and Final_OAC simulation are not large. The configuration of the Final_OAC simulation increases the relative contribution of BSOA at the expense of POM and SVOA, similar to what was seen in the OC and TC evaluation in Section 3.5.1. The increased relative

contribution of POM in the New_OAC case does not significantly impact model performance, as it improves model performance at some sites (e.g., Manchester) and degrades model performance at other sites (e.g., Duke Forest).

The impacts of the new OA treatments on SOA model performance are fairly complex. The NMB for SOA is reduced from a significant underprediction of -66.0% in the Base_OAC simulation to a more moderate underprediction of -26.3% in the New_OAC simulation. However, the NMB against the L13 SOA data becomes an overprediction of 53.2% in the Final_OAC simulation. It is important to note that caution must be used when interpreting these results. The L13 SOA data are derived based on tracers that represent oxidation products from a limited set of VOC precursors including: APIN, ISOP, TOL, naphthalene, β-Caryophyllene, and 2-Methyl-3-buten-2-ol (MBO). As a result, the L13 dataset has a very limited amount of anthropogenic SOA compared to the CESM-NCSU model that contains many additional anthropogenic precursors (XYL, IOLE, OLE, and ALKH). There are also inconsistencies in the biogenic precursors, as SOA formation from β-Caryophyllene and MBO are not explicitly simulated in CB05GE and are thus not treated in CESM-NCSU and the BPIN, OCI, LIM, and TER precursors are not part of the L13 dataset. Since the VBS approach is based on the lumping of precursors (Donahue et al., 2006), it is not computationally efficient to isolate the SOA formed from individual precursors for a more accurate comparison. With this understanding of the L13 dataset in mind, the large overprediction by the Final_OAC simulation likely represents improved model performance, since more ambient SOA exists than is reported in the dataset. Similarly, the large underprediction by the Base_OAC represents extremely poor model performance, which has

been corrected with the implementation of the final configuration of the new OA treatments. The increase in R values between the New_OAC and Final_OAC simulations (increase from 0.12 to 0.72) illustrates the importance of reducing the SVOC wet deposition in the Final_OAC simulation. Because of the larger amount of anthropogenic precursors in the new OA treatments CESM-NCSU overpredicts SOA at the three California sites included in L13 (i.e., Pasadena, Bakersfield, and Riverside), where many ASOA precursors are available. In the New_OAC simulation, CESM-NCSU underpredicts SOA at the sites from the Southeastern Aerosol Research and Characterization (SEARCH) network, that are located in a largely BVOC dominated environment with high precipitation rates. This makes the R value small, since there is an overprediction in the region with low estimated SOA and a slight underprediction in the region with larger estimated SOA. In the Final_OAC simulation, SOA is still overpredicted at the California sites, but SOA at the SEARCH sites are also slightly overpredicted due to the reduction in SVOC wet deposition. This leads to a better R value between simulated and observed values.

Figure 3.18 compares the relative contribution of ASOA to BSOA at four sites in the L13 dataset to those predicted by the New_OAC and Final_OAC simulations. A comparison was not possible from the Base_OAC simulation because all SOA are lumped into one species in the default OA treatments. The contributions of ASOA and BSOA at the RTP and Pensacola sites are similar between the L13 estimates and the CESM-NCSU simulations, with ASOA comprising 20.1%-25.4% and BSOA comprising 75.6%-79.9% in the L13 dataset, ASOA comprising 27.9%-21.7% and BSOA comprising 72.1%-78.3% in the New_OAC simulation, and ASOA comprising 24.9%-21 and BSOA comprising 75.1%-

78.2% in the Final_OAC simulation. This is different from the Bakersfield and Detroit sites where estimated ASOA contributions are slightly greater than BSOA contributions in the New_OAC (54.5%-51.2% ASOA and 45.5%-48.8% BSOA) and Final_OAC simulations (44.5%-51.3% ASOA and 55.6%-48.7% BSOA), than those in the L13 dataset (33.1%-38.0% ASOA and 66.9%-62.0% BSOA). The values at all four sites are in relatively good agreement; however it is difficult to attribute the differences at the low BVOC sites to errors in model performance. This is because the L13 dataset uses only two anthropogenic SOA components to estimate ASOA, which creates biases in the L13 estimate towards BSOA even in urban areas that have high AVOCs. Therefore, the biases in the L13 dataset may affect the model performance evaluation.

3.5.3 Evaluation and Comparison of $PM_{2.5}$ and PM_{10}

The impacts of the OA model updates on $PM_{2.5}$ and PM_{10} cannot be easily separated from those of other changes between simulations in a fully-coupled climate-chemistry model like CESM. For example, simulated wind speeds from the Base_OAC, New_OAC, and Final_OAC simulations are different because of feedbacks from different chemical predictions of chemistry into climate, which in turn change concentrations of dust and thus $PM_{2.5}$ and PM_{10}. These changes in dust concentrations dominate the changes in $PM_{2.5}$ of many regions in the Final_OAC simulation (Figure 3.13), although some of the changes from TOM are apparent. These impacts of TOM include decreasing $PM_{2.5}$ over South America, Indonesia, South Asia, central Africa, as well as, increases in $PM_{2.5}$ levels over most of North America, southeastern China, and northern Asia. Similar patterns occur in PM_{10} changes (Figure not shown), but are harder to differentiate from stronger perturbations in dust and

sea-salt. These perturbations have a stronger impact on PM_{10} since the MAM7 module does not treat any coarse mode OA formation (Liu et al., 2012). This is confirmed by correlation analysis which reveals that the R value between the changes in dust and $PM_{2.5}$ is 0.98, whereas the R value between the changes in TOM and $PM_{2.5}$ is 0.26. The R values for changes in dust and PM_{10} are similar (0.97), while the R value for changes between TOM and PM_{10} is weaker (0.09). Since the changes in $PM_{2.5}$ and PM_{10} are not entirely related to changes in OA, it is difficult to estimate the impacts of the changes in OA treatment on $PM_{2.5}$ and PM_{10} model performance. This is especially true in the CONUS and Europe regions, as the trends in model biases of the New_OAC and Final_OAC simulations change randomly compared to the Base_OAC simulation. The impact on $PM_{2.5}$ and PM_{10} in these regions from the final configuration of the new OA treatments in the Final_OAC simulation appears insignificant in Europe, as there is no trend in $PM_{2.5}$ and PM_{10} values shown in the Figure 3.13 scatter plots. In the CONUS region the new OA treatments in the Final_OAC simulation tend to cause slight overpredictions in $PM_{2.5}$ and minimal changes in PM_{10} performance. The CONUS $PM_{2.5}$ and PM_{10} scatterplots in Figure 3.14 both show increases in PM at sites with smaller $PM_{2.5}$ and PM_{10} levels and negligible changes at sites with larger PM levels. This impact is consistent with both the increased North American background $PM_{2.5}$ level from TOM in Figure 3.13 and the overprediction of OC at IMPROVE sites. There is a consistent trend in East Asian PM_{10} from the new OA treatments with the NMB decreasing in magnitude from -38.6% in the Base_OAC simulation to approximately -26% in the New_OAC and Final_OAC simulations. This slight improvement in East Asian PM_{10} is also apparent in the Figure 3.14 scatter plot. While it is not possible to rule out dust changes as a

cause of this improvement due to increased dust concentration in northeastern China (Figure not shown), there are strong increases in TOM over southeastern China that likely contribute to this PM_{10} enhancement. The improved TOM model performance in the Z07 & J09 dataset containing East Asian sites and the improved East Asia PM_{10} model performance appear to indicate improved East Asian OA performance. However, the lack of publically available large scale OC observations means this improvement cannot be directly confirmed.

3.5.4 Impacts and Evaluation of Aerosol/Climate Interactions

The addition of the OA conucleation treatment increases the global NUM level by 3.0×10^{17} cm^{-2} on global average in the Final_OAC simulation. The impact is the strongest in the tropics and subtropics (30ºS to 30ºN), where NUM increases by $8.0\times10^{17} – 2.0\times10^{18}$ cm^{-2} due to relatively high SVOC levels. The increase in NUM combined with the increase in OOA/TOM leads to a global average increase in CCN of 8.4×10^{6} cm^{-2}. The increases in CCN are the largest in eastern China, the southeastern U. S., central Africa, and South Asia (e.g., $4.0\times10^{7} – 1.2\times10^{8}$). These regions correspond to regions with the largest increases in OOA between the Base_OAC and Final_OAC simulations. The OOA impact on CCN is stronger than that of TOM for two primary reasons. The first is that POM is more hydrophobic than OOA in the CESM-NCSU model, with a κ value of 0.1 compared to 0.14 for OOA species. Secondly, the POM mass in the MAM7 aerosol module is divided between the primary carbon and accumulation modes. The POM in the primary carbon mode is both smaller and externally-mixed from other aerosols, making them less likely to act as CCN. The POM that ages into to accumulation mode is larger and internally-mixed with other aerosols, making it more likely to activate into cloud droplets (Liu et al., 2012). However, the

bulk of OOA mass partitions into the accumulation mode allowing it to dominate the losses of POM in this mode. The increase in CCN, from either increased NUM or increases in OOA, increases global average CDNC by 10.2 cm^{-3}. However, changes in CDNC are complex because increased CCN does not guarantee an increase in CDNC, as different feedbacks from chemistry into climate could impact cloud formation differently. In terms of model performance CCN is largely underpredicted in CESM-NCSU with a -73.6% NMB in the Base_OAC simulation. This can be attributed to a lack of a marine organic aerosol treatment and errors in sea-salt concentrations (He et al., 2015a). The NMB is improved slightly in the Final_OAC simulation to -70.4%. Model improvements in CCN are not dramatic, since the satellite estimate only exists in marine regions and the bulk of the CCN improvements occur over continental environments. CDNC is largely overpredicted in the BASE_OAC, with a NMB of 52.9%. This overprediction is enhanced in the Final_OAC simulation to a NMB of 66.2%. The large overprediction in CDNC does not occur in the work of Gantt et al. (2014) and He et al. (2015a) because primary particle number emissions were neglected in these studies. This has been corrected as part of this work resulting in higher simulated CDNC levels. This overprediction could be attributed to either the aerosol activation updates in the work of Gantt et al, (2014) or due to a potential underestimates of CDNC by the Bennartz (2007) dataset, from errors in the MODIS products used to derived these estimates (He et al., 2015a).

AOD decreases nearly domain wide by 0.06 on global average in the Final_OAC simulation. The decreased AOD is caused by decreases in POM in the final configuration of the new OA treatments. The impact of reduced POM dominates because biomass burning

emissions of POM are prescribed a vertical profile to mirror the injection of aerosol from fires at higher altitudes. As a result, POM has a greater impact throughout the depth of the troposphere compared to OOA as the SOA component of OOA originates from VOC sources near the earth's surface. However in eastern China, the OOA increases are large enough to compensate the POM decrease and increase AOD. The increase in CDNC from the new OA treatments also increases the aerosol cloud lifetime effect, increasing LWP on global average by 2.8 g m^{-2} (Figure not shown). This combined with increases in cloud albedo from increased CDNC result in an increase in COT of 0.7 on global average (Figure 3.13). In terms of model performance AOD is overpredicted, with an NMB of 15.8%. After the inclusion of the new OA treatments in the Final_OAC simulation the sign of the NMB changes to -19.9%. This is a slight degradation in model performance that results from the POM being too volatile in the new OA treatments. LWP and COT are underpredicted in the CESM-NCSU model, with NMBs of -37.5% and -43.2% in the Base_OAC simulation, respectively. This type of moderate underpredictions in cloud parameters is common in many global models (Lauer and Hamilton, 2013) and regional air quality models (Zhang et al., 2012b), indicating important model limitations in simulating cloud properties that need to be addressed by the scientific community in order to better understand the indirect forcing of aerosols. The underpredictions in both LWP and COT are reduced in the Final_OAC simulation to -33.6% and -39.2%, respectively. These improvements in model performance are small but based on the students' t-test analysis they are statistically significant.

The enhancements in COT from the enhanced cloud albedo and cloud lifetime affects in the Final_OAC simulation lead to increases in SWCF of 2.9 W m^{-2} on global average. The

increases are the largest in marine environments. These environments have less CCN and greater LWP compared to continental clouds. As a result, these clouds are more sensitive to changes in aerosol levels than their continental counterparts. Thus, even though the new OA treatments have the strongest impact on continental aerosol levels, the strongest climate impact occurs in the marine environments. The increase in SWCF from increases OOA levels is compensated by the increase in FSDS from reductions in AOD. As a result, the global average change in FSDS is an increase of ~0.6 W m^{-2} on global average. The absolute difference plot of FSDS between the Base_OAC simulation and the Final_OAC simulation shows that the AOD reduction dominates the changes in radiation over the continents, while the enhanced SWCF dominates the changes in FSDS in marine environments. SWCF is slightly underpredicted in the Base_OAC simulation with an MB of -1.3 W m^{-2} and slightly overpredicted with an MB of 1.6 W m^{-2} in the Final_OAC simulation. The magnitude of the bias is similar in both simulations, but slightly larger in the Final_OAC simulation. FSDS is also slightly underpredicted in the Base_OAC simulation by -1.1 W m^{-2}, which is reduced slightly to a MB of -0.6 W m^{-2} in the Final_OAC simulation. These values are also very similar but with a slight improvement in the Final_OAC simulation due to the underprediction of AOD that compensates the overprediction in SWCF.

3.6 World Region OA Comparison

Table 3.15 summarizes the maximum and spatial mean annual average concentrations of each OA component from the Final_OAC simulation, as well as the maximum and spatial mean relative contributions of these components to TOM in eight world regions. BSOA is the dominant component of TOM in the North America (NAM), South America (SAM), East

Asia (EA), Southeast Asia (SEA), and Australia (AUS) regions comprising 34.1%-47.0% of TOM on annual average, with maximum contributions of 71.8%-81.1% to TOM. Due to large BVOC emissions, it would be expected for SAM, SEA, and Africa (AF) to have the highest maximum BSOA values. However, this is not the case in CESM-NCSU, where maximum annual average BSOA values are the largest in the NHIR of NAM and EA (3.5 and 4.5 μg m^{-3}). This reflects the importance of the photochemical aging processes in new OA treatments. However, this may also be related to potential overpredictions of SVOC wet deposition, discussed in Sections 3.4 and 3.5, that limit OA formation in rainforest regions (e.g., SAM with a maximum BSOA value of 1.3 μg m^{-3}). The annual average BSOA level over the Amazon in CESM-NCSU is largely in the range of 0.5-0.7 μg m^{-3}. This is in the range of mean water soluble OA concentrations reported for the Amazon of 0.07-0.22 μg m^{-3} and 0.79-1.17 μg m^{-3} reported during wet and transition periods, respectively, but less than values reported during dry periods of 4.58-5.73 μg m^{-3} (Fuzzi et al., 2007). This does indicate that BSOA levels in the Amazon may be somewhat under predicted as the annual average would be comprised of all three periods. Additionally, there is a slight discrepancy in size of the simulated and measured OA, as the accumulation mode of MAM7 represents particles with diameters ranging 0.056-0.26 μm (Liu. et al., 2012) and the measurements represent a size range of 0.05-0.14 μm (Fuzzi et al., 2007).

ASOA comprises a significant portion of TOM in all world regions on annual average (21.7-33.7%). Maximum ASOA levels occur in EA, South Asia (SA), AF, and SEA (5.3-3.8 μg m^{-3}). The high ASOA levels in EA, SOA, and SEA are related to large anthropogenic VOC sources throughout these regions, while in the AF region large maximum ASOA levels

primarily occur in the Arabian Peninsula. Europe (EU) has smaller overall OA levels compared to all analyzed world regions except AUS. As results, even though the maximum annual average ASOA value (1.2 μg m^{-3}) is small compared to other world regions, ASOA is the dominant form of ASOA in EU as simulated by CESM-NCSU (33.7%) with the new OA treatments. This is only slightly larger than the annual average BSOA concentration (33.1%). The dominance of ASOA in EU is not consistent with findings of biogenic sources as the largest contributor to background European aerosol (May et al., 2008). This likely indicates errors in both anthropogenic and biogenic emissions in Europe within CESM-NCSU, as evidenced by the poor R values for all European chemical species (He et al., 2015a), including ISOP (Table 3.14).

The contribution of POM to TOM is smaller compared to all OOA components except GLSOA, comprising 7.7%-23.5% of TOM across the world regions. POM contributions are large in EA and SA (19.2% and 23.5%, respectively), reflecting large anthropogenic emissions in these regions. In the large biomass burning regions of SAM, AF, and SEA, POM comprises roughly 12.4%-14.8% of TOM. The smaller POM contribution in these regions is likely caused by strong influences from OOA species and because biomass burning emissions are injected at higher altitudes than the anthropogenic emissions in EA and SA. POM has very small relative contributions in both NAM and AUS (9.6% and 7.7%) because of the dominance in OOA species in NAM and the low overall anthropogenic emissions in AUS. The small overall contribution of POM to TOM in the Final_OAC simulation is likely an artifact of the underprediction of POM to HOA observations discussed in Section 3.5.1.

SVOA comprises a significant fraction of TOM in all world regions (e.g., 12.4%-34.5%). SVOA is the dominant form of aerosol in the SA and AF regions (28.2% and 34.5%, respectively). This dominance of SVOA is due to high POM emissions and strong radiation for photochemistry in both regions. The SAM and SEA regions also have high biomass burning POM emissions and stronger radiation for photochemistry reflected in strong annual average SVOA contributions (24.3% and 21.9%, respectively). SVOA contributions in the NAM and AUS regions are smaller (16.2% and 16.5%, respectively), but significantly larger than NAM and AUS regional POM contributions. This indicates that ambient OA from combustion sources in these regions is largely aged within the new OA treatments. EA and EU are the only two analyzed world regions in which the annual average SVOA contributions to TOM are smaller than POM contributions to TOM. In EA this is likely due to the overall high OA level that keeps POM less diluted and reduces POM evaporation compared to other world regions. In EU the small contribution of SVOA likely reflects the weaker radiation and thus weaker photochemical aging due to the higher latitudes of this region.

GLSOA is the smallest component of TOM in all world regions with mean contributions of 1.6%-7.0% across the world regions and a maximum contribution of no more than 21.8% in any world region. GLSOA is generated in the new OA treatments using a very simplified treatment. However, this simplicity means that this approach is likely an upper estimate of GLSOA formation (Knote et al., 2014). However, there is uncertainty in the glyoxal simulated by CB05GE, since CB05GE is a more concise gas-phase mechanism than the Master Chemical Mechanism (MCM) used in most glyoxal global modeling studies

(Fu et al., 2008; Stavrakou et al., 2009). The MCM provides a much better representation of isoprene chemistry, which is important for glyoxal as the primary source of glyoxal is secondary formation from ISOP (Fu et al., 2008). However, this complexity makes the MCM non-ideal for climate simulations, like those of CESM-NCSU, due to poor computational efficiency.

3.7 Conclusions

In this work, CESM-NCSU, a modified version of the CESM/CAM5.1 model, has been further improved in its capability in simulating organic aerosols. The new OA treatments implemented in CESM-NCSU include a VBS approach for simulating OA from VOCs, POM, and SVOA formed from oxidized POM and emitted S-IVOCs from combustion, a simplified treatment for SOA formation from glyoxal, and a treatment for the simulation of organic conucleation with sulfuric acid. This work differs from many past VBS treatments in global models by accounting for both functionalization and fragmentation of SVOCs and by including the aging biogenic SVOCs. There are similarities between this work and the work of Shrivastava et al. (2015), but this work has a greater focus on the comprehensive evaluation of OA against surface observations and the impact of OA on cloud properties. The primary objective of both studies also differs, as the objective of this study is to develop a version of CESM to that can adequately represent OA and its climate interactions within the current atmosphere for use in future climate simulations, while the objective of Shrivastava et al. (2015) is to understand the implications of different OA formation processes on spatial distribution, loadings, and lifetime of OA.

Sensitivity analysis has been conducted on various parameters controlling the new OA treatment in the CESM-NCSU model that affect both the prediction of OA and its impact on the climate system. The POM emission factors and conservative aging approaches used in previous studies have been shown to underpredict OA when wet deposition of SVOCs is considered. The impact of wet deposition of SVOCs has the strongest impact on TOM compared to all other parameters examined, indicating that an accurate representation of this process is important for accurate simulation of OA. The choice of ΔHvap values also shows a substantial impact on OA predictions, especially in the middle and higher latitudes of the NH where OA sources and the seasonality of temperatures are maximized. The amount of fragmentation considered in the VBS treatment has a significant, but smaller impact on TOM predictions compared to wet deposition or ΔHvap values. Ultimately, the sensitivity simulation that contains reduced SVOC wet deposition, reduced fragmentation, and the E10 ΔHvap values is chosen as the final configuration of the new OA updates. This adjustment is justified by improved model performance of most OA metrics and aerosol/cloud interaction variables.

Assumptions regarding OA hygroscopicity are shown to impact the vertical domain averaged predictions of CCN by ± 9.2 cm^{-3}. However, the general impact on various cloud and radiation parameters from these changes is difficult to distinguish from other complex interactions. The conucleation treatment shows an impact on simulated aerosol-cloud interactions by enhancing mean levels of CCN, CDNC, COT, LWP, and SWCF. Sensitivity analysis removing S-IVOCs from oxidized POM and combustion in the conucleation treatment shows a much smaller impact relative to full conucleation treatment, indicating that

the conucleation effect is dominated by condensable gases from oxidized VOCs. In addition to strong impacts on the surface OA predictions, the choices in enthalpies of vaporization and SVOC wet deposition affect the simulated OA and SVOC levels throughout the atmosphere. The changes in OA and SVOC levels throughout the atmosphere impact not only AOD but also COT due to changes in aerosol activation from changes in aerosol size and hygroscopicity as well as changes in aerosol number from the conucleation treatment. The relatively strong impact of SVOC wet deposition and enthalpies of vaporization on the aerosol direct and indirect effects of OA indicate that constraining and providing the best representation of these parameters is critical in order to accurately simulate the impacts of OA on the climate system. The impact of OA on aerosol/cloud interactions would also be aided by the incorporation of a more detailed treatment for organic aerosol nucleation.

A comparison of results from the final OA treatments in CESM-NCSU with the unmodified model reveals that these final OA treatments increase OOA levels globally by 0.33 $\mu g\ m^{-3}$ mainly in the NHIR due to the additional precursors and pathways for OOA formation, but decrease POM levels by 0.22 $\mu g\ m^{-3}$ on global average from treating POM volatility. The result is a global mean increase of 0.11 $\mu g\ m^{-3}$ in TOM, largely in the NH. The simulation with the final OA treatments shows significantly-improved model performance against European OC, CONUS TC, NH TOM, and NH OOA. There is only slight improvement in model performance for CONUS OC and SOA as the final OA treatments change the sign of model biases, resulting in overpredicted OC and SOA levels at several sites. There is only degradation in the OA performance of simulated POM against NH HOA measurements, due to treating POM volatility in the final OA treatments. Additionally, this

degradation may be worse than discussed in this work since biomass burning observation are not considered when evaluating POM. The reduced POM level from POM volatility reduces the OA direct effect by reducing AOD by 0.06 on global average. However, the increase in OOA increases the OA indirect effect by increasing SWCF by 2.9 W m^{-2} on global average. The net impact of the new treatments is an increase in FSDS of 0.6 W m^{-2}, indicating that the reduced OA direct effect dominates over the enhanced OA indirect effect.

The CESM-NCSU model with the final OA treatments provides a very good bulk representation of OA globally during the current climate period, but there are deviations from observations at specific locations and during certain seasons. The final OA treatments overpredict OC during the JJA period at the GRSM site due to the adjustments in fragmentation, ΔHvap, and SVOC wet deposition. This indicates that these adjustments do not provide improved model performance in all regimes. There are also large overpredictions at the European ISP site, which are likely from errors induced by coarse horizontal resolution and emission estimates. The poor R values in the evaluation of many European chemical species and the missed peaks in OC during various seasons also indicate possible errors in the spatial and temporal allocation of the emissions used in this work, There are large underpredictions of OC and TC during the JFD season due to a combination of overpredicted POM volatility and coarse horizontal resolution. The overpredicted POM volatility also leads to underpredictions in the relative contribution of POM to TOM in locations that have high photochemistry or contain mostly aged aerosol, such as the Beijing, China and NEAQS sites in the Z07 & J09 dataset. Overpredictions in the POM contribution to TOM in rural sites (e.g., Okinawa, Japan and Duke Forest, U.S.) are also likely caused by the use of a

coarse horizontal resolution in those simulations. Despite these deviations from observations, the final OA treatments in CESM-NCSU improve model performance of the magnitude and seasonal patterns of OC and TC and the relative contribution of POM and OOA to TOM, compared to the unmodified model.

In addition to limitations of the OA treatments and the CESM-NCSU model mentioned above, the VBS treatments included in the CESM-NCSU model have some general limitations. These include missing pathways for OA formation. One such pathway is the lack of SOA formation from aqueous processes. This could be addressed in future work by attempting to hybrid the VBS approach with the molecular approach similar to the hydrophilic/hydrophobic organic aerosol model (Couvidat et al., 2012), which would provide additional insights or improvements in the OA predictions. This could be accomplished by using the molecular approach to split the OA precursors into hydrophobic and hydrophilic classes and then using the VBS approach to simulate the hydrophobic component, while the molecular approach is to simulate the hydrophilic component. The treatments included in this work also do not include detailed treatments for oligomerization and acid-catalyzed chemistry of glyoxal or other carbonyl species which would provide more pathways for OA formation. The VBS treatments shown here may also be limited by using a 1.5-D basis set as the two dimensional basis set that simulates O:C ratio may be better suited to accurately represent OA hygroscopicity (Jimenez et al., 2009). Another key limitation is that the VBS treatments all assume that OA forms pseudo ideal solutions and behaves in much the same manner as a liquid. This has been shown to not be the case in certain situations such as when OA is coated by very hydrophobic organic substances (Vaden et al., 2011) and for certain

types of OA that behave like semi-solids (Virtanen et al., 2010). There are also emerging findings that show OA formation and removal may differ from the VBS approach, these include greater formation of OA from ELVOCs (Ehn et al., 2014; Jokinen et al., 2015) and greater removal through photolysis and heterogeneous oxidation (Hodzic et al., 2016). Overall, despite these limitations, CESM-NCSU with the finalized OA treatments can reasonably reproduce OA levels and aerosol/cloud interactions in the current atmosphere and is thus suitable for long-term climate simulations. A preliminary version of this treatment was used for such long-term climate simulations and the results of that study are presented in Chapter 4.

Table 3.1. Comparison of Organic Aerosol Modeling Approaches

Attribute	Traditional Approach	VBS Approach	Molecular Approach
Basis	Multi-product	Volatility	Molecular Surrogates
POM Treatment	Tracer-like	Volatile	Tracer-like/Volatile
SVOCs/IVOCs	Not Treated	Treated	Optional
Photochemical Aging	Not Treated	Treated	Optional
Partitioning	Pseudo-ideal	Pseudo-ideal	Non-ideal
Aqueous OA	Not Treated	Not Treated	Treated
Oligomerization	Not Treated	Not Treated	Treated
Complexity	Simple	Adjustable	Complex
Examples	SORGAM[1]/MADRID[2]	PMCAMx-2008[3]/MADE-VBS[4]	H2O[5]/SOAP[6]

[1]SORGAM: Secondary Organic Aerosol Model (Schell et al., 2001); [2]MADRID: Model of Aerosol, Dynamics, Ionization, and Dissolution (Zhang et al., 2004, 2010, 2012c); [3]PMCAMx-2008: 2008 version of the Comprehensive Air-quality Model with extension to treat particulate matter (Murphy and Pandis, 2009; Tsimpidi et al., 2010); [4]MADE-VBS: Modal Aerosol Dynamics Model for Europe with a Volatility Basis Set Treatment for SOA (Ahmadov et al., 2012; Wang et al., 2015); [5]H2O: Hydrophilic/Hydrophobic Organic Aerosol Model (Couvidat et al. 2012); [6]SOAP: The Secondary Organic Aerosol Processor (Couvidat and Sartelet, 2014)

Table 3.2. Comparison of VBS Treatments in the Literature.

Study	Model	Scale	Location	Period	GPM	AM	POV	PES	OAV	Func.	Frag.	BA	SDD	SWD
A12	WRF/Chem	R	CONUS	Aug.-Sep. 2006	RACM	MADE	NT	N/A	SV	1	NT	T	25% HNO_3	NT
B12	EMEP MSC-W	R	Europe	2002-2007	EmChem09	EmChem09	T	U	SV	1	NT	T	Higher Aldehydes	NT
F10	UGISS GCM II	G	Globe	Climatology	M99, W00	A99,N99	NT	N/A	SV	0	NT	NT	Organic Di-acids	T
J11	UGISS GCM II	G	Globe	Climatology	L03	A99,CS02, L04,F10	T	U	SV	0	NT	NT	Organic Di-acids	T
J13	GEOS-Chem	G	Globe	2009	UCx	UCx	T	U	SV	1	NT	NT	IN	IN
L08	$PMCAM_X$	R	Eastern U.S.	Jul. 2001	SAPRC99	G07	NT	N/A	SV	0	NT	T	IN	IN
MP09	$PMCAM_X$	R	Eastern U.S.	Jul. 2001	SAPRC99	G07	T	U	SV	1	NT	NT	HL 2700	IN
S08	$PMCAM_X$	R	Eastern U.S.	Jul. 2001 Jan 2002	CB4	G07	T	U	N/A	1	NT	NT	G07	T
S11	WRF/Chem	L	Mexico	Mar. 2006	SAPRC99	MOSAIC	T	S	SV	2P	NT	T	HL 2700	NT
S13	WRF/Chem	L	Mexico	Mar. 2006	SAPRC99	MOSAIC	T	S	NV	2	T	T	HL 2700	NT
S15	CESM-CAM5	G	Globe	2007-2011	MOZART-4	MAM3	T	S	NV	2	T	T	Methyl Hydroperoxide	IN
T10	$PMCAM_X$	L	Mexico	April 2003	SAPRAC99	G07, K03	T	U	SV	1	NT	T	HL 2700	IN
W15	WRF/Chem	R	CONUS	Jul. 2006	CB05	MADE	NT	N/A	SV	1	NT	T	25% HNO_3	NT
G16	CESM-NCSU	G	Globe	Climatology	Cb05GE	MAM7	T	S	SV	2	T	T	25% HNO_3	T

GPM-Gas-phase Mechanism, AM-Aerosol Module, POV-Primary Organic Volatility, PES-POM Emissions Spectrum; OAV-Organic Aerosol Volatility, Func.-Functionalization, Frag.-Fragmentation, BA-Biogenic Aging, SDD-SVOC Dry Deposition, SWD-SVOC Wet Deposition, R-Regional, G-Global, L-Local, CONUS-Conterminous U.S., RACM-Regional Atmospheric Chemistry Mechanism, CB4-Carbon Bond Mechanism version 4, CB05-2005 Carbon Bond Mechanism, CB05GE-2005 Carbon Bond Mechanism with Global Extension, MOZART-4-Model of Ozone and Related Chemical Tracers version 4, UCx-Universal Tropospheric-Stratospheric Chemistry Extension Mechanism, MADE-Aerosol Dynamic Model for Europe, MOSAIC-Model for Simulating Aerosol Interactions and Chemistry, MAM3-3 Mode Modal Aerosol Model, MAM7-7 Mode Modal Aerosol Model, T-Treated in study, NT-Not treated in study, IN-Insufficient information in text and supplement, N/A-Not Available, U-Uniform emissions spectrum for POM, S-Separated emission spectrum of POM between anthropogenic and biomass burning sources, SV-Semi-volatile, NV-Considers non-volatile OA, 0-No Functionalization, 1-Addition of 1 oxygen atom, 2-Addition of 2 oxygen atoms, 2P-Addition of 2 oxygen atoms for only POM, HL 2700-Wesely (1989) deposition assuming a Henry's Law constant of 2700 M atm^{-1}, A99-Adams et al. (1999), A12-Ahmadov et al. (2012), B12- Bergstrom et al. (2012), CS02-Chuang and Seinfeld (2002), F10- Farina et al. (2010), G07-Gaydos et al. (2007), G16-Glofelty et al. (2016a) and this work, J11- Jathar et al. (2011), J13- Jo et al. (2013), K03-Koo et al. (2003), L08- Lane et al. (2008a), L03-Liao et al. 2003, L04-Liao et al. (2004), M99-Mickley et al. (1999), MP09- Murphy and Pandis (2009), N99-Nenes et al. 1999, S08- Shrivastava et al. (2008), S11- Shrivastava et al. (2011), S13- Shrivastava et al. (2013), S15- Shrivastava et al. (2015), T10- Tsimpidi et al. (2010), W15-Wang et al. (2015), W00-Wild et al. 2000.

Table 3.3. Comparison of Performance Statistics of OA over CONUS.

Obs. Network	Statistic	A12[a]	F10	J11	J13[a]	L08[a]	MP09[a]	S08[a]	S15	W15[b]	G16[b]
IMPROVE	MB (μg m^{-3})	-0.43 to 1.30	-0.65 to -0.36	-1.1 to 0.5	N/A	0.33 to 6.44	0.29	-0.41 to 0.45	-0.12 to 1.66*	N/A	-0.26 to 0.32
OC	MAE (μg m^{-3})	N/A	0.92 to 0.95	N/A	N/A	1.11 to 6.45	0.72	0.79 to 1.00	N/A	N/A	0.42 to 0.45
(CONUS)	FB[c]/NMB[d]	N/A	-0.41 to -0.26[c]	-0.98 to 0.03[c]	-30.0 to 2.0[d]	0.21 to 1.06[c]	0.17[c]	-0.02 to 0.27[c]	N/A	60.5[d]	-0.38 to 0.19[c] /-25.3 to 31.5[d]
	FE[e]/NME[f]	N/A	0.49 to 0.55[e]	0.52 to 1.04[e]	41.0 to 47.0[f]	0.45 to 1.06[e]	0.39[e]	0.38 to 0.44[e]	N/A	83.0[f]	0.33 to 0.50[e] / 41.6 to 44.2[f]
	R	0.55 to 0.65	0.66	N/A	0.46 to 0.50	N/A	0.62	N/A	N/A	0.57	0.56 to 0.65
STN	MB (μg m^{-3})	-1.77 to 0.57	N/A	N/A	N/A	-1.23 to 3.60	-0.88	-2.24 to -0.95	N/A	N/A	-0.96 to -0.02
OC[a]/TC[b]	MAE (μg m^{-3})	N/A	N/A	N/A	N/A	1.80 to 3.94	1.33	1.76 to 2.59	N/A	N/A	0.93 to 1.16
(CONUS)	FB[c]/NMB[d]	N/A	N/A	N/A	N/A	-0.21 to 0.43[c]	-0.29[c]	-0.50 to -0.08[c]	N/A	53.1[d]	-0.39 to 0.08[c] / -38.7 to -0.08[d]
	FE[e]/NME[f]	N/A	N/A	N/A	N/A	0.37 to 0.50[e]	0.52[e]	0.58 to 0.64[e]	N/A	76.8[f]	0.39 to 0.50[e] / 37.5 to 46.7[f]
	R	0.68 to 0.76	N/A	N/A	N/A	N/A	0.52	N/A	N/A	0.54	0.57 to 0.59

[a]STN statistics based on organic carbon, [b]STN statistics based on total carbon, [c]FB, [d]NMB, [e]FE, [f]NME, [*]Statistics based on median bias rather than mean bias, MB: Mean Bias, MAE: Mean Absolute Error, FB: Fractional Bias, FE: Fractional Error, NMB: Normalized Mean Bias, NME: Normalized Mean Error, R: Pearson's Correlation Coefficient, A12-Ahmadov et al. (2012), F10- Farina et al. (2010), G16-Glofelty et al. (2016a) and this work, J11- Jathar et al. (2011), J13- Jo et al. (2013), L08- Lane et al. (2008a), MP09- Murphy and Pandis (2009), S08- Shrivastava et al. (2008), S15- Shrivastava et al. (2015), W15-Wang et al. (2015)

Table 3.4. Comparison of Performance Statistics against European EMEP OC Observations.

Statistics	B12	F10	J13	G16
MB (μg m^{-3})	-1.88 to -1.39	1.6 to 1.9	N/A	-1.98 to -1.42
MAE (μg m^{-3})	1.99 to 2.21	6.2	N/A	2.03 to 1.61
FB[c]/NMB[d]	N/A	0.13 to 0.18[c]	-42.0 to -58.0[d]	-0.90 to -0.48[c] / -68.6 to -49.3[d]
FE[e]/NME[f]	N/A	0.73 to 0.74[e]	53.0 to 63.0[f]	0.63 to 0.97[e] / 55.8 to 71.0[f]
R	0.38 to 0.46	0.2	0.26 to 0.28	0.37 to 0.38

[c]FB, [d]NMB, [e]FE, [f]NME, MB: Mean Bias, MAE: Mean Absolute Error, FB: Fractional Bias, FE: Fractional Error, NMB: Normalized Mean Bias, NME: Normalized Mean Error, R: Pearson's Correlation Coefficient, B12- Bergstrom et al. (2012), F10- Farina et al. (2010), G16-Glofelty et al. (2016a) and this work, J11- Jathar et al. (2011)

Table 3.5. Comparison of Performance Statistics against Z07 & J09. Observations

OA Type	Statistic	J13	G16
HOA	RMSE (μg m^{-3})	3.11	2.54-2.60
	NMB	85.0	-59.2 to -62.1
	NME	107.0	66.0 to 67.2
	R	0.43	0.91
OOA	RMSE (μg m^{-3})	3.47 to 3.92	2.27 to 3.30
	NMB	-71.0 to -43.0	-52.0 to -27.3
	NME	61.0 to 76.0	33.6 to 53.2
	R	0.22 to 0.26	0.89 to 0.92
TOA	RMSE (μg m^{-3})	4.26 to 4.44	4.01-7.11
	NMB	-8.0 to -29.0	-61.9 to -45.5
	NME	58.0 to 62.0	50.8 to 62.5
	R	0.45 to 0.47	0.82 to 0.89

RMSE: Root Mean Square Error, NMB: Normalized Mean Bias, NME: Normalized Mean Error, R: Pearson's Correlation Coefficient, G16-Glofelty et al. (2016a) and this work, J13-Jo et al. (2013)

Table 3.6. The CESM-NCSU Model Configurations for SOA Modeling.

Attribute	Configuration
Approximate Time Periods	2001, 2006, and 2010
Horizontal Resolution	0.9° × 1.25°, 192 (latitudes) × 288 (longitudes)
Vertical Resolution	30 layers from ~1000.0 - ~3.0 mb
Atmospheric Process	**Parameterization**
Deep Convection	Zhang and MacFarlane (1995); Neale et al. (2008)
Shallow Convection	Park and Bretherton (2009)
Cloud Microphysics	Morrison and Gettelman (2008)
Cloud Macrophysics	Park et al. (2014)
Planetary Boundary Layer	Bretherton and Park (2009)
Radiation	RRTMG (Iacono et al., 2004, 2008)
Gas-phase Chemistry	CB05GE (Karamchandani et al., 2012)
Aqueous Chemistry	Barth et al. (2000)
Aerosol Mechanism	MAM7 (Liu et al., 2012)
Inorganic Aerosol Thermodynamics	ISORROPIA II (Fountoukis and Nenes, 2007)
Aerosol Activation	Fountoukis and Nenes (2005); Barahona et al. (2010); Kumar et al. (2009)

RRTMG-Rapid Radiative Transfer Model for General Circulation Models, CB05GE-Carbon Bond Mechanism 2005 with Global Extension, MAM7-Modal Aerosol Model with Seven modes.

Table 3.7. SOA Mass Yields for VOC Precursors (Murphy and Pandis, 2009; Ahmadov et al., 2012) used in this work.

	High NO_x Conditions				Low NO_x Conditions			
VOC	**1[a]**	**10[a]**	**100[a]**	**1000[a]**	**1[a]**	**10[a]**	**100[a]**	**1000[a]**
ALKH	0.0000	0.1500	0.0000	0.0000	0.0000	0.3000	0.0000	0.0000
PAH	0.0753	0.3349	0.0000	1.7693	0.6996	0.0000	0.0000	0.0000
OLE	0.0008	0.0450	0.0375	0.1500	0.0045	0.0090	0.0600	0.2250
IOLE	0.0030	0.0225	0.0825	0.2700	0.0225	0.0435	0.1290	0.3750
TOL	0.0030	0.1650	0.3000	0.4350	0.0750	0.2250	0.3750	0.5250
XYL, CRES	0.0015	0.1950	0.3000	0.4350	0.0750	0.0300	0.3750	0.5250
ISOP	0.0003	0.0225	0.0150	0.0000	0.0090	0.0300	0.0150	0.0000
HUM	0.0750	0.1500	0.7500	0.9000	0.0750	0.1500	0.7500	0.9000
APIN, BPIN, TER, OCI, LIM	0.0120	0.1215	0.2010	0.5070	0.1073	0.0918	0.3587	0.6075

[a]Effective saturation concentration (C^*) of each volatility bin in units of μg m^{-3}.

Table 3.8. VBS POA Emission Factors and Enthalpies used in the New_OA and Sensitivity Simulations

C*[a] at 298K (μg m^{-3})	EFA[b]	EFBB[c]	EFS08[d]	S08[e] ΔHvap (kJ mol^{-1})	E10[f] ΔHvap (kJ mol^{-1})
10_{-2}	0.14	0.20	0.03	112	153
10^{-1}	0.13	0.00	0.06	106	142
10^{0}	0.15	0.10	0.09	100	131
10^{1}	0.26	0.10	0.14	94	120
10^{2}	0.15	0.20	0.18	88	109
10^{3}	0.03	0.10	0.30	82	98
10^{4}	0.22	0.50	0.40	76	97
10^{5}	0.51	0.50	0.50	N/A	N/A
10^{6}	0.91	0.80	0.80	N/A	N/A

[a]Effective saturation concentration of each volatility bin; [b]EMA: Anthropogenic POA emission factors, [c]EMBB: Biomass Burning POA emission factors, [d]EMS08: POA emission factors from Shrivastava et al. (2008), [e]S08 ΔHvap: Enthalpy of vaporization from Shrivastava et al. (2008) used in the New_OA, New_OAC, and all sensitivity simulations except OA_HVAP and OA_Final_Mix, [f]E10 ΔHvap: Enthalpy of vaporization from Epstein et al. (2010) used in the OA_HVAP, OA_Final_Mix, and Final_OAC simulations.

Table 3.9. Sensitivity Simulation Design and Purpose

No.	Run I.D.	Process or parameter adjusted	Purpose
1	OA_HGLY	Simulation using artificially high glyoxal emissions. This includes the addition of biofuel emissions generated from the POET project (Granier et al., 2005), and CO emissions and the scaling factor used in Fu et al. (2008). The total biofuel + biomass burning emissions are then scaled up by a factor of 3, corresponding to the missing continental glyoxal source as discussed in Stavrakou et al. (2009).	Illustrates the uncertainty in simulating OA and glyoxal due to uncertain glyoxal sources
2	OA_POM_SH08	Simulation where the POM emissions are distributed based on the emissions spectrum of Shrivastava et al. (2008)	Illustrates the uncertainty in OA predictions due to uncertainty in the volatility of POM
3	OA_NO_FF_BIOAGE	Simulation without the functionalization and fragmentation treatments and biogenic aging. This follows the conservative assumptions of Farina et al. (2010) and Jathar et al. (2011)	Illustrates the differences between the traditional VBS aging approach and the functionalization and fragmentation approach on OA
4	OA_HI_Fragmentation	Simulation assuming that 75% of the organic vapors undergo fragmentation once they reach the 3rd generation of oxidation, 17.25% is functionalized to the lower volatility bin, and the remainder is lost to volatilities higher than the VBS structure. This is the high fragmentation case of Shrivastava et al. (2013)	Illustrates the uncertainty in OA formation based on assumptions about carbon bond fragmentation
5	OA_LOW_Fragmentation	Simulation assuming that 17.5% of the organic vapors undergo fragmentation once they reach the 3rd generation of oxidation, 90% is functionalized to the lower volatility bin, and the remainder is lost to volatilities higher than the VBS structure. This is the high fragmentation case of Shrivastava et al. (2013)	Illustrates the impact of the fragmentation treatment.
6	OA_NO_Fragmentation	Simulation without fragmentation of semi-volatile vapors	Illustrates the impact of the fragmentation treatment.
7	OA_HVAP	Simulation using the volatility bin dependent enthalpy of vaporizations from Epstein et al. (2010) for all OA species	Illustrates the uncertainty in OA predictions and temperature dependence due to uncertainty in the enthalpy of vaporization parameter
8	OA_NO_WDEP	Simulation with no wet deposition of the OA forming semi-volatile organic vapors	Provides some insights into the impact of organic vapor wet deposition on OA, especially in the tropics
9	OA_LOW_WDEP	Simulation with 25% of original wet deposition of the OA forming semi-volatile vapors	Provides some insights into the impact of organic vapor wet deposition on OA, especially in the tropics
10	OA_Final_Mix	Simulation combining the configurations of OA_HVAP_SOA, OA_LOW_Fragmentation, and OA_LOW_WDEP.	Provides best possible configuration to simulate OA.
11	OA_HI_κ	Simulates OA using a kappa value of 0.21 for BSOA and SVOA hygroscopicity based on (Liu and Wang, 2010)	Examines the sensitivity of simulated aerosol activation of OA to OA hygroscopicity by using the upper limit of OA hygroscopicity
12	OA_LOW_κ	Simulates OA with kappa values of 0.06 for BSOA, ASOA, and SVOA hygroscopicity and 0.0 for POA hygroscopicity (Liu and Wang, 2010)	Examines sensitivity of simulated aerosol activation of OA to OA hygroscopicity by using the lower limit of OA hygroscopicity
13	OA_NO_CONUC	Simulation without the conucleation treatment	Illustrates the impact of the conucleation treatment on particle number concentrations and CCN
14	OA_SOA_CONUC	Simulation where only semi-volatile vapors from the oxidation of AVOCs and BVOCs participate in conucleation	Illustrates the impact of the conucleation treatment in a manner that is more comparable to is the method of implementation in Fan et al. (2006), which does not include SVOC from oxidized POA.

Table 3.10. List of Datasets for OA, PM, Radiation, and Cloud Evaluation

Variable	Short Name	Dataset	Temporal Coverage	Spatial Coverage
Organic Carbon	OC	EMEP, IMPROVE	Europe, CONUS	2001-2010 (IMPROVE) Assumed Climatology (EMEP)
Total Carbon	TC	IMPROVE, STN	CONUS	2001-2010
Oxygenated Organic Aerosol	OOA	Zhang, Q. et al. (2007) and	Northern Hemisphere	Assumed Climatology
Hydrocarbon-like Organic Aerosol	HOA	Jimenez et al. (2009)		
Total Organic Matter	TOM			
Secondary Organic Aerosol	SOA	Lewondowski et al. (2013)	CONUS	Assumed Climatology
Particulate Matter with diameter less than 2.5 μm	$PM_{2.5}$	Airbase, BDQA, EMEP, IMPROVE, STN	Europe, CONUS	2001-2010
Particulate matter with diameter less than 10 μm	PM_{10}	MEPC, NIESJ, TAQMN, KMOE, Airbase, BDQA, EMEP, AQS	East Asia, Europe, CONUS	2001-2010 2006-2010 (KMOE)
Isoprene	ISOP	EMEP,PAMS	Europe, CONUS	2001-2010 (PAMS)
Toluene	TOL			Assumed Climatology (EMEP)
Xylene	XYL	PAMS	CONUS	2001-2010
Aerosol Optical Depth	AOD	Level 3 Moderate Resolution Imaging	Global (1°×1°)	2001-2010
Cloud Optical Thickness	COT	Spectroradiometer (MODIS)	Oceans (CCN5)	
Column CCN (ocean) at S = 0.5% (cm^{-2})	CCN5			
Cloud Droplet Number Concentration from Warm Clouds (cm^{-3})	CDNC	Bennartz (2007)	Global (1°×1°)	2001-2010
Liquid Water Path (g m^{-2})	LWP	O'dell et al. (2008)	Oceans (1°×1°)	2001-2008
Shortwave Cloud Forcing (W m^{-2})	SWCF	Clouds and Earth's Radiant Energy	Global (1°×1°)	2001-2010
Downwelling Shortwave Radiation at the Earth's Surface (W m^{-2})	FSDS	Systems (CERES)/ Energy Balanced and Filled (EBAF)		

Table 3.11. Normalized Mean Bias for OA Sensitivity Simulations

Variables	Coverage	0	1	2	3	4	5	6	7	8	9	10	11	12	13	14
OC (μg m^{-3})	CONUS[2]	-0.3	5.1	-11.8	-18.6	-3.1	7.8	9.0	30.4	35.8	17.6	45.7	4.8	5.3	-0.3	-1.2
	Europe[1]	-52.4	-52.1	-64.2	-56.6	-51.8	-51.5	-46.6	-40.4	-38.7	-51.1	-29.2	-52.0	-48.7	-51.8	-50.5
TC (μg m^{-3})	CONUS[1]	-37.4	-34.1	-42.7	-46.7	-38.7	-34.3	-33.8	-21.2	-17.8	-26.6	-12.3	-33.9	-33.9	-34.0	-38.4
HOA (μg m^{-3})	NH	-36.4	-35.9	-70.8	-35.6	-34.0	-32.9	-32.6	-30.4	-37.0	-34.6	-31.5	-35.8	-38.8	-36.7	-37.3
OOA (μg m^{-3})	NH	-45.9	-41.0	-45.4	-61.8	-48.8	-37.8	-38.2	-40.2	-22.0	-42.8	-27.0	-48.6	-50.1	-50.4	-49.3
TOM (μg m^{-3})	NH	-51.5	-48.4	-59.5	-61.5	-53.2	-45.9	-45.9	-47.1	-35.4	-49.7	-38.6	-53.0	-54.6	-54.2	-53.8
SOA (μg m^{-3})	CONUS	-0.5	10.2	-3.5	-31.1	-1.4	8.0	12.1	23.2	83.7	44.5	46.8	10.5	14.4	2.6	-1.6
AOD	Global	-24.7	-24.6	-23.0	-25.4	-26.1	-22.7	-22.8	-21.8	-18.0	-22.9	-18.9	-23.3	-25.1	-26.6	-24.2
COT	Global	-40.3	-41.1	-40.4	-41.2	-40.2	-40.3	-41.1	-40.9	-38.5	-39.6	-39.7	-41.5	-41.1	-43.0	-41.5
CCN (cm^{-2})	Ocean	-75.9	-75.5	-75.4	-76.0	-76.0	-75.1	-74.7	-73.8	-69.9	-74.5	-72.3	-74.8	-76.9	-76.3	-75.8
CDNC (cm^{-3})	Global	80.2	78.8	82.5	80.7	80.6	80.5	80.7	78.6	87.8	83.1	80.5	79.5	77.3	68.9	79.0
LWP (g m^{-2})	Ocean	-34.1	-34.3	-34.5	-34.5	-34.6	-34.2	-35.0	-33.9	-29.9	-33.2	-33.4	-33.6	-33.5	-36.4	-34.9
SWCF (W m^{-2})	Global	1.6	2.0	2.5	2.3	2.3	2.3	2.5	3.1	5.0	3.2	3.3	1.7	1.8	1.3	1.6
FSDS (W m^{-2})	Global	0.5	0.5	0.3	0.4	0.6	0.3	0.2	0.1	-0.7	-0.3	-0.1	0.6	0.6	0.7	0.0.6

[1]Assumes an OM:OC ratio of 1.4; [2]Assumes an OM:OC ratio of 1.8

Table 3.12. Probability of Difference in Simulated Fields from Sensitivity Experiments

Variables	1[a]	2[a]	3[a]	4[a]	5[a]	6[a]	7[a]	8[a]	9[a]	10[a]	11[a]	12[a]	13[a]	14[a]
POM	0.56	3.6×10^{-11}	0.85	0.88	0.63	0.55	0.17	0.17	0.53	0.02	0.84	0.77	0.83	0.62
OOA	0	0	0	0	5.0×10^{-11}	0	0	2.4×10^{-12}	2.3×10^{-11}	1.1×10^{-11}	0.06	8.0×10^{-4}	0.64	8.0×10^{-4}
AOD	0.95	5.8×10^{-11}	1.0×10^{-5}	5.2×10^{-11}	1.5×10^{-11}	4.1×10^{-11}	6.7×10^{-11}	7.1×10^{-11}	0	1.3×10^{-11}	1.6×10^{-11}	6.5×10^{-3}	6.1×10^{-11}	0.04
COT	0	0.31	0	1.0	0.55	0	1.0×10^{-3}	1.5×10^{-12}	0	6.0×10^{-11}	2.1×10^{-11}	0	5.3×10^{-11}	0
CCN	3.2×10^{-5}	7.9×10^{-3}	1.2×10^{-7}	0	0	5.7×10^{-11}	0	0	0	6.3×10^{-12}	8.2×10^{-12}	0	1.8×10^{-9}	0.81
CDNC	2.9×10^{-11}	2.7×10^{-4}	5.8×10^{-11}	0	1.1×10^{-3}	1.4×10^{-11}	0	3.1×10^{-11}	0.06	2.6×10^{-9}	9.6×10^{-11}	0	4.5×10^{-11}	0
LWP	5.6×10^{-4}	0.05	3.8×10^{-8}	0.5	0.08	4.1×10^{-11}	0.01	1.1×10^{-11}	0	2.5×10^{-10}	7.2×10^{-11}	6.4×10^{7}	0	1.8×10^{-11}
SWCF	0.02	9.3×10^{-7}	9.0×10^{-5}	2.8×10^{-3}	3.4×10^{-4}	2.5×10^{-7}	0	0	3.0×10^{-11}	1.3×10^{-11}	0.77	0.33	0.16	0.95
FSDS	0.78	0.06	0.38	0.35	0.09	0.01	3.3×10^{-3}	0	1.0×10^{-8}	6.4×10^{-7}	0.17	0.15	0.02	0.12

[a]: Sensitivity simulation number from Table 3 in main text; Probability values less than 0.05 indicate that the difference between the variables in the New_OA simulation and the sensitivity simulation are statistically significant.

Table 3.13. Probability of Difference in Simulated Fields between the Baseline and New OA Treatments

Variables	New_OAC	Final_OAC
POM	0	0
OOA	4.5×10^{-11}	4.2×10^{-11}
AOD	7.7×10^{-11}	0
COT	1.6×10^{-10}	7.7×10^{-11}
CCN	1.9×10^{-10}	0
NUM	0	0
CDNC	4.2×10^{-11}	2.0×10^{-10}
LWP	0	7.8×10^{-11}
SWCF	0	1.6×10^{-10}
FSDS	1.3×10^{-11}	3.0×10^{-8}

Probability values less than 0.05 indicate that the difference between the variables in the New_OA simulation and the sensitivity simulation are statistically significant.

Table 3.14. Statistical Performance Comparison of Base_OAC (Base), New OAC (New), and Final_OAC (Final) Simulations.

Variables	Region	Obs	Sim			MB[a]			NMB[b]			NME[c]			R[d]		
			Base	New	Final	Base	New	Final	Base	New	Final	Base	New	Final	Base	New	Final
OC (μg m^{-3})	CONUS[2]	1.0	0.6	0.8	1.3	-0.4	-0.3	0.3	-37.9	-25.3	31.4	49.6	41.6	44.1	0.55	0.56	0.66
	Europe[1]	2.9	1.1	0.9	1.5	-1.7	-2.0	-1.4	-60.5	-68.6	-49.3	64.8	70.9	55.8	0.17	0.37	0.38
TC (μg m^{-3})	CONUS[1]	2.5	1.3	1.5	2.5	-1.1	-1.0	0	-46.0	-38.7	-0.7	51.1	46.7	37.5	0.53	0.57	0.59
HOA (μg m^{-3})	NH	2.1	2.2	0.8	0.8	0.1	-1.3	--1.2	5.7	-62.1	-59.2	41.8	67.2	66.0	0.94	0.78	0.91
OOA (μg m^{-3})	NH	4.8	0.5	2.3	3.5	-4.4	-2.6	-1.3	-90.0	-52.8	-27.3	90.0	53.2	33.6	0.48	0.92	0.89
TOM (μg m^{-3})	NH	7.9	2.5	3.0	4.3	-5.4	-4.9	-3.6	-68.3	-61.9	-45.5	69.2	62.5	50.8	0.87	0.89	0.82
SOA (μg m^{-3})	CONUS	2.9	1.0	2.1	4.5	-1.9	-0.8	1.6	-66.0	-26.3	53.2	66.0	46.3	53.2	0.72	0.12	0.72
$PM_{2.5}$ (μg m^{-3})	CONUS	8.3	10.2	9.4	11.4	1.8	1.1	3.1	22.2	13.3	37.4	40.6	33.8	48.7	0.78	0.73	0.77
	Europe	14.1	11.1	9.9	10.5	-3.0	-4.2	-3.6	-21.4	-30.0	-25.6	35.5	37.2	38.9	0.20	0.28	0.13
PM_{10} (μg m^{-3})	CONUS	22.2	20.7	17.9	20.6	-1.6	-4.3	-1.6	-7.0	-19,3	-7.3	49.7	44.0	43.5	0.19	0.27	0.26
	Europe	24.4	23.0	21.6	23.6	-1.4	-2.8	-0.8	-5.6	-11.6	-3.3	34.7	36.0	36.6	0.22	0.17	0.21
	East Asia	94.6	58.0	69.8	69.5	-36.6	-24.7	-25.0	-38.6	-26.2	-26.5	40.6	34.6	33.4	0.65	0.62	0.63
ISOP (ppt)	CONUS	322.6	198.2	212.6	197.8	-124.4	-110.0	-124.8	-38.6	-34.1	-38.7	66.2	67.0	64.8	0.69	0.67	0.70
	Europe	162.1	109.4	98.2	97.8	-52.8	-64.0	-64.5	-32.6	-39.4	-39.8	78.8	73.6	76.1	-0.03	0.0	-0.06
TOL (ppt)	CONUS	734.2	355.1	342.2	349.3	-379.0	-392.0	-384.9	-51.6	-53.4	-52.4	69.2	69.7	69.3	-0.16	-0.15	-0.15
	Europe	250.5	265.2	252.0	259.8	14.7	1.5	9.2	5.8	0.6	3.7	63.4	59.3	62.1	-0.08	-0.06	-0.10
XYL (ppt)	CONUS	419.9	202.7	208.2	212.5	-217.2	-211.7	-207.4	-51.7	-50.4	-49.4	89.2	89.5	89.2	-0.13	-0.14	-0.13
AOD	Global	0.16	0.18	0.11	0.12	0.02	-0.05	-0.03	15.8	-31.7	-19.9	35.4	46.0	41.4	0.60	0.58	0.62
COT	Global	17.0	9.6	9.9	10.3	-7.4	-7.1	-6.7	-43.4	-41.5	-39.2	57.9	57.0	56.2	-0.11	-0.09	-0.10
CCN (cm^{-2})	Ocean	6.4×10^{8}	5.8×10^{7}	5.4×10^{7}	7.2×10^{7}	-1.8×10^{8}	-1.9×10^{8}	-1.7×10^{8}	-73.6	-77.6	-70.4	73.6	77.6	70.4	0.15	0.15	0.14
CDNC (cm^{-3})	Global	108.5	166.0	177.4	180.4	57.4	68.8	71.9	52.9	63.4	66.2	70.3	79.2	81.4	0.56	0.55	0.53
LWP (g m^{-2})	Ocean	85.7	53.5	54.4	56.9	-32.2	-31.3	-28.8	-37.5	-36.5	-33.6	40.6	40.3	39.0	0.45	0.44	0.46
SWCF (W m^{-2})	Global	-40.7	-39.4	--40.9	-42.4	-1.3	0.2	1.6	-3.3	0.4	4.0	21.4	21.0	22.2	0.90	0.91	0.91
FSDS (W m^{-2})	Global	163.5	162.3	165.5	162.9	-1.1	2.0	-0.6	-0.7	1.2	-0.3	5.2	5.5	5.6	0.98	0.98	0.97

[1]Assumes an OM:OC ratio of 1.4; [2]Assumes an OM:OC ratio of 1.8; [a]Mean Bias (MB); [b]Normalized Mean Bias (NMB); [c]Normalized Mean Error (NME); [d]Correlation Coefficient (R)

Table 3.15. Regional Maximum and Spatial Mean OA levels.

	POM		GLSOA		ASOA		BSOA		SVOA	
Region	Max.[1]	Mean[1]	Max[1]	Mean[1]	Max[1]	Mean[1]	Max[1]	Mean[1]	Max[1]	Mean[1]
North America	2.2/57.3	0.1/9.6	0.1/10.5	0.01/2.1	2.3/65.2	0.2/31.8	3.5/81.1	0.3/40.2	0.7/47.9	0.1/16.2
South America	6.5/62.9	0.1/12.4	0.7/11.7	0.03/3.9	1.4/57.4	0.1/24.3	1.3/74.5	0.2/35.1	3.9/50.7	0.2/24.3
Europe	4.4/67.4	0.4/18.9	0.1/5.2	0.03/1.8	1.2/53.8	0.4/33.7	1.0/60.1	0.4/33.1	0.6/27.1	0.2/12.4
Africa	4.6/55.5	0.3/13.9	0.7/9.1	0.04/3.2	4.4/88.0	0.4/29.5	2.8/41.8	0.2/18.8	3.5/56.3	0.5/34.5
South Asia	11.8/63.4	1.3/23.5	0.3/5.1	0.08/2.2	3.8/53.8	1.0/29.5	1.7/46.4	0.5/16.0	5.4/39.1	1.2/28.2
East Asia	14.2/64.2	1.1/19.2	0.3/4.6	0.06/1.6	5.3/58.9	0.9/30.8	4.5/76.4	0.8/34.7	5.4/37.4	0.5/13.6
Southeast Asia	175.4/82.0	0.6/14.8	9.7/12.2	0.07/4.2	4.0/46.2	0.3/24.9	3.3/71.8	0.4/34.1	21.5/39.2	0.4/21.9
Australia	0.3/42.5	0.01/7.7	0.06/21.8	0.01/7.0	0.1/34.8	0.02/21.7	0.3/77.4	0.05/47.0	0.2/44.7	0.02/16.6

[1]units of $\mu g\ m^{-3}$/ %

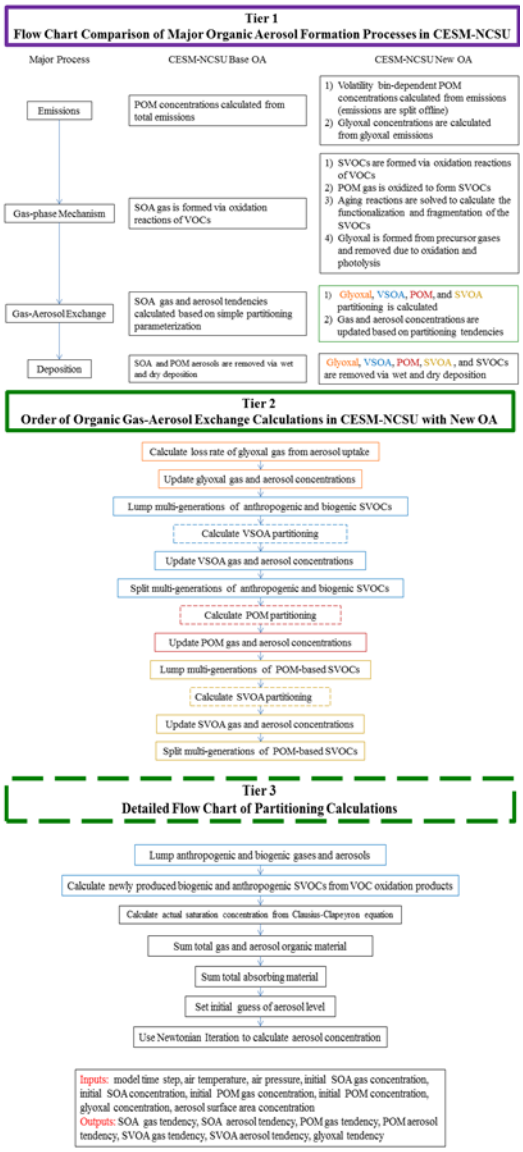

Figure 3.1. Flow chart that summarizes the differences between the CESM-NCSU Base organic aerosol treatment and the CESM-NCSU new organic aerosol treatments. Tier 1 illustrates the differences between the Base OA treatments and the New OA treatments, Tier 2 (Green Box) provides greater details on how the gas-aerosol partitioning is handles in the new OA treatments, and Tier 3 (Dashed Boxes) provides greater details on the partitioning calculations. Light blue boxes indicate VSOA specific calculations, red boxes indicate POM specific calculations, orange boxes indicate glyoxal specific calculations, and brown boxes indicate SVOA specific calculations.

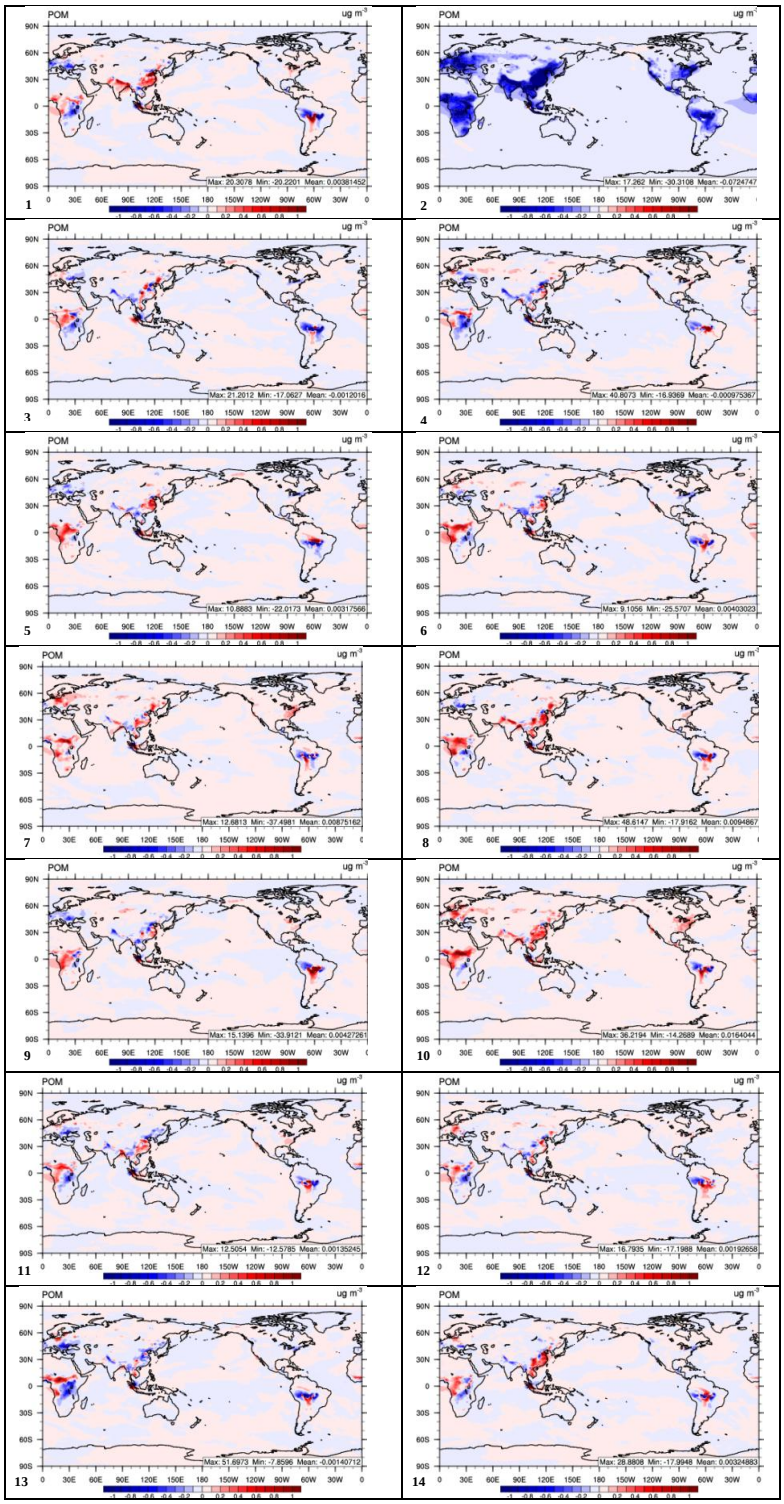

Figure 3.2. The absolute difference in the concentration of POM between the New OA simulation and sensitivity simulations 1-14 from Table 4.3.

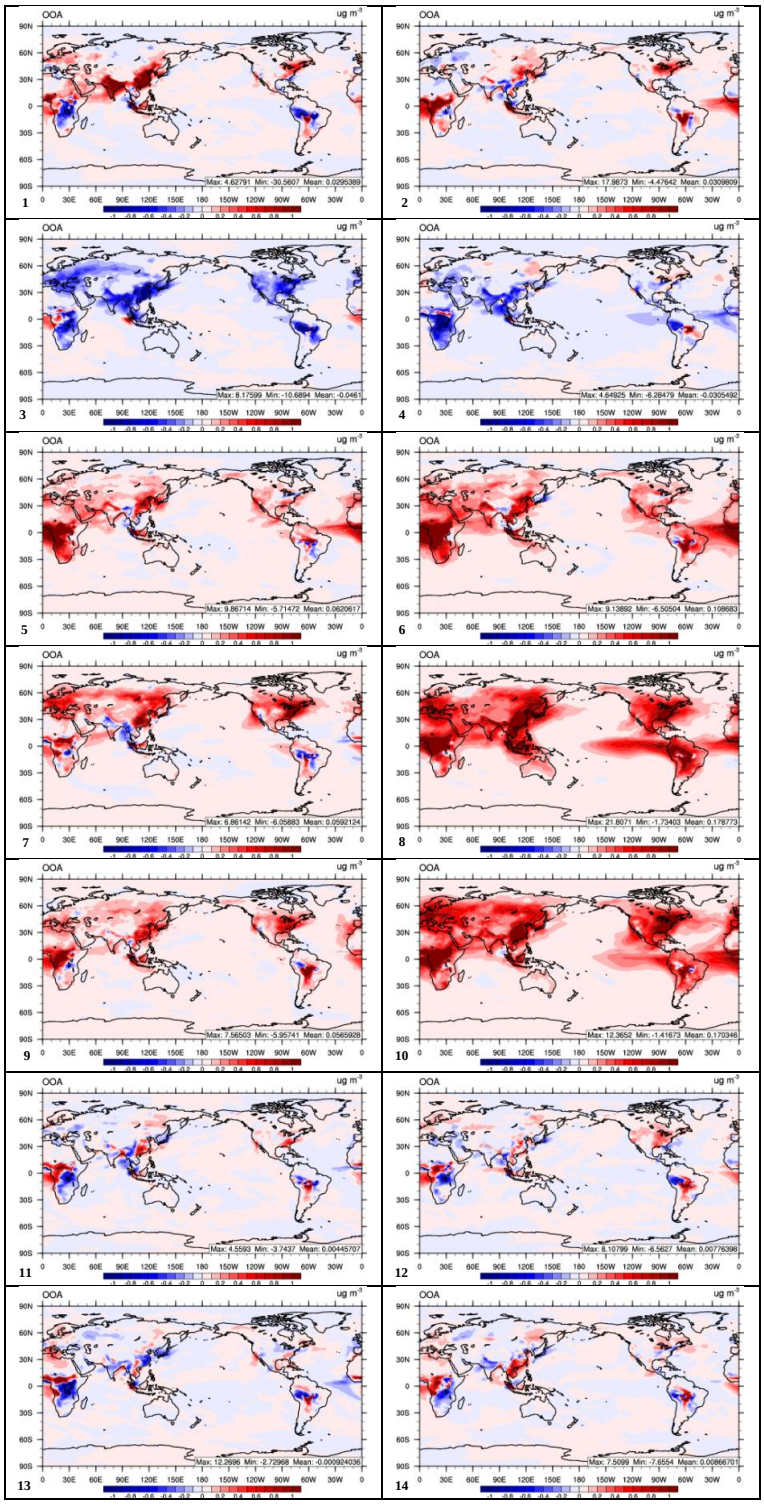

Figure 3.3. The absolute difference in the concentration of OOA between the New OA simulation and sensitivity simulations 1-14 from Table 4.3.

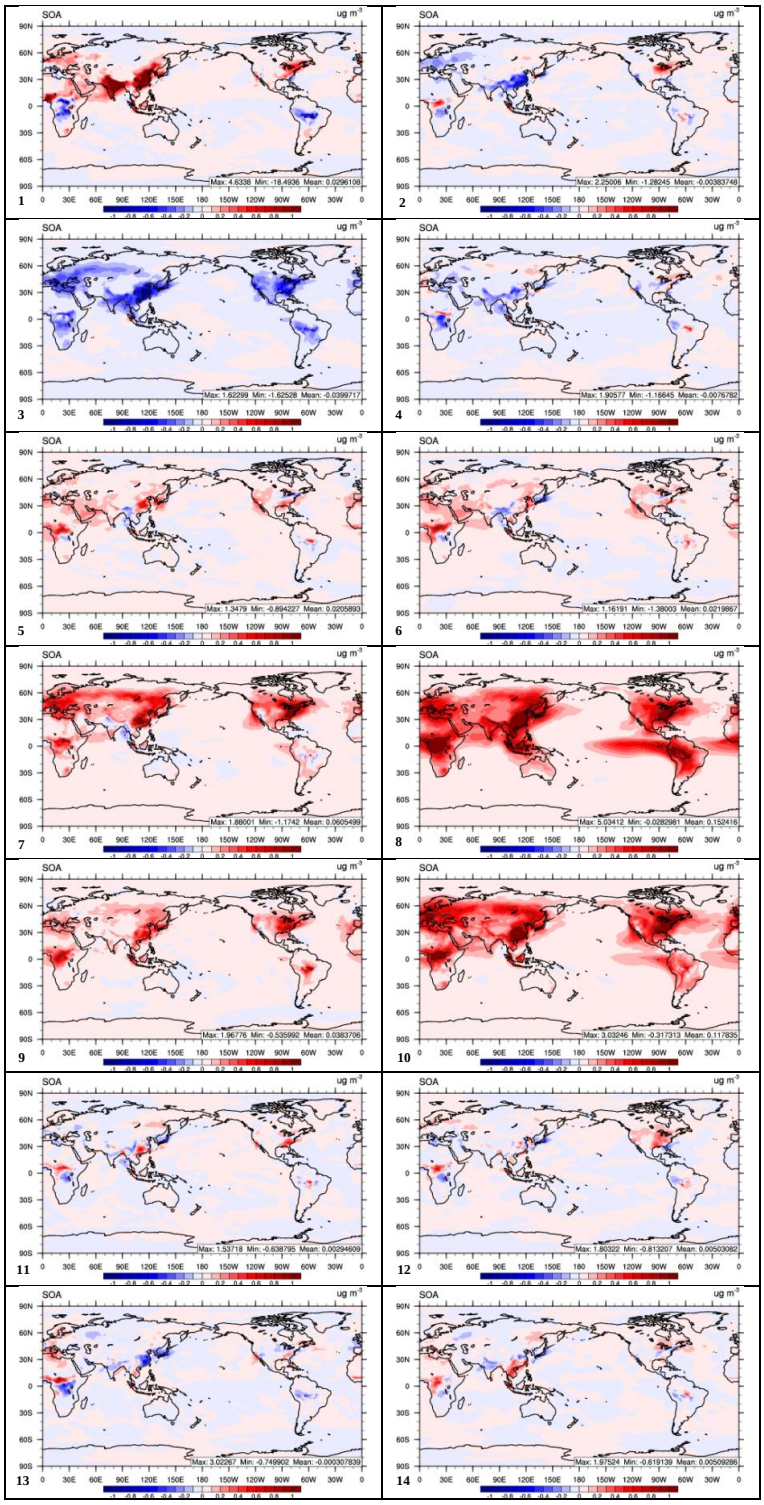

Figure 3.4. The absolute difference in the concentration of SOA between the New OA simulation and sensitivity simulations 1-14 from Table 4.3.

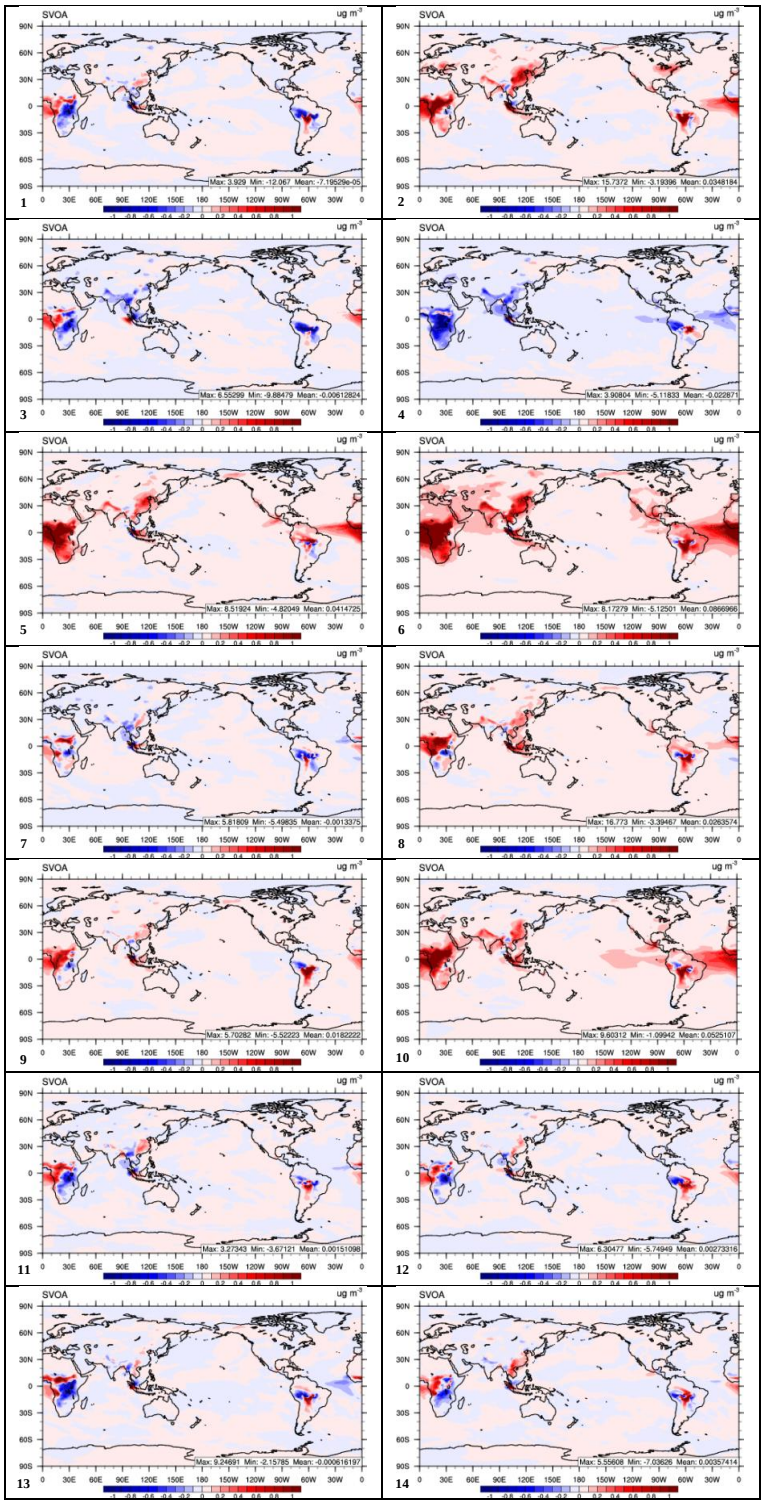

Figure 3.5. The absolute difference in the concentration of SVOA between the New OA simulation and sensitivity simulations 1-14 from Table 4.3.

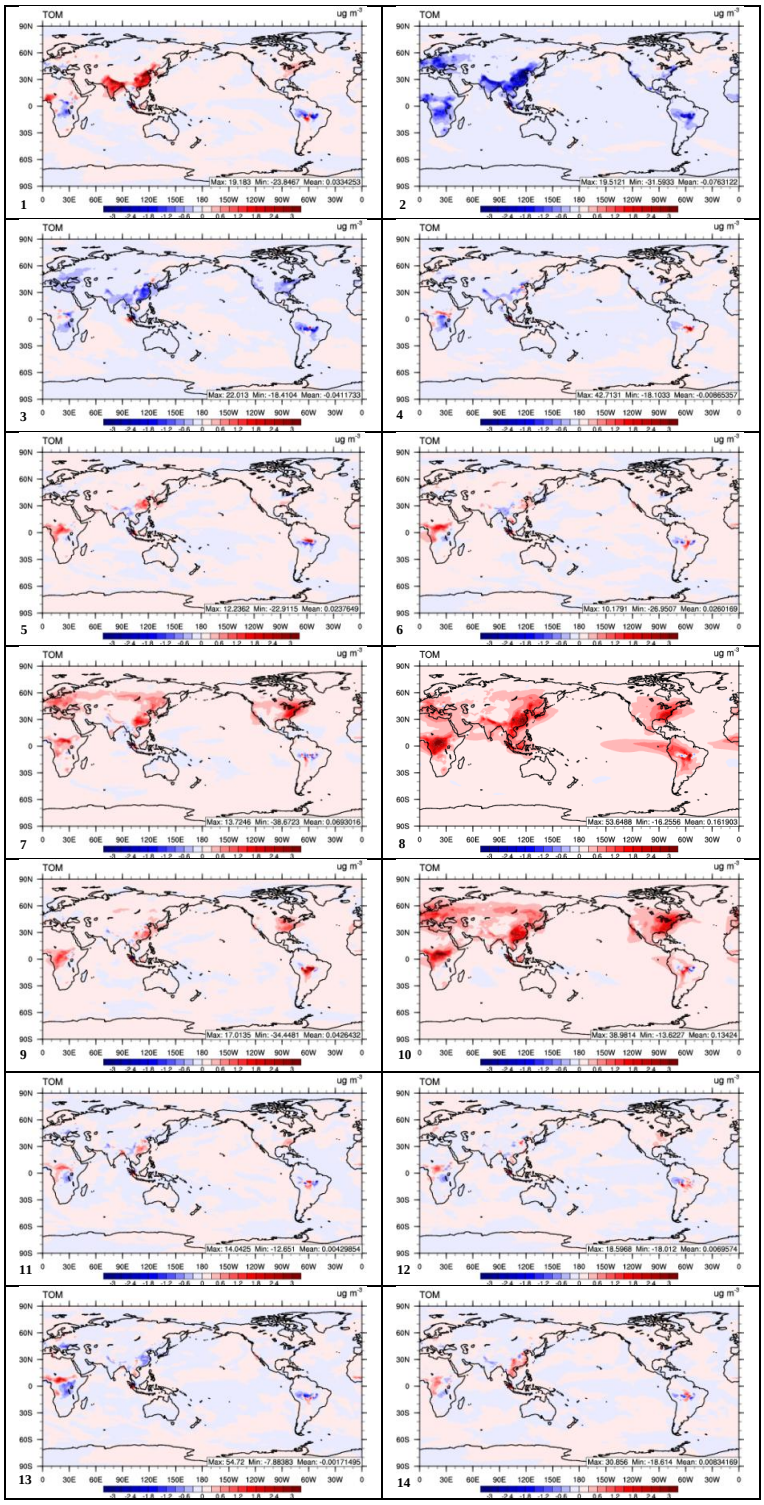

Figure 3.6**.** The absolute difference in the concentration of TOM between the New OA simulation and sensitivity simulations 1-14 from Table 4.3.

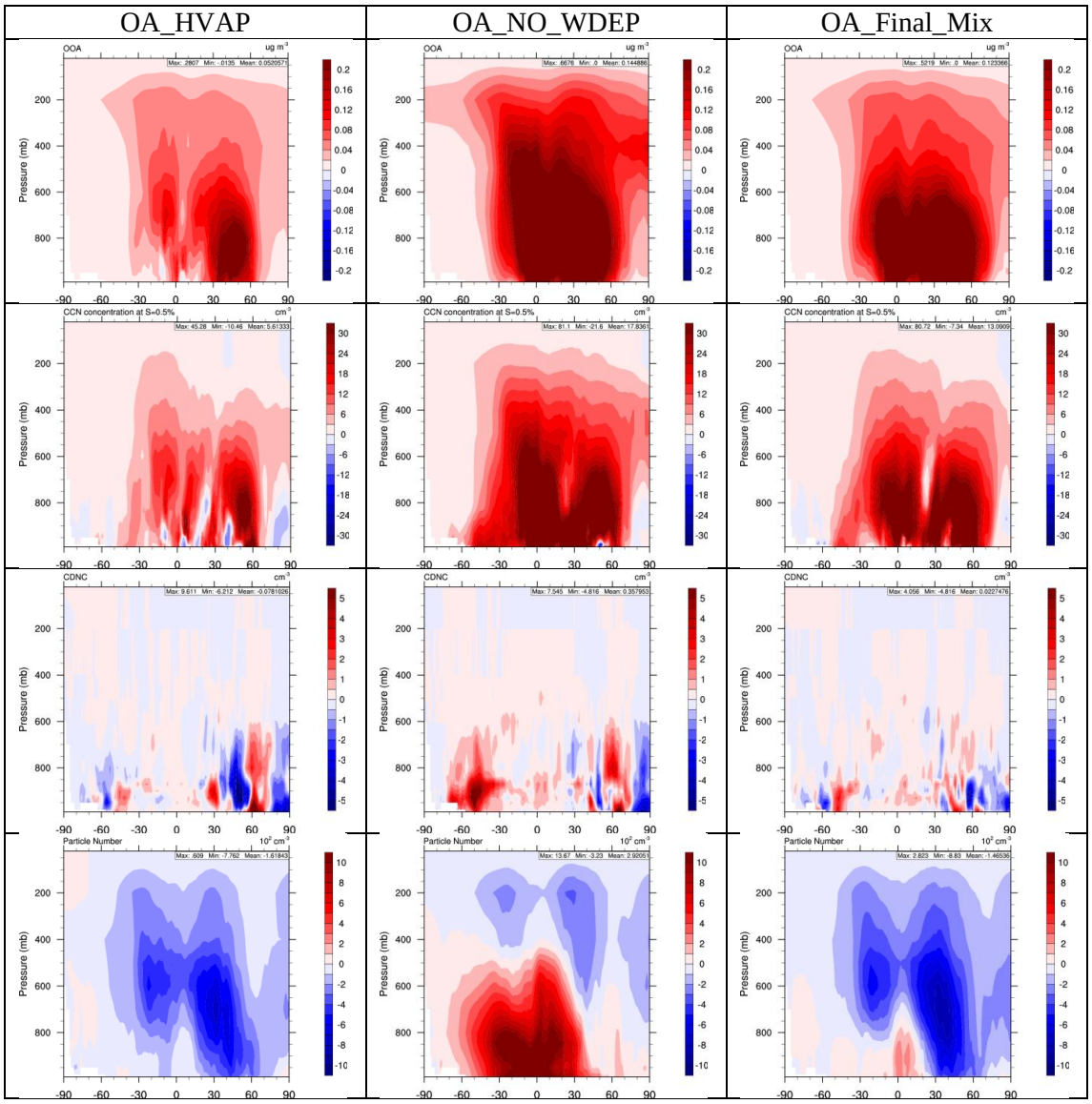

Figure 3.7. The zonally-averaged cross sectional absolute differences in the concentration of OOA, CCN at a supersaturation of 0.5%, cloud droplet number, and particle number between the OA_HVAP_SOA (left), OA_NO_WDEP (center), and OA_Final_Mix (right) simulations and the New OA simulation.

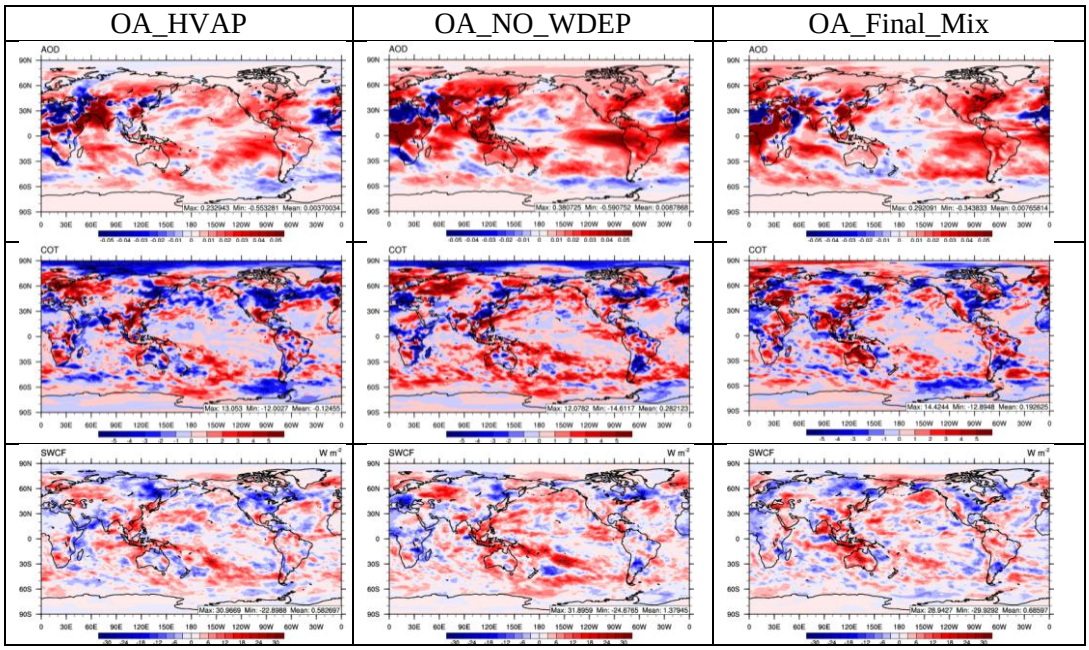

Figure 3.8. The absolute differences in AOD, COT, and SWCF between the OA_HVAP (left), OA_NO_WDEP (center), and OA_Final_Mix (right) simulations and the New_OA simulations.

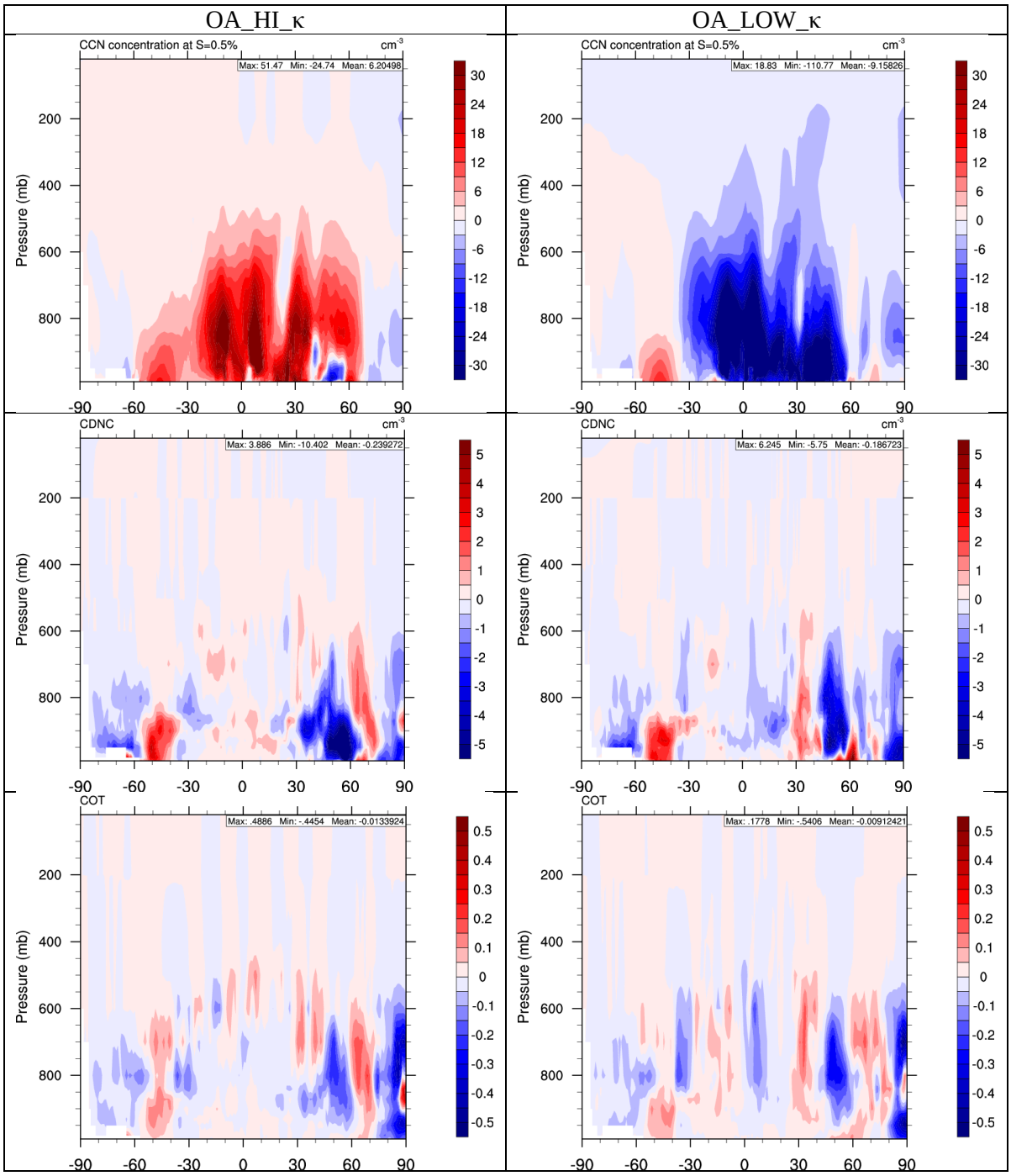

Figure 3.9. The zonally-averaged cross sectional absolute differences in CCN at a supersaturation of 0.5%, cloud droplet number concentration, and COT between the OA_HI_κ (left) and OA_LOW_κ (right) simulations and the New OA simulation.

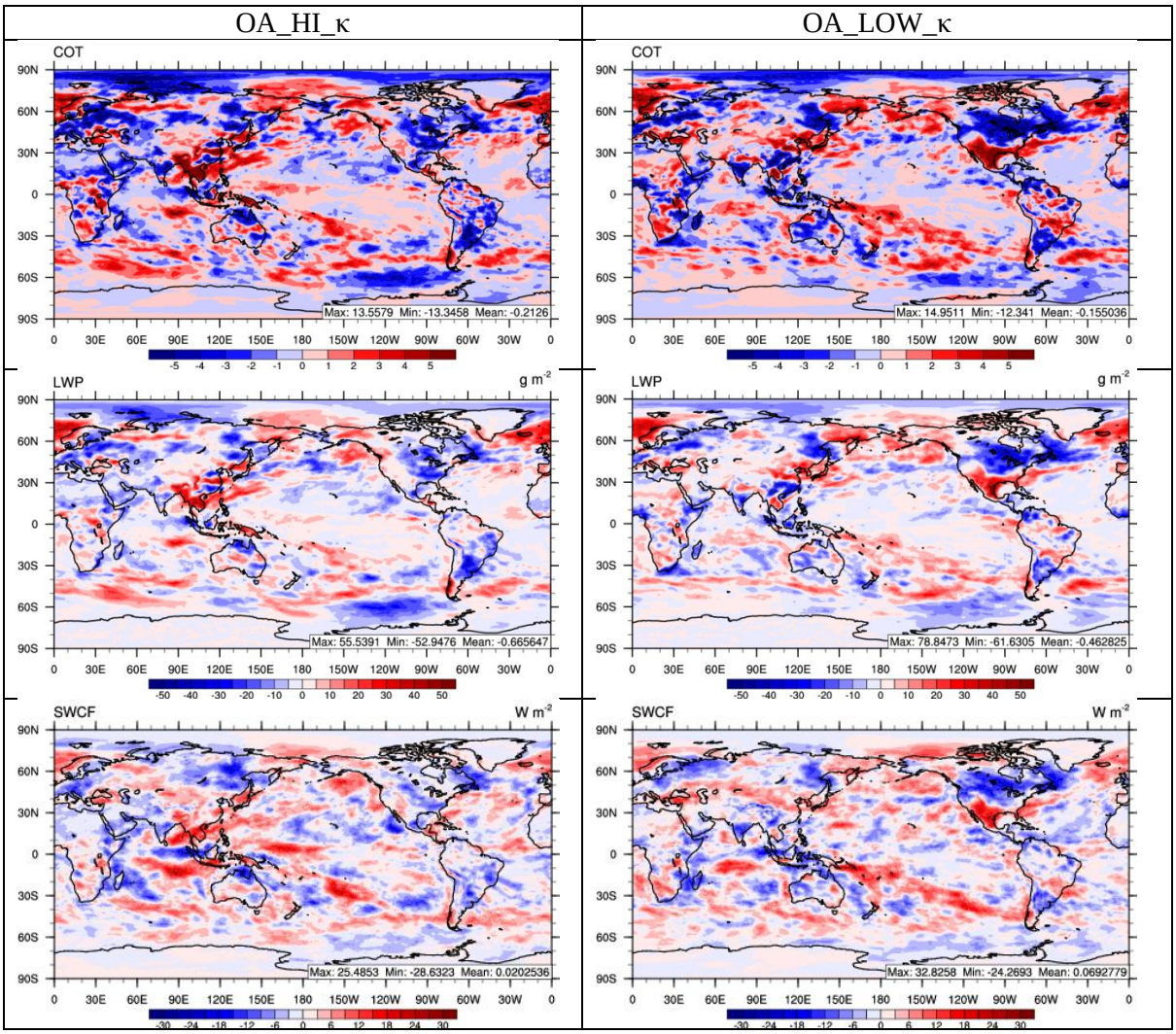

Figure 3.10**.** The absolute differences in COT, LWP, and SWCF between the OA_HI_κ (left) and OA_LOW_κ (right) simulations and the New_OA simulation.

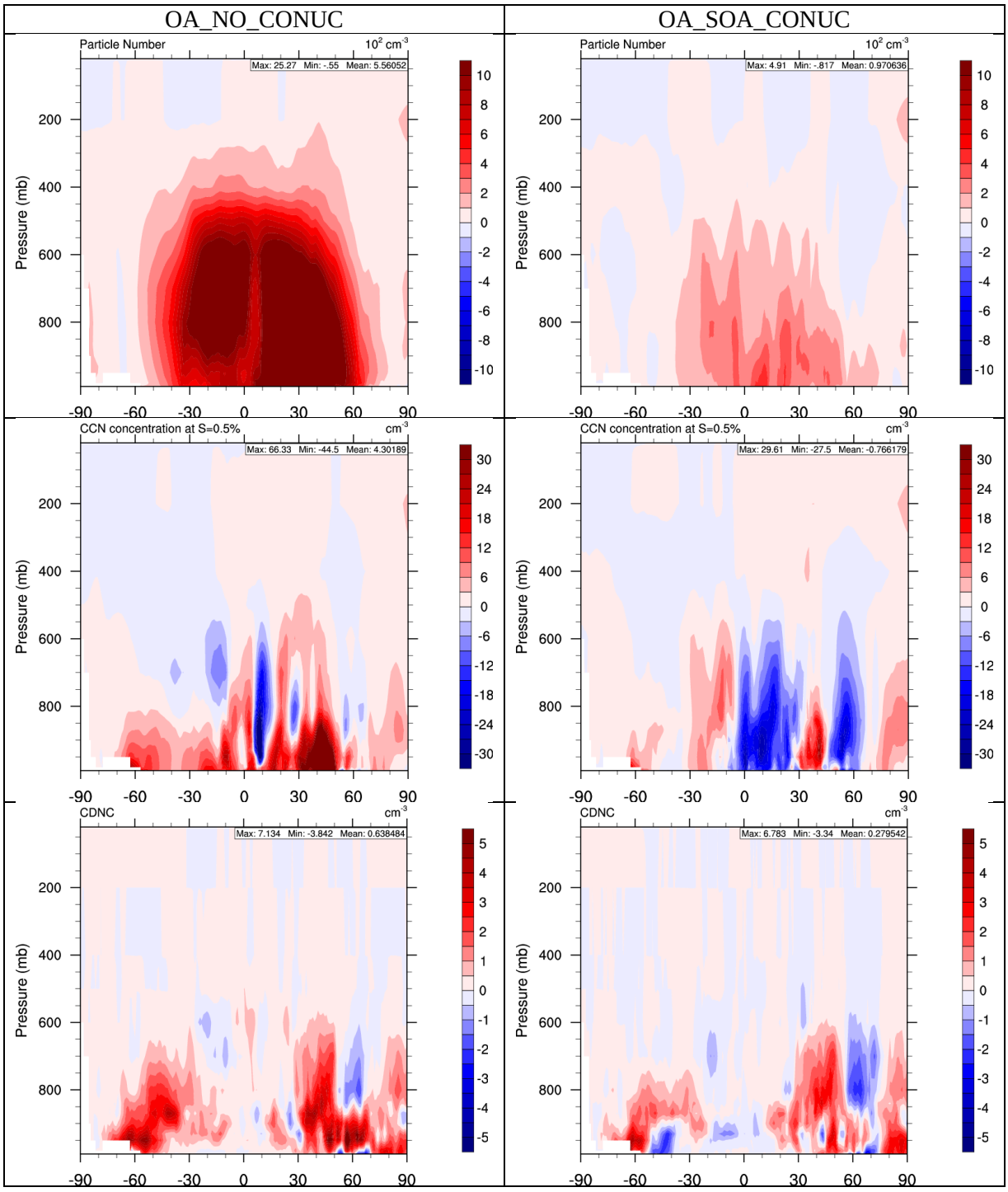

Figure 3.11. The zonally-averaged cross sectional differences in particle number concentrations, CCN at a supersaturation of 0.5%, and cloud droplet number concentrations between New OA simulation and the OA_NO_CONUC simulation (left) and the OA_SOA_CONUC simulation (right).

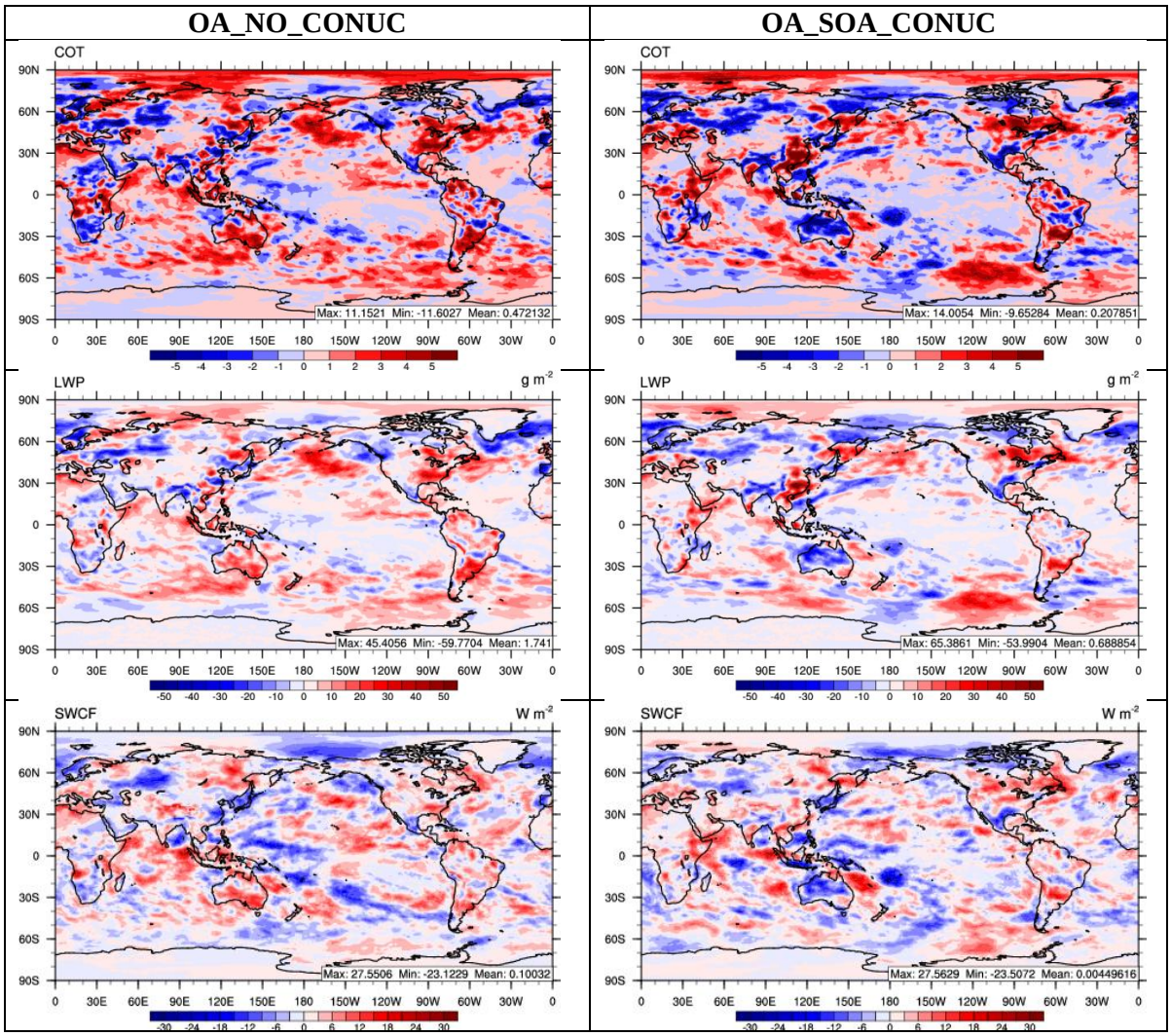

Figure 3.12**.** The absolute differences in COT, LWP, and SWCF between the New_OA simulation and the OA_NO_CONUC (left) and the OA_SOA_CONUC (right) simulations.

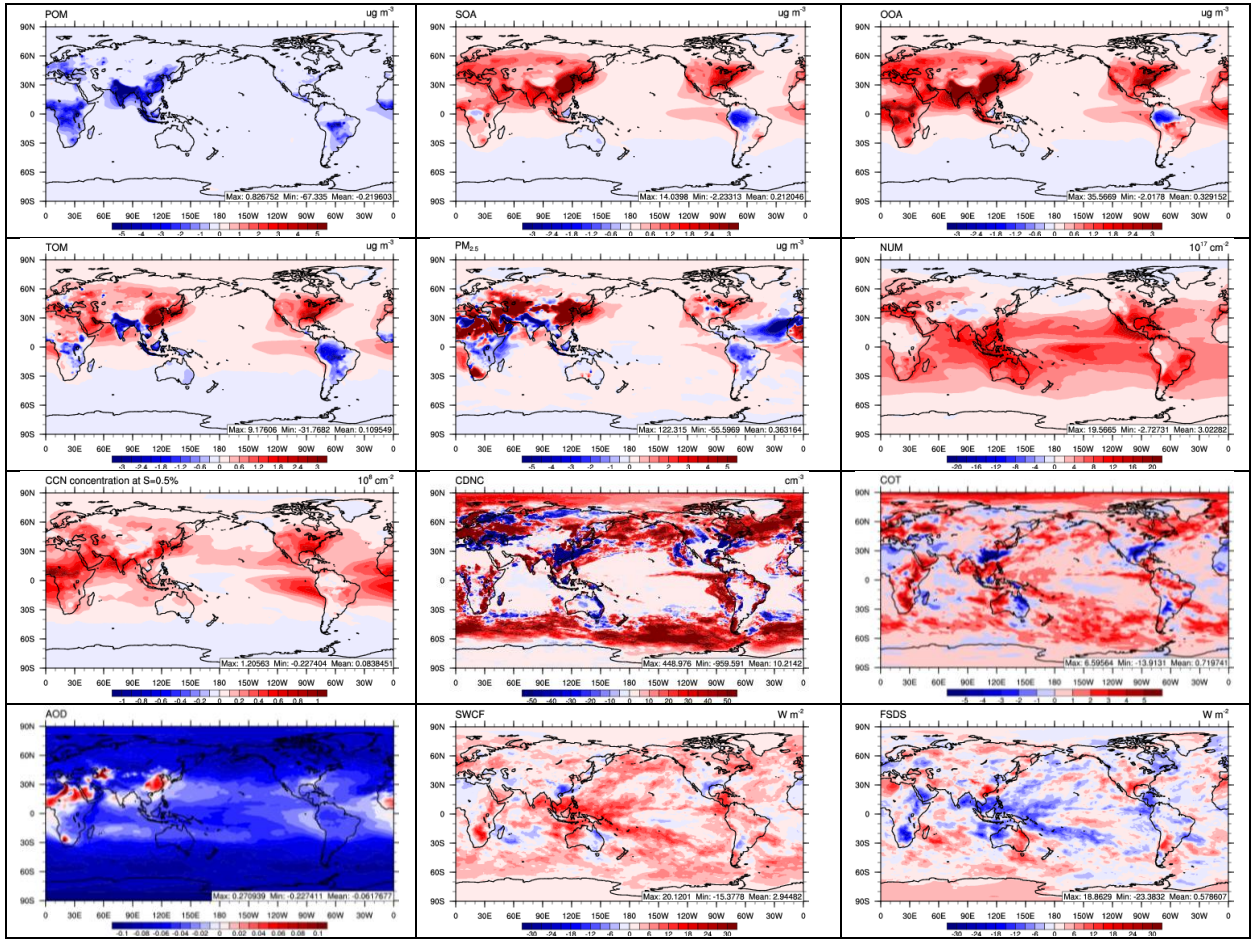

Figure 3.13. The absolute difference in the concentrations of POM, SOA, OOA, TOM, $PM_{2.5}$, AOD, NUM, CCN, CDNC, COT, SWCF, and FSDS between the Base_OAC and Final_OAC simulations for the average current time period.

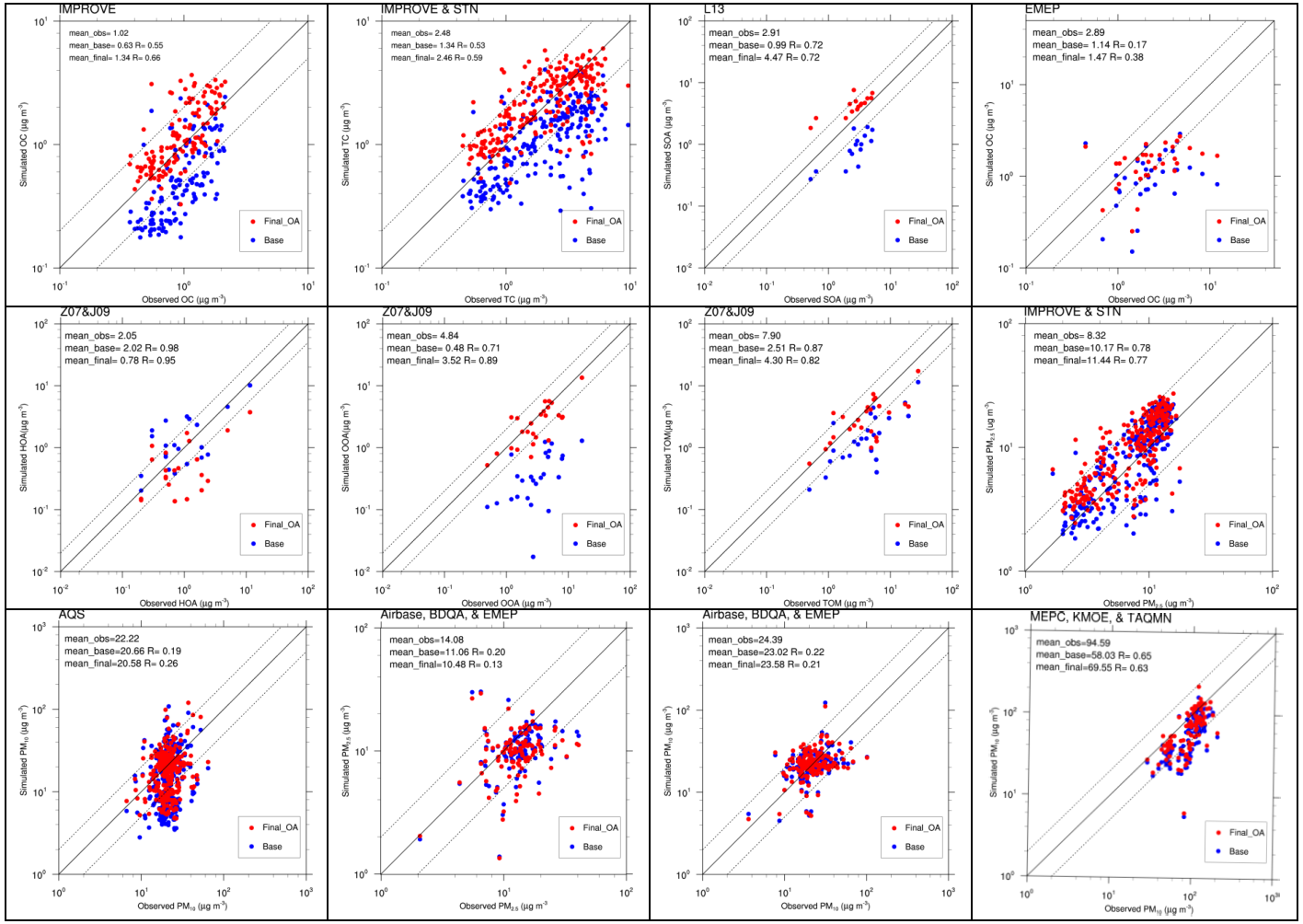

Figure 3.14. Scatter plots of observations versus simulation results from the averaged current time period Base_OAC and Final_OAC simulations for OC, TC, SOA, HOA, OOA, TOA, $PM_{2.5}$, and PM_{10}.

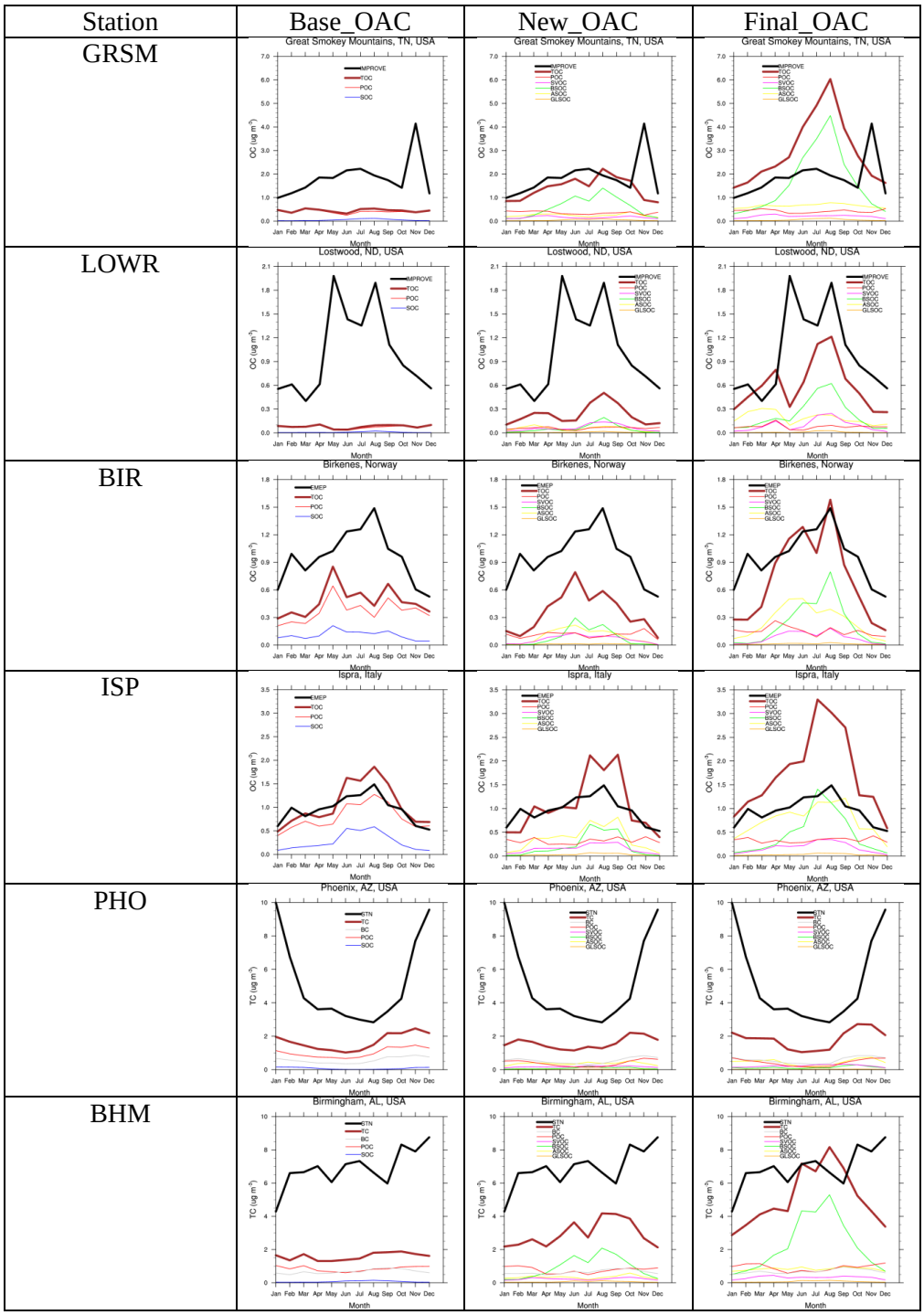

Figure 3.15. A comparison of the monthly time series of OC and its components from selected sites in the IMPROVE and EMEP networks and monthly time series of TC and its components from the select sites in the STN network from the Base_OAC, New_OAC, and Final_OAC simulations.

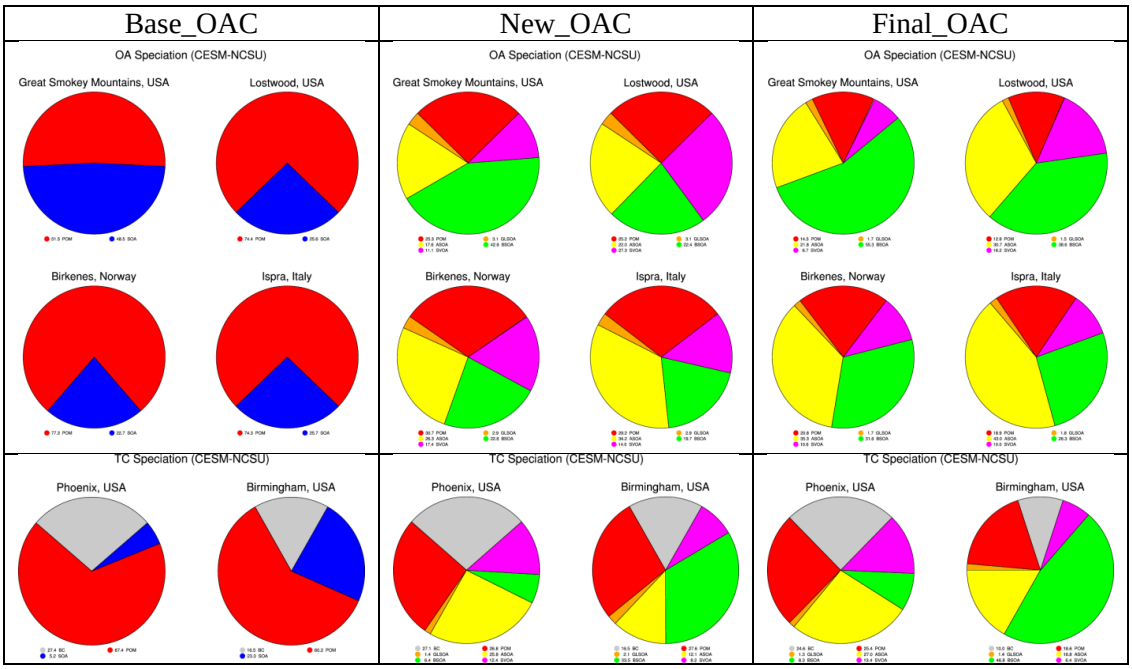

Figure 3.16. The relative contribution of simulated OA components to the total simulated OA and TC concentrations at selected IMPROVE, STN, and EMEP sites from the Base_OAC, New_OA, and Final_OAC simulations.

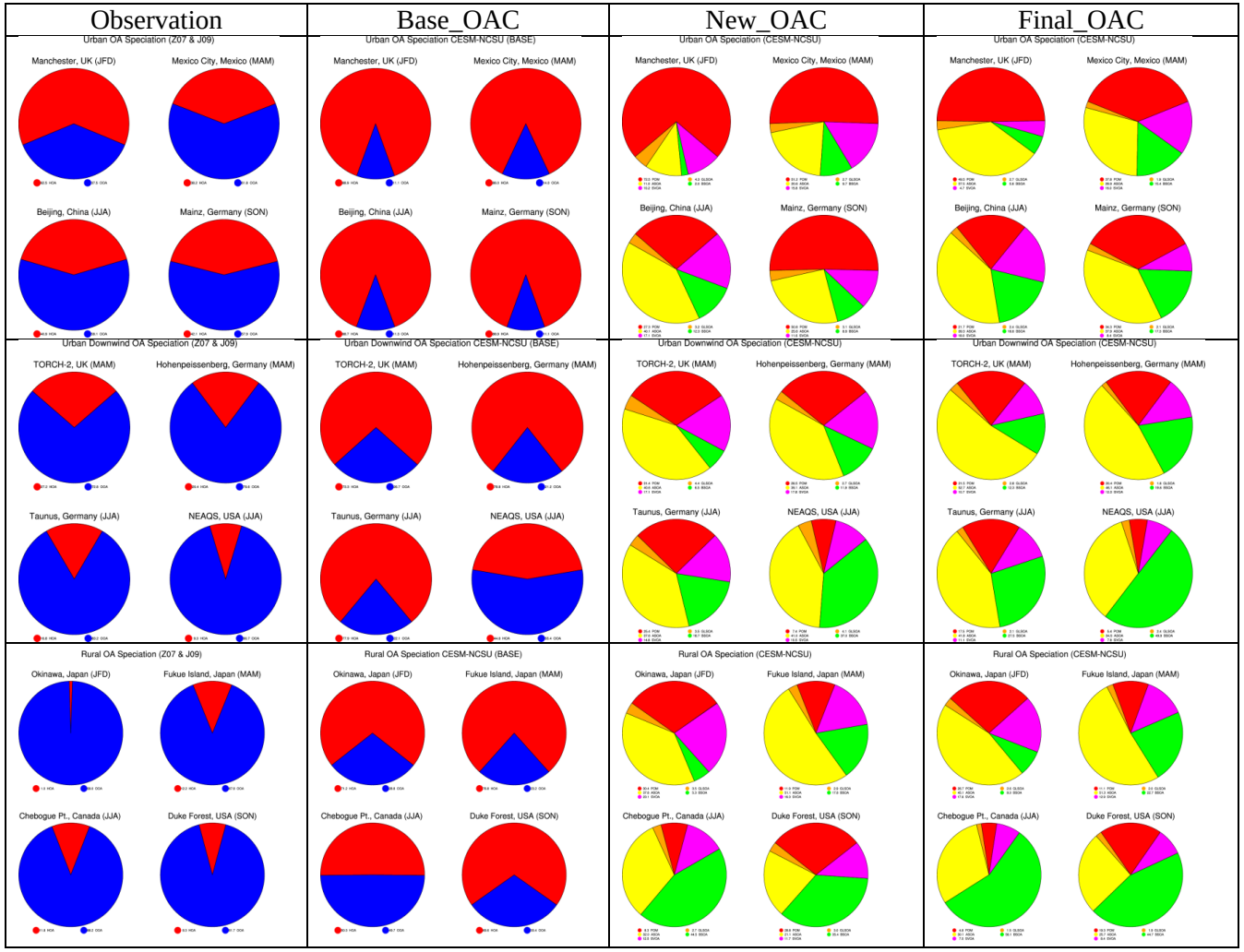

Figure 3.17. The relative contributions of HOA and OOA from selected sites in the Zhang, Q. et al. (2007) and Jimenez et al. (2009) dataset and the relative contribution of the OA species from the CESM-NCSU Base_OAC, New_OAC, and Final_OAC simulations.

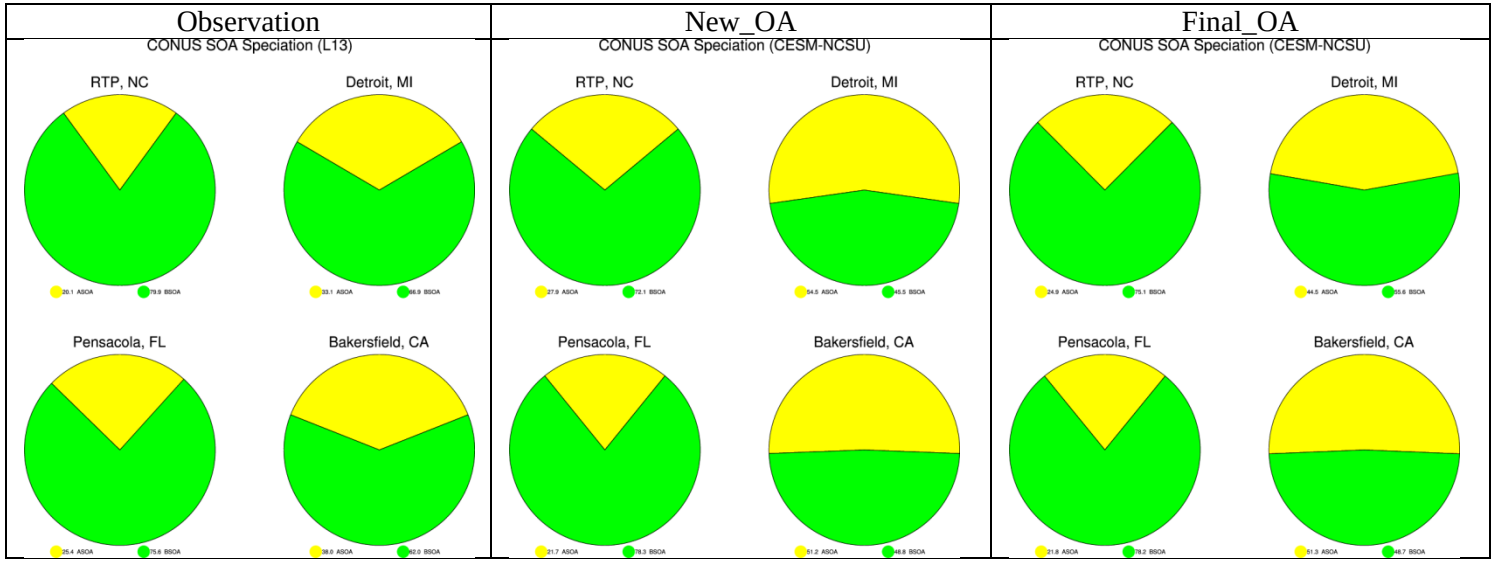

Figure 3.18. The relative contributions of ASOA and BSOA from selected sites of the Lewondowski et al. (2013) dataset and similar relative contributions at these sites from the CESM-NCSU New_OAC and Final_OAC simulations.

CHAPTER 4. CHANGES IN FUTURE AIR QUALITY, DEPOSITION, AND AEROSOL-CLOUD INTERACTIONS UNDER THE IPCC AR5 RCP SCENARIOS USING CESM-NCSU

4.1 Review of RCP Studies

The study of the future state of the atmosphere is of crucial importance as it will impact human and ecosystem health (Patz et al., 2005; Haines et al., 2006; Moore et al., 2008; Pereira et al., 2010; Shindell et al., 2012; West et al., 2013). However, these studies are limited since the true path of future climate and emissions of air pollutants are unknown and as a result the scientific community relies on many different scenarios to explore the range of possible future outcomes. The majority of future air quality studies have used either the older Intergovernmental Panel on Climate Change (IPCC) Fourth Assessment Report (AR4) Special Report on Emissions Scenarios (SRES) scenarios or the newer IPCC Fifth Assessment Report (AR5) Representative Concentration Pathway (RCP) scenarios (Fiore et al., 2012 and references therein). IPCC AR4 SRES scenarios are based primarily on socio-economic changes and as such the range in possible futures is described based on assumptions regarding the rate of globalization, population growth, and economic growth, as well as differences in future technology and energy generation (IPCC, 2001). The IPCC AR4 SRES scenarios are a limited projection of the future since none of these scenarios represent the implementation of climate policy initiatives and as a result scenarios with such policies were needed (IPCC, 2007). In a response to this need, the IPCC AR5 RCP scenarios were developed in a parallel process where information is exchanged between disciplines in a

rapid manner to develop climate policy scenarios with multiple ways to achieve specific anthropogenic radiative forcing goals (Moss et al., 2008; 2010).

Ultimately, four RCP scenarios were chosen by IPCC AR5 including: a scenario that peaks at approximately 3.0 W m^{-2} and declines to 2.6 W m^{-2} by 2100 (RCP2.6), two stabilization scenarios where radiative forcing stabilizes at target values of 4.5 W m^{-2} (RCP4.5) and 6.0 W m^{-2} (RCP6), respectively, by 2100, and a scenario in which radiative forcing never stabilizes, reaching a value of 8.5 W m^{-2} by 2100 (RCP8.5) (Moss et al., 2010; van Vuuren et al., 2011a). Some commonalities in all scenarios are the introduction of carbon capture and storage technologies (CCS) to reduce global carbon emissions and greater affluence of developing countries that will lead to greater implementation of emissions control policies for atmospheric pollutants (Masui et al., 2011; Riahi et al., 2011; Thomson et al., 2011; van Vuuren et al., 2011a,b). The RCP8.5 scenario provides a pseudo baseline for the other scenarios as it is the scenario reflecting the least climate mitigation due in part to slower economic growth and turnover in technology. As a result, this is the worst case scenario in terms of greenhouse gas (GHG) emissions, as there are minimal controls implemented over energy sector emission of carbon dioxide (CO_2) and methane (CH_4) and increased demand in food supplies from greater populations leads to strong enhancements in nitrous oxide (N_2O) emissions from greater fertilizer use and significant increases in CH_4 emissions from increases in livestock and rice cultivation. Despite representing the worst carbon policy of all RCP scenarios, air pollutants are strongly reduced in RCP8.5 due to assumed successful implementation of current and planned air quality policies and implementation of these policies in developing countries once sufficient affluence is

achieved (Riahi et al., 2011). The RCP2.6 scenario is the most optimistic of the RCP scenarios and achieves reduced radiative forcing through reductions in GHGs, largely from the introductions and large scale implementation of CCS systems on fossil fuel related emissions and introductions of alternative energy sources. Some of these climate policies provide additional air quality benefits as the introduction of CCS systems provides additional reductions in SO_2 emissions from coal and the implementation of hydrogen power sources in the transportation sector helps to reduce total non-methane volatile organic compound (TNMVOC) emissions (van Vuuren et al., 2011b). The more optimistic stabilization RCP4.5 scenario also relies strongly on CCS systems to achieve the radiative forcing target but includes greater reforestation as a process to control land use emissions and provide a carbon sink (Thomson et al., 2011). The less optimistic RCP6 scenario is possibly the most interesting pathway from an air quality perspective as Asian emissions in this scenario peak and then decline through the mid-21st century due to rapid expansion in Asian economies, resulting in the largest emissions of some pollutants (e.g., SO_2) under this scenario during the mid-21st century. Another key difference of this scenario compared to RCP4.5 is increases in deforestation and agriculture that drive greater emissions of CH_4 and N_2O that contribute to the larger radiative forcing target (Masui et al., 2011).

The projection of many air pollutants from these RCP scenarios is significantly different from the IPCC AR4 SRES scenarios where pollutant emissions increase mostly due to the lack of policy considerations (van Vuuren et al., 2011a). This results in key differences in future air quality, ecosystem health, and impacts from short lived climate forcers. For example, O_3 under the SRES scenarios is increased substantially in many scenarios (Prather

et al., 2003), while O_3 decreases by 2100 in a global sense under all RCP scenarios except RCP8.5 (Lamarque et al., 2011; Young et al., 2013; Kim et al., 2015). Subsequently, radiative forcing from O_3 under the SRES A1B scenario is a projected increase by 2100 (Levy et al., 2008), while all the RCP scenarios except RCP8.5 project decreases in O_3 radiative forcing by 2100 (Stevenson et al., 2013). In terms of aerosols and radiative forcing the SRES A1B scenario predicted decreases in sulfate (SO_4^{2-}) radiative forcing but large increase in black carbon (BC) radiative forcing associated with emissions changes by 2100 (Levy et al., 2008), while under the RCP scenarios the radiative forcing of both $SO4^{2-}$ and BC decrease by 2100 in response to declining emissions (Lamarque et al., 2011). Commonalities exist in nitrogen deposition between both types of scenario as the A2 scenario shows enhancements in nitrogen deposition largely from increases in oxidized nitrogen from NO emissions (Dentener et al., 2006); while the RCP scenarios have enhanced nitrogen deposition in certain regions largely from increases in agricultural emissions of NH_3 (Lamarque et al., 2011; Shindell et al., 2013).

Much work has been done to study how future global air quality will be impacted by climate change and emissions (Mickley et al., 2004; Murazaki and Hess, 2006; Liao et al., 2006; Stevenson et al., 2006; Unger et al., 2006; Tagaris et al., 2007; Vautard and Hauglaustaine, 2007; Heald et al., 2008; Hedegaard et al., 2008; Wu et al., 2008; Zeng et al., 2008; Jacob and Winner, 2009; Weaver et al., 2009; Lamarque et al., 2011; Fiore et al., 2012; Langner et al., 2012; Tai et al., 2012; Doherty et al., 2013; Stevenson et al., 2013; Voulgarakis et al., 2013; Young et al., 2013; Hauglaustaine et al., 2014; Kim et al., 2015, Rieder et al., 2015) . The changes in future air quality and radiative forcing under the RCP

scenarios as well as historical changes have been examined from time slice experiments of many online-coupled atmospheric chemistry and climate models as part of the Atmospheric Chemistry and Climate Model Intercomparison Project (ACCMIP) (Lamarque et al., 2013). A comparison of future O_3 burdens across the ACCMIP models reveals decreases under all scenarios except RCP8.5 by 2100 (Young et al., 2013) due to feedbacks from large increases in methane (CH_4) under this scenario, which is consistent the trend in future surface ozone (O_3) levels by 2050 predicted in the work of Kim et al. (2015). Although the models tend to predict similar global mean O_3 trends, the changes in O_3 in all ACCMIP models are not well correlated, indicating that different models are sensitive to climate and emissions changes in different ways (Young et al., 2013). Changes in O_3 radiative forcing mirror the changes in O_3 burden following these scenarios and while no true signal of climate change on O_3 radiative forcing is seen in the ACCMIP models, there are reductions in tropical O_3 levels from greater increases in humidity and greater increases in tropospheric O_3 at higher latitudes from greater lightning NO_x emissions (Stevenson et al., 2013). Changes in future oxidation state of the atmosphere via CH_4 lifetime and OH level have been examined in ACCMIP and findings show only minor changes in CH_4 lifetime and OH level under all scenarios except RCP8.5, where CH_4 lifetime increases and OH levels decline largely in response to increases in stratospheric O_3 recovery that limits O_3 photolysis and larger CH_4 levels (Voulgarakis et al., 2013). Reductions in aerosol levels under the RCP scenarios lead to reductions in aerosol radiative forcing from the aerosol direct and indirect effects, significantly reducing negative anthropogenic radiative forcing, which is reduced under the RCP2.6 scenario to larger extent than increases in GHG radiative forcing by 2100 (Shindell et al., 2013).

The impact of changes in aerosol radiative forgings on future climate under these scenarios need to be explored as the historical impact of aerosol effects have been shown to alter ocean circulations and heat transfer (Cai et al., 2006) and warming introduced under these scenarios has been shown to enhance sea ice retreat (Gagne et al., 2015). In this work a version of the Community Earth System Model version 1.2.2 (CESM1.2.2) is employed in order to simulate the impact of future climate policy scenarios on air quality and aerosol/cloud interactions. The first objective is to perform decadal simulations of the current atmosphere using emissions from both the RCP4.5 and RCP8.5 scenarios and to compare the state of the atmosphere predicted in these simulations to a current period decadal simulation using more detailed emissions. This will determine how well these scenarios represent the current atmosphere. The second objective is to quantitatively examine the changes in air quality, climate, and aerosol/cloud interactions expected under these scenarios by 2050 to assess the possible range of impacts from differences in climate policy scenario. The last objective is to isolate and quantify the impact that emission changes under a future climate policy scenario will have on future climate from aerosol/cloud interactions and the subsequent feedbacks from these interactions. This work differs from many previous climate-chemistry studies using detailed treatments for organic aerosol formation and aerosol-cloud interactions. This work also differs from the ACCMIP studies in that it is focused on the 2050 time frame, which was an optional experiment in the ACCIMIP studies that focus primarily on changes by 2030 and 2100.

4.2 Model Configuration, Evaluation Protocol, and Observational Datasets

4.2.1 Model Configuration

The CESM1.2.2 model used in this study contains a version of the Community Atmosphere Model version 5.3 (CAM5.3) that has been modified at the North Carolina State University (hereafter CESM-NCSU) (He et al., 2015a, b). Details of the default treatments within CESM1.2.2 are found on the web at http://www.cesm.ucar.edu/models/cesm1.2/tags/index.html#CESM1_2. CESM-NCSU contains several updated treatments for simulation of gases, aerosols, and aerosol/clout interactions. Gas-phase chemistry is simulated using the modified version of the 2005 Carbon Bond mechanism with global extension (CB05GE) (Karamchandani et al., 2012; He and Zhang, 2014). The version of CB05GE in CESM-NCSU also contains updated reactions for isoprene, toluene, xylene and their products, as well as, the inclusion of benzene, ethyne, glycolaldehyde, and glyoxal chemistry from the Carbon Bond Version 6 mechanism (CB6) (Yarwood et al., 2010) for improved simulation of organic aerosol. Inorganic aerosol thermodynamics is simulated using the computationally-efficient ISORROPIA II module that allows for the explicit simulation of NO_3^- and NH_4^+ in CESM, additionally sea-salt aerosol is split into Na^+ and Cl^- ions and ratios of Mg^{2+}, K^+, and Ca^{2+} ions are prescribed from dust concentrations that are not considered in the default model to be compatible with ISORROPIA-II (Fountoukis and Nenes, 2007; He and Zhang, 2014).

There are several updates in organic aerosol (OA) treatments. These include (1) a four bin volatility basis set (VBS) approach (Donahue et al., 2006) for simulating secondary organic aerosol (SOA) formation from volatile organic compounds (VOCs) (Ahmadov et al.,

2012), (2) a nine-bin VBS approach for simulating the volatility of primary organic aerosol (POA), (3) a nine-bin VBS approach for simulation the organic aerosol formed from semi-volatile organic compounds (SVOCs) and oxidized POA (SVOA) (Shrivastava et al., 2008; Shrivastava et al., 2013), (4) and a simple irreversible uptake approach for simulating SOA formation from glyoxal (Knote et al., 2014). More details on these OA treatments can be found in Chapter 3. However, there are some differences between the version of the OA treatments used in this work and those in Chapter 3, as this was a preliminary version of the treatments. The version of the OA treatments used here does not treat IVOCs as the values of IVOC emissions are not well constrained. This version is also similar to the New_OAC configuration as it uses moderate fragmentation and the ΔHvap values of the New_OAC simulation. In this version of CESM-NCSU, the gas wet deposition scheme has been updated to the Neu and Prather (2012) scheme, which eliminates the need for scaled down wet deposition.

CESM-NCSU also contains an updated aerosol nucleation parameterization that selects the largest nucleation rate from the available nucleation parameterizations within the model (He and Zhang, 2014), with two additional nucleation parameterizations included in the selection process. These additional parameterizations are the ion-mediated nucleation parameterization of Yu (2010) implemented by He and Zhang (2014) and the organic gas/ sulfuric acid conucleation parameterization of Fan et al. (2006) implemented in Chapter 4. Aerosol activation in CESM-NCSU (Gantt et al., 2014) is simulated following the Fountoukis and Nenes (2005) parameterization with additional updates for simulating the

impact of giant cloud condensation nuclei (CCN) (Barahona et al., 2010) and adsorptive activation of insoluble aerosols (Kumar et al., 2009).

The simulation periods are 2001-2010 that represent current climate conditions (hereafter current) and 2046-2055 that represent conditions of the mid-21st century around the year 2050 (hereafter future). Two RCP scenarios: RCP 4.5 and RCP 8.5 are selected. The RCP4.5 scenario is selected for this study since it is a more optimistic stabilization pathway and thus represents most likely future conditions with strict carbon policy implemented, and RCP8.5 is selected as it is the most pessimistic pathway among all RCP scenarios. Two sets of decadal simulations are therefore performed for one current decade and one future decade: one under the RCP4.5 scenario (hereafter RCP4C and RCP4F, respectively) and the other under the RCP8.5 scenario (hereafter RCP8C and RCP8F, respectively). Differences between simulations for the future decade and the current decade provide the impacts of changing emissions and climate on future air quality and its interactions with climate through various feedback mechanisms. An additional sensitivity decadal simulation is performed for the period of 2046-2055 which represents only future greenhouse gas forcing (GHGF) from the RCP4.5 scenario but utilizes RCP4.5 current decade emissions (RCP4F_GHGF). A comparison of RCP4F_GHGF with RCP4F illustrates the impacts of changing emissions on air quality and aerosol/cloud interactions and also their feedback to the climate system. A comparison of RCP4F_GHGF with RCP4C will illustrate the impacts of GHGF from the RCP4.5 scenario on future air quality. RCP4.5 is selected for the GHGF only scenario because it represents stronger emission control and climate

mitigation policies than RCP 8.5 and thus can better illustrate the impact that these types of policies can have on climate through aerosol/cloud interactions.

The RCP4C and RCP8C simulations are configured based on the CESM1.2.2 B_2000_STRATMAM7_CN component set. This component set represents a fully-coupled CESM configuration including prognostic simulation of the atmosphere, ocean, land, and sea ice from the various component models. The simulation is configured with GHGF comparable to the year 2000 for N_2O, CH_4, CO_2, and Chlorofluorocarbons (CFCs) but with O_3 radiative forcing free to change in response to chemistry. This component set also contains active stratospheric chemistry from CB05GE, aerosols simulated by the seven mode version of the Modal Aerosol Model (MAM7) (Liu, X. et al., 2012), as well as, carbon and nitrogen biogeochemical cycling in the land model. Initial conditions (ICs) for these current decadal simulations are the same as those for the CESM-NCSU current decadal simulations in He et al. (2015a), which are generated from a multi-step process. The first set of ICs are obtained from a 10 year (1990-2000) CAM5.1 standalone simulation using chemistry from the Model for Ozone and related chemical Tracers version 4 (MOZART-4) (Emmons et al., 2010) that is provided by the National Center for Atmospheric Research (NCAR). The MOZART-4 ICs are used to drive a one-year simulation of the CESM version 1.0.5 model using the B_1850-2000_CAM5_CN component set to provide initial meteorological conditions and chemical conditions for all species that exist in both MOZART and CB05GE gas-phase mechanism. The ICs from the land model are provided from an NCAR CESM/CAM4 B_1850-2000_CN simulation for the year 2000 and the ocean and sea ice models are initialized from CESM default settings. These ICs are then used to drive a three-

month spin up period that provides the final ICs for all meteorological parameters and chemical species; including those in CB05GE that are not available in MOZART-4, that have been spun up from clean conditions.

The ICs for all component models in the RCP4F and RCP4F_GHGF simulations are provided by NCAR from the 2044 restart files of the CESM Phase Five of the Coupled Model Intercomparison Project (CMIP5) b.e11.BRCP45C5CN.f09_g16.004 experiment. The year of 2044 was the closest time period to the starting year of 2046 in this work available from NCAR. These ICs correspond to a simulation using a similar component set as the current decadal simulations but with highly simplified chemistry and RCP4.5 GHGF. Due to the lack of chemical ICs, ICs of GHGs, CH_4, N_2O, CO_2, and O_3, are generated from output of the Whole Atmosphere Community Climate Model (WACCM) RCP4.5 r2i1p1 CMIP5 experiment. ICs of CFCs are generated from default IC files used to drive CESM stratospheric chemistry simulations for the year 2000 that are scaled to the year 2050 based on growth factors derived from the GHG levels used in the b.e11.BRCP45C5CN.f09_g16.004 experiment. These ICs drive a 1-year spin up simulation that generates the ICs for the chemical species used in the future decadal simulations in this work. The ICs for the RCP8F simulation are prepared in the same manner using restart files for the year 2047 from NCAR's CMIP5 b.e11.BRCP85C5CN.f09_g16.001 experiment and WACCM output of CH_4, N_2O, CO_2, and O_3 from the r2i1p1 CMIP5 experiment. The year 2047 was used as this is the closest available time period from NCAR for the starting year of 2046 in this work. All future decadal simulations have GHGF set to 2050 levels for either the RCP4.5 or RCP8.5 scenario.

In addition to the configurations mentioned above, the CESM-NCSU model underwent an additional tuning process for radiation variables. This tuning is necessary since the default tuning parameters in the model are no longer valid once the aerosol activation parameterizations of Gantt et al. (2014) were incorporated into the model framework. These aerosol activation treatments generally improved the performance of some cloud variables such as cloud optical thickness (COT) and cloud liquid water path (LWP) but resulted in an overprediction of shortwave cloud forcing (SWCF) and an associated underprediction in downwelling shortwave radiation at the Earth's surface (FSDS) (Gantt et al., 2014). These changes were responsible for the strong cold bias reported in He et al. (2015a). Additionally, both the work of Gantt et al. (2014) and He et al. (2015a) neglected primary number emissions from BC, primary organic carbon (POC), and primary sulfate (SO_4^{2-}). Once the primary number emissions were accounted for in the current decadal simulations, the radiation and temperature biases were further degraded without tuning.

NCAR tunes CESM radiation in climate simulations by adjusting various cloud parameters until top of the atmosphere annual net radiation flux (RESTOA) is equivalent to 0 W m^{-2} for the preindustrial period (Hannay et al., 2014). Model parameters that are typically adjusted during this process include the threshold relative humidity for formation of low level clouds (rhminl), the critical diameter for ice crystal autoconversion (Dcs), and the cloud fraction for deep convection (personal communication, Cecile Hannay, NCAR, 2014). The method employed to tune CESM-NCSU is slightly different as the time period of the current decadal simulations is not preindustrial. For CESM-NCSU, RESTOA was calibrated to match available estimates of RESTOA from the Cloud and Earth's Radiant Energy System

(CERES) / Energy Balanced and Filled (EBAF) dataset, which is roughly 0.8 W m^{-2} as a global area-weighted average for the averaged period of 2001-2010 (personal communication, Cecile Hannay, NCAR, 2014). A series of sensitivity simulations were carried out to find the appropriate tuning parameters. The final result was an adjustment of rhminl from 89.75% in the standard release to 95.5% for CESM-NCSU and an adjustment of Dcs from 400 μm in the standard release to 500 μm in CESM-NCSU. These changes are consistent with the possible ranges of the tuning parameter values (personal communication, Cecile Hannay, NCAR, 2014). Given computational constraints and the highly complex nature of the CESM model, the final model global area-weighted value of CESM-NCSU RESTOA was 0.7 W $m^{-2,}$ which was as close to the global area-weighted CERES/EBAF value of 0.8 W m^{-2} as possible without overshooting.

The RCP emission inventories used to drive the simulations are publicly available from version 2 of the RCP Database on the web at http://tntcat.iiasa.ac.at/RcpDb/dsd?Action=htmlpage&page=welcome. The current decadal simulations (RCP4C and RCP8C) are broken into three distinct emission periods with the years 2001-2003 utilizing the RCP year 2000 emissions, the years 2004-2006 utilizing the RCP year 2005 emissions, and the years 2007-2010 utilizing the RCP year 2010 emissions. The future decadal periods (RCP4F, RCP4f_GHGF, and RCP8F) utilize emissions based on RCP year 2050 emissions. Emissions of dust, sea-salt, and biogenic VOCs are calculated online in CESM1.2.2 following the parameterizations of Zender et al., (2003), Martensson et al. (2003), and the Model of Emissions of Gases and Aerosols from Nature version 2 (MEGAN2) (Guenther et al., 2006), respectively.

4.2.2 Evaluation and Analysis Protocol

The protocols for evaluation include assessing spatial distributions and statistical measures of model performance following a similar procedure to those used in Zhang et al. (2012) and He et al. (2015a). Statistical measures of interest include mean bias (MB), root mean square error (RMSE), normalized mean bias (NMB), normalized mean error (NME), and correlation coefficient (R). The radiation, cloud, and meteorological variables evaluated are listed in Table 4.1 along with the variables' short names used in the remainder of the text, the datasets against which the variables are compared, the spatial coverage and resolution (if applicable) of the datasets, and the temporal coverage during the CESM-NCSU current decadal simulations. Similar information for the chemical species evaluated is listed in Table 4.2.

All variables are evaluated on an annual basis and some dataset limitations exist. Chemical measurements in East Asia are very limited in terms of both chemical species (i.e., carbon monoxide (CO), nitrogen dioxide (NO_2), sulfur dioxide (SO_2) O_3, and PM_{10}) as well as spatial coverage, with all variables except PM_{10} only available from South Korea, Japan, and Taiwan. PM_{10} observations are limited to China and Taiwan for the entire period and available from South Korea beginning in 2006. Traffic and industrial sites are excluded from the Airbase and BDAQ observations because the horizontal grid resolution of these simulations is too coarse to represent these observations (Zhang et al., 2013). OC observations from EMEP sites have a coarse temporal resolution due to the lack of a routine observational program (Yttri et al., 2007). As a result, all available observations of OC spanning the time period of 2001-2013 are averaged into an annual climatology to compare

with the CESM-NCSU simulation. Similarly, the oxygenated organic aerosol (OOA), hydrocarbon-like organic aerosol (HOA), total organic matter (TOM), and SOA measurements compiled in the works of Zhang, Q. et al. (2007), Jimenez et al. (2009), and Lewondowski et al. (2013) are based on very limited time periods so these observations are assumed to represent the climatology of the season in which the measurements were taken and are compared against the corresponding seasonal climatology from the CESM-NCSU simulations.

In order to explore how well CESM-NCSU simulates aerosol/cloud interactions and trace gas levels, interannual variations of PM, CCN5, cloud droplet number concentration (CDNC), Aerosol Optical Depth (AOD), shortwave cloud forcing (SWCF), tropospheric NO_2 column (TNO_2), tropospheric formaldehyde column (THCHO), and tropospheric ozone residual (TOR) are analyzed over the marine stratocumulus regions identified in the work of Rausch et al. (2010). These regions were selected because the nearly continual presence of clouds in these regions makes them ideal for evaluating aerosol-cloud interactions and the remoteness of these regions provides insights into how well the background levels of trace gases and aerosols are simulated. These stratocumulus regions exist the vicinity of Australia (AUS, 30°S–40°S, 88°E–103°E), North America (NAM, 15°N–35°N, 115°W–140°W), South East Asia (SEA, 10°N–40°N, 105°E–150°E), Southern Africa (SAF, 5°S–25°S, 10°W–15°E), and South America (SAM, 8°S–28°S, 70°W–90°W). However, caution is taken when interpreting the simulated interannual variations in these regions as GHGF for all years is identical, thus year to year variations only result from internal model variability and the changes between the emissions periods. Additionally, the trends in radiation (FSDS and

Outgoing Longwave Radiation (OLR)), cloud (CF, cloud water path (CWP)), meteorological (2-m temperature (T2), 2-m specific humidity (Q2), 10-m wind speed (WSP10), and precipitation rate (PR)), and aerosol (AOD) variables between the current and future decadal simulations as predicted by CESM-NCSU will be compared against those predicted by a default version of CESM without complex chemistry from NCAR's RCP4.5 and RCP8.5 r1i1p1 CMIP5 experiments. This will illustrate the impacts of using the advanced chemical mechanisms to simulate these RCP pathways.

4.3 Evaluation of Current Climate Periods

4.3.1 Evaluation of Radiation, Cloud Properties, and Meteorological Parameters

Performance statistics for radiation, cloud, and meteorological parameters from both the RCP4C and RCP8C simulations are listed in Table 4.3. Zonal mean profiles of radiation and cloud parameters from the RCP4C, RCP8C, and He et al. (2015a) (HE15) CESM-NCSU simulations, as well as the CESM CMIP5 data that represent merged historical and RCP4.5 simulations (if available) are compared against satellite estimates in Figure 4.1. Similar zonal mean comparisons of meteorological and chemical parameters are shown in Figure 4.2. The performance of cloud, radiation, and meteorological variables are generally similar for both the RCP4C and RCP8C simulations. RESTOA is well simulated after tuning, with a slight underprediction of 3.9% in the RCP4C simulation and slight overprediction of 3.4% in the RCP8C simulation, NME values of ~26%, and R values of 0.99. The sensitivity simulations conducted to find the appropriate tuning parameters utilized the RCP8.5 emissions and as a result, the opposite signs in biases between the two scenarios are caused by their difference in emissions and GHGF. It is important to note that the mean satellite retrieval estimates and

mean simulation values of RESTOA in Table 4.3 are not the same as the RESTOA values mentioned in the model configuration section. This is because the average values mentioned in the model configuration section are area-weighted averages over the globe, while the values in Table 3 are the average grid cell values for model validation. Thus the area-weighted RESTOA average value is positive because grid cells with a positive RESTOA in the tropics are larger in terms of area than higher latitude grid cells where RESTOA is negative. The model performance for RESTOA is the poorest in the tropics with a general underprediction. This is likely caused by the overpredictions of COT in this region that increase outgoing shortwave radiation (OSR) and reduce FSDS compared to satellite estimates, thus reducing the shortwave contribution to RESTOA.

Other shortwave radiation variables are well simulated with NMBs less than ± 4%, NMEs less than 25%, and R values generally higher than 0.90 with the exception of OSR that has an R value of 0.83. FSDS and FSNS are both slightly underpredicted in response to overpredictions of SWCF and OSR. This indicates that generally clouds within the CESM-NCSU model overestimate reflectance. As shown in Figure 4.1, the CESM-NCSU model accurately captures the latitudinal variations in the shortwave radiation variables. The overpredictions in SWCF are the most pronounced in the tropics and result from the overpredictions in COT in this region. There is also a smaller overprediction that occurs in the northern hemisphere (NH) mid-latitudes that could potentially be attributed to the large overprediction in CDNC in this region. SWCF is underpredicted in polar regions and this is likely attributed to the underpredictions of cloud and aerosol variables in these environments discussed later in this section. The overpredictions in SWCF in the tropics and NH mid-

latitudes are responsible for the overpredicted OSR in these regions. OSR is also overpredicted in the polar regions, likely due to the overpredicted surface reflection from an overpredicted surface albedo. This overprediction of surface albedo could potentially be related to inaccuracies in snow or sea ice coverage or a limitation in the configuration of CESM. The configuration of CESM used in this study does not simulate the interaction between BC and snow albedo, which has been shown to affect the radiative forcing of the snow cover (Flanner et al., 2007). FSDS is underpredicted in the tropical regions in response the overpredicted SWCF and overpredicted in polar regions in response to underpredicted SWCF. This pattern is slightly different from FSNS that is also underpredicted in the tropics (due to the SWCF overprediction), but underpredicted in the polar regions. The underprediction in FSNS, despite overpredicted FSDS, in the polar regions provides further evidence of an overpredicted polar surface albedo. In general, the tuning of RESTOA brings all shortwave radiation variables into better agreement with satellite estimates compared to HE15 and also CMIP5 in the case of FSDS.

Longwave radiation variables are also well simulated in the RCP4C and RCP8C simulations with NMBs within ± 11%, NMEs less than 21%, and R values above 0.88. FLDS, OLR, and LWCF are all slightly underpredicted, while FSNS is slightly overpredicted. The bias in the longwave radiation variables is in part caused by the underpredictions in FSDS, since the lost energy leads to a cooler surface or less energy emitted as longwave radiation. Similar to the shortwave variables, the longwave variables from CESM-NCSU capture the satellite estimated latitudinal variations. FLDS performs well across the majority of the globe but has the strongest underpredictions in the polar regions

and slight overpredictions in the tropics. In the polar regions, this is caused in part by the underprediction in FSNS but may potentially be related to uncertainties in the complex refractive index of water (CRI) that has been shown to result in underestimates of the greenhouse effect in colder regions (Rowe et al., 2013). The slight overpredictions in the tropics are related to overpredictions in LWCF in this region. LWCF is generally underpredicted in the middle and higher latitudes but overpredicted in the tropics. The underprediction in the mid-latitude regions is likely caused by underpredictions in CF and COT that are maximized in these regions. At the higher latitudes, LWCF is underpredicted due to reduced surface longwave emissions as a result of underpredicted FSNS and the uncertainties in the CRI of water. The overpredicted LWCF in the tropics of the Southern Hemisphere (SH) is likely related to the overpredicted COT in this region. The co-location of the overpredicted COT and LWCF suggests that simulated clouds in this region are physically thick (i.e., the distance from cloud base to cloud top is large), which would explain the strong overpredictions of both SWCF and LWCF. OLR is underpredicted in tropical and subtropical regions of the SH and the higher latitudes of the NH. The underprediction of OLR in the SH is likely caused by a combination of underpredicted FSDS and the overprediction in LWCF in this region. The underprediction of OLR in the higher latitudes of the NH is likely caused by a combination of the underpredicted FSNS and overpredicted FLNS that leads to an underestimation of T2 as shown in Figure 4.2, and thus the reduced emission of longwave radiation. FLNS is underpredicted in the tropics similar to all longwave variables in response to underpredicted FSDS; but it is overpredicted in the poles. This is potentially due to the inaccuracies in the simulated land surface or the

uncertainties in the CRI of water. In general, the tuning of RESTOA has improved the simulation of longwave radiation variables compared to the HE15 simulation except in tropical regions. Compared to CMIP5, CESM-NCSU has slightly degraded performance for OLR but overall the differences are not substantial.

AOD is moderately well simulated in the RCP4C and RCP8C simulations with relatively low NMBs -16.2% to -14.5%), moderate error (NMEs of 40.7-41.7%) and moderately high R values (0.61-0.62). The zonal mean profile in Figure 4.1 shows that the latitudinal variations in AOD from satellite estimates are captured by the model but deviations exist, primarily in the polar regions. Underestimates of aerosol loadings in the polar regions have been reported with the unmodified version of the MAM aerosol module and are believed to reflect either underestimations in global emissions or too efficient wet deposition of aerosols (Liu, X. et al., 2012). The AOD predicted in the RCP4C and RCP8C simulations is larger and generally performs better than HE15 (e.g., NMBs of -14.5% and -16.2% vs. -35.4% and 49.2%), except in the subtropical regions of the NH and SH where AOD is overpredicted compared to satellite estimates. The larger AOD is the result of the vertically-structured emissions in the RCP inventories that allow for greater lofting of BC, POA, and SO_4^{2-} aerosols into the upper troposphere where they are more radiatively active. Inaccuracies in these emissions or their vertical structure likely cause the overpredictions in the subtropics as the subtropical regions of the NH contain large primary aerosol emissions from South Asia and Southeast Asia and the subtropical regions of the SH contain large biomass burning emissions from South America and Africa. In general all CESM-NCSU

simulations provide an AOD comparable to that of CMIP5 with the RCP simulations providing a slightly higher AOD in most latitudes

CF in CESM-NCSU is well simulated in terms of NMB (-0.9% to -0.7%) and NME (25.9-26.4%) but poor in terms of R value (0.28). This performance is slightly degraded in comparison to the HE15 current climate simulation that slightly overpredicted CF. with an NMB of 0.4%, an NME of 15.3%, and an R value of 0.7. This illustrates the negative aspects of tuning the model as not all variables will benefit. The cloud fraction is underpredicted in the RCP4C and RCP8C simulations because the increased rhminl value reduces low level cloud formation. The loss of low level clouds likely impacts the spatial distribution and thus results in the low R value. Despite this low R value, the RCP8C and RCP8F simulations do capture the latitudinal variations in CF from satellite estimates and are very similar to the values predicted in the CMIP5 experiment as shown in Figure 4.1. All CESM simulations generally overpredict CF in the polar regions, which is a historical model limitation of CESM and other global climate models (Vavrus and Waliser, 2008; Qian et al., 2012).

CCN5 is underpredicted in the RCP4C and RCP8C simulations with NMBs of -47.3% to -45.7%. The NMEs of 49.4-50.3% for CCN5 indicate that the majority of the simulation errors are a result of the bias. The zonal mean comparison shows that CCN5 values from the RCP4C and RCP8C simulations are generally comparable to MODIS estimates for regions in 30°S-45°N but are largely underpredicted in the middle and higher latitudes. As shown in Table 4.1, the MODIS CCN product is only available in marine environments, so the underpredictions in CCN5 are likely from uncertainties in marine aerosol treatments. For example, these underpredictions in CCN5 could potentially be

reduced with a treatment for marine organic aerosol. These aerosols are not treated in the version of CESM used in this study but have been shown to increase particulate matter with diameter less than and equal to 2.5 μm ($PM_{2.5}$) and CCN the most in middle and higher latitude marine environments (Gantt et al., 2012, 2015). CCN5 may also be underpredicted in part due to the overpredicted aerosol activation as evidenced by the overprediction of CDNC that will be discussed in detail below. The simulation of CCN5 is greatly improved compared to HE15 due to the addition of particle number emissions of BC, POC, and SO_4^{2-} that were neglected in HE15. Because these emissions are vertically-distributed in the RCP4C and RCP8C simulations, they are allowed to be transported further into the marine environment, thus improving CCN5 performance. The increased CCN5 levels may have also resulted from the inclusion of the organic gas/sulfuric acid conucleation treatment in this version of CESM-NCSU. CDNC is overpredicted in the RCP4C and RCP8C simulations with NMBs of 39.8-45.2%. NMEs are fairly large (58.6-62.6%) and R values are relatively low (0.42-0.43), indicating that the spatial distribution is only moderately captured. The zonal mean profiles show that the RCP4C and RCP8C simulations capture most of the latitudinal variability in CDNC but there is a discrepancy in the middle and higher latitudes of the NH with CDNC levels peaking at ~40°N in the simulation rather than peaking at ~50°N in the satellite estimate. This discrepancy is likely the cause of the moderately large errors and lower R values. The underpredictions at the higher latitudes are likely caused by underpredicted aerosol loadings in these environments as evidenced by the underpredicted AOD in this region. In addition to the aerosol loading uncertainties at these latitudes, there may be uncertainties associated the phase of the clouds. The Bennartz (2007) dataset only represents

CDNC from warm clouds and the simulated region for warm clouds in CESM is assumed to be between 960-850 hPa (Gantt et al., 2014; He et al., 2015a). However, this assumption may not be accurate at higher latitudes since these clouds are typically mixed-phase and are generally not well simulated by global climate models (Verlinde et al., 2007; Fan et al., 2011). The systematic overprediction of CDNC by CESM-NCSU can be linked to errors in the model treatment for aerosol activation and also uncertainties in the MODIS derived satellite product. In terms of model treatment, the overprediction can potentially be attributed to high activation fractions from the inclusions of insoluble aerosol activation and the use of 0.06 as the effective uptake coefficient (Gantt et al., 2014). Additionally, the treatment within CESM does not account for the effect of entrainment on aerosol activation which in general would suppress aerosol activation (Barahona and Nenes, 2007), although such an effect may be small. In terms of satellite uncertainties, the MODIS derived CDNC estimates are subject to the propagation of errors from the MODIS retrievals from which they are derived. One such example is the MODIS cloud effective radius (Bennartz, 2007). This parameter typically has very large values, especially in remote oceans regions due to the presence of broken cumulus clouds. This bias has been attributed to drizzle/rain contamination (Nakajima et al., 2010) and artifacts from cloud heterogeneity (Zhang and Platnick, 2011). The overestimation of cloud effective radius would result in an underestimate of satellite CDNC, thus leading to apparent overpredictions of simulated values. Compared to the HE15 simulation the CDNC overprediction is larger in the RCP4C and RCP8C simulations in response to higher CCN5 levels.

Precipitable Water Vapor (PWV) is very well simulated in the RCP4C and RCP8C simulations with low NMBs (2.8-3.4%), low NMEs (11.8%), and high R values (0.98). The zonal mean profile of PWV matches that of the MODIS estimates with slight underpredictions in the subtropical and mid-latitudes of the NH and slight overpredictions in the middle and higher latitudes of the SH. PWV is improved from the HE15 simulation due to the enhanced FSDS from model tuning in the tropical region that facilitates greater evapotranspiration. LWP in the RCP4C and RCP8C simulations is underpredicted (NMBs of -30.3% to -29.9%) and only moderately captures the spatial distribution of the satellite estimates (NMEs of 36.4-36.7% and R values of 0.42-0.44). The zonal mean profiles reveal that LWP from CESM-NCSU (RCP4C, RCP8C, and HE15) is generally comparable to satellite estimates in the mid-latitudes but underpredicted in the tropics, subtropics, and polar regions. Despite these underpredictions, the latitudinal variations in the satellite estimates are captured in the simulation in all but the polar regions. The underpredictions in the tropics and subtropics suggest that the model is not accurately representing LWP from convective clouds, as these clouds dominate this region, and may also be related to the underpredicted CF. The poor performance in the polar regions may be related to some of the common issues of CESM and other global climate models in simulating polar aerosols and clouds, as mentioned earlier in this section. It may also be due to inaccuracies in the satellite retrievals at these latitudes due to low solar zenith angles (Seethala and Horváth, 2010) and interference from snow cover (Kay et al., 2012). COT is also underpredicted (NMBs of ~ -41.0%) in the RCP4C and RCP8C simulations with even larger errors in spatial distribution compared to LWP (NMEs of 54.9% and R values of -0.12). The zonal mean profiles show

that COT is generally comparable to the MODIS estimates in the middle and lower latitudes but does not capture the high COT values of the polar regions. This is likely due to the same modeling and satellite uncertainties that cause LWP underpredictions in these regions. The general underprediction of COT over the remainder of the globe is likely cause by the underestimates of LWP and CF in these areas. COT and LWP from the RCP4C and RCP8C simulations are comparable to their performance reported by HE15, although some deviations exist, either from a lack of tuning of model radiation in HE15 or from the updates to the microphysics treatment that took place between CAM5.1 and CAM5.3 (http://www.cesm.ucar.edu/models/cesm1.2/tags/cesm1_2/whatsnew_science.html). All CESM-NCSU simulations show improvements in LWP compared to the CMIP5 simulations, illustrating the benefit of the updated aerosol formation and aerosol activation treatments. The moderate to poor performance of cloud related variables is common amongst many global climate models (Lauer and Hamilton, 2013) and regional air quality models (Zhang et al., 2012b). The strong performance of radiation variables compared to these cloud parameters suggests a disconnection between these two fields of study and may reflect offsetting errors in modeled radiation for different assumptions regarding cloud properties (Qian et al., 2012). The underprediction of LWP and other cloud parameters has been improved using a version of CESM that contains a cloud resolving model (CRM) within each CESM grid cell (Wang et al., 2011), illustrating CRM as a pathway for better representing aerosol-cloud interactions given the increasing availability of computational resources. Also, one important caveat of the results presented here is all simulated values are derived from

monthly averaged CESM output files and as a result the annual average simulated results may not necessarily reflect the overpass times of the satellite estimates.

PR is well simulated in the RCP4C and RCP8C simulations with low NMBs (8.3-8.9%) low NMEs (26.3-26.8%) and high R values (0.86-0.87). The zonal mean profiles show that CESM-NCSU captures the latitudinal variability of PR from GPCP but tends to overpredict deep tropical convective precipitation. In general the PR predicted in the current decadal simulation is very similar to that in both the HE15 and CMIP5 simulations. T2 is also simulated well in the RCP4C and RCP8C simulations although a cold bias still persists with MBs ranging from -1.3°C to -1.0°C and RMSEs ranging from 3.0-4.0°C comparing to the NCEP/NCAR and NCDC datasets. The R values are generally high (0.93-0.99). The zonal mean profile shows a very close matching to the T2 from the NCEP/NCAR analysis dataset with slight underpredictions occurring in the polar regions. These underpredictions are related to the underpredictions of FSNS in these regions. In general, the radiation tuning helps to correct the cold bias reported in the HE15 simulation but the T2 values from CESM-NCSU simulations are still slightly cooler than the T2 predicted by the CMIP5 version of the CESM model. The cool bias in T2 leads to reduced evapotranspiration and results in a slight dry bias in Q2 with an MB of -0.5 to -0.3 g kg^{-1}, however, Q2 is generally well simulated with RMSEs of 1.0-1.7 g kg^{-1} and R values of 0.93-0.99. The zonal mean profile of Q2 shows considerable improvement in Q2 compared to that of HE15 and CMIP5 in the tropics after tuning and similar to T2, the RCP4C and RCP8C simulations have better performance in Q2 than HE15 and weaker performance compared to CMIP5 in the NH. In general these deviations in T2 and Q2 from observations are comparable to those reported across the

different models participating in the CMIP5 project (Tian et al., 2013). WSP10 is moderately well simulated in terms of errors (RMSEs 1.8-3.3 m s^{-1}) and correlation (Rs of 0.47-0.58) comparing to both the NCDC and NCEP/NCAR datasets but there are differences in bias with an underprediction of 0.4 m s^{-1} against the NCDC observations and an overprediction of ~2.5 m s^{-1} against the NCEP/NCAR analysis. This inconsistency between the performance statistics using both observational datasets stems from two possible reasons. The first is that NCDC sites are primarily land based, while NCEP/NCAR has global coverage. This may indicate that CESM-NCSU underpredicts wind speeds over land but overpredicts wind speeds in marine environments. The second possibility is limitation different data processing procedure used for the NCDC observations, which requires values less than 1.5 knots be excluded from evaluation because of uncertainties in anemometer measurements (NOAA, 1998). This would artificially eliminate or limit overpredictions against WSP10 from NCDC if such biases exist. The zonal mean profile of WSP10 against the NCEP/NCAR analysis shows that despite the biases, the RCP4C and RCP8C simulations adequately capture the latitudinal variations in WSP10 and there is no substantial difference between these simulations and those of CMIP5 or HE15.

4.3.2 Evaluation of Trace Gases and Aerosols

CO evaluated against limited measurements from East Asia reveals a substantial underprediction with NMBs of -71.7% to -70.3%. The NMEs are identical to the NMBs indicating most of the error comes from the bias. This is likely caused by inaccuracies in emission levels and simulated vertical mixing in this region. Despite this poor performance in East Asia, TCO is well simulated with NMBs of -11.4% to -9.9%, NMEs of 15.2-16.2%, and

R values of 0.83-0.85. The zonal mean profile in Figure 4.2 reveals that the RCP4C and RCP8C simulations capture the profile from satellite estimates but slightly underpredict TCO in the NH mid-latitudes. This could be related to either underestimates of emissions in the RCP inventory or potentially from overestimated oxidation as evidenced by the O_3 overprediction that will be discussed later in this section. The overprediction of TCO in HE15 is reduced in the RCP4C and RCP8C simulations but the underprediction in the surface CO concentrations in East Asia is enhanced. This is caused by a correction to the CO reaction rate against OH that underestimates CO destruction by OH in the older version of CESM. This bug was reported in the supplementary material of Lamarque et al. (2012). THCHO is underpredicted (NMBs of ~-38.0%), resulting in moderate errors (NMEs ~42.0%) and a reasonable agreement of the spatial pattern (R values ~0.69). The zonal mean profiles from the RCP4.5 and RCP8.5 simulations are qualitatively similar to satellite estimates although the simulations predict less THCHO, especially in SH. These errors could potentially be related to underestimated emissions of formaldehyde or its precursors (e.g., isoprene and terpene) and uncertainties in secondary formation of HCHO. Such uncertainties have been shown to vary by approximately 20% among various commonly-used gas-phase chemical mechanisms including regional versions of CB05 (Knote et al., 2015). THCHO is improved compared to that in the HE15 simulation due to the inclusion of biogenic emissions that are part of the updated MEGAN2 in the CESM1.2.2 land model (http://www.cesm.ucar.edu/models/cesm1.2/tags/cesm1_2/whatsnew_science.html). Figure 4.3 shows absolute differences in the emissions of CO, HCHO, nitric oxide (NO), SO_2, NH_3, anthropogenic VOC (AVOC), BC, and POC between the RCP8.5 and RCP4.5 current

emission inventories . In general, CO and HCHO levels are reduced in the RCP8C simulation compared to the RCP4C simulation in response to lower emissions in the RCP8.5 inventory.

NO_2 is strongly underpredicted at surface sites in Europe and East Asia (NMBs of -80.0% to -70%) but TNO_2 is overpredicted (NMBs of 44.9-47.8%). The large errors and poor spatial correlations at the surface sites suggest inaccuracies in the spatial allocation of emissions. The disparity between the TNO_2 and surface NO_2 levels suggests errors in the vertical structure of NO_2 within the CESM-NCSU model. Such errors could include inaccurate magnitudes and vertical distributions of NO_2 emissions, excess lofting of NO_2 into the higher levels of the troposphere, which is consistent with the overpredicted TNO_2, or excess conversion of NO_2 to HNO_3, which is consistent with the overpredictions of HNO_3 and O_3. Similar errors in the vertical distributions of NO_2 emissions in 2005 over East Asia were reported by Zhang et al. (2015a). Zhang et al. (2015b) further showed that the adjusted magnitudes and vertical distributions of NO_2 emissions moderate to large improvement in simulated surface concentrations and column mass abundances of species in terms of domain mean performance statistics at individual sites. The zonal mean profiles show that despite these issues the RCP4C and RCP8C simulations capture the latitudinal changes in TNO_2, which is reflected in the high spatial correlation (R values of 0.82-0.86). The RCP8C and RCP4C simulations overpredict TNO_2 to a greater extent and underpredict surface NO_2 to a lesser extent than the HE15 simulation due to greater global average NO_2 emissions in the RCP emission inventories. The absolute differences in the emissions of CO, HCHO, NO, SO_2, NH_3, AVOC, BC, and POC between the RCP4.5 and RCP8.5 current emission inventories and the emission inventory of HE15 are shown in Figures 4.4 and 4.5,

respectively. HNO_3 is largely overpredicted in the CONUS region (NMBs of 82.7-93.1%) but only slightly overpredicted in Europe (NMBs of 0.4-12.3%). However, the small biases in Europe do not indicate excellent performance but are most likely from compensation errors, as evidenced by the high NMEs (63.6-71.2%) and low R values (~0.31). The errors in HNO_3 likely stem from the errors in NO_2 as its poor spatial performance in Europe is similar to that of NO_2 and also likely reflects the inaccuracies in the spatial allocation of emissions. As mentioned previously, the overpredictions of HNO_3 are consistent with overpredicted oxidation and may be potentially related to the inaccuracies in deposition and overestimated NO emissions, since the strong model performance of NO_3^- does not indicate inaccuracies in gas-to-aerosol partitioning.

O_3 is largely overpredicted in the RCP4C and RCP8C simulations across all NH regions (NMBs of 39.8-76.0%) with greater overpredictions in East Asia and Europe compared to CONUS. The overprediction in O_3 is primarily caused by insufficient O_3 titration and underpredictions in O_3 deposition. The underprediction of O_3 titration by CESM-NCSU has been reported in previous studies on global scale (He and Zhang, 2014; He et al., 2015a) and regional scale (Zhang et al., 2016a, b) and is linked to the underprediction of surface NO_X concentrations mentioned above. The O_3 overprediction is also caused in part by inaccuracies in O_3 deposition within CESM. In particular, the stomatal and leaf resistances in the CESM model are not linked to the leaf area index, which is an oversight that results in positive O_3 biases in both the MOZART-4 and CESM models (Val Martin et al., 2013). An additional possibility for the overprediction in O_3 is excess mixing of O_3 from higher levels of the troposphere to the surface due to the relative thickness of the CESM first

model layer (~99-130 m). Despite the large overpredictions of surface O_3, TOR is generally well simulated (NMBs of ~ 12.0%, NMEs of ~17.0%, and R values of ~0.8). The zonal mean profile of TOR in the RCP4C and RCP8C simulations is well captured in the SH and lower latitudes of the NH, but largely overpredicted in the NH mid-latitudes. This is consistent with O_3 deposition as the primary cause of the overprediction, since O_3 levels and land mass are both maximized in the NH mid-latitudes. In general surface O_3 overpredictions are greater than those of HE15 due to the slightly larger NO emissions from the RCP inventories. This emission difference helps to reduce the underpredicted TOR in the SH and lower latitudes of the NH but further enhances the overprediction of NH mid-latitudes.

SO_2 is underpredicted in Europe and East Asia (NMBs of -57.4% to -29.2%). These underpredictions likely reflect either overestimations of deposition or underestimation of emissions as the strong performance of SO_4^{2-} does not indicate that the errors are arising from gas-to-particle partitioning. SO_2 in the CONUS region is largely overpredicted (NMBs of 85.4-112.0%). This large overprediction of SO_2 in CONUS and underpredictions of SO_2 in the other NH locations mirror the performance statistics of HE15, although the underpredictions in Europe and East Asia are larger and the overprediction in CONUS is reduced. These reductions in biases of SO_2 reflect both reduced total column emissions of SO_2 in the RCP inventory compared to the HE15 inventory and reduced emissions of SO_2 in the surface layer in the vertically-structured RCP emissions, which inject more SO_2 at higher altitudes. The large overpredictions of SO_2 in CONUS are attributed to uncertainties in wet deposition, measurements, and emissions in this region and the model performance has been shown to be very sensitive to changes in SO_2 emission levels (He and Zhang, 2014; He et al.,

2015a). TSO_2 levels are generally underpredicted against SCIAMACHY satellite estimates (NMBs of -42.9% to -33.7%), with large errors and poor correlations (NMEs of 96.4-98.7% and R values of ~-0.8). This poor performance against the SCIAMACHY estimates is more likely associated with uncertainties in the satellite retrievals than with the model errors as TSO_2 satellite products are relatively new and subject to very large errors and biases especially for the year 2010, which makes them relatively unsuitable for use in data assimilation systems or model validation (Fioletov et al., 2013). NH_3 concentrations in Europe are overpredicted in the RCP4C and RCP8C simulations (NMBs of 71.2-110.2%). A weaker overprediction was reported in HE15 and was attributed to uncertainties in European emissions of NH_3. It is difficult to ascertain whether or not the increased overprediction in NH_3 is related to differences in the RCP inventories compared to the HE15 inventory as the spatial allocations of NH_3 appear different in both inventories, reflected in the dipole differences of NH_3 emissions in Figures 4.4 and 4.5. Extracting the average emission differences at the monitoring site locations reveals that NH_3 emission fluxes are approximately 1.7×10^{-7} molec. cm^{-2} s^{-1} less in the RCP4.5 inventory and 5.2×10^{9} molec. cm^{-2} s^{-1} greater in the RCP8.5 inventory compared to the HE15 inventory. This difference and the greater NH_3 emissions in the RCP8.5 inventory compared to the RCP4.5 inventory explain why the RCP8C has a much greater overprediction compared to both the RCP45 and HE15 simulations. The exact cause of the overprediction in the RCP4C simulation compared to the HE15 simulation is not apparent and may simply be related to compensation effects from different emission fluxes in grid cells surrounding the monitoring sites. Overall, the simulation of trace gases in the RCP4C and RCP8C reasonably represents the conditions of

the current atmosphere within model constraints. In addition to uncertainties in emissions and deposition of these species that seem be the primary driving force for deviations from observations, the CESM-NCSU simulations use fairly coarse horizontal (~0.9°×1.25°) and vertical resolution (30 layers). The model first layer with heights of ~ 99 -130 m is also considerable deeper than most regional air quality models that range in height from 25-45m (Zhang et al., 2013). The coarse grid resolution makes the model more susceptible to numerical diffusion, which in part accounts for underpredictions of many surface gases (e.g., CO, NO_2, and SO_2) and possibly the overprediction of O_3.

SO_4^{2-}, NH_4^+, and NO_3^- concentrations are all well simulated in the RCP4C and RCP8C simulations over the CONUS and European regions with NMBs generally within the range of ± 18.0%, The exception is NH_4^+ over Europe that is moderately overpredicted (NMBs of 33.0-42.0%) in response to overpredictions of European NH_3. It is important to note that all particle speciation measurements from Europe used in this study represent a size range consistent with particulate matter with diameter less than and equal to 10 μm (PM_{10}), while chemical speciation measurements from CONUS represent a size range consistent with $PM_{2.5}$. $PM_{2.5}$ from the CESM-NCSU MAM7 module is assumed to represent all aerosols within the Aiken, accumulation, primary carbon, fine dust, and fine sea-salt modes. With the exception of primary carbon mode, these are the only modes that treat inorganic aerosol thermodynamics. The coarse dust and coarse sea-salt modes treat only irreversible condensation of H_2SO_4, NH_3, HNO_3, and HCl, which may likely lead to overestimations of these species in PM_{10} measurements (He and Zhang, 2014). These factors explain the discrepancies between particle speciation model performance in the Europe and CONUS

regions found for NH_4^+ and Cl^- which will be discussed later in this section. Errors in the simulation of SO_4^{2-}, NH_4^+, and NO_3^- are moderate (NMEs ~25-60%) and correlations are reasonably high (0.52-0.87), indicating the spatial distributions of these inorganic aerosol species are captured reasonably well. Compared to the simulations of HE15, SO_4^{2-} levels are enhanced in the RCP4C and RCP8C simulations and generally in better agreement with the observations in terms of bias. This is likely caused greater oxidation related to greater O_3 levels and NO emissions. NH_4^+ levels are comparable to those of HE15 but the bias is reduced from reduced NH_3 emissions in portions of Europe and the eastern U.S. The reduced overprediction of NH_4^+ and reduced underprediction of SO_4^{2-} both serve to reduce the overprediction of NO_3^- compared to the HE15 simulation by reducing the free NH_4^+ available to from NH_4NO_3, which considerably improves NO_3^- performance in terms of bias and error. Coarse NO_3^- concentration in Europe is likely not overpredicted due to the small bias in HNO_3 in this region.

Cl^- is simulated poorly in both the RCP4C and RCP8C simulations. Cl^- is largely overpredicted (NMBs ~450-500%) in Europe, with similar large errors. The R values are high (0.73-0.75) for Cl^-, indicating that the majority of the errors are caused by the overprediction rather than errors in spatial distribution. These overpredictions of Cl^- are likely caused by the overpredicted WSP10 in marine regions that result in excess emissions of sea-salt and also as a result of the irreversible condensation of HCl. In the CONUS region Cl^- is underpredicted (NMBs of -22.0- -25.7%) with large errors (NMEs of 94%), and poor spatial correlation (R values of 0.17-0.20). These underpredictions are likely driven by either underestimates of HCl emissions or the overprediction of HNO_3, which competes against

HCl for partitioning into the particulate phase. The Cl^- performance of the RCP4C and RCP8C simulations is comparable to that of HE15.

BC, OC, and TC concentrations in the CONUS region are all underpredicted in the RCP4C and the RCP8C simulations (NMBs of ~-25- -59%), with moderate errors (NMEs of ~34-60%), and moderate spatial correlations (R values of 0.45-0.58). OC concentrations in Europe are strongly underpredicted (NMBs of ~-82%). This strong underprediction also occurs for HOA, OOA, and TOM, compared against data from the Zhang, Q. et al. (2007) and Jimenez et al. (2009) datasets (NMBs of ~ -93% to -65%). However, despite this large bias, there are moderate correlations for OC in Europe (0.46-0.51) and a strong correlation for OOA, HOA, and TOM (0.85-0.94), indicating that the spatial pattern of these species is reasonably captured. The strong underpredictions of carbonaceous aerosols in the RCP4C and RCP8C simulations are related to not only the low emissions of BC, POC, and AVOC in the RCP inventories compared to other global inventories (Liu, X. et al., 2012; Glotfelty et al., 2014), but also because the rapid aging of BC and POA within the MAM7 aerosol module leads to very efficient wet removal compared to other global models (Liu, X. et al., 2012). The large underprediction of HOA is also linked to an overpredicted volatility of POA within the VBS treatment. The errors and R values in the CONUS region are comparable to those from the HE15 simulation but there is a significant enhancement in the underpredictions. This is partially because the RCP biomass burning emissions are distributed vertically in the RCP4C and RCP8C simulations, which reduces surface OC and BC levels compared to the HE15 simulation where all emissions are injected in the bottom model layer. The levels of BC and OC are also reduced in the RCP4C and RCP8C

simulations due to large reductions in the emissions of BC, POC, and AVOC in the RCP emission inventories throughout the CONUS region compared to the HE15 inventory. Although HE15 did not evaluate against HOA, OOA, TOM, and European OC data, the underpredictions in the RCP4C and RCP8C simulations are considerably larger than those shown in the simulations of Chapter 3, which utilize the same emission inventory as HE15. This is also attributed to the reduced POC and AVOC emissions in the RCP inventories. SOA in the CONUS region performs well against observations from the Lewondowski et al. (2013) dataset (NMBs of -15.6% to -8.1%, NMEs of ~33-34%, and R values of 0.51-0.62). This is similar to the findings in Chapter 3 from the New_OAC simulation, however, caution must be taken when comparing SOA from CESM-NCSU to Lewondowski et al., (2013), as the anthropogenic and biogenic precursors used to derive observational SOA are not identical to those that contribute to SOA in CESM-NCSU.

Total $PM_{2.5}$ is well simulated over the CONUS region (NMBs of -6.4- -11.3%, NMEs of ~34%, and R values of 0.67), while $PM_{2.5}$ in Europe is reasonably well simulated in terms of bias (NMBs of -32.1% to -9.9%) and errors (NMEs of 31.9-36.1%) but has a poor correlation (0.03-0.06). This poor correlation is similar to other chemical species in Europe and again indicates possible inaccuracies in the spatial allocation of emissions. The larger underprediction in the RCP8C simulation in Europe is due to reduced emissions of all primary particles and $PM_{2.5}$ precursors, except $NH_{3,}$ in that region compared to the RCP4.5 inventory. Based on the evaluation of the various $PM_{2.5}$ species, the underpredictions can be attributed to the large underpredictions of primary carbonaceous aerosol. These results are generally comparable to $PM_{2.5}$ in the HE15 current decadal simulation, although the

underpredictions are larger in response to greater underpredictions of carbonaceous aerosols and reduced overpredictions of inorganic aerosols. PM_{10} in the CONUS region is not well simulated (NMBs of -43.5% to -42.7%), NMEs of 51.7-55.6%, and R values of 0.05-0.17). This large inconsistency compared with the simulation of $PM_{2.5}$ suggests that coarse particles are not well simulated in the CONUS region, which is likely linked to inaccuracies in the emissions of dust and also because the inorganic aerosol thermodynamics is not treated for these particles. PM_{10} in Europe is reasonably well simulated (NMBs of -5.4 to 15.3%, NMEs of 29.5-35.5%, and R values of ~0.22) and consistent with the performance of $PM_{2.5}$. PM_{10} in East Asia is underpredicted (NMBs of ~-56%) with the majority of the errors explained by the bias. The high R values (~0.67) suggest that the spatial pattern is reasonably well captured. The underprediction of PM_{10} in East Asia likely results from either underestimations of emissions in this region or from underpredicted dust emissions from underpredicted WSP10 over land areas. Similar to $PM_{2.5}$, the simulation of PM_{10} is comparable to that of the HE15 current decadal simulation accounting for emissions differences.

4.3.3 Temporal Evaluation Trace Gases, Aerosol, and Aerosol/Cloud Interactions

Figure 4.6 shows the time series of monthly averages from the RCP4C and RCP8C simulations for $PM_{2.5}/PM_{10}$, THCHO, TNO_2, and TOR, as well as the monthly average of the trace gas satellite estimates over five stratocumulus regions of Rausch et al. (2010). Figure 4.7 compares similar time series of simulated and satellite-estimated CCN5, CDNC, AOD, and SWCF. In general, PM_{10} and $PM_{2.5}$ are comparable in both the stratocumulus regions of NAM and SAM. However, the aerosol sources are likely slightly different with the NAM

region in the vicinity of greater anthropogenic emissions originating from Mexico and the SAM region in the vicinity of greater SOA from biogenic emissions in the Amazon and greater biomass burning emissions. The stratocumulus regions of SAF and SEA have greater aerosol loadings for both PM_{10} and $PM_{2.5}$ and stronger seasonality than the other regions. The enhanced aerosol loadings originate from greater anthropogenic emissions, greater biomass burning emissions, and greater dust emissions in the vicinity of these regions as evidenced by the spatial distributions of RCP4.5 emissions and natural emissions shown in Figure 4.8. In SEA, aerosol loadings peak in the boreal spring months (i.e., March, April, and May), this corresponds to the seasonality of dust storms in East Asia that occur primarily during this season (Zhao et al., 2006). In the SAF region, there are bi-modal peaks in aerosol loading with the largest peak in the boreal winter months (i.e., December, January, and February) and a smaller peak in the boreal summer months (i.e., June, July, and August). This bimodal seasonality is related to the movement of the intertropical convergence zone (ITCZ) and its subsequent impact on African biomass burning emissions. During the boreal winter months (DJF), the ITCZ moves southward, resulting in a dry season and greater fires in the savannas below the Sahara, while during the boreal summer months (JJA) the ITCZ moves northward, resulting in a dry season and greater fire activity in the savannas of southern Africa (Cahoon et al., 1992). The peak in DJF is larger because the emissions from the savannas below the Sahara are larger in the RCP emission inventory and closer to the stratocumulus region. The AUS region represents relatively clean conditions as evidenced by the large gap between $PM_{2.5}$ and PM_{10}, since natural aerosol sources typically contribute more to the PM_{10} size range (Artinano et al., 2003). This region also has prevailing winds from the Southern Ocean,

thus anthropogenic aerosols can only originate from either shipping and aircraft emissions or limited outflow from Australia. Overall the predictions of $PM_{2.5}$ and PM_{10} between the RCP4C and RCP8C simulations are similar in most regions, except SAF where aerosol loading from the RCP4.5 are greater during the first half of the current climate period (2001-2006) but less during the latter half of the current climate period (2007-2010).

THCHO in all stratocumulus regions is generally underpredicted as shown in the annual average statistics and can be attributed to uncertainties in emissions and secondary formation of HCHO. In the NAM region, the CESM-NCSU model fails to capture the seasonality of the satellite estimates and generally oscillates with peaks during JJA that are comparable to satellite estimates and valleys during DJF that show large deviations from satellite estimates. This pattern is related to the dual ITCZ bias that is persistent in all global models included in the CMIP5 project (Oueslati and Bellon, 2015). Due to this ITCZ bias, CESM underpredicts precipitation in the NAM region during the boreal spring (MAM) and JJA periods and overestimates precipitation during the boreal autumn (i.e., September, October, and November) and DJF periods, as shown in Figure 4.9. The impact of this bias is an artificial seasonality of THCHO within CESM-NCSU due to wet removal errors. In the SAM region, the simulated THCHO is comparable to satellite estimates during the 2001-2005 period but does not capture the observed trend of increasing THCHO in the 2006-2010 period. This indicates that the model is likely failing to capture either increasing trends in biogenic emissions or biomass burning emissions during the current climate period. However, considering the proximity of the SAM stratocumulus region to the Amazon and the lack of a similar trend in AOD and CCN5 from OC and BC in satellite estimates, it is likely

that the issue is related to inaccuracies in biogenic emissions. This is consistent with findings (Holm et al., 2014), namely, the MEGAN scheme within the CESM-NCSU land model does not adequately capture the climatic and biophysical process that control biogenic emissions of isoprene in the Amazon and thus may not capture the trends in biogenic emissions of HCHO or isoprene that contribute to secondary formation of HCHO. In the SAF region, CESM-NCSU fails to capture the trend of increasing THCHO but adequately captures the seasonality of THCHO satellite estimates despite underpredicted THCHO levels. The general underprediction is likely linked to overestimated wet removal as PR is consistently overpredicted in this region and the failure to capture the trend is likely linked to errors in biogenic emissions of HCHO and isoprene, similar to the SAM region. In the SEA region, THCHO is generally comparable to satellite estimates in JJA and the boreal autumn (SON) seasons but largely underpredicted during the DJF and MAM seasons, which is related to wet removal errors from the dual ITCZ bias. In the AUS region, CESM-NCSU predicted THCHO has an inverted artificial seasonality compared to SEA and NAM, resulting from overpredicted PR in JJA and underpredicted PR in DJF. The disparity in the seasonal patterns in this region likely also suggests poor model performance from either neglecting natural marine sources of HCHO emissions from phytoplankton or underestimated shipping emissions.

The seasonal variations of TNO_2 are captured in the NAM, SEA, and AUS regions. TNO_2 is generally overpredicted in the NAM and AUS regions, which is consistent with the global statistics and likely linked to overestimated NO emissions in the vicinity of these regions. In the SEA region, the TNO_2 levels are generally consistent with satellite estimates

and generally capture the slight upward trend in TNO_2 in both the RCP4C and RCP8C simulations, however, the RCP8C simulation generally captures the seasonality of TNO_2 better than the RCP4C simulation due to higher NO emissions. In the SAF and SAM regions TNO_2 is well simulated during the JJA months but the reductions in TNO_2 levels shown in satellite estimates during the DJF months are not captured. This suggests errors in photochemistry during this period that could be potentially linked to inaccuracies in biogenic emissions of VOCs, since both regions are in close proximity to the largest sources of biogenic VOCs, and photochemistry would be most active during this period since solar radiation is at its maximum.

TOR abundance and seasonality are generally well simulated against satellite estimates in all regions, although strong deviations exist in SON. The deviations in SON do not correspond well with deviations in TNO_2, which suggests poor model performance during this period is related to model dynamics rather than chemistry. SON is the season during which the exchange of mass between the troposphere and stratosphere (STE) is the largest, with the true maximums occurring late autumn in the NH and early autumn in the SH (Skerlack et al., 2014). In the NH regions of SEA and NAM, TOR is overestimated during this period, indicating a likely overestimation of STE in the NH, while in the SH regions of SAM, SAF, and AUS, TOR is underpredicted, indicating a likely underestimation of STE. The performance in these regions, with the exception of SEA and AUS, is generally consistent with other comparisons of global model output against satellite estimates (Ziemke et al., 2006).

AOD in all five regions is well simulated in terms of magnitude and seasonality. This is especially true in the NAM, SAM, and AUS regions, with the small deviations from satellite estimates that likely result from uncertainties in sea-salt emissions. In the SAF region, AOD is mostly well simulated but peak levels in the JJA period and the increasing trend in these peaks are not captured. These peak levels in JJA occur because dust transport from North Africa towards this region occurs at higher altitudes and thus has a greater impact on AOD (Gama et al., 2015). Therefore, it is likely that the underprediction of the peak AOD and the trend are related to the too efficient wet removal process that impacts aerosols within the MAM7 model (Liu, X. et al., 2012). AOD is underpredicted in SEA, likely due to underestimates of emissions of anthropogenic PM components such as OC and BC as well as PM precursors SO_2, NO, and NH_3in the region. This finding is also consistent with the underprediction of PM_{10} in East Asia in this work and during 2005, 2006, 2011 reported in Chen et al. (2015) and Zhang et al. (2015, 2016a, b).

CCN5 is well simulated in both the NAM and SAF regions, although the JJA maximum is not fully captured in the SAF region which is similar to AOD. CCN5 is generally underpredicted in both the SEA and AUS regions mirroring the global statistics. The underpredictions in SEA are likely from underestimated anthropogenic emissions of PM components such as OC and BC as well as PM precursors SO_2, NO, and NH_3 in that region, while the underprediction in the AUS region is likely related to neglecting marine organic aerosols. In the SAM region, CCN5 is generally comparable to satellite estimates but the seasonality is not captured. This poor seasonality mirrors the poor seasonality of TNO_2 and could thus be linked to errors in photochemistry that propagate into SOA formation and

subsequently new particle formation due to the inclusion of the organic gas/sulfuric acid conucleation parameterization. CDNC is overpredicted in all regions; consistent with the global statistics, but generally the simulation in all five regions captures the seasonality of CDNC. The variabilities in MODIS-derived and the simulated CDNC are not an exact match, but the CESM-NCSU model does at least capture the increased variability in CDNC compared to other variables. The magnitude of the overprediction is the largest in both the SAF and SEA regions, with the largest deviations from satellite estimates during JJA in SAF and MAM in SEA, when dust levels are maximized. It is further evidence that the aerosol activation parameterization within CESM-NCSU overpredicts aerosol activation of insoluble aerosols. Despite the deviations from satellite estimates of CDNC, SWCF is very well simulated in terms of both magnitude and seasonality in all five stratocumulus regions. However, there is a slight overprediction of SWCF in SEA, likely because CDNC levels in the region are the largest amongst the five regions.

4.4 Projected Trends in Climate, Air Quality, and Aerosol-Cloud Interactions

4.4.1 Trends in Meteorological, Cloud, and Radiation Parameters

Figure 4.10 shows the future trends in 2-m temperature (T2), 2-m specific humidity (Q2),, precipitable water vapor (PWV), precipitation rate (PR), 10-m wind speed (WSP10), aerosol optical depth (AOD), cloud fraction (CF), cloud water path (CWP = liquid water path (LWP) + cloud ice water path (IWP)), downwelling shortwave radiation at the Earth's surface (FSDS), and outgoing longwave radiation (OLR) between the future and current decade simulations under the RCP4.5 scenario (RCP4F and RCP4C, respectively) using CESM_NCSU compared to similar trends predicted by CESM from the CMIP5 project

(CESM1-CMIP5) under RCP4.5 scenario. Figure 4.11 shows similar trends in these variables between the future and current decade simulations under the RCP8.5 scenario (RCP8F and RCP8C, respectively) compared to CESM1-CMIP5 under RCP8.5 scenario. T2 projections between CESM-NCSU and CESM1-CMIP5 differ in magnitude with CESM-NCSU projections, predicting less warming for both the RCP4.5 and RCP8.5 scenarios (global mean increases of 1.1°C and 1.6°C, respectively) compared to CESM1-CMIP5 (global mean increases of 1.5°C and 2.3°C, respectively). This reduced warming trend is due to simulated cooling by CESM-NCSU that occurs in marine regions of the SH and the North Atlantic. These discrepancies in warming estimates are likely linked to three factors including: discrepancies in ocean and sea ice initial conditions, differences in how future greenhouse gas forcing (GHGF) is prescribed, and slight inconsistencies in the current year periods between CESM1-CMIP5 and CESM-NCSU. As mentioned in Section 4.2.1, the ocean and sea ice model components in RCP4C and RCP8C simulations are initialized based on CESM's default settings, consistent with the current decadal simulations of He et al. (2015a) (HE15). This differs from the current time period initialization of all component models in CESM1-CMIP5, which are initialized based on a transient 20^{th} century simulation. Thus sea ice coverage and sea surface temperatures could differ between the current periods of CESM-NCSU and CESM1-CMIP5, even though the RCP4F and RCP8F simulations are initialized from the CESM1-CMIP5 simulations. These differences likely account for the excess cooling simulated by CESM-NCSU shown in marine regions and Antarctica in Figures 4.10-4.11. GHGF in the CESM1-CMIP5 simulations is based on globally uniform prescribed values of carbon dioxide (CO_2), methane (CH_4), nitrous oxide (N_2O), O_3, and Chlorofluorocarbons

(CFCs) volume mixing ratios, while the GHGF in the standard release of CESM with advanced chemical treatments (CAM-Chem) (Lamarque et al., 2012), and subsequently CESM-NCSU, have GHGF based on GHG lower (i.e., the lowest model layer) boundary conditions that vary by latitude and higher altitude prognostic simulations of GHG chemistry. These lower boundary conditions for GHGs give greater GHG volume mixing ratios in the northern hemisphere (NH) compared to the Southern Hemisphere (SH) for CO_2 and CH_4, which is more consistent with observed distributions of GHGs like CH_4 (Frankenberg et al., 2006). This difference is primarily responsible for the larger latitudinal gradient in temperature changes simulated by CESM-NCSU. For example, maximum cooling of 4.7°C and 3.9°C occurs in the SH for the RCP4.5 and RCP8.5 scenarios, respectively, in the CESM-NCSU simulations compared to maximum cooling of -0.3°C under the RCP4.5 scenario and minimal warming of 0.1°C under the RCP8.5 scenario in the CESM-CMIP5 simulations. CESM-NCSU predicts greater maximum warming of 10.1°C in the NH compared to 6.2°C in the CESM1-CMIP5 simulation under the RCP4.5 scenario and more comparable maximum warming of 9.2°C compared to 10.0°C in the CESM1-CMIP5 simulation under the RCP8.5 scenario. These differences could also be related to the fact that the current year period in the CESM1-CMIP5 simulations is a subset (2006-2010) of the time period in the CESM-NCSU current year simulations, since the period of 2001-2005 is considered to be part of the historical 20th century period in the CMIP5 project. However, despite these discrepancies in the sign and magnitude of the T2 projections, the spatial patterns in T2 changes predicted by CESM-NCSU and CESM1-CMIP5 are qualitatively similar with greater temperature increases over land compared to marine environments and

greater warming at higher latitudes. There is also consistency in terms of cooling as the regions that cool in the CESM-NCSU simulation generally either cool or show minimal warming in the CESM1-CMIP5 simulations. The discrepancy in T2 projections could also be a factor of the chemistry as the aerosol changes under these scenarios can impact large scale circulations, which will be illustrated in Section 4.6.

The reduced warming in the CESM-NCSU simulation results in less evapotranspiration compared the CESM1-CMIP5 simulations, resulting in smaller increases in Q2 (e.g., global mean increases of 0.4 g kg^{-1} under RCP4.5 and 0.5 g kg^{-1} under RCP8.5) and PWV (e.g., global mean increases of 1.2 mm under RCP4.5 and 1.8 mm under RCP8.5) compared to CESM1-CMIP5 (e.g., global mean increases in Q2 of 0.5 g kg^{-1} under RCP4.5 and 0.8 g kg^{-1} under RCP8.5 and global mean increases in PWV of 1.5 mm under RCP4.5 and 2.3 mm under RCP8.5). Similar to T2, the spatial patterns of the changes in Q2 and PWV are qualitatively similar to those of CESM1-NCSU despite the differences in sign and magnitude. Overall, in addition to reduced warming and moistening of the atmosphere, the inconsistencies mentioned above also result in smaller differences between the RCP4.5 and RCP8.5 scenarios in the CESM-NCSU simulations compared to CESM1-CMIP5. PR in both scenarios and by both models increases on global average by ~0.05 mm day^{-1} in the CESM-NCSU simulations and by ~0.06 mm day^{-1} under the RCP4.5 scenario and ~0.09 mm day^{-1} under the RCP8.5 scenario in the CESM1-CMIP5 simulations. Both models under both scenarios generally experience increased PR in the tropics and higher latitudes and decreased PR in the subtropics, this is a consistent pattern of climate change from both CMIP5 models and models using older IPCC AR4 scenarios (Knutti and Sedlacek, 2012). The

inconsistencies between CESM-NCSU and CESM1-CMIP5 occur largely due to reductions of PR in the SH related to the cooling and drying seen in CESM-NCSU.

Changes in WSP10 from both the CESM-NCSU and CESM1-CMIP5 simulations are highly complex under both the RCP4.5 and RCP8.5 scenarios, but some commonalities exist. Under both scenarios, WSP10 changes predicted by both models over land are minimal compared to those in marine environments. These minimal changes over land make the trend in land WSP10 difficult to distinguish, but in a general sense the magnitude and spatial extent of WSP10 reductions appear to dominate. In the marine environments, there is a general trend for increasing WSP10 in the Arctic Ocean and Southern Ocean and reduced WSP10 in the Pacific Ocean. This pattern is consistent in the simulations with both models under both scenarios and is consistent with changes in WSP10 predicted under the RCP4.5 and RCP8.5 scenarios across the different models in the CMIP5 project (Dobrynin et al., 2012).

Changes in AOD simulated by both models are similar across both scenarios in the NH with large decreases in Europe, East Asia, and eastern U.S. in response to decreases in primary aerosol emissions and emissions of most anthropogenic aerosol precursors. The changes in anthropogenic (i.e., anthropogenic VOC (AVOC), nitric oxide (NO), carbon monoxide (CO), sulfur dioxide (SO_2) ammonia (NH_3), black carbon (BC), and organic carbon (OC)) and natural (i.e., biogenic VOC (BVOC), sea-salt, and dust) emissions between the current and future periods under the RCP4.5 and RCP8.5 scenarios are shown in Figures 4.12 and 4.13, respectively. Increases are simulated by both models in South Asia under both scenarios due to enhanced emissions of primary aerosols and aerosol precursors. Larger deviations in the AOD trends between CESM-NCSU and CESM1-CMIP5 are found in the

SH. In the CESM1-CMIP5 simulations, AOD remains similar to the current period or decreases slightly over most continents in response to declining biomass burning emissions of BC and OC in Africa and South America and reduced WSP10 and greater PR in central Australia. In the CESM-NCSU simulations AOD tends to increase in SH, which is in part related to decreased PR but also likely linked to strong enhancements in secondary organic aerosol (SOA) and related new particle formation in the Congo and Amazon predicted by the updated OA treatments in CESM-NCSU and increased WSP10 leading to greater dust emissions in central Australia and South Africa. Additionally, the magnitudes of changes in AOD are larger in the CESM-NCSU (e.g., maximum differences of ~ ± 0.6) compared to CESM1-CMIP5 (e.g., maximum differences of ~ ± 0.2), which is likely related to more advanced chemistry mentioned in Section 4.2.1.

Both models simulate decreases in CF on global average across both scenarios. Under the RCP4.5 scenario, the simulated decrease in CF is less by CESM-NCSU (~0.06%) compared to CESM1-CMIP5 (~28%). This discrepancy is related to the cooling in the SH that results in greater saturation and greater warming in the Arctic, leading to greater availability of water vapor to form clouds. Under the RCP8.5 scenario, the decreases in CF between both models are similar (~33% in CESM-NCSU and ~37% in CESM1-CMIP5). These findings are consistent with other CMIP5 model projections that showed declines in CF due to decreases in low and mid-level clouds resulting from greater vertical ascent related to increasing temperatures, with this effect maximized over land due to the greater increase in temperatures (Zelinka et al., 2013). CWP increases in both CESM-NCSU simulations (e.g., global mean increases of 0.1 g m^{-2} under RCP4.5 and 0.6 g m^{-2} under RCP8.5), unlike

CESM1-CMIP5 that experiences a general decrease under the RCP4.5 scenario (-0.5 g m^{-2}) and a small increase under the RCP8.5 scenario (0.1 g m^{-2}). The increased trend in CWP in CESM-NCSU is likely related to greater increases in CF in the Arctic and Southern Ocean and generally greater aerosol levels compared to CESM1-CMIP5. However, there are several commonalities between the two models under both scenarios including reduced CWP in East Asia, Europe, eastern U.S., southern Africa, and South America and increases of CWP in South Asia. These changes in CWP are mostly related to changes in CF in these regions but also mirror changes in AOD in NH, indicating that reductions in CWP in Europe, North America, and East Asia are caused by reduced formation of cloud droplets from reduced aerosol levels.

FSDS is reduced on global average by both models under both scenarios. Reductions are larger in CESM-NCSU (e.g., global mean reductions of 1.1 W m^{-2} under the RCP4.5 scenario and 2.1 W m^{-2} under the RCP8.5 scenario) compared to CESM1-CMIP5 (e.g., global mean reductions of 0.3 W m^{-2} under the RCP4.5 scenario and 1.0 W m^{-2} under the RCP8.5 scenario). The greater diming in CESM-NCSU is caused by the greater cloud formation in the Arctic and Southern Ocean and greater increases in AOD levels across the SH compared to CESM1-CMIP5. Despite these differences, the simulated spatial patterns of the trends in FSDS by both models match well with the simulated spatial patterns of the trends in AOD and CWP under both scenarios. Increasing FSDS over many land areas is in response to reductions in the strength of the aerosol direct and indirect effects from reduced emissions and reduced cloud formation. OLR is projected to increase in the future in response to greater warming with greater increases in CESM1-CMIP5 (e.g., global mean

reductions of 1.9 W m^{-2} under the RCP4.5 scenario and 2.3 W m^{-2} under the RCP8.5 scenario) compared to CESM-NCSU (e.g., global mean reductions of 0.6 W m^{-2} under the RCP4.5 scenario and 0.8 W m^{-2} under the RCP8.5 scenario). These differences are largely attributed to the cooling in the SH from differences in GHGF and ocean initial conditions between the simulations and also differences in trends in CF over in the tropics. Changes in OLR are generally consistent across the NH. Overall, the trends in radiation, cloud, aerosol, and meteorological parameters are comparable between CESM-NCSU and CESM1-CMIP5 and consistent with predictions of other CMIP5 models and thus can generally be considered representative of these climate policy scenarios.

4.4.2 Trends in Trace Gases

Figure 4.14 shows absolute differences in trace gas levels of total non-methane volatile organic compound (TNMVOC), NO_2, SO_2, NH_3, nitric acid (HNO_3), O_3, CO, hydroxyl radical (OH), hydroperoxy radical (HO_2), and hydrogen peroxide (H_2O_2) between the RCP4F and RCP4C simulations, as well as between the RCP8F and RCP8C simulations. Changes in TNMVOC, NO_2, SO_2, and NH_3 largely follow the trends in their emissions, or the emissions of NO in the case of NO_2. Figure 4.12 shows the absolute difference in emissions between the current and future periods under the RCP4.5 scenario for AVOC, NO, SO_2, NH_3, CO, BVOC, BC, OC, sea-salt, and dust. Figure 4.13 shows the trends in these species under the RCP8.5 scenario. TNMVOC levels increase with global average increases of 0.3 ppb and 0.7 ppb under the RCP4.5 and RCP8.5 scenarios, respectively. Increases are larger under the RCP8.5 scenario because the magnitude of the decrease in AVOC emissions in North America, Europe, and East Asia is less under the RCP8.5 scenario compared to the

decrease under the RCP4.5 scenario. AVOC emissions in tropical regions and the SH increase under the RCP8.5 scenario but decrease under RCP4.5 scenario, and BVOC emissions are larger under the RCP8.5 scenario compared to the RCP4.5 scenario. The greater enhancement in BVOC emissions is the result of greater warming in the RCP8.5 scenario compared to the RCP4.5 scenario, which is a consistent result for changes in BVOC emissions between both scenarios from the ACCMIP ensemble of models (Young et al., 2013). In general, the spatial distribution indicates that the enhanced BVOC emissions from warmer temperatures and greater FSDS over the continents will dominate the decreases in AVOC during the future decadal period. This is especially true in North America.

NO_2 levels decline on global average under both scenarios, with greater declines in the RCP4.5 scenario (~0.1 ppb) compared to the RCP8.5 (~0.06 ppb). NO_2 levels increase in South Asia and Africa, decrease in North America, East Asia, and Europe, and remain similar in the many other regions. This is a recurring pattern for the anthropogenic emissions and subsequently the atmospheric concentrations of many species in the RCP emission inventories by 2050. However, it is interesting to note that the increase in NO_2 is larger under the RCP4.5 scenario compared to the RCP8.5 scenario in response to greater increases in emissions in South Asia following RCP4.5. Changes in SO_2 levels follow a similar pattern as NO_2, with greater decreases under the RCP4.5 scenario (0.15 ppb) compared to those under the RCP8.5 scenario (0.08 ppb). This is in response to greater emission reductions across the NH under the RCP4.5 scenario and also greater increases in SO_2 emissions in South Asia under the RCP8.5 scenario. Unlike other inorganic gas species, NH_3 levels increase on global average under both scenarios due to increases in agricultural activities

(Riahi et al., 2011; Thomson et al., 2011), with greater increases under the RCP8.5 scenario (~0.2 ppb) compared to those under the RCP4.5 scenario (~0.1 ppb), resulting from larger emission increases under the RCP8.5 scenario. HNO_3 levels decrease on global average in both scenarios with greater decreases under RCP4.5 (0.04 ppb) compared to RCP8.5 (0.03 ppb). The primary cause of this reduction is the reductions in NO emissions. These decreased NO emissions reduce the levels of most oxidized nitrogen gas species including NO, NO_2, nitrate radical (NO_3g), N_2O_5, and organic nitrates, thus limiting the source species of HNO_3. However, there are also decreases in OH, which further limit HNO_3 formation resulted from the oxidation of NO_2 and organic nitrates, and reductions in aerosol levels that reduce the rates of heterogeneous reactions forming HNO_3 from N_2O_5 and NO_3g.

The O_3 mixing ratio decreases on global average under the RCP4.5 scenario by 1.4 ppb but increases on global average by 2.3 ppb under the RCP8.5 scenario. These differences in O_3 mixing ratio between these scenarios are consistent with future trends in surface O_3 from the ACCMIP model ensemble (Young et al., 2013) as well as the work of Kim et al. (2015) that predicted a global average decrease of 3.7 ppb under RCP4.5 and an increase of 2.1 ppb under RCP8.5 by 2050 using a version of GEOS-Chem driven by CESM. In both the RCP4.5 and RCP8.5 scenarios, NO emissions decline making the differences in future O_3 predictions slightly counter intuitive. In order to better understand these differences, Figure 4.15 shows the absolute difference in O_3, OH, and CO surface layer chemical production and net chemical production (production – loss) between the current and future periods for both the RCP4.5 and RCP8.5 scenarios. The decreases of O_3 mixing ratios under the RCP4.5 scenario in many of the models in the ACCMIP project are primarily attributed to reductions

in precursor NO and AVOC emissions (Young et al., 2013), which lead to a global average reduction in O_3 production. This is consistent with the global mean reduction in O_3 production (-1.7×10^{-2} ppb s^{-1}) shown under this scenario in Figure 4.15. However, the net chemical production (NCP) of O_3 under the RCP4.5 scenario is positive and increases on global average by 1.2×10^{-4} ppb s^{-1}. In South Asia and Africa the increases in NCP of O_3 are related to the increase in absolute production from greater precursor emissions, while the increases shown in eastern U.S., eastern China, and Europe are linked to strong decreases in O_3 chemical loss. These decreases are caused by reduced titration from reduced NO levels, less loss from the oxidation of AVOC, and less O_3 consumption from heterogeneous oxidation of SO_2 on the surface of aerosol due to reduced SO_2 and aerosol levels. The increased NCP of O_3 indicates that additional causes beyond chemistry result in the declining surface O_3 levels. The most likely cause is the increases in O_3 deposition in the future climate or reductions in production aloft. The enhanced O_3 deposition is not apparent in O_3 deposition flux differences shown in Figure 4.20 because the flux is a function of the O_3 concentration, except over the Arctic region where the O_3 deposition is enhanced despite a declining O_3 level. Increased O_3 deposition during the future period results from weaker aerodynamic resistances because of reduced wind speeds over land, general increases in planetary boundary layer height (PBLH) over land, and reductions in snow cover that have been shown to increase dry deposition (Andersson and Engardt, 2010).

Under the RCP8.5 scenario, the spatial extent of the reductions in NO emissions is less compared to the RCP4.5 scenario and the increases in background emissions from shipping and aviation are larger. Additionally, TNMVOC levels, temperatures, and CH_4

levels increase substantially in the RCP8F simulation, all of which result in a global mean increase in O_3 production (3.2×10^{-3} ppb s^{-1}) under the RCP8.5 scenario. The increase in CH_4 under the RCP8.5 scenario is especially large (~56.4%) compared to the RCP4.5 scenario (~4.7%). This contributes to the increased O_3 production by both enhancing O_3 production rates through warming (since CH_4 has a strong greenhouse effect), and by enhancing the conversion of NO to NO_2 which further enhances O_3 levels. This impact from CH_4 has been shown to contribute significantly to increases in O_3 in the RCP8.5 scenario compared to the RCP4.5 scenario on both the global and regional scales (Gao et al., 2013; Young et al., 2013). Under the RCP8.5 scenario, there is a reduction in surface OH, which may lead to reduced destruction of O_3 despite increases in TNMVOC and HO_2. This in addition to enhanced production leads to greater global average increase in NCP of O_3 (1.6×10^{-4} ppb s^{-1}) under the RCP8.5 scenario. Additionally, previous model simulations have shown that this increase in O_3 under the RCP8.5 scenario may be enhanced by greater troposphere and stratosphere (STE) due to a greater strengthening of the Brewer-Dobson Circulation from greater warming (Young et al., 2013).

In addition to changes in O_3 production and destruction it is also important to examine the impact of changing chemical regimes. Figure 4.16 in the supplementary material shows the changes in NO_x-VOC limited regimes under both the RCP4.5 and RCP8.5 scenarios using two different photochemical indicators suggested by Zhang et al. (2009). These photochemical indicators include the mixing ratio of $NO_{y,}$ which indicates a transition to VOC limited conditions when the NO_y level is less than or equal to 5.0 ppb, and the O_3/NO_y ratio which indicates a transition to VOC limited conditions when the value exceeds

15.0. These two indicators were found to be the most robust during a comparison of photochemical indicators from several regional online coupled air quality models as part of the Air Quality Model Evaluation International Initiative phase II (Campbell et al., 2015). Generally, both the RCP4.5 and RCP8.5 scenarios are dominated by a transition from VOC-limited conditions during the current period to NO_x-limited conditions in the future period over most of the NH industrial zones of the eastern U.S., Europe, and East Asia. While transitions from NO_x-limited conditions in the current period to VOC-limited conditions in the future period occur in some portions of South Asia and central Africa. Both indicators show similar changes under both RCP scenarios. The largest differences between scenarios occur in Asia. In East Asia there is not as strong a transition to NO_x-limited conditions in the future period under the RCP8.5 scenario. This is a result of smaller decreases in East Asian NO emissions under the RCP8.5 scenario. In South Asia there is a stronger transition to VOC-limited conditions under the RCP4.5 scenario, as a result of greater increases in South Asian NO emissions under the RCP4.5 scenario. Based on this analysis, it would seem the other factors mentioned earlier in this section have a much stronger impact on the global disparity in O_3 projections than chemical regime change, but it may still be important at the regional or smaller scales as indicated by Yahya et al. (2016).

Surface OH levels decline under both scenarios with a greater global average decrease under the RCP8.5 scenario (6.3×10^{-3} ppt) compared to the RCP4.5 scenario (1.8×10^{-3} ppt). Under the RCP4.5 scenario, OH production from the O_3 destruction by HO_2 and the reaction of water vapor with singlet oxygen (O^1D) formed through O_3 photolysis is reduced in East Asia, the U.S., South America, and Europe in response to decreased O_3

levels. OH production is enhanced in South Asia and Africa from increased O_3 levels due to the same processes. The change in NCP of OH is a global average increase (2.1×10^{-9} ppb s^{-1}) due to reductions in OH loss from the oxidation of SO_2, O_3, nitrogen species, and AVOCs. However, there are decreases in NCP of OH in regions with large ambient OH levels including the mountainous regions of western North America, the Tibetan Plateau, western South America, and northern and southern Africa, likely resulting from increases in BVOC levels which consume more OH. These decreases in NCP of OH are co-located with the largest decreases in surface OH levels and contribute to the global average surface OH reduction. Changes in OH in the RCP8.5 scenario are more complex. Under this scenario, there is both greater OH production and greater NCP of OH from greater O_3 levels and reductions in other species oxidized by OH, but surface OH levels decrease more than those under the RCP4.5 scenario. In both the RCP8C and RCP8F simulations, the NCP of OH is negative from the surface to roughly 936 hPa because the ambient trace gas and aerosol levels are relatively large due to surface emissions. In the region of the atmosphere from roughly 936 hPa to 760 hPa, the NCP of OH becomes positive because the levels of most species that destroy OH through oxidation decline and OH precursors (e.g., O and O_3) increase or remain elevated. Thus there is a pool of OH in this region of the atmosphere that can be mixed to the surface, especially in the tropical and subtropical marine environments. Under the RCP8.5 scenario there is greater diming of FSDS and reductions in PBLH in these regions from greater cloud formation that results in weaker vertical motion. This reduces mixing between the elevated region of large OH production and the lower region of OH loss. The net result is a compensation of the increase in the NCP of OH by the reduced mixing that

results in decreased surface OH levels. Reduced OH levels under the RCP8.5 scenario are consistent with decreases in OH burden from the ACCMIP ensemble of models (Voulgarakis et al., 2013).

Under both scenarios, the HO_2 and H_2O_2 levels increase on global average with larger increases under RCP8.5 (e.g., 0.46 ppt increase in HO_2 and 0.11 ppb increase in H_2O_2) compared to RCP4.5 (e.g., 0.16 ppt increase in HO_2 and 0.02 ppb increase in H_2O_2). The increase in HO_2 levels is likely from greater oxidation of TNMVOC, especially BVOC from enhanced BVOC emissions, and CH_4 under both scenarios. The increased levels of TNMVOC, CH_4, OH production, and O_3 under the RCP8.5 scenario relative to the RCP4.5 scenario explain the larger increase in HO_2 levels. H_2O_2 levels increase in a similar manner since HO_2 is one of the primary precursors of H_2O_2. Increases in H_2O_2 over land may also be related to reductions in aqueous chemistry from reduced LWP and SO_2 levels. This may also explain the further continental enhancement of HO_2 since HO_2 and H_2O_2 are connected by cyclical chemical reactions.

Similar to O_3, CO levels increase on global average under the RCP8.5 scenario (18.3 ppb) and decrease under RCP4.5 (-4.6 ppb). Under both scenarios, CO emissions decrease in almost all regions except South Asia and Africa, however, the magnitude and spatial extent of the CO emission reductions over land are reduced under the RCP8.5 scenario. Additionally, shipping emissions in the marine environments are projected to increase by ~30-40% under the RCP8.5 scenario compared to ~10-20% under the RCP4.5 scenario. Chemical production and the NCP of CO increase under both scenarios. However, chemical production of CO is much higher in the RCP8.5 scenario (1.4×10^{-4} ppb s^{-1}) compared to the

(3.5×10^{-5} ppb s^{-1}) because of greater formation from the oxidation of TNMVOC and CH_4. The NCP of CO between both scenarios is similar, although the magnitude is larger under the RCP8.5 scenario. The culmination of these factors explain the increase in CO under the RCP8.5 scenario where the enhanced shipping emissions and greater chemical production of CO lead to greater background levels of CO even though CO declines in industrial regions from reduced anthropogenic emissions. Under the RCP4.5 scenario chemical production of CO and increases in shipping emissions are less, allowing decreases in anthropogenic CO emissions to dominate the change in CO levels.

4.4.3 Trends in Aerosols

Figure 4.17 shows the tends in surface concentrations of individual aerosol species of sulfate (SO_4^{2-}), ammonium (NH_4^+), nitrate (NO_3^-), dust, sodium (Na^+), chloride (Cl^-), BC, PM, oxidized POA (SVOA), and SOA under the RCP4.5 and RCP8.5 scenarios. Figure 4.18 shows the total change in $PM_{2.5}$ and PM_{10} under these scenarios. Changes in SO_4^{2-} levels are dominated by changes in the emissions of SO_2 with decreases across Europe, East Asia, and North America under both scenarios and increase in South Asia and central Africa, with weaker decreases and stronger enhancements under the RCP8.5 scenario. The result is a global average decrease in SO_4^{2-} in both scenarios (e.g., -0.3 μg m^{-3} under RCP4.5 and -0.2 μg m^{-3} under RCP8.5). NH_4^+ levels follow a similar pattern to those of SO_4^{2-} despite increases in NH_3 levels in order to reach thermodynamic equilibrium with the reduced sulfuric acid (H_2SO_4) and nitric acid (HNO_3) levels. This leads to global average decreases in the NH_4^+ level by 0.06 μg m^{-3} under the RCP4.5 scenario and 0.03 μg m^{-3} under the RCP8.5 scenario. Changes in NO_3^- concentrations mirror those of SO_4^{2-} and NH_4^+ with the exception

of enhanced NO_3^- in the Middle East under both scenarios and southeastern China under the RCP8.5 scenario. The increases in the Middle East are related to increased HNO_3 levels, while the increase over southeastern China is likely a nonlinear effect of the reduced SO_4^{2-} allowing for more NO_3^- formation as described in Zhang et al. (2000) and Yu et al. (2005), since changes in meteorology and HNO_3 do not support this enhancement. The net result is a global average decrease in NO_3^- of 0.01 μg m^{-3} under the RCP4.5 scenario and a global average increase in NO_3^- of 0.02 under the RCP8.5 scenario.

The global level of dust decreases under both scenarios but with greater decreases under the RCP4.5 scenario (1.4 μg m^{-3}) compared to the RCP8.5 scenario (0.3 μg m^{-3}). The declining trend of dust levels in both scenarios is driven by decreases in WSP10 over land areas but especially in the dust emission source regions of North Africa, the Middle East, and East Asia. Dust concentrations and emissions in South Africa, Australia, and Patagonia increase under both scenarios in response to enhanced WSP10 in these regions. The weaker reduction in dust levels under the RCP8.5 scenario is due to greater complexity in the changes of WSP10 in the dust source regions of North Africa, the Middle East, and East Asia, leading to smaller reductions in dust emissions and some compensating increases in dust emissions. Na^+ and Cl^- concentrations both increase similarly on global average under both the RCP4.5 (e.g., 0.21 μg m^{-3} and 0.34 μg m^{-3}, respectively) and RCP8.5 scenarios (e.g., 0.24 μg m^{-3} and 0.37 μg m^{-3}, respectively) in response to greater emissions from the enhancements of marine WSP10. It is also interesting to note that sea-salt levels in the Arctic increase by up to 677% in response to greater emissions from sea ice retreat.

BC and primary organic matter (POM) both experience similar trends as other anthropogenic species with increases in South Asia and Africa and decreases in other regions. The only exception is an increase in POM over northern sections of North America and Asia under the RCP4.5 scenario in response to increases in biomass burring emissions. The global average decrease in BC concentrations is greater under the RCP8.5 scenario (1.6×10^{-2} μg m^{-3}) compared to that under the RCP4.5 scenario (1.2×10^{-2} μg m^{-3}) in response to greater emission increases in Africa and South Asia and smaller maximum reductions in the NH under the RCP4.5 scenario. The opposing trend exists for POM with a greater global average reduction of 2.2×10^{-2} μg m^{-3} under the RCP4.5 scenario compared to a global average reduction of 1.3×10^{-2} μg m^{-3} under the RCP8.5 scenario. This is in response to smaller reductions in SH biomass burning emissions and little change in emissions in North America under the RCP8.5 scenario. The changes in POM are also reflected in SVOA with a greater global average reduction under the RCP4.5 scenario (2.1×10^{-2} μg m^{-3}) compared to the RCP8.5 scenario (1.3×10^{-2} μg m^{-3}). This is related to the differences in OC emissions but may also be related to decreases in OH production in the RCP4.5 scenario that limits the aging of SVOCs.

SOA increases under both scenarios with a greater increase under the RCP8.5 scenario (7.8×10^{-2} μg m^{-3}) compared to those under the RCP4.5 scenario (3.0×10^{-2} μg m^{-3}). The spatial patterns in SOA changes are quite different between both scenarios. Under the RCP4.5 scenario, SOA enhancements of up to 5.1 μg m^{-3} occur in South Asia and central Africa. SOA is increased in these regions in response to increased O_3 levels that lead to

greater formation of condensable organic vapors from greater VOC oxidation and greater OH production, the latter enhances not only VOC oxidation but also photochemical aging of these organic vapors, leading to a reduction in volatility. There are also large enhancements in AVOC levels in South Asia and BVOC levels in central Africa that contribute to these enhancements. Minor increases in SOA exist over the Amazon (0.25-1.0 μg m^{-3}) in response to greater BVOC emissions but larger decreases in SOA of greater than 2.5 μg m^{-3} occur in central South America. The small increases and decreases in South America result from reductions in AVOC emissions, O_3 levels, and OH production. These factors also contribute to the reductions of up to 11.2 μg m^{-3} for SOA in Indonesia and East Asia. Under the RCP8.5 scenario, SOA levels are enhanced up to 6.4 μg m^{-3} in Africa, South America, South Asia, and East Asia. The nearly global enhancement in SOA under this scenario is related to the global enhancements of O_3, OH production, BVOC emissions, and enhanced AVOC emissions in the SH. Overall, the changes in both scenarios indicate that changes in oxidant levels have a stronger impact on SOA changes than changes in TNMVOC levels. This is especially true in East Asia where SOA levels increase under the RCP8.5 scenario despite decreases in TNMVOC levels.

The net impact from changes in all these species is global average decreases in $PM_{2.5}$ under both scenarios with a greater decrease under the RCP4.5 scenario (-0.7 μg m^{-3}) compared to the RCP8.5 scenario (-0.2 μg m^{-3}). The smaller decrease under the RCP8.5 scenario results from smaller decreases in the concentrations of most of the aforementioned species and greater increases in SOA. PM_{10} levels decrease on global average under the RCP4.5 (-1.2 μg m^{-3}) scenario but increase under the RCP8.5 scenario (0.2 μg m^{-3}). This is

related to the changes in $PM_{2.5}$ but the greater enhancements in PM_{10} under the RCP8.5 scenario result from greater increases in sea-salt emissions and weaker reductions in dust emissions.

4.4.4 Trends in Chemical Deposition

Figure 4.19 shows changes in total deposition of O_3, nitrogen, oxidized sulfur (SO_x) and BC, as well as the percentage of oxidized nitrogen, organic nitrogen, and reduced nitrogen that comprise total nitrogen deposition under the RCP4.5 and RCP8.5 scenarios. The changes in O_3 deposition under both scenarios largely mirror the changes in surface O_3 levels except in the Arctic regions under the RCP4.5 scenario, where O_3 deposition increases despite decreases in surface O_3 levels. The O_3 deposition decreases on global average under the RCP4.5 scenario by 1.1×10^{-12} kg m^{-2} s^{-1} and increases on global average by 3.8×10-12 kg m^{-2} s^{-1} under the RCP8.5 scenario. As mentioned in Section 4.4.1, the enhancements in Arctic O_3 deposition are likely linked to reduced snow cover since greater WSP10 and PBLH in this region would favor reduced deposition. Under both scenarios, O_3 deposition is enhanced in South Asia and central Africa, which indicates regardless of scenario there may be enhanced crop damage in these regions from greater O_3 deposition. The enhanced O_3 deposition over much of the globe under the RCP8.5 scenario may also result in greater ecological stress and thus underscores the importance of carbon control policies as well as emission control policies for climate mitigation and air pollution improvement. This is because the large increases in CH_4 under the RCP8.5 scenario result in greater climate change from greater warming, degradation of air quality from increases in O_3, and greater ecological stress from increases in O_3 deposition.

Nitrogen deposition (ND) from CESM-NCSU is defined as the sum of nitrogen deposited from the dry and wet deposition of NO, NO_2, peroxynitric acid (HO_2NO_2), HNO_3, NH_3, NO_3^-, NH_4^+, Peroxyacetylnitrate, and organic nitrates. ND decreases on global average (-2.1×10^{-13} kg m^{-2} s^{-1}) under the RCP4.5 scenario but increases (3.2×10^{-13} kg m^{-2} s^{-1}) under the RCP8.5 scenario. ND largely decreases under the RCP4.5 scenario in all regions except central Africa and South Asia in response to decreases in NO emissions that limit the formation of many oxidized nitrogen species. ND deposition is enhanced in almost all regions under the RCP8.5 scenario except the industrial regions of East Asia, northern Europe, and the western and eastern coasts of North America. This large increase in ND results from both smaller reductions in NO emissions that lead to smaller reductions in oxidized nitrogen species and greater increases in NH_3 emissions and concentrations that lead to greater deposition of reduced nitrogen species. This further indicates that the greater emission controls of the RCP4.5 scenario would be beneficial for ecosystem health as the enhancements in ND under the RCP8.5 scenario could lead to greater ecosystem stress, since 10.1% of current period ecosystems are exposed to ND greater the critical load estimated to cause ecological stress (Dentener et al., 2006).

The change in the source of ND is also explored by examining the changes in the percentage of ND from inorganic oxidized nitrogen (INON) species (NO, NO_2, HO_2NO_2, HNO_3, and NO_3^-), organic nitrogen (ON) species (Peroxyacetylnitrate and organic nitrates), and reduced nitrogen (RN) species (NH_3 +NH_4^+). Under both the RCP4.5 and RCP8.5 the percentage of INON deposition decreases due to reductions in projected NO emissions, with a greater global average reduction of 9.6% under the RCP8.5 scenario compared to the

RCP4.5 scenario reduction of 7.7%. Conversely, the amount of RN in the total ND increases under both scenarios with global average increases of 4.8% and 7.5% under the RCP4.5 and RCP8.5 scenarios, respectively. The increase in the relative amount of RN occurs largely in the interiors of continents in response to increases in future NH_3 emissions, with increases of ~30-40% occurring in North America, East Asia, and Europe. There are also increases in the relative amount of ON by 2.9% and 2.1% on global average following the RCP4.5 and RCP8.5 scenarios, respectively. The increases in the ON percentage is smaller in magnitude under the RCP8.5 scenario because increases in NH_3 emissions are much larger allowing this change to dominate, especially in regions like South America, where increases in the relative amount of RN lead to decreases in the relative amount of ON. Overall, ON amounts appear to increase more in remote regions of continents and the Arctic compared to continental interiors, indicating that ON deposition will increase and replace INON far from source regions and RN will replace INON more closer to populated areas.

BC deposition decreases in both the RCP4.5 and RCP8.5 scenarios in response to reductions in BC concentrations and emissions. The reduction in global average BC deposition is greater under the RCP8.5 scenario (-4.1×10^{-13} kg m^{-2} s^{-1}) compared to the RCP4.5 scenario (-2.0×10^{-13} kg m^{-2} s^{-1}) mirroring the trend in surface BC concentration in Section 2.3. These global reductions in BC deposition likely indicate a reduction in the snow albedo feedback (Warren and Wiscombe, 1980; Clarke and Noone, 1985) from BC in the future under both RCP scenarios. However, increases in BC deposition in South Asia including minor increases over the Tibetan Plateau may impact the snow melt of this region and thus have an impact on the region's water supply (Qian et al., 2011).

SO_x deposition ($SO_x = SO_2 + SO_4^{2-}$) decreases under both the RCP4.5 and RCP8,5 scenarios by 3.2×10^{-12} kg m^{-2} s^{-1} and 2.1×10^{-12} kg m^{-2} s^{-1}, respectively. The largest decreases in both scenarios occur in the eastern U.S., Mexico, East Asia, and Europe. This decrease is in response to decreasing SO_2 emissions in both scenarios. This implies that many of the industrial regions of the NH will be less susceptible to damage from acid deposition under these climate policy scenarios. There are areas of increasing SO_x deposition in both South Asia and central Africa under both the RCP4.5 and RCP8.5 scenarios in response to increasing SO_2 emissions with larger increases in South Asia under the RCP8.5 scenario (e.g., 1.0×10^{-11}- 1.6×10^{-10} kg m^{-2} s^{-1}) compared to the RCP4.5 scenario (general less than 1.0×10^{-11} kg m^{-2} s^{-1}). As a result both central Africa and South Asia will likely experience greater negative effects from acid deposition, especially following the RCP8.5 scenario by 2050.

4.4.5 Trends in Aerosol-Cloud Interactions

Figure 4.20 shows the differences in CCN5, CDNC, COT, and SWCF between the current and Future periods under the RCP4.5 and RCP8.5 scenarios. Reduced aerosol loadings from reduced emissions in both climate policy scenarios result in global average reductions in CCN5 with a greater reduction under RCP4.5 (-1.8×10^{7} cm^{-2}) compared to RCP8.5 (-8.4×10^{6} cm^{-2}). The smaller reductions in CCN5 under the RCP8.5 scenario are related to the smaller reduction in $PM_{2.5}$ and PM_{10} under this scenario but are also likely linked to smaller reductions in new particle formation, since the organic conucleation treatment in CESM-NCSU could compensate some of the reductions in H_2SO_4 levels due to higher SVOC levels from larger O_3 and OH production. Despite the smaller reductions in

CCN5 under the RCP8.5 scenario, the global average reductions in warm cloud CDNC are similar with global average reductions of 11.9 cm^{-3} under the RCP4.5 scenario and 11.6 cm^{-3} under the RCP8.5 scenario. The changes in CDNC are similar under both scenarios because, in addition to reduced aerosol loading, there is reduced cloud formation over the continents under both scenarios as discussed in Section 4.4.1. This reduces the ability of aerosols to activate, resulting in decreased CDNC regardless of changes in CCN5 levels. An example of this is South America under the RCP8.5 scenario, where CCN5 levels increase from increasing SOA but CDNC still decreases due to reduced CF. However, there is a possible inconsistency between the current and future simulations since the definition of "warm cloud CDNC" (defined as clouds between 960-850 mb from current decade simulation) may change for future years due to warmer temperatures and greater cloud heights.

COT declines on global average under the RCP4.5 scenario by ~0.04 but increases under the RCP8.5 scenario by ~0.10. Under both scenarios, COT is generally reduced over land, especially in Europe, East Asia, North America, and South America. These reductions largely result from reduced CF and CWP. However, the reductions in COT over Europe, East Asia, and eastern North America are enhanced via reduced CDNC from reduced aerosol loadings. Under both scenarios, COT is enhanced over the South Asia, Africa, the Arctic, the Southern Ocean, and the southern Pacific Ocean. Enhancements in South Asia and Africa are related to increases in aerosol loadings from enhanced emissions. Enhancements over the Arctic are largely result from increased cloud formation from the increased warming and evapotranspiration. Enhancements in the Southern Ocean are large related to increases in sea-salt aerosol from enhanced WSP10, while the enhancements in the southern Pacific Ocean

result from a combination of enhanced sea-salt and enhanced cloud formation. The global average increase under RCP8.5 occurs because cloud formation in the Arctic, sea-salt increases, and aerosol loading in South Asia and Africa are larger under this scenario and compensate the largely continental decreases.

SWCF is increased under both scenarios with a smaller increase of 0.4 W m^{-2} under the RCP4.5 scenario compared to an increase of 0.5 W m^{-2} under the RCP8.5 scenario. SWCF increases are dominant in both scenarios because the increase in COT over the Arctic and the oceans results in much stronger scattering compared to the reductions over the continents. This is especially true along the Arctic Ocean coastlines where increases in CF and CWP and relative increases in sea-salt are the largest, resulting in increases of 18-31 W m^{-2} in SWCF. Increases in SWCF over South Asia and Africa from enhanced aerosol loadings are much smaller (less than 9.0 W m^{-2}) and may also be partially related to enhanced cloud formation in these regions. SWCF is enhanced under the RCP8.5 scenario because of greater cloud formation in the Arctic. This enhanced SWCF in both scenarios causes the global average diming of FSDS discussed in Section 4.4.1.

4.5 Impact of Climate Change on Air Quality

In this study the impact of climate change on future air quality is examined following the RCP4.5 scenario. Figure 4.21 shows the absolute changes in CO, O_3, $PM_{2.5}$, PM_{10}, $PM_{2.5}$ (no dust), PM_{10} (no dust), dust, biogenic SOA (BSOA), SO_4^{2-}, and Na^+ between the RCP4F_GHGF and RCP4C simulations. CO increases globally with a 7.5 ppb on global average. This increase in CO is in response to both increases in CO biogenic emissions but also secondary formation from the increase in biogenic VOCs. The CESM-NCSU model

predicts an increase in surface O_3 of 0.3 ppb on global average due to climate change under the RCP4.5 scenario. This differs from the findings of both Dentener et al. (2006) and Doherty et al. (2013), that found decreases in surface O_3 in response to climate change from enhanced removal of excited atomic oxygen (O^1D) due to increases in the future water vapor level.

In the CESM-NCSU simulation O_3 is reduced in the tropics and the Arctic by up 4.7 ppb. While it is possible that these reductions in O_3 are caused by the increased water vapor level, it is more likely that the reductions in FSDS from increased cloud formation in these regions leads to the reduction in O_3. The increases in O_3 predicted by CESM-NCSU also do not follow similar patterns in previous studies, where O_3 increases from climate change largely occur in regions with high NO_x levels (Doherty et al., 2013). Instead the increases tend to occur in latitudinal bands ranging from approximately 10ºS to 30ºS in the SH and 20ºN to 50ºN in the NH. These areas do include industrialized regions like Asia, Europe, and North America, therefore increases in O_3 formation from increased temperatures in high NO_x conditions cannot be ruled out as a possible contributor to the increases in O_3. There may also be additional regional enhancements from meteorological changes as regions such as the eastern U.S. and Europe have the stronger increases in O_3 corresponding to increases in FSDS (not shown) and reductions in WSP10 that would both lead to enhancements in surface O_3. However, the most likely reason for increases in O_3 predicted by CESM-NCSU is increases STE of O_3 over these regions. Figure 4.22 shows the absolute difference in the zonal mean vertical cross section of O_3 between the RCP4F_GHGF and RCP4C simulations. This figure shows increases in O_3 descending from the upper atmosphere over the latitude

bands that experience increases in surface O_3. This increase in STE of O_3 is likely linked to the strengthening of the Brewer-Dobson circulation that has been projected to occur due to climate change (Buchart et al., 2010).

The deviation of the CESM-NCSU simulation from previous work may be linked to model biases. For example, in Section 4.3 it was shown that CESM-NCSU overpredicts surface O_3 due to errors in model deposition and titration and the evaluation of TOR in five stratocumulus regions reveled possible overpredictions of STE. These two biases combined may contribute to this predicted increasing trend in O_3 from climate change. The deviation in O_3 predictions may also be a limitation associated with the CB05GE gas phase mechanism. The CB05GE mechanism as part of the Global Weather Research and Forecasting Model with Chemistry (GU-WRF/Chem) (Zhang et al., 2012b) also predicts an increasing trend in O_3 due to climate change. These findings are based on future climate simulations using the older IPCC AR4 SRES A1B scenario discussed Chapter 2. The common trend of increasing O_3 using two different future climate scenarios and two different models that use CB05GE may indicate that the pathway of O_3 destruction due to enhanced water vapor is not well represented in CB05GE.

In response to climate change $PM_{2.5}$ and PM_{10} decrease on global average by ~0.3 and ~1.0 μg m^{-3}, respectively. This decrease in aerosol levels is dominated by decreases in dust concentrations of ~1.3 μg m^{-3} on global average. As mentioned in Section 4.4.3, this decrease in dust is driven by decreases in WSP10 over land that reduce dust emissions in the large dust source regions of North Africa, the Middle East, and East Asia.

In order to understand the impact of climate change on the remainder of the aerosol species, the differences in $PM_{2.5}$ and PM_{10} without considering the dust modes are shown in Figure 4.21. Without the influence of dust $PM_{2.5}$ increases by 0.04 μg m^{-3} on global average. This increase is driven by BSOA that increases by ~0.05 μg m^{-3} on global average in response to increasing biogenic VOCs and dominates non-dust aerosol changes in the tropics. There are also decreases in non-dust $PM_{2.5}$ (e.g., 0.6-3.0 μg m^{-3}) that occur over North America, Europe, and Southeast Asia. In order to examine the reasons for the additional changes in aerosol levels the remaining aerosol species including: POM, SVOA, anthropogenic SOA (ASOA), NH_4^+, NO_3^-, and Cl^-, as well as changes in planetary boundary layer height (PBLH), WSP10, and PR between the RCP4F_GHGF and RCP4C simulations are shown in Figure 4.23. BC is not shown because differences in this aerosol component are negligible. The decreases in non-dust $PM_{2.5}$ over North America and Europe are primarily the result of decreases in SO_4^{2-}, NH_4^+, and NO_3^-. These decreases occur in conjunction with increases in PBLH indicating that they are likely the result of enhanced vertical mixing in continental interiors from reduced cloud formation. However, the decreases in NO_3^- are greater over much of central North America, indicating that this reduction is also driven by enhanced volatility of NH_4NO_3 from the warmer climate. The decreases in non-dust $PM_{2.5}$ in Southeast Asia are largely the result of decreases in SO_4^{2-}, ASOA, NH_4^+, and SVOA. These decreases occur in conjunction with large increases in PR in this region. The increased PR and the fact that all four of the most impacted species are fairly hydrophilic indicate that this decrease is likely from enhanced wet removal.

Non-dust changes in PM_{10} (e.g., global average increase of 0.4 μg m^{-3}) are driven by increases in sea-salt (Na^+ + Cl^-) that occur from increases in marine WSP10. It is important to note that due to limited computational resources a non-forced future climate run was not completed and as a result the impact of internal model variability on the results discussed in this section cannot be ruled out. However, most of the changes in future aerosol levels are driven by: (1) reductions in continental cloud cover, (2) reductions in continental wind speeds, (3) increases in maritime wind speeds, (4) increases in near surface temperatures, and (5) increases in tropical precipitation that have been shown to be both consistent with not only CESM1-CMIP5 but also other models that are part of the CMIP5 comparison project. This indicates that these impacts of climate change are fairly robust and thus the results presented here are likely reliable.

4.6 Impact of Emission Changes on Aerosol Direct and Indirect Effects

In this section the changes between the RCP4F and RCP4F_GHGF simulations are compared to estimate the impacts of the changes in emissions under the RCP4.5 scenario on the future climate through the aerosol direct and indirect effects. In order to illustrate these impacts, Figure 4.24 shows the changes in AOD, CCN5, CDNC, CF, LWP, COT, PWV, PR, SWCF, FSDS, PBLH, and T2 between the RCP4F and RCP4F_GHGF. Figure 4.25 shows additional absolute differences in clear sky downwelling shortwave radiation at the surface (FSDSC), latent heat flux (LHX), sensible heat flux (SHX), average lower troposphere relative humidity (LTRH), average lower troposphere temperature (LTT), sea level pressure (SLP), convective precipitation rate (PRC), and large scale precipitation rate (PRL). The reduction in emissions of many primary aerosol and secondary aerosol precursors results in

an AOD reduction of 4.0×10^{-2} on global average. From a regional standpoint the changes are the largest in South Asia, East Asia, and Indonesia, with increases in the range of 0.02-0.14 over South Asia and strong decreases in the range of 0.05 – 0.20 over East Asia and Indonesia. There are more moderate decreases in AOD over Europe, North America, and central South America, with decreases typically in the range of $5.0\times10^{-2} – 5.0\times10^{-1}$. Trends in Australia and Africa are more difficult to discern due to small magnitudes and localized differences in the direction of changes. The global average reduction in AOD is larger than that between the current and future simulations shown in Figure 4.10, indicating the enhanced sea-salt from greater WSP10 and increased SOA from warming play an important role in future AOD. Regionally, these climate change differences are the strongest in South America, Africa, and Australia as illustrated by the large differences in AOD changes between Figure 4.10 and Figure 4.24, while the strong similarities in North America, East Asia, South Asia, and Europe indicate that these regions are more dominated by emission projections. The decreased AOD results in a global mean decrease of ~0.3 W m^{-2} in FSDSC, as shown in Figure 4.25. Regionally, AOD reductions increase FSDSC in the range of 0.2-3.0 W m^{-2} in South America and North America, 0.8-4.0 W m^{-2} in Europe, 0.4-7.0 W m^{-2} in Indonesia, and 1.3-12.9 W m^{-2} in East Asia. The increased AOD in South Asia results in diming of 1.0-9.4 W m^{-2}. In Africa and Australia, there is a mixed signal in radiation changes similar to those that occur in AOD, however, there is a pattern of dimming in the range of 0.6-2.0 W m^{-2} in central Africa where aerosol loadings increase.

The emission reductions decrease CCN5 on global average by 2.2×10^{7} cm^{-2}. Increasing emissions result in increased CCN5 levels of $3.2\times10^{7} – 1.2\times10^{8}$ cm^{-2} in South

Asia and smaller increases of 2.0×10^{7}-8.0×10^{7} cm^{-2} in portions of central Africa. Reductions in CCN5 are the smallest in Australia (e.g., 9.8×10^{6}-3.2×10^{7} cm^{-2}) and South America (e.g., 2.3×10^{7}-2.2×10^{8} cm^{-2}) and the largest in Indonesia (e.g., 2.1×10^{7}-4.3×10^{8} cm^{-2}) and East Asia (e.g., 1.5×10^{8}-5.7×10^{8} cm^{-2}). Reductions in CCN5 of 1.6×10^{8}-1.9×10^{8} cm^{-2} occur in Europe and reductions of 1.5×10^{7}-2.6×10^{8} cm^{-2} occur in North America. The larger range in reduction over North America reflects greater emission reductions in eastern North America compared to western North America. The global mean reduction in CCN5 leads to similar global mean reductions in "warm cloud" CDNC (-11.2 cm^{-3}) with decreases over Europe and much of North America ranging from 50.0-145.0 cm^{-3} and greater decreases of 50.0-267.0 cm^{-3} occurring in East Asia. Smaller decreases are simulated over Australia (1.0-20.0 cm^{-3}), Indonesia (6.0-80.0 cm^{-3}), South America (1.0-60.0 cm^{-3}), with greater complexity in the sign of the changes. The increasing CCN5 in the regions of South Asia and portions of central Africa results in increasing CDNC in the range of 13.0-62.0 cm^{-3}. Similar to changes in AOD, a comparison of changes in CCN5 and CDNC between Figure 4.24 and Figure 4.20 shows enhanced CCN5 and CDNC levels over the SH between the current and future periods that are not caused by anthropogenic emission changes. This differs from trends in the NH that mirror the changes caused by anthropogenic emissions. Overall, this indicates that emission changes under the RCP4.5 scenario have a stronger impact on aerosol cloud interactions in the NH than the SH. Despite these differences in the SH, the global mean changes in CCN5 and CDNC are quite similar to those shown in Figure 4.20, indicating that overall changes in emissions under the RCP4.5 scenario dominate the changes in aerosol-cloud interactions. The greater decrease in CDNC in Figure 4.20 compared to Figure 4.24

also lends further evidence to support the reduced cloud formation in the future climate as a reason for reduced aerosol activation and reduced CDNC in the future period.

The impacts of changes in aerosol loadings on CF are more complex than the changes in AOD or CDNC due to a number of complicating factors. CF decreases by 0.2% on global average under the RCP4.5 scenario due to emission projections. In general over the continental regions of Europe, South America, Indonesia, and Australia, CF is reduced by ~0.6-3.0%, with greater reductions of up to 5.5% in East Asia and South Asia. However, there are areas of greater cloud formation over the CONUS region where CF increases by 1.0-2.5% and the central Pacific where CF increases up to 8.7%. The reasons for the continental decrease in CF are difficult to discern as is the reason for the difference in behavior over North America. This is because CF can be impacted by changes in FSDSC from aerosol loadings but also changes in radiation from changes in CDNC. This is a cycle of feedbacks in which it is difficult to determine causes and effects since only the net impacts of the feedback cycle are apparent in the decadal averages. In general the increases in FSDSC from reduced AOD in Europe, North America, South America, and East Asia increase the surface LHX (see Figure 4.25) in the range of 2.0-6.0 W m^{-2} with larger increases in North America and East Asia compared to Europe and South America. Similarly, the decrease in FSDSC decreases the LHX in South Asia and central Africa by up to 22.3 W m^{-2}. The increased global average LHX increases PWV by 0.2 mm on global average. Increases occurring over Europe, South America, and East Asia are generally smaller (0.2-0.7 mm) than those in North America (0.5-1.0 mm). This somewhat mirrors the magnitude of the changes in LHX and does not correspond well with the magnitudes of changes in FSDSC.

This is likely caused by differences in land surface, as the impact of aerosol direct effects on ecosystems has been shown to vary significantly due to plant phenology (Chen and Zhuang, 2014). In addition to the continental changes, there are strong increases (up to 5.5 mm) in PWV in the central Pacific and strong decreases in PWV (up to 2.1 mm) in the Northern Indian Ocean and Indonesia.

These changes are likely linked to aerosol effects impacting atmospheric and ocean dynamics, as such aerosol radiative effects have been shown to impact oceanic heat transport and current systems (Cai et al., 2006). One of these dynamical feedbacks is a weakening of the Walker circulation. The Walker circulation is the large scale atmospheric flow pattern that describes meridional momentum flow in the tropics and is known at the surface as the Trade Winds. One indicator of the weakening in the Walker circulation is the reductions in sea level pressure (SLP) in the eastern Pacific and increases in SLP over the western Pacific and Indian Ocean. The weakening of the Walker circulation is consistent with the warming induced impact due to the emission projections under the RCP4.5 scenario, since similar weakening of the Walker circulation has occurred in response to warming from anthropogenic forcing (Vecchi et al., 2006). The weakening in the Walker circulation also explains the increase in cloud and convective activity in the central Pacific and central Africa and weakening in areas surrounding Indonesia, Australia, and South America. The decrease in LHX over South Asia also results in a PWV reduction of 0.2-1.4 mm. The loss of PWV in South Asia, Indonesia, and Australia and increases in PWV in North America and the central Pacific are adequate to account for the changes in CF in these regions from enhanced water vapor availability. However, these changes do not support the reductions in other continental

areas. The reductions in CF over the remaining continents are the result of reduced saturation as evidenced by the reductions in the average LTRH, which is defined here as the average RH from the surface to ~500 hPa shown in Figure 4.25. The average LTRH decreases over East Asia, Europe, South America, South Asia, central Africa, and Australia in the range of ~ 0.5-4.2%, while the average LTRH increases by 0.2-2.5% over the CONUS region. The decreased RH occurs because there is an increase in the average LTT, as shown in Figure 4.25, from greater warming associated with increases in FSDSC. LTT increases are greater over the East Asia, Europe, and South America regions typically in the range of 0.3-0.9°C, while warming over North America is smaller typically in the range of 0.1-0.7°C. This is related to both the changes in LHX and SHX, since in North America most of the increased radiation increases LHX, that do not directly increase atmospheric temperatures, while the remaining regions experienced stronger increases in SHX that warm the atmosphere. This disparity is likely linked to differences in the underlying land characteristics as mentioned previously. These factors contribute to the reduced warming and greater water vapor availability in North America and are the apparent cause of the enhanced cloud formation in this region compared to the other continents, however, the impact of dynamical changes this region cannot be ruled out as increases in moisture over portions North America is consistent with a weakening of the Walker circulation.

Reduced aerosol loadings from emission projections reduce LWP on global average by 1.3 g m^{-2}. The decreases of LWP in Europe (e.g., by 2.0-17.0 g m^{-2}), East Asia (e.g., by 5.0-51.3 g m^{-3}), South America (e.g., by 2.0-17.0 g m^{-2}), Indonesia (e.g., by 6.0-30.0 g m^{-2}), and eastern North America (e.g., by 1.6-12.0 g m^{-2}) are related to decreases in CCN5 that

reduce condensation. This is especially true in North America where LWP declines despite increases in LTRH and cloud formation. The changes in LWP are complex in South Asia but generally there is a dominant trend for decreases typically in the range of 0.7-12.0 g m^{-2} due to the reduction in cloud formation despite increases in CCN and CDNC. Additionally, LWP is reduced over Australia by 2.0-11.0 g m^{-2} in response to reduced cloud formation from the weakening of the Walker circulation. LWP is increased in central Africa (e.g., 0.2-15.0 g m^{-2}) from greater CCN5 levels and the central Pacific (e.g., 1.0-21.1 g m^{-2}) from greater cloud formation. COT is reduced on global average by ~0.4 in response to decreases in cloud albedo and cloud formation from reduced CF, CDNC, and LWP. The reductions in COT are smaller in Australia, South Asia, South America, and North America typically in the range of 0.02-0.11 compared to larger reductions of 0.06-0.17 in Europe, 0.05-0.21 in Indonesia, and 0.02-11.6 in East Asia. The largest increases in COT occur in central Africa (0.03-0.07) and the central Pacific (0.3-4.2). Globally the reductions in COT due to emission projections are greater than those shown in Figure 4.20 because of enhanced cloud formation in the Arctic, South Asia, and central Africa that enhance COT. However, over the continents COT reductions are larger than those that occur from declining emissions, illustrating the enhancement from reduced continental cloud formation.

Reduced COT and cloud formation result in a global mean reduction in SWCF of 0.23 W m^{-2}. The impact on SWCF is the strongest in the vicinity of Indonesia (decreases of 5.6-12.6 W m^{-2}) and the central Pacific (increases of 2.0-18.9 W m^{-2}). SWCF is reduced in Australia, Europe, and South America typically in the range of 0.5-7.0 W m^{-2}, while decreases are generally larger in South Asia (e.g., 1.2-11.5 W m^{-2}) and East Asia (e.g., 1.3-

8.0 W m^{-2}). In central Africa, COT enhancements lead to enhancements in SWCF of 0.5-5.5 W m^{-2}. The changes in SWCF are more complicated over North America with reductions of 0.2-4.5 W m^{-2} in the north and west from reductions in aerosol loading and increases of 1.5-5.0 W m^{-2} in the south and west from enhanced cloud formation. The global mean reductions in SWCF and AOD lead to reductions in FSDS of 0.7 W m^{-2} on global average. The impact of reduced AOD and SWCF enhances FSDS in the range of 1.0-11.0 W m^{-2} in Europe and South America with a greater enhancement of 2.0 – 18.7 W m^{-2} in East Asia. Although there is a strong direct impact on radiation in Indonesia from aerosol reductions, the changes in the Walker circulation have a greater impact on FSDS in this region, leading to increases in the range of 3.0-15.0 W m^{-2}. This process dominates over the aerosol impacts in Australia resulting in increases of FSDS in the range of 0.9-5.5 W m^{-2}. In central Africa, the increases in AOD and SWCF from emission projections lead to diming of 0.3-6.2 W m^{-2}. Changes in FSDS over North America and South Asia from emission projections are the most complex representing compensation of impacts from aerosol direct and indirect effects. In South Asia, FSDS is decreased in the range of 1.0-9.0 W m^{-2} over northern India in response to a dominance of the aerosol direct effect from enhanced emissions, while FSDS increases in the range of 1.0-9.0 W m^{-2} over the remainder of South Asia in response to dominant changes in aerosol indirect effects. In North America, FSDS increases in the north and west in the range of 0.2-7.5 W m^{-2} in response to reduced AOD and SWCF, while enhanced SWCF from greater cloud formation over the southwest North America leads to dimming in the range of 1.0-5.0 W m^{-2}. These changes in radiation from aerosol direct and indirect effects have a strong impact on air pollution meteorology and climate. In terms of air pollution

meteorology, the global increase in radiation results in a global average increase in PBLH of 1.0 m. The largest increases occur in Europe, South America, South Asia, East Asia, and Australia mirroring changes in SHX. These increases provide a positive feedback to emission reductions as the increase in PBLH will enhance vertical mixing, leading to greater reductions in surface pollution levels. The increases in FSDS also result in a general global warming trend of 0.2°C on global average with general warming of 0.2-1.2°C over most continental regions with greater increases in Europe, South America, and East Asia, compared to North America, Indonesia, Africa, South Asia, and Australia.

The impact of the RCP4.5 emission projection on global precipitation is dominated by changes in tropical convective precipitation related to the weakening of the Walker circulation, resulting in increases in PR over the central Pacific of 0.2-2.4 mm day^{-1}. This process also results in decreases of precipitation by 0.1-2.8 mm day^{-1} in the vicinity of Indonesia, South Asia, Australia, and South Asia. In the NH, PRC is increased in North America (e.g., 0.02-0.3 mm day^{-1}) and East Asia (e.g., 0.01-0.3 mm day^{-1}) in response to greater LHX in these regions and the warming from reduced aerosol loadings. The direction of the impact over Europe is more complicated likely from competing influences from the larger increase in SHX compared to LHX in this region. In North America the increase in large scale cloud formation also leads to increases in PRL of 1.0×10^{-3}-0.7 mm day^{-1} since the greater water level and reduced aerosol loading lead to bigger droplets as evidenced by the 0.01-0.7 μm increases in average cloud droplet effective radius (Figure not shown). There are mixed changes in PRL in East Asia and Europe with decreases in the range of 0.1-0.5 mm day^{-1} and increases in the range of 0.01-0.1 mm day^{-1}. These reflect similar complex changes

in average cloud drop radius likely from competing influences from reduced CDNC and reduced LWP. The combined effect in total PR is a mixed increase and decrease in East Asia, reflecting the dominant changes in PRL and a slight decrease in Europe.

The changes induced by the RCP4.5 emissions projections are similar to those of Westervelt et al. (2015) that reported global average changes of -0.87 g m^{-2}, ~0.08 mm day^{-1}, and 0.81ºC in LWP, PR, and T2, respectively. These changes are more extreme than the 0.2ºC and ~0.02 mm day^{-1} increases in T2 and PR, respectively, predicted by CESM-NCSU. This is likely because the work of Westervelt et al. (2015) examined the changes caused by emissions reductions by 2100 rather than 2050 when emissions reductions are stronger. However, the changes in LWP predicted by CESM-NCSU are more extreme with reductions of -1.3 g m^{-2}. This is likely due to differences in aerosol activation parameterizations between the models as well as differences in simulated time period.

4.7 Conclusions

In this work, the CESM-NCSU model is used to simulate the current atmosphere using emissions based on the RCP4.5 and RCP8.5 scenarios. The tuned version of CESM-NCSU simulates radiation variables consistent with satellite estimates from CERES/EBAF. Deviations from CERES-EBAF estimates indicate that CESM-NCSU overpredicts tropical cloudiness, while underpredicting the greenhouse effect and overpredicting surface albedo in the polar regions. Compared to satellite estimates, cloud parameters within CESM-NCSU are not as well simulated as radiation. This is common in many global modeling studies, indicating that more work is needed to better represent and link these individual processes. AOD is well simulated by CESM-NCSU given model limitations; and it generally performs

better or comparable to CMIP5. CCN5 and CDNC in CESM-NCSU are not as well simulated as AOD owing to uncertainties in aerosol treatments and satellite estimates. Meteorological parameters including T2, Q2, WSP10, and PR are all in good agreement with observations or reanalysis estimates, although there are deviations that result from errors in simulated radiation and the dual ITCZ bias.

In terms of atmospheric pollutants, CESM-NCSU generally captures the most features of the spatial distribution and the magnitudes of TNO_2, TOR, TCO, and THCHO. CESM-NCSU shows limited skills in simulating surface O_3 mixing ratios because of possible underestimations in O_3 deposition from the default model as released by NCAR, leading to moderate to large overpredictions. Overall, trace gas performance at surface sites is worse than the performance of column mass abundances. This may be due to inaccuracies in emissions, vertical mixing, and deposition but this evaluation is also limited by the use of a coarse spatial grid resolution in the simulations using the CESM-NCSU and subsequent numerical diffusion. In general, the concentrations of inorganic aerosol SO_4^{2-}, NH_4^+, and NO_3^- are all well simulated by CESM-NCSU, while the simulation of Cl^- concentrations is poor due to errors in WSP10 and competition of HCl with overpredicted HNO_3 in aerosol partitioning. The concentrations of carbonaceous aerosols are underpredicted due to the small magnitude in the emissions of the BC, OC, and AVOC in the RCP emission inventories, overestimates of POA volatility, and possible overpredictions in wet removal of these species by the MAM7 module. This underprediction in the concentrations of carbonaceous aerosols and the good performance of inorganic aerosols lead to underpredictions of $PM_{2.5}$ and PM_{10} using the RCP emission inventory in CESM-NCSU.

The evaluation of trace gas columns in the five stratocumulus cloud regions indicate that inaccuracies exist in tropical biogenic emissions within CESM-NCSU that may impact photochemistry in these regions and that the ITCZ bias likely plays an important role in the errors in simulating soluble trace gases in the tropics. Large biases in TOR levels during the SON period also imply biases in the STE of O_3 within the CESM-NCSU model. AOD, CCN5, and SWCF are all reasonably well simulated in these stratocumulus regions although some errors exist, and they can be attributed to the possible overpredictions of aerosol wet removal, underestimated emissions, or inaccuracies in tropical photochemistry. Compared to satellite estimates, the seasonality of CDNC in these regions is captured despite its overprediction. Given the potential inaccuracies in satellite CDNC estimates and the good performance of other variables, the evaluation of CDNC implies that the CESM-NCSU model represents aerosol-cloud and radiation processes reasonably well. Overall, the CESM-NCSU model does a reasonably good job in representing the current climate period in terms of radiation, clouds, meteorology, trace gases, aerosols, and aerosol-cloud interactions, making it suitable for use in predicting changes in these properties under future climate policy scenarios.

Changes in meteorological, radiation, cloud, and AOD between the CESM-CAM5.1 simulations from the CMIP5 project and CESM-NCSU are generally comparable under both the RCP4.5 and RCP8.5 scenarios with changes in cloud and wind patterns consistent with other CMIP5 models. However, differences exist in many meteorological variables in the SH due to cooling over this region in CESM-NCSU. This is potentially due to limitations in this comparison resulting from differences in ocean and sea ice initializations between the two

model applications, but the impact of chemistry cannot be discounted. For example, CESM-NCSU gives increases in tropical AOD due to the more advanced SOA treatments. Both models show the impact of changes in aerosol-climate interactions though reductions in CWP over the NH industrial areas in response to declining aerosol levels and increases in FSDS over continents for similar causes under both RCP4.5 and RCP8.5 climate policy scenarios. However, there are reductions in CF from climate change that amplify this decrease in CWP and increase in FSDS.

The changes in the trends of most trace gases at surface tend to follow the trends in their emissions which are typically decreasing in both scenarios by 2050 due to the implementation of emission control policies and projected reductions in the income gap between developing and developed countries. Global average surface O_3 experiences a decrease of 1.4 ppb under RCP4.5, due to decreased O_3 production from future NO emission reductions. However, O_3 increases by 2.4 ppb on global average under RCP8.5, due to increased O_3 production from weaker NO emission reductions, large increases in CH_4, larger increases in anthropogenic and biogenic TNMVOC emissions, and warmer temperatures. This trend is consistent with other modeling studies following these scenarios (Young et al., 2013; Kim et al., 2015). There are also decreases in OH under both scenarios from enhanced destruction by increases TNMVOC and CH_4 consistent with the ACCMIP modeling studies (Voulgarakis et al., 2013). This enhanced oxidation in conjunction with greater increases in shipping emissions increase the background CO level under the RCP8.5 scenario, while smaller increases in oxidation and shipping emissions and greater emissions reduction lead to a decrease in CO under the RCP4.5 scenario. $PM_{2.5}$ is reduced on global average by 0.7 μg m^{-}

^{3} under RCP4.5 and 0.2 μg m^{-3} under RCP8.5. These reductions are driven largely by reductions in primary BC and OC emissions and SO_2 and NO precursor emissions that limit the formation of SO_4^{2-}, NH_4^{+}, and NO_3^{-}. However, natural reductions in dust from reduced WSP10 in high dust emission regions play a role. Reductions in simulated $PM_{2.5}$ concentrations are less under RCP8.5 scenario due to smaller reductions in anthropogenic and dust emissions, larger sea-salt emissions, and larger SOA formation. These differences in sea-salt and dust emissions between the RCP4.5 and RCP8.5 scenarios lead to a global average reduction in PM_{10} of 1.2 μg m^{-3} under the RCP4.5 scenario but an increase of 0.2 μg m^{-3} under the RCP8.5 scenario.

Decreases in aerosol loading lead to global average decreases in CCN5 under both RCP scenarios and these decreases in CCN in conjunction with decreases in cloud formation over the continents lead to global average reductions in CDNC and CWP. Under the RCP4.5 scenario, COT is reduced on global average in response to the large reductions in CDNC, LWP, and CF over continental regions but under the RCP8.5 scenario this is compensated by stronger increases in cloud formation over the Arctic and Southern Ocean. The increase in cloud formation over the Arctic and the oceans dominates changes in SWCF, leading to a global average increase of 0.4 W m^{-2} and 0.5 W m^{-2} under the RCP4.5 and RCP8.5 scenarios, respectively. The increases in SWCF over the Arctic and oceans and greater AOD over South Asia and Africa compensate increases in FSDS from decreases in AOD and SWCF over the remaining continents, resulting in global dimming of 1.1 W m^{-1} under the RCP4.5 scenario and 2.0 W m^{-2} under the RCP8.5 scenario. In general, trends in air pollutants by the year 2050 under both the RCP4.5 and RCP8.5 climate policy scenarios are similar with reductions

in many pollutants due to similar changes in anthropogenic emissions. The key differences occur for O_3, OH, CO, and SOA due mainly to large feedbacks from large increases in CH_4 from the lack of widespread implementation of carbon capture and storage technologies (CCS) technologies in the RCP8.5 scenario. Thus this illustrates the importance of climate/carbon policies and international cooperation for future climate mitigation and air quality improvement as reductions in typical air pollution precursor emissions are not necessarily sufficient to reduce future air pollution levels.

Climate change following the RCP4.5 scenario increases O_3 by ~0.3 ppb on global average largely in response to enhanced STE of O_3. This differs from previous work that report decreases in global O_3 from climate change (Dentener et al., 2006; Doherty et al., 2013). This indicates that the enhancement of O_3 from climate change is possible either the result of model biases in surface O_3 and STE or a limitation of the CB05GE mechanism. Climate change leads to a reduction in both the global average $PM_{2.5}$ and PM_{10} level by ~0.3 and ~1.0 μg m^{-3}, respectively. These changes are dominated by reductions in dust concentrations but increases in BSOA, sea-salt, PBLH, and PR also play a role in future aerosol levels.

The reductions in pollutant emissions under the RCP4.5 scenario lead to reductions in future AOD that in turn increase clear sky downwelling solar radiation at the surface by 0.3 W m^{-2} on global average. This effect is further enhanced by reductions in cloud formation and cloud albedo caused by these aerosol reductions, which bring the total increase in all sky downwelling solar radiation to a global average increase of 0.7 W m^{-2}. The increase in solar radiation results in an increase in near surface air temperatures of 0.2°C on global average.

The higher incoming radiation and warmer temperatures result in increases in PBLH that would further reduce pollution levels through vertical mixing. However, the global warming signal induced from emission reductions leads to a weakening of the Walker circulation in the tropics, resulting in strong changes in tropical precipitation and cloud patterns and a general shift in global climate towards the negative phase of the El Nino Southern Oscillation. These findings illustrate the importance of utilizing an earth system modeling when conducting simulations of global aerosol effects since it allows for feedbacks of chemical species to atmospheric/oceanic circulation systems. These findings also imply a fairly strong "climate penalty" from the reduced emission levels. However, this should not imply that reduced air pollution emissions are poor policy decision as there will be benefits to human health. Rather, this further underscores the importance of climate/carbon policies as the best mechanism to mitigate the negative impacts from climate change. However, this does imply that the scientific community and policy makers would benefit from a cost/benefit analysis of the "climate penalty" versus the pollutant reductions under the RCP scenarios in terms of human health, ecosystem health, and economic consequences.

Table 4.1. List of Datasets for Meteorological, Cloud, and Radiation Evaluation

Variable (units)	Short Name	Dataset	Spatial Coverage	Temporal Coverage
Downwelling Longwave Radiation at the Earth's Surface (W m^{-2})	FLDS	Clouds and Earth's Radiant Energy Systems (CERES)/ Energy Balanced and Filled (EBAF)	Global (1°×1°)	2001-2010
Outgoing Longwave Radiation at the Top of the Atmosphere (W m^{-2})	OLR			
Longwave Cloud Forcing (W m^{-2})	LWCF			
Net Surface Longwave Flux (W m^{-2})	FLNS			
Downwelling Shortwave Radiation at the Earth's Surface (W m^{-2})	FSDS			
Outgoing Shortwave Radiation at the Top of the Atmosphere (W m^{-2})	OSR			
Shortwave Cloud Forcing (W m^{-2})	SWCF			
Net Surface Shortwave Flux (W m^{-2})	FSNS			
Top of the Atmosphere Net Flux (W m^{-2})	RESTOA			
Cloud fraction	CF	Level 3 Moderate Resolution Imaging Spectroradiometer (MODIS)	Global (1°×1°) Oceans (CCN5)	2001-2010
Column CCN (ocean) at S = 0.5% (cm^{-2})	CCN5			
Cloud Optical Thickness	COT			
Precipitable Water Vapor (cm)	PWV			
Aerosol Optical Depth	AOD			
Cloud Droplet Number Concentration from Warm Clouds (cm^{-3})	CDNC	Bennartz (2007)	Global (1°×1°)	2001-2010
Liquid Water Path (g m^{-2})	LWP	O'dell et al. (2008)	Oceans (1°×1°)	2001-2008
Precipitation Rate (mm day^{-1})	PR	Global Precipitation Climatology Project (GPCP)	Global (2.5°×2.5°)	2001-2010
2m Temperature (°C)	T2	National Climatic Data Center (NCDC) and National Centers for Environmental Prediction (NCEP)/ National Center for Atmospheric Research (NCAR)	Global (Intermittent Coverage) and Global (2.5°×2.5°)	2001-2010
2m Specific Humidity (g kg^{-1})	Q2			
10m Wind Speed (m s^{-1})	WSP10			

Table 4.2. List of Datasets for Chemical Evaluation

Variable	Short Name	Dataset	Spatial Coverage	Temporal Coverage
Carbon Monoxide	CO	NIESJ, TAQMN, KMOE	East Asia	2001-2010, 2006-2010 (KMOE)
Nitrogen Dioxide	NO_2	NIESJ, TAQMN, KMOE, Airbase, BDQA, EMEP	East Asia, Europe	2001-2010 2006-2010 (KMOE)
Ozone	O_3	TAQMN, KMOE, Airbase, BDQA, EMEP, CASTNET	East Asia, Europe, CONUS	2001-2010 2006-2010 (KMOE)
Sulfur Dioxide	SO_2	NIESJ, TAQMN, KMOE, Airbase, BDQA, EMEP, CASTNET	East Asia, Europe, CONUS	2001-2010 2006-2010 (KMOE)
Nitric Acid	HNO_3	EMEP, CASTNET	Europe, CONUS	2001-2010
Ammonia	NH_3	EMEP	Europe	2001-2010
Particulate Matter with diameter less than 2.5 μm	$PM_{2.5}$	Airbase, BDQA, EMEP, IMPROVE, STN	Europe, CONUS	2001-2010
Particulate matter with diameter less than 10 μm	PM_{10}	MEPC, NIESJ, TAQMN, KMOE, Airbase, BDQA, EMEP, AQS	East Asia, Europe, CONUS	2001-2010 2006-2010 (KMOE)
Sulfate	SO_4^{2-}	EMEP, CASTNET, IMPROVE, STN	Europe, CONUS	2001-2010
Ammonium	NH_4^+			
Nitrate	NO_3^-			
Chloride	Cl^-			
Black Carbon	BC	IMPROVE, STN	CONUS	2001-2010
Total Carbon	TC			
Organic Carbon	OC	EMEP, IMPROVE	Europe, CONUS	2001-2010 (IMPROVE) Assumed Climatology (EMEP)
Secondary Organic Aerosol	SOA	Lewondowski et al. (2013)	CONUS	Assumed Climatology
Oxygenated Organic Aerosol	OOA	Zhang, Q. et al. (2007) and Jimenez et al. (2009)	Northern Hemisphere	Assumed Climatology
Hydrocarbon-like Organic Aerosol	HOA			
Total Organic Aerosol	TOA			
Tropospheric CO	TCO	MOPITT	Global (1°×1°)	2001-2010
Tropospheric Formaldehyde	THCHO	GOME, SCIAMACHY	Global (0.25°×0.25°)	2001-2002 (GOME) 2003-2010 (SCIAMACHY)
Tropospheric NO_2	TNO_2			
Tropospheric SO_2	TSO_2	SCIAMACHY	Global (0.25°×0.25°)	2005-2010
Tropospheric Ozone Residual	TOR	OMI/MLS	Global (1.5°×1.25°)	2005-2010 (OMI/MLS)

*TOMS/SBUV: the Total Ozone Mapping Spectrometer/the Solar Backscatter UltraViolet; OMI: the Aura Ozone Monitoring Instrument; MOPITT: the Measurements Of Pollution In The Troposphere; the Global Ozone Monitoring Experiment; SCIAMCHY: the SCanning Imaging Absorption spectroMeter for Atmospheric CHartographY; GOME: the Global Ozone Monitoring Experiment; CASTNET: Clean Air Status and Trends Network; IMPROVE: Interagency Monitoring of Protected Visual Environments; STN: Speciation Trends Network; AQS: The U.S. Environmental Protection Agency's Air Quality System; EMEP: European Monitoring and Evaluation Program; BDQA: Base de Données sur la Qualité de l'Air; AirBase: European air quality database; MEPC: the Ministry of Environmental Protection of China; TAQMN: the Taiwan Air Quality Monitoring Network; NIESJ: the National Institute for Environmental Studies of Japan; KMOE: the Korean Ministry of Environment.

Table 4.3. Performance Statistics of Radiation, Cloud, and Meteorological Variables

Variable	Mean Obs.	Mean Sim.		MB*		RMSE*		NMB*		NME*		R*	
		RCP4.5	RCP8.5	RCP4.5	RCP8.5	RCP4.5	RCP8.5	RCP4.5	RCP8.5	RCP4.5	RCP8.5	RCP4.5	RCP8.5
RESTOA	-29.1	-30.2	-28.1	-1.1	1.0	10.3	9.2	-3.9	3.4	26.1	22.3	0.99	0.99
FSDS	163.5	161.5	161.7	-2.0	-1.8	12.5	12.2	-1.2	-1.1	5.5	5.4	0.98	0.98
OSR	102.7	106.4	106.3	3.7	3.6	11.9	11.5	3.6	3.5	8.7	8.5	0.82	0.83
SWCF	-40.7	-42.3	-42.2	1.6	1.5	12.2	11.9	3.8	3.7	21.6	21.1	0.92	0.92
FSNS	128.5	123.8	124.0	-4.7	-4.5	12.8	12.5	-3.7	-3.5	7.6	7.5	0.99	0.99
FLDS	306.3	300.5	300.7	-5.8	-5.6	13.2	13.5	-1.9	-1.8	3.4	3.5	0.99	0.99
OLR	223.7	217.9	219.6	-6.0	-4.2	9.2	7.9	-2.7	-1.9	3.2	2.7	0.98	0.98
LWCF	22.5	20.2	20.1	-2.4	-2.4	5.8	5.8	-10.6	-10.6	20.3	20.6	0.92	0.91
FLNS	-47.6	-49.8	-49.7	2.2	2.0	8.8	8.8	4.6	4.3	13.9	13.9	0.88	0.88
CF	67.2	66.6	66.7	-0.6	-0.5	22.4	22.0	-0.9	-0.7	26.4	25.9	0.28	0.28
CCN5	2.4×10^8	1.3×10^8	1.3×10^8	-1.1×10^8	-1.2×10^8	4.5×10^8	4.6×10^8	-45.7	-47.3	49.4	50.3	0.11	0.11
COT	17.0	10.1	10.0	-6.9	-7.0	12.8	12.8	-40.7	-41.0	54.9	54.9	-0.12	-0.12
PWV	1.9	2.0	2.0	0.05	0.06	0.3	0.3	2.8	3.4	11.8	11.8	0.98	0.98
AOD	0.16	0.13	0.13	-0.02	-0.03	0.1	0.1	-14.5	-16.2	40.7	41.4	0.62	0.61
CDNC	108.5	151.7	157.6	43.2	49.0	83.7	88.0	39.8	45.2	58.6	62.6	0.43	0.47
LWP	85.7	60.1	59.7	-25.6	-26.0	38.9	40.3	-29.9	-30.3	36.4	36.7	0.44	0.42
PR	2.3	2.4	2.5	0.2	0.2	1.0	1.0	8.3	8.9	26.3	26.8	0.87	0.86
T2[a]	13.1	11.8	11.8	-1.3	-1.3	3.9	4.0	-9.9	-10.1	21.1	20.9	0.94	0.93
T2[b]	5.4	4.3	4.3	-1.0	-1.0	3.0	3.1	-19.6	-19.5	39.1	39.0	0.99	0.99
Q2[a]	8.3	8.0	8.0	-0.3	-0.3	1.7	1.7	-3.6	-3.3	14.0	14.1	0.93	0.93
Q2[b]	8.2	7.6	7.7	-0.5	-0.5	1.0	1.0	-6.7	-6.2	9.4	9.5	0.99	0.99
WSP10[a]	3.7	3.3	3.3	-0.4	-.0.4	1.8	1.8	-9.7	-10.2	32.8	32.6	0.47	0.48
WSP10[b]	4.2	6.6	6.6	2.4	2.5	3.2	3.3	58.3	59.0	64.4	65.3	0.59	0.58

[a]Evaluated against NCDC dataset, [b]Evaluated against NCEP/NCAR dataset, *MB: mean bias; RMSE: root mean square error; NMB: normalized mean bias; NME: normalized mean error; R: correlation coefficient.

Table 4.4. Performance Statistics of Trace Gas and Aerosol Variables

Variable	Location	Mean Obs.	Mean Sim.		MB*		NMB*		NME*		R*	
			RCP4.5	RCP8.5	RCP4.5	RCP8.5	RCP4.5	RCP8.5	RCP4.5	RCP8.5	RCP4.5	RCP8.5
CO	East Asia[a]	503.9	149.5	142.8	-354.4	-361.2	-70.3	-71.7	70.3	71.7	0.23	0.27
NO_2	East Asia[a]	12.8	2.6	2.8	-10.2	-9.8	-80.0	-78.1	80.2	78.6	0.56	0.57
	Europe[b]	18.6	5.4	5.3	-13.2	-13.3	-71.1	-71.5	73.2	73.2	0.26	0.25
O_3	East Asia[a]	28.7	50.3	50.6	21.6	21.8	75.1	76.0	75.1	76.0	0.27	0.28
	Europe[b]	54.9	95.6	95.3	40.7	40.4	74.0	73.5	74.3	73.7	0.37	0.37
	CONUS[a]	35.1	49.2	49.0	14.1	13.9	40.1	39.8	40.7	40.3	0.48	0.49
SO_2	East Asia[a]	3.2	1.6	1.4	-1.6	-1.8	-48.7	-57.4	56.2	64.0	0.42	0.39
	Europe[b]	5.5	3.9	3.1	-1.6	-2.4	-29.2	-44.4	54.6	58.6	0.51	0.54
	CONUS[b]	2.7	5.8	5.1	3.1	2.3	112.0	85.4	114.6	89.7	0.82	0.85
HNO_3	Europe[b]	0.8	0.9	0.8	9.5×10^{-2}	3.0×10^{-3}	12.3	0.4	71.2	63.6	0.31	0.30
	CONUS[b]	1.2	2.3	2.2	1.1	1.0	93.1	82.7	98.6	88.7	0.66	0.66
NH_3	Europe[b]	1.0	1.7	2.1	0.7	1.1	71.2	110.2	130.9	156.5	0.25	0.28
$PM_{2.5}$	Europe[b]	13.6	12.7	9.5	-1.4	-4.5	-9.9	-32.1	31.9	36.1	0.03	0.06
	CONUS[b]	8.3	7.8	7.4	-0.5	-0.9	-6.4	-11.3	33.7	33.6	0.67	0.67
PM_{10}	East Asia[b]	112.8	50.6	50.5	-63.2	-63.4	-55.5	-55.7	56.5	57.2	0.67	0.66
	Europe[b]	23.2	26.8	22.0	3.6	-1.2	15.3	-5.4	35.5	29.5	0.22	0.21
	CONUS[b]	21.9	12.0	12.6	-9.9	-9.4	-43.5	-42.7	51.7	55.6	0.17	0.05
SO_4^{2-}	Europe[b]	2.0	2.4	2.0	0.4	4.2×10^{-3}	17.8	0.2	54.6	38.0	0.57	0.56
	CONUS[b]	2.3	2.5	2.2	0.2	-0.1	7.8	-4.0	28.4	25.4	0.85	0.87
NH_4^+	Europe[b]	0.9	1.3	1.2	0.4	0.3	42.4	33.0	54.5	49.7	0.69	0.67
	CONUS[b]	1.1	1.3	1.2	0.1	0.1	12.9	5.1	40.1	38,7	0.70	0.68
NO_3^-	Europe[b]	1.8	1.8	1.8	-2.1×10^{-2}	-1.1×10^{-3}	-1.1	-0.1	50.8	53.3	0.52	0.45
	CONUS[b]	1.0	1.2	1.2	0.1	0.2	11.9	15.5	57.8	59.9	0.58	0.58
Cl^-	Europe[b]	0.9	5.2	5.6	4.2	4.7	457.2	503.1	457.2	503.1	0.75	0.73
	CONUS[b]	0.1	0.1	0.1	-2.7×10^{-2}	-2.3×10^{-2}	-25.7	-22.0	94.0	94.0	0.17	0.20
BC	CONUS[b]	0.4	0.2	0.2	-0.1	-0.2	-37.3	-45.5	50.1	51.9	0.48	0.51
TC	CONUS[b]	2.6	1.2	1.1	-1.4	-1.6	-53.6	-59.2	55.7	60.1	0.45	0.47
OC	Europe[b]	2.9	0.5	0.5	-2.4	-2.4	-82.0	-82.2	83.0	83.2	0.46	0.51
	CONUS[b]	1.1	0.8	0.7	-0.3	-0.4	-24.9	-33.4	33.7	37.2	0.56	0.58
SOA	CONUS[b]	2.9	2.7	2.5	-0.2	-0.5	-8.1	-15.6	33.2	33.5	0.51	0.62
OOA	NH[b]	4.8	1.7	1.7	-3.1	-3.2	-64.6	-65.5	65.2	66.2	0.89	0.91
HOA	NH[b]	2.1	0.1	0.1	-1.9	-1.9	-92.9	-93.2	92.9	93.2	0.93	0.94
TOA	NH[b]	7.9	1.8	1.8	-6.0	-6.1	-76.6	-77.2	77.0	77.6	0.86	0.85
TCO	Global[c]	1.4×10^{18}	1.3×10^{18}	1.3×10^{18}	-1.4×10^{17}	-1.6×10^{17}	-9.9	-11.4	15.2	16.2	0.85	0.83
THCHO	Global[c]	4.2×10^{15}	2.6×10^{15}	2.7×10^{15}	-1.6×10^{15}	-1.5×10^{15}	-37.4	-37.8	42.0	41.7	0.69	0.69
TNO_2	Global[c]	5.3×10^{14}	7.7×10^{14}	7.9×10^{14}	2.4×10^{14}	2.6×10^{14}	44.9	47.8	62.0	62.8	0.82	0.86
TSO_2	Global[d]	0.2	0.1	0.1	-0.1	-0.1	-33.7	-42.9	98.7	96.4	-0.08	-0.08
TOR	Global[d]	28.4	31.8	31.6	3.4	3.2	11.9	11.2	17.2	17.2	0.80	0.79

[a]Units of ppb, [b]Units of μg m^{-3},[c]Units of molecules cm^{-2}, [d]Units of DU, *MB: mean bias; NMB: normalized mean bias; NME: normalized mean error; R: correlation coefficient.

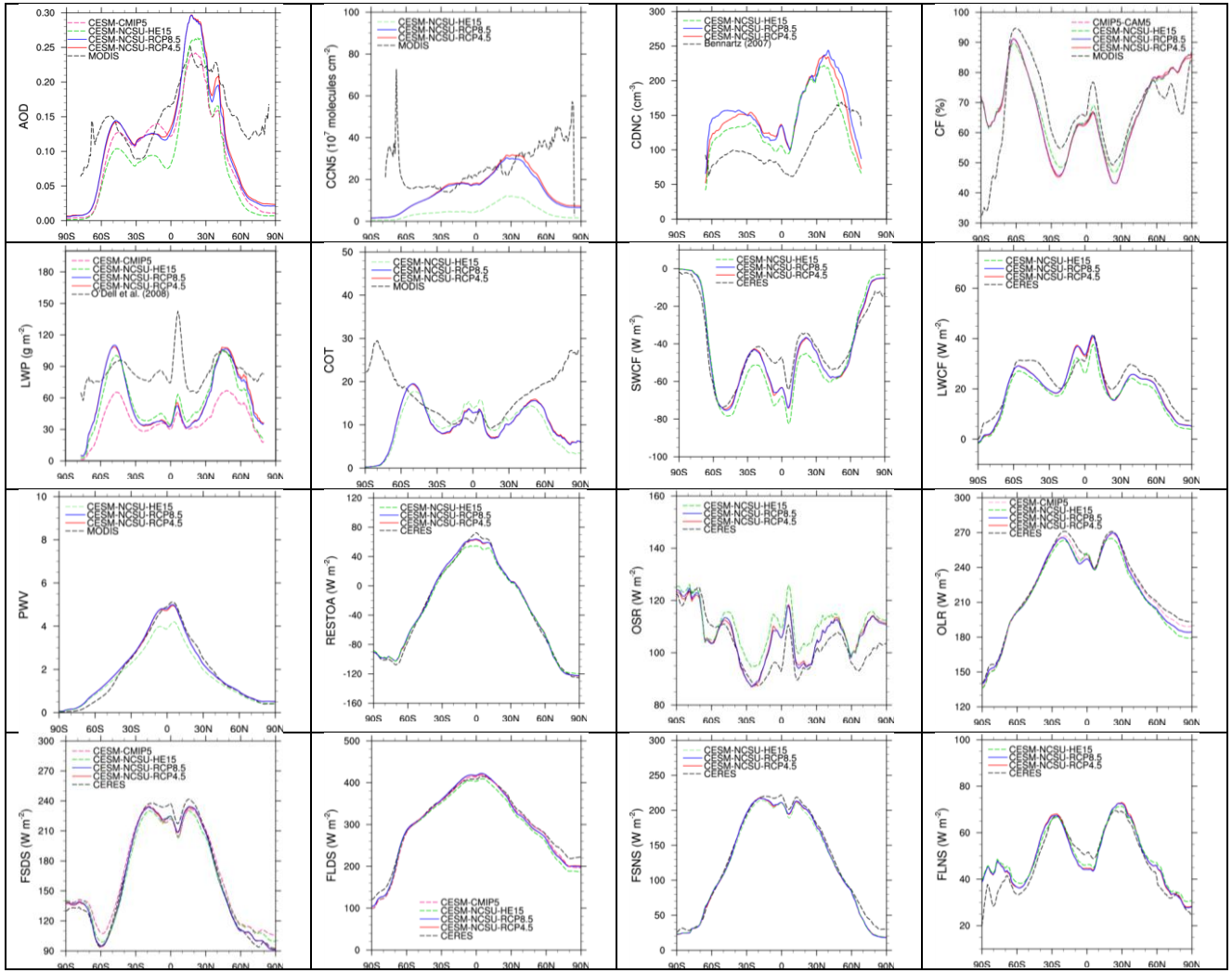

Figure 4.1. A comparison of the zonal mean profiles for cloud and radiation variables from the RCP4C, RCP8C, and He et al. (2015a) simulations using CESM-NCSU and available CESM1-CMIP5 simulations against satellite estimates.

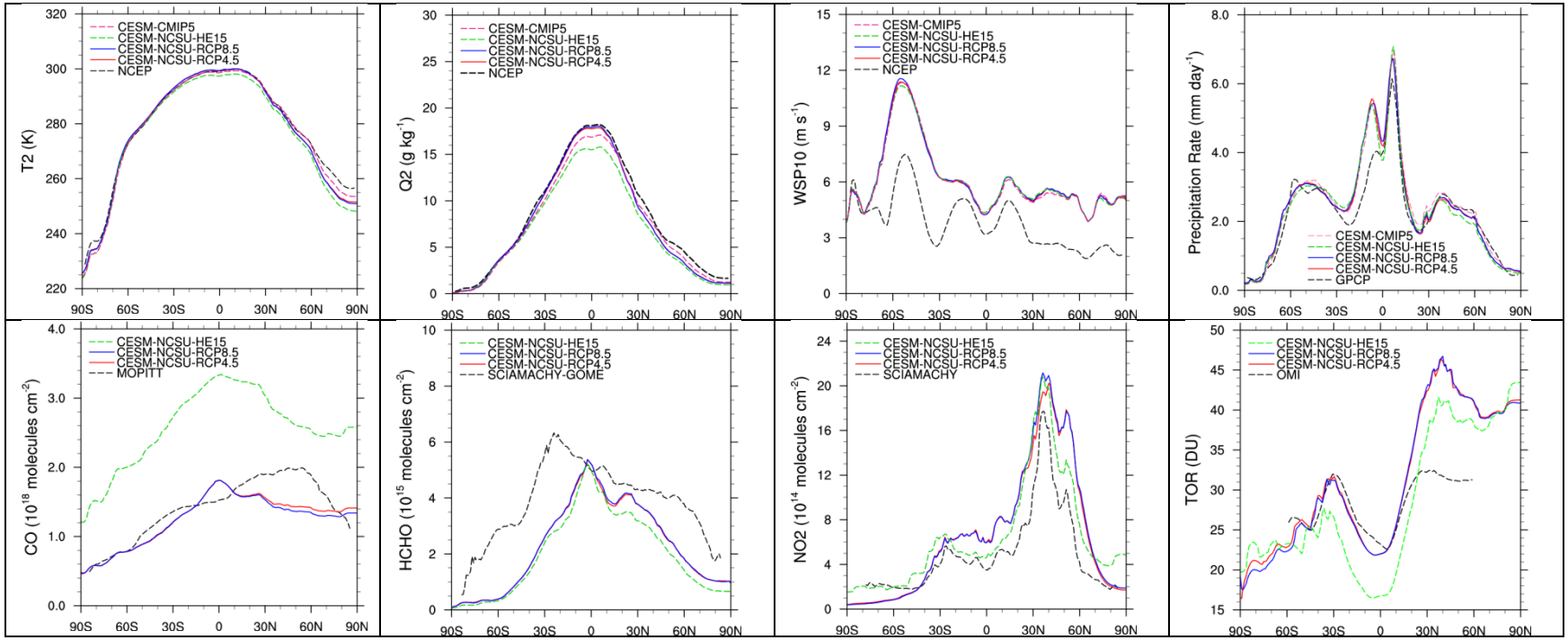

Figure 4.2. A comparison of the zonal mean profiles for surface meteorological variables and trace gas column mass abundances from the RCP4C, RCP8C, and He et al., (2015a) simulations using CESM-NCSU and available CESM-CMIP5 simulations against satellites/reanalysis estimates.

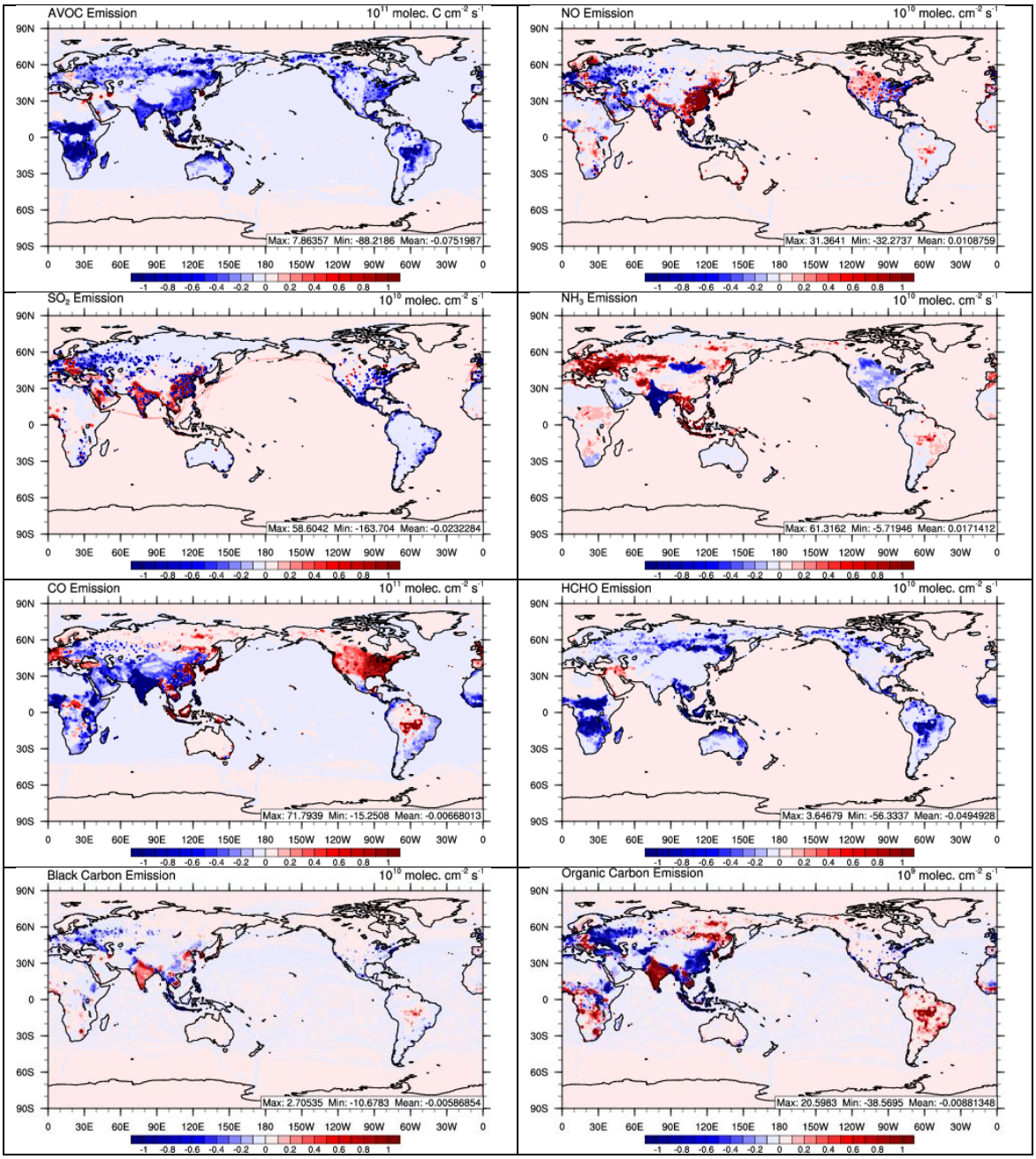

Figure 4.3. Absolute differences in the emissions of AVOC, NO, SO_2, NH_3, CO, HCHO, BC, and OC between the RCP8.5 and the RCP4.5 emission inventories for the current year period.

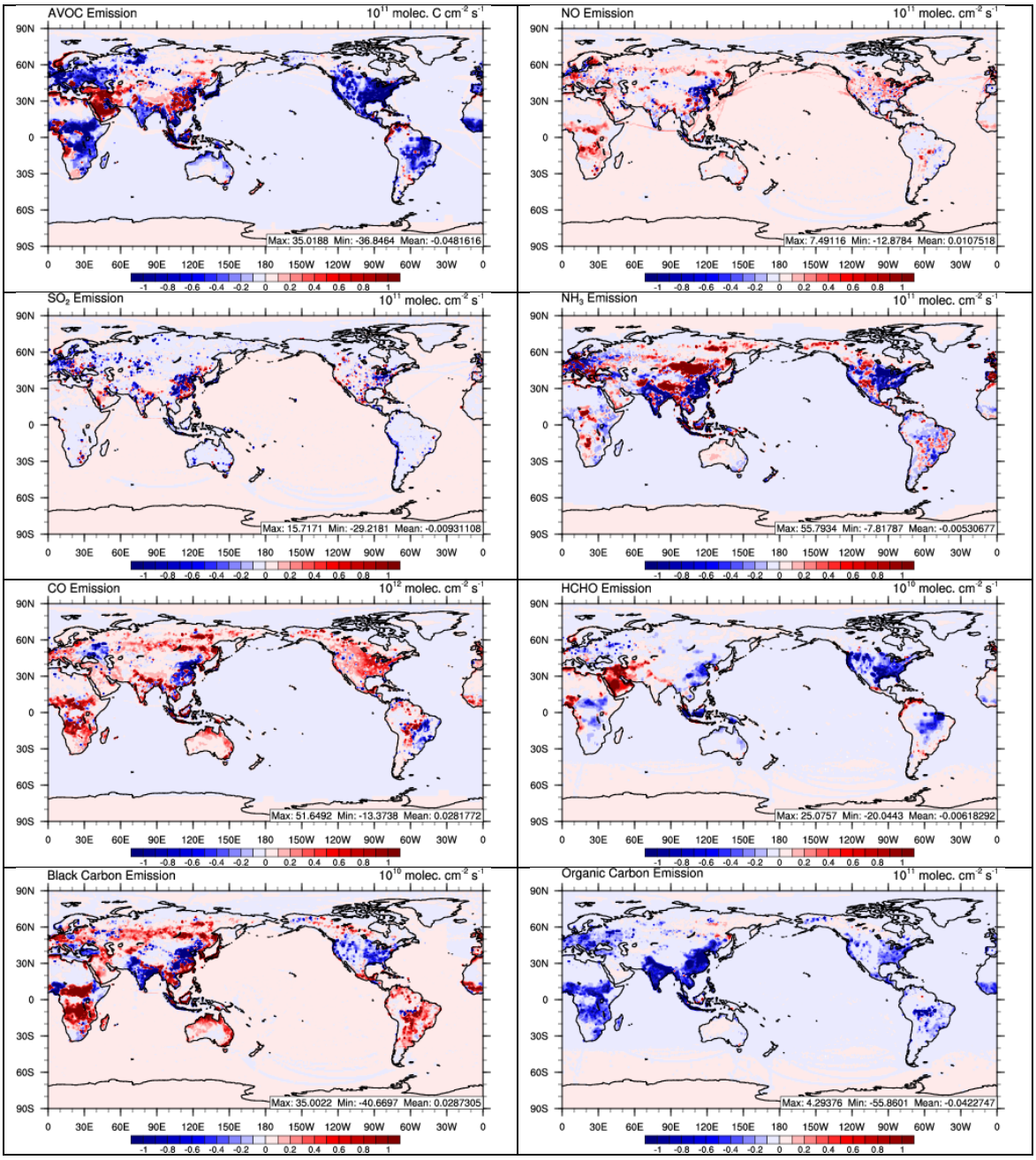

Figure 4.4. Absolute differences in the emissions of AVOC, NO, SO_2, NH_3, CO, HCHO, BC, and OC between the RCP8.5 and the He et al. (2015) emission inventories for the current year period.

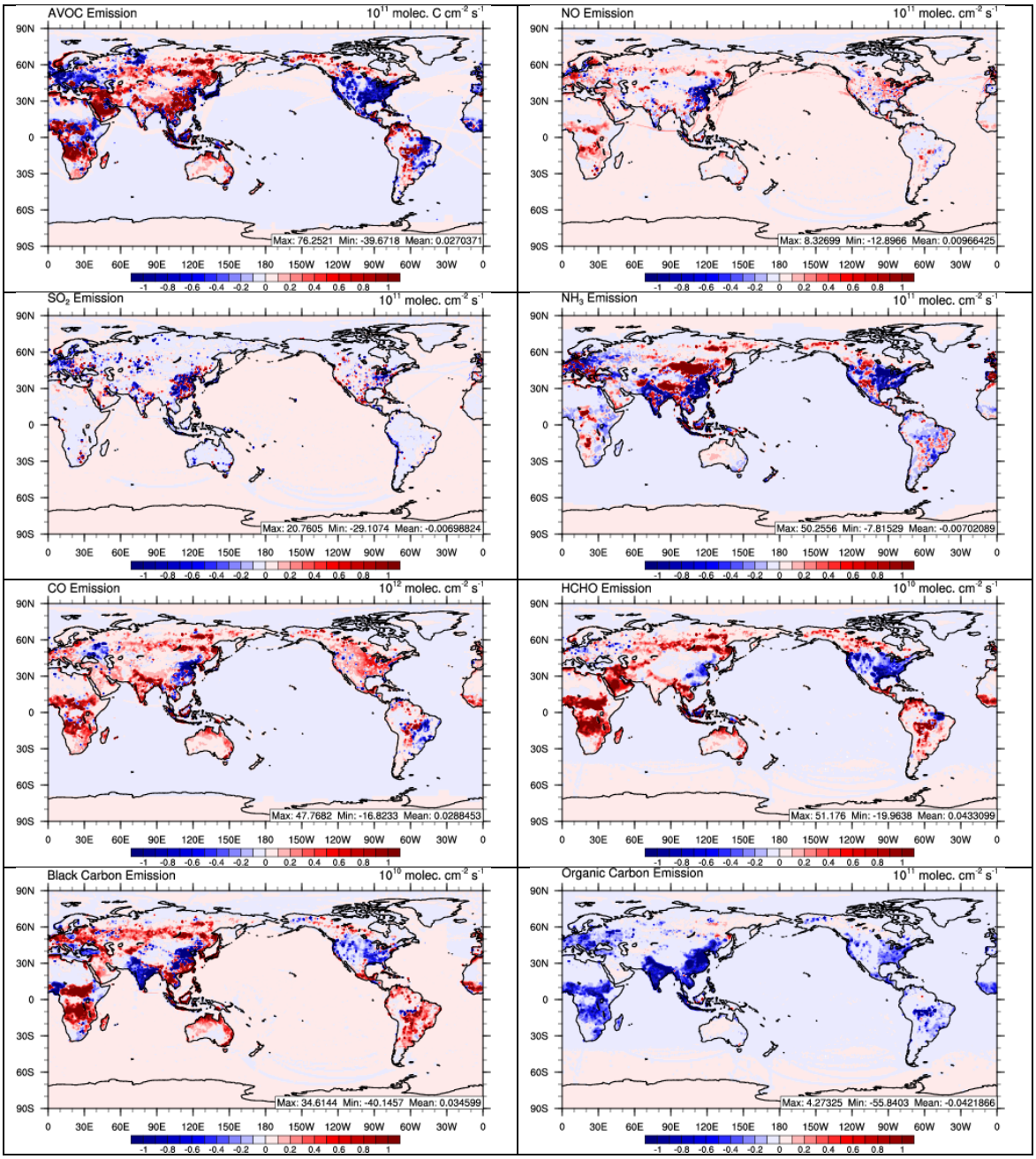

Figure 4.5. Absolute differences in the emissions of AVOC, NO, SO_2, NH_3, CO, HCHO, BC, and OC between the RCP4.5 and the He et al. (2015) emission inventories for the current year period.

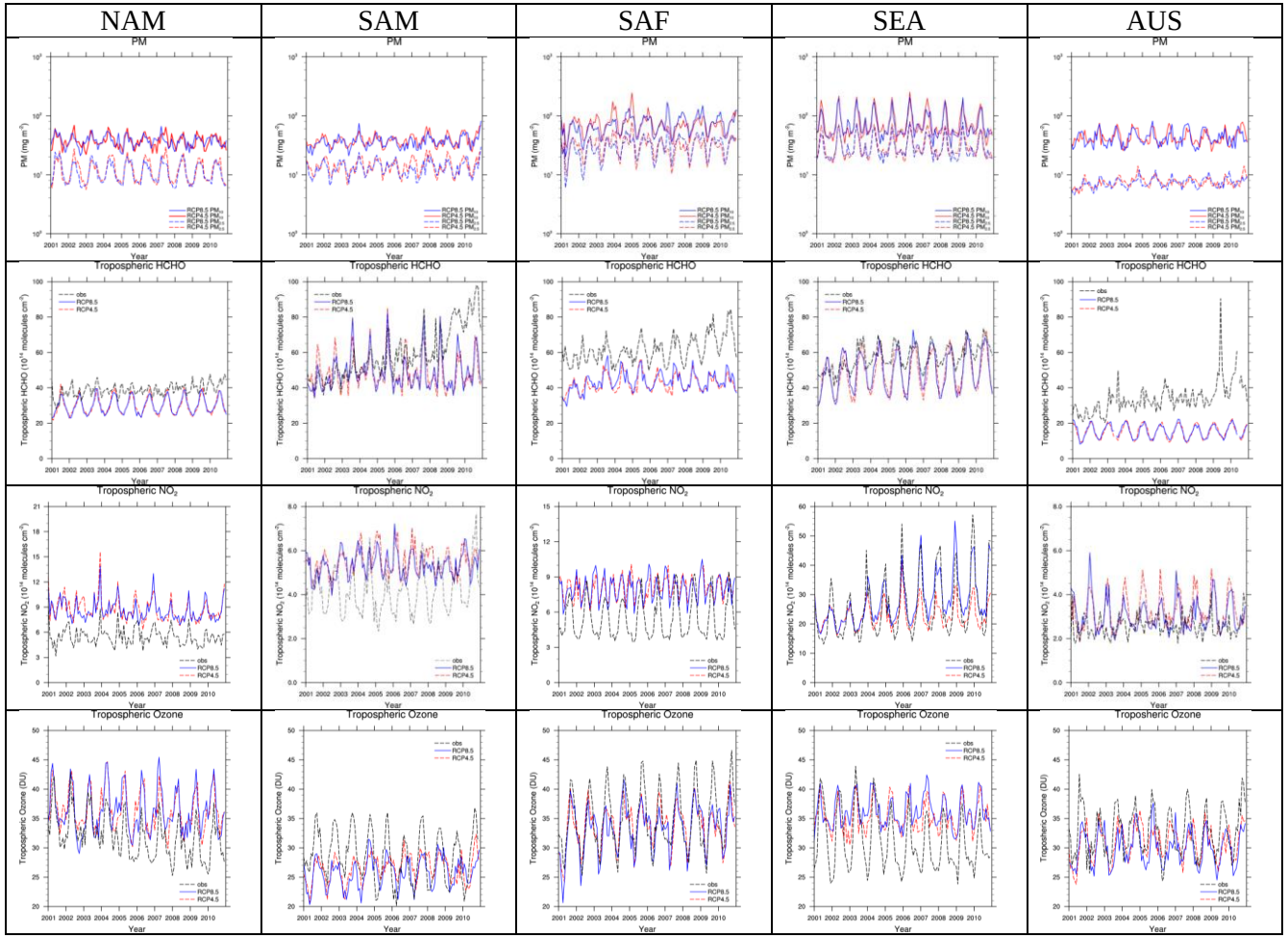

Figure 4.6. The monthly-mean times series of tropospheric $PM_{2.5}$, PM_{10}, and column mass abundances of HCHO, NO_2, and O_3 from the RCP4C and RCP8C simulations compared against available satellite estimates in the five stratocumulus cloud regions of North America (NAM), South America (SAM), South East Asia (SEA), South Africa (SAF), and Australia (AUS).

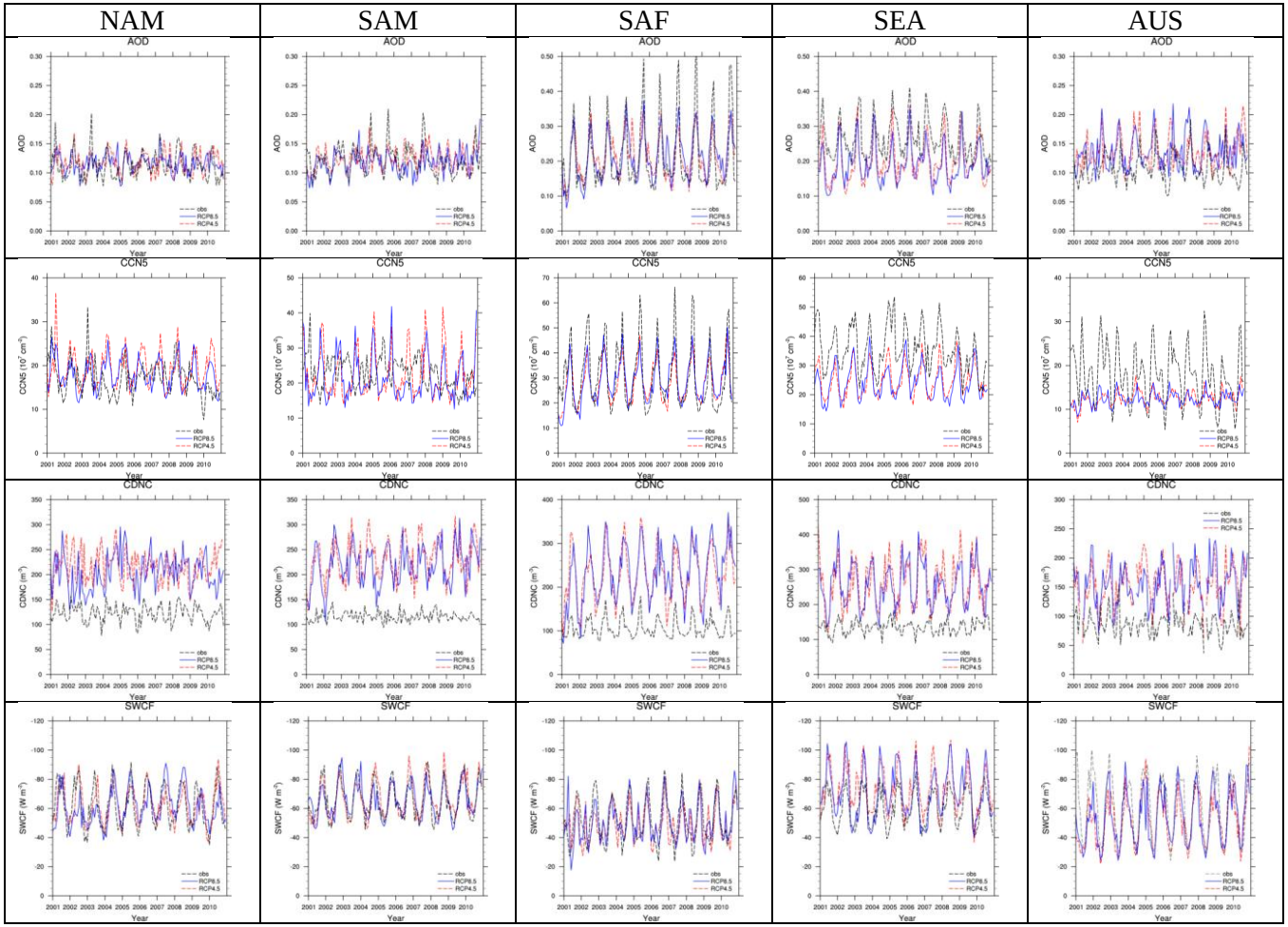

Figure 4.7. The monthly-mean times series (2001-2010) of AOD, column CCN5, column CDNC, and SWCF from the RCP4C and RCP8C simulations compared against available satellite estimates in the five stratocumulus cloud regions of NAM, SAM, SEA, SAF, and AUS.

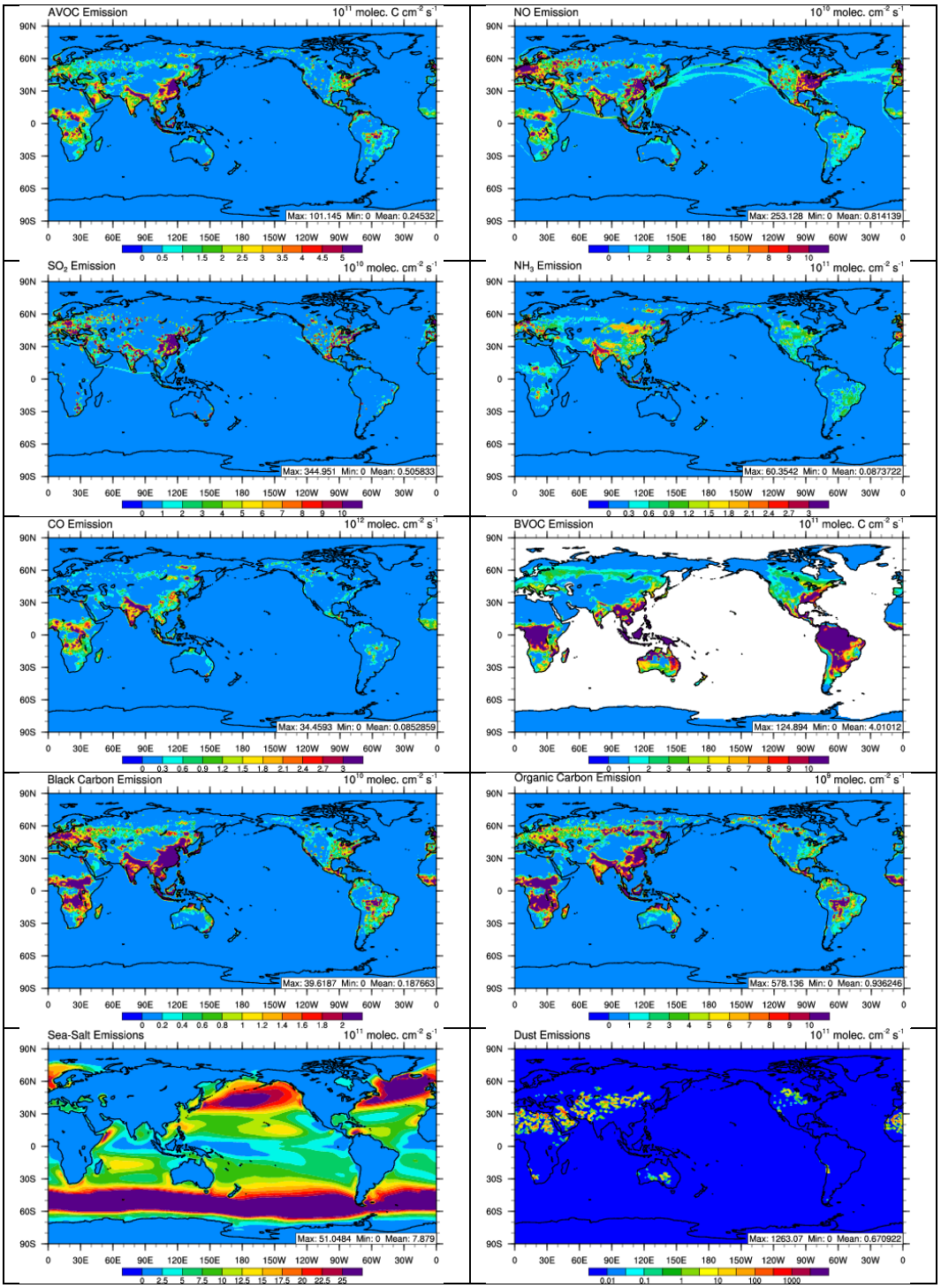

Figure 4.8. Spatial variability of AVOC, NO, SO_2, NH_3, CO, BVOC, BC, OC, sea-salt, and dust emissions from CESM and the RCP4.5 emission inventory for the current year period.

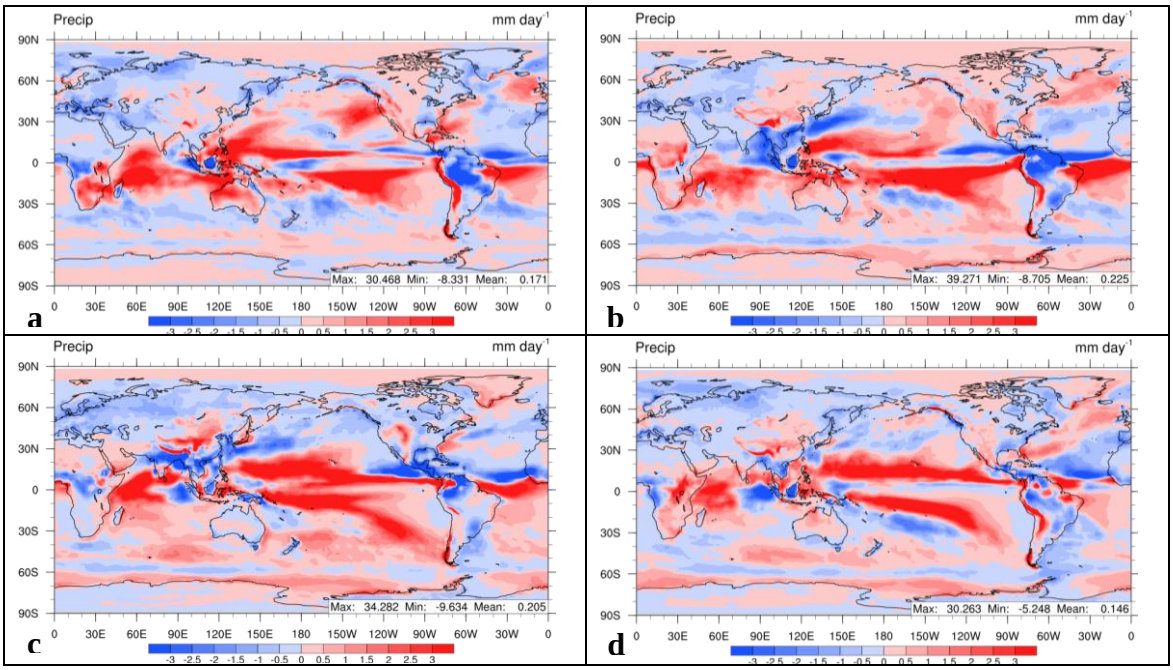

Figure 4.9. Absolute differences in precipitation rate between the RCP4C simulation and GPCP estimates during the four seasons: DJF (a), MAM (b), JJA (c), and SON (d).

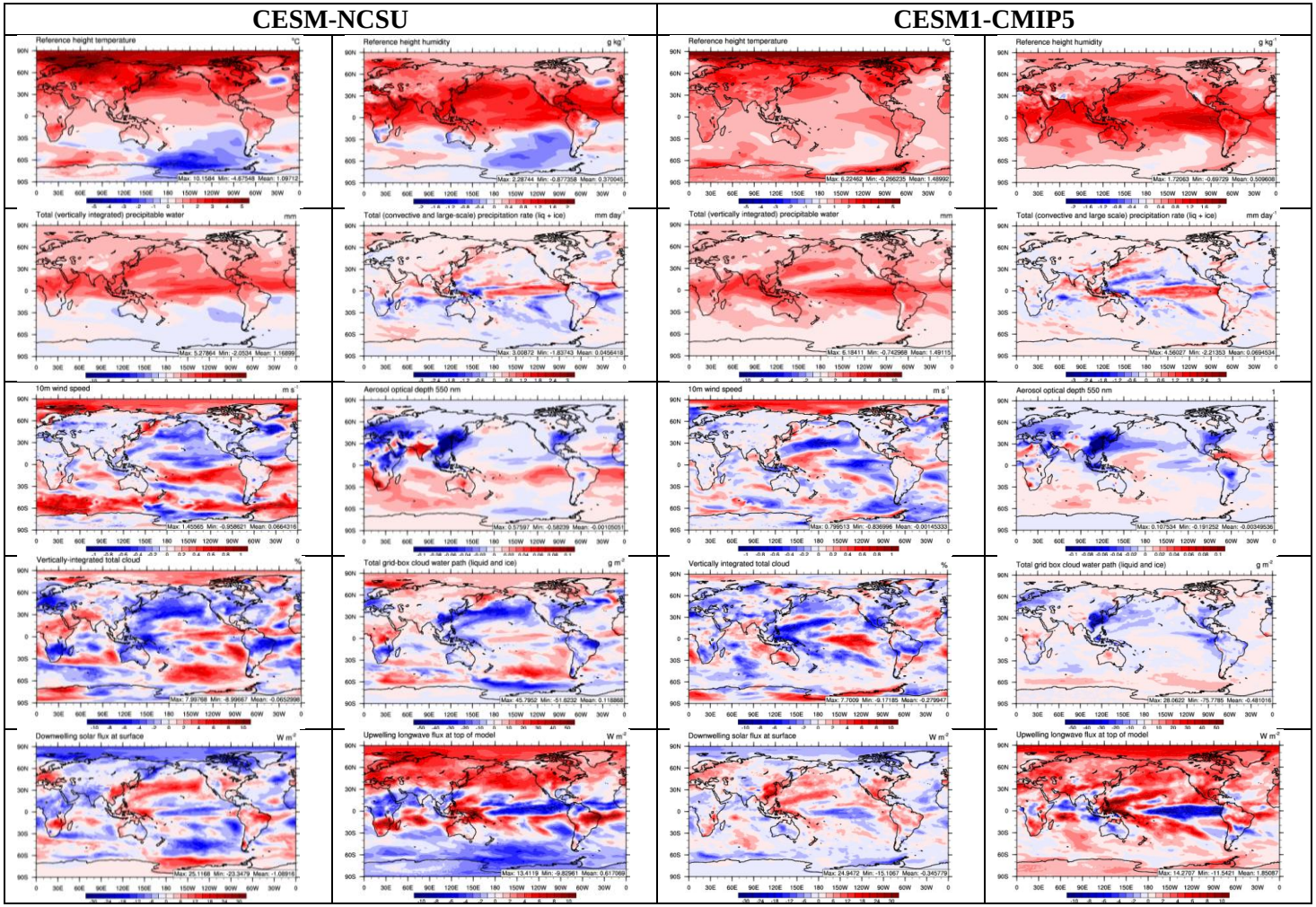

Figure 4.10. A comparison of the spatial trends in available meteorological, cloud, and radiation variables between CESM-NCSU and CESM1-CMIP5 simulations under the RCP4.5 scenario.

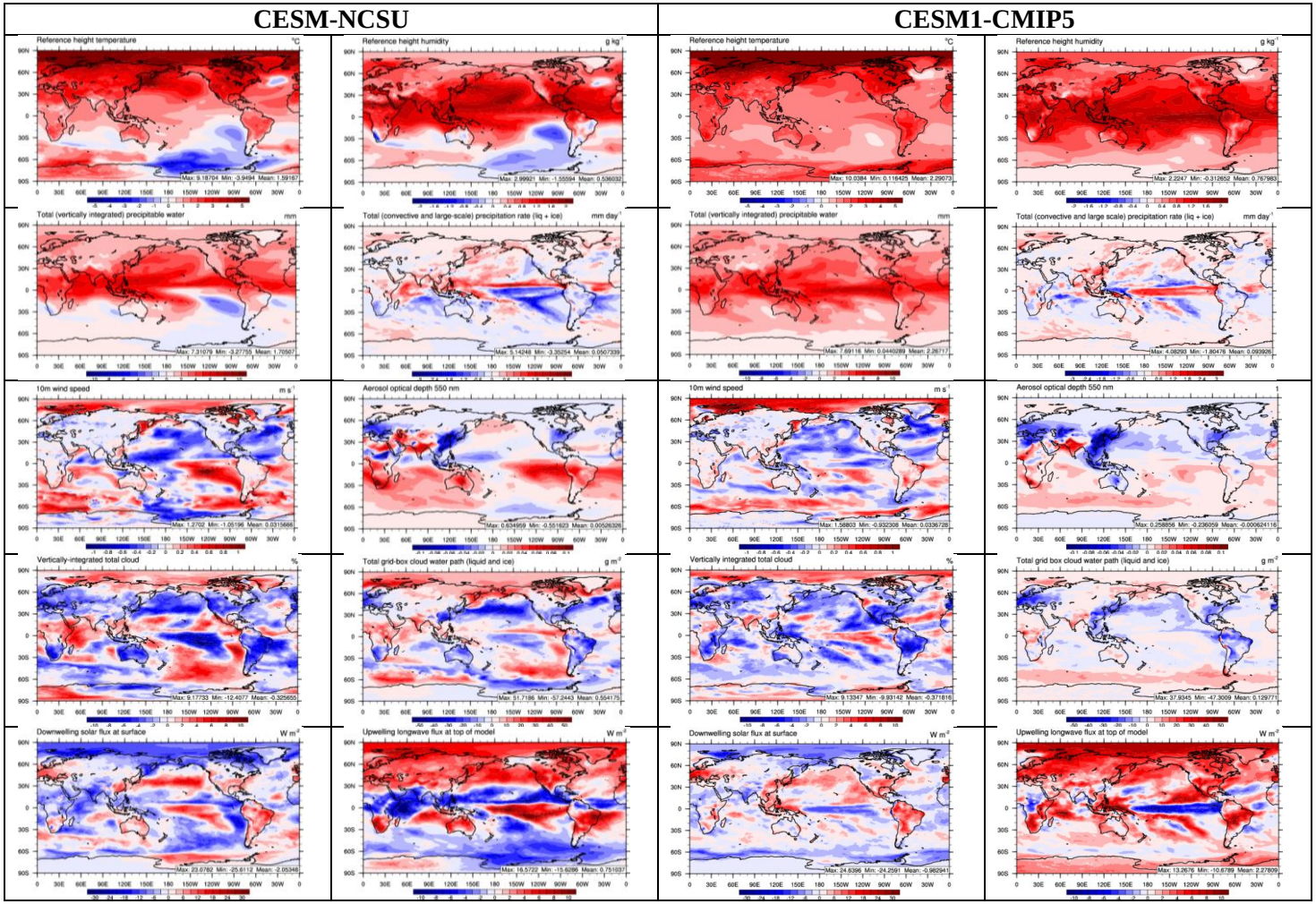

Figure 4.11. A comparison of the spatial trends in available meteorological, cloud, and radiation variables between CESM-NCSU and CESM1-CMIP5 simulations under the RCP8.5 scenario.

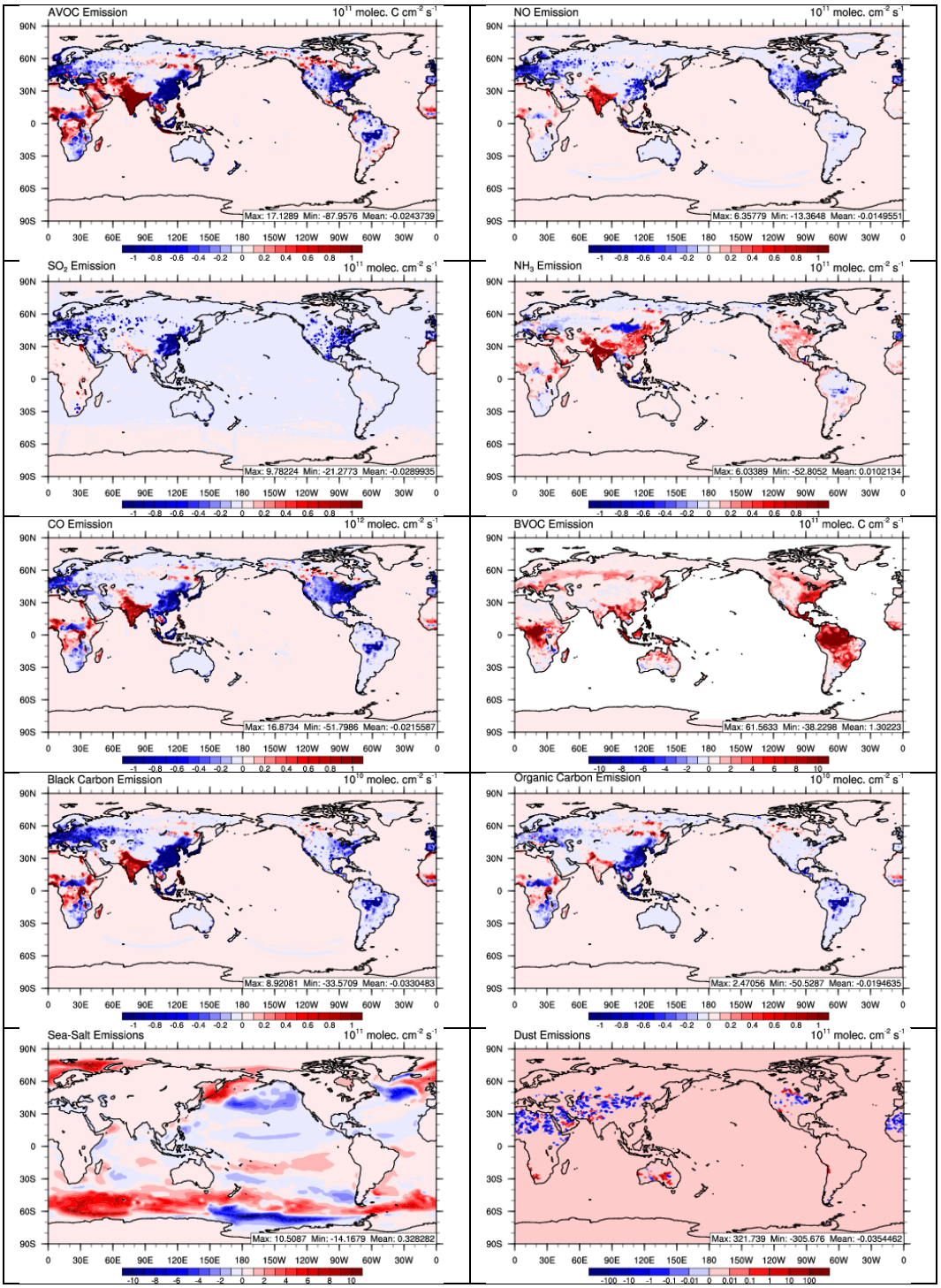

Figure 4.12. Absolute differences in the emissions of AVOC, NO, SO_2, NH_3, CO, BVOC, BC, OC, sea-salt, and dust between the RCP4F and RCP4C simulations.

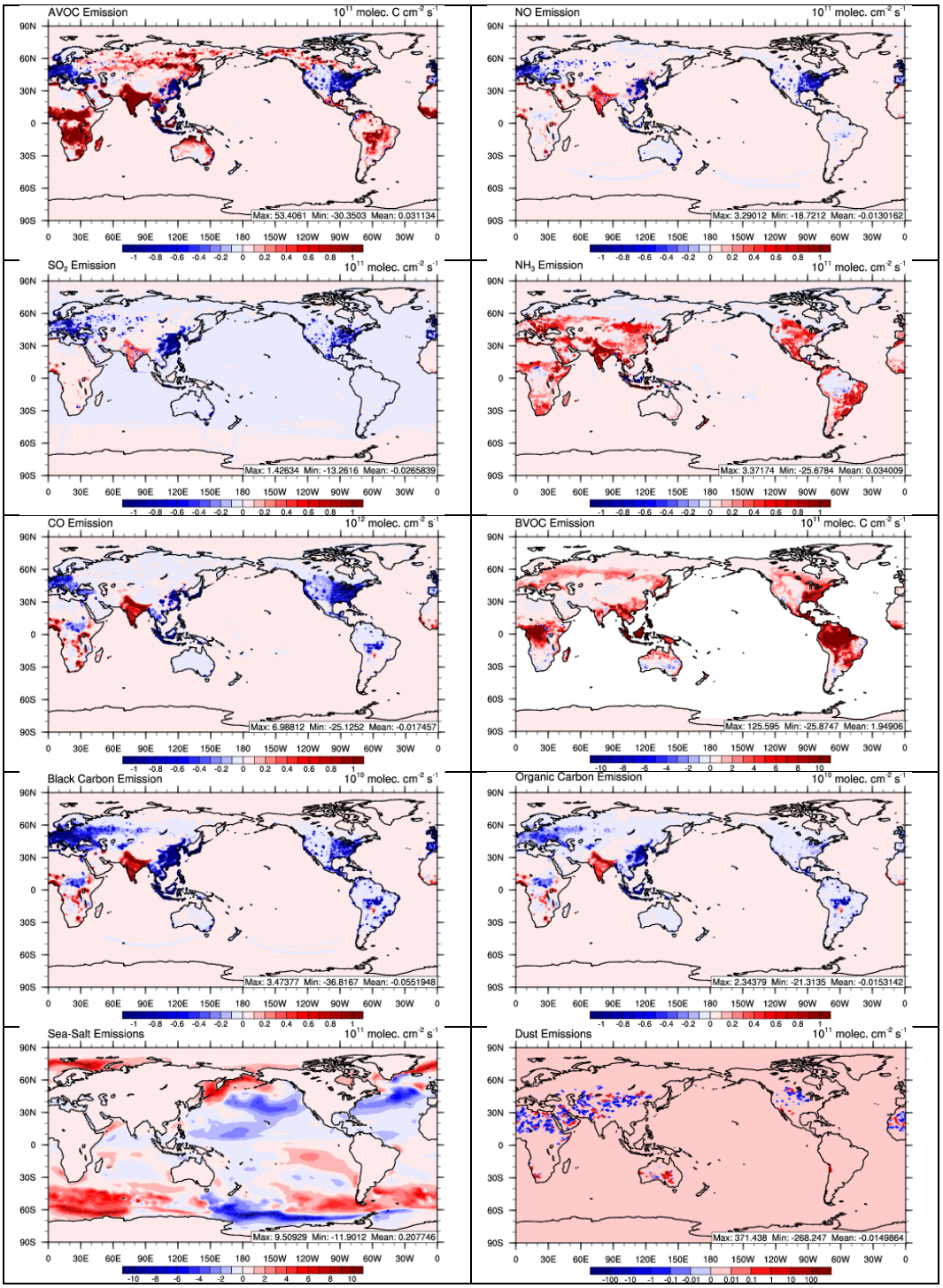

Figure 4.13. Absolute differences in the emissions of AVOC, NO, SO_2, NH_3, CO, BVOC, BC, OC, sea-salt, and dust emissions between the RCP8F and RCP8C simulations.

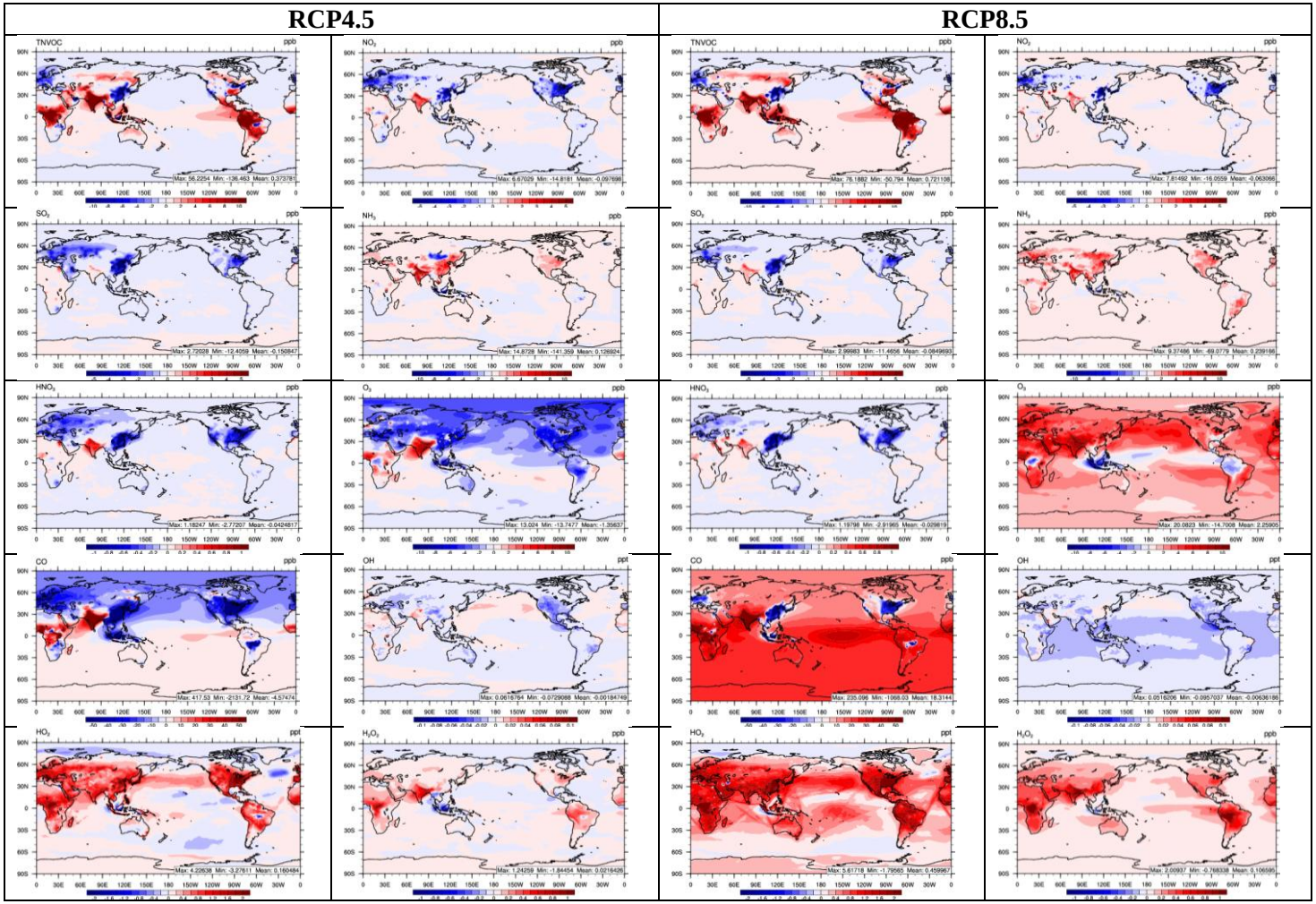

Figure 4.14. A comparison of trends in surface concentrations of trace gases predicted by CESM-NCSU between future and current decades under the RCP4.5 and RCP8.5 scenarios.

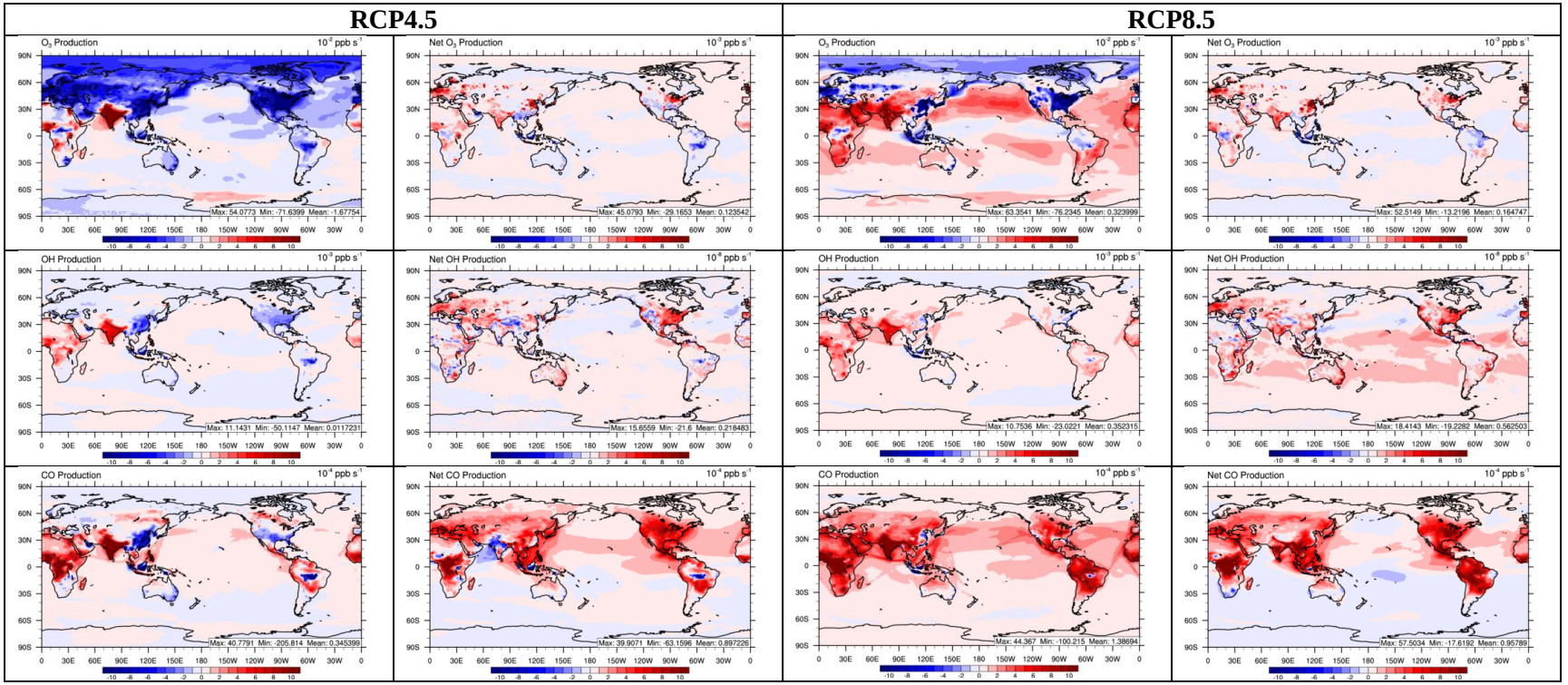

Figure 4.15. Absolute differences in surface total chemical production and net chemical production of O_3, OH, and CO between the current and future periods under the RCP4.5 and RCP8.5 scenarios.

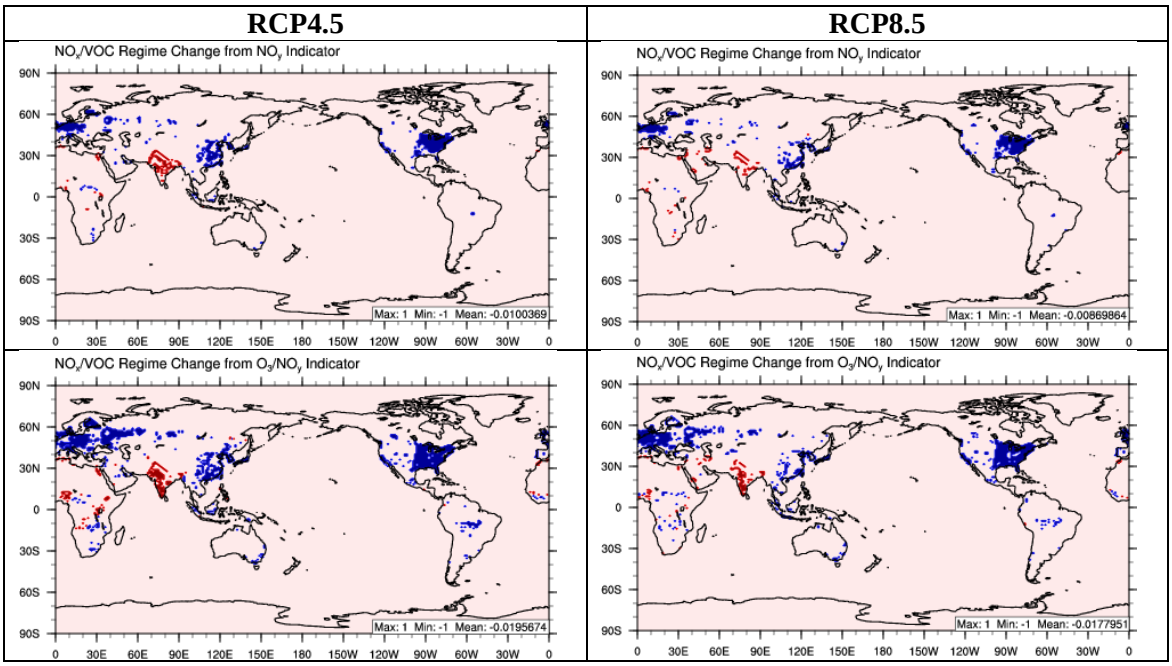

Figure 4.16. The changes in NO_x/VOC photochemical regimes using the NO_y level indicator (top) and O_3/NO_y ratio indicator (bottom) following the RCP4.5 (left) and RCP8.5 (right) scenarios. The blue color indicates a transition from VOC-limited conditions in the current period to NO_x limited conditions in the future period, while the red color indicates a transition from NO_x limited conditions during the current period to VOC-limited conditions during the future period.

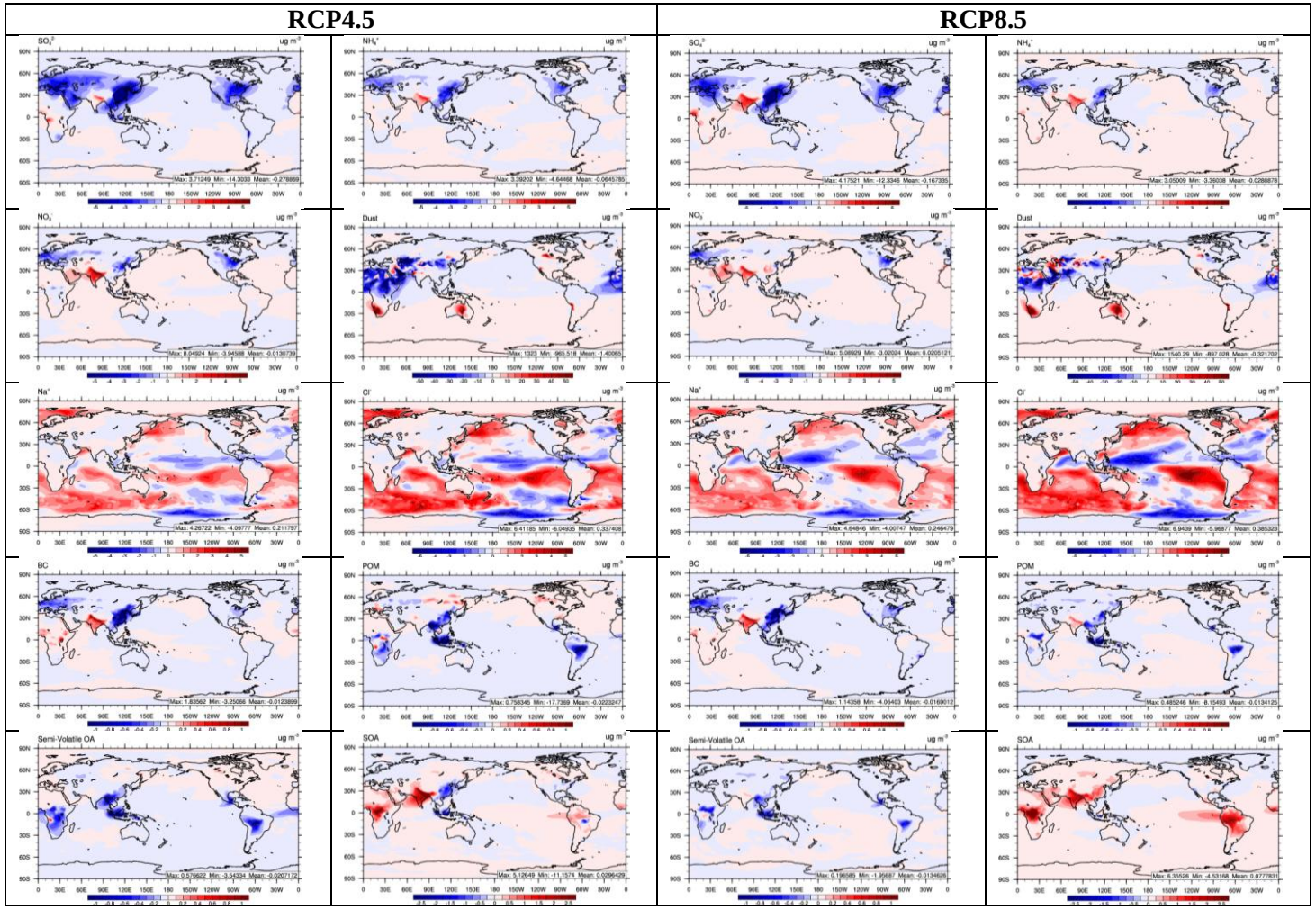

Figure 4.17. A comparison of trends in surface concentrations of aerosol species predicted by CESM-NCSU between future and current decades under the RCP4.5 and RCP8.5 scenarios.

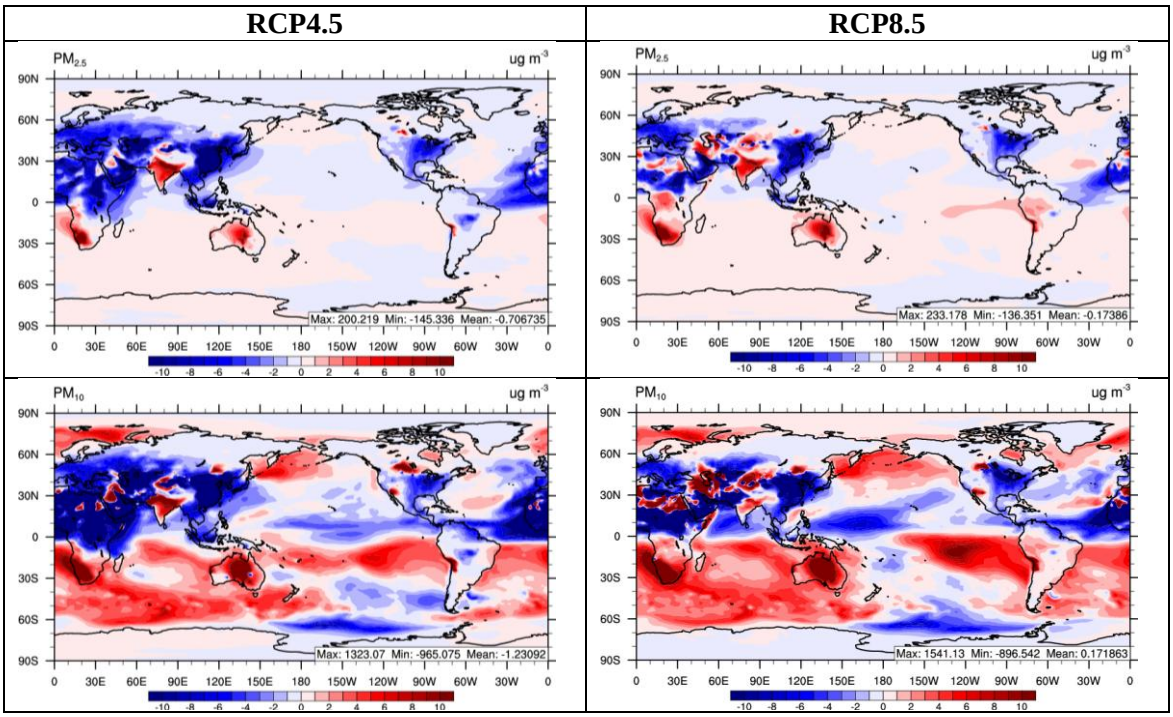

Figure 4.18. A comparison of trends in surface concentrations of $PM_{2.5}$ and PM_{10} predicted by CESM-NCSU between future and current decades under the RCP4.5 and RCP8.5 scenarios.

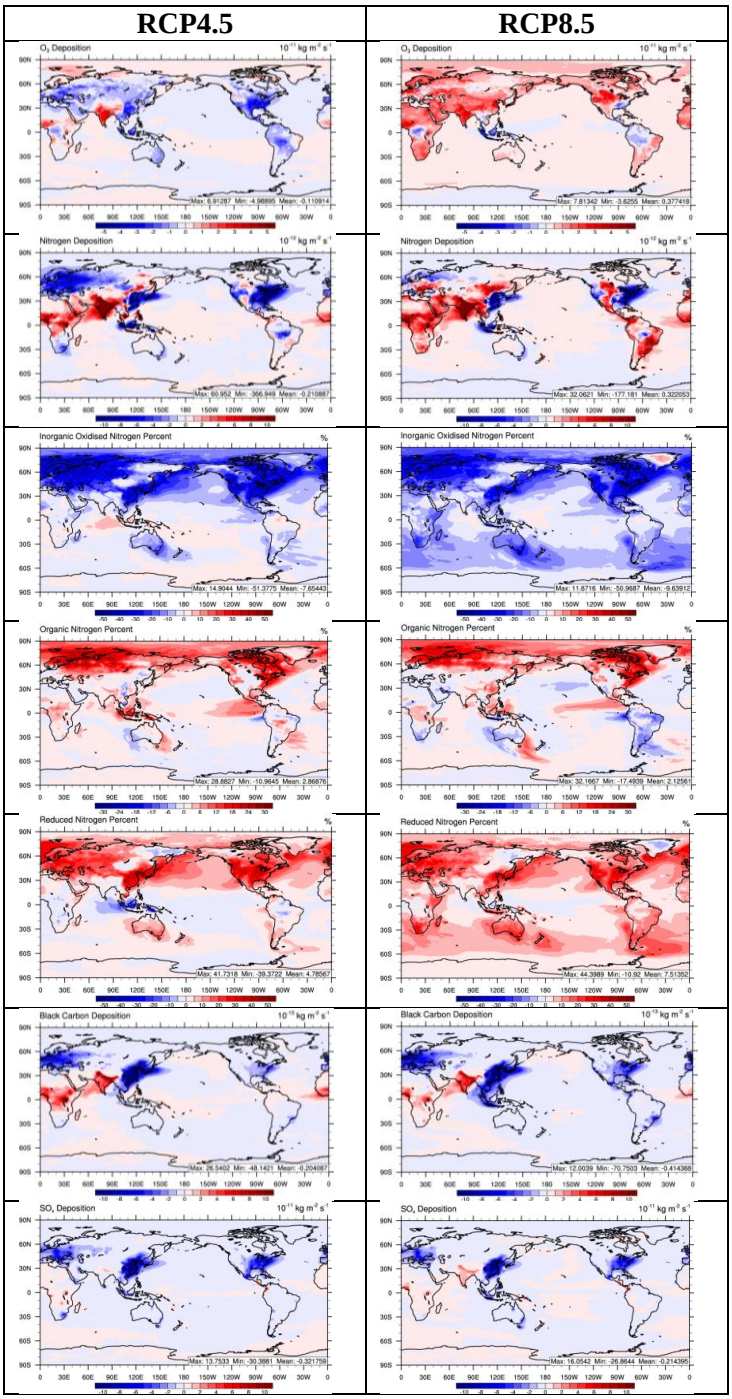

Figure 4.19. A comparison of trends in deposition of O_3, nitrogen, oxidized sulfur (SO_x), and black carbon, as well as trends in the percentage of oxidized nitrogen, organic nitrogen, and reduced nitrogen that compose the total nitrogen deposition predicted by CESM-NCSU between future and current decades under the RCP4.5 and RCP8.5 scenarios.

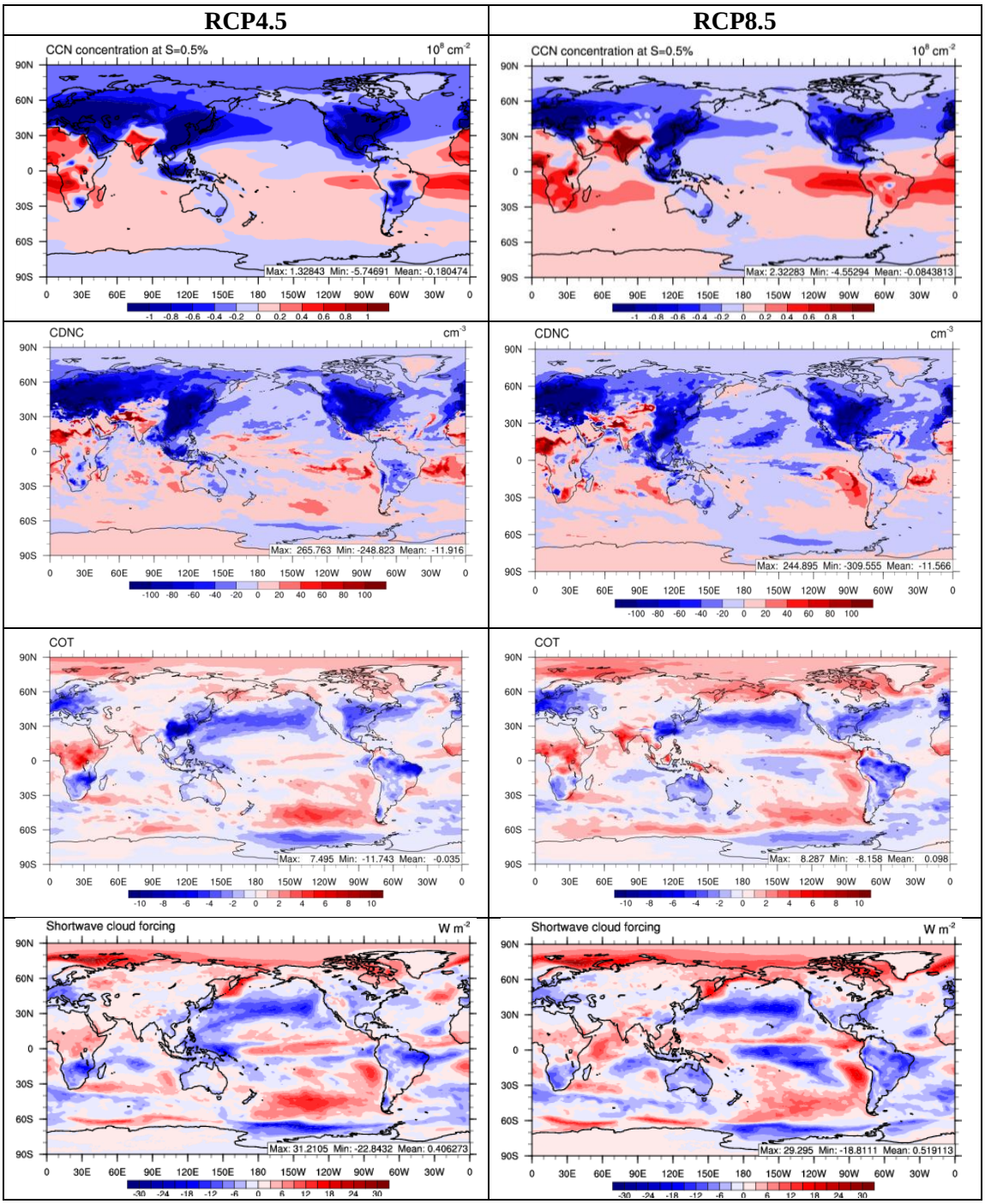

Figure 4.20. A comparison of trends in CCN5, CDNC, COT, and SWCF predicted by CESM-NCSU between future and current decades under the RCP4.5 and RCP8.5 scenarios.

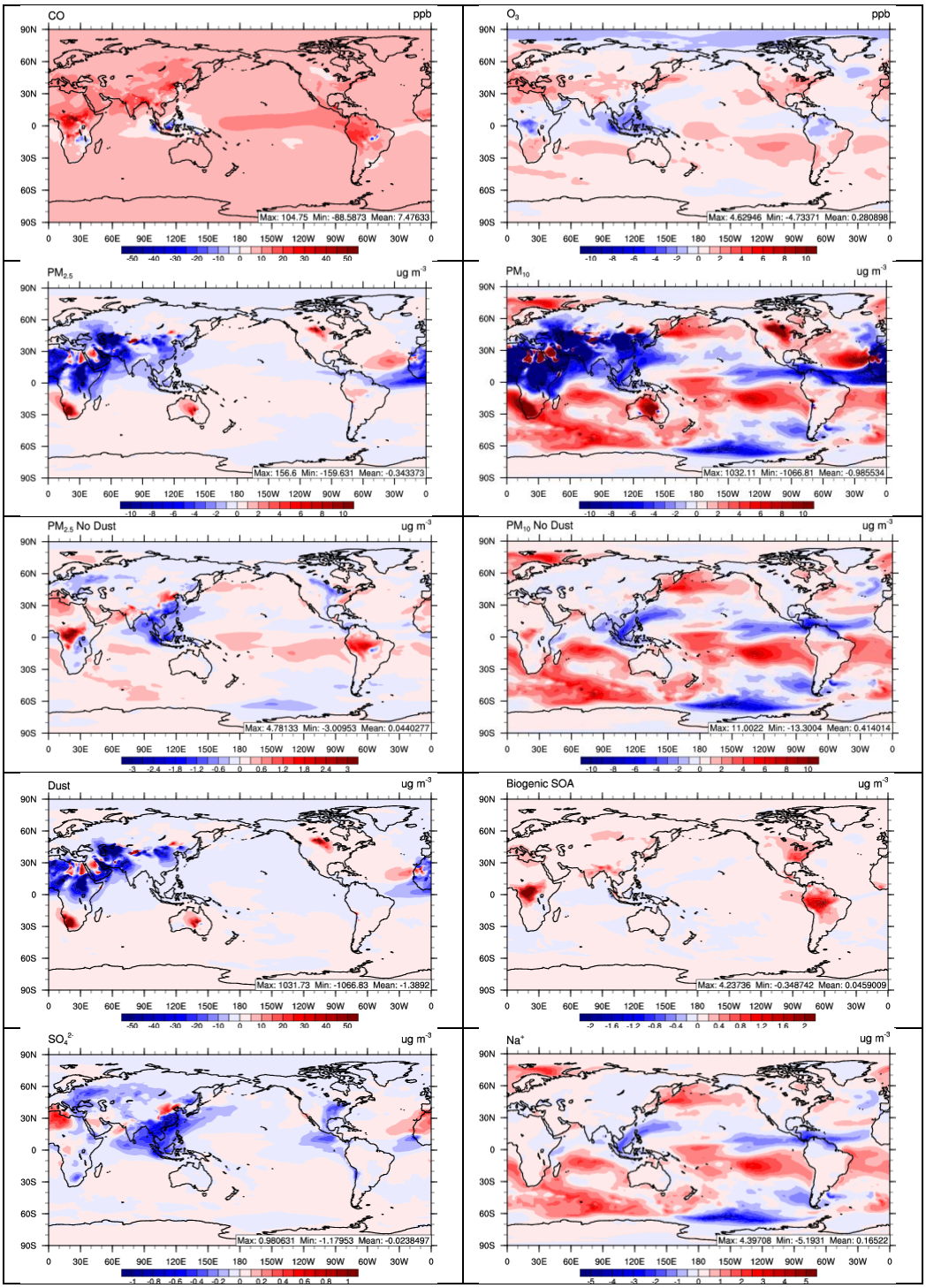

Figure 4.21. Absolute difference in O_3, CO, $PM_{2.5}$, PM_{10}, $PM_{2.5}$ (no dust), PM_{10} (no dust), dust, BSOA, SO_4^{2-}, and Na^+ between the RCP4F_GHGF and RCP4C simulations.

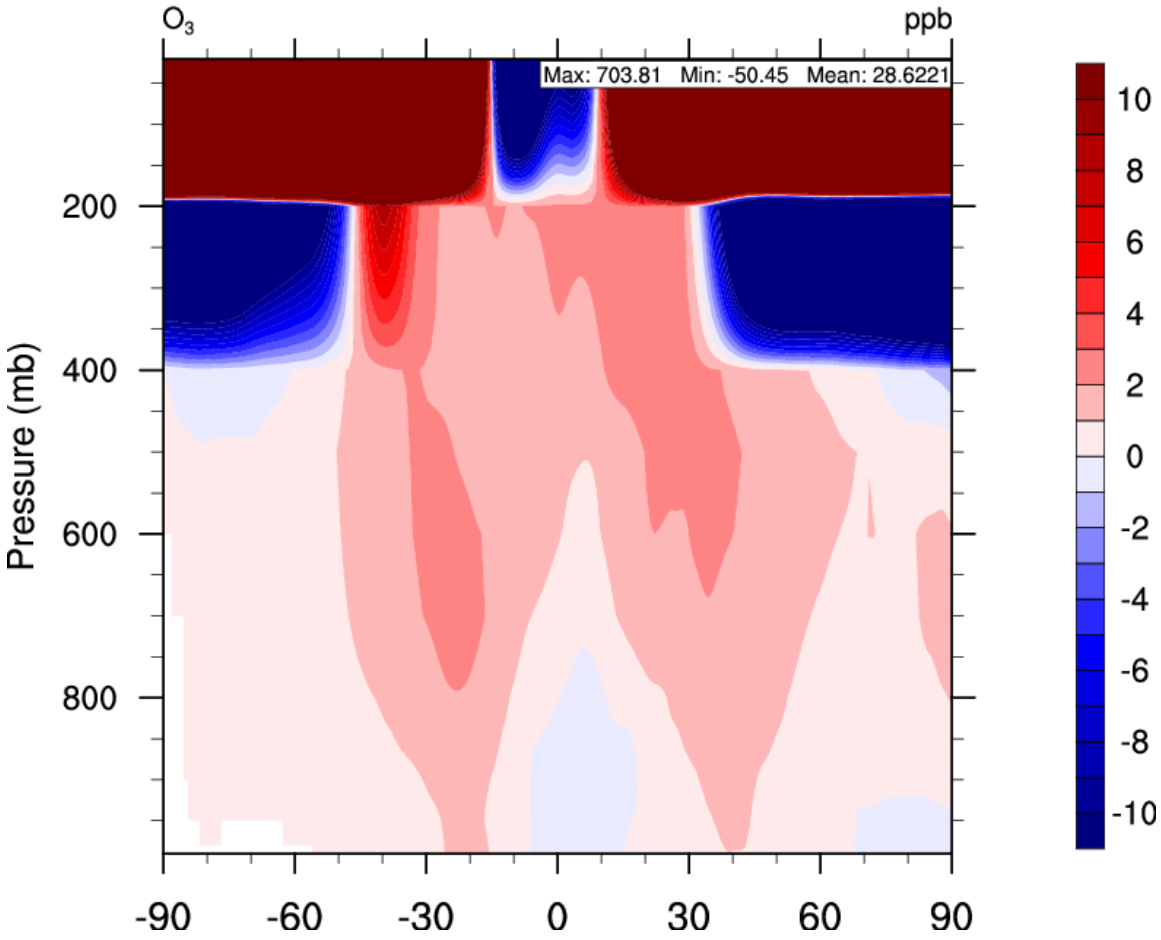

Figure 4.22. The absolute difference in the zonal mean vertical cross-section of O_3 between the RCP4F_GHGF and RCP4C simulations.

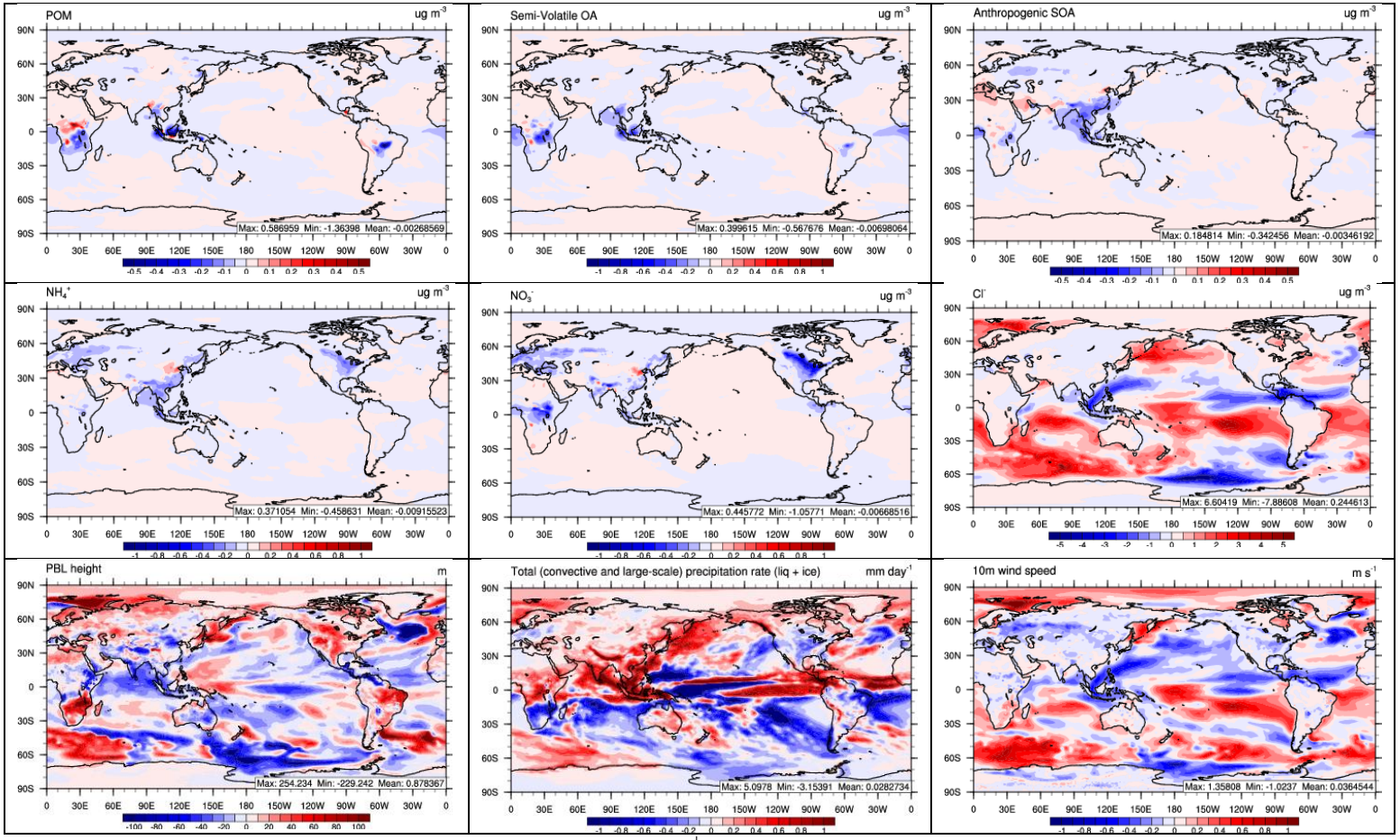

Figure 4.23. The absolute difference in POM, SVOA, ASOA, NH_4^+, NO_3^-, Cl^-, planetary boundary layer height, WSP10, and PR between the RCP4F_GHGF and RCP4C simulations.

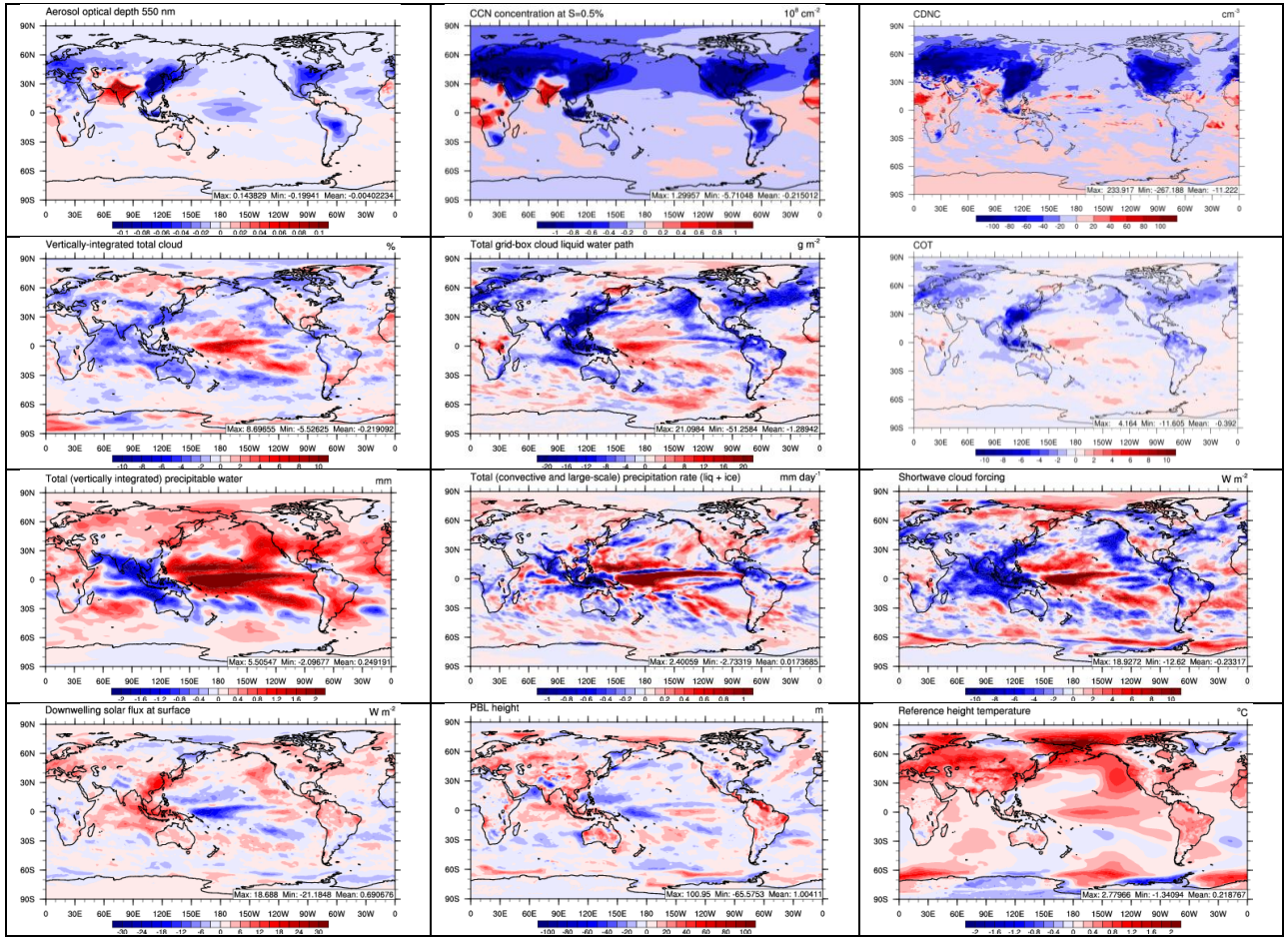

Figure 4.24. Absolute differences in meteorological, cloud, and radiation variables between the RCP4F and RCP4F_GHGF CESM-NCSU simulation, illustrating the impacts of changing emissions.

.

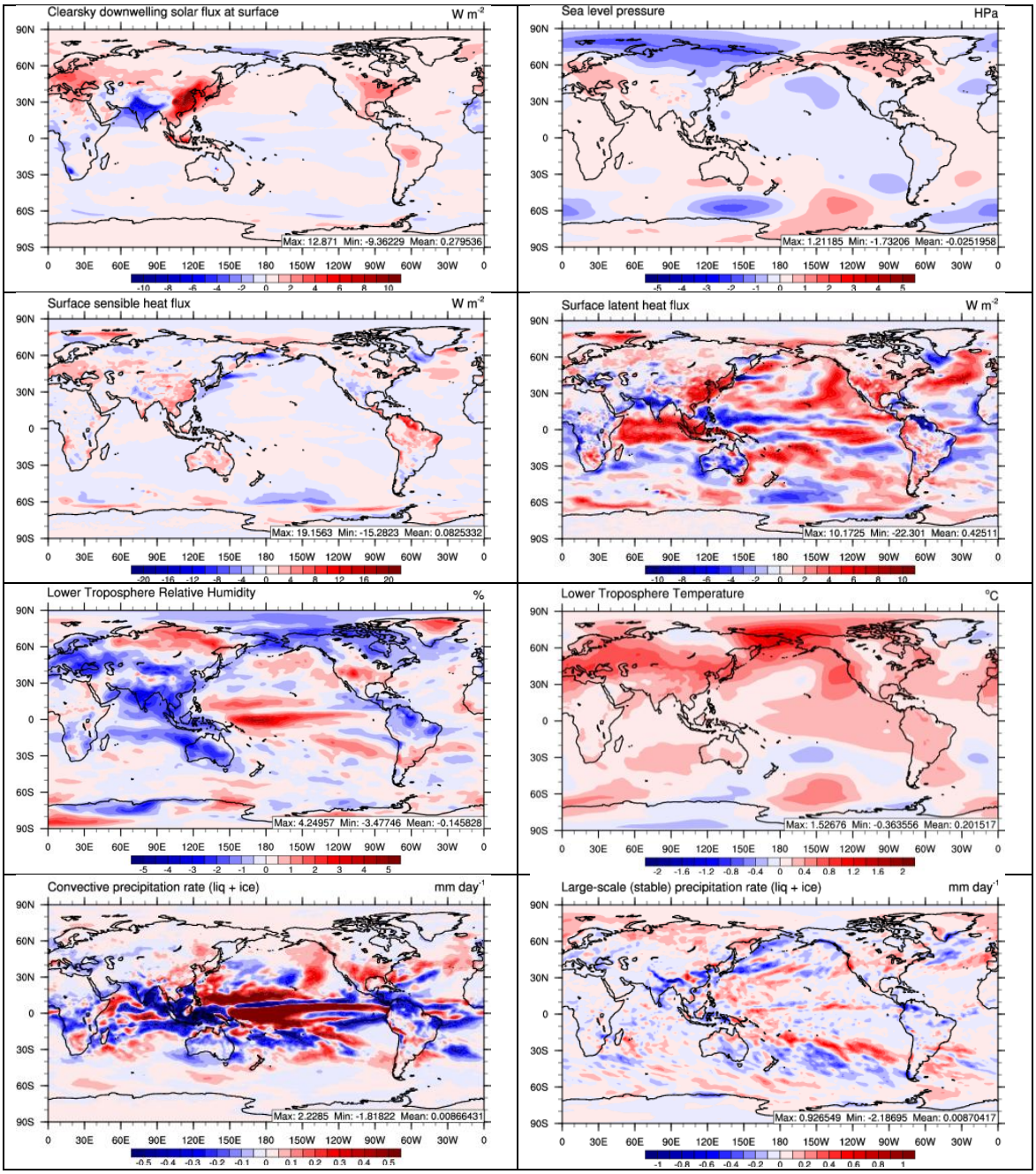

Figure 4.25. Absolute differences in clear sky FSDS, Sea Level Pressure, SHX, LHX, lower troposphere RH, lower troposphere temperature, PRC, and PRL between the RCP4F and RCP4F_GHGF simulations.

CHAPTER 5. SUMMARY

5.1 Summary

The prospect of global climate change will have wide scale impacts, such as ecological stress and human health hazards. One aspect of concern is future changes in air quality that will result from changes in both meteorological forcing and air pollutant emissions. The use of advanced modeling tools is necessary in order to understand the complex interactions between chemistry and climate in future climate simulations. In this work, the GU-WRF/Chem and CESM-NCSU models are applied to study the impact of future changes in air quality and aerosol/cloud interactions. The CESM-NCSU model is also further developed to better represent the formation of OA to aid in future climate simulations.

In the first half of this work, the GU-WRF/Chem model is employed to simulate the impact of changing climate and emissions following the IPCC AR4 SRES A1B scenario. An average of 4 future years (2020, 2030, 2040, and 2050) is compared against an average of 2 current years (2001 and 2010). Under this scenario, by the Mid-21st century, global air quality is projected to degrade with a global average increase of 2.5 ppb in the maximum 8-hr O_3 level and of 0.3 μg m^{-3} in 24-hr average $PM_{2.5}$. However, $PM_{2.5}$ changes are more regional due to regional variations in primary aerosol emissions and emissions of gaseous precursor for secondary $PM_{2.5}$. Increasing NO_x emissions in this scenario in conjunction with a wetter climate elevates the levels of OH, HO_2, H_2O_2, and the nitrate radical and increases the atmosphere's near surface oxidation state. This differs from findings under the RCP scenarios that experience declines in OH from reduced NO_x emissions, stratospheric recovery of O_3, and increases in CH_4 and VOCs. Increasing NO_x and O_3 levels enhances the nitrogen

and O_3 deposition, indicating potentially-enhanced crop damage and ecosystem stress under this scenario. The enhanced global aerosol level results in enhancements in aerosol optical depth, cloud droplet number concentration, and cloud optical thickness. This leads to dimming at the Earth's surface with a global average reduction in shortwave radiation of 1.2 W m^{-2}. This enhanced dimming leads to a more moderate warming trend and different trends in radiation than those found in NCAR's CCSM3 simulation, which does not include the advanced chemistry and aerosol treatment of GU-WRF/Chem and cannot simulate the impacts of changing climate and emissions with the same level of detailed treatments. This study indicates that effective climate mitigation and emission control strategies are needed to prevent future health impact and ecosystem stress. This study also highlights the need for a fully-coupled EaSM framework when conducting aerosol/climate interaction studies, as the use of prescribed SSTs prevents the complete simulation of the aerosol direct and indirect effects on climate.

GU-WRF/Chem is also used to determine the role of ITAP caused by EAAEs under the current and future climate following the IPCC AR4 SRES A1B scenario. ITAP can offset the impact of local emission control efforts, impact human and ecosystem health, and play a role in climate forcing. The contribution from EAAEs is determined using a Brute Force method, in which results from simulations with and without EAAEs are compared. ITAP from East Asia is enhanced in the future due to faster wind speeds aloft and a stronger low pressure center near eastern Russia that facilitate enhanced westerly export in the free troposphere and stronger southerly transport near the surface, increased gaseous precursor emissions, and increased temperatures. As a result, the contribution of O_3 generated by

EAAEs to the global average O_3 mixing ratio increases by ~0.8 ppb from 1.2 ppb in 2001 to 2.0 ppb in 2050. The contribution of $PM_{2.5}$ generated by EAAEs to the global $PM_{2.5}$ level increases by ~0.07 μg m^{-3} from 0.32 μg m^{-3} in 2001 to 0.39 μg m^{-3} in 2050, despite a non-homogenous response in $PM_{2.5}$ resulting from cloud and radiative feedbacks. EAAEs can increase East Asian biogenic secondary organic aerosol by 10-81%, indicating that it is largely controllable. EAAEs also increase the deposition of nitrogen, black carbon, and mercury both locally and downwind, implying that they may play a role in climate feedbacks and ecosystem health of these regions. These results show that EAAEs have a large impact on global air quality and climate, especially on downwind regions. Such impacts may be enhanced under future climate and emission scenarios, demonstrating a need to synergize global pollution control and climate mitigation efforts.

The second portion of this work focuses on further development and application of the CESM-NCSU model. This model is a version of the CESM model that has undergone extensive development at NCSU, focusing on the improving the treatment and representation of inorganic aerosol thermodynamics, new particle formation, and aerosol activation. The work presented here focuses on further improving the treatment of OA in CESM-NCSU, to make a more robust tool for future climate simulations. These treatments include a VBS treatment for the simulation of primary and secondary organic aerosols, a simplified treatment for organic aerosol formation from glyoxal, and a parameterization representing the impact of conucleation of organic gases and sulfuric acid. With the inclusion of these new treatments, the concentration of OOA increases on global average by 0.33 μg m^{-3} from the additional precursors and pathways for OA formation. The concentration of POM is reduced

by 0.22 μg m^{-3} on global average from treating this aerosol as volatile. The decrease in POM leads to a reduction in the direct effect of OA on climate, while the increased OOA increases the indirect effects of OA on climate. The reduced direct effect of OA dominates these changes, leading to a global average increase of 0.6 W m^{-2} in incoming shortwave radiation at the Earth's surface. Simulations with the new OA treatments show considerable improvement in simulated SOA, OOA, OC, TC, and TOM, but degradation in the performance of POM compared to a baseline simulation without these new treatments. This is the result of an overprediction in the volatility of POM by the new OA treatments that is further enhanced by efficient wet removal of POM in MAM7. In simulations of the current climate period, despite some deviations from observations, the CESM-NCSU model with the new OA treatments significantly improves the magnitude, spatial pattern, and seasonal pattern of OC and TC, as well as the speciation of TOM between POM and OOA compared to the unmodified model. Sensitivity analysis reveals that the inclusion of the conucleation treatment impacts the indirect effects of OA by enhancing cloud properties. The simulated OA level as well as the impact of OA on the climate system is most sensitive to choices in the enthalpy of vaporization and wet deposition of SVOCs, indicating that accurate representations of these parameters are critical for accurate OA climate simulations. This study differs from others in the literature by exploring not only the impact of detailed OA treatments on OA predictions but also the impact these detailed treatments have on aerosol/climate interactions. This study also examines the impact of organic gases on new particle formation not considered in most CCMs. Overall, the OA treatments included in the

CESM-NCSU model reasonably represent the current atmosphere and thus can be applied for long-term climate simulations.

A preliminary version of the new OA treatments in CESM-NCSU, corresponding to the New_OAC case from Chapter 3, has been ported to a newer version based on CESMv1.2.2. This version of CESM-NCSU is used to simulate the current and future atmosphere following the RCP4.5 and RCP8.5 scenarios. In order to determine the reliability of CESM-NCSU for future predictions, CESM-NCSU is comprehensively evaluated in this work. Radiation and most meteorological variables are well simulated in CESM-NCSU. Cloud parameters are not as well simulated due in part to the tuning of model radiation and general biases in cloud variables common to all global chemistry-climate models. The concentrations of most inorganic aerosol species (i.e., SO_4^{2-}, NH_4^+, and NO_3^-) are well simulated with normalized mean biases (NMBs) typically less than 20%. However, some notable exceptions are European NH_4^+, which is overpredicted by 33.0-42.2% due to high NH_3 emissions and irreversible coarse-mode condensation, and Cl^-, that is negatively impacted by errors in emissions driven by wind speed and overpredicted HNO_3. Carbonaceous aerosols are largely underpredicted following the RCP scenarios due to low emissions of black carbon, organic carbon, and anthropogenic volatile compounds in the RCP inventory and efficient wet removal. This results in underpredictions of $PM_{2.5}$ and PM_{10} ranging from 6.4 - 55.7 %. The column mass abundances are reasonably well simulated. Larger biases occur in surface mixing ratios of trace gases in CESM-NCSU, likely due to numerical diffusion from the coarse grid spacing of the CESM-NCSU simulations or errors in the magnitudes and vertical structure of emissions. This is especially true for SO_2 and

NO_2. The mixing ratio of O_3 is overpredicted by 38.9-76.0% due to the limitations in the O_3 deposition scheme used in CESM and insufficient titration resulted from large underpredictions in NO_2. Despite these limitations, CESM-NCSU reproduces reasonably well the current atmosphere in terms of radiation, clouds, meteorology, trace gases, aerosols, and aerosol-cloud interactions, making it suitable for future climate simulations.

Following the comprehensive evaluation, CESM-NCSU is used to examine the impact of climate change and emissions on future air quality under both the RCP4.5 and RCP8.5 scenarios and the impact of projected emission changes under the RCP4.5 scenario on future climate through aerosol direct and indirect effects. Both the RCP4.5 and RCP8.5 simulations predict similar changes in air quality by the 2050 period due to declining emissions under both scenarios. The largest differences occur in O_3, which decreases by global mean of 1.4 ppb under RCP4.5 but increases by global mean of 2.3 ppb under RCP8.5 due to greater methane levels, greater warming, smaller reductions in NO emissions, increases in AVOC emissions, and greater increases in BVOCs emissions. There are also differences in PM_{10}, which decreases by global mean of 1.2 $\mu g\ m^{-3}$ under RCP4.5 and increases by global mean of 0.2 $\mu g\ m^{-3}$ under RCP8.5 due to differences in dust and sea-salt emissions under both scenarios. Enhancements in cloud formation in the Arctic and Southern Ocean and increases of AOD in central Africa and South Asia dominate the change in surface radiation in both scenarios, leading to global average dimming of 1.1 $W\ m^{-2}$ and 2.0 $W\ m^{-2}$ in the RCP4.5 and RCP8.5 scenarios, respectively. Declines in AOD, cloud formation, and cloud optical thickness from reductions of emissions of primary aerosols and aerosol precursors under RCP4.5 result in near surface warming of 0.2°C from a global

average increase of 0.7 W m^{-2} in surface downwelling solar radiation. This warming leads to a weakening of the Walker Circulation in the tropics, leading to significant changes in cloud and precipitation that mirror a shift in climate towards the negative phase of the El Nino Southern Oscillation.

Both the GU-WRF/Chem and CESM-NCSU models show deviations from the CCSM3 and CESM-CMIP5 models, respectively, that do not treat chemistry with the same level of details. This indicates that these differences in chemistry treatments can impact the simulation of aerosol/climate interactions and thus provide different trends in climate/air quality predictions. However, these differences are usually regional in nature, such as the impacts of OA on AOD in South America between the CESM-NCSU and CESM-CMIP5 projections. This change in OA between the CESM-NCSU and CESM-CMIP5 simulations also underscores the importance of including more detailed OA treatments, since the more basic treatments in CESM-CMIP5 provide a much different prediction of AOD in this region dominated by OA. As a result, it is fair to conclude that the use of more advanced modeling tools is necessary to accurately develop future climate mitigation and emissions control policies. However, one caveat is that the more detailed chemical treatments will reduce the computational-efficiency of the CCMs. This is potentially problematic when conducting long-term simulations, but this limitation can be overcome as the strength and availability of computational resources increase.

The difference in climate changes induced by future emission projections between the GU-WRF/Chem and CESM-NCSU simulations is striking. This is caused in part by the use of different future climate projections; however, the most striking differences are the result of

the differences in the modeling frameworks. The online-coupled GCM-CTM framework in GU-WRF/Chem is unable to simulate changes in SSTs caused by aerosol/climate interactions. As a result, there is no robust change in meteorological variables such as T2 or Q2, even though some of the net impact on radiation and clouds can be determined. In the CESM-NCSU study, changes in climate from emission projections are strong, resulting in a global warming effect and significant changes in PR and cloud formation due to a weakening of the Walker circulation. Thus the work presented here clearly illustrates the importance of the EaSM framework compared to the coupled GCM-CTM model framework when conduction aerosol/climate interaction studies.

5.2 Limitations and Future Work

This work demonstrates the importance of using advanced modeling tools for future climate studies. Nonetheless, despite the greater details of the chemical treatments in GU-WRF/Chem and CESM-NCSU, both models and the new OA treatments in CESM-NCSU have limitations. In addition to the use of prescribed SSTs, the GU-WRF/Chem model also does not simulate projected changes in land use. Both of these limitations limit the accuracy of GU-WRF/Chem future predictions. Additionally, the lack of positive-definite advection scheme in GU-WRF/Chem induces errors in the simulated aerosol and trace gases. These general limitations of GU-WRF/Chem provide justifications for switching to the CESM-NCSU model for the second half of this work.

The new OA treatments in CESM-NCSU lead to a general improvement in simulated OA. However, deviations from observations still exist. The new VBS treatments in CESM-NCSU are based on pseudo ideal partitioning between organic material in the gas and aerosol

phases. This is not necessarily an accurate representation of OA formation, as not all organics behave in this pseudo ideal fashion (Virtanen et al., 2010; Vaden et al., 2011) and OA can form through aqueous processes (Couvidat et al., 2012). Thus, future work could potentially include treating the low/non-volatility of biogenic OA and developing a hybrid of the VBS and molecular approaches to better improve the simulation of OA. Also as discussed in Chapter 3, the glyoxal treatment and conucleation treatments incorporated in this work are highly simplified. Thus future work could also focus on the incorporation of more detailed GLSOA formation treatments, the formation of OA from other carbonyl species, and the incorporation of a more detailed conucleation treatment when such a treatment becomes available for 3-D models.

The comprehensive evaluation of the CESM-NCSU model also reveals several systematic errors and biases within the model. These include overpredicted O_3, underpredicted carbonaceous aerosols, and underpredictions in many cloud related parameters. Thus further development of the CESM-NCSU model should focus on the improvements in cloud/radiation parameterizations to bring both parameters into good agreement with observations, more advanced mechanisms that will improve titration and deposition of O_3, and improvements in carbonaceous aerosol to reduce the potential overly-efficient wet removal. The simulations completed as part of this study are on a global scale. As a result, these simulations can serve as a source of boundary and initial conditions for regional models, once they have undergone bias correction. Thus another key area for future work includes regional climate simulations using regional and urban scale models with more detailed model treatments than global models.

The future work mentioned in this section would require significant computational resources. Therefore it is logical that these items be given priorities. The most critical aspect of this future work would be to correct the biases in O_3, carbonaceous aerosols, and aerosol-cloud interactions, since these are deficiencies of the current simulations. However, addressing the limitations of aerosol-cloud interactions with climate models is likely an issue that must be addressed by the scientific community at large rather than individual researchers or research groups. The next most important future work would be regional climate simulations based on the global simulations carried out in this work. Regional climate studies provide additional details that are missing from global climate simulations due to higher horizontal resolution and generally more detailed model physics and chemistry, thus making them more relevant to policy makers at regional scales. Improving the OA representations in CESM-NCSU by incorporating pathways for aqueous SOA formation and ELVOCs through the above mentioned hybrid approach would rank third in terms of importance. These modifications would lead to more accurate representations of most OA in the model. Lastly, more detailed glyoxal and carbonyl OA treatments should be included. Although they do not contribute as much to global OA levels as indicated by this work, they may be of importance in specific regions.

REFERENCES

Abdul-Razzak, H., and S. J. Ghan (2002), A parameterization of aerosol activation. 3. Sectional representation, *J. Geophys. Res.*, *107*(D3), 4026, doi:10.1029/2001JD000483.

Ackermann, I. J., H. Hass, M. Memmesheimer, A. Ebel, F. S. Binkowaki, and U. Shankar (1998), Modal aerosol dynamics model for Europe: Development and first applications, *Atmos. Environ.*, *32*(17), 2981-2999, doi:10.1016/S1352-2310(98)00006-5.

Adams, P. J., J. H. Seinfeld, and D. M. Koch (1999), Global concentrations of tropospheric sulfate, nitrate, and ammonium aerosol simulated in a general circulation model, *J. Geophys. Res.*, *104*(D11), 13,791–13,823, doi:10.1029/1999JD900083.

Ahmadov, R., et al. (2012), A volatility basis set model for summertime secondary organic aerosols over the eastern United States in 2006, *J. Geophys. Res.*, *117*, D06301, doi:10.1029/2011JD016831.

Aiken, A. C., et al., (2008), O/C and OM/OC ratios of primary, secondary, and ambient organic aerosols with high-resolution time-of-flight aerosol mass spectrometry, *Environ. Sci. Technol.*, *42*, 4478-4485, doi: 10.1021/es703009q.

Alfarra, M. R., H. Coe, J. D. Allan, K. N. Bower, H. Boudries, M. R. Canagaratna, J. L. Jimenez, J. T. Jayne, A. A. Garforth, S.-M., Li, and D. R. Worsnap (2004), Characterization of urban and rural organic particulate in the Lower Fraser Valley using two Aerodyne Aerosol Mass Spectrometers, *Atmos. Environ.*, 38, 5745-5758, doi: 10.1016/j.atmosenv.2004.01.054.

Andreae, M. O., and P. Merlet (2001), Emissions of trace gases and aerosols from biomass burning, *Global Biogeochem. Cy.*, 15, 955-966, doi:10.1029/2000GB001382.

Andreae, M. O. (2009), A new look at aging aerosols, *Science*, *326*, 1493, doi:10.1126/science.1183158.

Andersson, C., and M. Engardt (2010), European ozone in a future climate: Importance of changes in dry deposition and isoprene emissions, *J. Geophys. Res.*, *115*, D02303, doi:10.1029/2008JD011690.

Anenberg, S. C., et al. (2009), Intercontinental impacts of ozone pollution on human mortality, *Environ. Sci. Technol.*, *43*, 6482-6487, doi: 10.1021/es900518z.

Arora, V., et al. (2013), Carbon-Concentration and Carbon-Climate feedbacks in CMIP5 Earth System Models, *J. Climate*, *26*, 5289-5314, doi:10.1175/JCLI-D-12-00494.1.

Artinano, B., P. Salvador, D. G. Alonso, X. Querol, and A. Alastuey (2003), Anthropogenic and natural influence on the PM_{10} and $PM_{2.5}$ aerosol in Madrid (Spain). Analysis of high concentration episodes, *Environmental Pollution*, *126*(3), 453-465, doi:10.1016/S0269-7491(03)00078-2.

Atkinson, R. (2000), Atmospheric chemistry of VOC and NO_x, *Atmos. Environ.*, *34*, 2063-2101, doi:10.1016/S1352-2310(99)00460-4.

Atkinson, R. and J. Arey (2003), Atmospheric degradation of volatile organic compounds, *Chem. Rev.*, *103*(12), 4605-4638, doi:10.1021/cr0206420.

Bader, D., K. Achuta Rao, C. Covey, C. Doutriaux, M. Fiorino, P. Gleckler, T. Phillips, K. Sperber, and K. Taylor (2004), An appraisal of coupled climate model simulations,

Lawrence Livermore National Laboratory, Livermore, CA, Open File Rep. UCRL-TR-202550, 197 pp.,

Barahona, D. and A. Nenes (2007), Parameterization of cloud droplet formation in large-scale models: including effects of entrainment, *J. Geophys. Res.*, *112*, D16206, doi:10.1029/2007JD008473.

Barahona, D., R. E. I. West, P. Steir, S. Romakkaniemi, H. Kokkola, and A. Nenes (2010), Comprehensively accounting for the effect of giant CCN in cloud activation parameterizations, *Atmos. Chem. Phys.*, *10*, 2467-2473, doi:10.1029/2006JD007547.

Barth, M. C., P. J. Rasch, J. T. Kiehl, C. M. Benkovitz, and S. E. Schwartz (2000), Sulfur chemistry in the National Center for Atmospheric Research Community Climate Model: Description, evaluation, features and sensitivity to aqueous chemistry, J. *Geophys. Res.*, *105*, 1387–1415, doi:10.1029/1999JD900773.

Bennartz, R. (2007), Global assessment of marine boundary layer cloud droplet number concentration from satellite, *J. Geophys. Res.,112*, D02201, doi:10.1029/2006JD007547.

Bergstrom, R., H. A. C. Denier van der Gon, A. S. H. Prevor, K. E. Yttri, and D. Simpson (2012), Modelling of organic aerosols over Europe (2002-2007) using a volatility basis set (VBS) framework: supplication of different assumptions regarding the formation of secondary organic aerosols, *Atmos. Chem. Phys.*, *12*, 8499-8527, doi:10.5194/acp-12-8499-2012.

Bessagnet, B., C. Seigneur, and L. Menut (2010), Impact of dry deposition of semi-volatile organic compounds on secondary organic aerosol, *Atmos. Environ.*, *44*, 1781-1787, doi:10.1016/j.atmosenv.2010.01.027.

Bey, I., D. L. Jacob, A. Logan, and R. M. Yantosca (2001), Asian chemical outflow to the Pacific in spring: Origins, pathways, and budgets, *J. Geophys. Res.*, *106*, 23,097–23,113, doi:10.1029/2001JD000806.

Bonn, B., M. Kulmala, I. Riipinen, S.-L. Sihto, and T. M. Ruuskanen (2008), How biogenic terpenes govern the correlation between sulfuric acid concentrations and new particle formation, *J. Geophys. Res.*, *113*, D12209, doi:10.1029/2007JD009327.

Brandt, J., J. D. Silver, L. M. Frohm, C. Geels, A. Gross, A. B. Hansen, K. M. Hansen, G. B. Hedegaard, C. A. Skjoth, H. Villadsen, A. Zare, and J. H. Christensen (2012), An integrated model study for Europe and North America using the Danish Eulerian Hemispheric Model with focus on intercontinental transport of air pollution, *Atmos. Environ.*, *53*, 156-176, doi:10.1016/j.atmosenv.2012.01.011.

Bretherton, C. S. and S. Park (2009), A new moist turbulence parameterization in the community atmosphere model, *J. Climate*, *22*, 3422–3448, doi: http://dx.doi.org/10.1175/2008JCLI2556.1.

Buchart, N,, et al. (2010), Chemistry-Climate Model Simulations of Twenty-First Century Stratospheric Climate and Circulation Changes, *J. Climate*, *23*, 5349–5374, doi: http://dx.doi.org/10.1175/2010JCLI3404.1.

Cahoon, D. R., B. J. Stocks, J. S. Levine, W. R. Cofer, and K. P. O'Neill (1992), Seasonal distributions of African savanna fires, *Nature*, *359*, 812-815, doi:10.1038/359812a0.

Campbell, P., et al. (2015), A multi-model assessment for 2006 and 2010 simulations under the Air Quality Model Evaluation International Initiative (AQMEII) phase 2 over North America: Part 1. Indicators of O_3 and $PM_{2.5}$ formation regimes, *Atmos. Environ.*, *115*, 569-586, doi:10.1016/j.atmosenv.2014.12.026.

Cai, W., D. Bi, J. Church, T. Cowan, M. Dix, and L. Rotstayn (2006), Pan-oceanic response to increasing anthropogenic aerosols: Impacts on the Southern Hemisphere oceanic circulation, *Geophys. Res. Lett.*, *33*, L21707, doi:10.1029/2006GL027513.

Carlton, A. G., R. W. Pinder, P. V. Bhave, and G. A. Pouliot (2010), To what extent can biogenic SOA be controlled?, *Environ. Sci. Technol.*, *44*, 3376-3380, doi: 10.1021/es903506b.

Carter, W. P. L. (2000), Programs and Files Implementing the SAPRC-99 Mechanism and its Associates Emissions Processing Procedures for Models-3 and Other Regional Models, http://www.engr.ucr.edu/~carter/SAPRC99/index.htm, Last updated: 30 March 2010.

Chalmers, N., E. J. Highwood, E. Hawkins, R. Sutton, and L. J. Wilcox (2012), Aerosol contribution to the rapid warming of near-term climate under RCP 2.6, *Geophys. Res. Lett.*, *39* L18709, doi:10.1029/2012GL052848.

Chan, A. W. H., K. E. Kautzman, P. S. Chhabra, J. D. Surratt, M. N. Chan, J. D. Crounse, A. Kurten, P. O. Wennberg, R. C. Flagan, and J. H. Seinfeld (2009), Secondary organic aerosol formation from photooxidation of naphthalene and alkylnaphthalenes: implications for oxidation of intermediate volatility organic compounds (IVOCs), *Atmos. Chem. Phys.*, *9*, 3049-3060, doi:10.5194/acp-9-3049-2009.

Chapin III, F. S., et al. (2005), Role of Land-Surface Changes in Arctic Summer Warming, *Science*, *310*, 657-660, doi:10.1126/science.1117368.

Chen, F., and J. Dudhia (2001a), Coupling an advanced land surface-hydrology model with the Penn State-NCAR MM5 modeling system. Part I: Model implementation and sensitivity, *Mon. Weather Rev.*, *129*, 569–585, doi: 10.1175/1520-0493(2001)129<0569:CAALSH>2.0.CO;2.

Chen, F. and J. Dudhia (2001b), Coupling an advanced land surface-hydrology model with the Penn State-NCAR MM5 modeling system Part II: Preliminary Model Validation, *Mon. Weather. Rev.*, *129*(4), 587-604, doi:10.1175/1520-0493(2001)129<0587:CAALSH>2.0.CO;2.

Chen, M. and Q. Zhuang (2014), Evaluating aerosol direct radiative effects on global terrestrial ecosystem carbon dynamics from 2003 to 2010, *Tellus B*, *66*, 21808, http://dx.doi.org/10.3402/tellusb.v66.21808.

Chen, S. H., and W. Y. Sun (2002), A one-dimensional time dependent cloud model, *J. Meteorol. Soc. Jpn.*, *80*, 99–118, doi:10.2151/jmsj.80.99.

Chen, Y., Y. Zhang, J. Fan, L.R. Leung, Q. Zhang, and K.-B. He (2015), Application of an Online-Coupled Regional Climate Model, WRF-CAM5, over East Asia for Examination of Ice Nucleation Schemes: Part I. Comprehensive Model Evaluation and Trend Analysis for 2006 and 2011, *Climate*, *3*(3), 627-667; doi:10.3390/cli3030627.

Chou, M. D., M. J. Suarez, C. H. Ho, M. M. H. Yan, and K. T. Lee (1998), Parameterizations for cloud overlapping and shortwave single-scattering properties for use in general

circulation and cloud ensemble models, *J. Clim.*, *11*, 202–214, doi:10.1175/1520-0442(1998)011<0202:PFCOAS>2.0.CO;2.

Chung, S. H., and J. H. Seinfeld (2002), Global distribution and climate forcing of carbonaceous aerosols, *J. Geophys. Res.*, *107*(D19), 4407, doi:10.1029/2001JD001397.

Clarke, A. D. and K. J. Noone (1985), Soot in the Arctic snowpack: A cause for perturbations in radiative transfer, *Atmos. Environ.*, *19*, 2045-2053, doi:10.1016/0004-6981(85)90113-1.

Claussen, M., et al. (2002), Earth System Models of intermediate complexity: closing the gap in the spectrum of climate system models, *Clim. Dynam.*, *18*, 579-586, doi:10.007/s00382-001-0200-1.

Cooper, O. R., et al. (2004), A case study of transpacific warm conveyor belt transport: Influence of merging airstreams on trace gas import to North America, *J. Geophys. Res.*, *109*, D23S08, doi:10.1029/2003JD003624.

Couvidat, F., and C. Seigneur (2011), Modeling secondary organic aerosol formation from isoprene oxidation under dry and humid conditions, *Atmos. Chem. Phys.*, *11*(2), 893–909, doi:10.5194/acp-11-893-2011.

Couvidat, F., É. Debry, K. Sartelet, and C. Seigneur (2012), A hydrophilic/hydrophobic organic (H2O) aerosol model: Development, evaluation and sensitivity analysis, *J. Geophys. Res.*, *117*, D10304, doi:10.1029/2011JD017214.

Couvidat, F., É. Debry, K. Sartelet, and C. Seigneur (2012), A hydrophilic/hydrophobic organic (H2O) aerosol model: Development, evaluation and sensitivity analysis, *J. Geophys. Res.*, *117*, D10304, doi:10.1029/2011JD017214.

Couvidat F. and Sartelet K. (2014), The Secondary Organic Aerosol Processor (SOAP v1.0) model: a unified model with different ranges of complexity based on the molecular surrogate approach, *Geosci. Model Dev. Discuss.*, *7*, 379-429, doi:10.5194/gmdd-7-379-2014

Dentener, F., et al., (2006), The global atmospheric environment for the next generation, *Environ. Sci. Technol.*, *40*, 3586-3594, doi:10.1021/es0523845.

Dobrynin, M., J. Murawsky, and S. Yang (2012), Evolution of the global wind wave climate in CMIP5 experiments, *Geophys. Res. Lett.*, *39*, L18606, doi:10.1029/2012GL052843.

Doherty, R. M., et al. (2013), Impacts of climate change on surface ozone and intercontinental ozone pollution: A multi-model study, *J. Geophys. Res. Atmos.*, *118*, 3744–3763, doi:10.1002/jgrd.50266.

Donahue, N. M., A. L. Robinson. C. O. Stanier, and S. N. Pandis (2006), Coupled partitioning, dilution, and chemical aging of semivolatile organics, *Environ. Sci. Technol.*, *40*, 2635-2643, doi:10.1021/es052297c.

Donahue, N. M., A. L. Robinson, and S. Pandis (2009), Atmospheric organic particulate matter: From smoke to secondary organic aerosol, *Atmos. Environ.*, *43*, 94-106, doi:10.1016/j.atmosenv.2008.09.055.

Donahue, N. M., S. A. Epstein, S. N. Pandis, and A. I. Robinson (2011), A two-dimensional volatility basis set: organic-aerosol mixing thermodynamics, *Atmos. Chem. Phys.*, *11*, 3303-3318, doi:10.5194/acp-11-3303-2011.

Donahue, N. M., J. H., Kroll, S. N. Pandis, and A. I. Robinson (2012), A two-dimensional volatility basis set – Part 2: Diagnostics of organic-aerosol evolution, *Atmos. Chem. Phys.*, *12*, 615-634, doi:10.5194/acp-12-615-2012.

Ehn, M. et al. (2014), A large source of low-volatility secondary organic aerosol, *Nature*, *506*, 476-479, doi:10.1038/nature13032.

Ek, M. B., K. E. Mitchell, Y. Lin, E. Rogers, P. Grunmann, V. Koren, G. Gayno, and J. D. Tarpley (2003), Implementation of Noah land surface model advances in the National Centers for Environmental Prediction operational mesoscale Eta model, *J. Geophys. Res.*, *108*(D22), 8851, doi:10.1029/2002JD003296.

Emmons, L. K. et al. (2010), Description and evaluation of the Modal for Ozone and Related chemical Tracers, version 4 (MOZART-4), *Geosci. Model. Dev*., *3*, 43-67, doi:10.5194/gmd-3-43-2010.

Epstein, S. A., I. Riipinen, and N. M. Donahue (2010), A semiempirical correlation between enthalpy of vaporization and saturation concentration for organic aerosol, *Environ. Sci. Technol.*, *44*. 743-748, doi: 10.1021/es902497z.

Ervens, B., A. G. Carlton, B. J. Turpin, K. E. Altieri, S. M. Kreidenweis, and G. Feingold (2008), Secondary organic aerosol yields from cloud-processing of isoprene oxidation products, *Geophys. Res. Lett.*, *35*, L02816, doi:10.1029/2007GL031828.

Ervens, B. and R. Volkamer (2010), Glyoxal processing by aerosol multiphase chemistry: towards a kinetic modeling framework of secondary organic aerosol formation in aqueous particles, *Atmos. Chem. Phys.*, *10*, 8219-8244, doi:10.5194/acp-10-8219-2010.

Eyring, V. et al. (2005), A strategy for process-oriented validation of coupled chemistry-climate models, *Bull. Am. Meteorol. Soc.*, *86*, 1117-1133, doi: 10.1175/BAMS-86-8-1117.

Eyring, V., et al. (2006), Assessment of temperature, trace species, and ozone in chemistry-climate model simulations of the recent past, *J. Geophys. Res.*, *111*, D22308, doi:10.1029/2006JD007327.

Fahey, K. M., and S. N. Pandis (2001), Optimizing model performance: Variable size resolution in cloud chemistry modeling, *Atmos. Environ.*, *35*, 4471–4478, doi:10.1016/S1352-2310(01)00224-2.

Fan, J., R. Zhang, D. Collins, and G. Li (2006), Contribution of secondary condensable organics to new particle formation: A case study in Houston, Texas, *Geophys. Res. Lett.*, *33*, L15802, doi:10.1029/2006GL026295.

Fan, J., S. Ghan, M. Ovchinnikov, X. Liu, P. J. Rasch, and A. Korolev (2011), Representation of Arctic mixed-phase clouds and the Wegener-Bergeron-Findeisen process in climate models: Perspectives from a cloud-resolving study, *J. Geophys. Res.*, *116*, D00T07, doi:10.1029/2010JD015375.

Fang, Y., A. M. Fiore, L. W. Horowitz, A. Gnanadesikan, I. Held, G. Chen, G. Vecchi, and H. Levy (2011), The impacts of changing transport and precipitation on pollutant

distributions in a future climate, *J. Geophys. Res.*, *116*, D18303, doi:10.1029/2011JD015642.

Farina, S. C., P. J. Adams, and S. N. Pandis (2010), Modeling global secondary organic aerosol formation and processing with the volatility basis set: Implications for anthropogenic secondary organic aerosol, *J. Geophys. Res.*, *115*, D09202, doi:10.1029/2009JD013046.

Felzer, B., D. Kicklighter, J. Melillo, C. Wang, Q. Zhuang, and R. Prinn (2004), Effects of ozone on net primary production and carbon sequestration in the conterminous United States using a biogeochemistry model, *Tellus B*, *56*, 230-248, doi:10.1111/j.1600-0889.2004.00097.x.

Fioletov, V. E., et al. (2013), Application of OMI, SCIAMACHY, and GOME-2 satellite SO2 retrievals for detection of large emission sources, *J. Geophys. Res. Atmos.*, *118*, 11,399–11,418, doi:10.1002/jgrd.50826.

Fiore, A. M., et al. (2009), Multimodel estimates of intercontinental source-receptor relationships for ozone pollution, *J. Geophys. Res.*, *114*, D04301, doi:10.1029/2008JD010816, 2009.

Fiore, A. M., et al. (2012), Global air quality and climate, *Chem. Soc. Rev.*, *41*(19), doi:10.1039/C2CS35095E.

Fisher, J. A., et al. (2010), Source attribution and interannual variability of Arctic pollution in the spring constrained by aircraft (ARCTAS, ARCPAC) and satellite (AIRS) observations of carbon monoxide, *Atmos. Chem. Phys.*, *10*, 977-996, doi: 10.5194/acp-10-977-2010.

Flanner, M. G., C. S. Zender, J. T. Randerson, and P. J. Rasch (2007), Present-day climate forcing and response from black carbon in snow, *J. Geophys. Res.*, *112*, D11202, doi:10.1029/2006JD008003.

Fountoukis, C. and A. Nenes (2005), Continued development of a cloud droplet formation parameterization for global climate models, *J. Geophys. Res.*, *110*, D11212, doi:10.1029/2004jd005591.

Fountoukis, C. and A. Nenes (2007), ISORROPIA II: a computationally efficient thermodynamic equilibrium model for K^+-Ca^{2+}-Mg^{2+}-NH_4^+-Na^+-SO_4^{2-}-NO_3^--Cl^--H_2O aerosols, *Atmos. Chem. Phys.*, *7*, 4639–4659, doi:10.5194/acp-7-4639-2007.

Frankenberg, C., J. F. Meirink, P. Bergamaschi, A. P. H. Goede, M. Heimann, S. Ko¨rner, U. Platt, M. van Weele, and T. Wagner (2006), Satellite chartography of atmospheric methane from SCIAMACHY on board ENVISAT: Analysis of the years2003 and 2004, *J. Geophys. Res.*, *111*, D07303, doi:10.1029/2005JD006235.

Fu, T.-M., D. J. Jacob, F. Wittrock, J. P. Burrows, M. Vrekoussis, and D. K. Henze (2008), Global budgets of atmospheric glyoxal and methylglyoxal, and implications for formation of secondary organic aerosols, *J. Geophys. Res.*, *113*, D15303, doi:10.1029/2007JD009505.

Fuzzi, S., et al. (2007), Overview of the inorganic and organic composition of size-segregated aerosol in Rondoˆnia, Brazil, from the biomass-burning period to the onset of the wet season, *J. Geophys. Res.*, *112*, D01201, doi:10.1029/2005JD006741.

Gagne, M.-E., N. P. Gillett, and J. C. Frye (2015), Impact of aerosol emission controls on future Arctic sea ice cover, *Geophys. Res. Lett.*, in press, doi:10.1002/2015GL065504.

Gama, C., O. Tchepel, J. M. Baldasano, S. Basart, J. Ferreira, C. Pio, J. Cardoso, and C. Borrego (2015), Seasonal patterns of Saharan dust over Cape Verde - a combined approach using observations and modeling, *Tellus*, *67*, 24410, http://dx.doi.org/10.3402/tellusb.v67.24410.

Gantt, B., J. Xu, N. Meskhidze, Y. Zhang, A. Nenes, S. J. Ghan, X. Liu, R. Easter, and R. Zaveri (2012), Global distribution and climate forcing of marine organic aerosol – Part 2: Effects on cloud properties and radiative forcing, *Atmos. Chem. Phys.*, *12*, 6555-6563, doi:10.5194/acp-12-6555-2012.

Gantt, B., J. He, X. Zhang, Y. Zhang, and A. Nenes (2013), Incorporation of advanced aerosol activation treatments into CESM-CAM5: model evaluation and impact on aerosol indirect effects, *Atmos. Chem. Phys.*, *14*, 7485-7497, doi:10.5194/ acp-14-7485-2014.

Gantt, B., J. He, X. Zhang, Y. Zhang, and A. Nenes (2014), Incorporation of advanced aerosol activation treatments into CESM/CAM5: model evaluation and impact on aerosol indirect effects, *Atmos. Chem. Phys.*, *14*, 7485-7497, doi: 10.5194/acp-14-7485-2014.

Gantt, B., T. Glotfelty, N. Meskhidze, and Y. Zhang (2015), Simulating the impacts of marine organic emissions on global atmospheric chemistry and aerosols using an

online-coupled meteorology and chemistry model, *Atmospheric and Climate Sciences*, 5, 266-274, doi: 10.4236/acs.2015.53020.

Gaydos, T. M., B. Koo, S. N. Pandis, and D. P. Chock (2003), Development and application of an efficient moving sectional approach for the solution of the atmospheric aerosol condensation/evaporation equations, *Atmos. Environ.*, *37*, 3303–3316. doi:10.1016/S1352-2310(03)00267-X.

Gaydos, T. M., R. W. Pinder, B. Koo, K. M. Fahey, and S. N. Pandis (2007), Development and application of a three-dimensional aerosol chemical transport model, PMCAMx, *Atmos. Environ.*, *41*, 2594–2611, doi:10.1016/j.atmosenv.2006.11.034.

Ghan, S. J., L. R. Leung, R. C. Easter, and H. Abdul-Razzak (1997), Prediction of cloud droplet number in a general circulation model, *J. Geophys. Res.*, *102*, 21,777–21,794, doi:10.1029/97JD01810.

Glotfelty, T., Y. Zhang, P. Karamchandani, and D. G. Streets (2014), Will the role of intercontinental transport change in a changing climate?, *Atmos. Chem. Phys.*, *14*, 9379-9402, doi:10.5194/acp-14-9379-2014.

Glotfelty, T., J. He, and Y. Zhang (2016a), New organic aerosol treatments in CESM-CAM5: Development and initial application, in preparation.

Glotfelty, T. Y. Zhang, P. Karamchandani, and D. G. Streets (2016b), Changes in future air quality, deposition, and aerosol-cloud interactions under future climate and emissions scenarios, *Atmos. Environ.*, *139*, 176-191, doi:10.1016/j.atmosenv.2016.05.008.

Glotfelty, T., J. He, and Y. Zhang (2016c), The impact of future climate policy scenarios on air quality and aerosol/cloud interactions using an advanced version of

CESM/CAM5: Part I. Model evaluation for the current decadal simulations, in preparation.

Glotfelty, T., J. He, and Y. Zhang (2016d), The impact of future climate policy scenarios on air quality and aerosol/cloud Interactions using an advanced version of CESM/CAM5: Part II. Future trend analysis and impacts of projected anthropogenic emissions, in preparation.

Goldstein, A., and I. Galbally (2007), Known and unexplored organic constituents of the Earth's atmosphere, *Environ. Sci. Technol.*, *41*(5) 1515-1521,doi: 10.1021/es072476p.

Gong, S., L. A. Barrie, and J. P. Blanchet (1997), Modeling sea salt aerosols in the atmosphere: 1. Model development, *J. Geophys. Res.*, *102*, 3805–3818, doi:10.1029/96JD02953.

Granier, C., A. Guenther, J.-F. Lamarque, A. Mieville, J.F. Muller, J. Oliver, J. Orlando, J. Peters, G. Petron, G. Tyndall, and S, Wallens, (2005), POET, a database of surface emissions of ozone precursors, [Available at: http://www.aero.jussieu.fr/project/ACCENT/POET.php].

Grell, G. A., and D. Devenyi (2002), A generalized approach to parameterizing convection combining ensemble and data assimilation techniques, *Geophys. Res. Lett.*, *29*(14), 1693, doi:10.1029/2002GL015311.

Grell, G. A., S. E. Peckham, R. Schmitz, S. A. McKeen, G. Frost, W. C. Skamarock, and B. Eder (2005), Fully coupled "online" chemistry within the WRF model, *Atmos. Environ.*, *39*(37), 6957–6975, doi:10.1016/j.atmosenv.2005.04.027.

Grieshop, A. P., J. M. Logue, N. M. Donahue, and A. L. Robinson (2009), Laboratory investigation of photochemical oxidation of organic aerosol from wood fires 1: measurements and simulation of organic aerosol evolution, Atmos. Chem. Phys., 9; 1283-1277, doi: 10.5194/acp-9-1263-2009.

Guenther, A., T. Karl, P. Harley, C. Wiedinmyer, P. I. Palmer, and C. Geron (2006), Estimates of global terrestrial isoprene emissions using MEGAN (Model of Emissions of Gases and Aerosols from Nature), *Atmos. Chem. Phys.*, 6, 3181-3210, doi:10.5194/acp-6-3181-2006.

Hadley, O. L., V. Ramanathan, G. R. Carmichael, Y. Tang, C. E. Corrigan, G. C. Roberts, and G. S. Mauger (2007), Trans-Pacific transport of black carbon and fine aerosols (D < 2.5 mm) into North America, *J. Geophys. Res., 112*, D05309, doi:10.1029/2006JD007632.

Hadley, O. L., C. E. Corrigan, T. W. Kirchstetter, S. S. Cliff, and V. Ramanathan (2010), Measured black carbon deposition on the Sierra Nevada snow pack and implication for snow pack retreat, *Atmos. Chem. Phys.*, *10*, 7505-7513, doi:10.5194/acp-10-7505-2010.

Haines, A., R. S. Kovats, D. Campbell-Lendrum, and C. Corvalen (2006), Climate change and human health: Impacts, vulnerability and public health, *Public Health, 120*(7), 585–596, doi:10.1016/j.puhe.2006.01.002.

Hallquist, M., et al. (2009), The formation, properties and impact of secondary organic aerosol: current and emerging issues, *Atmos. Chem. Phys.*, *9*, 5155-5236, doi:10.5194/acp-9-5155-2009.

Hannay, C., C. Jackson, G. Danabasoglu, J.-F. Lamarque, D. Lawrence, K. Lindsay, R. Neale, P. Rasch, and J. Trbbia (2014), Coupled model initialization and tuning, presentation at the 19th Annual CESM Workshop, June 16-19 , 2014, Breckenridge, CO.

Hauglustaine, D. A., J. Lathie`re, S. Szopa, and G. A. Folberth (2005), Future tropospheric ozone simulated with a climate-chemistry-biosphere model, *Geophys. Res. Lett., 32*, L24807, doi:10.1029/2005GL024031.

Hauglustaine, D. A., Y. Balkanski, and M Schultz (2014), A global model simulation of present and future nitrate aerosols and their direct radiative forcing of climate, Atmos. Chem. Phys., 14, 11031–11063, doi:10.5194/acp-14-11031-2014.

He, J. and Y. Zhang (2014), Improvement and further development in CESM/CAM5: gas-phase chemistry and inorganic aerosol treatments, *Atmos. Chem. Phys.*, *14*, 9171-9200, doi: 0.5194/acp-14-9171-2014.

He, J., Y. Zhang, T. Glotfelty, R. He, R. Bennartz, J. Rausch, and K. Sartelet (2015a), Decadal simulation and comprehensive evaluation of CESM/CAM5.1 with advanced chemistry, aerosol microphysics, and aerosol-cloud interactions, *J. Adv. Model. Earth Syst., 7*, 110–141, doi:10.1002/2014MS000360.

He, J., Y. Zhang, S. Tilmes, L. Emmons, J.-F. Lamarque, T. Glotfelty, A. Hodzic, and F. Vitt (2015b), CESM/CAM5 improvement and application: comparison and evaluation of updated CB05_GE and MOZART-4 gas-phase mechanisms and associated impacts on global air quality and climate, *Geosci. Model Dev., 8*, 3999-4025, doi:10.5194/gmd-8-3999-2015.

Heald, C. L., et al. (2008), Predicted change in global secondary organic aerosol concentrations in response to future climate, emissions, and land use change, *J. Geophys. Res.*, *113*, D05211, doi:10.1029/2007JD009092.

Hedegaard, G. B., J. Brandt, J. H. Christensen, L. M. Frohn, C. Geels, and K. M. Hansen (2008), Impacts of climate change on air pollution levels in the Northern Hemisphere with special focus on Europe and the Arctic, *Atmos. Chem. Phys.*, *8*, 3337-3367, doi:10.5194/acp-8-3337-2008 .

Hennigan, C. J., M. H. Bergin, J. E. Dibb, and R. J. Weber (2008), Enhanced secondary organic aerosol formation due to water uptake by fine particles, *Geophys. Res. Lett.*, *35*, L18801, doi:10.1029/2008GL035046.

Henze, D. K., and J. H. Seinfeld (2006), Global secondary organic aerosol from isoprene oxidation, *Geophys. Res. Lett.*, *33*, L09812, doi:10.1029/2006GL025976.

Henze, D. K., J. H. Seinfeld, and D. T. Shindell (2009), Inverse modeling and mapping US air quality influences of inorganic $PM_{2.5}$ precursor emissions using the adjoint of GEOS-Chem, *Atmos. Chem. Phys.*, *9*, 5877-5903, doi:10.5194/acp-9-5877-2009.

Hess, P. G., and T. Vukicevic (2003), Intercontinental transport, chemical transformations, and baroclinic systems, *J. Geophys. Res.*, 108, 4354, doi:10.1029/2002JD002798.

Hodzic, A., B. Aumont, C. Knote, J. Lee-Taylor, S. Madronich, and G. Tyndall (2014), Volatility dependence of Henry's law constants of condensable organics: Application to estimate depositional loss of secondary organic aerosols, *Geophys. Res. Lett.*, *41*, 4795–4804, doi:10.1002/2014GL060649.

Hodzic, A., P. S. Kasibhalta, D. S. Jo, C. Cappa, J. L. Jimenez, S. Mandonich, and R. J. Park

(2015), Rethinking the global secondary organic aerosol (SOA) budget: stronger production, faster removal, and shorter lifetime, *Atmos. Chem. Phys. Discuss.*, *15*, 32413-32468, doi:10.5194/acpd-15-32413-2015.

Holm, J. A., K. Jardine, A. B. Guenther, J. Q. Chambers, and E. Tribuzy (2014), Evaluation of MEGAN-CLM parameter sensitivity to predictions of isoprene emissions from an Amazonian rainforest, *Atmos. Chem. Phys. Discuss.*, *14*, 23995-24041, doi:10.5194/acpd-14-23995-2014.

Hong, S., Y. Noh, and J. Dudhia (2006), A new vertical diffusion package with an explicit treatment of entrainment processes, *Mon. Weather Rev.*, *134*, 2318–2341, doi:10.1175/MWR3199.1.

Horowitz, L. W., S. Walters, D. L. Mauzerall, L. K. Emmons, P. J. Rasch, C. Granier, X. X. Tie, J.-F. Lamarque, M. G. Schultz, G. S. Tyndall, J. J. Orlando, and G. P. Brasseur (2003), A global simulation of tropospheric ozone and related tracers: Description and evaluation of MOZART, version 2, *J. Geophys. Res.*, *108*, 4784, doi:10.1029/2002JD002853.

Hurrell, J. W., et al. (2013), The Community Earth System Model: A framework for collaborative research, *Bull. Am. Meteorol. Soc.*, *94*, 1339–1360, doi:10.1175/BAMS-D-12-00121.1.

Husar, R. B. et al. (2001), Asian dust events of April 1998, *J. Geophys. Res.*, *106*, 18,317–18,330, doi:10.1029/2000JD900788.

Iacono, M. J., J. S. Delamere, E. J. Mlawer, and S. A. Clough (2003), Evaluation of upper tropospheric water vapor in the NCAR Community Climate Model (CCM3) using

modeled and observed HIRS radiances, *J. Geophys. Res.*, *108*, 4037, doi:10.1029/2002jd002539.

Iacono, M. J., J. S. Delamere, E. J. Mlawer, M. W. Shephard, S. A. Clough, and W. D. Collins (2008), Radiative forcing by long-lived greenhouse gases: Calculations with the AER radiative transfer models, *J. Geophys. Res.*, *113*, D13103, doi:10.1029/2008jd009944.

Intergovernmental Panel on Climate Change (IPCC) (2000), *Special Report on Emission Scenarios (SRES), A Special Report of Working Group III of the Intergovernmental Panel on Climate Change*, edited by N. Nakicenovic and R. Swart, 570 pp., Cambridge Univ. Press, Cambridge, U. K.

Intergovernmental Panel on Climate Change (IPCC) (2007), *Report of the 26th session of the IPCC*. Bangkok. April 30- May 4 2007. Intergovernmental Panel on Climate Change, Geneva, Switzerland.

Ito, A., S. Sillman, and J. E. Penner (2009), Global chemical transport model study of ozone response to changes in chemical kinetics and biogenic volatile organic compounds emissions due to increasing temperatures: Sensitivities to isoprene nitrate chemistry and grid resolution, *J. Geophys. Res.*, *114*, D09301, doi:10.1029/2008JD011254.

Jacob, D. J., J. A. Logan, and P. P. Murti (1999), Effect of rising Asian emission on surface ozone in the United States, *Geophys. Res. Lett.*, *26*, 2175–2178, doi:10.1029/1999GL900450, 1999.

Jacob, D. J. and D. A. Winner (2009), Effect of climate change on air quality, *Atmos. Environ.*, *43*, 51-63, DOI:10.1016/j.atmosenv.2008.09.051.

Jacobson, M. Z., and D. G. Streets (2009), Influence of future anthropogenic emissions on climate, natural emissions, and air quality, *J. Geophys. Res.*, 114, D08118, doi:10.1029/2008JD011476.

Jaffe, D. A. et al. (1999), Transport of Asian air pollution to North America, *Geophys. Res. Lett.*, *26*, 711 –714, doi:10.1029/1999GL900100.

Jaffe, D. A., I. McKendry, T. Anderson, and H. Price (2003), Six 'new' episodes of trans-Pacific transport of air pollutants, *Atmos. Environ.*, *37*, 391–404, doi:10.1016/S1352-2310 (02)00862-2.

Janjic, Z. I. (2002), Nonsingular implementation of the Mellor-Yamada level 2.5 scheme in the NCEP Meso model, *NCEP Off. Note*, 437, 61 pp., Natl. Cent. for Environ. Predict., College Park, Md.

Jathar, S. H., S. C. Farina, A. L. Robinson, and P. J. Adams (2011), The influence of semi-volatile and reactive primary emissions on the abundance and properties of global organic aerosol, *Atmos. Chem. Phys.*, *11*, 7727-7746, doi:10.5194/acp-11-7727-2011.

Jimenez, J. L.., et al. (2009), Evolution of organic aerosols in the atmosphere, *Science, 326,* 1525-1529, doi:10.1126/science.1180353.

Jo, D. S., R. J. Park, M. J. Kim, and D. V. Spracklen (2013), Effects of chemical aging on global secondary organic aerosol using the volatility basis set approach, *Atmos. Environ.*, *81*, 230-244, doi:10.1016/j.atmosenv.2013.08.055.

John, V. O. and B. J. Soden (2007), Temperature and humidity biases in global climate models and their impact on climate feedbacks, *Geophys. Res. Lett.*, *34*, L18794, doi:10.1029/2007GL030429.

Jokinen, T., et al. (2015), Production of extremely low volatility organic compounds from biogenic emissions: Measured yields and atmospheric implications, *PNAS*, *112*(23), 7123–7128, doi: 10.1073/pnas.1423977112.

Jonson, J. E. et al. (2010), A multi-model analysis of vertical ozone profiles, *Atmos. Chem. Phys.*, *10*, 5759-5783, doi: 10.5194/acp-10-5759-2010.

Karamchandani, P., Y. Zhang, S. Y. Chen, and R. Balmori-Bronson (2012), Development and testing of an extended chemical mechanism for global-through-urban applications, *Atmos. Pollut. Res.*, *3*(1), 1–24, doi:10.5094/APR.2011.047.

Kay, J. E., B. R. Hillman, S. A. Klein, Y. Zhang, B. Medeiros, R. Pincus, A. Gettelman, B. Eaton, J. Boyle, R. Marchand, and T. P. Ackerman (2012), Exposing global cloud biases in the Community Atmosphere Model (CAM) using satellite observations and their corresponding instrument simulators, *J. Climate*, *25*, 5190-5207, doi:10.1175/JCLI-D-11-00469.1.

Kim, M. J., R. J. Park, C.-H. Ho, J.-H. Woo, K.-C. Choi, C.-K. Song, and J.-B. Lee (2015), Future ozone and oxidants change under the RCP scenarios, *Atmos. Environ.*, *101*, 103-115, doi:10.1016/j.atmosenv.2014.11.016.

Knote, C. et al. (2014), Simulation of semi-explicit mechanisms of SOA formation from glyoxal in aerosol in a 3-D model, *Atmos. Chem. Phys.*, *14*, 6213-6239, doi: 10.5194/acp-14-6213-2014.

Knote, C. et al. (2015), Influence of the choice of gas-phase mechanism on predictions of key gaseous pollutants during the AQMEII phase-2 intercomparison, *Atmos. Environ.*, 115, 553-568, doi:10.1016/j.atmosenv.2014.11.066.

Knutti, R., and J, Sedlacek (2013), Robustness and uncertainties in new CMIP5 climate model projections, *Nature Climate Change*, 3,369-373, doi:10.1038/nclimate1716.

Koo, B. Y., A. S. Ansari, and S. N. Pandis (2003), Integrated approaches to modeling the organic and inorganic atmospheric aerosol components, *Atmos. Environ., 37*, 4757–4768, doi:10.1016/j.atmosenv.2003.08.016.

Kriegler, E., B. C. O'Neill, S. Hallegatte, T. Kram, R. J. Lempert, R. H. Moss, and T. Wilbanks (2012), The need for and use of socio-economic scenarios for climate change analysis: A new approach based on shared socio-economic pathways, *Global Environ. Chang., 22*, 807–822, doi: doi:10.1016/j.gloenvcha.2012.05.005.

Kroll, J. H., et al. (2011), Carbon oxidation state as a metric for describing the chemistry of atmospheric organic aerosol, *Nat. Chem., 3*, 133–139. doi:10.1038/NCHEM.948.

Kumar, P., I. N. Sokolik, and A. Nenes (2009), Parameterization of cloud droplet formation for global and regional models: including adsorption activation from insoluble CCN, Atmos. Chem. Phys., 9, 2517-2532, doi:10.5194/acp-9-2517-2009.

Lamarque, J.-F., G. P. Kyle, M. Meinshausen, K. Riahi, S. J. Smith, D. P., van Vuuren, A. J. Conley, and F. Vitt (2011), Global and regional evolution of short-lived radiatively-active gases and aerosols in the Representative Concentration Pathways, *Clim. Change*, *109*, 191-212, doi:10.1007/s10584-011-0155-0.

Lamarque, J.-F., et al. (2012), CAM-chem: Description and evaluation of interactive atmospheric chemistry in CESM, *Geosci. Model Dev., 5*, 369–411, doi:10.5194/gmd-5-369-2012.

Lamarque, J.-F. et al. (2013), The Atmospheric Chemistry and Climate Model Intercomparison Project (ACCMIP): overview and description of models, simulations and climate diagnostics, *Geosci. Model Dev.*, *6*, 179–206, doi:10.5194/gmd-6-179-2013.

Lane, T. E., N. M. Donahue, and S. N. Pandis (2008a), Simulating secondary organic aerosol formation using the volatility basis-set approach in a chemical transport model, *Atmos. Environ.*, *42*(32), 7439–7451, doi:10.1016/j.atmosenv.2008.06.026.

Lane, T. E., N. M. Donahue, and S. N. Pandis (2008b), Effect of NOx on secondary organic aerosol concentrations, *Environ. Sci. Technol.*, *42*, 6022-6027, doi:10.1021/es703225a.

Langner, J., et al. (2012), A multi-model study of impacts of climate change on surface ozone in Europe, *Atmos. Chem. Phys.*, *12*, 10,423–10,440, doi:10.5194/acp-12-10423-2012.

Lau, K.-M., and K-M. Kim (2006a), Observational relationships between aerosol and Asian monsoon rainfall, and circulation, *Geophys. Res. Lett.*, *33*, L21810, doi:10.1029/2006GL027546.

Lau, K. M., M. K. Kim, and K. M. Kim (2006b), Asian monsoon anomalies induced by aerosol direct effects, *Clim. Dyn.*, *26*, 855– 864, doi:10.1007/s00382-006-0114-z.

Lauer, A. and K. Hamilton (2013), Simulating clouds with global climate models: A comparison of CMIP5 results with CMIP3 and satellite data, *J. Climate*, *26*, 3833-3845, doi: 10.1175/JCLI-D-12-00451.1.

Lee, S. S. (2011), Effect of aerosol on circulations and precipitation in deep convective clouds, *J. Atmos. Sci., 69*, 1957–1974, doi: http://dx.doi.org/10.1175/JAS-D-11-0111.1.

Leibensperger, E. M., L. J. Mickley, and D. J. Jacob (2008), Sensitivity of US air quality to mid-latitude cyclone frequency and implications of 1980-2006 climate change, *Atmos. Chem. Phys., 8*, 7075-7086, doi:10.5194/acp-8-7075-2008.

Leibensperger, E. M., L. J. Mickley, D. J. Jacob, and S. R. H. Barrett (2011), Intercontinental influence of NOx and CO on particulate matter air quality, *Atmos. Environ.*, *45*, 3318-3324, doi:10.1016/j.atmosenv.2011.02.023.

Leskinen, A. P. , M. Kulmala, and K. E. G. Lehtinen (2008), Growth of nucleation mode particles : Source rates of condensable vapor in smog chamber, *Atmos. Environ.*, *42*(32), 7405-5411, doi:10.1016/j.atmosenv.2008.06.024.

Levy, H., II, M. D. Schwarzkopf, L. Horowitz, V. Ramaswamy, and K. L. Findell (2008), Strong sensitivity of late 21st century climate to projected changes in short-lived air pollutants, *J. Geophys. Res.*, *113*, D06102, doi:10.1029/2007JD009176.

Li, Y. J., B. T. L. Lee, J. Z. Yu, N. L. Ng, and C. K. Chang (2013), Evaluating the degree of oxygenation of organic aerosol during foggy and hazy days in Hong Kong using high-resolution time-of-flight aerosol mass spectrometry (HR-ToF-AMS), *Atmos. Chem. Phys.*, *13*, 8739-8753, doi:10.5194/acp-13-8739-2013.

Liao, H., P. Adams, S. Chung, J. Seinfeld, L. Mickley, and D. Jacob (2003), Interactions between tropospheric chemistry and aerosols in a unified general circulation model, *J. Geophys. Res.*, *108*, D14001 doi:10.1029/2001JD001260.

Liao, H., J. Seinfeld, P. Adams, and L. Mickley (2004), Global radiative forcing of coupled tropospheric ozone and aerosols in a unified general circulation model, *J. Geophys. Res.*, *109*, D16207, doi:10.1029/2003JD004456.

Liao, H., W.-T. Chen, and J. H. Seinfeld (2006), Role of climate change in global predictions of future tropospheric ozone and aerosols, *J. Geophys. Res.*, *111*, D12304, doi:10.1029/2005JD006852.

Liggio, J., S.-M. Li, and R. McLaren (2005a), Reactive uptake of glyoxal by particulate matter, *J. Geophys. Res.*, *110*, D10304, doi:10.1029/2004JD005113.

Liggio, J., S.-M. Li, and R. McLaren (2005b), Heterogeneous reactions of glyoxal on particulate matter: Identification of acetals and sulfate esters, *Environ. Sci. Technol.*, *39*, 1632-1541, doi:10.1021/es048375y.

Lim, Y. B., Y. Tan, M. J. Perri, S. P. Seitzinger, and B. J, Turpin (2010), Aqueous chemistry and its role in secondary organic aerosol (SOA) formation, *Atmos. Chem. Phys.*, *10*, 10521-10539, doi: 10.5194/acp-10-10521-2010.

Lin, G., J. E. Penner, M. G. Flanner, S. Sillman, L. Xu, and C. Zhou (2014), Radiative forcing of organic aerosol in the atmosphere and on snow: Effects of SOA and brown carbon, *J. Geophys. Res. Atmos.*, *119*, 7453–7476, doi:10.1002/2013JD021186.

Lin, J.-T., J. T. Wuebbles, and X.-Z. Liang (2008), Effects of intercontinental transport on surface ozone over the United States: Present and future assessment with a global model, *Geophys. Res. Lett.*, *35*, L02805, doi:10.1029/ 2007GL031415.

Lin, Y.-L., R. D. Farley, and H. D. Orville (1983), Bulk parameterization of the snow field in a cloud model, *J. Clim. Appl. Meteorol., 22*, 1065–1092, doi:10.1175/1520-0450(1983)022<1065:BPOTSF>2.0.CO;2.

Lipsky, E. M., and A. L. Robinson (2006), Effects of dilution on fine particle mass and partitioning of semivolatile organics in diesel exhaust and wood smoke, Environ. Sci. Technol., 40. 155-162.doi: 10.1021/es050319p.

Liu, G., J. E. Penner, S. Sillman, D. Taraborrelli, and J, Lelieveld (2012), Global modeling of SOA formation from dicarbonyls, epoxides, organic nitrates, and peroxides, *Atmos. Chem. Phys., 12*, 4743-4774, doi:10.5194/acp-12-4743-2012.

Liu, H., D. J. Jacob, I. Bey, R. M. Yantosca, B. N. Duncan, and G. W. Sachse (2003), Transport pathways for Asian pollution outflow over the Pacific: Interannual and seasonal variations, *J. Geophys. Res., 108*, 8786, doi:10.1029/2002JD003102.

Liu, J., D. L. Mauzerall, and L. W. Horowitz (2008), Source-receptor relationships between East Asian sulfur dioxide emissions and Northern Hemisphere sulfate concentrations, *Atmos. Chem. Phys., 8*, 3721-3733, doi:10.5194/acp-8-3721-2008.

Liu, J., D. L. Mauzerall, and L. W. Horowitz (2009), Evaluating inter-continental transport of fine aerosol 2) global health impact, *Atmos. Environ., 43*, 4339-4347, doi:10.1016/j.atmosenv.2009.05.032.

Liu, X., and J. Wang (2010), How important is aerosol hygroscopicity to aerosol indirect forcing?, *Environ. Res. Lett., 5*, 044010, doi:10.1088/1748-9326/5/4/044010.

Liu, X., et al. (2012), Toward a minimal representation of aerosols in climate models: description and evaluation in the Community Atmosphere Model CAM5, *Geosci. Model Dev.*, *5*, 709-739, doi:10.5194/gmd-5-709-2012.

Liu, Y., F. Siekmann, P. Renard, A. El Zein, G. Salque, I. El Haddad, B. Temime-Roussel, D. Voisin, R. Thissen, and A. Monod (2012), Oligomer and SOA formation through aqueous phase photooxidation of methacrolein and methyl vinyl ketone, *Atmos. Environ.*, *49*, 123-129, doi:10.1016/j.atmosenv.2011.12.012.

Martensson, E. M., E. D. Nilsson, G. deLeeuw, L. H. Cohen, and H. C. Hansson (2003), Laboratory simulations and parameterizations of the primary marine aerosol production, *J. Geophys. Res.*, *108*(D9), 4297, doi:10.1029/2002JD0022263.

Masui, T., K., Y. Hijioka, T. Kinoshita, T. Nozawa, S. Ishiwatari, E. Kato, P. R. Shukla, Y. Yamaga, and M. Kainum (2011), An emission pathway for stabilization at 6 Wm^{-2} radiative forcing, *Clim. Chang.*, *109*, 59-76, doi: 10.1007/s10584-011-0150-5.

May, A. A., A. A. Presto, C. J. Hennigan, N. T. Nguyen, T. D. Gordon, and A. L. Robinon (2013a), Gas-particle partitioning of primary organic aerosol emissions: (1) Gasoline vehicle exhaust, *Atmos. Environ.*, *77*, 128-139, doi:10.1016/j.atmosenv.2013.04.060.

May, A. A., E. J. T. Levin, C. J. Hennigan, I. Riipinen, T. Lee, J. L. Collett Jr., J. L. Jimenez, S. M. Kreidenweis, and A. L. Robinson (2013b), Gas-particle partitioning of primary organic aerosol emissions: 3. Biomass burning, *J. Geophys. Res. Atmos.*, *118*, 11,327–11,338, doi:10.1002/jgrd.50828.

May, B., D. Wagenbach, S. Hammer, P. Steier, H. Pauxbaum, and C. Pio (2008), The anthropogenic influence on carbonaceous aerosol in the European background. *Tellus, 61B,* 464-472, doi:10.1111/j.1600-0889.2008.00379.x.

Meng, B., X. Feng, G. Qiu, P. Liang, P. Li, C. Chen, and L. Shang (2011), The process of methylmercury accumulation in rice (Oryza sativa L.), *Environ. Sci. Technol.*, *45*, 2711-2717, doi:10.1021/es103384v.

Menon, S., J. Hansen, L. Nazarenko, and Y. Luo (2002), Climate effects of black carbon aerosols in India and China, *Science, 297,* 2250-2253, doi:10.1126/science.1075159.

Mickley, L. J., P. P. Murti, D. J. Jacob, J. A. Logan, D. M. Koch, and D. Rind (1999), Radiative forcing from tropospheric ozone calculated with a unified chemistry-climate model, *J. Geophys. Res.*, *104*(D23), 30,153‑30,172, doi:10.1029/1999JD900439.

Mickley, L. J., D. J. Jacob, B. D. Field, and D. Rind (2004), Effects of future climate change on regional air pollution episodes in the United States, *Geophys. Res. Lett.*, *30*, L24103, doi:10.1029/2004GL021216.

Mlawer, E. J., S. J. Taubman, P. D. Brown, M. J. Iacono, and S. A. Clough (1997), Radiative transfer for inhomogeneous atmospheres: RRTM, a validated correlated-k model for the longwave, *J. Geophys. Res.*, *102*(D14), 16,663–16,682, doi:10.1029/97JD00237.

Monin, A. S., and A. M. Obukhov (1954), Basic laws of turbulent mixing in the surface layer of the atmosphere [in Russian], *Contrib. Geophys. Inst. Acad. Sci. USSR, 151*, 163–187.

Monks, P.S. et al. (2009), Atmospheric composition change – global and regional air quality, *Atmos. Environ. 43,* 5268-5350, doi:10.1016/j.atmosenv.2009.08.021.

Moore, S. K., V. L. Trainer, N. J. Mantua, M. S. Parker, E. A. Laws, L. C. Backer, and L. E. Fleming (2008), Impacts of climate variability and future climate change on harmful algal blooms and human health, *Environmental Health, 7,* S4, doi:10.1186/1476-069X-7-S2-S4.

Morrison, H., J. A. Curry, and V. I. Khvorostyanov (2005), A new Double-Moment microphysics parameterization for applications in cloud and climate models, Part 1: Description, *J. Atmos. Sci., 62,* 1665-1677, doi:10.1175/JAS3446.1.

Morrison, H. and A. Gettelman (2008), A new two-moment bulk stratiform cloud microphysics scheme in the community atmosphere model, version 3 (CAM3). Part I: Description and numerical tests, *J. Climate, 21*, 3642–3659, doi:http://dx.doi.org/10.1175/2008JCLI2105.1.

Moss, R., M. Babiker, S. Brinkman, E. Calvo, T, Carter, J. Edmonds, I. Elgizouli, S. Emori, L. Erda, K. Hibbard, R. Jones, M. Kainuma, J. Kelleher, J.-F. Lamarque, M. Manning, B. Matthews, J. Meehl, L. Meyer, J. Mitchell, N. Nakicenovic, B. O'Neill, R. Pichs, K. Riahi, S. Rose, P. Runci, R. Stouffer, D. van Vuuren, J. Weyant, T. Wilbanks, J.-P. van Ypersele, and M. Zurek (2008). *Towards New Scenarios for Analysis of Emissions, Climate Change, Impacts, and Response Strategies*. Technical Summary. Intergovernmental Panel on Climate Change, Geneva, 25 pp.

Moss, R. H., et al. (2010), The next generation of scenarios for climate change research and assessment, *Nature, 463,* 747–56, doi:10.1038/nature08823.

Murazaki, K., and P. Hess (2006), How does climate change contribute to surface ozone change over the United States?, *J. Geophys. Res.*, *111*, D05301, doi:10.1029/2005JD005873.

Murphy, B. N., and S. N. Pandis (2009), Simulating the formation of semivolatile primary and secondary organic aerosol in a regional chemical transport model, Environ. Sci. Technol., 43(13), 4722–4728, doi:10.1021/es803168a.

Murphy, B. N., N. M. Donahue, C. Fountoukis, and S. N. Pandis (2011), Simulating the oxygen content of ambient organic aerosol with the 2D volatility basis set, *Atmos. Chem. Phys.*, *11*, 7859-7873, doi:10.5194/acp-11-7859-2011.

Nakajima, T. Y., K. Suzuki, and G. L. Stephens (2010), Droplet Growth in Warm Water Clouds Observed by the A-Train. Part I: Sensitivity Analysis of the MODIS-Derived Cloud Droplet Sizes, *Journal of the Atmospheric Sciences*, *67*(6), 1884-189610.1175/2009jas3280.1.

Nakicenovic, N., O. Davidson, G. Davis, A. Grubler, T. Kram, E.L. La Rovere, B. Metz, T. Morita, W. Pepper, H. Pitcher, A. Sankovski, P. Shukla, R. Swart, R. Watson, and Z. Dadi (2000), *Emissions Scenarios: A Special Report of Working Group III of the Intergovernmental Panel on Climate Change*. Cambridge University Press, New York.

Neale, R. B., J. H. Richter and M. Jochum (2008), The impact of convection on ENSO: From a delayed oscillator to a series of events, *J. Climate*, *21***,** 5904-5924, doi: http://dx.doi.org/10.1175/2008JCLI2244.1.

Nel, A. (2005), Air pollution-related illness: Effects of particles, *Science*, *308*, 804-805, doi:10.1126/science.11108752.

Nenes, A., S. N. Pandis, and C. Pilinis (1998), ISORROPIA: A new thermodynamic equilibrium model for multiphase multicomponent inorganic aerosols, *Aquat. Geochem.*, *4*, 123–152, doi:10.1023/A:1009604003981.

Nenes, A., S. N. Pandis, and C. Pilinis (1999), Continued development and testing of a new thermodynamic aerosol module for urban and regional air quality models, *Atmos. Environ.*, *33*(10), 1553–1560, doi:10.1016/S1352-2310(98)00352-5.

Neu, J. L., and M. J. Prather (2012), Toward a more physical representation of precipitation scavenging in global chemistry models: cloud overlap and ice physics and their impact on tropospheric ozone, *Atmos. Chem. Phys.*, *12*, 3289-3310, doi:10.5194/acp-12-3289-2012.

NOAA, National Oceanic and Atmospheric Administration, (1998), Automated Surface Observing System User's Guide. http://www.nws.noaa.gov/asos/pdfs/aum-toc.pdf.

O'Dell, C. W., F. J. Wentz, and R. Bennartz (2008), Cloud liquid water path from satellite-based passive microwave observations: A new climatology over the global oceans, *J. Climate, 21*, 1721-1739, doi: http://dx.doi.org/10.1175/2007JCLI1958.1.

O'Dowd, C. D., H. S. Michael, I. E. Consterdine, and J. A. Lowe (1997), Marine aerosol, sea-salt, and the marine sulphur cycle: A short review, *Atmos. Environ.*, *31*, 73–80, doi:10.1016/S1352-2310(96)00106-9.

Odum, J. R., T. Hoffmann, F. Bowman, D. Collins, R. C. Flagan, and J. H. Seinfeld (1996) Gas/particle partitioning and secondary organic aerosol yields, *Environ. Sci. Technol.*, *30*, 2580–2585, doi:10.1021/es950943+.

Oueslati, B. and G. Bellon (2015), The double ITCZ bias in CMIP5 models: interaction between SST, large‐scale circulation and precipitation, *Clim. Dyn.*, *44*, 585-607, doi: 10.1007/s00382-015-2468-6.

Pankow, J. F. (1994), An absorption-model of the gas aerosol partitioning involved in the formation of secondary organic aerosol, *Atmos. Environ.*, *28*(2), 189–193, doi:10.1016/1352-2310(94)90094-9.

Park, R. J., D. J. Jacob, B. D. Field, R. M. Yantosca, and M. Chin (2004), Natural and transboundary pollution influences on sulfate-nitrate-ammonium aerosols in the United States: Implications for policy, *J. Geophys. Res.*, *109*, D15204, doi:10.1029/2003JD004473.

Park, S. and C. S. Bretherton (2009), The University of Washington shallow convection and moist turbulence schemes and their impact on climate simulations with the community atmosphere model, J. Climate, 22, 3449–3469, doi: http://dx.doi.org/10.1175/2008JCLI2557.1.

Park, S., C. S. Bretherton, and P. J. Rasch (2014), Integrating cloud processes in the Community Atmosphere Model, Version 5, J. Clim., 27, 6821-6856, doi: 10.1175/JCLI-D-14-00087.1.

Patz, J. A., D. Campbell-Lendrum, T. Holloway, and J. A. Foley (2005), Impact of regional climate change on human health, *Nature*, *438*, 310-317, doi:10.1038/nature04188.

Pereira, H. M. et al. (2010), Scenarios for Global Biodiversity in the 21st Century, *Science*, *330*, 1496-1501, doi:10.1126/science.1196624.

Pfister, G. G., L. K. Emmons, P. G. Hess, J.-F. Lamarque, A. M. Thompson, and J. E. Yorks (2008), Analysis of the Summer 2004 ozone budget over the United States using Intercontinental Transport Experiment Ozonesonde Network Study (IONS) observations and Model of Ozone and Related Tracers (MOZART-4) simulations, *J. Geophys. Res.*, *113*, D23306, doi:10.1029/2008JD010190.

Pierrehumbert, R. T. (2014), Short-lived climate pollution, *Annu. Rev. Earth Planet. Sci.*, *42*, 341-379, doi: 10.1146/annurev-earth-060313-054843.

Prather, M., et al., Fresh air in the 21st century? (2003), *Geophys. Res. Lett.*, *30*(2), 1100, doi:10.1029/2002GL016285.

Pun, B. K., R. J. Griffin, C. Seigneur, and J. H. Seinfeld, Secondary organic aerosol, 2, Thermodynamic model for gas/particle partitioning of molecular constituents, *J. Geophys. Res.*, *107*(D17), 4333, doi:10.1029/2001JD000542, 2002.

Puxbaum, H., A. Caseiro, A. Sanchex-Ochoa, A. Kasper-Giebl, M. Claeys, A. Gelencser, M. Legrand, S. Preunkert, and C. Pio (2007), Levoglucosan levels at background sites in Europe for assessing the impact of biomass combustion on the European aerosol background. *J. Geophys. Res.*, *112*, D23S05, doi:10.1029/2006JD008114.

Pye, H. O. T. and J. H. Seinfeld (2010), A global perspective on aerosol from low-volatility organic compounds, *Atmos. Chem. Phys.*, *10*, 4377-4401, doi:10.5194/acp-10-4377-2010.

Qian, Y., L. R. Leung, S. J. Ghan, and F. Giorgi (2003), Regional climate effects of aerosols over China: modeling and observation, *Tellus*, *55B*, 914-934, doi: 10.1046/j.1435-6935.2003.00070.x.

Qian, Y., D. P. Kaiser, L. R. Leung, and M. Xu (2006), More frequent cloud-free sky and less surface solar radiation in China from 1955 to 2000, *Geophys. Res. Lett.*, *33*, L01812, doi:10.1029/2005GL024586.

Qian, Y., W. Wang, L. R. Leung, and D. P. Kaiser (2007), Variability of solar radiation under cloud-free skies in China: The role of aerosols, *Geophys. Res. Lett.*, *34*, L12804, doi:10.1029/2006GL028800.

Qian, Y., M. G. Flanner, L. R. Leung, and W. Wang (2011), Sensitivity studies on the impacts of Tibetan Plateau snowpack pollution on the Asian hydrological cycle and monsoon climate, *Atmos. Chem. Phys.*, *11*, 1929-1948, doi:10.5194/acp-11-1929-2011.

Qian, Y., C. N. Long, H. Wang, J. M. Comstock, S. A. McFarlane, and S. Xie (2012), Evaluation of cloud fraction and its radiative effect simulated by IPCC AR4 global models against ARM surface observations, *Atmos. Chem. Phys.*, *12*, 1785–1810, doi:10.5194/acp-12-1785-2012.

Rausch, J., A. Heidinger, and R. Bennartz (2010), Regional assessment of microphysical properties of marine boundary layer cloud using the PATMOS-x dataset, *J. Geophys. Res.*, *115*, D23212, doi:10.1029/2010JD014468.

Ravetta, F., G. Ancellet, A. Colette, and H. Schlager (2007), Long-range transport and tropospheric ozone variability in the western Mediterranean region during the

Intercontinental Transport of Ozone and Precursors (ITOP-2004) campaign, *J. Geophys. Res.*, *112*, D10S46, doi:10.1029/2006JD007724.

Reidmiller, D. R., et al. (2009), The influence of foreign vs. North American emissions on surface ozone in the US, *Atmos. Chem. Phys.*, *9*, 5027-5042, doi:10.5194/acp-9-5027-2009.

Riahi, K., S. Rao, V. Krey, C. Cho, V. Chirkov, G. Fischer, G. Kindermann, N. Nakicenovic, and P. Rafaj (2011), RCP 8.5-A scenario of comparatively high greenhouse gas emissions, *Clim. Chang.*, *109*, 33-57, doi: 10.1007/s10584-011-0149-y.

Rieder, H. E., A. M. Fiore, L. W. Horowitz, and V. Naik (2015), Projecting policy-relevant metrics for high summertime ozone pollution events over the eastern United States due to climate and emission changes during the 21st century, *J. Geophys. Res. Atmos.*, *120*, 784–800, doi:10.1002/2014JD022303.

RIVM (National Institute for Public Health and the Environment), 2001. The IMAGE 2.2 Implementation of the SRES Scenarios [CD-ROM], RIVM Publication 481508018, Bilthoven, Netherlands.

Roberts, G., G. Mauger, O. Hadley, and V. Ramanathan (2006), North American and Asian aerosols over the eastern Pacific Ocean and their role in regulating cloud condensation nuclei, *J. Geophys. Res.*, *111*, D13205, doi:10.1029/2005JD006661.

Robinson, A. L. et al., (2007), Rethinking organic aerosols: Semivolatile emissions and photochemical aging, *Science*, *315*, 1259-1262, doi:10.1126/science.1133061.

Rosenfeld, D, U. Lohmann, G. B. Raga, C. D. O'Dowd, M. Kulmala, S. Fuzzi, A. Reissell, and M. O. Andreae (2008), Flood or Drought: How do aerosols affect precipitation?, *Science*, *321*, 1309-1313, doi: 10.1126/science.1160606.

Rowe, P. M., S. Neshyba, and V. P. Walden (2013), Radiative consequences of low-temperature infrared refractive indices for supercooled water clouds, *Atmos. Chem. Phys.*, *13*, 11925-11933, doi:10.5194/acp-13-11925-2013.

Saleh, R., et al., (2014), Brownness of organics in aerosols from biomass burning linked to their black carbon content, *Nature Geosci.*, *7*, 647-650, doi:10.1038/ngeo2220.

Sanderson, M. G., C. D. Jones, W. J. Collins, C. E. Johnson, and R. G. Derwent (2003), Effect of climate change on isoprene emissions and surface ozone levels, *Geophys. Res. Lett.*, *30*(18), 1936, doi:10.1029/2003GL017642.

Sanderson, M. G, et al. (2008), A multi-model study of the hemispheric transport and deposition of oxidized nitrogen, *Geophys. Res. Lett.*, *35*, L17815, doi:10.1029/2008GL035389.

SCAQMD – South Coast Air Quality Management District (2004), SCAQMD PAMS Assessment Review Task 1: Literature Review, C. L. Blanchard and H. R. Hafner, STI-904042-2569-TM, Sonoma Technology Inc., Petaluma, CA.

Schell, B., I. J. Ackermann, H. Hass, F. S. Binkowski, and A. Ebel (2001), Modeling the formation of secondary organic aerosol within a comprehensive air quality model system, *J. Geophys. Res.*, *106*, 28,275–28,293, doi:10.1029/2001JD000384.

Schindler, D. W. and S. E. Bayley (1993), The biosphere as an increasing sink for atmospheric carbon: Estimates from increased nitrogen deposition, *Glob. Biogeochem. Cycles*, 7, 717-733, doi:10.1029/93GB02562.

Seethala, C., and Á. Horvath (2010), Global assessment of AMSR-E and MODIS cloud liquid water path retrievals in warm oceanic clouds, *J. Geophys. Res.*, 115, D13202, doi:10.1029/2009JD012662.

Seigneur, C., K. Vijayaraghavan, K. Lohman, P. Karamchandani, P., and C. Scott (2004), Global source attribution for mercury deposition in the United States, *Environ. Sci. Technol.*, *28*, 555-569, doi: 10.1021/es034109t.

Shaw, P. (2008), Application of aerosol speciation data as an in situ dust proxy for validation of the Dust Regional Atmospheric Model (DREAM), *Atmos. Environ.*, 42, 7304–7309, doi:10.1016/j.atmosenv.2008.06.018.

Shindell, D. T., et al. (2008), A multi-model assessment of pollution transport to the Arctic, *Atmos. Chem. Phys.*, *8*, 5353-5372, doi:10.5194/acp-8-5353-2008.

Shindell, D., et al. (2012), Simultaneously Mitigating Near-Term Climate Change and Improving Human Health and Food Security, *Science*, 335, 183-189, doi:10.1126/science.1210026.

Shindell, D. T., et al. (2013), Radiative forcing in the ACCMIP historical and future climate simulations, *Atmos. Chem. Phys.*, *13*, 2939–2974, doi:10.5194/acp-13-2939-2013.

Shrivastava, M. K., E. M. Lipsky, C. O. Stanier, and A. L. Robinson (2006), Modeling semivolatile organic aerosol mass emissions from combustion systems, *Environ. Sci. Technol.*, *40*(8), 2671-2677, doi:10.1021/es0522231.

Shrivastava, M. K., T. E. Lane, N. M. Donahue, S. N. Pandis, and A. L. Robinson (2008), Effects of gas particle partitioning and aging of primary emissions on urban and regional organic aerosol concentrations, *J. Geophys. Res., 113*, D18301, doi:10.1029/2007JD009735.

Shrivastava, M.K., J. Fast, R. Easter, W. I. Gustafson, Jr., R. A. Zaveri, J. L. Jimenez, P. Saide, and A. Hodzic (2011), Modeling organic aerosols in a megacity: comparison of simple and complex representations of the volatility basis set approach, *Atmos. Chem. Phys., 11*, 6639-6662, doi: 10.5194/acp-11-6639-2011.

Shrivastava, M., A. Zelenyuk, D. Imre, R. Easter, J. Beranek, R. A. Zaveri, and J. Fast (2013), Implications of low volatility SOA and gas-phase fragmentation reactions on SOA loadings and their spatial and temporal evolution in the atmosphere, *J. Geophys. Res. Atmos., 118*, 3328–3342, doi:10.1002/jgrd.50160.

Shrivastava, M., et al. (2015), Global transformation and fate of SOA: Implications of low-volatility SOA and gas-phase fragmentation reactions, *J. Geophys. Res. Atmos., 120*, 4169–4195, doi:10.1002/2014JD022563.

Sitch, S., P. M. Cox, W. J. Collins, and C. Huntingford (2007), Indirect radiative forcing climate change through ozone effects on the land-carbon sink, *Nature, 448*, 791-794, doi:10.1038/nature06059.

Skerlack, B., Sprenger, and H. Weruli (2014), A global climatology of stratosphere–troposphere exchange using the ERA-Interim data set from 1979 to 2011, *Atmos. Chem. Phys., 14*, 913–937, doi:10.5194/acp-14-913-2014.

Stanier, C. O., N. Donahue, and S. N. Pandis (2008), Parameterization of secondary organic aerosol mass fractions from smog chamber data, *Atmos. Environ.*, *42*, 2276-2299, doi:10.1016/j.atmosenv.2007.12.042.

Stavrakou, T., J.-F. Muller, I. De Smedt, M. Van Roozendael, M,. Kanakidou, M. Vrekoussis, F. Wittrock, A. Richter, and J. P. Burrows (2009), The continental source of glyoxal estimated by synergistic use of spaceborne measurements and inverse modelling, *Atmos. Chem. Phys.*, *9*, 8431-8446, doi:10.5194/acp-9-8431-2009.

Steinacher, M., F. Joos, T. L. Frolicher, G.-K. Plattner, and S. C. Doney (2009), Imminent ocean acidification in the Arctic projected with the NCAR global coupled carbon cycle-climate model, Biogeosciences, 6, 515-533, doi:10.5194/bg-6-515-2009.

Stevenson, D. S., et al. (2006), Multimodel ensemble simulations of present-day and near-future tropospheric ozone, *J. Geophys. Res.*, *111*, D08301, doi:10.1029/2005JD006338.

Stevenson. D. S. et al., (2013), Tropospheric ozone changes, radiative forcing and attribution to emissions in the Atmospheric Chemistry and Climate Model Intercomparison Project (ACCMIP), *Atmos. Chem. Phys.*, *13*, 3063–3085, doi:10.5194/acp-13-3063-2013.

Stockwell, W. R., F. Kirchner, M. Kuhn, and S. Seefeld (1997), A new mechanism for regional atmospheric chemistry modeling, *J. Geophys. Res.*, *102*(D22), 25,847–25,879, doi:10.1029/97JD00849.

Stohl, A., S. Eckhardt, C. Forster, P. James, and N. Spichtinger (2002), On the pathways and timescales of intercontinental air pollution transport, *J. Geophys. Res.*, *107*, 4684, doi:10.1029/2001JD001396.

Streets, D. G., T. C. Bond, T. Lee, and C. Jang (2004), On the future of carbonaceous aerosol emissions, *J. Geophys. Res.*, *109*, D24212, doi:10.1029/2004JD004902.

Strode, S. A., L. Jaegle, D. A. Jaffe, P. C. Swartzendruber, N. E. Selin, C. Holmes, and R. M. Yantosca (2008), Trans-Pacific transport of mercury, *J. Geophys. Res.*, *113*, D15305, doi:10.1029/2007JD009428.

Sudo, K., and H. Akimoto (2007), Global source attribution of tropospheric ozone: Long-range transport from various source regions, *J. Geophys. Res.*, *112*, D12302, doi:10.1029/2006JD007992.

Sun, J., and P. A. Ariya (2006), Atmospheric organic and bio-aerosols as cloud condensation nuclei (CCN): A review, *Atmos. Environ.*, *40*, 795-820, doi: 10.1016/j.atmosenv.2005.05.052.

Tai, A. P. K., L. J. Mickley, and D. J. Jacob (2012), Impact of 2000-2050 climate change on fine particulate matter (PM2.5) air quality inferred from a multi-model analysis of meteorological modes, *Atmos. Chem. Phys.*, *12*, 11329-11337, doi:10.5194/acp-12-11329-2012.

Tagaris, E., K. Manomaiphiboon, K.-J. Liao, L. R. Leung, J.-H. Woo, S. He, P. Amar, and A. G. Russell (2007), Impacts of global climate change and emissions on regional ozone and fine particulate matter concentrations over the United States, *J. Geophys.Res.*,*112*, D14312, doi:10.1029/2006JD008262.

Takigawa, M., K. Sudo, H. Akimoto, K. Kita, N. Takegawa, Y. Kondo, and M. Takahashi (2005), Estimation of the contribution of intercontinental transport during the PEACE campaign by using a global model, *J. Geophys. Res.*, *110*, D21313, doi:10.1029/2005JD006226.

TF HTAP – Task Force on Hemispheric Transport of Air Pollution: Hemispheric Transport of Air Pollution 2010, Part A: Ozone and Particulate Matter, Air Pollut. Stud., 17, edited by: Dentener, F., T. J. Keating, and H. Akimoto, United Nations Economic Commission for Europe, Geneva, Switzerland, available at: www.htap.org, 2011.

Thomson, A., K. V. Calvin, S. J. Smith, G. P. Kyle, A. Volke, P. Patel, S. Delgado-Arias, B. Bond-Lamberty, M A. Wise, L. E. Clarke, and J. A. Edmonds (2011), RCP4.5: a pathway for stabilization of radiative forcing by 2100, *Clim. Change*, *109*, 77-94, doi: 10.1007/s10584-011-0151-4.

Tian, B., E. J. Fetzer, B. H. Kahn, J. Teixerira, E. Manning, and T. Hearty (2013), Evaluating CMIP5 models using AIRS tropospheric air temperature and specific humidity climatology, J. Geophys. Res., doi:10.1002/jgrd.50117.

Tie, X., S. Madronich, S. Walters, R. Zhang, P. Rasch, and W. Collins (2003), Effect of clouds on photolysis and oxidants in the troposphere, *J. Geophys. Res.*, *108*(D20), 4642, doi:10.1029/2003JD003659.

Tsigaridis, K. and M. Kanakidou (2003), Global modelling of secondary organic aerosol in the troposphere: a sensitivity analysis, *Atmos. Chem. Phys.*, *3*, 1849-1869, doi:10.5194/acp-3-1849-2003.

Tsimpidi, A. P., V. A. Karydis, M. Zavala, W. Lei, L. Molina, I. M. Ulbrich, J. L. Jimenez, and S. N. Pandis (2010), Evaluation of the volatility basis-set approach for the simulation of organic aerosol formation in the Mexico City metropolitan area, *Atmos. Chem. Phys*., *10*, 525-546, doi:10.5194/acp-10-525-2010.

Unger, N., D. T. Shindell, D. M. Koch, M. Amann, J. Cofala, and D. G. Streets (2006), Influences of man-made emissions and climate changes on tropospheric ozone, methane, and sulfate at 2030 from a broad range of possible futures, *J. Geophys. Res.*, *111*, D12313, doi:10.1029/2005JD006518.

Vaden, T. D., D. Imre, J. Beranek, M. Shrivastava, and A. Zelenyuk (2011), Evaporation kinetics and phase of laboratory and ambient secondary organic aerosol, *P. Natl. Acad. Sci. USA*, *108*, 2190-2195, doi: 10.1073/pnas.1013391108.

Val Martin, M., C. L. Heald, and S. R. Arnold (2014), Coupling dry deposition to vegetation phenology in the Community Earth System Model: Implications for the simulation of surface O_3, *Geophys. Res. Lett.*, *41*, 2988–2996, doi:10.1002/2014GL059651.

van Vuuren, D. P., J. Edmonds, M. Kainuma, K. Riahi, A. Thomson, K. Hibbard, G. C. Hurtt, T. Kram, V. Krey, J.-F. Lamarque, T. Masui, M. Meinshausen, N. Nakicenovic, S. J. Smith, and S. K. Rose (2011a), The representative concentration pathways: an overview, *Clim. Change*, *109*, 5-31, doi: 10.1007/s10584-011-0148-z.

van Vuuren, D. P., E. Stehfest, M. G. J. den Elzen, T. Kram, J. van Vliet, S. Deetman, M. Isaac, K. K. Glodewijk, A. Hof, A. M. Beltran, R. Oostenrijk, and B. van Ruijven (2011b), RCP2.6: exploring the possibility to keep global mean temperature increase below 2°C, *Clim. Change*, *109*, 95-116, doi: 10.1007/s10584-011-0152-3.

van Vuuren, D., K. Riahi, R. Moss, J. Edmonds, T. Allison, N. Nakicenovic, T. Kram, F. Berkhout, R. Swart, A. Janetos, S. K. Rose, and N. Arnell (2012), A proposal for a new scenario framework to support research and assessment in different climate research communities, *Global Environ. Chang.*, 22, 21–35, doi:10.1016/j.gloenvcha.2011.08.002.

Vautard, R. and D. Hauglaustaine (2007), Impact of global climate change on regional air quality: Introduction to the thematic issue, *C. R. Geosciences*, *339*, 703-708. doi:10.1016/j.crte.2007.08.012.

Vavrus, S. and D. Waliser (2008), An improved parameterization for simulating arctic cloud amount in the CCSM3 climate model, *J. Climate*, *21*, 5673–5687, doi:10.1175/2008JCLI2299.1.

Vavrus, S. J., M. M. Holland, A. Jahn, S. A. Bailey, and B. A. Blazey (2011), Twenty-First-Century Arctic climate change in CCSM4, *J. Clim.*, *25*, 2696-2710, doi: 10.1175/JCLI-D-11-00220.1.

Vecchi, G. A., B. J. Soden, A. T. Wittenberg, I. M. Held, A. Leetmaa, and M. J. Harrison (2006), Weakening of tropical Pacific atmospheric circulation due to anthropogenic forcing, *Nature*, *441*, 73-76, doi:10.1038/nature04744.

Verlinde, J., et al. (2007), the mixed-Phase Arctic Cloud Experiment, *B. Am. Meteorol. Soc.*, *88*, 205–221, doi:10.1175/BAMS-88-2-205.

Virtanen, A. et al., (2010), An amorphous solid state of biogenic secondary organic aerosol particles, *Nature*, *467*, 824-827, doi: 10.1038/nature09455.

Volkamer, R., F. San Martini, L. T. Molina, D. Salcedo, J. L. Jimenez, and M. J. Molina (2007), A missing sink for gas-phase glyoxal in Mexico City: Formation of secondary organic aerosol, *Geophys. Res. Lett.*, *34*, L19807, doi:10.1029/2007GL030752.

von Stackelberg, K. J. Buonocore, P. V. Bhave, and J. A. Schwartz (2013), Public health impacts of secondary particulate formation from aromatic hydrocarbons in gasoline, *Environmental Health*, *12*, doi: 10.1186/1476-069X-12-19.

Voulgarakis, A. et al. (2013), Analysis of present day and future OH and methane lifetime in the ACCMIP simulations, *Atmos. Chem. Phys.*, *13*, 2563–2587, doi:10.5194/acp-13-2563-2013.

Wang, K., Y. Zhang, C. Jang, S. Phillips, and B. Wang (2009), Modeling intercontinental air pollution transport over the trans-Pacific region in 2001 using the Community Multiscale Air Quality modeling system, *J. Geophys. Res.*, *114*, D04307, doi:10.1029/2008JD010807.

Wang, K., Y. Zhang, A. Nenes, and C. Fountoukis (2012), Implementation of dust emission and chemistry into the Community Multiscale Air Quality modeling system and initial application to an Asian dust storm episode, *Atmos. Chem. Phys.*, *12*, 10209–10237, doi:10.5194/acp-12-10209-2012.

Wang, K., Y. Zhang, K. Yahya, S.-Y. Wu, and G. Grell (2015), Implementation and initial application of new chemistry-aerosol options in WRF/Chem for simulation secondary organic aerosols and aerosol indirect effects for regional air quality, *Atmos. Environ.*, *115*, 716-732, doi:10.1016/j.atmosenv.2014.12.007.

Wang, M., S. Ghan, M. Ovchinnikov, X. Liu, R. Easter, E. Kassianov, Y. Qian, and H. Morrison (2011), Aerosol indirect effects in a multi-scale aerosol-climate model PNNL-MMF, *Atmos. Chem. Phys.*, *11*, 5431–5455, doi: 10.5194/acp-11-5431-2011.

Warren, S. G. and W. J. Wiscombe (1980), A model for the spectral albedo of snow. II: Snow containing atmospheric aerosols, *J. Atmos. Sci.*, *37*, 2734-2745, doi:10.1175/1520-0469(1980)037<2734:AMFTSA>2.0.CO;2.

Weaver, C. P., et al. (2009), A preliminary synthesis of modeled climate change impacts on U.S. regional ozone concentrations, *Bull. Amer. Met. Soc.*, *90*(12), 1843–1863, doi: 10.1175/2009BAMS2568.1.

Wesely, M. L. (1989), Parameterization of surface resistances to gaseous dry deposition in regional-scale numerical models, *Atmos. Environ.*, *23*, 1293-1304, doi:10.1016/0004-6981(89)90153-4.

Westervelt, D. M., L. W. Horowitz, V. Naik, and D. L. Mauzerall (2015), Radiative forcing and climate response to projected 21st century aerosol decreases, *Atmos. Chem. Phys. Discuss.*, *15*, 9293–9353, doi:10.5194/acpd-15-9293-2015.

Wild, O., X. Zhu, and M. J. Prather (2000), Fast-J: Accurate simulation of in- and below-cloud photolysis in tropospheric chemical models, *J. Atmos. Chem.*, *37*(3), 245–282, doi:10.1023/A:1006415919030.

Wild, O. and H. Akimoto (2001), Intercontinental transport of ozone and its precursors in three-dimensional CTM, *J. Geophys. Res.*, 106, 27,729-27,744,doi: 10.1029/2000JD000123.

Wu, S., L. J. Mickley, E. M. Leibensperger, D. J. Jacob, D. Rind, and D. G. Streets (2008), Effects of 2000 – 2050 global change on ozone air quality in the United States, *J. Geophys. Res.*, *113*, D06302, doi:10.1029/2007JD008917.

Wu, S., L. J. Mickley, J. O. Kaplan, and D. J. Jacob (2012), Impacts of changes in land use and land cover on atmospheric chemistry and air quality over the 21st century, *Atmos. Chem. Phys.*, *12*, 1597–1609, doi:10.5194/acp-12-1597-2012.

Yahya, K., K. Wang, M. Gudoshava, T. Glotfelty, and Y. Zhang (2014). Application of WRF/Chem over North America under the AQMEII Phase 2: Part 1. Comprehensive evaluation of 2006 simulation, *Atmos. Environ.*, *115*, 733-755, doi:10.1016/j.atmosenv.2014.08.063.

Yahya, K., K. Wang, Y. Zhang, and T. E. Kleindienst (2015), Application of WRF/Chem over North America under the AQMEII Phase 2 – Part 2: Evaluation of 2010 application and responses of air quality and meteorology–chemistry interactions to changes in emissions and meteorology from 2006 to 2010, *Geosci. Model Dev.*, *8*, 2095-2117, doi:10.F5194/gmd-8-2095-2015.

Yahya, K., P. Campbell, Y. Chen, T. Glotfelty, J. He, and Y. Zhang (2016), Downscaling CESM using WRF/Chem for Regional Air Quality and Climate Modeling over the U.S. under the Representative Concentration Pathways Scenarios, Part II. Future Air Quality and Sensitivity Simulation, *Atmospheric Environment*, in review.

Yarwood, G., S. Rao, M. Yocke, and G. Z. Whitten (2005), Final Report—Updates to the Carbon Bond Chemical Mechanism: CB05, Rep. RT-04-00675, 246 pp., Yocke and

Co., Novato, Calif. [Available at http://www.camx.com/publ/pdfs/CB05_Final_Report_120805.pdf.].

Yarwood, G., G. Z. Whitten, J. Jung, G. Heo, and D. T. Allen (2010), Final Report—Development, Evaluation, and Testing of Version 6 of the Carbon Bond Mechanism (CB6) , Rep. 582-7-84005-FY10-26, 119 pp., Center for Energy and Environmental Resources, The University of Texas at Austin, Austin, Texas. [Available at https://www.tceq.texas.gov/assets/public/implementation/air/am/contracts/reports/pm/5820784005FY1026-20100922-environ-cb6.pdf].

Yin, J. H. (2005), A consistent poleward shift of the storm tracks in simulations of 21st century climate, *Geophys. Res. Lett.*, *32*, L18701, doi:10.1029/2005GL023684.

Young, P. J., A. Arneth, G. Schurgers, G. Zeng, and J. A. Pyle (2009), The CO_2 inhibition of terrestrial isoprene emissions significantly affects future ozone projections, *Atmos. Chem. Phys.*, *9*, 2793-2803, doi:10.5194/acp-9-2793-2009.

Young, P. J. et al. (2013), Pre-industrial to end 21st century projections of tropospheric ozone from the Atmospheric Chemistry and Climate Model Intercomparison Project (ACCMIP), *Atmos. Chem. Phys.*, *13*, 2063–2090, doi:10.5194/acp-13-2063-2013.

Yu. F. (2010), Ion-mediated nucleation in the atmosphere: Key controlling parameters, implications, and look-up table, J. Geophys. Res., 115, D03206, doi:10.1029/2009JD012630.

Yu, H., L. A. Remer, M. Chin, H. Bian, R. G. Kleidman and T. Diehl (2008), A satellite-based assessment of transpacific transport of pollution aerosol, *J. Geophys. Res.*, *113*, D14S12, doi:10.1029/2007JD009349.

Yu, S., R. Dennis, S. Roselle, A. Nenes, J. Walker, B. Eder, K. Schere, J. Swall, and W. Robarge (2005). An assessment of the ability of 3-D air quality models with current thermodynamic equilibrium models to predict aerosol NO_3^- *J. Geophys. Res., 110*, D07S13, doi:10.1029/2004JD004718.

Zelinka, M. D., S. A. Klein, K. E. Taylor, T. Andrews, M. J. Webb, J. M. Gregory, and P. M. Forster (2013), Contributions of Different Cloud Types to Feedbacks and Rapid Adjustments in CMIP5, *J. Climate*, *26*, 5007–5027, doi: http://dx.doi.org/10.1175/JCLI-D-12-00555.1.

Zender, C. S., H. Bian, and D. Newman (2003), The mineral dust entrainment and deposition (DEAD) model: Description and 1990s dust climatology, *J. Geophys. Res.*, *108*(D14), 4416, doi:10.1029/2002JD002775.

Zeng, G., J. A. Pyle, and P. J. Young (2008), Impact of climate change on tropospheric ozone and its global budgets, *Atmos. Chem. Phys.*, *8*, 369–387, doi:10.5194/acp-8-369-2008.

Zhang, G. J. and N. A. McFarlane (1995), Sensitivity of climate simulations to the parameterization of cumulus convection in the Canadian Climate Centre general circulation model, *Atmos. Ocean*, *33*, 407–446, doi:10.1080/07055900.1995.9649539.

Zhang, H., X. Feng, T. Larssen, G. Qiu, and R. D. Vogt (2010), In inland China, rice, rather than fish, is the major pathway for methylmercury exposure, *Environ. Health Persp.*, *118*, 1183-1188, 10.1289/ehp.1001915.

Zhang, L., et al. (2008), Transpacific transport of ozone pollution and the effect of recent Asian emission increases on air quality in North America: an integrated analysis

using satellite, aircraft, ozonesonde, and surface observations, *Atmos. Chem. Phys.*, *8*, 6117-6136, doi:10.5194/acp-8-6117-2008.

Zhang, Q., M. R. Canagaratna, J. T. Jayne, D. R. Worsnop, and J.-L. Jimenez (2005a), Time- and size-resolved chemical composition of submicron particles in Pittsburgh: Implications for aerosol sources and processes, *J. Geophys. Res.*, *110*, D07S09, doi:10.1029/2004JD004649.

Zhang, Q., M. R. Alfarra, D. R. Worsnop, J. D. Allan, H. Coe, M. R. Canagaratna, and J. L. Jimenez (2005b), Deconvolution and quantification of hydrocarbon-like and oxygenated organic aerosols based on aerosol mass spectrometry, *Environ. Sci. Technol.*, *29*, 4938-4952, doi: 10.1021/es048568l.

Zhang, Q., et al. (2007), Ubiquity and dominance of oxygenated species in organic aerosols in anthropogenically-influenced Northern Hemisphere midlatitudes, *Geophys. Res. Lett.*, *34*, L13801, doi:10.1029/2007GL029979.

Zhang, Q., J. L. Jimenez, M. R. Canagaratna, I. M. Ulbrich, N. L. Ng, D. R. Worsnop, and Y. Sun (2011), Understanding atmospheric organic aerosols via factor analysis of aerosol mass spectrometry: a review, *Anal. Bioanal. Chem.*, *401*, 3045-3067, doi:10.1007/s00216-011-5355-y.

Zhang, R., I. Suh, J. Zhao, D. Zhang, E. Fortner, X. Tie, L. J. Molina, and M. J. Molina (2004), Atmospheric new particle formation enhanced by organic acids, *Science*, *304*, 1487-1490, doi:10.1126/science.1095139.

Zhang, R., G. Li, J. Fan, D. L. Wu, and M. J. Molina (2007), Intensification of Pacific storm track linked to Asian pollution, *PNAS*, *104*, 5295-5299,

doi:10.1073/pnas.0700618104.

Zhang, X., A. Hecobian, M. Zheng, N. H. Frank, and R. J. Weber (2010), Biomass burning impact on $PM_{2.5}$ over the southeastern US during 2007: integrating chemically speciated FRM filter measurements, MODIS fire counts and PMF analysis, *Atmos. Phys. Chem.*, *10*, 6839-6853, doi:10.5194/acp-10-6839-2010.

Zhang, Y., C. Seigneur, J.H. Seinfeld, M. Jacobson, S.L. Clegg, and F.S. Binkowski, 2000, A Comparative Review of Inorganic Aerosol Thermodynamic Equilibrium Modules: Similarities, Differences, and Their Likely Causes, *Atmospheric Environment*, 34, 117-137, doi:10.1016/S1352-2310(99)00236-8.

Zhang, Y., B. Pun, K. Vijayaraghavan, S.-Y. Wu, C. Seigneur, S. Pandis, M. Jacobson, A. Nenes, and J. H. Seinfeld (2004), Development and application of the Model of Aerosol Dynamics, Reaction, Ionization and Dissolution (MADRID), *J. Geophys. Res.*, *109*, D01202, doi:10.1029/2003JD003501.

Zhang, Y., X.-Y. Wen, K. Wang, and K. Vijayaraghavan, and M.Z. Jacobson (2009), Probing into Regional Ozone and Particulate Matter Pollution in the United States: 2. An Examination of Formation Mechanisms Through A Process Analysis Technique and Sensitivity Study, *Journal of Geophysical Research*, 114, D22305, doi:10.1029/2009JD011900.

Zhang, Y., Y. Pan, K. Wang, J. D. Fast, and G. A. Grell (2010), WRF/Chem-MADRID: Incorporation of an aerosol module into WRF/Chem and its initial application to the TexAQS2000 episode, *J. Geophys. Res.*, *115*, D18202, doi:10.1029/2009JD013443.

Zhang, Y., J. Hemperly, N. Meskhidze, and W. C. Skamarock (2012a), The Global Weather Research and Forecasting (GWRF) Model: Model evaluation, sensitivity study, and future year simulation, *Atmos. Clim. Sci.*, *2*(3), 231–253, doi:10.4236/acs.2012.23024.

Zhang, Y., P. Karamchandani, T. Glotfelty, D. G. Streets, G. Grell, A. Nenes, F. Yu, and R. Bennartz (2012b), Development and initial application of the global-through-urban weather research and forecasting model with chemistry (GU-WRF/Chem), *J. Geophys. Res.*, *117*, D20206, doi:10.1029/2012JD017966.

Zhang, Y., Y.-C. Chen, G. Sarwar, and K. Schere (2012c), Impact of Gas-Phase Mechanisms on Weather Research Forecasting Model with Chemistry (WRF/Chem) Predictions: Mechanism Implementation and Comparative Evaluation, *Journal of Geophysical Research,* 117, D1, doi:10.1029/2011JD015775.

Zhang, Y., K. Sartelet, S.-Y. Wu, and C. Seigneur (2013), Application of WRF/Chem-MADRID and WRF/Polyphemus in Europe, Part I: Model Description and Evaluation of Meteorological Predictions, *Atmos. Chem. Phys.*, *13*, 6807–6843, doi:10.5194/acp-13-6807-2013.

Zhang, Y., X. Zhang, K. Wang, J. He, L. R. Leung, J.-W. Fan, and A. Nenes (2015), Incorporating an Advanced Aerosol Activation Parameterization into WRF-CAM5: Model Evaluation and Parameterization Intercomparison, *Journal of Geophysical Research*, 120 (14), DOI: 10.1002/2014JD023051.

Zhang, Y., X. Zhang, L.-T. Wang, Q. Zhang, F.-K. Duan, and K.-B. He (2016a), Application of WRF/Chem over East Asia: Part I. Model Evaluation and Intercomparison with

MM5/CMAQ, *Atmospheric Environment*, 124, Part B, 285-300, doi:10.1016/j.atmosenv.2015.07.022.

Zhang, Y., X. Zhang, K. Wang, Q. Zhang, F.-K. Duan, and K.-B. He (2016b), Application of WRF/Chem over East Asia: Part II. Model Improvement and Sensitivity Simulations, *Atmospheric Environment*, 124, Part B, 301-320, doi:10.1016/j.atmosenv.2015.07.023.

Zhang, Z., and S. Platnick (2011), An assessment of differences between cloud effective particle radius retrievals for marine water clouds from three MODIS spectral bands, *J. Geophys. Res.*, *116*, doi:10.1029/2011jd016216.

Ziemke, J. R., S. Chandra, B. N. Duncan, L. Froidevaux, P. K. Bhartia, P. F. Levelt, and J. W. Waters (2006), Tropospheric ozone determined from Aura OMI and MLS: Evaluation of measurements and comparison with the Global Modeling Initiative's Chemical Transport Model, *J. Geophys. Res.*, *111*, D19303, doi:10.1029/2006JD007089.